
Precision Calculations for Gauge-Boson Pair Production with a Hadronic Jet at Hadron Colliders

Stefan Kallweit



München 2008

Precision Calculations for Gauge-Boson Pair Production with a Hadronic Jet at Hadron Colliders

Stefan Kallweit

Dissertation
an der Fakultät für Physik
der Ludwig-Maximilians-Universität
München

vorgelegt von
Stefan Kallweit
aus München

München, den 10.10.2008

Erstgutachter: PD Dr. Stefan Dittmaier
Zweitgutachter: Prof. Dr. Gerhard Buchalla
Tag der mündlichen Prüfung: 21.11.2008

Contents

Abstract	ix
Zusammenfassung	xi
1 Introduction and motivation	1
2 Theoretical preliminaries	5
2.1 Standard Model of particle physics	5
2.2 Parton model and Quantum Chromodynamics	11
3 VV+jet production at hadron colliders	13
3.1 CKM matrix dependence of the subprocesses	14
3.2 Treatment of external bottom (anti-)quarks	17
3.3 Strategy for the calculation of hadronic cross sections	17
3.4 Overview of the contributing subprocesses	19
4 Evaluation of helicity amplitudes for VV+jet production	31
4.1 Weyl–van-der-Waerden formalism for evaluating helicity amplitudes	31
4.1.1 Basic definitions	32
4.1.2 Discrete symmetries	36
4.2 Building blocks of VV+jet production amplitudes	37
4.2.1 Expressions with bispinor-like structure	37
4.2.2 Expressions with an initial-state quark–antiquark pair	40
4.3 Subamplitudes for VV+jet production	46
4.3.1 LO subprocesses	46
4.3.2 Real-emission subprocesses	47
4.4 Construction of full amplitudes for specified gauge bosons	54
4.4.1 Contributions with external gluons	54
4.4.2 Contributions with two fermion chains	56
4.5 Calculation of squared amplitudes	64
4.5.1 Colour structures of the amplitudes	64
4.5.2 Construction of squared amplitudes for all subprocesses	67
4.5.3 Combination of subprocesses with equal matrix elements	73

5	Evaluation of NLO QCD cross sections via dipole subtraction	77
5.1	Controlling divergences in NLO calculations	78
5.1.1	Definition of jet observables	78
5.1.2	Definition of NLO QCD cross sections	79
5.2	Real-correction contributions	83
5.2.1	Relevant dipole factorization formulae	83
5.2.2	Overview of the contributing subtraction counterterms	90
5.3	Virtual corrections to VV+jet production	105
5.3.1	Evaluation with FORMCALC/LOOPTOOLS	105
5.3.2	Bosonic corrections from virtual-gluon exchange	106
5.3.3	Fermionic corrections from closed quark loops	110
5.3.4	Counterterm contribution	114
5.3.5	Contribution from integrated subtraction counterterms	118
5.4	Collinear-subtraction counterterms	119
5.4.1	Redefinition of PDFs	119
5.4.2	Combined contribution of collinear terms and integrated dipoles . .	120
6	Inclusion of gauge-boson decays	121
6.1	Strategies for the description of leptonic gauge-boson decays	122
6.1.1	Full calculation with off-shell gauge bosons	122
6.1.2	Narrow-width approximation	124
6.1.3	Improved narrow-width approximation	126
6.2	Building blocks for leptonic gauge-boson decays	126
6.3	Implementation of decays into the production matrix elements	130
6.3.1	Full calculation with off-shell gauge bosons	130
6.3.2	Improved narrow-width approximation	136
7	Numerical phase-space integration	139
7.1	Multi-channel Monte Carlo integration	139
7.2	Generic phase-space construction	141
7.3	Improvements of the integrator performance	144
7.3.1	Extra channels for subtraction terms in the real corrections	144
7.3.2	Improving numerics in critical phase-space regions	146
8	Numerical results	149
8.1	Setup and input parameters	150
8.2	Survey of numerical checks	152
8.2.1	Comparison with available tools	152
8.2.2	Independent NLO QCD calculations for WW+jet	152
8.3	Discussion of VV+jet cross sections at LO	153
8.4	NLO QCD cross sections for VV+jet production	155
8.4.1	Four-flavour versus five-flavour scheme	156
8.4.2	Scale dependence of NLO QCD cross sections	159

8.4.3	Dependence on the transverse-momentum cut on the jet	160
8.5	LO analysis of the different decay descriptions	164
8.6	VV+jet with decays in improved NWA at NLO QCD	168
8.6.1	Integrated NLO QCD cross sections	168
8.6.2	Differential cross sections at NLO QCD	170
9	Summary and outlook	195
A	Definitions used in the dipole subtraction formalism	197
A.1	Colour charges	197
A.2	Operators in the collinear-subtraction counterterms	198
B	Dimensionally regularized scalar integrals	201
B.1	Integrals with vanishing internal masses	202
B.1.1	Two-point functions	202
B.1.2	Three-point functions	202
B.1.3	Four-point functions	203
B.2	Integrals with internal masses	204
B.2.1	Two-point functions	204
B.2.2	Three-point functions	204
B.2.3	Four-point functions	204
	Acknowledgement	213

Abstract

Gauge-boson pair-production processes with an additional hadronic jet are of particular interest as background to Higgs and new-physics searches at hadron colliders. Moreover, they enable—besides genuine gauge-boson pair production—a direct analysis of the non-Abelian gauge-boson self-interactions in the electroweak sector. In this work we provide precision calculations for the processes $pp/p\bar{p} \rightarrow VV + \text{jet} + X$.

In detail, corrections to $WW+\text{jet}$, $ZZ+\text{jet}$, and $WZ+\text{jet}$ production are evaluated at next-to-leading-order in the strong coupling (NLO QCD). Particular care has to be taken when treating the infrared singularities arising in the virtual and real corrections. The FORMCALC/LOOPTOOLS package is applied for the virtual corrections, where dimensionally regularized infrared-divergent integrals are added to the FF library which is used for the regular ones. The real-emission matrix elements are evaluated in terms of helicity amplitudes in the Weyl–van-der-Waerden formalism. The Catani–Seymour dipole subtraction formalism mediates the cancellation of infrared divergences between the two contributions. To perform the numerical integration a multi-channel Monte Carlo integrator is written in C++, which is designed to meet the requirements of integrating cross sections in the dipole subtraction formalism.

For all gauge-boson assignments, the NLO QCD corrections significantly stabilize the artificial dependence of the leading-order (LO) cross sections on renormalization and factorization scales for Tevatron. For LHC, however, only a modest reduction of the scale dependence results unless a veto on a second hard jet is applied.

Beyond investigating the production processes, leptonic decays of the gauge bosons are considered. To this end, a full amplitude calculation including resonant and non-resonant contributions to the leptonic final states, a simple narrow-width approximation (NWA), and an improved version of the NWA that takes into account spin correlations are performed at LO. Comparing these approaches the improved NWA turns out to deliver an appropriate approximation to the decays at a reasonable level of accuracy. Thus, an NLO QCD calculation to $VV+\text{jet}$ including leptonic decays is performed in the framework of the improved NWA. Several results on differential cross sections for quantities of the jet and the decay leptons are presented. For $WW+\text{jet}$, we discuss both proton–proton collisions at LHC and proton–antiproton collisions at Tevatron. For $WZ+\text{jet}$ and $ZZ+\text{jet}$, however, the cross sections at Tevatron are too small, so only results for LHC are presented.

The Monte Carlo generator developed in this thesis can be used as a tool in data analysis at LHC and Tevatron.

Zusammenfassung

Eichbosonpaarerzeugung mit einem zusätzlichen hadronischen Jet ist an Hadron-Beschleunigern ein bedeutender Untergrundprozess sowohl für die Suche nach dem Higgs-Boson als auch nach neuer Physik. Darüber hinaus ermöglicht diese Prozessklasse eine direkte Analyse der Selbst-Wechselwirkung der Elektroschwachen Eichbosonen. In dieser Arbeit werden Präzisionsrechnungen in nächstführender Ordnung der starken Kopplung (“next-to-leading order QCD”) für die Prozesse $pp/p\bar{p} \rightarrow VV + \text{jet} + X$ dargelegt.

Die Behandlung von Infrarotsingularitäten, die in den virtuellen und den reellen Korrekturen auftreten, erfordert besondere Sorgfalt. Das FORMCALC/LOOPTOOLS-Paket wird für die virtuellen Korrekturen verwendet, wobei dimensional regularisierte Integrale in die FF-Bibliothek eingebunden werden, die wiederum für die Auswertung regulärer Integrale herangezogen wird. Die Berechnung der reellen Korrekturen erfolgt in Form von Helizitätsamplituden im Weyl-van-der-Waerden-Formalismus. Die Aufhebung der Divergenzen zwischen den virtuellen und reellen Beiträgen vermittelt die Catani-Seymour-Dipolsubtraktionsmethode. Die numerisch stabile Auswertung wird durch ein Mehrkanal-Monte-Carlo-Integrationsprogramm in C++ gewährleistet, das für die Integration von Wirkungsquerschnitten im Dipolsubtraktionsformalismus optimiert ist.

Für alle betrachteten Prozesse stabilisieren die Korrekturen die künstliche Abhängigkeit der Wirkungsquerschnitte von Renormierungs- und Faktorisierungsskala am Tevatron erheblich. Am LHC wird eine wesentliche Verringerung der Skalenabhängigkeit erst erreicht, wenn Endzustände mit zwei harten Jets ausgeschlossen werden.

Um in den betrachteten Prozessen auch leptonische Zerfälle der Eichbosonen einzubinden, werden in führender Ordnung drei Verfahren angewandt: eine Berechnung unter Verwendung vollständiger Amplituden, also mit resonanten und nicht-resonanten Beiträgen zu den leptonischen Endzuständen, eine Näherung über Verzweigungsverhältnisse (“narrow-width approximation”, NWA) und eine verbesserte Variante der NWA, die Spin-Korrelationen miteinbezieht. Die verbesserte Version der NWA stellt sich als angemessene Näherung in der erforderlichen Genauigkeit heraus. Daher wird die Berechnung von Korrekturen für die Produktionsprozesse mit leptonischen Zerfällen unter Anwendung der verbesserten NWA durchgeführt, wobei differenzielle Wirkungsquerschnitte für verschiedene Observablen des Jets und der Leptonen präsentiert werden. Für WW+jet werden Resultate für LHC und Tevatron diskutiert. Da für WZ+jet und ZZ+jet die jeweiligen Wirkungsquerschnitte am Tevatron sehr klein sind, beschränkt sich die Betrachtung hier auf LHC.

Das für diese Arbeit entwickelte Monte-Carlo-Programm kann einen Beitrag zur Datenanalyse sowohl am LHC als auch am Tevatron liefern.

Chapter 1

Introduction and motivation

The constitutional aim of elementary particle physics is the description of the fundamental building blocks of matter and the understanding of the interactions among them. Already in the 1920s, the Quantum Electrodynamics (QED) was greatly successful particularly in explaining electromagnetic low-energy phenomena, such as the anomalous magnetic moment of the muon [1, 2, 3, 4]. In the 1930s, the Fermi model delivered an accurate description of weak decays. With a unitarity-violating high-energy behaviour, its predictive power was, however, limited to low energies. A great improvement in the direction of a uniform theory of particle physics was achieved by the Glashow–Salam–Weinberg (GSW) model [5, 6, 7]. Incorporating both QED and the Fermi model as low-energy limits, the GSW succeeded in unifying electromagnetism and weak interaction into one theory of electroweak interaction. Both renormalizability and a consistent high-energy behaviour were obtained by postulating massive vector bosons, the neutral Z and the charged W^\pm , which could be discovered at the “Super Proton Synchrotron” (SPS) at CERN in 1983 [8, 9, 10, 11, 12]. Most relations predicted by the GSW model, in particular the relations between the masses of the weak gauge bosons and the electroweak couplings that are determined by the Higgs mechanism [13, 14, 15, 16, 17, 18], could be experimentally confirmed so far. Thus, the GSW model delivers the electroweak sector of the Standard Model (SM) of particle physics.

The sector of strong interactions is described by the Quantum Chromodynamics (QCD). The postulate of three degrees of freedom for the quarks [19, 20, 21], which are later on called colours after the formulation of QCD, yielded a first understanding of the Δ^{++} resonance. Its seemingly symmetric wave function contradicted the spin-statistics theorem requiring antisymmetric wave functions for fermions. A solution to this contradiction was delivered by an antisymmetric colour part leading to the antisymmetry for the whole wave function [22, 23]. Besides, the decay width for $\pi^0 \rightarrow \gamma\gamma$ could be predicted by the inclusion of colours. Moreover, the running of the strong coupling provided an explanation for the feature of “asymptotic freedom” [24, 25]: The coloured particles are always confined in colourless bound states, but behave as free particles in scattering processes with high momentum transfer, which delivers an explanation for the validity of the naive parton model [26, 27]. Finally, the massless gluon [24, 28] that mediates the strong interaction

was discovered at DESY in 1979 [29]. Eventually, this discovery established the QCD as the description of strong interactions in the SM. From the theoretical side, besides the explanation of asymptotic freedom the proof of renormalizability of QCD [30] must be seen as a decisive step.

The matter content of the SM consists of three generations of quarks and leptons with only the quarks interacting strongly. Apart from increasing masses, the particles of the 2nd and the 3rd generation mirror the behaviour of the 1st generation particles with respect to strong and electroweak interactions. Each generation consists of two leptons and two quarks with different electric charges and masses. In 1995, the last one of the six quarks, the top quark, could be detected experimentally at the Tevatron [31, 32], the proton–antiproton collider with a center-of-mass (CM) energy of about 2 TeV at Fermilab. The existence of the last missing SM lepton, the τ neutrino, had been accepted from precision measurements of the Z-boson decay width at the “Large Electron-Positron Collider” (LEP) at CERN. Its direct proof, however, succeeded in 2000, again at Fermilab [33].

As the only SM particle that has not been discovered directly, the Higgs boson remains. Its existence is fundamental for the generation of particle masses, both in the sector of weak gauge bosons and of fermions. The mass of the Higgs boson is, however, a free parameter in the SM, but upper and lower bounds can be derived: The lower bound of $M_H > 114.4 \text{ GeV}$ [34] is given from the fact that its discovery failed in all present experiments. Upper bounds of $M_H \lesssim 200 \text{ GeV}$ [35] are provided by electroweak precision measurements that depend on the Higgs mass by means of radiative corrections. The whole range of allowed SM Higgs masses is expected to be covered by the “Large Hadron Collider” (LHC) [36], a proton–proton collider with a CM energy of 14 TeV at CERN. First collisions are planned for spring 2009. Precision measurements on mass and decay width would, however, require further experiments, e.g., at an “International Linear Collider” (ILC) [37].

Although the SM could be confirmed in all collider experiments performed so far, it is assumed to be the low-energy limit of a more fundamental theory. First of all, gravitational interactions are not included in the SM. Moreover, the SM does not provide explanations for the origin of dark matter and dark energy, which are, however, known to exist from cosmological data [38]. A further drawback of the SM can be seen in the fact that lots of parameters like masses and couplings cannot be predicted by the model, but have to be extracted from experiment. Besides, the hierarchy problem arises that is related to quadratic divergences in the loop corrections to the Higgs propagator. Some of these problems could be solved by a supersymmetric extension of the SM. In such models, supersymmetric partners are postulated for all fermions and bosons. The relations between the partner particles would naturally cancel the quadratic divergences arising in the Higgs propagator and, therefore, provide a solution to the hierarchy problem. Moreover, R -parity conserving versions of supersymmetry (SUSY) even deliver dark-matter candidates. Aside from SUSY, a large variety of models attempting to describe physics beyond the SM is studied, e.g. universal extra dimensions, Little Higgs models, Higgs-less models, etc. For the investigation of all of these models, however, an accurate knowledge of SM predictions is needed in order to distinguish “new-physics” signals from SM background.

At hadron colliders, it is in general not enough to consider such background processes only in a leading-order (LO) approximation, since QCD cross sections at LO suffer from a strong artificial dependence on the factorization and renormalization scales. Thus, they can only be seen as a rough estimate. At least next-to-leading-order (NLO) QCD calculations are in general required to evaluate results with sufficient accuracy to provide useful predictions.

In this thesis, NLO QCD calculations are provided for the process classes $pp/p\bar{p} \rightarrow VV + \text{jet} + X$. Their importance for the analysis of LHC and also Tevatron data can be read off the fact that VV+jet production made it to the top of the so-called “experimenters’ wishlist for NLO calculations” of the Les Houches workshops 2005 [39] and 2007 [40]. This list collects the most urgently required background processes whose NLO QCD calculations are still missing. The main arguments for VV+jet to be such important shall be pointed out in the following. In this thesis, all weak-gauge-boson assignments allowed from charge conservation are discussed, namely $W^+W^- + \text{jet}$, $ZZ + \text{jet}$, and $W^\pm Z + \text{jet}$.

Since the search for the Higgs boson may be seen as the primary objective of the LHC, the relevance of VV+jet as background processes to Higgs searches is discussed first. In this context we have to concentrate on WW+jet and ZZ+jet, since only these processes deliver relevant background. Depending on the value of the Higgs mass, both $H \rightarrow WW^*$ and $H \rightarrow ZZ^*$ belong to the most promising channels in Higgs searches [41, 42, 43, 44, 45, 46, 47, 48]. Since additional jet activity might arise from the production processes, not only the exclusive channels $H \rightarrow VV^*$ are worth considering, but also those with one or even more hard jets are relevant. The analysis of Ref. [49] makes clear that at least WW+jet production might also be useful as a background process for Higgs searches at the Tevatron. Here, the case of both W bosons decaying leptonically is discussed, and the emission of one or two hard hadronic jets is considered.

Moreover, the process classes involving outgoing W bosons, i.e. WW+jet and WZ+jet production, yield an important background for a variety of new-physics searches, especially in SUSY scenarios [50, 51]. The signature of leptons and missing transverse momentum arising from the decay neutrinos in these process classes mimics the signature of a number of SUSY decay chains. In SUSY scenarios with R -parity conservation, the missing transverse momentum is in general assigned to the lightest supersymmetric particle (LSP) that is expected to be the endpoint of each SUSY decay chain. These LSPs that leave the detector unseen would show up in pairs due to R -parity conservation. Additional jet activity could arise either in the production processes of the SUSY particles or in their decay chains.

Apart from their meaning as potential background sources to Higgs or new-physics searches, VV+jet processes are interesting in their own right because they enable a direct precise analysis of the non-Abelian gauge-boson self-interactions. For this purpose, the production of genuine gauge-boson pairs probably provides the best test ground. Since, however, a large fraction of massive gauge-boson pairs will show additional jet activity at the LHC, also VV+jet processes might be interesting here. Whereas no experimental evidence for deviations from the SM predictions has been found yet, the LHC enables the investigation of the three-gauge-boson interactions in the electroweak sector at much higher

energies. To this end, WW +jet, WZ +jet, and ZZ +jet are worth analyzing. The processes involving W bosons contain three-gauge-boson vertices with couplings determined by SM predictions. No such vertices with two Z bosons attached exist in the SM, but also this non-existence might be probed. Deviations from the SM predictions could provide an indication of anomalous couplings, which arise in some theories beyond the SM.

Last but not least, VV +jet also delivers the real-virtual contributions to the next-to-next-to-leading-order (NNLO) calculation of massive gauge-boson pair production. In this context, especially WW +jet production is interesting, since further building blocks for WW production at NNLO have been presented in Refs. [52, 53].

Chapter 2

Theoretical preliminaries

2.1 Standard Model of particle physics

All calculations of this work are based on the SM of particle physics. Therefore, a brief outline is given in this section. More details can be found, for instance, in Refs. [54, 55, 56].

The SM is a quantum field theory with the interactions therein governed by local symmetries, which are in general called gauge symmetries. A convenient formulation is delivered by the Lagrangian formalism, i.e. the ingredients of the theory such as kinetic, mass and interaction terms of the fields are incorporated into a single local functional, the Lagrangian density. The action of the theory is obtained by a space-time integration over this Lagrangian density. Its actual form is prescribed by symmetry principles and the requirement of renormalizability.

The feature of renormalizability is assigned to a quantum field theory if all ultraviolet (UV) divergences can be absorbed by an appropriate redefinition of fields and parameters of the Lagrangian. Such UV divergences arise in a perturbative evaluation of the theory, namely in higher-order terms involving loop integrals over internal momenta that yield divergences from the region of large integration momenta. A regularization of these divergences can be obtained in different ways. In this work, dimensional regularization is applied, i.e. the calculation of loop integrals is performed in $D = 4 - 2\varepsilon$ dimensions with the UV divergences showing up as poles $\frac{1}{\varepsilon}$. In the process of renormalization of the Lagrangian these divergences are absorbed into the bare parameters. After redefining the bare parameters, a part of the Lagrangian density can be extracted that has the same functional dependence on the renormalized parameters as the bare Lagrangian on the bare parameters. This part is called renormalized Lagrangian, and the remainder delivers the so-called counterterms. These counterterms do not only guarantee the UV finiteness of the theory at the considered perturbative order, but also the proper meaning of the input parameters, e.g. the definition of a particle mass as the pole of its propagator. This finite part and with it the precise meaning of the various quantities is defined by the applied renormalization conditions defining different renormalization schemes. Details on particular schemes are given, for example, in Ref. [54]. From power-counting, Lagrangian densities involving

only operators with four or less mass dimensions turn out to be renormalizable, i.e. the UV divergences can be cancelled by a finite number of counterterms in each perturbative order. In addition, the underlying symmetries have to be obeyed by the Lagrangian density including counterterms. Nevertheless, non-Abelian gauge theories with spontaneous symmetry breaking, and hence the SM, can be shown to be renormalizable [30, 57].

The symmetries that are obeyed by the SM are, on the one hand, space–time symmetries. Namely, it is invariant under Poincare transformations, excluding space and time inversions. These transformations form the Poincare group containing Lorentz boosts, rotations, and translations in the Minkowski space. All irreducible representations of the Poincare group can be classified by a real positive number m and a half-integer s that define mass and spin of the particular particle types.

On the other hand, there are symmetries among the fields at one and the same point x , which are therefore called internal symmetries. The SM Lagrangian is invariant under transformations of the group $SU(3)_C \otimes SU(2)_W \otimes U(1)_Y$, which can be written as

$$U(\boldsymbol{\theta}_S, \boldsymbol{\theta}_W, \theta_Y) = \exp \left\{ i g_s T^a \theta_S^a + i g_2 I^i \theta_W^i - i g_1 \frac{Y}{2} \theta_Y \right\} \equiv U(\boldsymbol{\theta}_S) U(\boldsymbol{\theta}_W) U(\theta_Y) . \quad (2.1)$$

Here, $\boldsymbol{\theta}_S$, $\boldsymbol{\theta}_W$ and θ_Y are arbitrary real group parameters, and g_s , g_1 , and g_2 the couplings of the respective gauge groups. The generators of the groups $SU(3)_C$, $SU(2)_W$, and $U(1)_Y$ are denoted as T^a ($a = 1, \dots, 8$), I^i ($i = 1, \dots, 3$), and Y , respectively. For these, the fundamental representations can be used, i.e. $T^a = \frac{\lambda^a}{2}$ with the Gell-Mann matrices λ^a and $I^i = \frac{\sigma^i}{2}$ with the Pauli matrices σ^i . The quantum numbers of T^a are related to the “colour”, which is a kind of a charge with respect to $SU(3)_C$. The quantum numbers of I^i define the weak isospin, and that of Y the weak hypercharge. The transformation of a fermion field reads

$$\Psi \rightarrow \Psi' = U(\boldsymbol{\theta}_S, \boldsymbol{\theta}_W, \theta_Y) \Psi . \quad (2.2)$$

When going from global to local symmetries, i.e. when the group parameters get a space–time dependence, new fields have to be introduced to keep the Lagrangian density invariant under this local transformation of the fermion fields. This is due to the fact that derivatives of fields appear in the Lagrangian density. These derivatives do not behave as the fields themselves under local gauge transformations. Therefore, the usual space–time derivative is substituted by a covariant derivative,

$$\partial_\mu \rightarrow D_\mu = \partial_\mu - i g_s G_\mu^a T^a - i g_2 W_\mu^i I^i + i g_1 B_\mu \frac{Y}{2} . \quad (2.3)$$

Here, the gauge fields G_μ^a ($a = 1, \dots, 8$), W_μ^i ($i = 1, \dots, 3$), and B_μ are introduced, which represent the vector fields mediating the respective interaction. These transform in the adjoint representation of their gauge groups for global transformations. For local ones, the transformation reads

$$G_\mu^a T^a \rightarrow G_\mu'^a T^a = U(\boldsymbol{\theta}_S) G_\mu^a T^a U(\boldsymbol{\theta}_S)^{-1} + \frac{i}{g_s} (\partial_\mu U(\boldsymbol{\theta}_S)) U(\boldsymbol{\theta}_S)^{-1} ,$$

		1 st gen.	2 nd gen.	3 rd gen.	I	I_3	Y	Q
quarks	Ψ_L^Q	$\begin{pmatrix} u \\ d \end{pmatrix}_L$	$\begin{pmatrix} c \\ s \end{pmatrix}_L$	$\begin{pmatrix} t \\ b \end{pmatrix}_L$	$\frac{1}{2}$ $\frac{1}{2}$	$\frac{1}{2}$ $-\frac{1}{2}$	$\frac{1}{3}$ $\frac{2}{3}$	$\frac{2}{3}$ $-\frac{1}{3}$
	Ψ_R^U	u_R	c_R	t_R	0	0	$\frac{4}{3}$	$\frac{2}{3}$
	Ψ_R^D	d_R	s_R	b_R	0	0	$-\frac{2}{3}$	$-\frac{1}{3}$
leptons	Ψ_L^L	$\begin{pmatrix} \nu_e \\ e \end{pmatrix}_L$	$\begin{pmatrix} \nu_\mu \\ \mu \end{pmatrix}_L$	$\begin{pmatrix} \nu_\tau \\ \tau \end{pmatrix}_L$	$\frac{1}{2}$ $\frac{1}{2}$	$\frac{1}{2}$ $-\frac{1}{2}$	-1 -1	0 -1
	Ψ_R^E	e_R	μ_R	τ_R	0	0	-2	-1

Table 2.1: Fermions of the SM and their quantum numbers weak isospin I , its third component I_3 , weak hypercharge Y , and electromagnetic charge Q .

$$\begin{aligned}
W_\mu^i I^i \rightarrow W_\mu^i I^i &= U(\boldsymbol{\theta}_W) W_\mu^i I^i U(\boldsymbol{\theta}_W)^{-1} + \frac{i}{g_2} (\partial_\mu U(\boldsymbol{\theta}_W)) U(\boldsymbol{\theta}_W)^{-1} , \\
B_\mu \rightarrow B'_\mu &= B_\mu - \partial_\mu \theta_Y .
\end{aligned} \tag{2.4}$$

With the covariant derivative of Eq. (2.3), the kinetic terms for fermions can be formulated in a gauge invariant way,

$$\begin{aligned}
\mathcal{L}_{\text{fermions}} &= \sum_Q \bar{\Psi}_L^Q i \not{D} \Psi_L^Q + \sum_U \bar{\Psi}_R^U i \not{D} \Psi_R^U + \sum_D \bar{\Psi}_R^D i \not{D} \Psi_R^D \\
&\quad + \sum_L \bar{\Psi}_L^L i \not{D} \Psi_L^L + \sum_E \bar{\Psi}_R^E i \not{D} \Psi_R^E .
\end{aligned} \tag{2.5}$$

The fermionic particle content of the SM and, hence, the range of the sums in Eq. (2.5) is provided in Table 2.1. With respect to $SU(3)_C$, the leptons transform trivially, since they do not carry so-called colour charges, and the quarks in the fundamental representation of the group. The sums over the three resulting colour charges are suppressed in Eq. (2.5). With respect to $SU(2)_W$, the fermions are left-chiral doublets Ψ_L and right-chiral singlets Ψ_R . In the case of vanishing fermion masses, which is used for all fermions but the third-generation quarks in this work, they can be identified with left-handed and right-handed particles. As a fundamental principle of gauge theories, the fermion–gauge-boson interactions are already introduced in terms of the covariant derivatives. The hypercharge Y can be chosen to reproduce the correct coupling to the photon, which is identified as a linear combination of B_μ and W_μ^3 , as explained below. The quantum numbers of all fermions with respect to $SU(2)_W$ and $U(1)_Y$ as well as the electric charge that is defined according to the Gell-Mann–Nishijima relation,

$$Q = I^3 + \frac{Y}{2} , \tag{2.6}$$

are collected in Table 2.1.

Besides, kinetic terms for the gauge fields can be constructed in a gauge-invariant way from the field-strength tensors,

$$\begin{aligned} G_{\mu\nu}^a &= \partial_\mu G_\nu^a - \partial_\nu G_\mu^a - g_s f^{abc} G_\mu^b G_\nu^c , \\ W_{\mu\nu}^i &= \partial_\mu W_\nu^i - \partial_\nu W_\mu^i - g_2 \epsilon^{ijk} W_\mu^j W_\nu^k , \\ B_{\mu\nu} &= \partial_\mu B_\nu - \partial_\nu B_\mu , \end{aligned} \quad (2.7)$$

where f^{abc} and ϵ^{ijk} are the structure constants of $SU(3)_C$ and $SU(2)_W$, respectively. Taking the trace of the squared field-strength tensors yields a gauge-invariant contribution to the Lagrangian density,

$$\mathcal{L}_{\text{gauge bosons}} = -\frac{1}{4} G_{\mu\nu}^a G^{a,\mu\nu} - \frac{1}{4} W_{\mu\nu}^i W^{i,\mu\nu} - \frac{1}{4} B_{\mu\nu} B^{\mu\nu} . \quad (2.8)$$

It contains kinetic terms for all the gauge bosons as well as three- and four-gauge-boson interaction terms in case of the non-Abelian groups.

So far, both fermions and gauge bosons are massless because explicit mass terms would violate gauge invariance. The Higgs mechanism for spontaneous symmetry breaking [13, 14, 15, 16, 17, 18] provides a solution by introducing the Higgs field,

$$\Phi = \begin{pmatrix} \phi^+ \\ \phi^0 \end{pmatrix} , \quad (2.9)$$

which transforms as a complex $SU(2)_W$ doublet and has a weak hypercharge $Y = 1$. Introducing a kinetic term and the most general form of renormalizable self-interactions, the contribution to the Lagrangian density is

$$\mathcal{L}_{\text{Higgs}} = (D_\mu \Phi)^\dagger (D^\mu \Phi) + \mu^2 (\Phi^\dagger \Phi) - \frac{\lambda}{4} (\Phi^\dagger \Phi)^2 , \quad \mu^2, \lambda > 0 . \quad (2.10)$$

The signs of μ and λ are chosen to deliver a non-vanishing vacuum expectation value Φ_0 of the Higgs field,

$$|\Phi_0|^2 = \frac{2\mu^2}{\lambda} \equiv \frac{v^2}{2} , \quad (2.11)$$

which breaks the $SU(2)_W \otimes U(1)_Y$ symmetry spontaneously. In an expansion of the Higgs field around its vacuum expectation value,

$$\Phi = \begin{pmatrix} \phi^+ \\ \frac{1}{\sqrt{2}}(v + H + i\chi) \end{pmatrix} , \quad \phi^- = (\phi^+)^\dagger , \quad (2.12)$$

so-called would-be Goldstone bosons arise. The fields ϕ^+ , ϕ^- , and χ turn out to be unphysical degrees of freedom, which can be seen from the fact that they can be eliminated by a suitable gauge transformation. However, they become manifest in the longitudinal degrees of freedom of the massive weak gauge bosons. The field H describes the physical Higgs boson.

Inserting the expansion of the Higgs field (2.12) into its contribution to the Lagrangian density (2.10) delivers mass terms for the electroweak gauge bosons arising from the vacuum expectation value of the Higgs field. However, the mass eigenstates are linear combinations of the fields W_μ^i and B_μ . They are obtained by diagonalizing the mass matrix arising in the Lagrangian density. For the W bosons, charge eigenstates are chosen. The following eigenstates result,

$$W_\mu^\pm = \frac{1}{\sqrt{2}} (W_\mu^1 \mp iW_\mu^2), \quad \begin{pmatrix} Z_\mu \\ A_\mu \end{pmatrix} = \begin{pmatrix} \cos \theta_W & -\sin \theta_W \\ \sin \theta_W & \cos \theta_W \end{pmatrix} \begin{pmatrix} W_\mu^3 \\ B_\mu \end{pmatrix}, \quad (2.13)$$

where the weak mixing angle is defined in terms of the couplings g_1 and g_2 as

$$\cos \theta_W = \frac{g_2}{\sqrt{g_1^2 + g_2^2}}, \quad \sin \theta_W = \frac{g_1}{\sqrt{g_1^2 + g_2^2}}. \quad (2.14)$$

After spontaneous symmetry breaking a $U(1)$ symmetry remains unbroken, and hence, one gauge boson stays massless. As anticipated in Eq. (2.6), the generator of this unbroken symmetry is the relative electric charge Q , and the respective gauge boson A_μ is identified with the photon. The elementary electric charge e and with it the fine-structure constant α can be expressed in terms of the couplings,

$$e \equiv \sqrt{4\pi\alpha} \equiv \frac{g_1 g_2}{\sqrt{g_1^2 + g_2^2}}. \quad (2.15)$$

To summarize, the four electroweak gauge bosons consist of three massive gauge bosons, the charged W^\pm and the neutral Z , which are often referred to as the weak gauge bosons, and the neutral massless photon A . Their masses are

$$M_W = \frac{v}{2} g_2 = \frac{ev}{2 \sin \theta_W}, \quad M_Z = \frac{v}{2} \sqrt{g_1^2 + g_2^2} = \frac{ev}{2 \sin \theta_W \cos \theta_W}, \quad M_A = 0. \quad (2.16)$$

Expressed by the masses of the weak gauge bosons, the weak mixing angle reads

$$\cos \theta_W = \frac{M_W}{M_Z}. \quad (2.17)$$

The mechanism of spontaneous symmetry breaking also provides a way to implement fermion masses into the Lagrangian. A naive construction of mass terms would fail due to the fact that left- and right-handed fermions belong to different representations of the gauge group $SU(2)_W \otimes U(1)_Y$ and have different quantum numbers. Again, the introduction of couplings of the fermions to the Higgs field yields mass terms due to its non-vanishing vacuum expectation value. The corresponding contribution to the Lagrangian density is

$$\mathcal{L}_{\text{Yukawa}} = \sum_{Q,D} \bar{\Psi}_L^Q G_D^{QD} \Psi_R^D \Phi + \sum_{Q,U} \bar{\Psi}_L^Q G_U^{QU} \Psi_R^U \tilde{\Phi} + \sum_{L,E} \bar{\Psi}_L^L G_E^{LE} \Psi_R^E \Phi + \text{h.c.}, \quad (2.18)$$

where ‘h.c.’ denotes the Hermitian conjugate of the convenient expression, and $\tilde{\Phi} = i\sigma_2 \Phi^*$ the charge-conjugate Higgs field. The matrices G_D , G_U , and G_E , which are 3×3 matrices in

generation space, contain the so-called Yukawa couplings. The fermionic mass eigenstates are obtained by diagonalizing these matrices via field transformations. For quarks, the change from weak-interaction to mass eigenstates is described by the Cabibbo–Kobayashi–Maskawa (CKM) matrix [58]. By convention, the rotation is applied to the down-type sector, yielding

$$\Psi_L^D \rightarrow V_{\text{CKM}} \Psi_L^D = \begin{pmatrix} V_{ud} & V_{us} & V_{ub} \\ V_{cd} & V_{cs} & V_{cb} \\ V_{td} & V_{ts} & V_{tb} \end{pmatrix} \begin{pmatrix} \Psi_L^d \\ \Psi_L^s \\ \Psi_L^b \end{pmatrix}. \quad (2.19)$$

for the left-handed quarks. This rotation in generation space affects only the couplings to W bosons. Since the right-handed quarks are singlets under $SU(2)_W$ and, hence, do not couple to W bosons, no rotation needs to be performed here. In the leptonic sector, the assumption of vanishing neutrino masses simplifies the situation, since the diagonalization matrices can be absorbed into the fields. This assumption is kept, although neutrino oscillation experiments have shown that neutrino masses do not vanish. They are, however, very small and can therefore be treated as zero for the purpose of this work.

The classical Lagrangian density of the SM is already completed by the contributions given so far. However, in order to quantize the theory in the path-integral formalism, the gauge must be fixed to avoid integrating over equivalent field configurations. To this end, gauge-fixing terms are added to the Lagrangian. In an R_ξ gauge, the respective functionals for all gauge-boson fields are chosen as

$$\begin{aligned} F^G &= \frac{1}{\sqrt{\xi^G}} \partial^\mu G_\mu^a, & F^{W^\pm} &= \frac{1}{\sqrt{\xi_1^W}} \partial^\mu W_\mu^\pm \mp i M_W \sqrt{\xi_2^W} \phi^\pm, \\ F^A &= \frac{1}{\sqrt{\xi^A}} \partial^\mu A_\mu^a, & F^Z &= \frac{1}{\sqrt{\xi_1^Z}} \partial^\mu Z_\mu - M_Z \sqrt{\xi_2^Z} \chi, \end{aligned} \quad (2.20)$$

where ξ_i^α are arbitrary gauge parameters. The case of $\xi^G = \xi^A = \xi_{1,2}^W = \xi_{1,2}^Z = 1$ is called 't Hooft–Feynman gauge. The corresponding contributions to the Lagrangian density read

$$\mathcal{L}_{\text{fix}} = -\frac{1}{2} \sum_\alpha |F^\alpha|^2, \quad (2.21)$$

where $\alpha = G, A, W^+, W^-, Z$. By adding the gauge-fixing term (2.21), the path integral measure is changed by the Fadeev–Popov determinant arising as a factor in the path integral,

$$\text{Det} \left(\frac{\delta F}{\delta \theta} \right), \quad (2.22)$$

where $\delta \theta$ denotes an infinitesimal gauge transformation. This functional determinant can be expressed as a functional integral over anticommuting fields $u^\alpha(x)$, the so-called Fadeev–Popov ghosts, leading to an additional contribution to the Lagrangian density,

$$\mathcal{L}_{\text{Fadeev–Popov}} = -\bar{u}^\alpha(x) \frac{\delta F^\alpha}{\delta \theta^\beta(x)} u^\beta(x). \quad (2.23)$$

The Fadeev-Popov ghosts are scalar anticommuting fields and, thus, violate the spin-statistics theorem. This is, however, unproblematic because they are unphysical degrees of freedom and do not correspond to physical states, but occur only inside loops in perturbative calculations.

With all contributions given in this section, the full Lagrangian density of the SM reads

$$\mathcal{L}_{\text{SM}} = \mathcal{L}_{\text{fermions}} + \mathcal{L}_{\text{gauge bosons}} + \mathcal{L}_{\text{Higgs}} + \mathcal{L}_{\text{Yukawa}} + \mathcal{L}_{\text{fix}} + \mathcal{L}_{\text{Fadeev-Popov}} . \quad (2.24)$$

The Feynman rules derived from this Lagrangian that are relevant for this work are collected in Section 4.1. An exhaustive survey can, e.g., be found in Ref. [59] for the electroweak part and in Ref. [60] for the strong part.

2.2 Parton model and Quantum Chromodynamics

The previous section introduces the elementary particles in the SM and the interactions among them. Perturbation theory enables the calculation of cross sections for scattering processes between these particles at in principle arbitrarily high accuracy. The applicability of perturbation theory is based on the smallness of the involved couplings that are used as ordering parameters. At low scales, however, this condition is no more true for QCD due to confinement. In hadron-hadron scattering processes, this applies to the description of the incoming partons that are bound in hadrons. These bound states are not accessible perturbatively and, hence, their description has to be extracted from experiment so far. A suitable way for calculating hadronic scattering processes is delivered by the parton model that is briefly outlined in the following. More details and field-theoretical background can be found in Ref. [60].

In the parton model, a hadron consists of point-like constituents, the so-called partons. The hadron momentum is distributed to these partons. The valence particles, which are e.g. uud for the proton and $\bar{u}\bar{u}\bar{d}$ for the antiproton, determine the quantum numbers of the hadron. Besides, the hadron consists of a sea of virtual particles which are gluons and light quark-antiquark pairs. The “infinite momentum frame” is applied to the description of the hadrons, i.e. the momenta are assumed to be large so that both hadron and constituent masses can be neglected. Further on, the parton momenta are assumed to be collinear to the hadron momentum. Only one parton from each hadron is involved into the hard scattering process, whereas the remaining partons of the hadrons are considered as spectator partons. For the hard scattering process, these incoming partons are treated as free particles. This is justified by the fact that the scale given by the momentum transfers in the hard process is much larger than the scale of the hadronic binding energies. Therefore, the partonic cross sections can be evaluated perturbatively.

The hadron structure is described in terms of parton distribution functions (PDFs). Hadronic cross sections are evaluated by convoluting the partonic cross sections $\hat{\sigma}$ with the

PDFs of the particular partons and summing over all partonic initial states,

$$\sigma_{h_1 h_2}(p_1, p_2) = \sum_{a,b} \int_0^1 dx_1 \int_0^1 dx_2 f_{a(h_1)}(x_1, \mu_{\text{fact}}) f_{b(h_2)}(x_2, \mu_{\text{fact}}) \hat{\sigma}_{ab}(x_1 p_1, x_2 p_2; \mu_{\text{fact}}), \quad (2.25)$$

where the explicit factorization-scale dependence of the partonic cross section only arises at NLO and beyond. The PDFs $f_{a(h)}(x, \mu_{\text{fact}})$ give the probability density for the parton a to carry the momentum fraction x of the total momentum of the respective hadron h . The factorization scale μ_{fact} introduced here is an arbitrary parameter. It can be viewed as the scale which separates the long- and short-distance parts of the cross-section calculation. Thus, a parton that is emitted with a transverse momentum smaller than this factorization scale is absorbed into the hadron structure. Since the factorization-scale dependence of the hadronic cross section is actually artificial, it is expected to decrease when going to higher orders in the perturbative expansion.

For LO cross sections, the partonic cross sections are evaluated in the same way as for parton scattering processes. If going to higher orders in perturbation theory, the short-distance scattering cross section is derived from the partonic cross section by removing the long-distance parts. These parts must be factored out and are absorbed into the PDFs. The resulting PDF redefinition in dimensional regularization with $D = 4 - 2\varepsilon$ space-time dimensions reads

$$f_a(x, \mu_{\text{fact}}) \rightarrow f_a(x, \mu_{\text{fact}}) + \sum_{a'} \int_x^1 \frac{dz}{z} f_{a'}\left(\frac{x}{z}, \mu_{\text{fact}}\right) P^{a'a}(z) \frac{\alpha_s}{2\pi} \frac{\Gamma(1+\varepsilon)}{\varepsilon} \left(\frac{4\pi\mu^2}{\mu_{\text{fact}}^2}\right)^\varepsilon, \quad (2.26)$$

where μ denotes the reference mass of dimensional regularization. The sum over a' runs over all partons with non-vanishing Altarelli–Parisi splitting functions [61] $P^{a'a}(z)$, which are provided in App. A.2. The choice to absorb only the divergence—including the ubiquitous $\ln(4\pi) - \gamma_E$ contribution—into the PDFs defines the $\overline{\text{MS}}$ factorization scheme, which is applied in the calculations of this thesis. In the deep inelastic scattering (DIS) scheme, for instance, the finite part is chosen such that the structure function F_2 does not get perturbative corrections.

At NLO, this absorption of divergences into the PDFs gives rise to so-called collinear-subtraction counterterms. A convenient way how to perform this factorization is delivered by the dipole subtraction formalism in Ref. [62]. It will be discussed in Chapter 5.

Chapter 3

VV+jet production at hadron colliders

In the class of the hadronic processes $pp/p\bar{p} \rightarrow VV + \text{jet} + X$ considered in this thesis, a large number of partonic subprocesses contributes to the same final state. This is due to the fact that in hadron–hadron scattering processes many combinations of initial-state partons, which are all contained in the scattering hadrons, have to be taken into account. Moreover, outgoing hard jets can result from each colour-charged parton, so both outgoing gluons and light (anti-)quarks must be considered as sources of hadronic jets. In this chapter, some preliminary remarks are made about the calculation of VV+jet production at hadron colliders.

In Section 3.1, the influence of the approximations applied in the calculation is discussed—namely the neglect of light-quark masses and the approximation of the CKM matrix, which is chosen to allow for mixing only between the two light generations of quarks.

The role played by bottom (anti-)quarks in the VV+jet-production processes is considered in Section 3.2. In this context, a principal problem arises in the process class $pp/p\bar{p} \rightarrow WW + \text{jet} + X$ from the fact that top resonances appear if bottom (anti-)quarks are allowed as final-state particles. These resonances result in large contributions to the cross section, but actually arise from a different class of processes, namely from the off-shell continuations of $t\bar{t}$, W^+t , and W^-t production. On the other hand, if the five-flavour scheme is applied, the same subprocesses also contain infrared singularities that are needed to cancel against those in the virtual corrections to non-resonant channels.

How this problem of top resonances and infrared finiteness is treated in this thesis is described in Section 3.3.

In Section 3.4, a generic overview over the Feynman diagrams and the subprocesses to be calculated is given. Finally, all subprocesses are listed for the four possible gauge-boson-pair assignments in the generic process class $pp/p\bar{p} \rightarrow VV + \text{jet} + X$.

3.1 CKM matrix dependence of the subprocesses

To limit the number of contributing subprocesses, the CKM matrix is used in a block-diagonal form, where mixing is allowed only between the two light generations, namely

$$V_{\text{CKM}} = \begin{pmatrix} V_{ud} & V_{us} & 0 \\ V_{cd} & V_{cs} & 0 \\ 0 & 0 & 1 \end{pmatrix} = \begin{pmatrix} \cos \theta_C & \sin \theta_C & 0 \\ -\sin \theta_C & \cos \theta_C & 0 \\ 0 & 0 & 1 \end{pmatrix}, \quad (3.1)$$

where θ_C is the Cabibbo angle [63]. The approximation is justified by the fact that the neglected off-diagonal matrix elements are very small. Since the masses of the light quarks are neglected, one could argue that CKM-mixing between quarks with degenerate (zero) masses is redundant. This is, however, only partially true, because the PDFs refer to mass eigenstates, which still holds if masses are neglected to simplify the calculation of amplitudes. The mass degeneracy, however, leads to simplifications, since the CKM dependence of amplitudes drops out for a remarkable set of subprocesses.

WW+jet

For $pp/p\bar{p} \rightarrow WW + \text{jet} + X$, this happens if both W bosons couple to the same fermion chain, as illustrated in Figure 3.1. Independent of gluonic couplings to this fermion chain, which do not affect the electroweak structure, the unitarity of the CKM matrix leads to

$$\sum_{D=d,s} V_{U'D} V_{UD}^* = \sum_{D=d,s} V_{U'D} V_{DU}^\dagger = \delta_{UU'}, \quad \sum_{U=u,c} V_{UD'}^* V_{UD} = \sum_{U=u,c} V_{D'U}^\dagger V_{UD} = \delta_{DD'}, \quad (3.2)$$

with the nomenclature of Figure 3.1, when the intermediate quark state is summed over. Diagrams with the W -boson pair coupling to the fermion chain by means of an intermediate vector boson (see Figure 3.2) are independent of the CKM matrix, anyway. Therefore, a remarkable set of subprocesses of $pp/p\bar{p} \rightarrow WW + \text{jet} + X$ is not influenced by the explicit entries of the CKM matrix due to its unitarity.

The only subprocesses contributing to $pp/p\bar{p} \rightarrow WW + \text{jet} + X$ that depend on the explicit entries of the CKM matrix, are those containing two fermion chains with the two W bosons coupling to different fermion chains at least in some diagrams. These are the

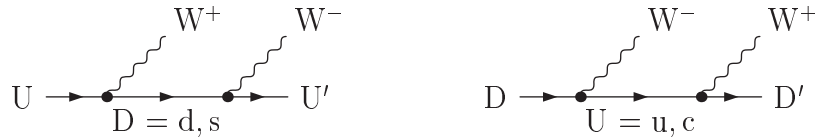


Figure 3.1: Electroweak part of diagrams with two W bosons coupling directly to the same fermion chain: With light-quark masses neglected, all contributions with $U \neq U'$ or $D \neq D'$ vanish in the block-diagonal approximation of the CKM matrix. Those contributions with $U = U'$ or $D = D'$ behave as in the case of a trivial (diagonal) CKM matrix.

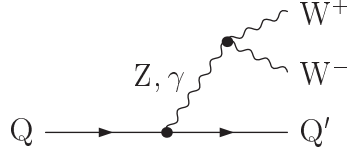


Figure 3.2: Electroweak part of diagrams with the two W bosons coupling to the fermion chain by means of an intermediate vector boson: These contributions are independent of the CKM matrix and contribute only if $Q = Q'$.

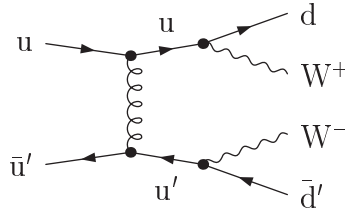


Figure 3.3: A sample diagram with two W bosons coupling to different fermion chains: Contributions of this kind explicitly depend on the CKM matrix elements.

subprocesses including both two external up- and two down-type (anti-)quarks. A sample diagram is shown in Figure 3.3.

ZZ+jet

Since no W bosons appear in any of the subprocesses contributing to $pp/p\bar{p} \rightarrow ZZ + \text{jet} + X$ in LO and NLO QCD, no CKM matrix dependence arises.

WZ+jet

When considering the subprocesses contributing to $pp/p\bar{p} \rightarrow WZ + \text{jet} + X$, the dependence on the CKM matrix does not drop out for any subprocess, at least if single partonic subprocesses are considered. It is, however, possible to reduce the number of subprocesses to be calculated by considering two partonic subprocesses together.

The two subprocesses to be combined differ from each other only in one outgoing parton that is the only external up-(down-)type (anti-)quark in both cases, e.g. $u\bar{u} \rightarrow W^+ Z d\bar{u}$ and $u\bar{u} \rightarrow W^+ Z s\bar{u}$. This example is illustrated on the left-hand side of Figure 3.4. Here, the squared amplitudes with the outgoing d/s quark are proportional to $|V_{ud}|^2$ and $|V_{us}|^2$, respectively. The sum over both squared amplitudes is proportional to $|V_{ud}|^2 + |V_{us}|^2$, which is equal to 1 due to the unitarity of the CKM matrix in the approximation of Eq. (3.1). In this step, we make use of the fact that the initial states are identical and, correspondingly, the PDFs are the same in both contributions.

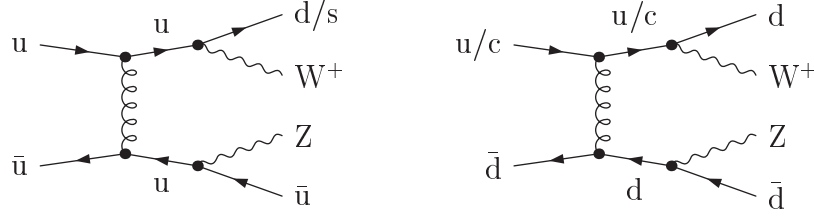


Figure 3.4: The two subprocesses depicted by the left diagram are summed over yielding a CKM-independent result. The two subprocesses illustrated by the diagram on the right-hand side are not combined due to the different PDFs involved.

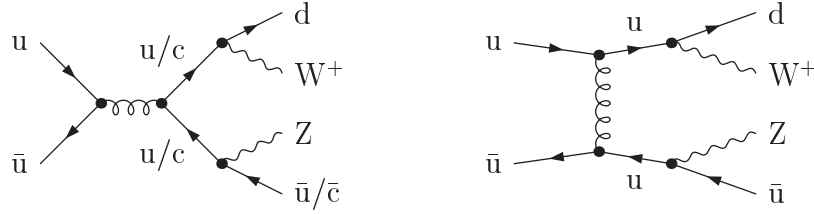


Figure 3.5: Two subprocesses that cannot be calculated simultaneously: The diagrams with changed fermion-number flow (right-hand plot) only contribute for $u\bar{u} \rightarrow W^+Zd\bar{u}$.

If the external parton that makes the difference between the two subprocesses belongs to the initial state, this procedure is not applied, since the PDFs are different for the two subprocesses. The right-hand side of Figure 3.4 illustrates this situation. One could absorb the CKM factors into the PDFs, and the remainders of the amplitudes of the two partonic subprocesses would be identical again. This is, however, not done in the calculations of this thesis.

If the external parton differing between the two subprocesses is not the only external up-(down-)type (anti-)quark, the described procedure cannot be applied for general reasons. This shall be made clear in the following on the basis of the sample subprocesses $u\bar{u} \rightarrow W^+Zd\bar{u}$ and $u\bar{u} \rightarrow W^+Zd\bar{c}$. An illustration is provided in Figure 3.5. The diagrams represented by the left-hand plot are relevant for both subprocesses. The decisive difference is that the Feynman diagrams with a changed fermion-number flow, which are represented by the right-hand plot, contribute only to the subprocess $u\bar{u} \rightarrow W^+Zd\bar{u}$. Such diagrams are not present for $u\bar{u} \rightarrow W^+Zd\bar{c}$. For WZ+jet, this situation can be generalized as follows: Two subprocesses do not have—up to CKM factors—identical matrix elements if the differing parton is not the only external up-(down-)type (anti-)quark.

The same procedure can be applied for the gluonic processes. It is, however, much simpler in this case, because only one fermion chain exists.

3.2 Treatment of external bottom (anti-)quarks

The situation of a hard jet resulting from an outgoing bottom (anti-)quark has to be considered with care: Since the weak decay of the bottom (anti-)quark is mediated only by the small non-diagonal CKM matrix elements, its lifetime is long enough to result in a resolvable second vertex that is significantly displaced from the primary interaction point. Therefore, events containing outgoing bottom (anti-)quarks can be isolated from such events with light hadronic jets by anti-b-tagging.

This is no more true in case of some real-emission subprocesses, because here only one of the two outgoing jets must be detected: This can be the light jet as well, while the b-jet leaves the detector unseen in direction of the beam axis. Moreover, the b-tagging efficiency lies far below 100%, so that not all “b-jet events” can be isolated [64, 65, 66, 67, 68]. The influence of incoming bottom (anti-)quarks on the hadronic cross section is suppressed by the small bottom PDFs in the colliding hadrons.

In the process class $pp/p\bar{p} \rightarrow WW + \text{jet} + X$, however, the suppression of subprocesses with external bottom (anti-)quarks is overcompensated by top resonances always showing up along with final-state bottom (anti-)quarks. Moreover, outgoing $b\bar{b}$ pairs appearing in real-emission subprocesses even contain two resonant top-quark propagators in some diagrams without PDF suppression. These subprocesses should, however, in general not be assigned to $WW + \text{jet}$ production, since they are actually off-shell continuations to $t\bar{t}$ production. From this point of view, the subprocesses with only one outgoing bottom (anti-)quark can be seen as contributions to W^-t production and $W^+\bar{t}$ production, respectively, with the off-shell decay of the top (anti-)quark implied.

In order to face this problem, all generic amplitudes that could contain external bottom (anti-)quarks are evaluated with non-vanishing internal quark masses in the next chapter. In this context, the only complication concerning the evaluation of amplitudes is due to the appearance of massive top propagators in some diagrams contributing to $pp/p\bar{p} \rightarrow WW + \text{jet} + X$. Whenever the top propagators can become resonant in any diagrams of a subprocess, the top (anti-)quarks have to be treated as unstable particles with a non-vanishing width, e.g. by application of the complex-mass scheme [69, 70, 71]. If external bottom (anti-)quarks are taken into account, they are treated as massless particles. Therefore, no new types of amplitudes for $pp/p\bar{p} \rightarrow ZZ + \text{jet} + X$ and $pp/p\bar{p} \rightarrow WZ + \text{jet} + X$ have to be evaluated, but only some new subprocesses with another massless quark are to be added.

3.3 Strategy for the calculation of hadronic cross sections

For the calculation of the cross sections to $pp/p\bar{p} \rightarrow VV + \text{jet} + X$, two different strategies regarding the treatment of bottom (anti-)quarks are applied:

In the first scenario, bottom (anti-)quarks are treated as massless particles, so five-flavour PDFs and a five-flavour running of α_s are applied. In this framework, the strategy is

to neglect all contributions containing external bottom (anti-)quarks. For the initial state, this approach is justified by the smallness of their PDFs. Final-state bottom (anti-)quarks are excluded by the assumption that their signal can be distinguished from that of a light-quark jet by means of b-tagging.

For the process class $pp/p\bar{p} \rightarrow WW + \text{jet} + X$, an advantage of this procedure can be seen in the fact that the influence of the off-shell continuations of $t\bar{t}$, W^-t , and $W^+\bar{t}$ production, which is explained in the foregoing passage, is simply left away. A drawback arises from the fact that divergences from the $g \rightarrow b\bar{b}$ splitting are contained in the virtual corrections, but the respective subprocesses contributing to the real corrections, which are essentially needed to cure these divergences, are left out. This problem of getting a divergent cross section is solved by adding the integrated dipole terms to the virtual corrections in the way described in Chapter 5. The corresponding real-correction contributions and the subtracted dipoles are, however, neglected. This approach can also be described as follows: All real-correction subprocesses containing external bottom (anti-)quarks are approximated by the dipole terms which solely contain the divergences related to subprocesses whose virtual corrections are taken into account. This procedure is justified by the fact that the neglected contribution only delivers sizeable contributions from diagrams including resonant top quarks. Exactly these contributions, however, are meant to be left out, because they should actually be assigned to different process classes.

In the process classes $pp/p\bar{p} \rightarrow ZZ + \text{jet} + X$ and $pp/p\bar{p} \rightarrow WZ + \text{jet} + X$, no top-quark resonances are to be treated, since, with no more than one flavour-changing coupling appearing in these process classes, internal top quarks do not show up at all—except for closed top loops. As for $WW + \text{jet}$, we perform the five-flavour-scheme calculation omitting external bottom-(anti-)quark contributions, because these are expected to be small, which will be proven in Section 8.3 on the LO level. The problem of divergences related to external bottom (anti-)quarks is treated as explained above.

In the second scenario, the bottom (anti-)quarks are understood as massive particles. Consequently, four-flavour PDFs are used. The running of α_s is driven only by the four remaining light quarks with both bottom- and top-quark loops in the gluon self-energies subtracted at zero momentum. In this context, no large corrections arise from terms proportional to $\alpha_s \ln m_b$, because counterterms always contribute in the combination $\frac{1}{2}\delta Z_A + \delta Z_{g_s}$, which will be shown in Section 5.3.4. Thus, the $\alpha_s \ln m_b$ term from the renormalization of the strong coupling cancels against the corresponding term from the wave-function renormalization of the gluon. In this four-flavour scheme, such a cancellation always takes place if the number of external gluons is equal to the number of strong couplings in the considered LO process.

Here, no top resonances show up, since no bottom-(anti-)quark densities exist in the four-flavour scheme and no mixing between the two light and the third generation takes place in the chosen approximation of the CKM matrix. No $b\bar{b}$ pairs are taken into account in final states—single outgoing bottom (anti-)quarks could only show up along with initial-state ones—, which is justified by anti-b-tagging. In this framework, the calculation is performed for all four gauge-boson-pair assignments in the process class $pp/p\bar{p} \rightarrow VV + \text{jet} + X$.

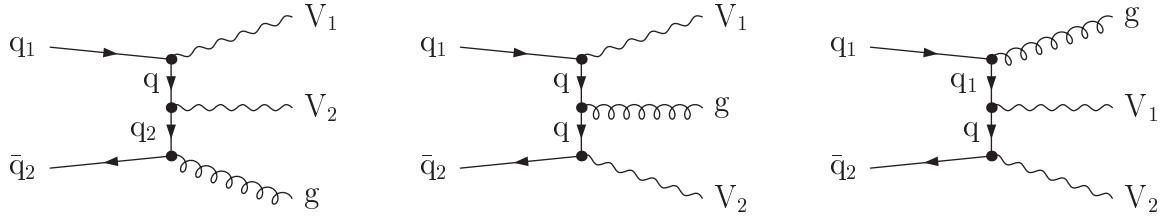


Figure 3.6: Diagrams contributing to the LO subprocesses with both weak gauge bosons coupling directly to the fermion chain.

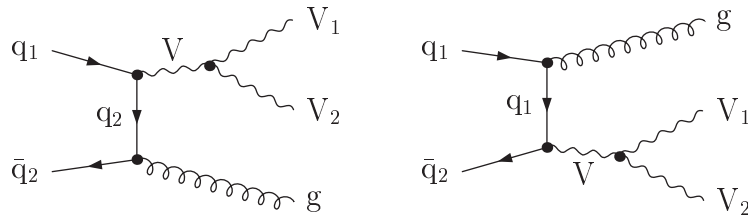


Figure 3.7: Diagrams contributing to the LO subprocesses with the two weak gauge bosons coupling to the fermion chain by means of an intermediate gauge boson.

3.4 Overview of the contributing subprocesses

Two different groups of diagrams contribute to the LO subprocesses. These are, on the one side, diagrams with both weak gauge bosons coupling directly to the fermion chain; such graphs are illustrated in Figure 3.6. In the other group of diagrams, which is shown in Figure 3.7, the weak-gauge-boson pair couples to the fermion chain by means of an intermediate gauge boson and a three-vector-boson vertex. Of course, the latter diagrams only contribute if a respective three-gauge-boson vertex exists. This is the case for all process classes other than ZZ +jet production.

A list of all subprocesses contributing at LO—and also in the virtual corrections which agree in initial and final states with the LO subprocesses if only NLO contributions are taken into account—is given in Table 3.1.

The real-emission subprocesses with two external gluons show a similar structure compared to the LO subprocesses. The main differences are the appearance of three-gluon vertices as a consequence of the non-Abelian structure of QCD and a larger number of contributing diagrams, which is mainly due to combinatorics. The diagrams with the weak gauge bosons coupling directly to the fermion chain are shown in Figure 3.8, those with an intermediate electroweak gauge boson in Figure 3.9. Again, the latter diagrams do not contribute to ZZ +jet production. In the calculation of both groups of diagrams, every diagram without a three-gluon-vertex has to be taken into account also with the two outgoing gluons crossed. A list of all subprocesses with two external gluons is provided in Table 3.2.

$Q\bar{Q} \rightarrow W^+W^-g$	$Q\bar{Q} \rightarrow ZZg$	$U\bar{D} \rightarrow W^+Zg$	$D\bar{U} \rightarrow W^-Zg$
$d\bar{d} \rightarrow W^+W^-g$	$d\bar{d} \rightarrow ZZg$	$u\bar{d} \rightarrow W^+Zg$	$d\bar{u} \rightarrow W^-Zg$
$s\bar{s} \rightarrow W^+W^-g$	$s\bar{s} \rightarrow ZZg$	$c\bar{s} \rightarrow W^+Zg$	$s\bar{c} \rightarrow W^-Zg$
$u\bar{u} \rightarrow W^+W^-g$	$u\bar{u} \rightarrow ZZg$	$u\bar{s} \rightarrow W^+Zg$	$d\bar{c} \rightarrow W^-Zg$
$c\bar{c} \rightarrow W^+W^-g$	$c\bar{c} \rightarrow ZZg$	$c\bar{d} \rightarrow W^+Zg$	$s\bar{u} \rightarrow W^-Zg$
$b\bar{b} \rightarrow W^+W^-g$	$b\bar{b} \rightarrow ZZg$		
$Qg \rightarrow W^+W^-Q$	$Qg \rightarrow ZZQ$	$Ug \rightarrow W^+ZU$	$Dg \rightarrow W^-Z\bar{U}$
$dg \rightarrow W^+W^-d$	$dg \rightarrow ZZd$	$ug \rightarrow W^+Zd$	$dg \rightarrow W^-Zu$
$sg \rightarrow W^+W^-s$	$sg \rightarrow ZZs$	$cg \rightarrow W^+Zs$	$sg \rightarrow W^-Zc$
$ug \rightarrow W^+W^-u$	$ug \rightarrow ZZu$	$ug \rightarrow W^+Zs$	$dg \rightarrow W^-Zc$
$cg \rightarrow W^+W^-c$	$cg \rightarrow ZZc$	$cg \rightarrow W^+Zd$	$sg \rightarrow W^-Zu$
$bg \rightarrow W^+W^-b *$	$bg \rightarrow ZZb$		
$g\bar{Q} \rightarrow W^+W^-\bar{Q}$	$g\bar{Q} \rightarrow ZZ\bar{Q}$	$g\bar{D} \rightarrow W^+Z\bar{U}$	$g\bar{U} \rightarrow W^-Z\bar{D}$
$g\bar{d} \rightarrow W^+W^-\bar{d}$	$g\bar{d} \rightarrow ZZ\bar{d}$	$g\bar{d} \rightarrow W^+Z\bar{u}$	$g\bar{u} \rightarrow W^-Z\bar{d}$
$g\bar{s} \rightarrow W^+W^-\bar{s}$	$g\bar{s} \rightarrow ZZ\bar{s}$	$g\bar{s} \rightarrow W^+Z\bar{c}$	$g\bar{c} \rightarrow W^-Z\bar{s}$
$g\bar{u} \rightarrow W^+W^-\bar{u}$	$g\bar{u} \rightarrow ZZ\bar{u}$	$g\bar{d} \rightarrow W^+Z\bar{c}$	$g\bar{u} \rightarrow W^-Z\bar{s}$
$g\bar{c} \rightarrow W^+W^-\bar{c}$	$g\bar{c} \rightarrow ZZ\bar{c}$	$g\bar{s} \rightarrow W^+Z\bar{u}$	$g\bar{c} \rightarrow W^-Z\bar{d}$
$g\bar{b} \rightarrow W^+W^-\bar{b} *$	$g\bar{b} \rightarrow ZZ\bar{b}$		

Table 3.1: All partonic subprocesses contributing to $pp/p\bar{p} \rightarrow VV+\text{jet}+X$ at LO. The subprocesses collected in pairs contain identical matrix elements, since they are connected by exchanging all first-generation (anti-)quarks by the respective second-generation particles and vice versa. Subprocesses with external bottom (anti-)quarks contribute only in the five-flavour scheme and are treated as described in the text. Those marked with an asterisk contain diagrams with top resonances. In case of WZ+jet production, vertical spacing separates subprocesses suppressed by a non-diagonal CKM matrix factor (second section) from those leading to non-zero contributions also in case of a trivial CKM matrix (first section). Subprocesses with CKM-suppression are only present in WZ+jet production at LO.

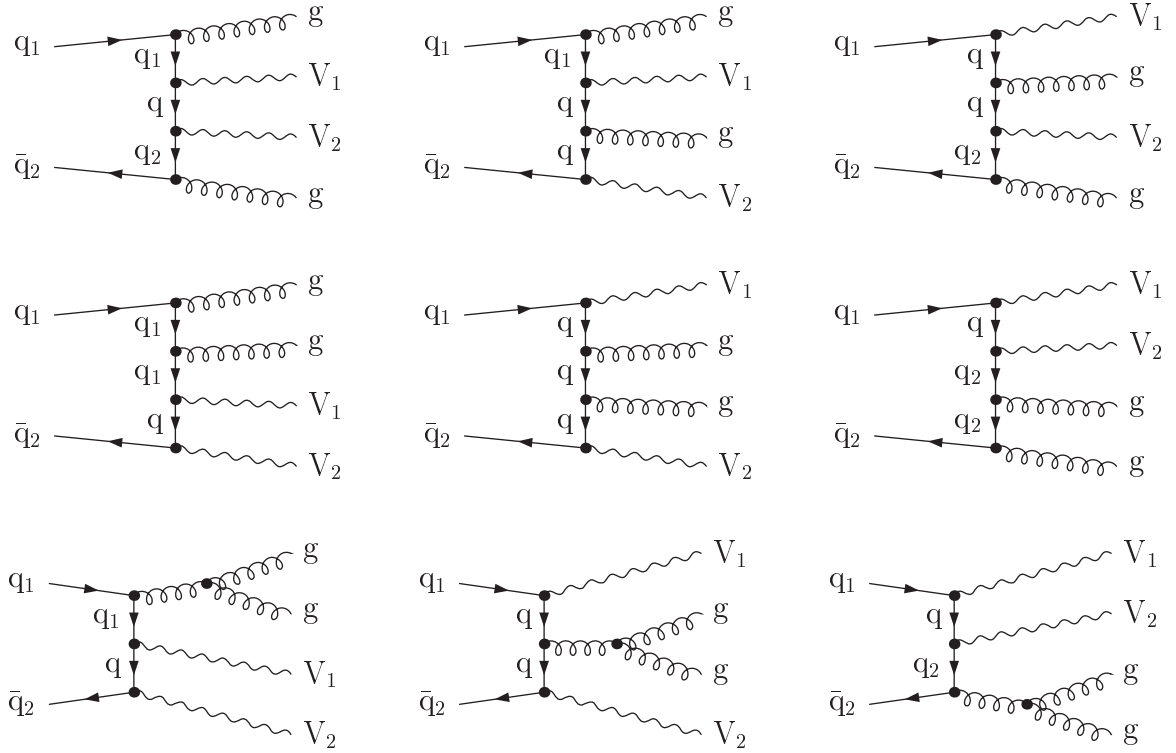


Figure 3.8: Diagrams with two external gluons contributing to the real-emission subprocesses with both weak gauge bosons coupling directly to the fermion chain.

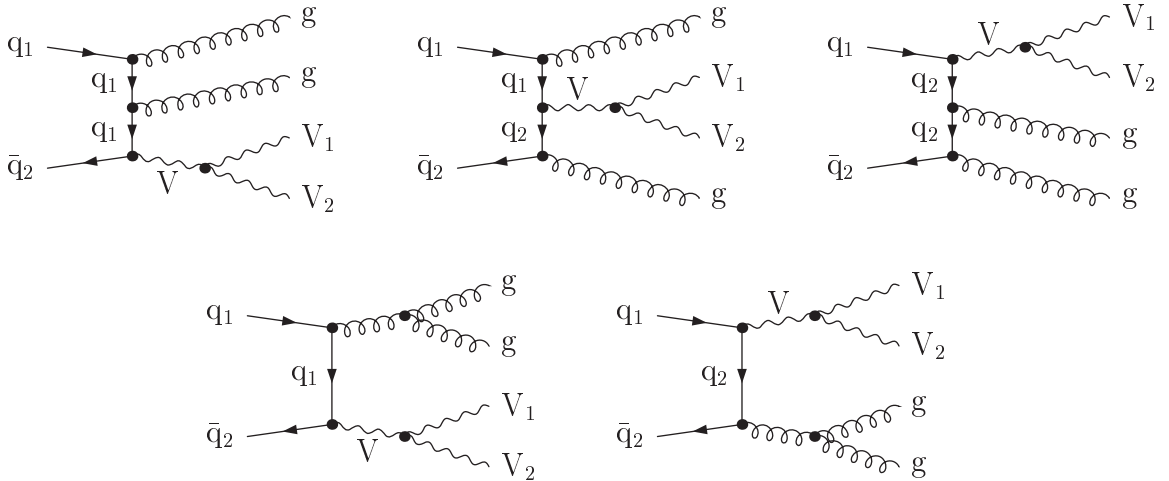


Figure 3.9: Diagrams with two external gluons contributing to the real-emission subprocesses with the two weak gauge bosons coupling to the fermion chain by an intermediate gauge boson.

$Q\bar{Q} \rightarrow W^+W^-gg$	$Q\bar{Q} \rightarrow ZZgg$	$U\bar{D} \rightarrow W^+Zgg$	$D\bar{U} \rightarrow W^-Zgg$
$d\bar{d} \rightarrow W^+W^-gg$	$d\bar{d} \rightarrow ZZgg$	$u\bar{d} \rightarrow W^+Zgg$	$d\bar{u} \rightarrow W^-Zgg$
$s\bar{s} \rightarrow W^+W^-gg$	$s\bar{s} \rightarrow ZZgg$	$c\bar{s} \rightarrow W^+Zgg$	$s\bar{c} \rightarrow W^-Zgg$
$u\bar{u} \rightarrow W^+W^-gg$	$u\bar{u} \rightarrow ZZgg$	$u\bar{s} \rightarrow W^+Zgg$	$d\bar{c} \rightarrow W^-Zgg$
$c\bar{c} \rightarrow W^+W^-gg$	$c\bar{c} \rightarrow ZZgg$	$c\bar{d} \rightarrow W^+Zgg$	$s\bar{u} \rightarrow W^-Zgg$
$b\bar{b} \rightarrow W^+W^-gg$	$b\bar{b} \rightarrow ZZgg$		
$Qg \rightarrow W^+W^-Qg$	$Qg \rightarrow ZZQg$	$Ug \rightarrow W^+ZUg$	$Dg \rightarrow W^-Z\bar{U}g$
$dg \rightarrow W^+W^-dg$	$dg \rightarrow ZZdg$	$ug \rightarrow W^+Zdg$	$dg \rightarrow W^-Zug$
$sg \rightarrow W^+W^-sg$	$sg \rightarrow ZZsg$	$cg \rightarrow W^+Zsg$	$sg \rightarrow W^-Zcg$
$ug \rightarrow W^+W^-ug$	$ug \rightarrow ZZug$	$ug \rightarrow W^+Zsg$	$dg \rightarrow W^-Zcg$
$cg \rightarrow W^+W^-cg$	$cg \rightarrow ZZcg$	$cg \rightarrow W^+Zdg$	$sg \rightarrow W^-Zug$
$bg \rightarrow W^+W^-bg *$	$bg \rightarrow ZZbg$		
$g\bar{Q} \rightarrow W^+W^-g\bar{Q}$	$g\bar{Q} \rightarrow ZZg\bar{Q}$	$g\bar{D} \rightarrow W^+Zg\bar{U}$	$g\bar{U} \rightarrow W^-Zg\bar{D}$
$g\bar{d} \rightarrow W^+W^-g\bar{d}$	$g\bar{d} \rightarrow ZZg\bar{d}$	$g\bar{d} \rightarrow W^+Zg\bar{u}$	$g\bar{u} \rightarrow W^-Zg\bar{d}$
$g\bar{s} \rightarrow W^+W^-g\bar{s}$	$g\bar{s} \rightarrow ZZg\bar{s}$	$g\bar{s} \rightarrow W^+Zg\bar{c}$	$g\bar{c} \rightarrow W^-Zg\bar{s}$
$g\bar{u} \rightarrow W^+W^-g\bar{u}$	$g\bar{u} \rightarrow ZZg\bar{u}$	$g\bar{d} \rightarrow W^+Zg\bar{c}$	$g\bar{u} \rightarrow W^-Zg\bar{s}$
$g\bar{c} \rightarrow W^+W^-g\bar{c}$	$g\bar{c} \rightarrow ZZg\bar{c}$	$g\bar{s} \rightarrow W^+Zg\bar{u}$	$g\bar{c} \rightarrow W^-Zg\bar{d}$
$g\bar{b} \rightarrow W^+W^-g\bar{b} *$	$g\bar{b} \rightarrow ZZg\bar{b}$		
$gg \rightarrow W^+W^-Q\bar{Q}$	$gg \rightarrow ZZQ\bar{Q}$	$gg \rightarrow W^+ZD\bar{U}$	$gg \rightarrow W^-ZU\bar{D}$
$gg \rightarrow W^+W^-d\bar{d}$	$gg \rightarrow ZZd\bar{d}$	$gg \rightarrow W^+Zd\bar{u}$	$gg \rightarrow W^-Zu\bar{d}$
$gg \rightarrow W^+W^-s\bar{s}$	$gg \rightarrow ZZs\bar{s}$	$gg \rightarrow W^+Zs\bar{c}$	$gg \rightarrow W^-Zc\bar{s}$
$gg \rightarrow W^+W^-u\bar{u}$	$gg \rightarrow ZZu\bar{u}$	$gg \rightarrow W^+Zd\bar{c}$	$gg \rightarrow W^-Zc\bar{d}$
$gg \rightarrow W^+W^-c\bar{c}$	$gg \rightarrow ZZc\bar{c}$	$gg \rightarrow W^+Zs\bar{u}$	$gg \rightarrow W^-Zu\bar{s}$
$gg \rightarrow W^+W^-b\bar{b} **$	$gg \rightarrow ZZb\bar{b}$		

Table 3.2: All partonic subprocesses containing two external gluons, which contribute to $pp/p\bar{p} \rightarrow VV+\text{jet}+X$ at NLO QCD. Subprocesses with external bottom (anti-)quarks contribute only in the five-flavour scheme. Details on the notation are explained in the caption of Table 3.1. In addition, two asterisks denote subprocesses with two top resonances arising simultaneously.

$D\bar{D} \rightarrow W^+W^-D\bar{D}$	$U\bar{U} \rightarrow W^+W^-U\bar{U}$	$D\bar{D} \rightarrow ZZD\bar{D}$	$U\bar{U} \rightarrow ZZU\bar{U}$
$d\bar{d} \rightarrow W^+W^-d\bar{d}$	$u\bar{u} \rightarrow W^+W^-u\bar{u}$	$d\bar{d} \rightarrow ZZd\bar{d}$	$u\bar{u} \rightarrow ZZu\bar{u}$
$s\bar{s} \rightarrow W^+W^-s\bar{s}$	$c\bar{c} \rightarrow W^+W^-c\bar{c}$	$s\bar{s} \rightarrow ZZs\bar{s}$	$c\bar{c} \rightarrow ZZc\bar{c}$
$d\bar{d} \rightarrow W^+W^-s\bar{s}$	$u\bar{u} \rightarrow W^+W^-c\bar{c}$	$d\bar{d} \rightarrow ZZs\bar{s}$	$u\bar{u} \rightarrow ZZc\bar{c}$
$s\bar{s} \rightarrow W^+W^-d\bar{d}$	$c\bar{c} \rightarrow W^+W^-u\bar{u}$	$s\bar{s} \rightarrow ZZd\bar{d}$	$c\bar{c} \rightarrow ZZu\bar{u}$
$d\bar{s} \rightarrow W^+W^-d\bar{s}$	$u\bar{c} \rightarrow W^+W^-u\bar{c}$	$d\bar{s} \rightarrow ZZd\bar{s}$	$u\bar{c} \rightarrow ZZu\bar{c}$
$s\bar{d} \rightarrow W^+W^-s\bar{d}$	$c\bar{u} \rightarrow W^+W^-c\bar{u}$	$s\bar{d} \rightarrow ZZs\bar{d}$	$c\bar{u} \rightarrow ZZc\bar{u}$
$b\bar{b} \rightarrow W^+W^-b\bar{b} **$		$b\bar{b} \rightarrow ZZb\bar{b}$	
$d\bar{d} \rightarrow W^+W^-b\bar{b} **$		$d\bar{d} \rightarrow ZZb\bar{b}$	
$s\bar{s} \rightarrow W^+W^-b\bar{b} **$		$s\bar{s} \rightarrow ZZb\bar{b}$	
$b\bar{b} \rightarrow W^+W^-d\bar{d}$		$b\bar{b} \rightarrow ZZd\bar{d}$	
$b\bar{b} \rightarrow W^+W^-s\bar{s}$		$b\bar{b} \rightarrow ZZs\bar{s}$	
$d\bar{b} \rightarrow W^+W^-d\bar{b} *$		$d\bar{b} \rightarrow ZZd\bar{b}$	
$s\bar{b} \rightarrow W^+W^-s\bar{b} *$		$s\bar{b} \rightarrow ZZs\bar{b}$	
$b\bar{d} \rightarrow W^+W^-b\bar{d} *$		$b\bar{d} \rightarrow ZZb\bar{d}$	
$b\bar{d} \rightarrow W^+W^-b\bar{s} *$		$b\bar{s} \rightarrow ZZb\bar{s}$	

Table 3.3: Partonic subprocesses with quark–antiquark pairs in the initial and final states, which contribute to $pp/p\bar{p} \rightarrow WW+\text{jet}+X$ and $pp/p\bar{p} \rightarrow ZZ+\text{jet}+X$, respectively, at NLO QCD. Here, only subprocesses with all external (anti-)quarks of the same type (up- or down-type) are shown. Due to charge conservation no such subprocesses exist for $pp/p\bar{p} \rightarrow WZ+\text{jet}+X$. Details on the notation are explained in the caption of Table 3.1. Again, two asterisks denote subprocesses with two top resonances arising simultaneously.

The real-emission subprocesses with four external (anti-)quarks get contributions from three different types of diagrams. A subset of diagrams with the two gauge bosons coupling to the same fermion chain is presented in Figure 3.10. Explicitly, only diagrams with both gauge bosons coupling to the fermion chain of the initial-state quark–antiquark pair are depicted. Depending on the specific assignments of gauge bosons and (anti-)quarks, also diagrams with the two gauge bosons coupling to a different fermion chain contribute, e.g. the one of the final-state quark–antiquark pair. The corresponding diagrams are not shown explicitly, but they can be obtained by applying crossing relations to one or two pairs of external (anti-)quarks. The same is true for the diagrams given in Figure 3.11, where contributions with three-vector-boson vertex are depicted. Depending again on the gauge-boson and (anti-)quark assignments, some diagrams contribute with the two gauge bosons coupling to different fermion chains. These diagrams are presented in Figure 3.12. All subprocesses with two fermion chains are collected in Tables 3.3 – 3.6 for $pp/p\bar{p} \rightarrow WW + \text{jet} + X$ and $pp/p\bar{p} \rightarrow ZZ + \text{jet} + X$. Those contributing to $pp/p\bar{p} \rightarrow WZ + \text{jet} + X$ are given in Tables 3.7 – 3.9.

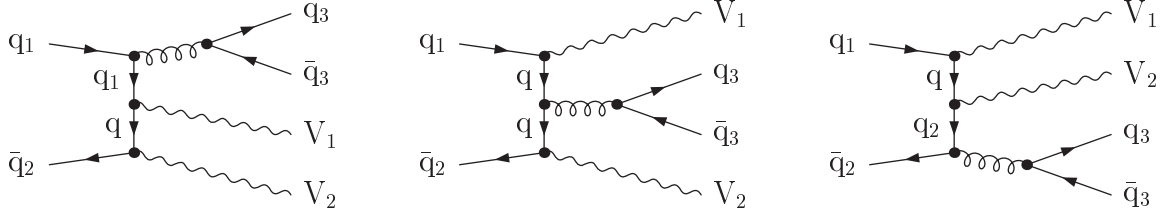


Figure 3.10: Diagrams with four external (anti-)quarks contributing to the real-emission subprocesses at NLO QCD with the two weak gauge bosons coupling directly to the same fermion chain.

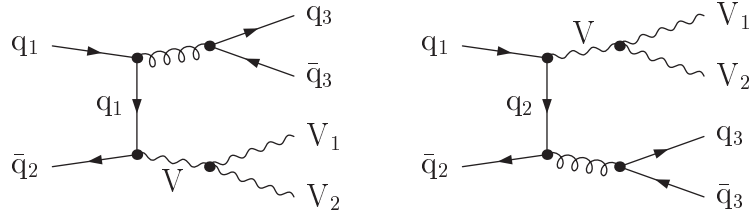


Figure 3.11: Diagrams with four external (anti-)quarks contributing to the real-emission subprocesses at NLO QCD with the two weak gauge bosons coupling to the fermion chain by an intermediate gauge boson.

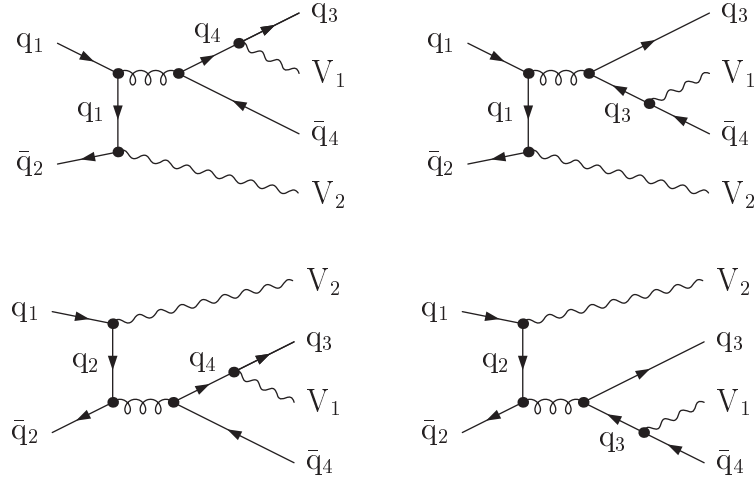


Figure 3.12: Diagrams with four external (anti-)quarks contributing to the real-emission subprocesses at NLO QCD. Here, the diagrams with the two gauge bosons coupling to different fermion chains are shown.

$D\bar{D} \rightarrow W^+W^-U\bar{U}$	$U\bar{U} \rightarrow W^+W^-D\bar{D}$	$D\bar{D} \rightarrow ZZU\bar{U}$	$U\bar{U} \rightarrow ZZD\bar{D}$
$d\bar{d} \rightarrow W^+W^-u\bar{u}$	$u\bar{u} \rightarrow W^+W^-d\bar{d}$	$d\bar{d} \rightarrow ZZu\bar{u}$	$u\bar{u} \rightarrow ZZd\bar{d}$
$s\bar{s} \rightarrow W^+W^-c\bar{c}$	$c\bar{c} \rightarrow W^+W^-s\bar{s}$	$s\bar{s} \rightarrow ZZc\bar{c}$	$c\bar{c} \rightarrow ZZs\bar{s}$
$d\bar{d} \rightarrow W^+W^-c\bar{c}$	$u\bar{u} \rightarrow W^+W^-s\bar{s}$	$d\bar{d} \rightarrow ZZc\bar{c}$	$u\bar{u} \rightarrow ZZs\bar{s}$
$s\bar{s} \rightarrow W^+W^-u\bar{u}$	$c\bar{c} \rightarrow W^+W^-d\bar{d}$	$s\bar{s} \rightarrow ZZu\bar{u}$	$c\bar{c} \rightarrow ZZd\bar{d}$
$d\bar{s} \rightarrow W^+W^-u\bar{c}$	$u\bar{c} \rightarrow W^+W^-d\bar{s}$		
$s\bar{d} \rightarrow W^+W^-c\bar{u}$	$c\bar{u} \rightarrow W^+W^-s\bar{d}$		
$d\bar{d} \rightarrow W^+W^-u\bar{c}$	$u\bar{u} \rightarrow W^+W^-d\bar{s}$		
$s\bar{s} \rightarrow W^+W^-c\bar{u}$	$c\bar{c} \rightarrow W^+W^-s\bar{d}$		
$d\bar{d} \rightarrow W^+W^-c\bar{u}$	$u\bar{u} \rightarrow W^+W^-s\bar{d}$		
$s\bar{s} \rightarrow W^+W^-u\bar{c}$	$c\bar{c} \rightarrow W^+W^-d\bar{s}$		
$d\bar{s} \rightarrow W^+W^-u\bar{u}$	$u\bar{c} \rightarrow W^+W^-d\bar{d}$		
$s\bar{d} \rightarrow W^+W^-c\bar{c}$	$c\bar{u} \rightarrow W^+W^-s\bar{s}$		
$d\bar{s} \rightarrow W^+W^-c\bar{c}$	$u\bar{c} \rightarrow W^+W^-s\bar{s}$		
$s\bar{d} \rightarrow W^+W^-u\bar{u}$	$c\bar{u} \rightarrow W^+W^-d\bar{d}$		
$d\bar{s} \rightarrow W^+W^-c\bar{u}$	$u\bar{c} \rightarrow W^+W^-s\bar{d}$		
$s\bar{d} \rightarrow W^+W^-u\bar{c}$	$c\bar{u} \rightarrow W^+W^-d\bar{s}$		
$b\bar{b} \rightarrow W^+W^-u\bar{u}$	$u\bar{u} \rightarrow W^+W^-b\bar{b} **$	$b\bar{b} \rightarrow ZZu\bar{u}$	$u\bar{u} \rightarrow ZZb\bar{b}$
$b\bar{b} \rightarrow W^+W^-c\bar{c}$	$c\bar{c} \rightarrow W^+W^-b\bar{b} **$	$b\bar{b} \rightarrow ZZc\bar{c}$	$c\bar{c} \rightarrow ZZb\bar{b}$

Table 3.4: As in Table 3.3, but for subprocesses with an initial state consisting of a down-type quark–antiquark pair and a final state consisting of an up-type quark–antiquark pair (columns 1 and 3) and vice versa (columns 2 and 4). WW+jet subprocesses suppressed by one (second section) or two (third section) non-diagonal CKM matrix factors are separated from those giving non-zero contributions also in the case of a trivial CKM matrix (first section) by vertical spacing.

$D\bar{U} \rightarrow W^+W^-D\bar{U}$	$U\bar{D} \rightarrow W^+W^-U\bar{D}$	$D\bar{U} \rightarrow ZZD\bar{U}$	$U\bar{D} \rightarrow ZZU\bar{D}$
$d\bar{u} \rightarrow W^+W^-d\bar{u}$	$u\bar{d} \rightarrow W^+W^-u\bar{d}$	$d\bar{u} \rightarrow ZZd\bar{u}$	$u\bar{d} \rightarrow ZZu\bar{d}$
$s\bar{c} \rightarrow W^+W^-s\bar{c}$	$c\bar{s} \rightarrow W^+W^-c\bar{s}$	$s\bar{c} \rightarrow ZZs\bar{c}$	$c\bar{s} \rightarrow ZZc\bar{s}$
$d\bar{c} \rightarrow W^+W^-d\bar{c}$	$u\bar{s} \rightarrow W^+W^-u\bar{s}$	$d\bar{c} \rightarrow ZZd\bar{c}$	$u\bar{s} \rightarrow ZZu\bar{s}$
$s\bar{u} \rightarrow W^+W^-s\bar{u}$	$c\bar{d} \rightarrow W^+W^-c\bar{d}$	$s\bar{u} \rightarrow ZZs\bar{u}$	$c\bar{d} \rightarrow ZZc\bar{d}$
$d\bar{u} \rightarrow W^+W^-s\bar{c}$	$u\bar{d} \rightarrow W^+W^-c\bar{s}$		
$s\bar{c} \rightarrow W^+W^-d\bar{u}$	$c\bar{s} \rightarrow W^+W^-u\bar{d}$		
$d\bar{u} \rightarrow W^+W^-d\bar{c}$	$u\bar{d} \rightarrow W^+W^-u\bar{s}$		
$s\bar{c} \rightarrow W^+W^-s\bar{u}$	$c\bar{s} \rightarrow W^+W^-c\bar{d}$		
$d\bar{u} \rightarrow W^+W^-s\bar{u}$	$u\bar{d} \rightarrow W^+W^-c\bar{d}$		
$s\bar{c} \rightarrow W^+W^-d\bar{c}$	$c\bar{s} \rightarrow W^+W^-u\bar{s}$		
$d\bar{c} \rightarrow W^+W^-d\bar{u}$	$u\bar{s} \rightarrow W^+W^-u\bar{d}$		
$s\bar{u} \rightarrow W^+W^-s\bar{c}$	$c\bar{d} \rightarrow W^+W^-c\bar{s}$		
$d\bar{c} \rightarrow W^+W^-s\bar{c}$	$u\bar{s} \rightarrow W^+W^-c\bar{s}$		
$s\bar{u} \rightarrow W^+W^-d\bar{u}$	$c\bar{d} \rightarrow W^+W^-u\bar{d}$		
$d\bar{c} \rightarrow W^+W^-s\bar{u}$	$u\bar{s} \rightarrow W^+W^-c\bar{d}$		
$s\bar{u} \rightarrow W^+W^-d\bar{c}$	$c\bar{d} \rightarrow W^+W^-u\bar{s}$		
$b\bar{u} \rightarrow W^+W^-b\bar{u}$	$u\bar{b} \rightarrow W^+W^-u\bar{b}$	$b\bar{u} \rightarrow ZZb\bar{u}$	$u\bar{b} \rightarrow ZZu\bar{b}$
$b\bar{c} \rightarrow W^+W^-b\bar{c}$	$c\bar{b} \rightarrow W^+W^-c\bar{b}$	$b\bar{c} \rightarrow ZZb\bar{c}$	$c\bar{b} \rightarrow ZZc\bar{b}$

Table 3.5: As in Table 3.4, but for both initial and final states consisting of a down-type quark and an up-type antiquark (column 1 and 3) and vice versa (column 2 and 4).

$DD \rightarrow W^+W^-DD$	$\bar{D}\bar{D} \rightarrow W^+W^-\bar{D}\bar{D}$	$DD \rightarrow ZZDD$	$\bar{D}\bar{D} \rightarrow ZZ\bar{D}\bar{D}$
$dd \rightarrow W^+W^-dd$	$\bar{d}\bar{d} \rightarrow W^+W^-\bar{d}\bar{d}$	$dd \rightarrow ZZdd$	$\bar{d}\bar{d} \rightarrow ZZ\bar{d}\bar{d}$
$ss \rightarrow W^+W^-ss$	$\bar{s}\bar{s} \rightarrow W^+W^-\bar{s}\bar{s}$	$ss \rightarrow ZZss$	$\bar{s}\bar{s} \rightarrow ZZ\bar{s}\bar{s}$
$ds \rightarrow W^+W^-sd$	$\bar{d}\bar{s} \rightarrow W^+W^-\bar{s}\bar{d}$	$ds \rightarrow ZZsd$	$\bar{d}\bar{s} \rightarrow ZZ\bar{s}\bar{d}$
$bb \rightarrow W^+W^-bb *$	$\bar{b}\bar{b} \rightarrow W^+W^-\bar{b}\bar{b} *$	$bb \rightarrow ZZbb$	$\bar{b}\bar{b} \rightarrow ZZ\bar{b}\bar{b}$
$db \rightarrow W^+W^-bd *$	$\bar{d}\bar{b} \rightarrow W^+W^-\bar{b}\bar{d} *$	$db \rightarrow ZZbd$	$\bar{d}\bar{b} \rightarrow ZZ\bar{b}\bar{d}$
$sb \rightarrow W^+W^-bs *$	$\bar{s}\bar{b} \rightarrow W^+W^-\bar{b}\bar{s} *$	$sb \rightarrow ZZbs$	$\bar{s}\bar{b} \rightarrow ZZ\bar{b}\bar{s}$
$UU \rightarrow W^+W^-UU$	$\bar{U}\bar{U} \rightarrow W^+W^-\bar{U}\bar{U}$	$UU \rightarrow ZZUU$	$\bar{U}\bar{U} \rightarrow ZZ\bar{U}\bar{U}$
$uu \rightarrow W^+W^-uu$	$\bar{u}\bar{u} \rightarrow W^+W^-\bar{u}\bar{u}$	$uu \rightarrow ZZuu$	$\bar{u}\bar{u} \rightarrow ZZ\bar{u}\bar{u}$
$cc \rightarrow W^+W^-cc$	$\bar{c}\bar{c} \rightarrow W^+W^-\bar{c}\bar{c}$	$cc \rightarrow ZZcc$	$\bar{c}\bar{c} \rightarrow ZZ\bar{c}\bar{c}$
$uc \rightarrow W^+W^-cu$	$\bar{u}\bar{c} \rightarrow W^+W^-\bar{c}\bar{u}$	$uc \rightarrow ZZcu$	$\bar{u}\bar{c} \rightarrow ZZ\bar{c}\bar{u}$
$DU \rightarrow W^+W^-UD$	$\bar{D}\bar{U} \rightarrow W^+W^-\bar{U}\bar{D}$	$DU \rightarrow ZZUD$	$\bar{D}\bar{U} \rightarrow ZZ\bar{U}\bar{D}$
$du \rightarrow W^+W^-ud$	$\bar{d}\bar{u} \rightarrow W^+W^-\bar{u}\bar{d}$	$du \rightarrow ZZud$	$\bar{d}\bar{u} \rightarrow ZZ\bar{u}\bar{d}$
$sc \rightarrow W^+W^-cs$	$\bar{s}\bar{c} \rightarrow W^+W^-\bar{c}\bar{s}$	$sc \rightarrow ZZcs$	$\bar{s}\bar{c} \rightarrow ZZ\bar{c}\bar{s}$
$dc \rightarrow W^+W^-cd$	$\bar{d}\bar{c} \rightarrow W^+W^-\bar{c}\bar{d}$	$dc \rightarrow ZZcd$	$\bar{d}\bar{c} \rightarrow ZZ\bar{c}\bar{d}$
$su \rightarrow W^+W^-us$	$\bar{s}\bar{u} \rightarrow W^+W^-\bar{u}\bar{s}$	$su \rightarrow ZZus$	$\bar{s}\bar{u} \rightarrow ZZ\bar{u}\bar{s}$
$dc \rightarrow W^+W^-su$	$\bar{d}\bar{c} \rightarrow W^+W^-\bar{s}\bar{u}$		
$su \rightarrow W^+W^-dc$	$\bar{s}\bar{u} \rightarrow W^+W^-\bar{d}\bar{c}$		
$du \rightarrow W^+W^-us$	$\bar{d}\bar{u} \rightarrow W^+W^-\bar{u}\bar{s}$		
$sc \rightarrow W^+W^-cd$	$\bar{s}\bar{c} \rightarrow W^+W^-\bar{c}\bar{d}$		
$du \rightarrow W^+W^-cd$	$\bar{d}\bar{u} \rightarrow W^+W^-\bar{c}\bar{d}$		
$sc \rightarrow W^+W^-us$	$\bar{s}\bar{c} \rightarrow W^+W^-\bar{u}\bar{s}$		
$dc \rightarrow W^+W^-cs$	$\bar{d}\bar{c} \rightarrow W^+W^-\bar{c}\bar{s}$		
$su \rightarrow W^+W^-ud$	$\bar{s}\bar{u} \rightarrow W^+W^-\bar{u}\bar{d}$		
$dc \rightarrow W^+W^-ud$	$\bar{d}\bar{c} \rightarrow W^+W^-\bar{u}\bar{d}$		
$su \rightarrow W^+W^-cs$	$\bar{s}\bar{u} \rightarrow W^+W^-\bar{c}\bar{s}$		
$du \rightarrow W^+W^-cs$	$\bar{d}\bar{u} \rightarrow W^+W^-\bar{c}\bar{s}$		
$sc \rightarrow W^+W^-ud$	$\bar{s}\bar{c} \rightarrow W^+W^-\bar{u}\bar{d}$		
$bu \rightarrow W^+W^-ub *$	$\bar{b}\bar{u} \rightarrow W^+W^-\bar{u}\bar{b} *$	$bu \rightarrow ZZub$	$\bar{b}\bar{u} \rightarrow ZZ\bar{u}\bar{b}$
$bc \rightarrow W^+W^-cb *$	$\bar{b}\bar{c} \rightarrow W^+W^-\bar{c}\bar{b} *$	$bc \rightarrow ZZcb$	$\bar{b}\bar{c} \rightarrow ZZ\bar{c}\bar{b}$

Table 3.6: As in Table 3.4, but for all partonic subprocesses containing four external quarks or four external antiquarks, which contribute to $pp/p\bar{p} \rightarrow WW+\text{jet}$ or $pp/p\bar{p} \rightarrow ZZ+\text{jet}$, respectively, at NLO QCD. The subprocesses of column 1 and 2 as well as those of column 3 and 4 are charge conjugated to each other.

$D\bar{D} \rightarrow W^+ Z D\bar{U}$	$U\bar{U} \rightarrow W^+ Z D\bar{U}$	$D\bar{D} \rightarrow W^- Z U\bar{D}$	$U\bar{U} \rightarrow W^- Z U\bar{D}$
$d\bar{d} \rightarrow W^+ Z d\bar{u}$	$u\bar{u} \rightarrow W^+ Z d\bar{u}$	$d\bar{d} \rightarrow W^- Z u\bar{d}$	$u\bar{u} \rightarrow W^- Z u\bar{d}$
$s\bar{s} \rightarrow W^+ Z s\bar{c}$	$c\bar{c} \rightarrow W^+ Z s\bar{c}$	$s\bar{s} \rightarrow W^- Z c\bar{s}$	$c\bar{c} \rightarrow W^- Z c\bar{s}$
$d\bar{d} \rightarrow W^+ Z s\bar{c}$	$u\bar{u} \rightarrow W^+ Z s\bar{c}$	$d\bar{d} \rightarrow W^- Z c\bar{s}$	$u\bar{u} \rightarrow W^- Z c\bar{s}$
$s\bar{s} \rightarrow W^+ Z d\bar{u}$	$c\bar{c} \rightarrow W^+ Z d\bar{u}$	$s\bar{s} \rightarrow W^- Z u\bar{d}$	$c\bar{c} \rightarrow W^- Z u\bar{d}$
$d\bar{s} \rightarrow W^+ Z d\bar{c}$	$u\bar{c} \rightarrow W^+ Z d\bar{c}$	$s\bar{d} \rightarrow W^- Z c\bar{d}$	$c\bar{u} \rightarrow W^- Z c\bar{d}$
$s\bar{d} \rightarrow W^+ Z s\bar{u}$	$c\bar{u} \rightarrow W^+ Z s\bar{u}$	$d\bar{s} \rightarrow W^- Z u\bar{s}$	$u\bar{c} \rightarrow W^- Z u\bar{s}$
$d\bar{d} \rightarrow W^+ Z d\bar{c}$	$u\bar{u} \rightarrow W^+ Z s\bar{u}$	$d\bar{d} \rightarrow W^- Z c\bar{d}$	$u\bar{u} \rightarrow W^- Z u\bar{s}$
$s\bar{s} \rightarrow W^+ Z s\bar{u}$	$c\bar{c} \rightarrow W^+ Z d\bar{c}$	$s\bar{s} \rightarrow W^- Z u\bar{s}$	$c\bar{c} \rightarrow W^- Z c\bar{d}$
$d\bar{d} \rightarrow W^+ Z s\bar{u}$	$u\bar{u} \rightarrow W^+ Z d\bar{c}$	$d\bar{d} \rightarrow W^- Z u\bar{s}$	$u\bar{u} \rightarrow W^- Z c\bar{d}$
$s\bar{s} \rightarrow W^+ Z d\bar{c}$	$c\bar{c} \rightarrow W^+ Z s\bar{u}$	$s\bar{s} \rightarrow W^- Z c\bar{d}$	$c\bar{c} \rightarrow W^- Z u\bar{s}$
$d\bar{s} \rightarrow W^+ Z d\bar{u}$	$u\bar{c} \rightarrow W^+ Z s\bar{c}$	$s\bar{d} \rightarrow W^- Z u\bar{d}$	$c\bar{u} \rightarrow W^- Z c\bar{s}$
$s\bar{d} \rightarrow W^+ Z s\bar{c}$	$c\bar{u} \rightarrow W^+ Z d\bar{u}$	$d\bar{s} \rightarrow W^- Z c\bar{s}$	$u\bar{c} \rightarrow W^- Z u\bar{d}$
$b\bar{b} \rightarrow W^+ Z d\bar{u}$		$b\bar{b} \rightarrow W^- Z u\bar{d}$	
$b\bar{b} \rightarrow W^+ Z s\bar{c}$		$b\bar{b} \rightarrow W^- Z c\bar{s}$	
$b\bar{d} \rightarrow W^+ Z b\bar{u}$		$d\bar{b} \rightarrow W^- Z u\bar{b}$	
$b\bar{s} \rightarrow W^+ Z b\bar{c}$		$s\bar{b} \rightarrow W^- Z c\bar{b}$	
$b\bar{b} \rightarrow W^+ Z d\bar{c}$		$b\bar{b} \rightarrow W^- Z c\bar{d}$	
$b\bar{b} \rightarrow W^+ Z s\bar{u}$		$b\bar{b} \rightarrow W^- Z u\bar{s}$	
$b\bar{d} \rightarrow W^+ Z b\bar{c}$		$d\bar{b} \rightarrow W^- Z c\bar{b}$	
$b\bar{s} \rightarrow W^+ Z b\bar{u}$		$s\bar{b} \rightarrow W^- Z u\bar{b}$	

Table 3.7: Partonic subprocesses with quark–antiquark both in initial and final states, which contribute to $pp/p\bar{p} \rightarrow WZ+\text{jet}$ at NLO QCD. All subprocesses contain either one down-type (anti-)quark and three up-type (anti-)quarks as external partons or vice versa with a charge difference of ± 1 between initial and final states for $W^\pm Z+\text{jet}$ production, respectively. This table shows all such subprocesses with two quarks of different types in the final state. The subprocesses of column 1 and 3 as well as those of column 2 and 4 are charge conjugated to each other. Vertical spacing separates subprocesses suppressed by a non-diagonal CKM matrix factor (second section) from those giving non-zero contributions also in case of a trivial CKM matrix (first section). Further details on the notation are explained in the caption of Table 3.1.

$U\bar{D} \rightarrow W^+Z D\bar{D}$	$U\bar{D} \rightarrow W^+Z U\bar{U}$	$D\bar{U} \rightarrow W^-Z D\bar{D}$	$D\bar{U} \rightarrow W^-Z U\bar{U}$
$u\bar{d} \rightarrow W^+Z d\bar{d}$	$u\bar{d} \rightarrow W^+Z u\bar{u}$	$d\bar{u} \rightarrow W^-Z d\bar{d}$	$d\bar{u} \rightarrow W^-Z u\bar{u}$
$c\bar{s} \rightarrow W^+Z s\bar{s}$	$c\bar{s} \rightarrow W^+Z c\bar{c}$	$s\bar{c} \rightarrow W^-Z s\bar{s}$	$s\bar{c} \rightarrow W^-Z c\bar{c}$
$u\bar{d} \rightarrow W^+Z s\bar{s}$	$u\bar{d} \rightarrow W^+Z c\bar{c}$	$d\bar{u} \rightarrow W^-Z d\bar{d}$	$d\bar{u} \rightarrow W^-Z c\bar{c}$
$c\bar{s} \rightarrow W^+Z d\bar{d}$	$c\bar{s} \rightarrow W^+Z u\bar{u}$	$s\bar{c} \rightarrow W^-Z s\bar{s}$	$s\bar{c} \rightarrow W^-Z u\bar{u}$
$u\bar{s} \rightarrow W^+Z d\bar{s}$	$u\bar{s} \rightarrow W^+Z u\bar{c}$	$d\bar{c} \rightarrow W^-Z s\bar{s}$	$s\bar{u} \rightarrow W^-Z c\bar{u}$
$c\bar{d} \rightarrow W^+Z s\bar{d}$	$c\bar{d} \rightarrow W^+Z c\bar{u}$	$s\bar{u} \rightarrow W^-Z d\bar{d}$	$d\bar{c} \rightarrow W^-Z u\bar{c}$
$c\bar{d} \rightarrow W^+Z d\bar{d}$	$u\bar{s} \rightarrow W^+Z u\bar{u}$	$d\bar{c} \rightarrow W^-Z d\bar{d}$	$s\bar{u} \rightarrow W^-Z u\bar{u}$
$u\bar{s} \rightarrow W^+Z s\bar{s}$	$c\bar{d} \rightarrow W^+Z c\bar{c}$	$s\bar{u} \rightarrow W^-Z s\bar{s}$	$d\bar{c} \rightarrow W^-Z c\bar{c}$
$u\bar{s} \rightarrow W^+Z d\bar{d}$	$u\bar{s} \rightarrow W^+Z c\bar{c}$	$d\bar{u} \rightarrow W^-Z d\bar{d}$	$s\bar{u} \rightarrow W^-Z c\bar{c}$
$c\bar{d} \rightarrow W^+Z s\bar{s}$	$c\bar{d} \rightarrow W^+Z u\bar{u}$	$s\bar{c} \rightarrow W^-Z s\bar{s}$	$d\bar{c} \rightarrow W^-Z u\bar{u}$
$u\bar{d} \rightarrow W^+Z s\bar{d}$	$u\bar{d} \rightarrow W^+Z u\bar{c}$	$d\bar{c} \rightarrow W^-Z d\bar{d}$	$d\bar{u} \rightarrow W^-Z c\bar{u}$
$c\bar{s} \rightarrow W^+Z d\bar{s}$	$c\bar{s} \rightarrow W^+Z c\bar{u}$	$s\bar{u} \rightarrow W^-Z s\bar{s}$	$s\bar{c} \rightarrow W^-Z u\bar{c}$
$u\bar{d} \rightarrow W^+Z b\bar{b}$		$d\bar{u} \rightarrow W^-Z b\bar{b}$	
$c\bar{s} \rightarrow W^+Z b\bar{b}$		$s\bar{c} \rightarrow W^-Z b\bar{b}$	
$u\bar{b} \rightarrow W^+Z d\bar{b}$		$b\bar{u} \rightarrow W^-Z b\bar{d}$	
$c\bar{b} \rightarrow W^+Z s\bar{b}$		$b\bar{c} \rightarrow W^-Z b\bar{s}$	
$u\bar{s} \rightarrow W^+Z b\bar{b}$		$s\bar{u} \rightarrow W^-Z b\bar{b}$	
$c\bar{d} \rightarrow W^+Z b\bar{b}$		$d\bar{c} \rightarrow W^-Z b\bar{b}$	
$u\bar{b} \rightarrow W^+Z s\bar{b}$		$b\bar{u} \rightarrow W^-Z b\bar{s}$	
$c\bar{b} \rightarrow W^+Z d\bar{b}$		$b\bar{c} \rightarrow W^-Z b\bar{d}$	

Table 3.8: As in Table 3.7, but for all the subprocesses with two (anti-)quarks of different types in the initial state. The subprocesses of column 1 and 3 as well as those of column 2 and 4 are charge conjugated to each other.

$UU \rightarrow W^+ZUD$	$\bar{D}\bar{D} \rightarrow W^+Z\bar{U}\bar{D}$	$DD \rightarrow W^-ZDU$	$\bar{U}\bar{U} \rightarrow W^-Z\bar{D}\bar{U}$
$uu \rightarrow W^+Zud$	$\bar{d}\bar{d} \rightarrow W^+Z\bar{u}\bar{d}$	$dd \rightarrow W^-Zdu$	$\bar{u}\bar{u} \rightarrow W^-Z\bar{d}\bar{u}$
$cc \rightarrow W^+Zcs$	$\bar{s}\bar{s} \rightarrow W^+Z\bar{c}\bar{s}$	$ss \rightarrow W^-Zsc$	$\bar{c}\bar{c} \rightarrow W^-Z\bar{s}\bar{c}$
$uc \rightarrow W^+Zcd$	$\bar{d}\bar{s} \rightarrow W^+Z\bar{c}\bar{d}$	$sd \rightarrow W^-Zdc$	$\bar{c}\bar{u} \rightarrow W^-Z\bar{d}\bar{c}$
$cu \rightarrow W^+Zus$	$\bar{s}\bar{d} \rightarrow W^+Z\bar{u}\bar{s}$	$ds \rightarrow W^-Zsu$	$\bar{u}\bar{c} \rightarrow W^-Z\bar{s}\bar{u}$
$uu \rightarrow W^+Zus$	$\bar{d}\bar{d} \rightarrow W^+Z\bar{c}\bar{d}$	$dd \rightarrow W^-Zdc$	$\bar{u}\bar{u} \rightarrow W^-Z\bar{s}\bar{u}$
$cc \rightarrow W^+Zcd$	$\bar{s}\bar{s} \rightarrow W^+Z\bar{u}\bar{s}$	$ss \rightarrow W^-Zsu$	$\bar{c}\bar{c} \rightarrow W^-Z\bar{d}\bar{c}$
$uc \rightarrow W^+Zcs$	$\bar{d}\bar{s} \rightarrow W^+Z\bar{u}\bar{d}$	$sd \rightarrow W^-Zdu$	$\bar{c}\bar{u} \rightarrow W^-Z\bar{s}\bar{c}$
$cu \rightarrow W^+Zud$	$\bar{s}\bar{d} \rightarrow W^+Z\bar{c}\bar{s}$	$ds \rightarrow W^-Zsc$	$\bar{u}\bar{c} \rightarrow W^-Z\bar{d}\bar{u}$
	$\bar{b}\bar{d} \rightarrow W^+Z\bar{u}\bar{b}$	$bd \rightarrow W^-Zub$	
	$\bar{b}\bar{s} \rightarrow W^+Z\bar{c}\bar{b}$	$bs \rightarrow W^-Zcb$	
	$\bar{b}\bar{d} \rightarrow W^+Z\bar{c}\bar{b}$	$bd \rightarrow W^-Zcb$	
	$\bar{b}\bar{s} \rightarrow W^+Z\bar{u}\bar{b}$	$bs \rightarrow W^-Zub$	
$UD \rightarrow W^+ZDD$	$\bar{U}\bar{D} \rightarrow W^+Z\bar{U}\bar{D}$	$DU \rightarrow W^-ZUU$	$\bar{D}\bar{U} \rightarrow W^-Z\bar{D}\bar{D}$
$ud \rightarrow W^+Zdd$	$\bar{u}\bar{d} \rightarrow W^+Z\bar{u}\bar{u}$	$du \rightarrow W^-Zuu$	$\bar{d}\bar{u} \rightarrow W^-Z\bar{d}\bar{d}$
$cs \rightarrow W^+Zss$	$\bar{c}\bar{s} \rightarrow W^+Z\bar{c}\bar{c}$	$sc \rightarrow W^-Zcc$	$\bar{s}\bar{c} \rightarrow W^-Z\bar{s}\bar{s}$
$us \rightarrow W^+Zsd$	$\bar{u}\bar{s} \rightarrow W^+Z\bar{c}\bar{u}$	$su \rightarrow W^-Zuc$	$\bar{s}\bar{u} \rightarrow W^-Z\bar{d}\bar{s}$
$cd \rightarrow W^+Zds$	$\bar{c}\bar{d} \rightarrow W^+Z\bar{u}\bar{c}$	$dc \rightarrow W^-Zcu$	$\bar{d}\bar{c} \rightarrow W^-Z\bar{s}\bar{d}$
$us \rightarrow W^+Zss$	$\bar{u}\bar{s} \rightarrow W^+Z\bar{u}\bar{u}$	$su \rightarrow W^-Zuu$	$\bar{s}\bar{u} \rightarrow W^-Z\bar{s}\bar{s}$
$cd \rightarrow W^+Zdd$	$\bar{c}\bar{d} \rightarrow W^+Z\bar{c}\bar{c}$	$dc \rightarrow W^-Zcc$	$\bar{d}\bar{c} \rightarrow W^-Z\bar{d}\bar{d}$
$ud \rightarrow W^+Zds$	$\bar{u}\bar{d} \rightarrow W^+Z\bar{c}\bar{u}$	$du \rightarrow W^-Zuc$	$\bar{d}\bar{u} \rightarrow W^-Z\bar{s}\bar{d}$
$cs \rightarrow W^+Zsd$	$\bar{c}\bar{s} \rightarrow W^+Z\bar{u}\bar{c}$	$sc \rightarrow W^-Zcu$	$\bar{s}\bar{c} \rightarrow W^-Z\bar{d}\bar{s}$
$ub \rightarrow W^+Zbd$			$\bar{b}\bar{u} \rightarrow W^-Z\bar{d}\bar{b}$
$cb \rightarrow W^+Zbs$			$\bar{b}\bar{c} \rightarrow W^-Z\bar{s}\bar{b}$
$ub \rightarrow W^+Zbs$			$\bar{b}\bar{u} \rightarrow W^-Z\bar{s}\bar{b}$
$cb \rightarrow W^+Zbd$			$\bar{b}\bar{c} \rightarrow W^-Z\bar{d}\bar{b}$

Table 3.9: As in Table 3.7, but for all partonic subprocesses containing four external quarks or four external antiquarks, which contribute to $pp/p\bar{p} \rightarrow WZ+\text{jet}$ at NLO QCD. The subprocesses of column 1 and 4 as well as those of column 2 and 3 are charge conjugated to each other.

Chapter 4

Evaluation of helicity amplitudes for VV+jet production

The evaluation of matrix elements for all subprocesses contributing to VV+jet production at NLO QCD is performed in this chapter with the gauge bosons considered as stable particles. The complete evaluation of the LO amplitudes and the real-emission amplitudes is performed by application of the Weyl–van-der-Waerden (WvdW) spinor technique for helicity amplitudes [72], which is briefly outlined in Section 4.1.

Since the number of contributing subprocesses is $\mathcal{O}(100)$ for each of the gauge-boson assignments, the matrix elements must be built in a generic way. For this purpose, general building blocks to construct the amplitudes are evaluated in Section 4.2 without specifying the gauge bosons.

In Section 4.3, the building blocks are combined to subamplitudes representing the minimal selections of diagrams which are gauge invariant with respect to $SU(3)_C$. In general, they do not describe full amplitudes yet.

The composition of these subamplitudes to full amplitudes for specific gauge-boson pairs is performed in Section 4.4.

In Section 4.5, absolute squares of the matrix elements are taken. For this purpose, the different colour structures in the amplitudes of the subprocesses are considered. Spins and colours of outgoing particles are summed over, those of initial state particles are averaged. Symmetry factors for identical final-state particles arising from the phase-space integration are already included at this point.

4.1 Weyl–van-der-Waerden formalism for evaluating helicity amplitudes

From the SM Lagrangian density presented in Section 2.1, Feynman rules can be derived that are used to perform the perturbative calculation of the matrix elements for scattering processes. These Feynman rules are usually given in terms of the Dirac formalism where fermionic wave functions are expressed in terms of four-component spinors, and the

absolute-squared amplitudes are evaluated by making use of the completeness relations for the external particles. One of the main drawbacks of this formalism is the quadratic growth of the number of terms to be evaluated with the number of contributing Feynman diagrams. Therefore, in the calculations of this thesis, the WvdW formalism in the form presented in Ref. [72] is applied in order to calculate helicity amplitudes, which leads only to a linear growth of complexity with the number of diagrams. This advantage is partially compensated by the fact that the amplitudes have to be calculated for each helicity configuration. In practice, this is not as problematic as squaring amplitudes, because discrete symmetries between different helicity channels can be applied to reduce the number of independent contributions to be evaluated.

The general idea of the WvdW formalism is to express particle momenta and wave functions in terms of two-component spinors, which form fundamental representations of the Lorentz group. A detailed introduction to the WvdW formalism and the relevant derivations are given in Ref. [72]. Further details including the extensions for treating QCD amplitudes can be found in the references therein. The formulae that are relevant for this work are already presented in Ref. [73].

4.1.1 Basic definitions

At this point, only a brief overview of the most relevant definitions and a collection of all Feynman rules needed in this thesis are given. All arising spinor and bispinor expressions can be written in terms of the following two spinors,

$$n_{1,A} = \begin{pmatrix} e^{-i\varphi} \cos \frac{\theta}{2} \\ \sin \frac{\theta}{2} \end{pmatrix}, \quad n_{2,A} = \begin{pmatrix} \sin \frac{\theta}{2} \\ -e^{+i\varphi} \cos \frac{\theta}{2} \end{pmatrix}, \quad (4.1)$$

where φ and θ are the polar angles of the respective momentum $k^\mu = (k^0, |\mathbf{k}| \sin \theta \cos \varphi, |\mathbf{k}| \sin \theta \sin \varphi, |\mathbf{k}| \cos \theta)$. The spinors used in the description of the wave functions of all massless particles are defined by

$$k_A = \sqrt{2k_0} n_{1,A}. \quad (4.2)$$

The spinors with dotted indices are obtained by complex conjugation. By the spinor metric, which is defined for upper and lower, dotted and undotted indices as

$$\epsilon_{AB} = \epsilon^{AB} = \epsilon_{\dot{A}\dot{B}} = \epsilon^{\dot{A}\dot{B}} = \begin{pmatrix} 0 & +1 \\ -1 & 0 \end{pmatrix}, \quad (4.3)$$

an antisymmetric spinor product is defined for both types,

$$\langle \phi \psi \rangle = \phi_A \epsilon^{AB} \psi_B, \quad \langle \phi \psi \rangle^* = \phi_{\dot{A}} \epsilon^{\dot{A}\dot{B}} \psi_{\dot{B}}. \quad (4.4)$$

The momentum bispinor, which corresponds to a momentum translated to the WvdW formalism, can be written as

$$K_{\dot{A}B} = \sum_{i=1,2} \kappa_{i,\dot{A}} \kappa_{i,B}, \quad \text{where } \kappa_{i,A} = \sqrt{\lambda_i} n_{i,A} \text{ with } \lambda_{1,2} = k_0 \pm |\mathbf{k}|. \quad (4.5)$$

Incoming fields	Outgoing fields
Right-handed massless fermions ($\sigma = R$)	
$\xrightarrow{A} \bullet \quad \Psi_1^{(+)}(p) \longrightarrow \begin{pmatrix} \phi_A \\ 0 \end{pmatrix}$	$\bullet \xrightarrow{A} \quad \bar{\Psi}_1^{(+)}(p) \longrightarrow (0, \phi_{\dot{A}})$
Left-handed massless fermions ($\sigma = L$)	
$\xrightarrow{A} \bullet \quad \Psi_2^{(+)}(p) \longrightarrow \begin{pmatrix} 0 \\ \phi^{\dot{A}} \end{pmatrix}$	$\bullet \xrightarrow{A} \quad \bar{\Psi}_2^{(+)}(p) \longrightarrow (\phi^A, 0)$
Right-handed massless antifermions ($\sigma' = L$)	
$\xleftarrow{A} \bullet \quad \Psi_2^{(-)}(p') \longrightarrow (\phi'^A, 0)$	$\bullet \xleftarrow{A} \quad \bar{\Psi}_2^{(-)}(p') \longrightarrow \begin{pmatrix} 0 \\ \phi'^{\dot{A}} \end{pmatrix}$
Left-handed massless antifermions ($\sigma' = R$)	
$\xleftarrow{A} \bullet \quad \Psi_1^{(-)}(p') \longrightarrow (\phi'_{\dot{A}}, 0)$	$\bullet \xleftarrow{A} \quad \bar{\Psi}_1^{(-)}(p') \longrightarrow \begin{pmatrix} \phi'_A \\ 0 \end{pmatrix}$

Table 4.1: Translation rules from the Dirac to the WvdW formalism for the wave functions of massless fermions.

In case of massless particles, the momentum bispinor factorizes to

$$K_{\dot{A}B} = k_{\dot{A}} k_B , \quad (4.6)$$

where again the definition of Eq. (4.2) is applied.

In Table 4.1, the wave functions for massless fermions are collected, using the definitions for spinors derived from massless momenta. Massive fermions appear only as intermediate states in the calculations of this thesis. Hence, no respective wave functions are needed.

The rules how to translate polarization vectors to the respective bispinors are collected in Table 4.2 for all vector particles relevant in VV+jet production.

The polarization bispinors of outgoing massive gauge bosons—incoming ones are naturally not considered in this context—are given by

$$v_{\dot{A}B}^*(k, +) = \sqrt{2} n_{1,\dot{A}} n_{2,B} , \quad v_{\dot{A}B}^*(k, -) = \sqrt{2} n_{2,\dot{A}} n_{1,B} , \quad (4.7)$$

$$v_{\dot{A}B}^*(k, 0) = \frac{1}{M_V} (\kappa_{1,\dot{A}} \kappa_{1,B} - \kappa_{2,\dot{A}} \kappa_{2,B}) , \quad (4.8)$$

for the two transversal polarizations and the longitudinal one, where again the definitions of Eqs. (4.1) and (4.5) are used.

Electroweak massive gauge bosons ($\lambda = \pm, 0$)			
$\begin{array}{c} AB \\ \sim \\ \mu \end{array}$	$v_\mu(k, \lambda) \longrightarrow v_{\dot{A}\dot{B}}(k, \lambda)$	$\begin{array}{c} AB \\ \bullet \sim \\ \mu \end{array}$	$v_\mu^*(k, \lambda) \longrightarrow v_{\dot{A}\dot{B}}^*(k, \lambda)$
Gluons ($\tau = \pm$)			
$\begin{array}{c} AB \\ \sim \\ \mu \end{array}$	$\varepsilon_\mu^a(k, \tau) \longrightarrow \varepsilon_{\dot{A}\dot{B}}^a(k, \tau)$	$\begin{array}{c} AB \\ \bullet \sim \\ \mu \end{array}$	$\varepsilon_\mu^{*a}(k, \tau) \longrightarrow \varepsilon_{\dot{A}\dot{B}}^{*a}(k, \tau)$

Table 4.2: Translation rules from the Dirac to the WvdW formalism for the wave functions of all external vector particles appearing in the calculation of VV+jet production.

Propagators			
$\begin{array}{c} B \quad k \quad A \\ \bullet \longrightarrow \bullet \\ f \end{array}$	$\frac{i(\not{k} + m_f)}{k^2 - m_f^2}$	\longrightarrow	$\frac{i}{k^2 - m_f^2} \begin{pmatrix} m_f \delta_A^B & K_{A\dot{B}} \\ K^{\dot{A}B} & m_f \delta_{\dot{B}}^A \end{pmatrix}$
$\begin{array}{c} AB \quad CD \\ \bullet \sim \bullet \\ \mu \quad V \quad \nu \end{array}$	$\frac{-ig_{\mu\nu}}{k^2 - M_V^2}$	\longrightarrow	$\frac{-2i\epsilon_{\dot{A}\dot{C}}\epsilon_{BD}}{k^2 - M_V^2}$
$\begin{array}{c} AB \quad CD \\ \bullet \sim \bullet \\ \mu \quad g \quad \nu \end{array}$	$\frac{-i\delta^{ab}g_{\mu\nu}}{k^2}$	\longrightarrow	$\frac{-2i\delta^{ab}\epsilon_{\dot{A}\dot{C}}\epsilon_{BD}}{k^2}$

Table 4.3: Translation rules from the Dirac to the WvdW formalism for propagators.

In case of massless vector particles like gluons, the longitudinal polarization does not exist with the corresponding degree of freedom manifesting itself in the arbitrariness of gauge for the remaining transversal polarizations. Therefore, an arbitrary spinor $g_{\pm, A}$ with $\langle g_{\pm} k \rangle \neq 0$, the so-called gauge spinor, shows up in the definitions of polarization bispinors for incoming and outgoing gluons, respectively,

$$\varepsilon_{\dot{A}\dot{B}}(k, +) = \frac{\sqrt{2} g_{+, \dot{A}} k_B}{\langle g_+ k \rangle^*}, \quad \varepsilon_{\dot{A}\dot{B}}(k, -) = \frac{\sqrt{2} k_{\dot{A}} g_{-, B}}{\langle g_- k \rangle}, \quad (4.9)$$

$$\varepsilon_{\dot{A}\dot{B}}^*(k, +) = \frac{\sqrt{2} k_{\dot{A}} g_{+, B}}{\langle g_+ k \rangle}, \quad \varepsilon_{\dot{A}\dot{B}}^*(k, -) = \frac{\sqrt{2} g_{-, \dot{A}} k_B}{\langle g_- k \rangle^*}. \quad (4.10)$$

The translation rules for fermionic and bosonic propagators are collected in Table 4.3, those for all relevant vertices in Table 4.4. In the following, the definitions of the couplings listed in Table 4.4 are given, starting with the fermion–gauge–boson couplings,

$$C_{\gamma\text{ff}}^\pm = -Q_f, \quad (4.11)$$

$$C_{\text{Zff}}^+ = -Q_f \frac{\cos \theta_W}{\sin \theta_W}, \quad C_{\text{Zff}}^- = -Q_f \frac{\cos \theta_W}{\sin \theta_W} + \frac{I_f^3}{\sin \theta_W \cos \theta_W}, \quad (4.12)$$

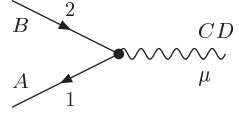
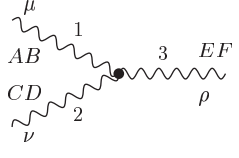
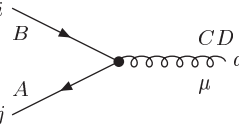
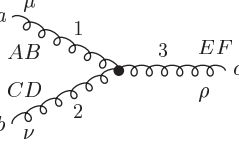
Vertices		
	$ie\gamma^\mu C_{V\bar{f}_1 f_2}^\tau \omega_\tau$	$\longrightarrow ie \begin{pmatrix} 0 & C_{V\bar{f}_1 f_2}^- \delta_B^{\dot{C}} \delta_A^{\dot{D}} \\ C_{V\bar{f}_1 f_2}^+ \epsilon^{\dot{A}\dot{C}} \epsilon^{BD} & 0 \end{pmatrix}$
	$ieC_{V_1 V_2 V_3} [g^{\mu\nu}(k_1 - k_2)^\rho + g^{\nu\rho}(k_2 - k_3)^\mu + g^{\mu\rho}(k_3 - k_1)^\nu]$	$\longrightarrow \frac{i}{4}eC_{V_1 V_2 V_3} \left[\epsilon^{\dot{A}\dot{C}} \epsilon^{BD} (K_1 - K_2)^{\dot{E}F} + \epsilon^{\dot{C}\dot{E}} \epsilon^{DF} (K_2 - K_3)^{\dot{A}B} + \epsilon^{\dot{A}\dot{E}} \epsilon^{BF} (K_3 - K_1)^{\dot{C}D} \right]$
	$-ig_s T_{ji}^a \gamma^\mu$	$\longrightarrow -ig_s T_{ji}^a \begin{pmatrix} 0 & \delta_B^{\dot{C}} \delta_A^{\dot{D}} \\ \epsilon^{\dot{A}\dot{C}} \epsilon^{BD} & 0 \end{pmatrix}$
	$-g_s f^{abc} [g^{\mu\nu}(k_1 - k_2)^\rho + g^{\nu\rho}(k_2 - k_3)^\mu + g^{\mu\rho}(k_3 - k_1)^\nu]$	$\longrightarrow -\frac{1}{4}g_s f^{abc} \left[\epsilon^{\dot{A}\dot{C}} \epsilon^{BD} (K_1 - K_2)^{\dot{E}F} + \epsilon^{\dot{C}\dot{E}} \epsilon^{DF} (K_2 - K_3)^{\dot{A}B} + \epsilon^{\dot{A}\dot{E}} \epsilon^{BF} (K_3 - K_1)^{\dot{C}D} \right]$

Table 4.4: Translation rules from the Dirac to the WvdW formalism for all vertices relevant in VV+jet production. The couplings are defined for all particles incoming.

$$\begin{aligned}
C_{W^\pm \bar{f}_i f_j}^+ &= 0, \quad C_{W^+ \bar{u}_i d_j}^- = V_{u_i d_j} C_W^-, \quad C_{W^- \bar{d}_j u_i}^- = V_{u_i d_j}^* C_W^-, \\
C_{W^+ \bar{\nu}_i l_j}^- &= \delta_{ij} C_W^-, \quad C_{W^- \bar{l}_j \nu_i}^- = \delta_{ij} C_W^-, \quad C_W^- = \frac{1}{\sqrt{2} \sin \theta_W},
\end{aligned} \tag{4.13}$$

where $f = u_i, d_i, l_i, \nu_i$, $u_i = u, c, t$, $d_i = d, s, b$, $\nu_i = \nu_e, \nu_\mu, \nu_\tau$, $l_i = e, \mu, \tau$ and $i, j = 1, 2, 3$ corresponding to the three families of quarks and leptons. The quantities $V_{u_i d_j}$ denote the entries of the CKM matrix given in Eq. (3.1) in the applied approximation. Q_f and I_f^3 are the electric charge and the third component of the weak isospin of the fermion f as given in Table 2.1.

The remaining definitions refer to three-gauge-boson vertices, where the non-vanishing couplings are, again with all particles incoming,

$$C_{\gamma W^- W^+} = -1, \quad C_{ZW^- W^+} = \frac{\cos \theta_W}{\sin \theta_W}. \tag{4.14}$$

All cyclic permutations of the same gauge bosons in the vertex result in the identical coupling, whereas anti-cyclic permutations lead to a relative minus sign, which can be easily understood from the symmetry properties of the vertex definition.

4.1.2 Discrete symmetries

To reduce the number of helicity amplitudes to be explicitly evaluated, discrete symmetries can be applied to relate amplitudes or subamplitudes of different processes or of one and the same process. The discrete symmetries used in the calculations of this thesis are crossing symmetry, a modified parity transformation \mathcal{P} , and the combined application of parity transformation and charge conjugation \mathcal{CP} , which is again a symmetry in the SM in the used approximation for the CKM matrix. Details on the derivation of these transformations can be found in Ref. [72]. Here, only the recipes to apply these transformations are given.

Crossing symmetry transforms an incoming particle into the corresponding outgoing antiparticle and vice versa. The inversion of the respective momenta is—apart from irrelevant phase factors—realized by inverting only the signs of the dotted spinors derived from this momentum, but leaving the undotted ones unchanged. Since only $2 \rightarrow n$ scattering processes are considered, crossing symmetry is always applied to pairs of particles. The crossing of an incoming/outgoing particle with momentum k_1 and an outgoing/incoming particle with momentum k_2 is denoted by $\mathcal{X}[k_1 \leftrightarrow k_2]$. In addition, the helicities of the crossed partons are exchanged, i.e. an incoming left-handed fermion becomes a right-handed outgoing antifermion, etc. Applying crossing symmetry to unpolarized squared matrix elements means that the crossing has to be applied to all helicity amplitudes needed in the evaluation. The rearrangement of helicity channels due to particle crossing is irrelevant here since all external helicities are summed over.

The amplitude for opposite helicities of all external particles and inverted spatial parts of their momenta can be obtained—up to an irrelevant phase factor—by complex conjugation of an amplitude if in addition all chirality-dependent couplings are exchanged, i.e. $C_{\dots}^+ \leftrightarrow C_{\dots}^-$. The corresponding transformation is denoted by \mathcal{P} , although exchanging chirality-dependent couplings is not included in the usual parity transformation. However, since parity is not a symmetry in the SM, the \mathcal{P} transformation is defined in this way in order to relate amplitudes for different helicity channels of SM subprocesses.

The combined application of parity transformation and charge conjugation is a symmetry in the SM if phases in the CKM matrix are neglected as in the used approximation. Therefore, taking the complex conjugate of a helicity amplitude reproduces an amplitude to another subprocess up to an irrelevant sign factor, as if the amplitude was calculated directly from the rules presented in this section. This subprocess involves the respective antiparticles with the spatial parts of the momenta inverted and all external helicities reversed, but without interchanging chiral couplings. The transformation, which is indicated by \mathcal{CP} , is also applied to unpolarized squared matrix elements. This is meant in the sense that all helicity amplitudes are obtained from the respective amplitudes by applying \mathcal{CP} symmetry, and the squared amplitudes are finally summed over all external spins. For unpolarized matrix elements the rearrangement of helicity channels is again irrelevant.

The phase factors mentioned in this section are irrelevant for the evaluation of squared tree-level matrix elements. When calculating dipole terms from helicity amplitudes as in Section 5.2, the phase conventions have to be known in some constellations. The needed phase conventions are taken from Ref. [72].

4.2 Building blocks of VV+jet production amplitudes

The evaluation of matrix elements for all contributing subprocesses is performed by application of the WvdW spinor technique for helicity amplitudes in the form presented in Ref. [72], which is briefly outlined in the previous section. Making use of helicity amplitudes is especially convenient in this case, since all external fermions are treated as massless particles, which reduces the number of non-vanishing helicity channels significantly. A further reduction of the number of channels results from the maximal parity violation of the W boson.

The bispinors describing the polarizations of the outgoing massive gauge bosons are not inserted analytically into the expressions given in this section, since no further simplifications are expected from this step. Besides, the number of expressions to be evaluated analytically is reduced by a factor of nine due to the two massive gauge bosons in the final state. Furthermore, this approach is very useful for the implementation of leptonic decays of the gauge bosons. To this end, the polarization bispinors are replaced by a gauge-boson propagator and the leptonic current of the decay products in order to obtain resonant diagrams. Details on this procedure will be given in Chapter 6.

The notation used in this chapter provides all relevant parameters for each particle: In the brackets after the particle first its momentum is given. The upper entry is the colour index for all colour-charged partons: The letters $a, b, c = 1, \dots, 8$ are used for gluons, $i, j, k, l = 1, 2, 3$ for quarks and antiquarks. All other particles do not carry colour charges, so the corresponding entry is omitted. The lower entry gives the polarization or helicity of the corresponding particle: In case of (anti-)fermions, ‘L’ is used for left-handed and ‘R’ for right-handed particles. For vector bosons, the polarization is either given by ‘+’ or ‘−’. Otherwise, the entry is the polarization vector if the polarization of the particle is not specified yet. For incoming massive vector particles, it is denoted by v , for outgoing ones by v^* . For incoming and outgoing gluons we use g and g^* , respectively. In the construction of amplitudes, “products” of production and decay building blocks for the same vector boson are taken. This is understood in the sense that the polarization bispinor of the outgoing particle, v^*/g^* , is omitted, which is additionally indicated by a hat over the reduced building block. The bispinor-valued expression containing v/g is contracted with the resulting open spinor indices of the reduced amplitude.

The spinor and bispinor expressions used in the building blocks and the (sub-)amplitudes are in one-to-one correspondence to the particle momenta. This correspondence is declared in Tables 4.5 and 4.6 for all particles appearing in the calculation. Only building blocks for amplitudes with an incoming quark–antiquark pair are calculated, because all other amplitudes needed can be obtained from these by application of crossing symmetry—either to full amplitudes or to subamplitudes.

4.2.1 Expressions with bispinor-like structure

We start with the calculation of building blocks with bispinor-like structure, i.e. with two open spinor indices, which are used to replace polarization bispinors of outgoing bosons.

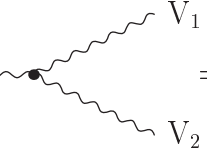
(Anti-)quark	momentum vector	spinor	momentum bispinor
incoming quark	p^μ	ϕ_A	$P_{\dot{A}B}$
incoming antiquark	p'^μ	ϕ'_A	$P'_{\dot{A}B}$
outgoing quark	q^μ	η_A	$Q_{\dot{A}B}$
outgoing antiquark	q'^μ	η'_A	$Q'_{\dot{A}B}$

Table 4.5: Notation for (anti-)quarks: momenta, spinors and bispinors.

Vector boson	momentum vector	momentum bispinor	spinor	polarization bispinor
outgoing gluon	k^μ	$K_{\dot{A}B}$	k_A	$g_{k\tau, \dot{A}B}^*$
outgoing gluon	l^μ	$L_{\dot{A}B}$	l_A	$g_{l\tau', \dot{A}B}^*$
outgoing gauge boson	k_1^μ	$K_{1, \dot{A}B}$	—	$v_{1, \dot{A}B}^*$
outgoing gauge boson	k_2^μ	$K_{2, \dot{A}B}$	—	$v_{2, \dot{A}B}^*$

Table 4.6: Notation for vector particles: momenta, polarization and momentum bispinors.

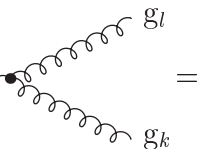
The first building block is needed for all diagrams containing vertices of three electroweak gauge bosons, which are shown in Figures 3.7, 3.9, and 3.11,

$$\mathcal{A}\left(V\left[\begin{smallmatrix} y \\ v \end{smallmatrix}\right] \rightarrow V_1\left[\begin{smallmatrix} k_1 \\ v_1^* \end{smallmatrix}\right] V_2\left[\begin{smallmatrix} k_2 \\ v_2^* \end{smallmatrix}\right]\right) \equiv \text{Diagram} = \frac{1}{2} e C_{V\bar{V}_1\bar{V}_2} \frac{\mathcal{V}_{\dot{K}L}}{(y^2 - M_V^2)}, \quad (4.15)$$


$$\mathcal{V}_{\dot{K}L} = v_{1, \dot{U}V}^* v_2^{* \dot{U}V} (K_2 - K_1)_{\dot{K}L} + 2 v_{2, \dot{U}V}^* K_1^{\dot{U}V} v_{1, \dot{K}L}^* - 2 v_{1, \dot{U}V}^* K_2^{\dot{U}V} v_{2, \dot{K}L}^*. \quad (4.16)$$

The intermediate gauge boson V can be either a photon or a Z boson in case of WW +jet production. For $W^\pm Z$ +jet production, only diagrams with $V = W^\pm$ contribute, respectively. In ZZ +jet production, no diagrams with intermediate gauge bosons show up, since all vertices with only neutral gauge bosons attached, namely γZZ and ZZZ , vanish.

In the real-emission subprocesses with two outgoing gluons, which are shown in the diagrams in the last rows of Figures 3.8 and 3.9, respectively, the following building block is needed due to the non-Abelian structure of QCD,

$$\mathcal{A}\left(g\left[\begin{smallmatrix} c \\ k+l \\ g \end{smallmatrix}\right] \rightarrow g\left[\begin{smallmatrix} a \\ k \\ g_k^* \end{smallmatrix}\right] g\left[\begin{smallmatrix} b \\ l \\ g_l^* \end{smallmatrix}\right]\right) \equiv \text{Diagram} = \frac{i}{2} g_s f^{abc} \frac{\mathcal{G}(k, l)_{\dot{A}B}}{(k+l)^2}, \quad (4.17)$$


$$\mathcal{G}(k, l)_{\dot{A}B} = g_{k, \dot{U}V}^* g_l^{* \dot{U}V} (L - K)_{\dot{A}B} + 2 g_{l, \dot{U}V}^* K^{\dot{U}V} g_{k, \dot{A}B}^* - 2 g_{k, \dot{U}V}^* L^{\dot{U}V} g_{l, \dot{A}B}^*. \quad (4.18)$$

In the real-emission amplitudes with two different fermion chains, some diagrams contribute where the intermediate gluon decays into a quark–antiquark pair with the gauge-boson pair coupling to the other fermion chain. For these diagrams, which are shown in Figures 3.10 and 3.11, one needs

$$\begin{aligned}
 \mathcal{A}\left(g\left[\begin{smallmatrix} a \\ q+q' \\ g \end{smallmatrix}\right] \rightarrow q_3\left[\begin{smallmatrix} k \\ q \\ \tau \end{smallmatrix}\right] \bar{q}_4\left[\begin{smallmatrix} l \\ q' \\ \tau' \end{smallmatrix}\right]\right) &\equiv g \bullet \text{---} \text{---} \text{---} \text{---} \text{---} \text{---} \bullet \begin{array}{l} \nearrow q_3 \\ \searrow \bar{q}_4 \end{array} \\
 &= \begin{cases} -2 g_s T_{kl}^a \frac{\eta_A' \eta_B'}{(q+q')^2} & \text{for } \tau = L, \tau' = R, \\ -2 g_s T_{kl}^a \frac{\eta_A' \eta_B}{(q+q')^2} & \text{for } \tau = R, \tau' = L. \end{cases} \quad (4.19)
 \end{aligned}$$

Diagrams with both weak gauge bosons coupling to the fermion chain of the outgoing quark–antiquark pair do not have to be evaluated separately, since their amplitudes can be obtained by application of crossing symmetry. Consequently, no such building blocks need to be given here.

Some of the real-emission amplitudes with two fermion chains also contain diagrams with the two gauge bosons coupling to different chains, which are presented in Figure 3.12. If $V_1 = Z$, q_3 and \bar{q}_4 belong to the same flavour. For $V_1 = W^\pm$, q_3 is of up/down-type and \bar{q}_4 of down/up-type according to charge conservation. In the latter case, only (anti-)quarks of the two light generations contribute, since top (anti-)quarks are not taken into account as final-state particles, and mixing between the first two and the third generation is neglected in the applied approximation of the CKM matrix. Therefore, no internal quark masses have to be taken into account, and the corresponding building blocks read

$$\begin{aligned}
 \mathcal{A}\left(g\left[\begin{smallmatrix} a \\ g \\ g \end{smallmatrix}\right] \rightarrow V_1\left[\begin{smallmatrix} k_1 \\ v_1^* \end{smallmatrix}\right] q_3\left[\begin{smallmatrix} k \\ q \\ \tau \end{smallmatrix}\right] \bar{q}_4\left[\begin{smallmatrix} l \\ q' \\ \tau' \end{smallmatrix}\right]\right) &\equiv g \bullet \text{---} \text{---} \text{---} \text{---} \text{---} \bullet \begin{array}{l} \nearrow q_3 \\ \searrow \bar{q}_3 \end{array} \text{---} \text{---} \text{---} \text{---} \text{---} \text{---} \bullet \begin{array}{l} \nearrow q_3 \\ \searrow \bar{q}_4 \end{array} + g \bullet \text{---} \text{---} \text{---} \text{---} \text{---} \bullet \begin{array}{l} \nearrow q_3 \\ \searrow \bar{q}_4 \end{array} \text{---} \text{---} \text{---} \text{---} \text{---} \text{---} \bullet \begin{array}{l} \nearrow q_3 \\ \searrow \bar{q}_4 \end{array} \\
 &= 2 g_s T_{kl}^a e^2 v_{1,\dot{E}F}^* \frac{1}{y^2} \\
 &\quad \times \begin{cases} C_{V_1 \bar{q}_3 q_4}^- \left[\frac{\eta_A'(Q+K_2)^{\dot{E}V} \epsilon_{VB} \eta^F}{(q+k_2)^2} - \frac{\eta'^{\dot{E}}(Q'+K_2)^{\dot{U}F} \epsilon_{\dot{U}A} \eta_B}{(q'+k_2)^2} \right] & \text{for } \tau = L, \tau' = R, \\ C_{V_1 \bar{q}_3 q_4}^+ \left[\frac{\eta^{\dot{E}}(Q+K_2)^{\dot{U}F} \epsilon_{\dot{U}A} \eta_B'}{(q+k_2)^2} - \frac{\eta_A(Q'+K_2)^{\dot{E}V} \epsilon_{VB} \eta'^F}{(q'+k_2)^2} \right] & \text{for } \tau = R, \tau' = L. \end{cases} \quad (4.20)
 \end{aligned}$$

4.2.2 Expressions with an initial-state quark–antiquark pair

To obtain the subamplitudes given in the following section, one needs to calculate building blocks containing an initial-state quark–antiquark pair. For the vector bosons that couple to this fermion chain, generic polarization bispinors are inserted in the first step. These bispinors can be replaced either by polarization bispinors for specific outgoing particles or by the expressions of the previous subsection if the respective boson is an intermediate particle. Only one helicity configuration $\sigma\sigma'$ of the incoming quark–antiquark pair has to be evaluated explicitly for all building blocks provided in this subsection. Whereas the helicity combinations $\sigma\sigma' = \text{RR}, \text{LL}$ vanish for massless quarks, $\sigma\sigma' = \text{LR}, \text{RL}$ can be obtained from each other by application of a \mathcal{P} transformation. Thus, only building blocks for $\sigma\sigma' = \text{LR}$ are calculated.

The first group of diagrams to be evaluated here contains one gluon and one electroweak gauge boson attached to the fermion chain, where both possible orders have to be taken into account. The resulting expression can also be obtained from Eq. (4.20) by crossing the outgoing quark–antiquark pair into the initial state,

$$\begin{aligned}
 \mathcal{A}\left(q_1 \begin{bmatrix} i \\ p \\ \sigma \end{bmatrix} \bar{q}_2 \begin{bmatrix} j \\ p' \\ \sigma' \end{bmatrix} \rightarrow V \begin{bmatrix} y \\ v^* \end{bmatrix} g \begin{bmatrix} a \\ k \\ g^* \end{bmatrix}\right) &\equiv \text{diagram 1} + \text{diagram 2} \\
 \mathcal{A}\left(q_1 \begin{bmatrix} i \\ p \\ \text{L} \end{bmatrix} \bar{q}_2 \begin{bmatrix} j \\ p' \\ \text{R} \end{bmatrix} \rightarrow V \begin{bmatrix} y \\ v^* \end{bmatrix} g \begin{bmatrix} a \\ k \\ g^* \end{bmatrix}\right) &= i g_s T_{ji}^a e C_{V\bar{q}_2 q_1}^- g_{AB}^* v_{KL}^* \\
 &\times \left[\frac{\phi'^B (K - P')^{\dot{A}L} \phi^{\dot{K}}}{(k - p')^2} + \frac{\phi^{\dot{A}} (P - K)^{\dot{K}B} \phi'^L}{(p - k)^2} \right]. \tag{4.21}
 \end{aligned}$$

Combining Eqs. (4.15) and (4.21) and summing over all possible intermediate gauge bosons results in

$$\begin{aligned}
 \mathcal{A}_V\left(q_1 \begin{bmatrix} i \\ p \\ \sigma \end{bmatrix} \bar{q}_2 \begin{bmatrix} j \\ p' \\ \sigma' \end{bmatrix} \rightarrow V_1 \begin{bmatrix} k_1 \\ v_1^* \end{bmatrix} V_2 \begin{bmatrix} k_2 \\ v_2^* \end{bmatrix} g \begin{bmatrix} a \\ k \\ g^* \end{bmatrix}\right) \\
 \equiv \text{diagram 3} + \text{diagram 4} \\
 = \sum_V \hat{\mathcal{A}}\left(q_1 \begin{bmatrix} i \\ p \\ \sigma \end{bmatrix} \bar{q}_2 \begin{bmatrix} j \\ p' \\ \sigma' \end{bmatrix} \rightarrow V \begin{bmatrix} y \\ v^* \end{bmatrix} g \begin{bmatrix} a \\ k \\ g^* \end{bmatrix}\right) \mathcal{A}\left(V \begin{bmatrix} y \\ v \end{bmatrix} \rightarrow V_1 \begin{bmatrix} k_1 \\ v_1^* \end{bmatrix} V_2 \begin{bmatrix} k_2 \\ v_2^* \end{bmatrix}\right),
 \end{aligned}$$

$$\mathcal{A}_V\left(q_1\begin{bmatrix}i\\p\\L\end{bmatrix}\bar{q}_2\begin{bmatrix}j\\p'\\R\end{bmatrix}\rightarrow V_1\begin{bmatrix}k_1\\v_1^*\end{bmatrix}V_2\begin{bmatrix}k_2\\v_2^*\end{bmatrix}g\begin{bmatrix}a\\k\\g^*\end{bmatrix}\right) = \frac{i}{2}g_s T_{ji}^a e^2 g_{AB}^* \sum_V \frac{C_{V\bar{q}_2q_1}^- C_{V\bar{V}_1\bar{V}_2} \mathcal{V}_{KL}}{y^2 - M_V^2} \\ \times \left[\frac{\phi'^B(K-P')^{\dot{A}L}\phi^{\dot{K}}}{(k-p')^2} + \frac{\phi^{\dot{A}}(P-K)^{\dot{K}B}\phi'^L}{(p-k)^2} \right], \quad (4.22)$$

where \mathcal{V}_{KL} is given in Eq. (4.16). Since W bosons couple only to left-handed fermions and right-handed antifermions, the inverse helicity configuration delivers a non-vanishing contribution only if the intermediate vector boson is not a W boson, but a Z boson or a photon, which is the case for WW+jet production. The resulting expression with the polarization bispinors for all outgoing vector bosons inserted already gives one of two sub-amplitudes contributing at LO.

For the second subamplitude, the following group of diagrams is needed, where the two weak gauge bosons couple directly to the fermion chain. Here, only the diagram group for one order of the two weak gauge bosons is calculated, whereas the other order can be obtained by interchanging V_1 and V_2 ,

$$\mathcal{A}_Q\left(q_1\begin{bmatrix}i\\p\\L\end{bmatrix}\bar{q}_2\begin{bmatrix}j\\p'\\R\end{bmatrix}\rightarrow V_1\begin{bmatrix}k_1\\v_1^*\end{bmatrix}V_2\begin{bmatrix}k_2\\v_2^*\end{bmatrix}g\begin{bmatrix}a\\k\\g^*\end{bmatrix}\right)$$

$$\equiv$$

$$\mathcal{A}_Q\left(q_1\begin{bmatrix}i\\p\\L\end{bmatrix}\bar{q}_2\begin{bmatrix}j\\p'\\R\end{bmatrix}\rightarrow V_1\begin{bmatrix}k_1\\v_1^*\end{bmatrix}V_2\begin{bmatrix}k_2\\v_2^*\end{bmatrix}g\begin{bmatrix}a\\k\\g^*\end{bmatrix}\right) = -i g_s T_{ji}^a e^2 g_{AB}^* v_{1,\dot{E}F}^* v_{2,\dot{G}H}^* \sum_q C_{V_2\bar{q}_2q}^- C_{V_1\bar{q}q_1}^- \\ \times \left[\frac{\phi^{\dot{E}}(P-K_1)^{\dot{A}F}(K_2-P')^{\dot{G}B}\phi'^H}{((p-k_1)^2 - m_q^2)((k_2-p')^2 - m_q^2)} + \frac{\phi^{\dot{A}}(P-K)^{\dot{E}B}(K_2-P')^{\dot{G}F}\phi'^H}{(p-k)^2((k_2-p')^2 - m_q^2)} \right. \\ \left. + \frac{\phi^{\dot{E}}(P-K_1)^{\dot{G}F}(K-P')^{\dot{A}H}\phi'^B}{(k-p')^2((p-k_1)^2 - m_q^2)} + \frac{m_q^2 \phi^{\dot{E}}\epsilon^{\dot{A}\dot{G}}\epsilon^{BF}\phi'^H}{((p-k_1)^2 - m_q^2)((k_2-p')^2 - m_q^2)} \right]. \quad (4.23)$$

The diagram group with the inverse order of the two gauge bosons can be constructed from this expression by interchanging their momenta and polarization bispinors, as well as the respective couplings. Both orders contribute to the same subprocess only for ZZ+jet and WZ+jet production. In case of WW+jet production, the order of the W bosons is determined by charge conservation, since no intermediate quark state with an electric charge of $\frac{5}{3}e$ or $-\frac{4}{3}e$ exists. The sum over the intermediate quark q runs over all quarks with non-vanishing couplings for the respective weak-gauge-boson and external (anti-)quark assignments.

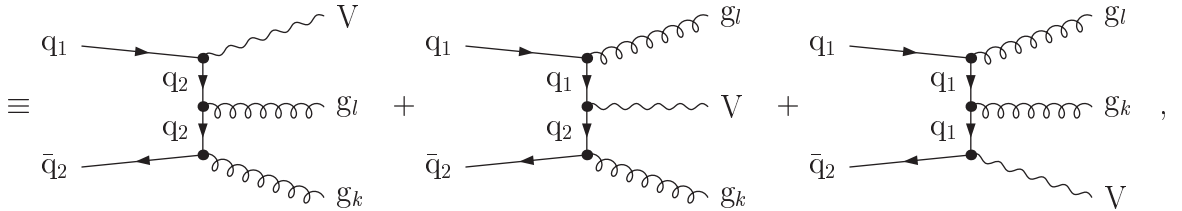
For ZZ+jet production, only $q = q_1 = q_2$ contributes because no flavour-changing neutral currents exist in the SM. Since no external top-quark contributions are taken into account, $m_q^2 = 0$ holds for all subprocesses, and thus the term proportional to m_q^2 always vanishes.

The same is true for WZ+jet production, where non-vanishing contributions stem from $q = q_1$ or $q = q_2$. The former holds if $V_1 = Z$, and the latter if $V_2 = Z$. However, subprocesses that are suppressed by non-diagonal CKM matrix elements contribute to $pp/p\bar{p} \rightarrow WZ + \text{jet} + X$.

The only process class with massive intermediate quarks is WW+jet production. In the chosen approximation of the CKM matrix, this is the case for $q_1 = q_2 = b$, where only $q = t$ contributes to the sum. As discussed in Section 3.1, for external quarks of the two light generations the unitarity of the CKM matrix can be used for simplification. Namely, all subprocesses with $q_1 \neq q_2$ vanish if the intermediate quark state is summed over. For $q_1 = q_2$, the CKM factors, which are hidden in $C_{V_2 \bar{q}_2 q}^-$ and $C_{V_1 \bar{q}_1 q}^-$ for $V_{1,2} = W^\pm$, can be factorized off the rest of the amplitude. The sum over intermediate quarks yields a factor 1 (see context of Eq. (3.2)), which is the same result as for a diagonal CKM matrix.

For the evaluation of the real-emission amplitudes with external gluons, the following building block is needed,

$$\mathcal{A}_Q \left(q_1 \begin{bmatrix} i \\ p \\ \sigma \end{bmatrix} \bar{q}_2 \begin{bmatrix} j \\ p' \\ \sigma' \end{bmatrix} \rightarrow V \begin{bmatrix} y \\ v^* \end{bmatrix} g \begin{bmatrix} a \\ k \\ g_k^* \end{bmatrix} g \begin{bmatrix} b \\ l \\ g_l^* \end{bmatrix} \right)$$



$$\begin{aligned} \mathcal{A}_Q \left(q_1 \begin{bmatrix} i \\ p \\ L \end{bmatrix} \bar{q}_2 \begin{bmatrix} j \\ p' \\ R \end{bmatrix} \rightarrow V \begin{bmatrix} y \\ v^* \end{bmatrix} g \begin{bmatrix} a \\ k \\ g_k^* \end{bmatrix} g \begin{bmatrix} b \\ l \\ g_l^* \end{bmatrix} \right) &= i g_s^2 [T^a T^b]_{ji} e C_{V \bar{q}_2 q_1}^- g_{k, \dot{A} B}^* g_{l, \dot{M} N}^* v_{\dot{K} L}^* \\ &\times \left[\frac{\phi^{\dot{M}}(P-L)^{\dot{A} N} (Y-P')^{\dot{K} B} \phi'^{L}}{(y-p')^2 (p-l)^2} + \frac{\phi^{\dot{K}}(P-Y)^{\dot{M} L} (K-P')^{\dot{A} N} \phi'^{B}}{(p-y)^2 ((k-p')^2)} \right. \\ &\quad \left. + \frac{\phi^{\dot{M}}(P-L)^{\dot{K} N} (K-P')^{\dot{A} L} \phi'^{B}}{(k-p')^2 (p-l)^2} \right]. \end{aligned} \quad (4.24)$$

The calculation needs to be performed only for one order of the two gluons; the other order can be obtained by interchanging momenta, polarization bispinors and colour indices of the two gluons.

By combining Eqs. (4.15) and (4.24), one part of the real-emission subamplitude including a vertex of three weak gauge bosons results, namely the part describing the diagrams

in the first row of Figure 3.9,

$$\begin{aligned}
& \mathcal{A}_{\text{VQ}} \left(q_1 \begin{bmatrix} i \\ p \\ \sigma \end{bmatrix} \bar{q}_2 \begin{bmatrix} j \\ p' \\ \sigma' \end{bmatrix} \rightarrow V_1 \begin{bmatrix} k_1 \\ v_1^* \end{bmatrix} V_2 \begin{bmatrix} k_2 \\ v_2^* \end{bmatrix} g \begin{bmatrix} a \\ k \\ g_k^* \end{bmatrix} g \begin{bmatrix} b \\ l \\ g_l^* \end{bmatrix} \right) \\
& \equiv \text{Diagram 1} + \text{Diagram 2} + \text{Diagram 3} \\
& = \hat{\mathcal{A}}_{\text{Q}} \left(q_1 \begin{bmatrix} i \\ p \\ \sigma \end{bmatrix} \bar{q}_2 \begin{bmatrix} j \\ p' \\ \sigma' \end{bmatrix} \rightarrow V \begin{bmatrix} y \\ v^* \end{bmatrix} g \begin{bmatrix} a \\ k \\ g_k^* \end{bmatrix} g \begin{bmatrix} b \\ l \\ g_l^* \end{bmatrix} \right) \mathcal{A} \left(V \begin{bmatrix} y \\ v \end{bmatrix} \rightarrow V_1 \begin{bmatrix} k_1 \\ v_1^* \end{bmatrix} V_2 \begin{bmatrix} k_2 \\ v_2^* \end{bmatrix} \right), \\
& \mathcal{A}_{\text{VQ}} \left(q_1 \begin{bmatrix} i \\ p \\ \sigma \end{bmatrix} \bar{q}_2 \begin{bmatrix} j \\ p' \\ \sigma' \end{bmatrix} \rightarrow V_1 \begin{bmatrix} k_1 \\ v_1^* \end{bmatrix} V_2 \begin{bmatrix} k_2 \\ v_2^* \end{bmatrix} g \begin{bmatrix} a \\ k \\ g_k^* \end{bmatrix} g \begin{bmatrix} b \\ l \\ g_l^* \end{bmatrix} \right) = i g_s^2 [T^a T^b]_{ji} e^2 g_{k,AB}^* g_{l,\dot{M}N}^* \\
& \quad \times \sum_V \frac{C_{\text{V}\bar{q}_2 q_1}^- C_{\text{V}\bar{V}_1 \bar{V}_2} \mathcal{V}_{\dot{K}L}}{y^2 - M_V^2} \left[\frac{\phi^{\dot{M}}(P-L)^{\dot{A}N}(Y-P')^{\dot{K}B} \phi'^L}{(y-p')^2 (p-l)^2} \right. \\
& \quad \left. + \frac{\phi^{\dot{K}}(P-Y)^{\dot{M}L}(K-P')^{\dot{A}N} \phi'^B}{(p-y)^2 ((k-p')^2)} + \frac{\phi^{\dot{M}}(P-L)^{\dot{K}N}(K-P')^{\dot{A}L} \phi'^B}{(k-p')^2 (p-l)^2} \right]. \quad (4.25)
\end{aligned}$$

The second part of this subamplitude can be constructed from already known results: Replacing the polarization bispinor of the gluon in Eq. (4.22) by the expression (4.17) delivers the remaining contributions including a three-gluon vertex (last row of Figure 3.9),

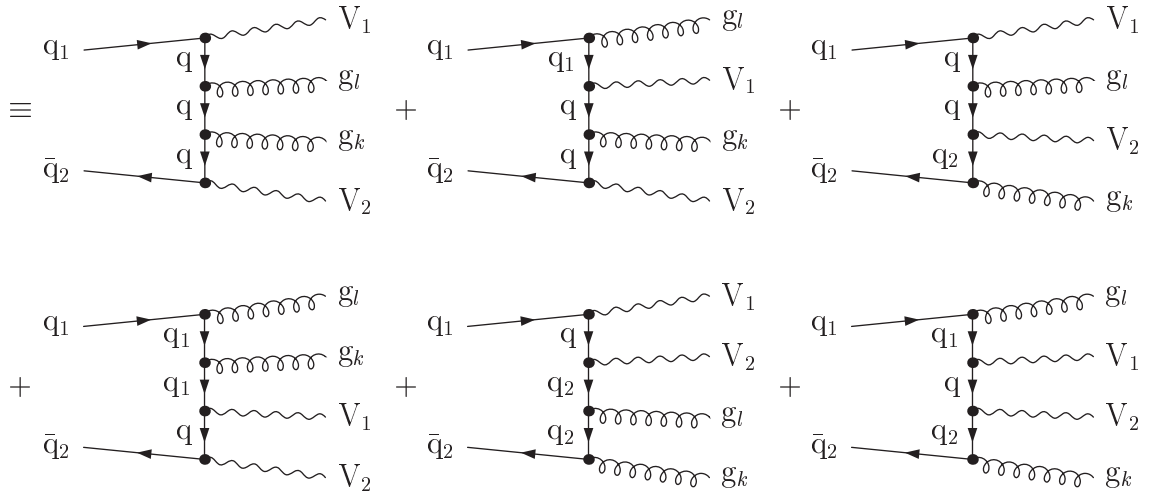
$$\begin{aligned}
& \mathcal{A}_{\text{VG}} \left(q_1 \begin{bmatrix} i \\ p \\ \sigma \end{bmatrix} \bar{q}_2 \begin{bmatrix} j \\ p' \\ \sigma' \end{bmatrix} \rightarrow V_1 \begin{bmatrix} k_1 \\ v_1^* \end{bmatrix} V_2 \begin{bmatrix} k_2 \\ v_2^* \end{bmatrix} g \begin{bmatrix} a \\ k \\ g_k^* \end{bmatrix} g \begin{bmatrix} b \\ l \\ g_l^* \end{bmatrix} \right) \\
& \equiv \text{Diagram 4} + \text{Diagram 5} \\
& = \hat{\mathcal{A}}_{\text{V}} \left(q_1 \begin{bmatrix} i \\ p \\ \sigma \end{bmatrix} \bar{q}_2 \begin{bmatrix} j \\ p' \\ \sigma' \end{bmatrix} \rightarrow V_1 \begin{bmatrix} k_1 \\ v_1^* \end{bmatrix} V_2 \begin{bmatrix} k_2 \\ v_2^* \end{bmatrix} g \begin{bmatrix} c \\ k+l \\ g^* \end{bmatrix} \right) \mathcal{A} \left(g \begin{bmatrix} c \\ k+l \\ g \end{bmatrix} \rightarrow g \begin{bmatrix} a \\ k \\ g_k^* \end{bmatrix} g \begin{bmatrix} b \\ l \\ g_l^* \end{bmatrix} \right), \\
& \mathcal{A}_{\text{VG}} \left(q_1 \begin{bmatrix} i \\ p \\ \sigma \end{bmatrix} \bar{q}_2 \begin{bmatrix} j \\ p' \\ \sigma' \end{bmatrix} \rightarrow V_1 \begin{bmatrix} k_1 \\ v_1^* \end{bmatrix} V_2 \begin{bmatrix} k_2 \\ v_2^* \end{bmatrix} g \begin{bmatrix} a \\ k \\ g_k^* \end{bmatrix} g \begin{bmatrix} b \\ l \\ g_l^* \end{bmatrix} \right) = \frac{i}{4} g_s^2 [T^a, T^b]_{ji} e^2 \frac{\mathcal{G}(k, l)_{\dot{A}B}}{(k+l)^2} \\
& \quad \times \sum_V \frac{C_{\text{V}\bar{q}_2 q_1}^- C_{\text{V}\bar{V}_1 \bar{V}_2} \mathcal{V}_{\dot{K}L}}{y^2 - M_V^2} \left[\frac{\phi'^B (K+L-P')^{\dot{A}L} \phi^{\dot{K}}}{(k+l-p')^2} + \frac{\phi^{\dot{A}} (P-K-L)^{\dot{K}B} \phi'^L}{(p-k-l)^2} \right]. \quad (4.26)
\end{aligned}$$

Here, $\mathcal{V}_{\dot{K}L}$ is defined in Eq. (4.16) and $\mathcal{G}(k, l)_{\dot{A}B}$ in Eq. (4.18).

The building blocks that are still needed for the calculation of the amplitudes of the real-emission subprocesses with two external gluons describe the diagrams with both weak gauge bosons coupling directly to the fermion chain. These can again be subdivided into diagrams with and without a three-gluon vertex, which are given in the first two rows and the last row of Figure 3.8, respectively.

First, the contribution without three-boson vertices is calculated. Again, only one specified order of the gauge bosons and the gluons is evaluated, because the others can be obtained by interchanging momenta and polarization bispinors as well as couplings,

$$\mathcal{A}_{\text{QQ}}\left(q_1 \begin{bmatrix} i \\ p \\ \sigma \end{bmatrix} \bar{q}_2 \begin{bmatrix} j \\ p' \\ \sigma' \end{bmatrix} \rightarrow V_1 \begin{bmatrix} k_1 \\ v_1^* \end{bmatrix} V_2 \begin{bmatrix} k_2 \\ v_2^* \end{bmatrix} g \begin{bmatrix} a \\ k \\ g_k^* \end{bmatrix} g \begin{bmatrix} b \\ l \\ g_l^* \end{bmatrix}\right)$$



$$\begin{aligned} \mathcal{A}_{\text{QQ}}\left(q_1 \begin{bmatrix} i \\ p \\ L \end{bmatrix} \bar{q}_2 \begin{bmatrix} j \\ p' \\ R \end{bmatrix} \rightarrow V_1 \begin{bmatrix} k_1 \\ v_1^* \end{bmatrix} V_2 \begin{bmatrix} k_2 \\ v_2^* \end{bmatrix} g \begin{bmatrix} a \\ k \\ g_k^* \end{bmatrix} g \begin{bmatrix} b \\ l \\ g_l^* \end{bmatrix}\right) &= -i g_s^2 [T^a T^b]_{ji} e^2 g_{k,AB}^* g_{l,MN}^* v_{1,\dot{E}F}^* v_{2,\dot{G}H}^* \\ &\times \sum_q C_{V_2 \bar{q}_2 q}^- C_{V_1 q \bar{q}_1}^- \left\{ \frac{\phi^{\dot{E}}(P - K_1)^{\dot{M}F} (P - L - K_1)^{\dot{A}N} (K_2 - P')^{\dot{G}B} \phi'^H}{((p - k_1)^2 - m_q^2)((p - l - k_1)^2 - m_q^2)((k_2 - p')^2 - m_q^2)} \right. \\ &+ \frac{\phi^{\dot{E}}(P - K_1)^{\dot{M}F} (P - L - K_1)^{\dot{G}N} (K - P')^{\dot{A}H} \phi'^B}{((p - k_1)^2 - m_q^2)((p - l - k_1)^2 - m_q^2)(k - p')^2} \\ &+ \frac{\phi^{\dot{M}}(P - L)^{\dot{E}N} (P - L - K_1)^{\dot{A}F} (K_2 - P')^{\dot{G}B} \phi'^H}{(p - l)^2((p - l - k_1)^2 - m_q^2)((k_2 - p')^2)} \\ &+ \frac{\phi^{\dot{M}}(P - L)^{\dot{A}N} (P - L - K)^{\dot{E}B} (K_2 - P')^{\dot{G}F} \phi'^H}{(p - l)^2((p - l - k)^2 - m_q^2)((k_2 - p')^2 - m_q^2)} \\ &+ \frac{\phi^{\dot{E}}(P - K_1)^{\dot{G}F} (L + K - P')^{\dot{M}H} (K - P')^{\dot{A}N} \phi'^B}{(k - p')^2(l + k - p')^2((p - k_1)^2 - m_q^2)} \\ &+ \frac{\phi^{\dot{M}}(P - L)^{\dot{E}N} (P - L - K_1)^{\dot{G}F} (K - P')^{\dot{A}H} \phi'^B}{(p - l)^2(k - p')^2((p - l - k_1)^2 - m_q^2)} \end{aligned}$$

$$\begin{aligned}
& + \frac{m_q^2}{(p-l-k_1)^2 - m_q^2} \left[\frac{\phi^{\dot{E}} \phi'^B \epsilon^{\dot{G}\dot{M}} \epsilon^{FN} (K-P')^{\dot{A}H}}{(k-p')^2 ((p-k_1)^2 - m_q^2)} + \frac{\phi^{\dot{M}} \phi'^H \epsilon^{\dot{G}\dot{A}} \epsilon^{FB} (P-L)^{\dot{E}N}}{(p-l)^2 ((k_2-p')^2 - m_q^2)} \right. \\
& + \left(\epsilon^{\dot{G}\dot{A}} \epsilon^{NB} (P-K_1)^{\dot{M}F} + \epsilon^{\dot{A}\dot{M}} \epsilon^{FN} (K_2-P')^{\dot{G}B} + \epsilon^{\dot{G}\dot{A}} \epsilon^{FN} (P-L-K_1)^{\dot{M}B} \right) \\
& \left. \times \frac{\phi^{\dot{E}} \phi'^H}{((p-k_1)^2 - m_q^2)((k_2-p')^2 - m_q^2)} \right] \Bigg\}. \quad (4.27)
\end{aligned}$$

The discussion of the contributing insertions for the intermediate quark q , which is summed over, is not affected by the second gluon. The result is the same as given in succession of Eq. (4.23) and shall not be repeated here. The same is also true for the possible orders of the gauge bosons coupling to the fermion chain.

The argumentation also holds in the remaining case with the two gluons coupling to the fermion chain by means of an intermediate gluon and a three-gluon vertex. This building block can be constructed by inserting the expression (4.17) instead of the gluon polarization bispinor into Eq. (4.23). The result is

$$\begin{aligned}
& \mathcal{A}_{\text{QG}} \left(q_1 \begin{bmatrix} i \\ p \\ \sigma \end{bmatrix} \bar{q}_2 \begin{bmatrix} j \\ p' \\ \sigma' \end{bmatrix} \rightarrow V_1 \begin{bmatrix} k_1 \\ v_1^* \end{bmatrix} V_2 \begin{bmatrix} k_2 \\ v_2^* \end{bmatrix} g \begin{bmatrix} a \\ k \\ g_k^* \end{bmatrix} g \begin{bmatrix} b \\ l \\ g_l^* \end{bmatrix} \right) \\
& \equiv \text{[Three diagrams showing different gluon couplings to the fermion chain]} \\
& = \hat{\mathcal{A}}_{\text{Q}} \left(q_1 \begin{bmatrix} i \\ p \\ \sigma \end{bmatrix} \bar{q}_2 \begin{bmatrix} j \\ p' \\ \sigma' \end{bmatrix} \rightarrow V_1 \begin{bmatrix} k_1 \\ v_1^* \end{bmatrix} V_2 \begin{bmatrix} k_2 \\ v_2^* \end{bmatrix} g \begin{bmatrix} c \\ k+l \\ g^* \end{bmatrix} \right) \mathcal{A} \left(g \begin{bmatrix} c \\ k+l \\ g^* \end{bmatrix} \rightarrow g \begin{bmatrix} a \\ k \\ g_k^* \end{bmatrix} g \begin{bmatrix} b \\ l \\ g_l^* \end{bmatrix} \right), \\
& \mathcal{A}_{\text{QG}} \left(q_1 \begin{bmatrix} i \\ p \\ L \end{bmatrix} \bar{q}_2 \begin{bmatrix} j \\ p' \\ R \end{bmatrix} \rightarrow V_1 \begin{bmatrix} k_1 \\ v_1^* \end{bmatrix} V_2 \begin{bmatrix} k_2 \\ v_2^* \end{bmatrix} g \begin{bmatrix} a \\ k \\ g_k^* \end{bmatrix} g \begin{bmatrix} b \\ l \\ g_l^* \end{bmatrix} \right) = -\frac{i}{2} g_s^2 [T^a, T^b]_{ji} e^2 v_{1,\dot{E}F}^* v_{2,\dot{G}H}^* \frac{\mathcal{G}(k,l)_{\dot{A}B}}{(k+l)^2} \\
& \times \sum_q C_{V_2 \bar{q}_2 q}^- C_{V_1 \bar{q} q_1}^- \left[\frac{\phi^{\dot{A}}(P-K)^{\dot{E}B} (K_2-P')^{\dot{G}F} \phi'^H}{(p-k)^2 ((k_2-p')^2 - m_q^2)} + \frac{\phi^{\dot{E}}(P-K_1)^{\dot{G}F} (K-P')^{\dot{A}H} \phi'^B}{(k-p')^2 ((p-k_1)^2 - m_q^2)} \right. \\
& \left. + \frac{\phi^{\dot{E}}(P-K_1)^{\dot{A}F} (K_2-P')^{\dot{G}B} \phi'^H}{((p-k_1)^2 - m_q^2)((k_2-p')^2 - m_q^2)} + \frac{m_q^2 \phi^{\dot{E}} \epsilon^{\dot{A}\dot{G}} \epsilon^{BF} \phi'^H}{((p-k_1)^2 - m_q^2)((k_2-p')^2 - m_q^2)} \right]. \quad (4.28)
\end{aligned}$$

Replacing the polarization bispinor of the gluon by the expression (4.19) in the building blocks of Eqs. (4.22) and (4.23) provides the expressions needed for the evaluation of the real-emission subamplitudes with two fermion chains, which are shown in Figures 3.10 and 3.11. The contributions from the remaining diagrams, which are presented in Figure 3.12, can be obtained by inserting the expression (4.20) into Eq. (4.21) instead of the gluon polarization bispinor.

4.3 Subamplitudes for VV+jet production

The building blocks calculated in the last section can be combined to subamplitudes. These subamplitudes are, in general, no full amplitudes yet, but gauge-invariant groups of diagrams with respect to $SU(3)_C$. Thus, they have to be calculated together to deliver gauge-invariant results. The invariance under $SU(3)_C$ gauge transformations can be checked analytically by keeping the generic gauge spinors in the polarization vectors of the external gluons and showing the independence of this gauge spinor for the particular subamplitude. This check has been performed for all helicity combinations in the LO subamplitudes and for a selection of helicity combinations in the real-emission subamplitudes with external gluons. For the remaining helicity channels, convenient choices of the gauge spinors are made to simplify the resulting expressions as far as possible. The polarizations of the outgoing weak gauge bosons remain unspecified.

Since the full amplitudes are sums of the subamplitudes given in this section or of subamplitudes that can be obtained from these by crossing, the conventional factor $(-i)$ is already included here.

The formulae presented in this section refer to generic VV+jet-production processes. Therefore, masses of intermediate quarks are kept, although they only appear in WW+jet production subprocesses. Some of the given subamplitudes or at least some helicity channels do not contribute to subprocesses of all gauge-boson-pair assignments. All helicity combinations with $\sigma\sigma' = \text{RR, LL}$ vanish, since all external (anti-)quarks are treated as massless particles.

4.3.1 LO subprocesses

Starting with the LO subprocesses, two different subamplitudes have to be evaluated. The one describes all diagrams with the two weak gauge bosons coupling to the fermion chain by means of an intermediate gauge boson, which are shown in Figure 3.7. With Eq. (4.15), the subamplitude is

$$\mathcal{M}_V \left(q_1 \begin{bmatrix} i \\ p \\ \sigma \end{bmatrix} \bar{q}_2 \begin{bmatrix} j \\ p' \\ \sigma' \end{bmatrix} \rightarrow V_1 \begin{bmatrix} k_1 \\ v_1^* \end{bmatrix} V_2 \begin{bmatrix} k_2 \\ v_2^* \end{bmatrix} g \begin{bmatrix} a \\ k \\ \tau \end{bmatrix} \right) = -i \mathcal{A}_V \left(q_1 \begin{bmatrix} i \\ p \\ \sigma \end{bmatrix} \bar{q}_2 \begin{bmatrix} j \\ p' \\ \sigma' \end{bmatrix} \rightarrow V_1 \begin{bmatrix} k_1 \\ v_1^* \end{bmatrix} V_2 \begin{bmatrix} k_2 \\ v_2^* \end{bmatrix} g \begin{bmatrix} a \\ k \\ \tau \end{bmatrix} \right). \quad (4.29)$$

The subamplitudes for specified gluon polarizations and (anti-)quark helicities are calculated from Eq. (4.29) by inserting the polarization bispinors defined in Eq. (4.10). After simplifications, the resulting subamplitudes, which are independent of the gauge spinor g_{\pm} , read

$$\mathcal{M}_V \left(q_1 \begin{bmatrix} i \\ p \\ L \end{bmatrix} \bar{q}_2 \begin{bmatrix} j \\ p' \\ R \end{bmatrix} \rightarrow V_1 V_2 g \begin{bmatrix} a \\ k \\ + \end{bmatrix} \right) = \frac{1}{\sqrt{2}} g_s T_{ji}^a e^2 \sum_V \frac{C_{V\bar{q}_2 q_1}^- C_{V\bar{V}_1 \bar{V}_2} V_{\dot{K}L} \phi'_V Y^{\dot{K}V} \phi'^{IL}}{y^2 - M_V^2} \frac{\phi'_V Y^{\dot{K}V} \phi'^{IL}}{\langle k\phi \rangle \langle k\phi' \rangle}, \quad (4.29a)$$

$$\mathcal{M}_V \left(q_1 \begin{bmatrix} i \\ p \\ L \end{bmatrix} \bar{q}_2 \begin{bmatrix} j \\ p' \\ R \end{bmatrix} \rightarrow V_1 V_2 g \begin{bmatrix} a \\ k \\ - \end{bmatrix} \right) = \frac{1}{\sqrt{2}} g_s T_{ji}^a e^2 \sum_V \frac{C_{V\bar{q}_2 q_1}^- C_{V\bar{V}_1 \bar{V}_2} \mathcal{V}_{\dot{K}L} - \phi^{\dot{K}} \phi_{\dot{U}} Y^{\dot{U}L}}{y^2 - M_V^2} \frac{1}{\langle k\phi \rangle \langle k\phi' \rangle^*}, \quad (4.29b)$$

where the shorthand $y = k_1 + k_2$, $Y_{AB} = (K_1 + K_2)_{AB}$ is used. The arguments of the weak gauge bosons are dropped. The remaining non-vanishing helicity channels are related to the given subamplitudes by a \mathcal{P} transformation,

$$\mathcal{M}_V\left(q_1 \begin{bmatrix} i \\ p \\ R \end{bmatrix} \bar{q}_2 \begin{bmatrix} j \\ p' \\ L \end{bmatrix} \rightarrow V_1 V_2 g \begin{bmatrix} a \\ k \\ + \end{bmatrix}\right) = \mathcal{P}\left\{\mathcal{M}_V\left(q_1 \begin{bmatrix} i \\ p \\ L \end{bmatrix} \bar{q}_2 \begin{bmatrix} j \\ p' \\ R \end{bmatrix} \rightarrow V_1 V_2 g \begin{bmatrix} a \\ k \\ - \end{bmatrix}\right)\right\}, \quad (4.29c)$$

$$\mathcal{M}_V\left(q_1 \begin{bmatrix} i \\ p \\ R \end{bmatrix} \bar{q}_2 \begin{bmatrix} j \\ p' \\ L \end{bmatrix} \rightarrow V_1 V_2 g \begin{bmatrix} a \\ k \\ - \end{bmatrix}\right) = \mathcal{P}\left\{\mathcal{M}_V\left(q_1 \begin{bmatrix} i \\ p \\ L \end{bmatrix} \bar{q}_2 \begin{bmatrix} j \\ p' \\ R \end{bmatrix} \rightarrow V_1 V_2 g \begin{bmatrix} a \\ k \\ + \end{bmatrix}\right)\right\}. \quad (4.29d)$$

The subamplitudes with both weak gauge bosons coupling directly to the fermion chain are obtained in the same way from Eq. (4.23),

$$\mathcal{M}_Q\left(q_1 \begin{bmatrix} i \\ p \\ \sigma \end{bmatrix} \bar{q}_2 \begin{bmatrix} j \\ p' \\ \sigma' \end{bmatrix} \rightarrow V_1 \begin{bmatrix} k_1 \\ v_1^* \end{bmatrix} V_2 \begin{bmatrix} k_2 \\ v_2^* \end{bmatrix} g \begin{bmatrix} a \\ k \\ \tau \end{bmatrix}\right) = -i \mathcal{A}_Q\left(q_1 \begin{bmatrix} i \\ p \\ \sigma \end{bmatrix} \bar{q}_2 \begin{bmatrix} j \\ p' \\ \sigma' \end{bmatrix} \rightarrow V_1 \begin{bmatrix} k_1 \\ v_1^* \end{bmatrix} V_2 \begin{bmatrix} k_2 \\ v_2^* \end{bmatrix} g \begin{bmatrix} a \\ k \\ \tau \end{bmatrix}\right). \quad (4.30)$$

By inserting the gluon polarization bispinors (4.10) into Eq. (4.29), subamplitudes of the following helicity channels are obtained,

$$\begin{aligned} \mathcal{M}_Q\left(q_1 \begin{bmatrix} i \\ p \\ L \end{bmatrix} \bar{q}_2 \begin{bmatrix} j \\ p' \\ R \end{bmatrix} \rightarrow V_1 V_2 g \begin{bmatrix} a \\ k \\ + \end{bmatrix}\right) &= \sqrt{2} g_s T_{ji}^a e^2 v_{1,\dot{E}F}^* v_{2,\dot{G}H}^* \sum_q \frac{C_{V_2 \bar{q}_2 q}^- C_{V_1 \bar{q} q_1}^-}{\langle k \phi' \rangle ((k_2 - p')^2 - m_q^2)} \\ &\times \left[\frac{\phi^{\dot{E}} \phi^H k_{\dot{U}} (P - K_1)^{\dot{U}F} \phi'_V K_2^{\dot{G}V}}{((p - k_1)^2 - m_q^2)} - \frac{\phi'_V Y^{\dot{E}V} (K_2 - P')^{\dot{G}F} \phi'^H}{\langle k \phi \rangle} + \frac{m_q^2 \phi^{\dot{E}} \phi'^F k^{\dot{G}} \phi'^H}{((p - k_1)^2 - m_q^2)} \right], \end{aligned} \quad (4.30a)$$

$$\begin{aligned} \mathcal{M}_Q\left(q_1 \begin{bmatrix} i \\ p \\ L \end{bmatrix} \bar{q}_2 \begin{bmatrix} j \\ p' \\ R \end{bmatrix} \rightarrow V_1 V_2 g \begin{bmatrix} a \\ k \\ - \end{bmatrix}\right) &= \sqrt{2} g_s T_{ji}^a e^2 v_{1,\dot{E}F}^* v_{2,\dot{G}H}^* \sum_q \frac{C_{V_2 \bar{q}_2 q}^- C_{V_1 \bar{q} q_1}^-}{\langle k \phi \rangle^* ((p - k_1)^2 - m_q^2)} \\ &\times \left[-\frac{\phi^{\dot{E}} \phi_{\dot{U}} K_1^{\dot{U}F} k_V (K_2 - P')^{\dot{G}V} \phi'^H}{((k_2 - p')^2 - m_q^2)} + \frac{\phi^{\dot{E}} (P - K_1)^{\dot{G}F} \phi_{\dot{U}} Y^{\dot{U}H}}{\langle k \phi' \rangle^*} + \frac{m_q^2 \phi^{\dot{E}} k^F \phi^{\dot{G}} \phi^H}{((k_2 - p')^2 - m_q^2)} \right]. \end{aligned} \quad (4.30b)$$

A \mathcal{P} transformation again delivers the results for the remaining helicity combinations,

$$\mathcal{M}_Q\left(q_1 \begin{bmatrix} i \\ p \\ R \end{bmatrix} \bar{q}_2 \begin{bmatrix} j \\ p' \\ L \end{bmatrix} \rightarrow V_1 V_2 g \begin{bmatrix} a \\ k \\ + \end{bmatrix}\right) = \mathcal{P}\left\{\mathcal{M}_Q\left(q_1 \begin{bmatrix} i \\ p \\ L \end{bmatrix} \bar{q}_2 \begin{bmatrix} j \\ p' \\ R \end{bmatrix} \rightarrow V_1 V_2 g \begin{bmatrix} a \\ k \\ - \end{bmatrix}\right)\right\}, \quad (4.30c)$$

$$\mathcal{M}_Q\left(q_1 \begin{bmatrix} i \\ p \\ R \end{bmatrix} \bar{q}_2 \begin{bmatrix} j \\ p' \\ L \end{bmatrix} \rightarrow V_1 V_2 g \begin{bmatrix} a \\ k \\ - \end{bmatrix}\right) = \mathcal{P}\left\{\mathcal{M}_Q\left(q_1 \begin{bmatrix} i \\ p \\ L \end{bmatrix} \bar{q}_2 \begin{bmatrix} j \\ p' \\ R \end{bmatrix} \rightarrow V_1 V_2 g \begin{bmatrix} a \\ k \\ + \end{bmatrix}\right)\right\}. \quad (4.30d)$$

4.3.2 Real-emission subprocesses

Contributions with two external gluons

As in the LO case discussed in the previous subsection, two different real-emission subamplitudes have to be evaluated. The first one again contains all diagrams with an intermediate gauge boson, which are presented in Figure 3.9. The corresponding subamplitude is

calculated from Eqs. (4.25) and (4.26) as follows,

$$\begin{aligned} \mathcal{M}_V \left(q_1 \begin{bmatrix} i \\ p \\ \sigma \end{bmatrix} \bar{q}_2 \begin{bmatrix} j \\ p' \\ \sigma' \end{bmatrix} \rightarrow V_1 \begin{bmatrix} k_1 \\ v_1^* \end{bmatrix} V_2 \begin{bmatrix} k_2 \\ v_2^* \end{bmatrix} g \begin{bmatrix} a \\ k \\ \tau \end{bmatrix} g \begin{bmatrix} b \\ l \\ \tau' \end{bmatrix} \right) = -i \mathcal{A}_{VG} \left(q_1 \begin{bmatrix} i \\ p \\ \sigma \end{bmatrix} \bar{q}_2 \begin{bmatrix} j \\ p' \\ \sigma' \end{bmatrix} \rightarrow V_1 \begin{bmatrix} k_1 \\ v_1^* \end{bmatrix} V_2 \begin{bmatrix} k_2 \\ v_2^* \end{bmatrix} g \begin{bmatrix} a \\ k \\ \tau \end{bmatrix} g \begin{bmatrix} b \\ l \\ \tau' \end{bmatrix} \right) \\ -i \left\{ \mathcal{A}_{VQ} \left(q_1 \begin{bmatrix} i \\ p \\ \sigma \end{bmatrix} \bar{q}_2 \begin{bmatrix} j \\ p' \\ \sigma' \end{bmatrix} \rightarrow V_1 \begin{bmatrix} k_1 \\ v_1^* \end{bmatrix} V_2 \begin{bmatrix} k_2 \\ v_2^* \end{bmatrix} g \begin{bmatrix} a \\ k \\ \tau \end{bmatrix} g \begin{bmatrix} b \\ l \\ \tau' \end{bmatrix} \right) + \mathcal{A}_{VQ} \left(\dots \rightarrow \dots g \begin{bmatrix} b \\ l \\ \tau' \end{bmatrix} g \begin{bmatrix} a \\ k \\ \tau \end{bmatrix} \right) \right\}. \end{aligned} \quad (4.31)$$

The constellation with the two gluons interchanged is included by adding the contribution of Eq. (4.25) for a second time with the two gluons interchanged. Precisely, the expression in the last contribution to Eq. (4.31) means an interchange of momenta, polarization bispinors and colour indices of the two gluons.

The polarization bispinors of the two outgoing gluons are inserted into Eq. (4.31) according to Eq. (4.10). After analytical simplifications, the resulting subamplitudes read

$$\begin{aligned} \mathcal{M}_V \left(q_1 \begin{bmatrix} i \\ p \\ L \end{bmatrix} \bar{q}_2 \begin{bmatrix} j \\ p' \\ R \end{bmatrix} \rightarrow V_1 V_2 g \begin{bmatrix} a \\ k \\ + \end{bmatrix} g \begin{bmatrix} b \\ l \\ + \end{bmatrix} \right) \\ = 2 g_s^2 [T^a T^b]_{ji} e^2 \sum_V \frac{C_{V\bar{q}_2 q_1}^- C_{V\bar{V}_1 \bar{V}_2}}{y^2 - M_V^2} \mathcal{V}_{\dot{K}L} \frac{-\phi'_V Y^{\dot{K}V} \phi'^L}{\langle k\phi' \rangle \langle l\phi' \rangle \langle kl \rangle} + \left\{ \begin{matrix} a \leftrightarrow b \\ k \leftrightarrow l \end{matrix} \right\}, \end{aligned} \quad (4.31a)$$

$$\begin{aligned} \mathcal{M}_V \left(q_1 \begin{bmatrix} i \\ p \\ L \end{bmatrix} \bar{q}_2 \begin{bmatrix} j \\ p' \\ R \end{bmatrix} \rightarrow V_1 V_2 g \begin{bmatrix} a \\ k \\ - \end{bmatrix} g \begin{bmatrix} b \\ l \\ - \end{bmatrix} \right) \\ = 2 g_s^2 [T^a T^b]_{ji} e^2 \sum_V \frac{C_{V\bar{q}_2 q_1}^- C_{V\bar{V}_1 \bar{V}_2}}{y^2 - M_V^2} \mathcal{V}_{\dot{K}L} \frac{\phi^{\dot{K}} \phi_{\dot{U}} Y^{\dot{U}L}}{\langle k\phi' \rangle^* \langle l\phi' \rangle^* \langle kl \rangle^*} + \left\{ \begin{matrix} a \leftrightarrow b \\ k \leftrightarrow l \end{matrix} \right\}, \end{aligned} \quad (4.31b)$$

$$\begin{aligned} \mathcal{M}_V \left(q_1 \begin{bmatrix} i \\ p \\ L \end{bmatrix} \bar{q}_2 \begin{bmatrix} j \\ p' \\ R \end{bmatrix} \rightarrow V_1 V_2 g \begin{bmatrix} a \\ k \\ + \end{bmatrix} g \begin{bmatrix} b \\ l \\ - \end{bmatrix} \right) = 2 g_s^2 e^2 \sum_V \frac{C_{V\bar{q}_2 q_1}^- C_{V\bar{V}_1 \bar{V}_2}}{y^2 - M_V^2} \mathcal{V}_{\dot{K}L} \frac{1}{\langle k\phi' \rangle \langle l\phi' \rangle^*} \\ \times \left\{ [T^b T^a]_{ji} \left[\frac{\phi_{\dot{U}}(L - P')^{\dot{U}L} \phi'_V(P - K)^{\dot{K}V}}{\langle k\phi \rangle \langle l\phi' \rangle^*} - \frac{\langle l\phi' \rangle^* \langle l\phi' \rangle \phi^{\dot{K}} k_{\dot{U}}(L - P')^{\dot{U}L}}{\langle l\phi' \rangle^* (p - y)^2} \right. \right. \\ \left. \left. + \frac{\langle k\phi \rangle^* \langle k\phi' \rangle l_V(P - K)^{\dot{K}V} \phi'^L}{\langle k\phi \rangle (y - p')^2} \right] + [T^a, T^b]_{ji} \frac{1}{(k + l)^2} \left[\langle l\phi' \rangle \langle k\phi \rangle^* \phi^{\dot{K}} \phi'^L \right. \right. \\ \left. \left. - \frac{\langle l\phi' \rangle^2 \langle l\phi \rangle^* \phi^{\dot{K}} k_{\dot{U}}(L - P')^{\dot{U}L}}{(p - y)^2} + \frac{\langle k\phi \rangle^{*2} \langle k\phi' \rangle l_V(P - K)^{\dot{K}V} \phi'^L}{(y - p')^2} \right] \right\}. \end{aligned} \quad (4.31c)$$

The brace $\left\{ \begin{matrix} a \leftrightarrow b \\ k \leftrightarrow l \end{matrix} \right\}$ in Eqs. (4.31a) and (4.31b) means the whole preceding expression with momenta and colour indices of the two gluons interchanged.

The subamplitudes with different polarizations of the two gluons are directly related to each other. From the subamplitude for $\tau\tau' = +- (4.31c)$ the subamplitude for $\tau\tau' = --$ is obtained by exchanging momenta and colour indices of the two gluons,

$$\mathcal{M}_V \left(q_1 \begin{bmatrix} i \\ p \\ L \end{bmatrix} \bar{q}_2 \begin{bmatrix} j \\ p' \\ R \end{bmatrix} \rightarrow V_1 V_2 g \begin{bmatrix} a \\ k \\ - \end{bmatrix} g \begin{bmatrix} b \\ l \\ + \end{bmatrix} \right) = \mathcal{M}_V \left(q_1 \begin{bmatrix} i \\ p \\ L \end{bmatrix} \bar{q}_2 \begin{bmatrix} j \\ p' \\ R \end{bmatrix} \rightarrow V_1 V_2 g \begin{bmatrix} b \\ l \\ + \end{bmatrix} g \begin{bmatrix} a \\ k \\ - \end{bmatrix} \right). \quad (4.31d)$$

The four remaining helicity channels are again delivered by a \mathcal{P} transformation of the subamplitudes in Eqs. (4.31a) – (4.31d),

$$\mathcal{M}_V\left(q_1 \begin{bmatrix} i \\ p \\ R \end{bmatrix} \bar{q}_2 \begin{bmatrix} j \\ p' \\ L \end{bmatrix} \rightarrow V_1 V_2 g \begin{bmatrix} a \\ k \\ \tau \end{bmatrix} g \begin{bmatrix} b \\ l \\ \tau' \end{bmatrix}\right) = \mathcal{P}\left\{\mathcal{M}_V\left(q_1 \begin{bmatrix} i \\ p \\ L \end{bmatrix} \bar{q}_2 \begin{bmatrix} j \\ p' \\ R \end{bmatrix} \rightarrow V_1 V_2 g \begin{bmatrix} a \\ k \\ -\tau \end{bmatrix} g \begin{bmatrix} b \\ l \\ -\tau' \end{bmatrix}\right)\right\}, \quad (4.31e)$$

for the helicity combinations $\tau\tau' = ++, --, +-, -+$.

The second subamplitude with the two weak gauge bosons coupling directly to the fermion chain, whose diagrams can be found in Figure 3.8, is calculated analogously to the previous case. Eqs. (4.27) and (4.28) deliver the generic subamplitude

$$\begin{aligned} \mathcal{M}_Q\left(q_1 \begin{bmatrix} i \\ p \\ \sigma \end{bmatrix} \bar{q}_2 \begin{bmatrix} j \\ p' \\ \sigma' \end{bmatrix} \rightarrow V_1 \begin{bmatrix} k_1 \\ v_1^* \end{bmatrix} V_2 \begin{bmatrix} k_2 \\ v_2^* \end{bmatrix} g \begin{bmatrix} a \\ k \\ \tau \end{bmatrix} g \begin{bmatrix} b \\ l \\ \tau' \end{bmatrix}\right) &= -i \mathcal{A}_{QQ}\left(q_1 \begin{bmatrix} i \\ p \\ \sigma \end{bmatrix} \bar{q}_2 \begin{bmatrix} j \\ p' \\ \sigma' \end{bmatrix} \rightarrow V_1 \begin{bmatrix} k_1 \\ v_1^* \end{bmatrix} V_2 \begin{bmatrix} k_2 \\ v_2^* \end{bmatrix} g \begin{bmatrix} a \\ k \\ \tau \end{bmatrix} g \begin{bmatrix} b \\ l \\ \tau' \end{bmatrix}\right) \\ &- i \left\{ \mathcal{A}_{QQ}\left(q_1 \begin{bmatrix} i \\ p \\ \sigma \end{bmatrix} \bar{q}_2 \begin{bmatrix} j \\ p' \\ \sigma' \end{bmatrix} \rightarrow V_1 \begin{bmatrix} k_1 \\ v_1^* \end{bmatrix} V_2 \begin{bmatrix} k_2 \\ v_2^* \end{bmatrix} g \begin{bmatrix} a \\ k \\ \tau \end{bmatrix} g \begin{bmatrix} b \\ l \\ \tau' \end{bmatrix}\right) + \mathcal{A}_{QQ}\left(\dots \rightarrow \dots g \begin{bmatrix} b \\ l \\ \tau' \end{bmatrix} g \begin{bmatrix} a \\ k \\ \tau \end{bmatrix}\right) \right\}, \end{aligned} \quad (4.32)$$

where again both orders of the two outgoing gluons have to be taken into account.

By inserting the gluon polarization bispinors (4.10) and performing analytical simplifications, the following results for the different helicity combinations are obtained,

$$\begin{aligned} \mathcal{M}_Q\left(q_1 \begin{bmatrix} i \\ p \\ L \end{bmatrix} \bar{q}_2 \begin{bmatrix} j \\ p' \\ R \end{bmatrix} \rightarrow V_1 V_2 g \begin{bmatrix} a \\ k \\ + \end{bmatrix} g \begin{bmatrix} b \\ l \\ + \end{bmatrix}\right) &= 2 g_s^2 [T^a T^b]_{ji} e^2 v_{1,\dot{E}F}^* v_{2,\dot{G}H}^* \sum_q \frac{C_{V_2 \bar{q}_2 q}^- C_{V_1 q q_1}^-}{(k_2 - p')^2 - m_q^2} \\ &\times \frac{1}{\langle k \phi' \rangle \langle l \phi' \rangle} \left[\frac{\langle l \phi' \rangle \phi_V' Q^{\dot{E}V} (K_2 - P')^{\dot{G}F} \phi'^H}{\langle kl \rangle \langle l \phi' \rangle} - \left(\frac{k_{\dot{U}} \phi_V' K_2^{\dot{U}V} \phi^{\dot{E}} l_{\dot{W}} (P - K_1)^{\dot{W}F}}{((p - k_1)^2 - m_q^2)((p - l - k_1)^2 - m_q^2)} \right. \right. \\ &- \frac{k_{\dot{U}} (K_2 - P')^{\dot{U}F} \phi_V' (P - L)^{\dot{E}V}}{\langle l \phi' \rangle ((p - l - k_1)^2 - m_q^2)} + \left. \frac{\phi^{\dot{E}} (K + L)_{\dot{U}V} \phi'^V (P - K_1)^{\dot{U}F}}{\langle kl \rangle ((p - k_1)^2 - m_q^2)} \right) \phi_X' K_2^{\dot{G}X} \phi'^H \\ &- \frac{m_q^2 \phi^{\dot{E}} \phi'^F \phi'^H}{(p - k_1)^2 - m_q^2} \left(\frac{\langle kl \rangle^* \phi_V' K_2^{\dot{G}V}}{(p - l - k_1)^2 - m_q^2} - \frac{\phi_V' (K + L)^{\dot{G}V}}{\langle kl \rangle} \right) - \frac{m_q^2 k^{\dot{G}} \phi'^H \phi'^F}{(p - l - k_1)^2 - m_q^2} \\ &\times \left(\frac{l_{\dot{U}} \phi_V' (P - k_1)^{\dot{U}V} \phi^{\dot{E}}}{(p - k_1)^2 - m_q^2} - \frac{\phi_V' (P - L)^{\dot{E}V}}{\langle l \phi' \rangle} \right) \Bigg] + \left\{ \begin{array}{l} a \leftrightarrow b \\ k \leftrightarrow l \end{array} \right\}, \end{aligned} \quad (4.32a)$$

$$\begin{aligned} \mathcal{M}_Q\left(q_1 \begin{bmatrix} i \\ p \\ L \end{bmatrix} \bar{q}_2 \begin{bmatrix} j \\ p' \\ R \end{bmatrix} \rightarrow V_1 V_2 g \begin{bmatrix} a \\ k \\ - \end{bmatrix} g \begin{bmatrix} b \\ l \\ - \end{bmatrix}\right) &= -2 g_s^2 [T^a T^b]_{ji} e^2 v_{1,\dot{E}F}^* v_{2,\dot{G}H}^* \sum_q \frac{C_{V_2 \bar{q}_2 q}^- C_{V_1 q q_1}^-}{(p - k_1)^2 - m_q^2} \\ &\times \frac{1}{\langle k \phi' \rangle^* \langle l \phi' \rangle^*} \left[\frac{\langle k \phi' \rangle^* \phi^{\dot{E}} (P - K_1)^{\dot{G}F} \phi_{\dot{U}}' Q^{\dot{U}H}}{\langle k \phi' \rangle^* \langle kl \rangle^*} + \left(\frac{\phi_{\dot{W}} l_V K_1^{\dot{W}V} k_X (K_2 - P')^{\dot{G}X} \phi'^H}{((p - l - k_1)^2 - m_q^2)((k_2 - p')^2 - m_q^2)} \right. \right. \\ &+ \frac{l_V (P - K_1)^{\dot{G}V} \phi_{\dot{W}}' (K - P')^{\dot{W}H}}{\langle k \phi' \rangle^* ((p - l - k_1)^2 - m_q^2)} - \left. \frac{(K + L)_{\dot{W}V} \phi^{\dot{W}} (K_2 - P')^{\dot{G}V} \phi'^H}{\langle kl \rangle^* ((k_2 - p')^2 - m_q^2)} \right) \phi^{\dot{E}} \phi_{\dot{U}}' K_1^{\dot{U}F} \\ &+ \frac{m_q^2 \phi^{\dot{E}} l^F \phi^{\dot{G}}}{(p - l - k_1)^2 - m_q^2} \left(\frac{\phi_{\dot{U}}' k_V (K_2 - P')^{\dot{U}V} \phi'^H}{(k_2 - p')^2 - m_q^2} - \frac{\phi_{\dot{U}}' (K - P')^{\dot{U}H}}{\langle k \phi' \rangle^*} \right) + \frac{m_q^2 \phi^{\dot{E}} \phi^{\dot{G}} \phi'^H}{(k_2 - p')^2 - m_q^2} \end{aligned}$$

$$\begin{aligned}
& \times \left(\frac{\langle kl \rangle \phi_{\dot{U}} K_1^{\dot{U}F}}{(p-l-k_1)^2 - m_q^2} - \frac{\phi_{\dot{U}}(K+L)^{\dot{U}F}}{\langle kl \rangle^*} \right) \Bigg] + \left\{ \begin{array}{c} a \leftrightarrow b \\ k \leftrightarrow l \end{array} \right\}, \quad (4.32b) \\
\mathcal{M}_Q \left(q_1 \begin{bmatrix} i \\ p \\ L \end{bmatrix} \bar{q}_2 \begin{bmatrix} j \\ p' \\ R \end{bmatrix} \rightarrow V_1 V_2 g \begin{bmatrix} a \\ k \\ + \end{bmatrix} g \begin{bmatrix} b \\ l \\ - \end{bmatrix} \right) &= 2 g_s^2 e^2 v_{1,\dot{E}F}^* v_{2,\dot{G}H}^* \sum_q \frac{C_{V_2 \bar{q}_2 q}^- C_{V_1 \bar{q} q_1}^-}{\langle k \phi' \rangle \langle l \phi \rangle^*} \\
&\times \left\{ [T^a T^b]_{ji} \left[\frac{k_{\dot{U}} l_V (P - K_1)^{\dot{U}V} \phi_{\dot{W}}^{\dot{E}} K_1^{\dot{W}F} \phi_X^{\dot{G}X} K_2^{\dot{G}X} \phi'^H}{((p-k_1)^2 - m_q^2)((p-l-k_1)^2 - m_q^2)((k_2-p')^2 - m_q^2)} \right. \right. \\
&\quad \left. \left. + \frac{m_q^2 \phi_{\dot{E}}^{\dot{E}} \left(\langle l \phi' \rangle \phi_{\dot{U}} K_1^{\dot{U}F} k_{\dot{G}}^{\dot{G}} - \langle k \phi \rangle^* \phi_V' K_2^{\dot{G}V} l^F - \phi_{\dot{U}} \phi_V' (K_2 + K)^{\dot{U}V} l^F k_{\dot{G}}^{\dot{G}} \right) \phi'^H}{((p-k_1)^2 - m_q^2)((p-l-k_1)^2 - m_q^2)((k_2-p')^2 - m_q^2)} \right] \right. \\
&\quad + [T^b T^a]_{ji} \left[\frac{\phi_{\dot{U}} \phi_V' (K + K_1)^{\dot{U}V} \phi_{\dot{W}}^{\dot{E}} k_{\dot{W}}^{\dot{E}} (P - K_1)^{\dot{W}F} l_X (K_2 - P')^{\dot{G}X} \phi'^H}{((p-k_1)^2 - m_q^2)((p-l-k_1)^2 - m_q^2)((k_2-p')^2 - m_q^2)} \right. \\
&\quad + \frac{\phi_{\dot{E}}^{\dot{E}} k_{\dot{U}} (P - K_1)^{\dot{U}F} \phi_V' (L + K_2)^{\dot{G}V} \phi_{\dot{W}}^{\dot{E}} (L - P')^{\dot{W}H}}{\langle l \phi' \rangle^* ((p-k_1)^2 - m_q^2)((p-k-k_1)^2 - m_q^2)} \\
&\quad - \frac{\phi_V' (P - K)^{\dot{E}V} \phi_{\dot{U}} (K + K_1)^{\dot{U}F} l_X (K_2 - P')^{\dot{G}X} \phi'^H}{\langle k \phi \rangle ((p-k-k_1)^2 - m_q^2)((k_2-p')^2 - m_q^2)} \\
&\quad - \frac{\langle k \phi \rangle^* \langle k \phi' \rangle l_V (P - K)^{\dot{E}V} (K_2 - P')^{\dot{G}F} \phi'^H}{\langle k \phi \rangle (p-l-k)^2 ((k_2-p')^2 - m_q^2)} \\
&\quad + \frac{\langle l \phi \rangle^* \langle l \phi' \rangle \phi_{\dot{E}}^{\dot{E}} (P - K_1)^{\dot{G}F} k_{\dot{U}} (L - P')^{\dot{U}H}}{\langle l \phi' \rangle^* (l+k-p')^2 ((p-k_1)^2 - m_q^2)} \\
&\quad - \frac{\phi_V' (P - K)^{\dot{E}V} (P - K - K_1)^{\dot{G}F} \phi_{\dot{U}} (L - P')^{\dot{U}H}}{\langle k \phi \rangle \langle l \phi' \rangle^* ((p-k-k_1)^2 - m_q^2)} \\
&\quad + \frac{m_q^2}{(p-k-k_1)^2 - m_q^2} \left(\frac{\phi_{\dot{E}}^{\dot{E}} \langle l \phi' \rangle k_{\dot{U}} (P - K_1)^{\dot{U}F} \phi_{\dot{G}}^{\dot{G}} \phi'^H}{((p-k_1)^2 - m_q^2)((k_2-p')^2 - m_q^2)} \right. \\
&\quad + \frac{\langle k \phi \rangle^* \phi_{\dot{E}}^{\dot{E}} \phi'^F l_V (K_2 - P')^{\dot{G}V} \phi'^H - k_{\dot{U}} l_V (P - K_1)^{\dot{U}V} \phi_{\dot{E}}^{\dot{E}} \phi'^F \phi_{\dot{G}}^{\dot{G}} \phi'^H}{((p-k_1)^2 - m_q^2)((k_2-p')^2 - m_q^2)} \\
&\quad \left. + \frac{\phi_{\dot{E}}^{\dot{E}} \phi'^F k_{\dot{G}}^{\dot{G}} \phi_{\dot{U}} (L - P')^{\dot{U}H}}{\langle l \phi' \rangle^* ((p-k_1)^2 - m_q^2)} + \frac{\phi_V' (P - K)^{\dot{E}V} l^F \phi_{\dot{G}}^{\dot{G}} \phi'^H}{\langle k \phi \rangle ((k_2-p')^2 - m_q^2)} \right) \Bigg] \\
&+ [T^a, T^b]_{ji} \frac{-1}{2(k+l)^2} \left[\langle k \phi \rangle^* \langle l \phi' \rangle \phi_{\dot{E}}^{\dot{E}} \phi'^H \left(\frac{(P - K_1)^{\dot{G}F}}{(p-k_1)^2 - m_q^2} + \frac{(K_2 - P')^{\dot{G}F}}{(k_2-p')^2 - m_q^2} \right) \right. \\
&\quad \left. + \left(\langle k \phi \rangle^* \langle l \phi' \rangle (L - K)_{\dot{U}V} + 2(K - L)_{\dot{W}X} \phi_{\dot{W}}^{\dot{W}} \phi'^X k_{\dot{U}} l_V \right) \right]
\end{aligned}$$

$$\begin{aligned}
& \times \frac{\phi^{\dot{E}}(P - K_1)^{\dot{U}F}(K_2 - P')^{\dot{G}V}\phi'^H}{((p - k_1)^2 - m_q^2)((k_2 - p')^2 - m_q^2)} \\
& + 2 \left(\frac{\langle k\phi \rangle^{*2} \langle k\phi' \rangle l_V (P - K)^{\dot{E}V}(K_2 - P')^{\dot{G}F}\phi'^H}{(p - l - k)^2((k_2 - p')^2 - m_q^2)} \right. \\
& \quad \left. - \frac{\langle l\phi' \rangle^2 \langle l\phi \rangle^* \phi^{\dot{E}}(P - K_1)^{\dot{G}F} k_{\dot{U}}(L - P')^{\dot{U}H}}{(k + l - p')^2((p - k_1)^2 - m_q^2)} \right) \\
& + \frac{m_q^2 \phi^{\dot{E}} \left(\langle k\phi \rangle^* \langle l\phi' \rangle (L - K)^{\dot{G}F} + 2(K - L)_{\dot{U}V} \phi^{\dot{U}} \phi'^V k^{\dot{G}} l^{\dot{F}} \right) \phi'^H}{((p - k_1)^2 - m_q^2)((k_2 - p')^2 - m_q^2)} \Bigg\}. \tag{4.32c}
\end{aligned}$$

The brace $\left\{ \begin{smallmatrix} a \leftrightarrow b \\ k \leftrightarrow l \end{smallmatrix} \right\}$ in Eqs. (4.32a) and (4.32b) again means the whole preceding expression with momenta and colour indices of the two gluons interchanged.

The subamplitudes for $\tau\tau' = -+$ can be obtained from that one for $\tau\tau' = +-$ by interchanging momenta and colour indices, which leads to

$$\mathcal{M}_{\text{Q}} \left(q_1 \begin{bmatrix} i \\ p \\ \text{R} \end{bmatrix} \bar{q}_2 \begin{bmatrix} j \\ p' \\ \text{R} \end{bmatrix} \rightarrow V_1 V_2 g \begin{bmatrix} a \\ k \\ - \end{bmatrix} g \begin{bmatrix} b \\ l \\ + \end{bmatrix} \right) = \mathcal{M}_{\text{Q}} \left(q_1 \begin{bmatrix} i \\ p \\ \text{L} \end{bmatrix} \bar{q}_2 \begin{bmatrix} j \\ p' \\ \text{R} \end{bmatrix} \rightarrow V_1 V_2 g \begin{bmatrix} b \\ l \\ + \end{bmatrix} g \begin{bmatrix} a \\ k \\ - \end{bmatrix} \right). \tag{4.32d}$$

By applying a \mathcal{P} transformation, the remaining amplitudes can be evaluated from those given in Eqs. (4.32a) – (4.32d),

$$\mathcal{M}_{\text{Q}} \left(q_1 \begin{bmatrix} i \\ p \\ \text{R} \end{bmatrix} \bar{q}_2 \begin{bmatrix} j \\ p' \\ \text{L} \end{bmatrix} \rightarrow V_1 V_2 g \begin{bmatrix} a \\ k \\ \tau \end{bmatrix} g \begin{bmatrix} b \\ l \\ \tau' \end{bmatrix} \right) = \mathcal{P} \left\{ \mathcal{M}_{\text{Q}} \left(q_1 \begin{bmatrix} i \\ p \\ \text{L} \end{bmatrix} \bar{q}_2 \begin{bmatrix} j \\ p' \\ \text{R} \end{bmatrix} \rightarrow V_1 V_2 g \begin{bmatrix} a \\ k \\ -\tau \end{bmatrix} g \begin{bmatrix} b \\ l \\ -\tau' \end{bmatrix} \right) \right\}, \tag{4.32e}$$

for the helicity combinations $\tau\tau' = ++, --, +-, -+$.

Contributions with two fermion chains

The real-emission amplitudes without external gluons, but with two fermion chains connected by an intermediate gluon, get contributions from three different kinds of subamplitudes. Two of them are similar to those in the gluonic case, with the gluon splitting into a quark–antiquark pair here. Only subamplitudes for diagrams with both weak gauge bosons coupling to the fermion chain of the initial-state quark–antiquark pair—directly or mediated by a third gauge boson—are evaluated. All other contributions can be constructed from these by the application of crossing. This means that, differing from the case with external gluons, crossing is applied here already on the level of subamplitudes, not only for full amplitudes. This step will be performed in the following section, where the particle insertions for gauge bosons and (anti-)quarks are specified. These insertions determine the selection of contributing diagrams.

One of the subamplitudes describes all diagrams with an intermediate gauge boson coupling to the fermion chain of the initial-state quark–antiquark pair, which are shown in

Figure 3.11. It is constructed from Eq. (4.22) by inserting (4.19) instead of the polarization bispinor of the outgoing gluon,

$$\begin{aligned} \mathcal{M}_V \left(q_1 \begin{bmatrix} i \\ p \\ \sigma \end{bmatrix} \bar{q}_2 \begin{bmatrix} j \\ p' \\ \sigma' \end{bmatrix} \rightarrow V_1 \begin{bmatrix} k_1 \\ v_1^* \end{bmatrix} V_2 \begin{bmatrix} k_2 \\ v_2^* \end{bmatrix} q_3 \begin{bmatrix} k \\ q \\ \tau \end{bmatrix} \bar{q}_4 \begin{bmatrix} l \\ q' \\ \tau' \end{bmatrix} \right) \\ = -i \hat{\mathcal{A}}_V \left(q_1 \begin{bmatrix} i \\ p \\ \sigma \end{bmatrix} \bar{q}_2 \begin{bmatrix} j \\ p' \\ \sigma' \end{bmatrix} \rightarrow V_1 \begin{bmatrix} k_1 \\ v_1^* \end{bmatrix} V_2 \begin{bmatrix} k_2 \\ v_2^* \end{bmatrix} g \begin{bmatrix} a \\ q+q' \\ g^* \end{bmatrix} \right) \mathcal{A} \left(g \begin{bmatrix} a \\ q+q' \\ g \end{bmatrix} \rightarrow q_3 \begin{bmatrix} k \\ q \\ \tau \end{bmatrix} \bar{q}_4 \begin{bmatrix} l \\ q' \\ \tau' \end{bmatrix} \right). \end{aligned} \quad (4.33)$$

The subamplitudes for the following helicity configurations result,

$$\begin{aligned} \mathcal{M}_V \left(q_1 \begin{bmatrix} i \\ p \\ L \end{bmatrix} \bar{q}_2 \begin{bmatrix} j \\ p' \\ R \end{bmatrix} \rightarrow V_1 V_2 q_3 \begin{bmatrix} k \\ q \\ L \end{bmatrix} \bar{q}_4 \begin{bmatrix} l \\ q' \\ R \end{bmatrix} \right) = -2 g_s^2 T_{ji}^a T_{kl}^a e^2 \sum_V \frac{C_{V\bar{q}_2 q_1}^- C_{V\bar{V}_1 \bar{V}_2} \mathcal{V}_{KL}}{y^2 - M_V^2} \\ \times \frac{1}{(q+q')^2} \left[\frac{\langle \eta' \phi \rangle^* \eta'_V (P-K)^{\dot{K}V} \phi'^L}{(p-k)^2} + \frac{\langle \eta' \phi \rangle \phi^{\dot{K}} \eta'_{\dot{U}} (K-P')^{\dot{U}L}}{(k-p')^2} \right], \end{aligned} \quad (4.33a)$$

$$\begin{aligned} \mathcal{M}_V \left(q_1 \begin{bmatrix} i \\ p \\ L \end{bmatrix} \bar{q}_2 \begin{bmatrix} j \\ p' \\ R \end{bmatrix} \rightarrow V_1 V_2 q_3 \begin{bmatrix} k \\ q \\ R \end{bmatrix} \bar{q}_4 \begin{bmatrix} l \\ q' \\ L \end{bmatrix} \right) = -2 g_s^2 T_{ji}^a T_{kl}^a e^2 \sum_V \frac{C_{V\bar{q}_2 q_1}^- C_{V\bar{V}_1 \bar{V}_2} \mathcal{V}_{KL}}{y^2 - M_V^2} \\ \times \frac{1}{(q+q')^2} \left[\frac{\langle \eta' \phi \rangle^* \eta'_V (P-K)^{\dot{K}V} \phi'^L}{(p-k)^2} + \frac{\langle \eta' \phi \rangle \phi^{\dot{K}} \eta'_{\dot{U}} (K-P')^{\dot{U}L}}{(k-p')^2} \right]. \end{aligned} \quad (4.33b)$$

The remaining helicity channels are obtained by means of a \mathcal{P} transformation,

$$\mathcal{M}_V \left(q_1 \begin{bmatrix} i \\ p \\ R \end{bmatrix} \bar{q}_2 \begin{bmatrix} j \\ p' \\ L \end{bmatrix} \rightarrow V_1 V_2 q_3 \begin{bmatrix} k \\ q \\ R \end{bmatrix} \bar{q}_4 \begin{bmatrix} l \\ q' \\ L \end{bmatrix} \right) = \mathcal{P} \left\{ \mathcal{M}_V \left(q_1 \begin{bmatrix} i \\ p \\ L \end{bmatrix} \bar{q}_2 \begin{bmatrix} j \\ p' \\ R \end{bmatrix} \rightarrow V_1 V_2 q_3 \begin{bmatrix} k \\ q \\ L \end{bmatrix} \bar{q}_4 \begin{bmatrix} l \\ q' \\ R \end{bmatrix} \right) \right\}, \quad (4.33c)$$

$$\mathcal{M}_V \left(q_1 \begin{bmatrix} i \\ p \\ R \end{bmatrix} \bar{q}_2 \begin{bmatrix} j \\ p' \\ L \end{bmatrix} \rightarrow V_1 V_2 q_3 \begin{bmatrix} k \\ q \\ L \end{bmatrix} \bar{q}_4 \begin{bmatrix} l \\ q' \\ R \end{bmatrix} \right) = \mathcal{P} \left\{ \mathcal{M}_V \left(q_1 \begin{bmatrix} i \\ p \\ L \end{bmatrix} \bar{q}_2 \begin{bmatrix} j \\ p' \\ R \end{bmatrix} \rightarrow V_1 V_2 q_3 \begin{bmatrix} k \\ q \\ R \end{bmatrix} \bar{q}_4 \begin{bmatrix} l \\ q' \\ L \end{bmatrix} \right) \right\}. \quad (4.33d)$$

The subamplitudes with the two weak gauge bosons coupling directly to the fermion chain of the incoming quark-antiquark pair are constructed from Eq. (4.23) with the gluon polarization bispinor replaced by (4.19),

$$\begin{aligned} \mathcal{M}_Q \left(q_1 \begin{bmatrix} i \\ p \\ \sigma \end{bmatrix} \bar{q}_2 \begin{bmatrix} j \\ p' \\ \sigma' \end{bmatrix} \rightarrow V_1 \begin{bmatrix} k_1 \\ v_1^* \end{bmatrix} V_2 \begin{bmatrix} k_2 \\ v_2^* \end{bmatrix} q_3 \begin{bmatrix} k \\ q \\ \tau \end{bmatrix} \bar{q}_4 \begin{bmatrix} l \\ q' \\ \tau' \end{bmatrix} \right) \\ = -i \hat{\mathcal{A}}_Q \left(q_1 \begin{bmatrix} i \\ p \\ \sigma \end{bmatrix} \bar{q}_2 \begin{bmatrix} j \\ p' \\ \sigma' \end{bmatrix} \rightarrow V_1 \begin{bmatrix} k_1 \\ v_1^* \end{bmatrix} V_2 \begin{bmatrix} k_2 \\ v_2^* \end{bmatrix} g \begin{bmatrix} a \\ q+q' \\ g^* \end{bmatrix} \right) \mathcal{A} \left(g \begin{bmatrix} a \\ q+q' \\ g \end{bmatrix} \rightarrow q_3 \begin{bmatrix} k \\ q \\ \tau \end{bmatrix} \bar{q}_4 \begin{bmatrix} l \\ q' \\ \tau' \end{bmatrix} \right). \end{aligned} \quad (4.34)$$

By specifying the (anti-)quark helicities, the subamplitudes for the following helicity configurations result,

$$\begin{aligned} \mathcal{M}_Q \left(q_1 \begin{bmatrix} i \\ p \\ L \end{bmatrix} \bar{q}_2 \begin{bmatrix} j \\ p' \\ R \end{bmatrix} \rightarrow V_1 V_2 q_3 \begin{bmatrix} k \\ q \\ L \end{bmatrix} \bar{q}_4 \begin{bmatrix} l \\ q' \\ R \end{bmatrix} \right) = g_s^2 T_{ji}^a T_{kl}^a e^2 v_{1,\dot{E}F}^* v_{2,\dot{G}H}^* \sum_q C_{V_2 \bar{q}_2 q}^- C_{V_1 q q_1}^- \frac{1}{(q+q')^2} \\ \times \left[\frac{\phi^{\dot{E}} \eta'_{\dot{U}} (P-K_1)^{\dot{U}F} \eta_V (K_2-P')^{\dot{G}V} \phi'^H}{((k_2-p')^2 - m_q^2)((p-k_1)^2 - m_q^2)} + \frac{\langle \eta' \phi \rangle^* \eta'_V (P-K)^{\dot{E}V} (K_2-P')^{\dot{G}F} \phi'^H}{(p-k)^2((k_2-p')^2 - m_q^2)} \right] \end{aligned}$$

$$+ \frac{\langle \eta \phi' \rangle \phi^{\dot{E}}(P - K_1)^{\dot{G}F} \eta'_U(K - P')^{\dot{U}H}}{(k - p')^2((p - k_1)^2 - m_q^2)} + \frac{m_q^2 \phi^{\dot{E}} \eta^F \eta'^{\dot{G}} \phi'^H}{((k_2 - p')^2 - m_q^2)((p - k_1)^2 - m_q^2)} \Big], \quad (4.34a)$$

$$\begin{aligned} \mathcal{M}_Q \left(q_1 \begin{bmatrix} i \\ p \\ L \end{bmatrix} \bar{q}_2 \begin{bmatrix} j \\ p' \\ R \end{bmatrix} \rightarrow V_1 V_2 q_3 \begin{bmatrix} k \\ q \\ R \end{bmatrix} \bar{q}_4 \begin{bmatrix} l \\ q' \\ L \end{bmatrix} \right) &= g_s^2 T_{ji}^a T_{kl}^a e^2 v_{1,\dot{E}F}^* v_{2,\dot{G}H}^* \sum_q C_{V_2 \bar{q}_2 q}^- C_{V_1 \bar{q}_1 q}^- \frac{1}{(q + q')^2} \\ &\times \left[\frac{\phi^{\dot{E}} \eta'_U(P - K_1)^{\dot{U}F} \eta'_V(K_2 - P')^{\dot{G}V} \phi'^H}{((k_2 - p')^2 - m_q^2)((p - k_1)^2 - m_q^2)} + \frac{\langle \eta \phi \rangle^* \eta'_V(P - K)^{\dot{E}V} (K_2 - P')^{\dot{G}F} \phi'^H}{(p - k)^2((k_2 - p')^2 - m_q^2)} \right. \\ &\left. + \frac{\langle \eta' \phi' \rangle \phi^{\dot{E}}(P - K_1)^{\dot{G}F} \eta'_U(K - P')^{\dot{U}H}}{(k - p')^2((p - k_1)^2 - m_q^2)} + \frac{m_q^2 \phi^{\dot{E}} \eta'^F \eta^{\dot{G}} \phi'^H}{((k_2 - p')^2 - m_q^2)((p - k_1)^2 - m_q^2)} \right]. \quad (4.34b) \end{aligned}$$

Again, a \mathcal{P} transformation yields the remaining helicity channels,

$$\mathcal{M}_Q \left(q_1 \begin{bmatrix} i \\ p \\ R \end{bmatrix} \bar{q}_2 \begin{bmatrix} j \\ p' \\ L \end{bmatrix} \rightarrow V_1 V_2 q_3 \begin{bmatrix} k \\ q \\ R \end{bmatrix} \bar{q}_4 \begin{bmatrix} l \\ q' \\ L \end{bmatrix} \right) = \mathcal{P} \left\{ \mathcal{M}_Q \left(q_1 \begin{bmatrix} i \\ p \\ L \end{bmatrix} \bar{q}_2 \begin{bmatrix} j \\ p' \\ R \end{bmatrix} \rightarrow V_1 V_2 q_3 \begin{bmatrix} k \\ q \\ L \end{bmatrix} \bar{q}_4 \begin{bmatrix} l \\ q' \\ R \end{bmatrix} \right) \right\}, \quad (4.34c)$$

$$\mathcal{M}_Q \left(q_1 \begin{bmatrix} i \\ p \\ R \end{bmatrix} \bar{q}_2 \begin{bmatrix} j \\ p' \\ L \end{bmatrix} \rightarrow V_1 V_2 q_3 \begin{bmatrix} k \\ q \\ L \end{bmatrix} \bar{q}_4 \begin{bmatrix} l \\ q' \\ R \end{bmatrix} \right) = \mathcal{P} \left\{ \mathcal{M}_Q \left(q_1 \begin{bmatrix} i \\ p \\ L \end{bmatrix} \bar{q}_2 \begin{bmatrix} j \\ p' \\ R \end{bmatrix} \rightarrow V_1 V_2 q_3 \begin{bmatrix} k \\ q \\ R \end{bmatrix} \bar{q}_4 \begin{bmatrix} l \\ q' \\ L \end{bmatrix} \right) \right\}. \quad (4.34d)$$

The third subamplitude contains all diagrams with the two gauge bosons coupling to different fermion chains, which are presented in Figure 3.12. For its construction, the gluon polarization bispinor in Eq. (4.21) is replaced by (4.20),

$$\begin{aligned} \mathcal{M}_F \left(q_1 \begin{bmatrix} i \\ p \\ \sigma \end{bmatrix} \bar{q}_2 \begin{bmatrix} j \\ p' \\ \sigma' \end{bmatrix} \rightarrow V_1 \begin{bmatrix} k_1 \\ v_1^* \end{bmatrix} V_2 \begin{bmatrix} k_2 \\ v_2^* \end{bmatrix} q_3 \begin{bmatrix} k \\ q \\ \tau \end{bmatrix} \bar{q}_4 \begin{bmatrix} l \\ q' \\ \tau' \end{bmatrix} \right) \\ = -i \hat{\mathcal{A}} \left(q_1 \begin{bmatrix} i \\ p \\ \sigma \end{bmatrix} \bar{q}_2 \begin{bmatrix} j \\ p' \\ \sigma' \end{bmatrix} \rightarrow V_1 \begin{bmatrix} k_1 \\ v_1^* \end{bmatrix} g \begin{bmatrix} a \\ p + p' - k_1 \\ g^* \end{bmatrix} \right) \mathcal{A} \left(g \begin{bmatrix} a \\ p + p' - k_1 \\ g \end{bmatrix} \rightarrow V_2 \begin{bmatrix} k_2 \\ v_2^* \end{bmatrix} q_3 \begin{bmatrix} k \\ q \\ \tau \end{bmatrix} \bar{q}_4 \begin{bmatrix} l \\ q' \\ \tau' \end{bmatrix} \right). \quad (4.35) \end{aligned}$$

One obtains the subamplitudes for the following helicity channels,

$$\begin{aligned} \mathcal{M}_F \left(q_1 \begin{bmatrix} i \\ p \\ L \end{bmatrix} \bar{q}_2 \begin{bmatrix} j \\ p' \\ R \end{bmatrix} \rightarrow V_1 V_2 q_3 \begin{bmatrix} k \\ q \\ L \end{bmatrix} \bar{q}_4 \begin{bmatrix} l \\ q' \\ R \end{bmatrix} \right) &= g_s^2 T_{ji}^a T_{kl}^a e^2 v_{1,\dot{E}F}^* v_{2,\dot{G}H}^* \frac{1}{(q + q')^2} \sum_q C_{V_2 \bar{q}_2 q}^- C_{V_1 \bar{q}_1 q}^- \\ &\times \left[\frac{\phi^{\dot{E}} \eta'_U(P - K_1)^{\dot{U}F} \eta'_V(K_2 - P')^{\dot{G}V} \phi'^H}{((k_2 - p')^2 - m_q^2)((p - k_1)^2 - m_q^2)} + \frac{\langle \eta' \phi \rangle^* \eta'_V(P - K)^{\dot{E}V} (K_2 - P')^{\dot{G}F} \phi'^H}{(p - k)^2((k_2 - p')^2 - m_q^2)} \right. \\ &\left. + \frac{\langle \eta \phi' \rangle \phi^{\dot{E}}(P - K_1)^{\dot{G}F} \eta'_U(K - P')^{\dot{U}H}}{(k - p')^2((p - k_1)^2 - m_q^2)} + \frac{m_q^2 \phi^{\dot{E}} \eta^F \eta'^{\dot{G}} \phi'^H}{((k_2 - p')^2 - m_q^2)((p - k_1)^2 - m_q^2)} \right], \quad (4.35a) \end{aligned}$$

$$\begin{aligned} \mathcal{M}_F \left(q_1 \begin{bmatrix} i \\ p \\ L \end{bmatrix} \bar{q}_2 \begin{bmatrix} j \\ p' \\ R \end{bmatrix} \rightarrow V_1 V_2 q_3 \begin{bmatrix} k \\ q \\ R \end{bmatrix} \bar{q}_4 \begin{bmatrix} l \\ q' \\ L \end{bmatrix} \right) &= g_s^2 T_{ji}^a T_{kl}^a e^2 v_{1,\dot{E}F}^* v_{2,\dot{G}H}^* \frac{1}{(q + q')^2} \sum_q C_{V_2 \bar{q}_2 q}^- C_{V_1 \bar{q}_1 q}^- \\ &\times \left[\frac{\phi^{\dot{E}} \eta'_U(P - K_1)^{\dot{U}F} \eta'_V(K_2 - P')^{\dot{G}V} \phi'^H}{((k_2 - p')^2 - m_q^2)((p - k_1)^2 - m_q^2)} + \frac{\langle \eta \phi \rangle^* \eta'_V(P - K)^{\dot{E}V} (K_2 - P')^{\dot{G}F} \phi'^H}{(p - k)^2((k_2 - p')^2 - m_q^2)} \right. \\ &\left. + \frac{\langle \eta' \phi' \rangle \phi^{\dot{E}}(P - K_1)^{\dot{G}F} \eta'_U(K - P')^{\dot{U}H}}{(k - p')^2((p - k_1)^2 - m_q^2)} + \frac{m_q^2 \phi^{\dot{E}} \eta'^F \eta^{\dot{G}} \phi'^H}{((k_2 - p')^2 - m_q^2)((p - k_1)^2 - m_q^2)} \right], \quad (4.35b) \end{aligned}$$

the remaining ones result from a \mathcal{P} transformation,

$$\mathcal{M}_F\left(q_1 \begin{bmatrix} i \\ p \\ R \end{bmatrix} \bar{q}_2 \begin{bmatrix} j \\ p' \\ L \end{bmatrix} \rightarrow V_1 V_2 q_3 \begin{bmatrix} k \\ q \\ R \end{bmatrix} \bar{q}_4 \begin{bmatrix} l \\ q' \\ L \end{bmatrix}\right) = \mathcal{P}\left\{\mathcal{M}_F\left(q_1 \begin{bmatrix} i \\ p \\ L \end{bmatrix} \bar{q}_2 \begin{bmatrix} j \\ p' \\ R \end{bmatrix} \rightarrow V_1 V_2 q_3 \begin{bmatrix} k \\ q \\ L \end{bmatrix} \bar{q}_4 \begin{bmatrix} l \\ q' \\ R \end{bmatrix}\right)\right\}, \quad (4.35c)$$

$$\mathcal{M}_F\left(q_1 \begin{bmatrix} i \\ p \\ R \end{bmatrix} \bar{q}_2 \begin{bmatrix} j \\ p' \\ L \end{bmatrix} \rightarrow V_1 V_2 q_3 \begin{bmatrix} k \\ q \\ L \end{bmatrix} \bar{q}_4 \begin{bmatrix} l \\ q' \\ R \end{bmatrix}\right) = \mathcal{P}\left\{\mathcal{M}_F\left(q_1 \begin{bmatrix} i \\ p \\ L \end{bmatrix} \bar{q}_2 \begin{bmatrix} j \\ p' \\ R \end{bmatrix} \rightarrow V_1 V_2 q_3 \begin{bmatrix} k \\ q \\ R \end{bmatrix} \bar{q}_4 \begin{bmatrix} l \\ q' \\ L \end{bmatrix}\right)\right\}. \quad (4.35d)$$

4.4 Construction of full amplitudes for specified gauge bosons

In the previous section, subamplitudes for the generic process class $pp/p\bar{p} \rightarrow VV + \text{jet} + X$ are evaluated. These subamplitudes are groups of diagrams that are gauge invariant with respect to $SU(3)_C$. In order to construct full amplitudes out of these, the weak gauge bosons must be specified. The different charges of the gauge bosons and the flavour-changing property of the W boson have a strong influence on which initial- and final-state (anti-)quarks deliver contributing subprocesses. In this section, we use the notation $Q = d, u, s, c, b$, $U = u, c$, and $D = d, s, b$.

4.4.1 Contributions with external gluons

Which subamplitudes and which helicity channels contribute, is determined only by the electroweak structure of the subprocesses, i.e. the number of emitted gluons is not relevant for this distinction. Therefore, the LO subprocesses with one emitted gluon and the real-emission subprocesses with two emitted gluons can be treated simultaneously.

WW+jet

Considering the process class $pp/p\bar{p} \rightarrow WW + \text{jet} + X$, the order of the gauge bosons coupling directly to the fermion chain is determined by the charge of the external (anti-)quarks: A W^+ boson only couples to incoming up-type quarks or down-type antiquarks, whereas a W^- boson only couples to incoming down-type quarks and up-type antiquarks. Otherwise, intermediate quark states with charges of $+\frac{5}{3}e$ or $-\frac{4}{3}e$ would have to exist, which is not the case in the SM. Owing to the maximal parity violation of the W bosons, the helicity of the fermion chain is restricted to left-handed quarks and right-handed antiquarks in case of direct gauge-boson coupling. This is not the case for the subamplitude with an intermediate gauge boson, because photons and Z bosons couple to both possible helicity chains. For this reason, the left-handed quark chain gets contributions from both subamplitudes, which are given in Eqs. (4.29) and (4.30) for the LO case and in Eqs. (4.31) and (4.32) for the real-emission case. For the subprocesses with an external up-type quark–antiquark

pair the corresponding amplitudes read

$$\mathcal{M}\left(\mathrm{U}\begin{bmatrix} i \\ p \\ \mathrm{L} \end{bmatrix} \bar{\mathrm{U}}\begin{bmatrix} j \\ p' \\ \mathrm{R} \end{bmatrix} \rightarrow \mathrm{W}^+\begin{bmatrix} k_1 \\ w_+^* \end{bmatrix} \mathrm{W}^-\begin{bmatrix} k_2 \\ w_-^* \end{bmatrix} g\begin{bmatrix} a \\ k \\ \tau \end{bmatrix} \left(g\begin{bmatrix} b \\ l \\ \tau' \end{bmatrix}\right)\right) = (\mathcal{M}_{\mathrm{V}} + \mathcal{M}_{\mathrm{Q}})\left(\dots \rightarrow \dots\right). \quad (4.36a)$$

The right-handed quark chain only gets contributions from the subamplitudes including a three-gauge-boson vertex provided in Eqs. (4.29) and (4.31), respectively. They are

$$\mathcal{M}\left(\mathrm{U}\begin{bmatrix} i \\ p \\ \mathrm{R} \end{bmatrix} \bar{\mathrm{U}}\begin{bmatrix} j \\ p' \\ \mathrm{L} \end{bmatrix} \rightarrow \mathrm{W}^+\begin{bmatrix} k_1 \\ w_+^* \end{bmatrix} \mathrm{W}^-\begin{bmatrix} k_2 \\ w_-^* \end{bmatrix} g\begin{bmatrix} a \\ k \\ \tau \end{bmatrix} \left(g\begin{bmatrix} b \\ l \\ \tau' \end{bmatrix}\right)\right) = \mathcal{M}_{\mathrm{V}}\left(\dots \rightarrow \dots\right). \quad (4.36b)$$

For an external down-type quark–antiquark pair, the discussion of the helicity dependence of contributing subamplitudes is identical to the up-type case. The respective amplitudes can be obtained from those in Eq. (4.36) via

$$\begin{aligned} & \mathcal{M}\left(\mathrm{D}\begin{bmatrix} i \\ p \\ \sigma \end{bmatrix} \bar{\mathrm{D}}\begin{bmatrix} j \\ p' \\ \sigma' \end{bmatrix} \rightarrow \mathrm{W}^+\begin{bmatrix} k_1 \\ w_+^* \end{bmatrix} \mathrm{W}^-\begin{bmatrix} k_2 \\ w_-^* \end{bmatrix} g\begin{bmatrix} a \\ k \\ \tau \end{bmatrix} \left(g\begin{bmatrix} b \\ l \\ \tau' \end{bmatrix}\right)\right) \\ &= \mathcal{M}\left(\mathrm{U}\begin{bmatrix} i \\ p \\ \sigma \end{bmatrix} \bar{\mathrm{U}}\begin{bmatrix} j \\ p' \\ \sigma' \end{bmatrix} \rightarrow \mathrm{W}^+\begin{bmatrix} k_1 \\ w_+^* \end{bmatrix} \mathrm{W}^-\begin{bmatrix} k_2 \\ w_-^* \end{bmatrix} g\begin{bmatrix} a \\ k \\ \tau \end{bmatrix} \left(g\begin{bmatrix} b \\ l \\ \tau' \end{bmatrix}\right)\right) \Big|_{\mathrm{U} \leftrightarrow \mathrm{D}, \mathrm{W}^+ \leftrightarrow \mathrm{W}^-}, \end{aligned} \quad (4.37)$$

i.e. by interchanging momenta and polarization bispinors of W^+ and W^- . Moreover, U and D as well as W^+ and W^- have to be interchanged in the respective couplings. The latter exchange influences, of course, also the contributing flavours in the sum over intermediate quark states, which appears in the subamplitudes with both W bosons coupling directly to the fermion chain. However, only the CKM factors in the W-boson couplings are changed, which give unity when summed over all intermediate quark states in any possible cases. This point is discussed in the context of Eq. (4.23), where this situation shows up for the first time. Consequently, all these subprocesses can be evaluated as in the situation of a trivial (diagonal) CKM matrix.

ZZ+jet

In the process class $\mathrm{pp}/\mathrm{p}\bar{\mathrm{p}} \rightarrow \mathrm{ZZ} + \text{jet} + \mathrm{X}$, only the subamplitudes with both Z bosons coupling directly to the fermion chain contribute. Since the Z bosons are neutral, their order can be exchanged, giving rise to a second contribution. Since no flavour-changing neutral currents exist in the SM, only subprocesses initiated by a quark–antiquark pair of the same flavour arise. The intermediate quark must belong to this flavour, too. With the subamplitudes taken from Eqs. (4.30) and (4.32), respectively, the amplitudes read

$$\begin{aligned} & \mathcal{M}\left(\mathrm{Q}\begin{bmatrix} i \\ p \\ \sigma \end{bmatrix} \bar{\mathrm{Q}}\begin{bmatrix} j \\ p' \\ \sigma' \end{bmatrix} \rightarrow \mathrm{Z}\begin{bmatrix} k_1 \\ z_1^* \end{bmatrix} \mathrm{Z}\begin{bmatrix} k_2 \\ z_2^* \end{bmatrix} g\begin{bmatrix} a \\ k \\ \tau \end{bmatrix} \left(g\begin{bmatrix} b \\ l \\ \tau' \end{bmatrix}\right)\right) \\ &= \mathcal{M}_{\mathrm{Q}}\left(\mathrm{Q}\begin{bmatrix} i \\ p \\ \sigma \end{bmatrix} \bar{\mathrm{Q}}\begin{bmatrix} j \\ p' \\ \sigma' \end{bmatrix} \rightarrow \mathrm{Z}\begin{bmatrix} k_1 \\ z_1^* \end{bmatrix} \mathrm{Z}\begin{bmatrix} k_2 \\ z_2^* \end{bmatrix} g\begin{bmatrix} a \\ k \\ \tau \end{bmatrix} \left(g\begin{bmatrix} b \\ l \\ \tau' \end{bmatrix}\right)\right) + \mathcal{M}_{\mathrm{Q}}\left(\dots \rightarrow \mathrm{Z}\begin{bmatrix} k_2 \\ z_2^* \end{bmatrix} \mathrm{Z}\begin{bmatrix} k_1 \\ z_1^* \end{bmatrix} \dots\right), \end{aligned} \quad (4.38)$$

where non-vanishing contributions stem from the helicity channels $\sigma\sigma' = \mathrm{LR}, \mathrm{RL}$ in the relevant case of vanishing quark masses.

WZ+jet

The subprocesses of $pp/p\bar{p} \rightarrow WZ + \text{jet} + X$ get contributions from both subamplitudes again. In the subamplitude with a three-gauge-boson vertex, a W boson shows up as an intermediate particle, so this subamplitude contributes only in case of a left-handed quark chain. In the second subamplitude with W and Z boson coupling directly to the fermion chain, both orders of the gauge bosons contribute, but again only for a left-handed quark chain. The flavour of the intermediate quark is given either by the flavour of the incoming quark or antiquark, depending on the order of the weak gauge bosons. In case of W^+Z +jet production, charge conservation allows only initial states with an up-type quark and a down-type antiquark in the considered process class. With the subamplitudes taken from Eqs. (4.29) and (4.30) for the LO case and from Eqs. (4.31) and (4.32) for the real-emission case, the only contributing helicity amplitudes are

$$\begin{aligned} \mathcal{M}\left(\text{U}\begin{bmatrix} i \\ p \\ \text{L} \end{bmatrix} \bar{\text{D}}\begin{bmatrix} j \\ p' \\ \text{R} \end{bmatrix} \rightarrow \text{W}^+\begin{bmatrix} k_1 \\ w_+^* \end{bmatrix} \text{Z}\begin{bmatrix} k_2 \\ z^* \end{bmatrix} \text{g}\begin{bmatrix} a \\ k \\ \tau \end{bmatrix} \left(\text{g}\begin{bmatrix} b \\ l \\ \tau' \end{bmatrix}\right)\right) &= \mathcal{M}_{\text{V}}(\dots \rightarrow \dots) \\ &+ \mathcal{M}_{\text{Q}}\left(\text{U}\begin{bmatrix} i \\ p \\ \text{L} \end{bmatrix} \bar{\text{D}}\begin{bmatrix} j \\ p' \\ \text{R} \end{bmatrix} \rightarrow \text{W}^+\begin{bmatrix} k_1 \\ w_+^* \end{bmatrix} \text{Z}\begin{bmatrix} k_2 \\ z^* \end{bmatrix} \text{g}\begin{bmatrix} a \\ k \\ \tau \end{bmatrix} \left(\text{g}\begin{bmatrix} b \\ l \\ \tau' \end{bmatrix}\right)\right) + \mathcal{M}_{\text{Q}}\left(\dots \rightarrow \text{Z}\begin{bmatrix} k_2 \\ z^* \end{bmatrix} \text{W}^+\begin{bmatrix} k_1 \\ w_+^* \end{bmatrix} \dots\right). \end{aligned} \quad (4.39)$$

The amplitudes for W^-Z +jet production are not needed explicitly, since they can be obtained from the given ones by means of a \mathcal{CP} -transformation. This transformation is performed on the level of matrix elements in the following section.

4.4.2 Contributions with two fermion chains

In the real-emission subprocesses with two fermion chains, the number of different amplitudes to be calculated is much larger. This is mainly due to the fact that the two weak gauge bosons can couple to the same fermion chain or to different ones. Moreover, not only subprocesses contribute with one fermion chain of the quark–antiquark pair in the initial state and a second one of the pair in the final state. Also subprocesses with a changed fermion-number flow exist: Here, one chain contains the external quarks and the second one the external antiquarks. In some constellations of external (anti-)quarks, even diagrams of both types contribute to the same subprocess.

WW+jet

To compactify the expressions appearing in the amplitudes of $pp/p\bar{p} \rightarrow WW + \text{jet} + X$, the following abbreviation is introduced for the situation that both W bosons couple—directly or mediated by a third gauge boson—to the left-handed fermion chain connecting the initial-state quark–antiquark pair,

$$\mathcal{M}_{\text{V+Q}}\left(\text{q}_1\begin{bmatrix} i \\ p \\ \text{L} \end{bmatrix} \bar{\text{q}}_2\begin{bmatrix} j \\ p' \\ \text{R} \end{bmatrix} \rightarrow \text{W}^+\begin{bmatrix} k_1 \\ w_+^* \end{bmatrix} \text{W}^-\begin{bmatrix} k_2 \\ w_-^* \end{bmatrix} \text{q}_3\begin{bmatrix} k \\ q \\ \tau \end{bmatrix} \bar{\text{q}}_4\begin{bmatrix} l \\ q' \\ \tau' \end{bmatrix}\right) = \left(\mathcal{M}_{\text{V}} + \mathcal{M}_{\text{Q}}\right)(\dots \rightarrow \dots). \quad (4.40)$$

The two subamplitudes used in this expression are given in Eqs. (4.33) and (4.34), respectively.

The first amplitude to be calculated contains four up-type (anti-)quarks of the same generation as external particles. This enables four possibilities for the two W bosons to couple to fermion chains, namely the chains of the initial- and the final-state quark-antiquark pairs and those with the incoming and the outgoing (anti-)quark as endpoints. Since—in the relevant case of massless external fermions—only (anti-)quarks with the same helicity or a quark and an antiquark with opposite helicities can form a quark chain, not all four possibilities contribute to each helicity channel. Just the helicity amplitudes with only left-handed quarks and right-handed antiquarks or vice versa get contributions from all four configurations. With the definitions of Eqs. (4.33) and (4.40), they read

$$\begin{aligned} \mathcal{M}\left(\mathrm{U}\begin{bmatrix} i \\ p \\ \mathrm{L} \end{bmatrix} \bar{\mathrm{U}}\begin{bmatrix} j \\ p' \\ \mathrm{R} \end{bmatrix} \rightarrow \mathrm{W}^+\begin{bmatrix} k_1 \\ w_+^* \end{bmatrix} \mathrm{W}^-\begin{bmatrix} k_2 \\ w_-^* \end{bmatrix} \mathrm{U}\begin{bmatrix} k \\ q \\ \mathrm{L} \end{bmatrix} \bar{\mathrm{U}}\begin{bmatrix} l \\ q' \\ \mathrm{R} \end{bmatrix}\right) \\ = \left(1 + \mathcal{X}\begin{bmatrix} p \leftrightarrow q' \\ p' \leftrightarrow q \end{bmatrix} - \mathcal{X}[p \leftrightarrow q'] - \mathcal{X}[p' \leftrightarrow q]\right) \left\{ \mathcal{M}_{\mathrm{V}+\mathrm{Q}}(\dots \rightarrow \dots) \right\}, \end{aligned} \quad (4.41a)$$

$$\begin{aligned} \mathcal{M}\left(\mathrm{U}\begin{bmatrix} i \\ p \\ \mathrm{R} \end{bmatrix} \bar{\mathrm{U}}\begin{bmatrix} j \\ p' \\ \mathrm{L} \end{bmatrix} \rightarrow \mathrm{W}^+\begin{bmatrix} k_1 \\ w_+^* \end{bmatrix} \mathrm{W}^-\begin{bmatrix} k_2 \\ w_-^* \end{bmatrix} \mathrm{U}\begin{bmatrix} k \\ q \\ \mathrm{R} \end{bmatrix} \bar{\mathrm{U}}\begin{bmatrix} l \\ q' \\ \mathrm{L} \end{bmatrix}\right) \\ = \left(1 + \mathcal{X}\begin{bmatrix} p \leftrightarrow q' \\ p' \leftrightarrow q \end{bmatrix} - \mathcal{X}[p \leftrightarrow q'] - \mathcal{X}[p' \leftrightarrow q]\right) \left\{ \mathcal{M}_{\mathrm{V}}(\dots \rightarrow \dots) \right\}. \end{aligned} \quad (4.41b)$$

The remaining non-vanishing helicity channels get only two contributions,

$$\begin{aligned} \mathcal{M}\left(\mathrm{U}\begin{bmatrix} i \\ p \\ \mathrm{L} \end{bmatrix} \bar{\mathrm{U}}\begin{bmatrix} j \\ p' \\ \mathrm{R} \end{bmatrix} \rightarrow \mathrm{W}^+\begin{bmatrix} k_1 \\ w_+^* \end{bmatrix} \mathrm{W}^-\begin{bmatrix} k_2 \\ w_-^* \end{bmatrix} \mathrm{U}\begin{bmatrix} k \\ q \\ \mathrm{R} \end{bmatrix} \bar{\mathrm{U}}\begin{bmatrix} l \\ q' \\ \mathrm{L} \end{bmatrix}\right) = \mathcal{M}_{\mathrm{V}+\mathrm{Q}}(\dots \rightarrow \dots) \\ + \mathcal{X}\begin{bmatrix} p \leftrightarrow q' \\ p' \leftrightarrow q \end{bmatrix} \left\{ \mathcal{M}_{\mathrm{V}}\left(\mathrm{U}\begin{bmatrix} i \\ p \\ \mathrm{R} \end{bmatrix} \bar{\mathrm{U}}\begin{bmatrix} j \\ p' \\ \mathrm{L} \end{bmatrix} \rightarrow \mathrm{W}^+\begin{bmatrix} k_1 \\ w_+^* \end{bmatrix} \mathrm{W}^-\begin{bmatrix} k_2 \\ w_-^* \end{bmatrix} \mathrm{U}\begin{bmatrix} k \\ q \\ \mathrm{L} \end{bmatrix} \bar{\mathrm{U}}\begin{bmatrix} l \\ q' \\ \mathrm{R} \end{bmatrix}\right) \right\}, \end{aligned} \quad (4.41c)$$

$$\begin{aligned} \mathcal{M}\left(\mathrm{U}\begin{bmatrix} i \\ p \\ \mathrm{R} \end{bmatrix} \bar{\mathrm{U}}\begin{bmatrix} j \\ p' \\ \mathrm{L} \end{bmatrix} \rightarrow \mathrm{W}^+\begin{bmatrix} k_1 \\ w_+^* \end{bmatrix} \mathrm{W}^-\begin{bmatrix} k_2 \\ w_-^* \end{bmatrix} \mathrm{U}\begin{bmatrix} k \\ q \\ \mathrm{L} \end{bmatrix} \bar{\mathrm{U}}\begin{bmatrix} l \\ q' \\ \mathrm{R} \end{bmatrix}\right) = \mathcal{M}_{\mathrm{V}}(\dots \rightarrow \dots) \\ + \mathcal{X}\begin{bmatrix} p \leftrightarrow q' \\ p' \leftrightarrow q \end{bmatrix} \left\{ \mathcal{M}_{\mathrm{V}+\mathrm{Q}}\left(\mathrm{U}\begin{bmatrix} i \\ p \\ \mathrm{L} \end{bmatrix} \bar{\mathrm{U}}\begin{bmatrix} j \\ p' \\ \mathrm{R} \end{bmatrix} \rightarrow \mathrm{W}^+\begin{bmatrix} k_1 \\ w_+^* \end{bmatrix} \mathrm{W}^-\begin{bmatrix} k_2 \\ w_-^* \end{bmatrix} \mathrm{U}\begin{bmatrix} k \\ q \\ \mathrm{R} \end{bmatrix} \bar{\mathrm{U}}\begin{bmatrix} l \\ q' \\ \mathrm{L} \end{bmatrix}\right) \right\}, \end{aligned} \quad (4.41d)$$

$$\begin{aligned} \mathcal{M}\left(\mathrm{U}\begin{bmatrix} i \\ p \\ \mathrm{L} \end{bmatrix} \bar{\mathrm{U}}\begin{bmatrix} j \\ p' \\ \mathrm{L} \end{bmatrix} \rightarrow \mathrm{W}^+\begin{bmatrix} k_1 \\ w_+^* \end{bmatrix} \mathrm{W}^-\begin{bmatrix} k_2 \\ w_-^* \end{bmatrix} \mathrm{U}\begin{bmatrix} k \\ q \\ \mathrm{L} \end{bmatrix} \bar{\mathrm{U}}\begin{bmatrix} l \\ q' \\ \mathrm{L} \end{bmatrix}\right) \\ = -\mathcal{X}[p \leftrightarrow q'] \left\{ \mathcal{M}_{\mathrm{V}}\left(\mathrm{U}\begin{bmatrix} i \\ p \\ \mathrm{R} \end{bmatrix} \bar{\mathrm{U}}\begin{bmatrix} j \\ p' \\ \mathrm{L} \end{bmatrix} \rightarrow \mathrm{W}^+\begin{bmatrix} k_1 \\ w_+^* \end{bmatrix} \mathrm{W}^-\begin{bmatrix} k_2 \\ w_-^* \end{bmatrix} \mathrm{U}\begin{bmatrix} k \\ q \\ \mathrm{L} \end{bmatrix} \bar{\mathrm{U}}\begin{bmatrix} l \\ q' \\ \mathrm{R} \end{bmatrix}\right) \right\} \\ - \mathcal{X}[p' \leftrightarrow q] \left\{ \mathcal{M}_{\mathrm{V}+\mathrm{Q}}\left(\mathrm{U}\begin{bmatrix} i \\ p \\ \mathrm{L} \end{bmatrix} \bar{\mathrm{U}}\begin{bmatrix} j \\ p' \\ \mathrm{R} \end{bmatrix} \rightarrow \mathrm{W}^+\begin{bmatrix} k_1 \\ w_+^* \end{bmatrix} \mathrm{W}^-\begin{bmatrix} k_2 \\ w_-^* \end{bmatrix} \mathrm{U}\begin{bmatrix} k \\ q \\ \mathrm{R} \end{bmatrix} \bar{\mathrm{U}}\begin{bmatrix} l \\ q' \\ \mathrm{L} \end{bmatrix}\right) \right\}, \end{aligned} \quad (4.41e)$$

$$\begin{aligned} \mathcal{M}\left(\mathrm{U}\begin{bmatrix} i \\ p \\ \mathrm{R} \end{bmatrix} \bar{\mathrm{U}}\begin{bmatrix} j \\ p' \\ \mathrm{R} \end{bmatrix} \rightarrow \mathrm{W}^+\begin{bmatrix} k_1 \\ w_+^* \end{bmatrix} \mathrm{W}^-\begin{bmatrix} k_2 \\ w_-^* \end{bmatrix} \mathrm{U}\begin{bmatrix} k \\ q \\ \mathrm{R} \end{bmatrix} \bar{\mathrm{U}}\begin{bmatrix} l \\ q' \\ \mathrm{R} \end{bmatrix}\right) \\ = -\mathcal{X}[p \leftrightarrow q'] \left\{ \mathcal{M}_{\mathrm{V}+\mathrm{Q}}\left(\mathrm{U}\begin{bmatrix} i \\ p \\ \mathrm{L} \end{bmatrix} \bar{\mathrm{U}}\begin{bmatrix} j \\ p' \\ \mathrm{R} \end{bmatrix} \rightarrow \mathrm{W}^+\begin{bmatrix} k_1 \\ w_+^* \end{bmatrix} \mathrm{W}^-\begin{bmatrix} k_2 \\ w_-^* \end{bmatrix} \mathrm{U}\begin{bmatrix} k \\ q \\ \mathrm{L} \end{bmatrix} \bar{\mathrm{U}}\begin{bmatrix} l \\ q' \\ \mathrm{L} \end{bmatrix}\right) \right\} \\ - \mathcal{X}[p' \leftrightarrow q] \left\{ \mathcal{M}_{\mathrm{V}}\left(\mathrm{U}\begin{bmatrix} i \\ p \\ \mathrm{R} \end{bmatrix} \bar{\mathrm{U}}\begin{bmatrix} j \\ p' \\ \mathrm{L} \end{bmatrix} \rightarrow \mathrm{W}^+\begin{bmatrix} k_1 \\ w_+^* \end{bmatrix} \mathrm{W}^-\begin{bmatrix} k_2 \\ w_-^* \end{bmatrix} \mathrm{U}\begin{bmatrix} k \\ q \\ \mathrm{R} \end{bmatrix} \bar{\mathrm{U}}\begin{bmatrix} l \\ q' \\ \mathrm{R} \end{bmatrix}\right) \right\}. \end{aligned} \quad (4.41f)$$

The relative minus signs between the contributions with an odd and an even number of particle crossings are Fermi signs and result from the change of the fermion-number flow.

The respective amplitudes for external down-type (anti-)quarks are obtained by interchanging W^+ and W^- , i.e. their momenta and polarization bispinors, and of W^+ and W^- as well as U and D in all couplings,

$$\begin{aligned} & \mathcal{M}\left(D\begin{bmatrix} i \\ p \\ \sigma \end{bmatrix} \bar{D}\begin{bmatrix} j \\ p' \\ \sigma' \end{bmatrix} \rightarrow W^+\begin{bmatrix} k_1 \\ w_+^* \end{bmatrix} W^-\begin{bmatrix} k_2 \\ w_-^* \end{bmatrix} D\begin{bmatrix} k \\ q \\ \tau \end{bmatrix} \bar{D}\begin{bmatrix} l \\ q' \\ \tau' \end{bmatrix}\right) \\ &= \mathcal{M}\left(U\begin{bmatrix} i \\ p \\ \sigma \end{bmatrix} \bar{U}\begin{bmatrix} j \\ p' \\ \sigma' \end{bmatrix} \rightarrow W^+\begin{bmatrix} k_1 \\ w_+^* \end{bmatrix} W^-\begin{bmatrix} k_2 \\ w_-^* \end{bmatrix} U\begin{bmatrix} k \\ q \\ \tau \end{bmatrix} \bar{U}\begin{bmatrix} l \\ q' \\ \tau' \end{bmatrix}\right) \Big|_{U \leftrightarrow D, W^+ \leftrightarrow W^-}. \end{aligned} \quad (4.42)$$

The treatment of intermediate quarks is performed analogously to the discussion in the context of Eq. (4.37).

The subprocesses with only external up-type (anti-)quarks, but with different generations in the initial- and the final-state quark-antiquark pairs, do not get contributions from diagrams with a changed fermion-number flow.

The remaining contributions are identical to the subprocess class discussed before and give, again with the subamplitudes from Eqs. (4.33) and (4.40),

$$\begin{aligned} & \mathcal{M}\left(U\begin{bmatrix} i \\ p \\ \text{L} \end{bmatrix} \bar{U}\begin{bmatrix} j \\ p' \\ \text{R} \end{bmatrix} \rightarrow W^+\begin{bmatrix} k_1 \\ w_+^* \end{bmatrix} W^-\begin{bmatrix} k_2 \\ w_-^* \end{bmatrix} U'\begin{bmatrix} k \\ q \\ \text{L} \end{bmatrix} \bar{U}'\begin{bmatrix} l \\ q' \\ \text{R} \end{bmatrix}\right) = \mathcal{M}_{V+Q}(\dots \rightarrow \dots) \\ & + \mathcal{X}\left[p \leftrightarrow q' \atop p' \leftrightarrow q\right] \left\{ \mathcal{M}_{V+Q}\left(U'\begin{bmatrix} i \\ p \\ \text{L} \end{bmatrix} \bar{U}'\begin{bmatrix} j \\ p' \\ \text{R} \end{bmatrix} \rightarrow W^+\begin{bmatrix} k_1 \\ w_+^* \end{bmatrix} W^-\begin{bmatrix} k_2 \\ w_-^* \end{bmatrix} U\begin{bmatrix} k \\ q \\ \text{L} \end{bmatrix} \bar{U}\begin{bmatrix} l \\ q' \\ \text{R} \end{bmatrix}\right) \right\}, \end{aligned} \quad (4.43a)$$

$$\begin{aligned} & \mathcal{M}\left(U\begin{bmatrix} i \\ p \\ \text{R} \end{bmatrix} \bar{U}\begin{bmatrix} j \\ p' \\ \text{L} \end{bmatrix} \rightarrow W^+\begin{bmatrix} k_1 \\ w_+^* \end{bmatrix} W^-\begin{bmatrix} k_2 \\ w_-^* \end{bmatrix} U'\begin{bmatrix} k \\ q \\ \text{R} \end{bmatrix} \bar{U}'\begin{bmatrix} l \\ q' \\ \text{L} \end{bmatrix}\right) = \mathcal{M}_V(\dots \rightarrow \dots) \\ & + \mathcal{X}\left[p \leftrightarrow q' \atop p' \leftrightarrow q\right] \left\{ \mathcal{M}_V\left(U'\begin{bmatrix} i \\ p \\ \text{R} \end{bmatrix} \bar{U}'\begin{bmatrix} j \\ p' \\ \text{L} \end{bmatrix} \rightarrow W^+\begin{bmatrix} k_1 \\ w_+^* \end{bmatrix} W^-\begin{bmatrix} k_2 \\ w_-^* \end{bmatrix} U\begin{bmatrix} k \\ q \\ \text{R} \end{bmatrix} \bar{U}\begin{bmatrix} l \\ q' \\ \text{L} \end{bmatrix}\right) \right\}, \end{aligned} \quad (4.43b)$$

$$\begin{aligned} & \mathcal{M}\left(U\begin{bmatrix} i \\ p \\ \text{L} \end{bmatrix} \bar{U}\begin{bmatrix} j \\ p' \\ \text{R} \end{bmatrix} \rightarrow W^+\begin{bmatrix} k_1 \\ w_+^* \end{bmatrix} W^-\begin{bmatrix} k_2 \\ w_-^* \end{bmatrix} U'\begin{bmatrix} k \\ q \\ \text{R} \end{bmatrix} \bar{U}'\begin{bmatrix} l \\ q' \\ \text{L} \end{bmatrix}\right) = \mathcal{M}_{V+Q}(\dots \rightarrow \dots) \\ & + \mathcal{X}\left[p \leftrightarrow q' \atop p' \leftrightarrow q\right] \left\{ \mathcal{M}_V\left(U'\begin{bmatrix} i \\ p \\ \text{R} \end{bmatrix} \bar{U}'\begin{bmatrix} j \\ p' \\ \text{L} \end{bmatrix} \rightarrow W^+\begin{bmatrix} k_1 \\ w_+^* \end{bmatrix} W^-\begin{bmatrix} k_2 \\ w_-^* \end{bmatrix} U\begin{bmatrix} k \\ q \\ \text{L} \end{bmatrix} \bar{U}\begin{bmatrix} l \\ q' \\ \text{R} \end{bmatrix}\right) \right\}, \end{aligned} \quad (4.43c)$$

$$\begin{aligned} & \mathcal{M}\left(U\begin{bmatrix} i \\ p \\ \text{R} \end{bmatrix} \bar{U}\begin{bmatrix} j \\ p' \\ \text{L} \end{bmatrix} \rightarrow W^+\begin{bmatrix} k_1 \\ w_+^* \end{bmatrix} W^-\begin{bmatrix} k_2 \\ w_-^* \end{bmatrix} U'\begin{bmatrix} k \\ q \\ \text{L} \end{bmatrix} \bar{U}'\begin{bmatrix} l \\ q' \\ \text{R} \end{bmatrix}\right) = \mathcal{M}_V(\dots \rightarrow \dots) \\ & + \mathcal{X}\left[p \leftrightarrow q' \atop p' \leftrightarrow q\right] \left\{ \mathcal{M}_{V+Q}\left(U'\begin{bmatrix} i \\ p \\ \text{L} \end{bmatrix} \bar{U}'\begin{bmatrix} j \\ p' \\ \text{R} \end{bmatrix} \rightarrow W^+\begin{bmatrix} k_1 \\ w_+^* \end{bmatrix} W^-\begin{bmatrix} k_2 \\ w_-^* \end{bmatrix} U\begin{bmatrix} k \\ q \\ \text{R} \end{bmatrix} \bar{U}\begin{bmatrix} l \\ q' \\ \text{L} \end{bmatrix}\right) \right\}. \end{aligned} \quad (4.43d)$$

The analogous amplitudes for external down-type (anti-)quarks belonging to different generations can again be obtained by interchanging the momenta and polarization bispinors of the W bosons, accompanied by an exchange of W^+ and W^- , U and D, and U' and D'

in all couplings,

$$\begin{aligned} & \mathcal{M}\left(D\begin{bmatrix} i \\ p \\ \sigma \end{bmatrix} \bar{D}\begin{bmatrix} j \\ p' \\ \sigma' \end{bmatrix} \rightarrow W^+\begin{bmatrix} k_1 \\ w_+^* \end{bmatrix} W^-\begin{bmatrix} k_2 \\ w_-^* \end{bmatrix} D'\begin{bmatrix} k \\ q \\ \tau \end{bmatrix} \bar{D}'\begin{bmatrix} l \\ q' \\ \tau' \end{bmatrix}\right) \\ &= \mathcal{M}\left(U\begin{bmatrix} i \\ p \\ \sigma \end{bmatrix} \bar{U}\begin{bmatrix} j \\ p' \\ \sigma' \end{bmatrix} \rightarrow W^-\begin{bmatrix} k_2 \\ w_-^* \end{bmatrix} W^+\begin{bmatrix} k_1 \\ w_+^* \end{bmatrix} U'\begin{bmatrix} k \\ q \\ \tau \end{bmatrix} \bar{U}'\begin{bmatrix} l \\ q' \\ \tau' \end{bmatrix}\right) \Bigg|_{U \leftrightarrow D, U' \leftrightarrow D', W^+ \leftrightarrow W^-}. \end{aligned} \quad (4.44)$$

The subprocesses with an up-type quark–antiquark pair in the initial state and a down-type quark–antiquark pair in the final state are evaluated quite similarly to the previous case. The main difference is that the subamplitude with the two W bosons coupling to different fermion chains contributes here. Due to the maximal parity violation of the W coupling to fermions, it only appears in the helicity configuration with only left-handed quarks and right-handed antiquarks. Exactly these diagrams give the only dependence on the explicit entries of the CKM matrix. In all other subamplitudes, the summation over the intermediate quark state results in a Kronecker delta for the flavours of the external quarks that build the endpoints of the fermion chain with the W bosons attached. With the definitions of Eqs. (4.33), (4.35), and (4.40), the following amplitudes result,

$$\begin{aligned} & \mathcal{M}\left(U\begin{bmatrix} i \\ p \\ L \end{bmatrix} \bar{U}\begin{bmatrix} j \\ p' \\ R \end{bmatrix} \rightarrow W^+\begin{bmatrix} k_1 \\ w_+^* \end{bmatrix} W^-\begin{bmatrix} k_2 \\ w_-^* \end{bmatrix} D\begin{bmatrix} k \\ q \\ L \end{bmatrix} \bar{D}\begin{bmatrix} l \\ q' \\ R \end{bmatrix}\right) = \mathcal{M}\left(\dots \rightarrow \dots\right) \\ & + \mathcal{X}\left[\begin{smallmatrix} p \leftrightarrow q' \\ p' \leftrightarrow q \end{smallmatrix}\right] \left\{ \mathcal{M}_{V+Q}\left(D\begin{bmatrix} i \\ p \\ L \end{bmatrix} \bar{D}\begin{bmatrix} j \\ p' \\ R \end{bmatrix} \rightarrow W^-\begin{bmatrix} k_2 \\ w_-^* \end{bmatrix} W^+\begin{bmatrix} k_1 \\ w_+^* \end{bmatrix} U\begin{bmatrix} k \\ q \\ L \end{bmatrix} \bar{U}\begin{bmatrix} l \\ q' \\ R \end{bmatrix}\right) \right\} \\ & - \mathcal{X}\left[p' \leftrightarrow q\right] \left\{ \mathcal{M}_F\left(U\begin{bmatrix} i \\ p \\ L \end{bmatrix} \bar{D}\begin{bmatrix} j \\ p' \\ R \end{bmatrix} \rightarrow W^+\begin{bmatrix} k_1 \\ w_+^* \end{bmatrix} W^-\begin{bmatrix} k_2 \\ w_-^* \end{bmatrix} U\begin{bmatrix} k \\ q \\ L \end{bmatrix} \bar{D}\begin{bmatrix} l \\ q' \\ R \end{bmatrix}\right) \right\}, \end{aligned} \quad (4.45a)$$

$$\begin{aligned} & \mathcal{M}\left(U\begin{bmatrix} i \\ p \\ L \end{bmatrix} \bar{U}\begin{bmatrix} j \\ p' \\ L \end{bmatrix} \rightarrow W^+\begin{bmatrix} k_1 \\ w_+^* \end{bmatrix} W^-\begin{bmatrix} k_2 \\ w_-^* \end{bmatrix} D\begin{bmatrix} k \\ q \\ R \end{bmatrix} \bar{D}\begin{bmatrix} l \\ q' \\ L \end{bmatrix}\right) = \mathcal{M}\left(\dots \rightarrow \dots\right) \\ & + \mathcal{X}\left[\begin{smallmatrix} p \leftrightarrow q' \\ p' \leftrightarrow q \end{smallmatrix}\right] \left\{ \mathcal{M}_V\left(D\begin{bmatrix} i \\ p \\ R \end{bmatrix} \bar{D}\begin{bmatrix} j \\ p' \\ L \end{bmatrix} \rightarrow W^-\begin{bmatrix} k_2 \\ w_-^* \end{bmatrix} W^+\begin{bmatrix} k_1 \\ w_+^* \end{bmatrix} U\begin{bmatrix} k \\ q \\ R \end{bmatrix} \bar{U}\begin{bmatrix} l \\ q' \\ L \end{bmatrix}\right) \right\}, \end{aligned} \quad (4.45b)$$

$$\begin{aligned} & \mathcal{M}\left(U\begin{bmatrix} i \\ p \\ L \end{bmatrix} \bar{U}\begin{bmatrix} j \\ p' \\ R \end{bmatrix} \rightarrow W^+\begin{bmatrix} k_1 \\ w_+^* \end{bmatrix} W^-\begin{bmatrix} k_2 \\ w_-^* \end{bmatrix} D\begin{bmatrix} k \\ q \\ R \end{bmatrix} \bar{D}\begin{bmatrix} l \\ q' \\ L \end{bmatrix}\right) = \mathcal{M}\left(\dots \rightarrow \dots\right) \\ & + \mathcal{X}\left[\begin{smallmatrix} p \leftrightarrow q' \\ p' \leftrightarrow q \end{smallmatrix}\right] \left\{ \mathcal{M}_V\left(D\begin{bmatrix} i \\ p \\ R \end{bmatrix} \bar{D}\begin{bmatrix} j \\ p' \\ L \end{bmatrix} \rightarrow W^-\begin{bmatrix} k_2 \\ w_-^* \end{bmatrix} W^+\begin{bmatrix} k_1 \\ w_+^* \end{bmatrix} U\begin{bmatrix} k \\ q \\ L \end{bmatrix} \bar{U}\begin{bmatrix} l \\ q' \\ R \end{bmatrix}\right) \right\}, \end{aligned} \quad (4.45c)$$

$$\begin{aligned} & \mathcal{M}\left(U\begin{bmatrix} i \\ p \\ R \end{bmatrix} \bar{U}\begin{bmatrix} j \\ p' \\ L \end{bmatrix} \rightarrow W^+\begin{bmatrix} k_1 \\ w_+^* \end{bmatrix} W^-\begin{bmatrix} k_2 \\ w_-^* \end{bmatrix} D\begin{bmatrix} k \\ q \\ L \end{bmatrix} \bar{D}\begin{bmatrix} l \\ q' \\ R \end{bmatrix}\right) = \mathcal{M}\left(\dots \rightarrow \dots\right) \\ & + \mathcal{X}\left[\begin{smallmatrix} p \leftrightarrow q' \\ p' \leftrightarrow q \end{smallmatrix}\right] \left\{ \mathcal{M}_{V+Q}\left(D\begin{bmatrix} i \\ p \\ L \end{bmatrix} \bar{D}\begin{bmatrix} j \\ p' \\ R \end{bmatrix} \rightarrow W^-\begin{bmatrix} k_2 \\ w_-^* \end{bmatrix} W^+\begin{bmatrix} k_1 \\ w_+^* \end{bmatrix} U\begin{bmatrix} k \\ q \\ R \end{bmatrix} \bar{U}\begin{bmatrix} l \\ q' \\ L \end{bmatrix}\right) \right\}. \end{aligned} \quad (4.45d)$$

The amplitudes for the subprocesses with a down-type quark–antiquark pair in the initial state and an up-type quark–antiquark pair in the final state could be constructed by crossing from the results given before. It seems, however, convenient to define also

these amplitudes for simplification of the expressions in later sections. As an alternative to crossing symmetry, an exchange of W^+ and W^- accompanied by interchanging U and D in all couplings is performed like for the previous amplitudes, leading to

$$\begin{aligned} & \mathcal{M}\left(D\begin{bmatrix} i \\ p \\ \sigma \end{bmatrix} \bar{D}\begin{bmatrix} j \\ p' \\ \sigma' \end{bmatrix} \rightarrow W^+\begin{bmatrix} k_1 \\ w_+^* \end{bmatrix} W^-\begin{bmatrix} k_2 \\ w_-^* \end{bmatrix} U\begin{bmatrix} k \\ q \\ \tau \end{bmatrix} \bar{U}\begin{bmatrix} l \\ q' \\ \tau' \end{bmatrix}\right) \\ &= \mathcal{M}\left(U\begin{bmatrix} i \\ p \\ \sigma \end{bmatrix} \bar{U}\begin{bmatrix} j \\ p' \\ \sigma' \end{bmatrix} \rightarrow W^+\begin{bmatrix} k_1 \\ w_+^* \end{bmatrix} W^-\begin{bmatrix} k_2 \\ w_-^* \end{bmatrix} D\begin{bmatrix} k \\ q \\ \tau \end{bmatrix} \bar{D}\begin{bmatrix} l \\ q' \\ \tau' \end{bmatrix}\right) \Bigg|_{U \leftrightarrow D, W^+ \leftrightarrow W^-} \end{aligned} \quad (4.46)$$

for all contributing helicity channels.

The amplitude that remains to be calculated contains only external up-type quarks and down-type antiquarks with in total more than two different flavours involved, i.e. either $U \neq U'$, $D \neq D'$, or both. (If the up-type quarks and the down-type antiquarks belong to the same flavour, respectively, the amplitude is calculated from the previous one via crossing relations.) Here, only the subamplitude with both W bosons coupling to different fermion chains contributes. Consequently, all helicity channels but the one containing only left-handed quarks and right-handed antiquarks vanish. With Eq. (4.35), the amplitude is

$$\mathcal{M}\left(U\begin{bmatrix} i \\ p \\ L \end{bmatrix} \bar{D}\begin{bmatrix} j \\ p' \\ R \end{bmatrix} \rightarrow W^+\begin{bmatrix} k_1 \\ w_+^* \end{bmatrix} W^-\begin{bmatrix} k_2 \\ w_-^* \end{bmatrix} U\begin{bmatrix} k \\ q \\ L \end{bmatrix} \bar{D}'\begin{bmatrix} l \\ q' \\ R \end{bmatrix}\right) = \mathcal{M}_F(\dots \rightarrow \dots). \quad (4.47)$$

As before, it is not necessary but convenient to define also the corresponding amplitude with only external down-type quarks and up-type-antiquarks,

$$\begin{aligned} & \mathcal{M}\left(D\begin{bmatrix} i \\ p \\ L \end{bmatrix} \bar{U}\begin{bmatrix} j \\ p' \\ R \end{bmatrix} \rightarrow W^+\begin{bmatrix} k_1 \\ w_+^* \end{bmatrix} W^-\begin{bmatrix} k_2 \\ w_-^* \end{bmatrix} D'\begin{bmatrix} k \\ q \\ L \end{bmatrix} \bar{U}'\begin{bmatrix} l \\ q' \\ R \end{bmatrix}\right) \\ &= \mathcal{M}\left(U'\begin{bmatrix} i \\ p \\ L \end{bmatrix} \bar{D}'\begin{bmatrix} j \\ p' \\ R \end{bmatrix} \rightarrow W^-\begin{bmatrix} k_2 \\ w_-^* \end{bmatrix} W^+\begin{bmatrix} k_1 \\ w_+^* \end{bmatrix} U\begin{bmatrix} k \\ q \\ L \end{bmatrix} \bar{D}\begin{bmatrix} l \\ q' \\ R \end{bmatrix}\right) \Bigg|_{U \leftrightarrow D, U' \leftrightarrow D', W^+ \leftrightarrow W^-}. \end{aligned} \quad (4.48)$$

Again, momenta and polarization bispinors of W^+ and W^- are exchanged. Additionally, W^+ and W^- , U and D, and U' and D' are interchanged in all couplings.

The selection of amplitudes is neither unique nor minimal, but seems to be an appropriate choice for the calculation of squared amplitudes in Section 4.5.

ZZ+jet

For the amplitudes of the process class $pp/p\bar{p} \rightarrow ZZ + \text{jet} + X$, the following two abbreviations are introduced for subamplitudes only differing by an interchange of the two Z bosons. With the subamplitudes from Eqs. (4.34) and (4.35), these definitions are

$$\begin{aligned} & \mathcal{M}_{Q^2}\left(q_1\begin{bmatrix} i \\ p \\ \sigma \end{bmatrix} \bar{q}_2\begin{bmatrix} j \\ p' \\ \sigma' \end{bmatrix} \rightarrow Z\begin{bmatrix} k_1 \\ z_1^* \end{bmatrix} Z\begin{bmatrix} k_2 \\ z_2^* \end{bmatrix} q_3\begin{bmatrix} k \\ q \\ \tau \end{bmatrix} \bar{q}_4\begin{bmatrix} l \\ q' \\ \tau' \end{bmatrix}\right) \\ &= \mathcal{M}_Q\left(q_1\begin{bmatrix} i \\ p \\ \sigma \end{bmatrix} \bar{q}_2\begin{bmatrix} j \\ p' \\ \sigma' \end{bmatrix} \rightarrow Z\begin{bmatrix} k_1 \\ z_1^* \end{bmatrix} Z\begin{bmatrix} k_2 \\ z_2^* \end{bmatrix} q_3\begin{bmatrix} k \\ q \\ \tau \end{bmatrix} \bar{q}_4\begin{bmatrix} l \\ q' \\ \tau' \end{bmatrix}\right) + \mathcal{M}_Q\left(\dots \rightarrow Z\begin{bmatrix} k_2 \\ z_2^* \end{bmatrix} Z\begin{bmatrix} k_1 \\ z_1^* \end{bmatrix} \dots\right), \end{aligned} \quad (4.49)$$

$$\begin{aligned}
& \mathcal{M}_{\text{F2}} \left(q_1 \begin{bmatrix} i \\ p \\ \sigma \end{bmatrix} \bar{q}_2 \begin{bmatrix} j \\ p' \\ \sigma' \end{bmatrix} \rightarrow Z \begin{bmatrix} k_1 \\ z_1^* \end{bmatrix} Z \begin{bmatrix} k_2 \\ z_2^* \end{bmatrix} q_3 \begin{bmatrix} k \\ q \\ \tau \end{bmatrix} \bar{q}_4 \begin{bmatrix} l \\ q' \\ \tau' \end{bmatrix} \right) \\
&= \mathcal{M}_{\text{F}} \left(q_1 \begin{bmatrix} i \\ p \\ \sigma \end{bmatrix} \bar{q}_2 \begin{bmatrix} j \\ p' \\ \sigma' \end{bmatrix} \rightarrow Z \begin{bmatrix} k_1 \\ z_1^* \end{bmatrix} Z \begin{bmatrix} k_2 \\ z_2^* \end{bmatrix} q_3 \begin{bmatrix} k \\ q \\ \tau \end{bmatrix} \bar{q}_4 \begin{bmatrix} l \\ q' \\ \tau' \end{bmatrix} \right) + \mathcal{M}_{\text{F}} \left(\dots \rightarrow Z \begin{bmatrix} k_2 \\ z_2^* \end{bmatrix} Z \begin{bmatrix} k_1 \\ z_1^* \end{bmatrix} \dots \right). \tag{4.50}
\end{aligned}$$

Since no flavour-changing couplings appear in ZZ+jet-production subprocesses, only two different kinds of amplitudes are to be evaluated. The first one contains four (anti-)quarks of the same flavour. With the definitions of Eqs. (4.49) and (4.50) the amplitudes for the following three helicity configurations are calculated,

$$\begin{aligned}
& \mathcal{M} \left(Q \begin{bmatrix} i \\ p \\ \text{L} \end{bmatrix} \bar{Q} \begin{bmatrix} j \\ p' \\ \text{R} \end{bmatrix} \rightarrow Z \begin{bmatrix} k_1 \\ z_1^* \end{bmatrix} Z \begin{bmatrix} k_2 \\ z_2^* \end{bmatrix} Q \begin{bmatrix} k \\ q \\ \text{L} \end{bmatrix} \bar{Q} \begin{bmatrix} l \\ q' \\ \text{R} \end{bmatrix} \right) = (1 - \mathcal{X}[p \leftrightarrow q']) \left\{ (\mathcal{M}_{\text{Q2}} + \mathcal{M}_{\text{F2}}) (\dots \rightarrow \dots) \right\} \\
&+ \left(\mathcal{X} \left[\begin{smallmatrix} p \leftrightarrow q' \\ p' \leftrightarrow q \end{smallmatrix} \right] - \mathcal{X}[p' \leftrightarrow q] \right) \left\{ \mathcal{M}_{\text{Q2}} (\dots \rightarrow \dots) \right\}, \tag{4.51a}
\end{aligned}$$

$$\begin{aligned}
& \mathcal{M} \left(Q \begin{bmatrix} i \\ p \\ \text{L} \end{bmatrix} \bar{Q} \begin{bmatrix} j \\ p' \\ \text{R} \end{bmatrix} \rightarrow Z \begin{bmatrix} k_1 \\ z_1^* \end{bmatrix} Z \begin{bmatrix} k_2 \\ z_2^* \end{bmatrix} Q \begin{bmatrix} k \\ q \\ \text{R} \end{bmatrix} \bar{Q} \begin{bmatrix} l \\ q' \\ \text{L} \end{bmatrix} \right) = (\mathcal{M}_{\text{Q2}} + \mathcal{M}_{\text{F2}}) (\dots \rightarrow \dots) \\
&+ \mathcal{X} \left[\begin{smallmatrix} p \leftrightarrow q' \\ p' \leftrightarrow q \end{smallmatrix} \right] \left\{ \mathcal{M}_{\text{Q2}} \left(Q \begin{bmatrix} i \\ p \\ \text{R} \end{bmatrix} \bar{Q} \begin{bmatrix} j \\ p' \\ \text{L} \end{bmatrix} \rightarrow Z \begin{bmatrix} k_1 \\ z_1^* \end{bmatrix} Z \begin{bmatrix} k_2 \\ z_2^* \end{bmatrix} Q \begin{bmatrix} k \\ q \\ \text{L} \end{bmatrix} \bar{Q} \begin{bmatrix} l \\ q' \\ \text{R} \end{bmatrix} \right) \right\}, \tag{4.51b}
\end{aligned}$$

$$\begin{aligned}
& \mathcal{M} \left(Q \begin{bmatrix} i \\ p \\ \text{L} \end{bmatrix} \bar{Q} \begin{bmatrix} j \\ p' \\ \text{L} \end{bmatrix} \rightarrow Z \begin{bmatrix} k_1 \\ z_1^* \end{bmatrix} Z \begin{bmatrix} k_2 \\ z_2^* \end{bmatrix} Q \begin{bmatrix} k \\ q \\ \text{L} \end{bmatrix} \bar{Q} \begin{bmatrix} l \\ q' \\ \text{L} \end{bmatrix} \right) \\
&= -\mathcal{X}[p \leftrightarrow q'] \left\{ (\mathcal{M}_{\text{Q2}} + \mathcal{M}_{\text{F2}}) \left(Q \begin{bmatrix} i \\ p \\ \text{R} \end{bmatrix} \bar{Q} \begin{bmatrix} j \\ p' \\ \text{L} \end{bmatrix} \rightarrow Z \begin{bmatrix} k_1 \\ z_1^* \end{bmatrix} Z \begin{bmatrix} k_2 \\ z_2^* \end{bmatrix} Q \begin{bmatrix} k \\ q \\ \text{L} \end{bmatrix} \bar{Q} \begin{bmatrix} l \\ q' \\ \text{R} \end{bmatrix} \right) \right\} \\
&- \mathcal{X}[p' \leftrightarrow q] \left\{ \mathcal{M}_{\text{Q2}} \left(Q \begin{bmatrix} i \\ p \\ \text{R} \end{bmatrix} \bar{Q} \begin{bmatrix} j \\ p' \\ \text{L} \end{bmatrix} \rightarrow Z \begin{bmatrix} k_1 \\ z_1^* \end{bmatrix} Z \begin{bmatrix} k_2 \\ z_2^* \end{bmatrix} Q \begin{bmatrix} k \\ q \\ \text{L} \end{bmatrix} \bar{Q} \begin{bmatrix} l \\ q' \\ \text{R} \end{bmatrix} \right) \right\}. \tag{4.51c}
\end{aligned}$$

The relative minus signs between the contributions follow again from the changed fermion-number flow. The remaining non-vanishing helicity channels are obtained from these amplitudes by application of a \mathcal{P} transformation,

$$\mathcal{M} \left(Q \begin{bmatrix} i \\ p \\ \text{R} \end{bmatrix} \bar{Q} \begin{bmatrix} j \\ p' \\ \text{L} \end{bmatrix} \rightarrow Z \begin{bmatrix} k_1 \\ z_1^* \end{bmatrix} Z \begin{bmatrix} k_2 \\ z_2^* \end{bmatrix} Q \begin{bmatrix} k \\ q \\ \text{R} \end{bmatrix} \bar{Q} \begin{bmatrix} l \\ q' \\ \text{L} \end{bmatrix} \right) = \mathcal{P} \left\{ \mathcal{M} \left(Q \begin{bmatrix} i \\ p \\ \text{L} \end{bmatrix} \bar{Q} \begin{bmatrix} j \\ p' \\ \text{R} \end{bmatrix} \rightarrow Z \begin{bmatrix} k_1 \\ z_1^* \end{bmatrix} Z \begin{bmatrix} k_2 \\ z_2^* \end{bmatrix} Q \begin{bmatrix} k \\ q \\ \text{L} \end{bmatrix} \bar{Q} \begin{bmatrix} l \\ q' \\ \text{R} \end{bmatrix} \right) \right\}, \tag{4.51d}$$

$$\mathcal{M} \left(Q \begin{bmatrix} i \\ p \\ \text{R} \end{bmatrix} \bar{Q} \begin{bmatrix} j \\ p' \\ \text{L} \end{bmatrix} \rightarrow Z \begin{bmatrix} k_1 \\ z_1^* \end{bmatrix} Z \begin{bmatrix} k_2 \\ z_2^* \end{bmatrix} Q \begin{bmatrix} k \\ q \\ \text{L} \end{bmatrix} \bar{Q} \begin{bmatrix} l \\ q' \\ \text{R} \end{bmatrix} \right) = \mathcal{P} \left\{ \mathcal{M} \left(Q \begin{bmatrix} i \\ p \\ \text{L} \end{bmatrix} \bar{Q} \begin{bmatrix} j \\ p' \\ \text{R} \end{bmatrix} \rightarrow Z \begin{bmatrix} k_1 \\ z_1^* \end{bmatrix} Z \begin{bmatrix} k_2 \\ z_2^* \end{bmatrix} Q \begin{bmatrix} k \\ q \\ \text{R} \end{bmatrix} \bar{Q} \begin{bmatrix} l \\ q' \\ \text{L} \end{bmatrix} \right) \right\}, \tag{4.51e}$$

$$\mathcal{M} \left(Q \begin{bmatrix} i \\ p \\ \text{R} \end{bmatrix} \bar{Q} \begin{bmatrix} j \\ p' \\ \text{R} \end{bmatrix} \rightarrow Z \begin{bmatrix} k_1 \\ z_1^* \end{bmatrix} Z \begin{bmatrix} k_2 \\ z_2^* \end{bmatrix} Q \begin{bmatrix} k \\ q \\ \text{R} \end{bmatrix} \bar{Q} \begin{bmatrix} l \\ q' \\ \text{R} \end{bmatrix} \right) = \mathcal{P} \left\{ \mathcal{M} \left(Q \begin{bmatrix} i \\ p \\ \text{L} \end{bmatrix} \bar{Q} \begin{bmatrix} j \\ p' \\ \text{L} \end{bmatrix} \rightarrow Z \begin{bmatrix} k_1 \\ z_1^* \end{bmatrix} Z \begin{bmatrix} k_2 \\ z_2^* \end{bmatrix} Q \begin{bmatrix} k \\ q \\ \text{L} \end{bmatrix} \bar{Q} \begin{bmatrix} l \\ q' \\ \text{L} \end{bmatrix} \right) \right\}. \tag{4.51f}$$

The second class of subprocesses contains a quark–antiquark pair in the initial state and a quark–antiquark pair of a different flavour in the final state. With the definitions of Eqs. (4.49) and (4.50), the amplitudes for two helicity channels are given by

$$\begin{aligned} \mathcal{M}\left(Q\begin{bmatrix} i \\ p \\ L \end{bmatrix} \bar{Q}\begin{bmatrix} j \\ p' \\ R \end{bmatrix} \rightarrow Z\begin{bmatrix} k_1 \\ z_1^* \end{bmatrix} Z\begin{bmatrix} k_2 \\ z_2^* \end{bmatrix} Q'\begin{bmatrix} k \\ q \\ L \end{bmatrix} \bar{Q}'\begin{bmatrix} l \\ q' \\ R \end{bmatrix}\right) &= \left(\mathcal{M}_{Q2} + \mathcal{M}_{F2}\right)\left(\dots \rightarrow \dots\right) \\ &+ \mathcal{X}\left[p \leftrightarrow q' \atop p' \leftrightarrow q\right] \left\{ \mathcal{M}_{Q2}\left(Q'\begin{bmatrix} i \\ p \\ L \end{bmatrix} \bar{Q}'\begin{bmatrix} j \\ p' \\ R \end{bmatrix} \rightarrow Z\begin{bmatrix} k_1 \\ z_1^* \end{bmatrix} Z\begin{bmatrix} k_2 \\ z_2^* \end{bmatrix} Q\begin{bmatrix} k \\ q \\ L \end{bmatrix} \bar{Q}\begin{bmatrix} l \\ q' \\ R \end{bmatrix}\right) \right\}, \end{aligned} \quad (4.52a)$$

$$\begin{aligned} \mathcal{M}\left(Q\begin{bmatrix} i \\ p \\ R \end{bmatrix} \bar{Q}\begin{bmatrix} j \\ p' \\ L \end{bmatrix} \rightarrow Z\begin{bmatrix} k_1 \\ z_1^* \end{bmatrix} Z\begin{bmatrix} k_2 \\ z_2^* \end{bmatrix} Q'\begin{bmatrix} k \\ q \\ R \end{bmatrix} \bar{Q}'\begin{bmatrix} l \\ q' \\ L \end{bmatrix}\right) &= \left(\mathcal{M}_{Q2} + \mathcal{M}_{F2}\right)\left(\dots \rightarrow \dots\right) \\ &+ \mathcal{X}\left[p \leftrightarrow q' \atop p' \leftrightarrow q\right] \left\{ \mathcal{M}_{Q2}\left(Q'\begin{bmatrix} i \\ p \\ R \end{bmatrix} \bar{Q}'\begin{bmatrix} j \\ p' \\ L \end{bmatrix} \rightarrow Z\begin{bmatrix} k_1 \\ z_1^* \end{bmatrix} Z\begin{bmatrix} k_2 \\ z_2^* \end{bmatrix} Q\begin{bmatrix} k \\ q \\ R \end{bmatrix} \bar{Q}\begin{bmatrix} l \\ q' \\ L \end{bmatrix}\right) \right\}, \end{aligned} \quad (4.52b)$$

the remaining ones can again be obtained by a \mathcal{P} transformation,

$$\mathcal{M}\left(Q\begin{bmatrix} i \\ p \\ R \end{bmatrix} \bar{Q}\begin{bmatrix} j \\ p' \\ L \end{bmatrix} \rightarrow Z\begin{bmatrix} k_1 \\ z_1^* \end{bmatrix} Z\begin{bmatrix} k_2 \\ z_2^* \end{bmatrix} Q'\begin{bmatrix} k \\ q \\ R \end{bmatrix} \bar{Q}'\begin{bmatrix} l \\ q' \\ L \end{bmatrix}\right) = \mathcal{P}\left\{ \mathcal{M}\left(Q\begin{bmatrix} i \\ p \\ L \end{bmatrix} \bar{Q}\begin{bmatrix} j \\ p' \\ R \end{bmatrix} \rightarrow Z\begin{bmatrix} k_1 \\ z_1^* \end{bmatrix} Z\begin{bmatrix} k_2 \\ z_2^* \end{bmatrix} Q'\begin{bmatrix} k \\ q \\ L \end{bmatrix} \bar{Q}'\begin{bmatrix} l \\ q' \\ R \end{bmatrix}\right) \right\}, \quad (4.52c)$$

$$\mathcal{M}\left(Q\begin{bmatrix} i \\ p \\ L \end{bmatrix} \bar{Q}\begin{bmatrix} j \\ p' \\ R \end{bmatrix} \rightarrow Z\begin{bmatrix} k_1 \\ z_1^* \end{bmatrix} Z\begin{bmatrix} k_2 \\ z_2^* \end{bmatrix} Q'\begin{bmatrix} k \\ q \\ L \end{bmatrix} \bar{Q}'\begin{bmatrix} l \\ q' \\ R \end{bmatrix}\right) = \mathcal{P}\left\{ \mathcal{M}\left(Q\begin{bmatrix} i \\ p \\ R \end{bmatrix} \bar{Q}\begin{bmatrix} j \\ p' \\ L \end{bmatrix} \rightarrow Z\begin{bmatrix} k_1 \\ z_1^* \end{bmatrix} Z\begin{bmatrix} k_2 \\ z_2^* \end{bmatrix} Q'\begin{bmatrix} k \\ q \\ R \end{bmatrix} \bar{Q}'\begin{bmatrix} l \\ q' \\ L \end{bmatrix}\right) \right\}. \quad (4.52d)$$

WZ+jet

In the amplitude calculation for the process class $pp/p\bar{p} \rightarrow WZ + \text{jet} + X$, only the case of $W^+Z + \text{jet}$ production has to be considered. All $W^-Z + \text{jet}$ amplitudes can be obtained from these by application of a \mathcal{CP} transformation, as for the gluonic subprocesses.

The following abbreviation is useful for a compact notation of the amplitudes,

$$\begin{aligned} \mathcal{M}_A\left(q_1\begin{bmatrix} i \\ p \\ \sigma \end{bmatrix} \bar{q}_2\begin{bmatrix} j \\ p' \\ \sigma' \end{bmatrix} \rightarrow W^+\begin{bmatrix} k_1 \\ w_+^* \end{bmatrix} Z\begin{bmatrix} k_2 \\ z^* \end{bmatrix} q_3\begin{bmatrix} k \\ q \\ \tau \end{bmatrix} \bar{q}_4\begin{bmatrix} l \\ q' \\ \tau' \end{bmatrix}\right) &= \left(\mathcal{M}_V + \mathcal{M}_F\right)\left(\dots \rightarrow \dots\right) \\ &+ \mathcal{M}_Q\left(q_1\begin{bmatrix} i \\ p \\ \sigma \end{bmatrix} \bar{q}_2\begin{bmatrix} j \\ p' \\ \sigma' \end{bmatrix} \rightarrow W^+\begin{bmatrix} k_1 \\ w_+^* \end{bmatrix} Z\begin{bmatrix} k_2 \\ z^* \end{bmatrix} q_3\begin{bmatrix} k \\ q \\ \tau \end{bmatrix} \bar{q}_4\begin{bmatrix} l \\ q' \\ \tau' \end{bmatrix}\right) + \mathcal{M}_Q\left(\dots \rightarrow Z\begin{bmatrix} k_2 \\ z^* \end{bmatrix} W^+\begin{bmatrix} k_1 \\ w_+^* \end{bmatrix} \dots\right). \end{aligned} \quad (4.53)$$

Unlike in the cases of WW+jet or ZZ+jet production, where the gauge-boson pair is neutral, the fermion chain at which the WZ pair is attached is already determined by the charge of the W boson. Besides, the number of non-vanishing helicity channels is reduced by the fact that a W boson always couples directly to one of the fermion chains.

In the amplitudes calculated explicitly, the incoming quark–antiquark pair always couples to the W^+ boson. Thus, it has to consist of an up-type quark and a down-type antiquark. Since the final-state quark–antiquark pair has to belong to one flavour, three different cases of the outgoing quark–antiquark pair are to be distinguished: It belongs

either to the same flavour as the incoming quark, or as the incoming antiquark, or to a different flavour.

In the first case, the W boson couples to the fermion chain that contains the initial-state down-type antiquark and either the incoming up-type quark or the outgoing up-type antiquark. Only helicity channels with a right-handed down-type antiquark contribute, since the W boson always couple to that chain. With the abbreviation (4.53), the amplitudes read

$$\mathcal{M}\left(\mathrm{U}\begin{bmatrix} i \\ p \\ \mathrm{L} \end{bmatrix} \bar{\mathrm{D}}\begin{bmatrix} j \\ p' \\ \mathrm{R} \end{bmatrix} \rightarrow \mathrm{W}^+ \begin{bmatrix} k_1 \\ w_+^* \end{bmatrix} \mathrm{Z}\begin{bmatrix} k_2 \\ z^* \end{bmatrix} \mathrm{U}\begin{bmatrix} k \\ q \\ \mathrm{L} \end{bmatrix} \bar{\mathrm{U}}\begin{bmatrix} l \\ q' \\ \mathrm{R} \end{bmatrix}\right) = (1 - \mathcal{X}[p \leftrightarrow q']) \left\{ \mathcal{M}_{\mathrm{A}}(\dots \rightarrow \dots) \right\}, \quad (4.54a)$$

$$\mathcal{M}\left(\mathrm{U}\begin{bmatrix} i \\ p \\ \mathrm{L} \end{bmatrix} \bar{\mathrm{D}}\begin{bmatrix} j \\ p' \\ \mathrm{R} \end{bmatrix} \rightarrow \mathrm{W}^+ \begin{bmatrix} k_1 \\ w_+^* \end{bmatrix} \mathrm{Z}\begin{bmatrix} k_2 \\ z^* \end{bmatrix} \mathrm{U}\begin{bmatrix} k \\ q \\ \mathrm{R} \end{bmatrix} \bar{\mathrm{U}}\begin{bmatrix} l \\ q' \\ \mathrm{L} \end{bmatrix}\right) = \mathcal{M}_{\mathrm{A}}(\dots \rightarrow \dots), \quad (4.54b)$$

$$\begin{aligned} & \mathcal{M}\left(\mathrm{U}\begin{bmatrix} i \\ p \\ \mathrm{R} \end{bmatrix} \bar{\mathrm{D}}\begin{bmatrix} j \\ p' \\ \mathrm{R} \end{bmatrix} \rightarrow \mathrm{W}^+ \begin{bmatrix} k_1 \\ w_+^* \end{bmatrix} \mathrm{Z}\begin{bmatrix} k_2 \\ z^* \end{bmatrix} \mathrm{U}\begin{bmatrix} k \\ q \\ \mathrm{R} \end{bmatrix} \bar{\mathrm{U}}\begin{bmatrix} l \\ q' \\ \mathrm{R} \end{bmatrix}\right) \\ &= -\mathcal{X}[p \leftrightarrow q'] \left\{ \mathcal{M}_{\mathrm{A}}\left(\mathrm{U}\begin{bmatrix} i \\ p \\ \mathrm{L} \end{bmatrix} \bar{\mathrm{D}}\begin{bmatrix} j \\ p' \\ \mathrm{R} \end{bmatrix} \rightarrow \mathrm{W}^+ \begin{bmatrix} k_1 \\ w_+^* \end{bmatrix} \mathrm{Z}\begin{bmatrix} k_2 \\ z^* \end{bmatrix} \mathrm{U}\begin{bmatrix} k \\ q \\ \mathrm{R} \end{bmatrix} \bar{\mathrm{U}}\begin{bmatrix} l \\ q' \\ \mathrm{L} \end{bmatrix}\right) \right\}, \end{aligned} \quad (4.54c)$$

where the the relative minus signs stem from the change in the fermion-number flow again.

In the case of an incoming up-type quark and three down-type (anti-)quarks of the same flavour, the W boson always couples to the up-type quark whose fermion chain contains either the incoming down-type antiquark or the outgoing down-type quark. Due to the maximal parity violation of the W coupling, only helicity configurations with a left-handed up-type quark contribute. With the abbreviation (4.53), the amplitudes are

$$\mathcal{M}\left(\mathrm{U}\begin{bmatrix} i \\ p \\ \mathrm{L} \end{bmatrix} \bar{\mathrm{D}}\begin{bmatrix} j \\ p' \\ \mathrm{R} \end{bmatrix} \rightarrow \mathrm{W}^+ \begin{bmatrix} k_1 \\ w_+^* \end{bmatrix} \mathrm{Z}\begin{bmatrix} k_2 \\ z^* \end{bmatrix} \mathrm{D}\begin{bmatrix} k \\ q \\ \mathrm{L} \end{bmatrix} \bar{\mathrm{D}}\begin{bmatrix} l \\ q' \\ \mathrm{R} \end{bmatrix}\right) = (1 - \mathcal{X}[p' \leftrightarrow q]) \left\{ \mathcal{M}_{\mathrm{A}}(\dots \rightarrow \dots) \right\}, \quad (4.55a)$$

$$\mathcal{M}\left(\mathrm{U}\begin{bmatrix} i \\ p \\ \mathrm{L} \end{bmatrix} \bar{\mathrm{D}}\begin{bmatrix} j \\ p' \\ \mathrm{R} \end{bmatrix} \rightarrow \mathrm{W}^+ \begin{bmatrix} k_1 \\ w_+^* \end{bmatrix} \mathrm{Z}\begin{bmatrix} k_2 \\ z^* \end{bmatrix} \mathrm{D}\begin{bmatrix} k \\ q \\ \mathrm{R} \end{bmatrix} \bar{\mathrm{D}}\begin{bmatrix} l \\ q' \\ \mathrm{L} \end{bmatrix}\right) = \mathcal{M}_{\mathrm{A}}(\dots \rightarrow \dots) \quad (4.55b)$$

$$\begin{aligned} & \mathcal{M}\left(\mathrm{U}\begin{bmatrix} i \\ p \\ \mathrm{L} \end{bmatrix} \bar{\mathrm{D}}\begin{bmatrix} j \\ p' \\ \mathrm{L} \end{bmatrix} \rightarrow \mathrm{W}^+ \begin{bmatrix} k_1 \\ w_+^* \end{bmatrix} \mathrm{Z}\begin{bmatrix} k_2 \\ z^* \end{bmatrix} \mathrm{D}\begin{bmatrix} k \\ q \\ \mathrm{L} \end{bmatrix} \bar{\mathrm{D}}\begin{bmatrix} l \\ q' \\ \mathrm{L} \end{bmatrix}\right) \\ &= -\mathcal{X}[p' \leftrightarrow q] \left\{ \mathcal{M}_{\mathrm{A}}\left(\mathrm{U}\begin{bmatrix} i \\ p \\ \mathrm{L} \end{bmatrix} \bar{\mathrm{D}}\begin{bmatrix} j \\ p' \\ \mathrm{R} \end{bmatrix} \rightarrow \mathrm{W}^+ \begin{bmatrix} k_1 \\ w_+^* \end{bmatrix} \mathrm{Z}\begin{bmatrix} k_2 \\ z^* \end{bmatrix} \mathrm{D}\begin{bmatrix} k \\ q \\ \mathrm{R} \end{bmatrix} \bar{\mathrm{D}}\begin{bmatrix} l \\ q' \\ \mathrm{L} \end{bmatrix}\right) \right\}. \end{aligned} \quad (4.55c)$$

The last case to be discussed is that of an outgoing quark–antiquark pair which belongs neither to the flavour of the incoming quark nor of the antiquark. Here, only diagrams with one fermion chain containing the initial-state quark–antiquark pair, whose helicity must be left-handed due to the W coupling, and the other one containing the final-state quark–antiquark pair contribute. With the abbreviation (4.53), the non-vanishing amplitudes read

$$\mathcal{M}\left(\mathrm{U}\begin{bmatrix} i \\ p \\ \mathrm{L} \end{bmatrix} \bar{\mathrm{D}}\begin{bmatrix} j \\ p' \\ \mathrm{R} \end{bmatrix} \rightarrow \mathrm{W}^+ \begin{bmatrix} k_1 \\ w_+^* \end{bmatrix} \mathrm{Z}\begin{bmatrix} k_2 \\ z^* \end{bmatrix} \mathrm{Q}\begin{bmatrix} k \\ q \\ \mathrm{L} \end{bmatrix} \bar{\mathrm{Q}}\begin{bmatrix} l \\ q' \\ \mathrm{R} \end{bmatrix}\right) = \mathcal{M}_{\mathrm{A}}(\dots \rightarrow \dots), \quad (4.56a)$$

$$\mathcal{M}\left(\mathrm{U}\begin{bmatrix} i \\ p \\ \mathrm{L} \end{bmatrix} \bar{\mathrm{D}}\begin{bmatrix} j \\ p' \\ \mathrm{R} \end{bmatrix} \rightarrow \mathrm{W}^+ \begin{bmatrix} k_1 \\ w_+^* \end{bmatrix} \mathrm{Z}\begin{bmatrix} k_2 \\ z^* \end{bmatrix} \mathrm{Q}\begin{bmatrix} k \\ q \\ \mathrm{R} \end{bmatrix} \bar{\mathrm{Q}}\begin{bmatrix} l \\ q' \\ \mathrm{L} \end{bmatrix}\right) = \mathcal{M}_{\mathrm{A}}\left(\dots \rightarrow \dots\right). \quad (4.56\mathrm{b})$$

From the amplitudes presented in this section, the matrix elements for all subprocesses with two fermion chains that contribute to the real corrections of the process class $\mathrm{pp}/\mathrm{p}\bar{\mathrm{p}} \rightarrow \mathrm{VV} + \mathrm{jet} + \mathrm{X}$ —including quark–quark and antiquark–antiquark scattering subprocesses—can be received either directly or by applying crossing symmetry.

4.5 Calculation of squared amplitudes

For the calculation of cross sections, the absolute squares of the amplitudes presented in the previous section are used, which have to be averaged over spins and colours of the incoming partons. For the investigated processes, no helicities of outgoing particles are observed, so spins and colours of final-state particles are summed over. The explicit colour structure of the amplitudes is not spelled out explicitly in the last section, since it is quite simple with not more than four colour-charged external particles involved. It can be reconstructed from the subamplitudes given in Section 4.3.

4.5.1 Colour structures of the amplitudes

In this subsection, all different colour structures of amplitudes arising in the subprocesses contributing to $\mathrm{pp}/\mathrm{p}\bar{\mathrm{p}} \rightarrow \mathrm{VV} + \mathrm{jet} + \mathrm{X}$ are explained. At LO, all subprocesses have the same colour structure, whereas three different structures arise in the real corrections.

For all LO subprocesses (all subprocesses of Section 4.4.1 with the gluon in parentheses omitted), the colour structure is trivial: All amplitudes can be written as

$$\mathbb{M} = \mathrm{T}_{ji}^a \times \mathcal{M}^\alpha \quad (4.57)$$

by extracting the only $\mathrm{SU}(3)_{\mathrm{C}}$ generator T^a . Full amplitudes with colour are labelled by \mathbb{M} , \mathcal{M}^α is a colour-stripped amplitude. Taking the absolute square results in

$$\sum_{\mathrm{col}} |\mathbb{M}|^2 = \mathrm{Tr} \{ \mathrm{T}^a \mathrm{T}^a \} \times |\mathcal{M}^\alpha|^2 = 4 |\mathcal{M}^\alpha|^2. \quad (4.58)$$

For all real-emission subprocesses containing two external gluons (all subprocesses of Section 4.4.1 with the gluon in parentheses included), two different colour structures arise due to the two possibilities of ordering the external gluons coupling to the only fermion chain. An illustration is given in Figure 4.1. The amplitudes get the generic form

$$\mathbb{M} = [\mathrm{T}^a \mathrm{T}^b]_{ji} \times \mathcal{M}^\alpha + [\mathrm{T}^b \mathrm{T}^a]_{ji} \times \mathcal{M}^\beta \quad (4.59)$$

by extracting all $\mathrm{SU}(3)_{\mathrm{C}}$ generators. Taking the absolute square now results in

$$\begin{aligned} \sum_{\mathrm{col}} |\mathbb{M}|^2 &= \mathrm{Tr} \{ \mathrm{T}^a \mathrm{T}^a \mathrm{T}^b \mathrm{T}^b \} (|\mathcal{M}^\alpha|^2 + |\mathcal{M}^\beta|^2) + 2 \mathrm{Tr} \{ \mathrm{T}^a \mathrm{T}^b \mathrm{T}^a \mathrm{T}^b \} \mathrm{Re} (\mathcal{M}^\alpha \mathcal{M}^{\beta*}) \\ &= \frac{16}{3} (|\mathcal{M}^\alpha|^2 + |\mathcal{M}^\beta|^2) - \frac{4}{3} \mathrm{Re} (\mathcal{M}^\alpha \mathcal{M}^{\beta*}), \end{aligned} \quad (4.60)$$

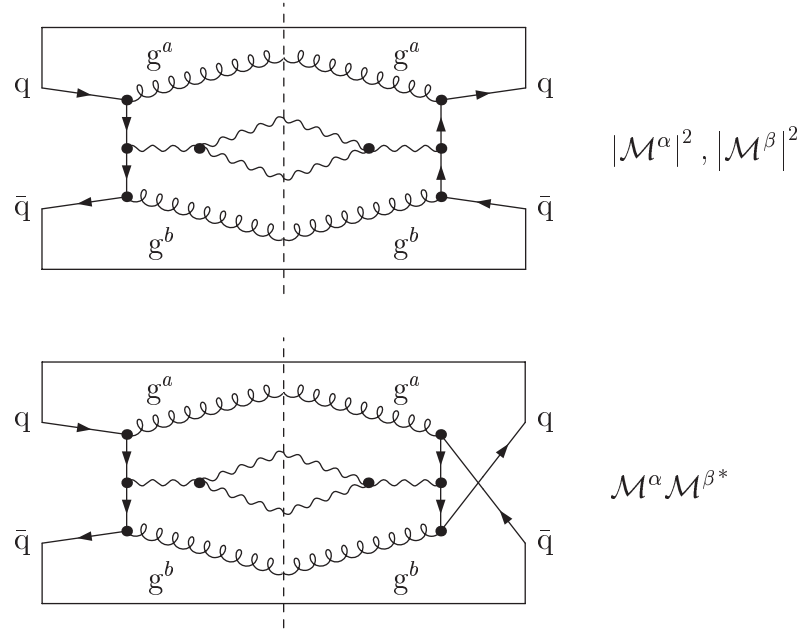


Figure 4.1: Illustration of the two different ways how the fermion chains close in case of two external gluons. As an example a subprocess with a quark–antiquark pair in the initial state and two outgoing gluons in WW+jet production is taken. The upper plot shows a squared diagram with the SU(3)_C generators in the (cyclic) sequence $T^a T^a T^b T^b$. The lower plot shows an interference term between two diagrams with the outgoing gluons ordered differently, leading to the sequence $T^a T^b T^a T^b$ of SU(3)_C generators.

where the cyclic property of traces has been used.

For the real-emission amplitudes involving no external gluons (given in Section 4.4.2), two different colour structures show up: If all contributing diagrams have the same fermion-number flow, the colour structure always looks like

$$\mathbb{M} = T_{ji}^a T_{kl}^b \times \mathcal{M}^\alpha, \quad (4.61)$$

at least after renaming indices if necessary (namely in helicity channels getting only contributions from crossed subamplitudes).

Taking the absolute square now results in the product of two traces over chains of SU(3)_C generators which are connected by colour indices,

$$\sum_{\text{col}} |\mathbb{M}|^2 = \text{Tr} \{T^a T^b\} \text{Tr} \{T^a T^b\} \times |\mathcal{M}^\alpha|^2 = 2 |\mathcal{M}^\alpha|^2. \quad (4.62)$$

For some classes of subprocesses with two fermion chains, the colour structure is a bit more involved, namely for subprocesses containing three (in case of WZ+jet production) or four (in case of WW+jet or ZZ+jet production) (anti-)quarks of the same flavour. In case of WW+jet production, the same is true for the subprocesses given in Eq. (4.45), where the two W bosons can couple either to the same or to two different fermion chains. In these

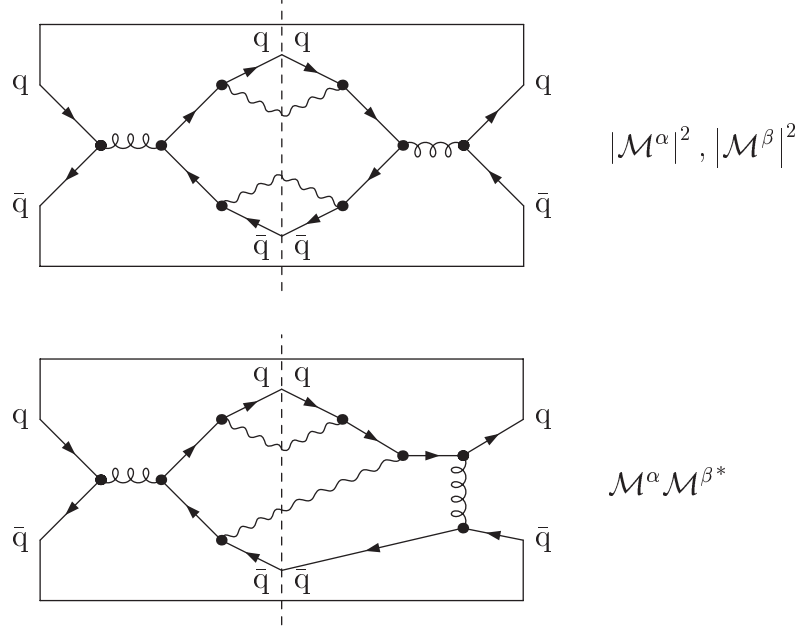


Figure 4.2: Illustration of the two different possibilities how fermion chains close in the case that diagrams with different colour structures contribute to the same subprocess. As an example, a subprocess with all external (anti-)quarks belonging to the same flavour in ZZ+jet or WW+jet production is taken. The upper plot shows a squared diagram, resulting in a product of two fermion chains connected by colour indices. The lower one shows the interference of two diagrams with different colour structures, resulting in only one fermion chain in the squared amplitude.

situations, the amplitude involves two different colour structures arising along with two different fermion-number flows contributing to the particular subprocesses. In these cases, the amplitudes can—at least for some helicity channels (the others show the simpler colour structure of Eq. (4.62))—be written as

$$\mathbb{M} = T_{ji}^a T_{kl}^b \times \mathcal{M}^\alpha + T_{ki}^a T_{jl}^b \times \mathcal{M}^\beta. \quad (4.63)$$

Squaring this amplitude results in contributions with the squared diagram containing only one fermion chain and others with two chains connected by colour indices, which is illustrated in Figure 4.2. Taking the absolute square yields

$$\begin{aligned} \sum_{\text{col}} |\mathbb{M}|^2 &= \text{Tr} \{T^a T^b\} \text{Tr} \{T^a T^b\} (|\mathcal{M}^\alpha|^2 + |\mathcal{M}^\beta|^2) + 2 \text{Tr} \{T^a T^b T^a T^b\} \text{Re} (\mathcal{M}^\alpha \mathcal{M}^{\beta*}) \\ &= 2 (|\mathcal{M}^\alpha|^2 + |\mathcal{M}^\beta|^2) - \frac{4}{3} \text{Re} (\mathcal{M}^\alpha \mathcal{M}^{\beta*}). \end{aligned} \quad (4.64)$$

4.5.2 Construction of squared amplitudes for all subprocesses

Using the amplitudes given in Section 4.4, the different colour structures from the previous subsection, and crossing symmetry, all matrix elements needed for the evaluation of $pp/p\bar{p} \rightarrow VV + \text{jet} + X$ cross sections can be obtained. In this subsection, the matrix elements are collected with all factors from averaging over spins and colours of the initial-state particles included. The colour averaging factors are $\frac{1}{3}$ for incoming (anti-)quarks and $\frac{1}{8}$ for incoming gluons. The factor from averaging over polarizations and helicities, respectively, is $\frac{1}{2}$ for each relevant incoming particle. Symmetry factors for identical outgoing particles are also already included here, but are not combined with the averaging factors for the sake of transparency. In the process class $WZ + \text{jet}$, only the matrix elements of $W^+Z + \text{jet}$ are explicitly given, because each subprocess has its $W^-Z + \text{jet}$ counterpart that can be obtained by application of a \mathcal{CP} transformation.

LO matrix elements

For all process classes of $VV + \text{jet}$ production, the sum over external colours and spins reads

$$\begin{aligned} & |\mathcal{M}(q_1[p] \bar{q}_2[p'] \rightarrow V_1[k_1] V_2[k_2] g[k])|^2 \\ &= \sum_{\sigma, \sigma'} \sum_{\tau} \sum_{\lambda_1, \lambda_2} \sum_{i, j} \sum_a \left| \mathcal{M}\left(q_1 \begin{bmatrix} i \\ p \\ \sigma \end{bmatrix} \bar{q}_2 \begin{bmatrix} j \\ p' \\ \sigma' \end{bmatrix} \rightarrow V_1 \begin{bmatrix} k_1 \\ \lambda_1 \end{bmatrix} V_2 \begin{bmatrix} k_2 \\ \lambda_2 \end{bmatrix} g \begin{bmatrix} a \\ k \\ \tau \end{bmatrix}\right) \right|^2. \end{aligned} \quad (4.65)$$

The momentum assignment applied for each matrix element in this paragraph is understood to be $\mathcal{M}(a[p] b[p'] \rightarrow c[k_1] d[k_2] e[k])$. In particular, all applications of particle crossings refer to this notation. The colour structure is taken from Eq. (4.58), and the LO cross sections get contributions from quark–antiquark, quark–gluon, and gluon–antiquark initial states for all $VV + \text{jet}$ process classes.

For $WW + \text{jet}$ and $ZZ + \text{jet}$ production, the external (anti-)quarks belong to the same flavour, $q_2 = q_1 = Q$, for all subprocesses. For $WW + \text{jet}$ production, the amplitudes for $Q = u, c$ are given in Eq. (4.36), and those for $Q = d, s, b$ in Eq. (4.37). Including the averaging factors for the respective initial states, the following matrix elements result,

$$\overline{|\mathcal{M}(Q\bar{Q} \rightarrow W^+W^-g)|^2} = \frac{1}{36} |\mathcal{M}(Q\bar{Q} \rightarrow W^+W^-g)|^2, \quad (4.66)$$

$$\overline{|\mathcal{M}(Qg \rightarrow W^+W^-Q)|^2} = \frac{1}{96} \mathcal{X}[p' \leftrightarrow k] \left\{ |\mathcal{M}(Q\bar{Q} \rightarrow W^+W^-g)|^2 \right\}, \quad (4.67)$$

$$\overline{|\mathcal{M}(g\bar{Q} \rightarrow W^+W^-\bar{Q})|^2} = \frac{1}{96} \mathcal{X}[p \leftrightarrow k] \left\{ |\mathcal{M}(Q\bar{Q} \rightarrow W^+W^-g)|^2 \right\}. \quad (4.68)$$

For $ZZ + \text{jet}$ production, the amplitudes can be found in Eq. (4.38) for $Q = d, u, s, c, b$. With averaging factors and the symmetry factor for the identical Z bosons in the final state, the matrix elements read

$$\overline{|\mathcal{M}(Q\bar{Q} \rightarrow ZZg)|^2} = \frac{1}{2} \times \frac{1}{36} |\mathcal{M}(Q\bar{Q} \rightarrow ZZg)|^2, \quad (4.69)$$

$$\overline{|\mathcal{M}(\text{Qg} \rightarrow \text{ZZQ})|^2} = \frac{1}{2} \times \frac{1}{96} \mathcal{X}[p' \leftrightarrow k] \left\{ |\mathcal{M}(\text{Q}\bar{\text{Q}} \rightarrow \text{ZZg})|^2 \right\}, \quad (4.70)$$

$$\overline{|\mathcal{M}(\text{g}\bar{\text{Q}} \rightarrow \text{ZZ}\bar{\text{Q}})|^2} = \frac{1}{2} \times \frac{1}{96} \mathcal{X}[p \leftrightarrow k] \left\{ |\mathcal{M}(\text{Q}\bar{\text{Q}} \rightarrow \text{ZZg})|^2 \right\}. \quad (4.71)$$

For WZ+jet production, the relevant amplitudes are given in Eq. (4.39). With averaging factors included, the matrix elements for U = u, c and D = d, s are

$$\overline{|\mathcal{M}(\text{U}\bar{\text{D}} \rightarrow \text{W}^+ \text{Zg})|^2} = \frac{1}{36} |\mathcal{M}(\text{U}\bar{\text{D}} \rightarrow \text{W}^+ \text{Zg})|^2, \quad (4.72)$$

$$\overline{|\mathcal{M}(\text{Ug} \rightarrow \text{W}^+ \text{ZD})|^2} = \frac{1}{96} \mathcal{X}[p' \leftrightarrow k] \left\{ |\mathcal{M}(\text{U}\bar{\text{D}} \rightarrow \text{W}^+ \text{Zg})|^2 \right\}, \quad (4.73)$$

$$\overline{|\mathcal{M}(\text{g}\bar{\text{D}} \rightarrow \text{W}^+ \text{Z}\bar{\text{U}})|^2} = \frac{1}{96} \mathcal{X}[p \leftrightarrow k] \left\{ |\mathcal{M}(\text{U}\bar{\text{D}} \rightarrow \text{W}^+ \text{Zg})|^2 \right\}. \quad (4.74)$$

Real-emission matrix elements with two external gluons

For all process classes, the sum over external colours and spins reads

$$\begin{aligned} & |\mathcal{M}(q_1[p] \bar{q}_2[p'] \rightarrow V_1[k_1] V_2[k_2] g[k] g[l])|^2 \\ &= \sum_{\sigma, \sigma'} \sum_{\tau, \tau'} \sum_{\lambda_1, \lambda_2} \sum_{i, j} \sum_{a, b} \left| \mathcal{M} \left(q_1 \begin{bmatrix} i \\ p \\ \sigma \end{bmatrix} \bar{q}_2 \begin{bmatrix} j \\ p' \\ \sigma' \end{bmatrix} \rightarrow V_1 \begin{bmatrix} k_1 \\ \lambda_1 \end{bmatrix} V_2 \begin{bmatrix} k_2 \\ \lambda_2 \end{bmatrix} g \begin{bmatrix} a \\ k \\ \tau \end{bmatrix} g \begin{bmatrix} b \\ l \\ \tau' \end{bmatrix} \right) \right|^2. \end{aligned} \quad (4.75)$$

Accordingly, the momentum assignment used for all matrix elements in this paragraph is $\mathcal{M}(a[p] b[p'] \rightarrow c[k_1] d[k_2] e[k] f[l])$. All amplitudes of this kind of subprocesses are decomposed with respect to their colour structures as described in Eq. (4.59). The prefactors for the particular terms resulting from the sum over colour indices are given in Eq. (4.60). The contributing initial states are quark–antiquark, quark–gluon, gluon–antiquark, and—in addition to the channels already present in LO—gluon–gluon for all VV+jet process classes. For all subprocesses with two gluons in the final state, a symmetry factor $\frac{1}{2}$ arises.

As in the LO case, for all subprocesses of WW+jet and ZZ+jet production the external (anti-)quarks belong to the same flavour, $q_2 = q_1 = Q$. For WW+jet production, the amplitudes are given in Eq. (4.36) for $Q = u, c$ and in Eq. (4.37) for $Q = d, s, b$. Including averaging factors and—if needed—symmetry factors, the matrix elements are

$$\overline{|\mathcal{M}(\text{Q}\bar{\text{Q}} \rightarrow \text{W}^+ \text{W}^- \text{gg})|^2} = \frac{1}{2} \times \frac{1}{36} |\mathcal{M}(\text{Q}\bar{\text{Q}} \rightarrow \text{W}^+ \text{W}^- \text{gg})|^2, \quad (4.76)$$

$$\overline{|\mathcal{M}(\text{Qg} \rightarrow \text{W}^+ \text{W}^- \text{Qg})|^2} = \frac{1}{96} \mathcal{X}[p' \leftrightarrow k] \left\{ |\mathcal{M}(\text{Q}\bar{\text{Q}} \rightarrow \text{W}^+ \text{W}^- \text{gg})|^2 \right\}, \quad (4.77)$$

$$\overline{|\mathcal{M}(\text{g}\bar{\text{Q}} \rightarrow \text{W}^+ \text{W}^- \text{g}\bar{\text{Q}})|^2} = \frac{1}{96} \mathcal{X}[p \leftrightarrow l] \left\{ |\mathcal{M}(\text{Q}\bar{\text{Q}} \rightarrow \text{W}^+ \text{W}^- \text{gg})|^2 \right\}, \quad (4.78)$$

$$\overline{|\mathcal{M}(\text{gg} \rightarrow \text{W}^+ \text{W}^- \text{Q}\bar{\text{Q}})|^2} = \frac{1}{256} \mathcal{X} \left[\begin{matrix} p \leftrightarrow l \\ p' \leftrightarrow k \end{matrix} \right] \left\{ |\mathcal{M}(\text{Q}\bar{\text{Q}} \rightarrow \text{W}^+ \text{W}^- \text{gg})|^2 \right\}. \quad (4.79)$$

The amplitudes of the ZZ+jet subprocesses for $Q = d, u, s, c, b$ are given in Eq. (4.38). With all averaging factors and symmetry factors for identical final-state particles, the following matrix elements result,

$$\overline{|\mathcal{M}(\text{Q}\bar{\text{Q}} \rightarrow \text{ZZgg})|^2} = \frac{1}{2} \times \frac{1}{2} \times \frac{1}{36} |\mathcal{M}(\text{Q}\bar{\text{Q}} \rightarrow \text{ZZgg})|^2, \quad (4.80)$$

$$\overline{|\mathcal{M}(\text{Qg} \rightarrow \text{ZZQg})|^2} = \frac{1}{2} \times \frac{1}{96} \mathcal{X}[p' \leftrightarrow k] \left\{ |\mathcal{M}(\text{Q}\bar{\text{Q}} \rightarrow \text{ZZgg})|^2 \right\}, \quad (4.81)$$

$$\overline{|\mathcal{M}(\text{g}\bar{\text{Q}} \rightarrow \text{ZZg}\bar{\text{Q}})|^2} = \frac{1}{2} \times \frac{1}{96} \mathcal{X}[p \leftrightarrow l] \left\{ |\mathcal{M}(\text{Q}\bar{\text{Q}} \rightarrow \text{ZZgg})|^2 \right\}, \quad (4.82)$$

$$\overline{|\mathcal{M}(\text{gg} \rightarrow \text{ZZQ}\bar{\text{Q}})|^2} = \frac{1}{2} \times \frac{1}{256} \mathcal{X}\left[\begin{smallmatrix} p \leftrightarrow l \\ p' \leftrightarrow k \end{smallmatrix}\right] \left\{ |\mathcal{M}(\text{Q}\bar{\text{Q}} \rightarrow \text{ZZgg})|^2 \right\}. \quad (4.83)$$

The relevant amplitudes for WZ+jet production are delivered in Eq. (4.39). With all factors included, the matrix elements for $U = u, c$ and $D = d, s$ read

$$\overline{|\mathcal{M}(\text{U}\bar{\text{D}} \rightarrow \text{W}^+ \text{Zgg})|^2} = \frac{1}{2} \times \frac{1}{36} |\mathcal{M}(\text{U}\bar{\text{D}} \rightarrow \text{W}^+ \text{Zgg})|^2, \quad (4.84)$$

$$\overline{|\mathcal{M}(\text{Ug} \rightarrow \text{W}^+ \text{ZDg})|^2} = \frac{1}{96} \mathcal{X}[p' \leftrightarrow k] \left\{ |\mathcal{M}(\text{U}\bar{\text{D}} \rightarrow \text{W}^+ \text{Zgg})|^2 \right\}, \quad (4.85)$$

$$\overline{|\mathcal{M}(\text{g}\bar{\text{D}} \rightarrow \text{W}^+ \text{Zg}\bar{\text{U}})|^2} = \frac{1}{96} \mathcal{X}[p \leftrightarrow k] \left\{ |\mathcal{M}(\text{U}\bar{\text{D}} \rightarrow \text{W}^+ \text{Zgg})|^2 \right\}, \quad (4.86)$$

$$\overline{|\mathcal{M}(\text{gg} \rightarrow \text{W}^+ \text{ZD}\bar{\text{U}})|^2} = \frac{1}{256} \mathcal{X}\left[\begin{smallmatrix} p \leftrightarrow l \\ p' \leftrightarrow k \end{smallmatrix}\right] \left\{ |\mathcal{M}(\text{U}\bar{\text{D}} \rightarrow \text{W}^+ \text{Zgg})|^2 \right\}. \quad (4.87)$$

Real-emission matrix elements without external gluons

For all VV+jet process classes, the sum over external colours and spins reads

$$\begin{aligned} & |\mathcal{M}(q_1[p] \bar{q}_2[p'] \rightarrow V_1[k_1] V_2[k_2] q_3[q] \bar{q}_4[q'])|^2 \\ &= \sum_{\sigma, \sigma', \tau, \tau'} \sum_{\lambda_1, \lambda_2} \sum_{i, j, k, l} \left| \mathcal{M}\left(q_1 \begin{bmatrix} i \\ p \\ \sigma \end{bmatrix} \bar{q}_2 \begin{bmatrix} j \\ p' \\ \sigma' \end{bmatrix} \rightarrow V_1 \begin{bmatrix} k_1 \\ \lambda_1 \end{bmatrix} V_2 \begin{bmatrix} k_2 \\ \lambda_2 \end{bmatrix} q_3 \begin{bmatrix} k \\ q \\ \tau \end{bmatrix} \bar{q}_4 \begin{bmatrix} l \\ q' \\ \tau' \end{bmatrix}\right) \right|^2. \end{aligned} \quad (4.88)$$

The momentum assignment for all matrix elements in this paragraph is understood to be $\mathcal{M}(a[p] b[p'] \rightarrow c[k_1] d[k_2] e[q] f[q'])$. The colour structures of the amplitudes for this group of subprocesses depend on the particular (anti-)quark assignments. In general, the following rule can be applied: If the contributions to one helicity channel contain two different fermion-number flows, the respective amplitude shows two different colour structures as well. Thus, it has to be decomposed according to Eq. (4.63). The prefactors corresponding to this decomposition are given in Eq. (4.64). For all other helicity channels and the remaining subprocesses, only one colour structure appears, leading to the prefactor given in Eq. (4.62). Crossing symmetry delivers the matrix elements for a set of subprocesses from each amplitude, where in every case quark–antiquark, quark–quark, and antiquark–antiquark initial states are involved. In the following, the matrix elements are given for the various gauge-boson assignments.

WW+jet

For subprocesses based on $Q\bar{Q} \rightarrow W^+W^-Q\bar{Q}$, the amplitudes are provided in Eqs. (4.41) and (4.42) for $Q = u, c$ and $Q = d, s, b$, respectively. Including averaging factors and—in the case of identical outgoing partons—symmetry factors, the matrix elements are

$$\overline{|\mathcal{M}(Q\bar{Q} \rightarrow W^+W^-Q\bar{Q})|^2} = \frac{1}{36} |\mathcal{M}(Q\bar{Q} \rightarrow W^+W^-Q\bar{Q})|^2, \quad (4.89)$$

$$\overline{|\mathcal{M}(QQ \rightarrow W^+W^-QQ)^2} = \frac{1}{2} \times \frac{1}{36} \mathcal{X}[p' \leftrightarrow q'] \left\{ |\mathcal{M}(Q\bar{Q} \rightarrow W^+W^-Q\bar{Q})|^2 \right\}, \quad (4.90)$$

$$\overline{|\mathcal{M}(\bar{Q}\bar{Q} \rightarrow W^+W^-\bar{Q}\bar{Q})|^2} = \frac{1}{2} \times \frac{1}{36} \mathcal{X}[p \leftrightarrow q] \left\{ |\mathcal{M}(Q\bar{Q} \rightarrow W^+W^-Q\bar{Q})|^2 \right\}. \quad (4.91)$$

The amplitudes for subprocesses derived from $Q\bar{Q} \rightarrow W^+W^-Q'\bar{Q}'$ with $Q \neq Q'$, but both Q and Q' either of up- or of down-type, are given in Eqs. (4.43) and (4.44). For the particles insertions $(Q, Q') = (u, c), (c, u), (d, s), (s, d), (d, b), (s, b), (b, d), (b, s)$, the matrix elements with averaging factors included read

$$\overline{|\mathcal{M}(Q\bar{Q} \rightarrow W^+W^-Q'\bar{Q}')|^2} = \frac{1}{36} |\mathcal{M}(Q\bar{Q} \rightarrow W^+W^-Q'\bar{Q}')|^2, \quad (4.92)$$

$$\overline{|\mathcal{M}(Q\bar{Q}' \rightarrow W^+W^-Q\bar{Q}')|^2} = \frac{1}{36} \mathcal{X}[p' \leftrightarrow q] \left\{ |\mathcal{M}(Q\bar{Q} \rightarrow W^+W^-Q'\bar{Q}')|^2 \right\}, \quad (4.93)$$

$$\overline{|\mathcal{M}(QQ' \rightarrow W^+W^-Q'\bar{Q})|^2} = \frac{1}{36} \mathcal{X}[p' \leftrightarrow q'] \left\{ |\mathcal{M}(Q\bar{Q} \rightarrow W^+W^-Q'\bar{Q}')|^2 \right\}, \quad (4.94)$$

$$\overline{|\mathcal{M}(\bar{Q}\bar{Q}' \rightarrow W^+W^-\bar{Q}'\bar{Q})|^2} = \frac{1}{36} \mathcal{X}[p \leftrightarrow q] \left\{ |\mathcal{M}(Q'\bar{Q}' \rightarrow W^+W^-Q\bar{Q})|^2 \right\}. \quad (4.95)$$

For the subprocesses based on $U\bar{U} \rightarrow W^+W^-D\bar{D}$, the amplitudes can be found in Eqs. (4.45) and (4.46). With the factors from averaging over colours and spins, the matrix elements for the flavour insertions $U = u, c$ and $D = d, s, b$ are

$$\overline{|\mathcal{M}(U\bar{U} \rightarrow W^+W^-D\bar{D})|^2} = \frac{1}{36} |\mathcal{M}(U\bar{U} \rightarrow W^+W^-D\bar{D})|^2, \quad (4.96)$$

$$\overline{|\mathcal{M}(D\bar{D} \rightarrow W^+W^-U\bar{U})|^2} = \frac{1}{36} |\mathcal{M}(D\bar{D} \rightarrow W^+W^-U\bar{U})|^2, \quad (4.97)$$

$$\overline{|\mathcal{M}(U\bar{D} \rightarrow W^+W^-U\bar{D})|^2} = \frac{1}{36} \mathcal{X}[p' \leftrightarrow q] \left\{ |\mathcal{M}(U\bar{U} \rightarrow W^+W^-D\bar{D})|^2 \right\}, \quad (4.98)$$

$$\overline{|\mathcal{M}(D\bar{U} \rightarrow W^+W^-D\bar{U})|^2} = \frac{1}{36} \mathcal{X}[p' \leftrightarrow q] \left\{ |\mathcal{M}(D\bar{D} \rightarrow W^+W^-U\bar{U})|^2 \right\}, \quad (4.99)$$

$$\overline{|\mathcal{M}(DU \rightarrow W^+W^-UD)^2} = \frac{1}{36} \mathcal{X}[p' \leftrightarrow q'] \left\{ |\mathcal{M}(D\bar{D} \rightarrow W^+W^-U\bar{U})|^2 \right\}, \quad (4.100)$$

$$\overline{|\mathcal{M}(\bar{D}\bar{U} \rightarrow W^+W^-\bar{U}\bar{D})|^2} = \frac{1}{36} \mathcal{X}[p \leftrightarrow q] \left\{ |\mathcal{M}(U\bar{U} \rightarrow W^+W^-D\bar{D})|^2 \right\}. \quad (4.101)$$

The remaining real-emission subprocesses are constructed from $U\bar{U}' \rightarrow W^+W^-D\bar{D}'$ with either $U \neq U'$, $D \neq D'$, or both. The amplitudes are taken from Eqs. (4.47) and (4.48).

With averaging factors, the matrix elements for the flavour insertions $U, U' = u, c$ and $D, D' = d, s$ that are not covered in the previous passage are

$$\overline{|\mathcal{M}(\bar{U}\bar{D} \rightarrow W^+W^-U'\bar{D}')|^2} = \frac{1}{36} |\mathcal{M}(\bar{U}\bar{D} \rightarrow W^+W^-U'\bar{D}')|^2, \quad (4.102)$$

$$\overline{|\mathcal{M}(\bar{D}\bar{U} \rightarrow W^+W^-D'\bar{U}')|^2} = \frac{1}{36} |\mathcal{M}(\bar{D}\bar{U} \rightarrow W^+W^-D'\bar{U}')|^2, \quad (4.103)$$

$$\overline{|\mathcal{M}(U\bar{U}' \rightarrow W^+W^-D\bar{D}')|^2} = \frac{1}{36} \mathcal{X}[p' \leftrightarrow q] \left\{ |\mathcal{M}(\bar{U}\bar{D} \rightarrow W^+W^-U'\bar{D}')|^2 \right\}, \quad (4.104)$$

$$\overline{|\mathcal{M}(D\bar{D}' \rightarrow W^+W^-U\bar{U}')|^2} = \frac{1}{36} \mathcal{X}[p' \leftrightarrow q] \left\{ |\mathcal{M}(\bar{D}\bar{U} \rightarrow W^+W^-D'\bar{U}')|^2 \right\}, \quad (4.105)$$

$$\overline{|\mathcal{M}(D\bar{U}' \rightarrow W^+W^-D'\bar{U})|^2} = \frac{1}{36} \mathcal{X}[p' \leftrightarrow q'] \left\{ |\mathcal{M}(\bar{D}\bar{U} \rightarrow W^+W^-D'\bar{U}')|^2 \right\}, \quad (4.106)$$

$$\overline{|\mathcal{M}(\bar{D}'\bar{U} \rightarrow W^+W^-D\bar{U}')|^2} = \frac{1}{36} \mathcal{X}[p \leftrightarrow q] \left\{ |\mathcal{M}(\bar{D}\bar{U} \rightarrow W^+W^-D'\bar{U}')|^2 \right\}. \quad (4.107)$$

ZZ+jet

For subprocesses based on $Q\bar{Q} \rightarrow ZZQ\bar{Q}$ with $Q = d, u, s, c, b$, the amplitudes are provided in Eq. (4.51). With all averaging factors for colours and spins and the symmetry factors for the two identical Z bosons and, if existing, identical partons in the final state, the matrix elements read

$$\overline{|\mathcal{M}(Q\bar{Q} \rightarrow ZZQ\bar{Q})|^2} = \frac{1}{2} \times \frac{1}{36} |\mathcal{M}(Q\bar{Q} \rightarrow ZZQ\bar{Q})|^2, \quad (4.108)$$

$$\overline{|\mathcal{M}(Q\bar{Q} \rightarrow ZZQ\bar{Q})|^2} = \frac{1}{2} \times \frac{1}{2} \times \frac{1}{36} \mathcal{X}[p' \leftrightarrow q'] \left\{ |\mathcal{M}(Q\bar{Q} \rightarrow ZZQ\bar{Q})|^2 \right\}, \quad (4.109)$$

$$\overline{|\mathcal{M}(\bar{Q}\bar{Q} \rightarrow ZZQ\bar{Q})|^2} = \frac{1}{2} \times \frac{1}{2} \times \frac{1}{36} \mathcal{X}[p \leftrightarrow q] \left\{ |\mathcal{M}(Q\bar{Q} \rightarrow ZZQ\bar{Q})|^2 \right\}. \quad (4.110)$$

The remaining real-emission subprocesses are constructed from $Q\bar{Q} \rightarrow ZZQ'\bar{Q}'$ with $Q, \bar{Q}' = d, u, s, c, b$, but $Q \neq Q'$. The needed amplitudes can be taken from Eq. (4.52). With averaging factors and the symmetry factor for the two outgoing Z bosons included, the matrix elements are

$$\overline{|\mathcal{M}(Q\bar{Q} \rightarrow ZZQ'\bar{Q}')|^2} = \frac{1}{2} \times \frac{1}{36} |\mathcal{M}(Q\bar{Q} \rightarrow ZZQ'\bar{Q}')|^2, \quad (4.111)$$

$$\overline{|\mathcal{M}(Q\bar{Q}' \rightarrow ZZQ\bar{Q}')|^2} = \frac{1}{2} \times \frac{1}{36} \mathcal{X}[p \leftrightarrow q'] \left\{ |\mathcal{M}(Q\bar{Q} \rightarrow ZZQ'\bar{Q}')|^2 \right\}, \quad (4.112)$$

$$\overline{|\mathcal{M}(Q\bar{Q}' \rightarrow ZZQ'\bar{Q})|^2} = \frac{1}{2} \times \frac{1}{36} \mathcal{X}[p' \leftrightarrow q'] \left\{ |\mathcal{M}(Q\bar{Q} \rightarrow ZZQ'\bar{Q}')|^2 \right\}, \quad (4.113)$$

$$\overline{|\mathcal{M}(\bar{Q}\bar{Q}' \rightarrow ZZQ'\bar{Q})|^2} = \frac{1}{2} \times \frac{1}{36} \mathcal{X}[p \leftrightarrow q] \left\{ |\mathcal{M}(Q'\bar{Q}' \rightarrow ZZQ\bar{Q})|^2 \right\}. \quad (4.114)$$

WZ+jet

In the process class WZ+jet, only the real-emission matrix elements for W^+Z +jet have to be calculated. The subprocesses contributing to W^-Z +jet can be received from the previous ones by applying a \mathcal{CP} transformation. The amplitudes for all subprocesses based on $U\bar{D} \rightarrow W^+W^-U\bar{U}$ are provided in Eq. (4.54). With the average factors for colours and spins as well as for identical partons in the final state if existent, the matrix elements for the flavour assignments $U = u, c$ and $D = d, s$ are

$$\overline{|\mathcal{M}(U\bar{D} \rightarrow W^+ZU\bar{U})|^2} = \frac{1}{36} |\mathcal{M}(U\bar{D} \rightarrow W^+ZU\bar{U})|^2, \quad (4.115)$$

$$\overline{|\mathcal{M}(U\bar{U} \rightarrow W^+ZD\bar{U})|^2} = \frac{1}{36} \mathcal{X}[p' \leftrightarrow q] \left\{ |\mathcal{M}(U\bar{D} \rightarrow W^+ZU\bar{U})|^2 \right\}, \quad (4.116)$$

$$\overline{|\mathcal{M}(UU \rightarrow W^+ZUD)^2} = \frac{1}{36} \mathcal{X}[p' \leftrightarrow q'] \left\{ |\mathcal{M}(U\bar{D} \rightarrow W^+ZU\bar{U})|^2 \right\}, \quad (4.117)$$

$$\overline{|\mathcal{M}(\bar{U}\bar{D} \rightarrow W^+Z\bar{U}\bar{U})|^2} = \frac{1}{2} \times \frac{1}{36} \mathcal{X}[p \leftrightarrow q] \left\{ |\mathcal{M}(U\bar{D} \rightarrow W^+ZU\bar{U})|^2 \right\}. \quad (4.118)$$

The amplitudes for subprocesses derived from $U\bar{D} \rightarrow W^+W^-D\bar{D}$ can be taken from Eq. (4.55). Including averaging factors and symmetry factors for identical outgoing partons, the matrix elements for the flavour assignments $U = u, c$ and $D = d, s$ read

$$\overline{|\mathcal{M}(U\bar{D} \rightarrow W^+ZD\bar{D})|^2} = \frac{1}{36} |\mathcal{M}(U\bar{D} \rightarrow W^+ZD\bar{D})|^2, \quad (4.119)$$

$$\overline{|\mathcal{M}(D\bar{D} \rightarrow W^+ZD\bar{U})|^2} = \frac{1}{36} \mathcal{X}[p \leftrightarrow q'] \left\{ |\mathcal{M}(U\bar{D} \rightarrow W^+ZD\bar{D})|^2 \right\}, \quad (4.120)$$

$$\overline{|\mathcal{M}(UD \rightarrow W^+ZDD)^2} = \frac{1}{2} \times \frac{1}{36} \mathcal{X}[p' \leftrightarrow q'] \left\{ |\mathcal{M}(U\bar{D} \rightarrow W^+ZD\bar{D})|^2 \right\}, \quad (4.121)$$

$$\overline{|\mathcal{M}(\bar{D}\bar{D} \rightarrow W^+Z\bar{U}\bar{D})|^2} = \frac{1}{36} \mathcal{X}[p \leftrightarrow q] \left\{ |\mathcal{M}(U\bar{D} \rightarrow W^+ZD\bar{D})|^2 \right\}. \quad (4.122)$$

The remaining real-emission subprocesses are based on $U\bar{D} \rightarrow W^+W^-Q\bar{Q}$, whose amplitudes are given in Eq. (4.56). With averaging factors, the matrix elements for the flavour insertions $U = u, c$, $D = d, s$, and $Q = d, u, s, c, b$ with the restrictions $Q \neq U$ and $Q \neq D$ are

$$\overline{|\mathcal{M}(U\bar{D} \rightarrow W^+ZQ\bar{Q})|^2} = \frac{1}{36} |\mathcal{M}(U\bar{D} \rightarrow W^+ZQ\bar{Q})|^2, \quad (4.123)$$

$$\overline{|\mathcal{M}(Q\bar{Q} \rightarrow W^+ZD\bar{U})|^2} = \frac{1}{36} \mathcal{X} \left[\begin{smallmatrix} p \leftrightarrow q' \\ p' \leftrightarrow q \end{smallmatrix} \right] \left\{ |\mathcal{M}(U\bar{D} \rightarrow W^+ZQ\bar{Q})|^2 \right\}, \quad (4.124)$$

$$\overline{|\mathcal{M}(Q\bar{D} \rightarrow W^+ZQ\bar{U})|^2} = \frac{1}{36} \mathcal{X}[p \leftrightarrow q'] \left\{ |\mathcal{M}(U\bar{D} \rightarrow W^+ZQ\bar{Q})|^2 \right\}, \quad (4.125)$$

$$\overline{|\mathcal{M}(U\bar{Q} \rightarrow W^+ZD\bar{Q})|^2} = \frac{1}{36} \mathcal{X}[p' \leftrightarrow q] \left\{ |\mathcal{M}(U\bar{D} \rightarrow W^+ZQ\bar{Q})|^2 \right\}, \quad (4.126)$$

$$\overline{|\mathcal{M}(UQ \rightarrow W^+ZQ\bar{D})|^2} = \frac{1}{36} \mathcal{X}[p' \leftrightarrow q'] \left\{ |\mathcal{M}(U\bar{D} \rightarrow W^+ZQ\bar{Q})|^2 \right\}, \quad (4.127)$$

$$\overline{|\mathcal{M}(\bar{Q}\bar{D} \rightarrow W^+ Z \bar{U} \bar{Q})|^2} = \frac{1}{36} \mathcal{X}[p \leftrightarrow q] \left\{ |\mathcal{M}(\bar{U}\bar{D} \rightarrow W^+ Z Q \bar{Q})|^2 \right\}. \quad (4.128)$$

The matrix elements for W^-Z +jet subprocesses are obtained from those presented for W^+Z +jet by application of a \mathcal{CP} transformation. For any possible insertion of the partons p_i , $i = 1, \dots, 4$, the matrix element reads

$$\begin{aligned} & \left| \mathcal{M}(p_1[p_1] \bar{p}_2[p_2] \rightarrow W^-[k_1] Z[k_2] p_3[k_3] \bar{p}_4[k_4]) \right|^2 \\ &= \mathcal{CP} \left\{ \left| \mathcal{M}(p_2[p_2] \bar{p}_1[p_1] \rightarrow W^+[k_1] Z[k_2] p_4[k_4] \bar{p}_3[k_3]) \right|^2 \right\}, \end{aligned} \quad (4.129)$$

where the interchanged order of the partons is just a convention. The LO matrix elements are obtained by an analogous operation with the parton p_4 omitted.

4.5.3 Combination of subprocesses with equal matrix elements

With the matrix elements provided in the previous subsection, the contributions of all processes listed in Tables 3.1 – 3.9 to the particular cross sections can be calculated. Due to their large number especially in the real corrections, it makes sense to calculate as many subprocesses as possible simultaneously in order to reduce the needed computational time.

A trivial way to reduce the number of subprocesses by nearly a factor 2 is provided by the fact that two subprocesses with interchanged incoming partons are related to each other point-wise, i.e. for related phase-space points. This relation is not a parity transformation, which can be easily understood, since the electroweak interactions of the SM violate parity symmetry. However, the invariance of the SM under proper Lorentz transformations and, in particular, under rotations, delivers a way to relate two phase-space points with identical matrix elements for exchanged initial states. Precisely, a rotation by 180° around an axis perpendicular to the beam axis has to be performed: For all momenta, this means a sign change of the components in beam direction and a second spatial component, but not in the third. Whereas the matrix elements are identical, different contributions to the hadronic cross sections arise from the related phase-space points in proton–antiproton collisions due to the different PDFs. The rotated process may only be taken into account if the two initial-state partons are not identical, since no new contribution results otherwise.

In Table 4.7, the initial states leading to subprocesses contributing to WW +jet and ZZ +jet production are collected. Initial states consisting of identical partons are denoted by ‘1’, because the respective matrix-element calculation is used for one subprocess only. The matrix elements for initial states denoted by ‘2’ are used for the original and the rotated subprocess. Those with a ‘0’ do not have to be calculated separately, because they are already contained in the previous case.

Another way to combine processes is based on the fact that—for massless quarks and in the applied approximation of the CKM matrix—subprocesses are described by the same matrix elements if each first-generation (anti-)quark is replaced by its second-generation counterpart and vice versa. For instance, the matrix elements of the subprocesses $u\bar{d} \rightarrow W^+ W^- c\bar{s}$ and $c\bar{s} \rightarrow W^+ W^- u\bar{d}$ are the same. Only the PDFs have to be calculated separately for the subprocesses related by exchange of first- and second-generation

	g	d	u	s	c	b	\bar{d}	\bar{u}	\bar{s}	\bar{c}	\bar{b}
g	1	0	0	0	0	0	2	2	2	2	2
d	2	1	2	2	2	2	2	2	2	2	2
u	2	0	1	2	2	2	2	2	2	2	2
s	2	0	0	1	2	2	2	2	2	2	2
c	2	0	0	0	1	2	2	2	2	2	2
b	2	0	0	0	0	1	2	2	2	2	2
\bar{d}	0	0	0	0	0	0	1	2	2	2	2
\bar{u}	0	0	0	0	0	0	0	1	2	2	2
\bar{s}	0	0	0	0	0	0	0	0	1	2	2
\bar{c}	0	0	0	0	0	0	0	0	0	1	2
\bar{b}	0	0	0	0	0	0	0	0	0	0	1

Table 4.7: All partonic initial states contributing to $pp/p\bar{p} \rightarrow WW/ZZ+\text{jet}+X$ are collected in this table. The entries of the tabular are explained in the text. The selection of the subprocesses being evaluated is based on the matrix elements provided in Section 4.4. For the given selection, the number of crossings of momenta to be applied is minimal. This explains the deviations from the expected diagonal structure, which is ‘1’ on the diagonal, ‘2’ top right, and ‘0’ left bottom.

(anti-)quarks. Initial states of subprocesses that can be obtained by this procedure are labelled by gray numbers. Care has to be taken for subprocesses with the initial states ds , uc , $\bar{d}\bar{s}$, and $\bar{u}\bar{c}$: For $WW+\text{jet}$ and $ZZ+\text{jet}$, the described generation exchange reproduces the subprocesses that are already obtained by exchanging the incoming partons. Therefore, only the exchange of initial state partons is applied here to avoid double counting of subprocesses. For the gg initial state, the exchange of the (anti-)quarks of the two light generations can also be used. E.g. the subprocesses $gg \rightarrow W^+W^-d\bar{d}$ and $gg \rightarrow W^+W^-s\bar{s}$ can be calculated simultaneously. Since the PDFs are identical in the two cases, only one of them has to be evaluated, multiplied with a factor 2.

By applying these two symmetries, four subprocesses can be calculated with the same matrix elements in general. The exceptions to this are discussed in the previous passages. Finally, the procedure is illustrated by the following chart for a sample subprocess,

$$\begin{array}{ccc}
u\bar{c} \rightarrow W^+W^-d\bar{s} & \xrightarrow{\text{gen.}} & c\bar{u} \rightarrow W^+W^-s\bar{d} \\
\downarrow 1 \leftrightarrow 2 & & \downarrow 1 \leftrightarrow 2 \\
\bar{c}u \rightarrow W^+W^-s\bar{d} & \xrightarrow{\text{gen.}} & \bar{u}c \rightarrow W^+W^-d\bar{s} \quad .
\end{array} \tag{4.130}$$

The label ‘ $1 \leftrightarrow 2$ ’ denotes the interchanged parton assignments to the incoming hadrons, and ‘gen.’ the exchange of all first-generation (anti-)quarks by their second-generation counterparts.

	g	d	u	s	c	b	\bar{d}	\bar{u}	\bar{s}	\bar{c}	\bar{b}
g	1	–	0	–	0	–	2	–	2	–	2
d	–	–	0	–	0	–	2	–	2	–	2
u	2	2	1	2	2	2	2	2	2	2	2
s	–	–	0	–	2	–	2	–	2	–	2
c	2	2	0	0	1	2	2	2	2	2	2
b	–	–	0	–	0	–	2	–	2	–	2
\bar{d}	0	0	0	0	0	0	1	0	2	0	2
\bar{u}	–	–	0	–	0	–	2	–	2	–	2
\bar{s}	0	0	0	0	0	0	0	0	1	2	2
\bar{c}	–	–	0	–	0	–	2	–	0	–	2
\bar{b}	0	0	0	0	0	0	0	0	0	0	1

Table 4.8: As in Table 4.7, but for the initial states yielding subprocesses that contribute to $pp/p\bar{p} \rightarrow W^+Z+\text{jet}+X$.

For the subprocesses contributing to $WZ+\text{jet}$, the two described symmetries can also be applied in order to reduce the number of subprocesses to be calculated. In addition, we make use of the fact that pairs of subprocesses can be combined if the unitarity of the CKM matrix is employed, as described in Section 3.1. In the way it is used in the calculations of this thesis, this does not influence the contributing initial states and is hence not spelled out here. In Tables 4.8 and 4.9, all initial states delivering subprocesses contributing to $W^+Z+\text{jet}$ and $W^-Z+\text{jet}$ production, respectively, are collected. Due to the charged gauge-boson pair in these process classes, some initial states do not contribute at all. These are the initial states that do not contain at least one up-type quark or one down-type antiquark for $W^+Z+\text{jet}$, and vice versa for $W^-Z+\text{jet}$. These initial states are denoted by ‘–’, while the remaining notation is given in the previous passages.

In contrast to $WW+\text{jet}$ and $ZZ+\text{jet}$, no exception has to be made for the initial states ds , uc , $\bar{d}\bar{s}$, and $\bar{u}\bar{c}$: In $WZ+\text{jet}$ production, the exchange of the first-generation (anti-)quarks with their counterparts of the second generation yields new subprocesses. This is due to the fact only one of the two incoming partons in each subprocess belongs to the fermion chain with the W boson attached.

To illustrate this situation, the following chart shows the eight subprocesses for the sample initial state uc that can be calculated simultaneously,

$$\begin{array}{ccc}
\text{unit.} \left\{ \begin{array}{l} uc \rightarrow W^+Zcd \\ uc \rightarrow W^+Zcs \end{array} \right\} & \xrightarrow{\text{gen.}} & \left\{ \begin{array}{l} cu \rightarrow W^+Zus \\ cu \rightarrow W^+Zud \end{array} \right\} \text{unit.} \\
\downarrow 1 \leftrightarrow 2 & & \downarrow 1 \leftrightarrow 2 \\
\text{unit.} \left\{ \begin{array}{l} cu \rightarrow W^+Zdc \\ cu \rightarrow W^+Zsc \end{array} \right\} & \xrightarrow{\text{gen.}} & \left\{ \begin{array}{l} uc \rightarrow W^+Zsu \\ uc \rightarrow W^+Zdu \end{array} \right\} \text{unit.} .
\end{array} \tag{4.131}$$

	g	d	u	s	c	b	\bar{d}	\bar{u}	\bar{s}	\bar{c}	\bar{b}
g	1	0	–	0	–	0	–	2	–	2	–
d	2	1	2	2	2	2	2	2	2	2	2
u	–	0	–	2	–	2	–	2	–	2	–
s	2	0	0	1	2	2	2	2	2	2	2
c	–	0	–	0	–	2	–	2	–	2	–
b	2	0	0	0	0	1	2	2	2	2	2
\bar{d}	–	0	–	0	–	0	–	2	–	2	–
\bar{u}	0	0	0	0	0	0	0	1	2	2	2
\bar{s}	–	0	–	0	–	0	–	0	–	2	–
\bar{c}	0	0	0	0	0	0	0	0	0	1	2
\bar{b}	–	0	–	0	–	0	–	0	–	0	–

Table 4.9: As in Table 4.7, but for the initial states yielding subprocesses that contribute to $pp/p\bar{p} \rightarrow W^-Z+\text{jet}+X$.

The labels ‘1 \leftrightarrow 2’ and ‘gen.’ are explained in the context of Eq. (4.130). The subprocesses in curly brackets, which are marked by ‘unit.’, can be combined by making use of the unitarity relation $|V_{ud}|^2 + |V_{us}|^2 = 1$, which is valid for the applied approximation of the CKM matrix.

Chapter 5

Evaluation of NLO QCD cross sections via dipole subtraction

For the treatment of infrared (soft and collinear) divergences, the dipole subtraction formalism for massless partons, presented in Ref. [62], is used. The conception of this formalism manifests in a rearrangement of divergences between the different NLO contributions, resulting in separately finite contributions which can then be evaluated numerically. This rearrangement is mediated by the so-called dipole terms that provide a process-independent description of the singularities.

The definition of hadronic observables as infrared-safe jet quantities and the general idea how the rearrangement of the NLO contributions and the dipole terms is actually performed are reviewed in Section 5.1.

Section 5.2 shows how the dipole terms needed to compensate divergences in the real corrections can be calculated from the LO matrix elements and further process-independent constituents. Explicit results are given for all the dipoles needed in subprocesses of $pp/p\bar{p} \rightarrow VV + \text{jet} + X$.

The second part of the NLO QCD calculation, the virtual corrections, are described in Section 5.3. They involve the subprocesses already present at LO, to which diagrams with an exchange of a virtual gluon and diagrams with closed fermion loops contribute. These corrections contain integrals that are divergent both in the infrared and in the ultraviolet region. To guarantee UV finiteness, the Lagrangian of the theory is renormalized. The resulting counterterm Feynman rules also contribute at one-loop level and compensate all UV divergences. The infrared divergences cancel against those contained in the real corrections where the transfer of divergent terms between the two NLO contributions is mediated by subtraction and re-addition of dipole terms. The integration over the one-parton phase space is performed analytically for the re-added terms, leading to singularities in terms of poles $\frac{1}{\epsilon}$ and $\frac{1}{\epsilon^2}$.

In the presence of initial-state QCD partons, collinear divergences related to those incoming particles are not cancelled between real and virtual corrections. Since they do not depend on the specific process, they can be absorbed into the structure of the incoming hadrons resulting in so-called collinear-subtraction counterterms. They can be understood

as a redefinition of PDFs. Their combination with the remaining divergent terms which do not cancel between real and virtual corrections can be performed in a process-independent way. The result of this procedure is given in Section 5.4.

5.1 Controlling divergences in NLO calculations

In general, different kinds of singularities have to be handled when evaluating NLO QCD cross sections. Both real-emission contributions with one additional QCD parton emitted and virtual corrections containing loop diagrams have to be considered. Ultraviolet singularities arising from high-momentum regions in some loop integrals of the virtual corrections are removed by renormalization, which is considered in Section 5.3. The more problematic divergences originate from either low-momentum (soft) partons or configurations with small angles between two partons (collinear), which are summarized as infrared singularities and show up both in real and virtual corrections. However, if the considered observable is properly defined as a jet observable, i.e. its actual value is independent of the number of soft and collinear final-state particles, a cancellation between these singularities is guaranteed by factorization theorems [60, 74]. Left-over collinear singularities with respect to the initial-state partons are process-independent and can therefore be absorbed into the structure functions of the incoming partons in the respective hadrons, leading to a well-defined finite NLO QCD cross section.

In the following, the definition of jet observables is discussed in more detail. Afterwards, a brief overview of the dipole subtraction formalism used to perform the cancellations of infrared divergences in an appropriate form for a numerical phase-space integration is given.

5.1.1 Definition of jet observables

Jet observables must be defined in such a way that their values are independent of the number of soft and collinear partons in the final state. The general features these jet functions have to obey are collected, for instance, in Ref. [62]. Here, only the situation relevant for $pp/p\bar{p} \rightarrow VV + \text{jet} + X$ with only one outgoing parton in the LO process is discussed. Since the processes are calculated at NLO QCD, only one additional soft and/or collinear parton has to be considered at this order of perturbation theory.

Jet observables are obtained by introducing so-called jet functions $F_{\text{jet}}^{(m)}$ into the general definition of the partonic cross section on an m -particle phase space,

$$d\sigma_{ab}(p_a, p_b) = d\Phi^{(m)}(p_a, p_b) F_{\text{jet}}^{(m)}(p_a, p_b; \dots) \overline{|\mathcal{M}_{ab}^{(m)}(p_a, p_b; \dots)|^2}, \quad (5.1)$$

where $d\Phi^{(m)}$ denotes the m -particle phase space including flux factors, as defined in more detail in Chapter 7, and $\mathcal{M}_{ab}^{(m)}$ is the matrix element of the considered subprocess. The jet functions in general contain the realization of experimental cuts in terms of θ -functions.

The finiteness of the LO cross section is guaranteed by the condition

$$F_{\text{jet}}^{(m)}(p_a, p_b; \dots, p_i) \rightarrow 0, \text{ if } p_i \cdot p_a \rightarrow 0 \text{ or } p_i \cdot p_b \rightarrow 0, \quad (5.2)$$

where the upper index gives the number of final-state particles in the LO process. The dots stand for the remaining $(m - 1)$ non-QCD particles. These particles, which are massive gauge bosons in the discussed process class, do not affect the structure of QCD singularities. The jet function in Eq. (5.2) is realized in the gauge-boson pair production processes by the requirement of a minimal transverse momentum of the outgoing parton.

The jet function applied for the real-emission subprocesses contributing at NLO QCD, which contain one additional QCD parton in the final state, has to guarantee the soft and collinear safety of the jet observable. This implies the property $F_{\text{jet}}^{(m+1)} \rightarrow F_{\text{jet}}^{(m)}$ for any kinematically degenerate configurations, i.e. soft and collinear limits, namely

$$F_{\text{jet}}^{(m+1)}(p_a, p_b; \dots, p_i, p_j = \lambda q) \rightarrow F_{\text{jet}}^{(m)}(p_a, p_b; \dots, p_i) \quad \text{if } \lambda \rightarrow 0, \quad (5.3)$$

$$F_{\text{jet}}^{(m+1)}(p_a, p_b; \dots, p_i, p_j) \rightarrow F_{\text{jet}}^{(m)}(p_a, p_b; \dots, p_{ij}) \quad \text{if } p_i \rightarrow z p_{ij}, p_j \rightarrow (1 - z) p_{ij}, \quad (5.4)$$

where q stands for an arbitrary light-like momentum and z is a real number. Eq. (5.3) also must hold, of course, if the roles of the partons i and j are interchanged. In the limits $z \rightarrow 0, 1$ soft and collinear regions overlap. These features of the jet functions are in general realized by application of a jet algorithm; in this thesis, the successive combination jet algorithm described in Ref. [77] is applied.

Moreover, the jet functions with the properties of Eqs. (5.2) – (5.4) fulfill the property of factorizability of initial-state collinear singularities, which implies

$$F_{\text{jet}}^{(m+1)}(p_a, p_b; \dots, p_i, p_j) \rightarrow F_{\text{jet}}^{(m)}(x p_a, p_b; \dots, p_j) \quad \text{if } p_i \rightarrow (1 - x) p_a, \quad (5.5)$$

and the same for interchanged roles of the final-state partons i and j and/or the initial-state partons a and b , respectively.

5.1.2 Definition of NLO QCD cross sections

Using the jet-function definition given in the previous subsection, finite cross sections can be defined at LO and at NLO QCD.

The LO cross section is defined by

$$\sigma_{\text{pp/pp}}^{\text{LO}}(p_1, p_2) = \sum_{a,b} \int_0^1 dx_1 \int_0^1 dx_2 f_{a(\text{p})}^{\text{LO}}(x_1, \mu_{\text{fact}}) f_{b(\text{p/p})}^{\text{LO}}(x_2, \mu_{\text{fact}}) \hat{\sigma}_{ab}^{\text{LO}}(x_1 p_1, x_2 p_2), \quad (5.6)$$

where the PDFs of the partons a and b in the respective hadrons are denoted by f . The upper index ‘LO’ prescribes that LO fits for the respective PDFs are to be used. All QCD partons contained in each incoming hadron are summed over. The partonic momentum fractions with respect to the hadrons, which are named x_1 and x_2 , are integrated over. The label $\hat{\sigma}_{ab}^{\text{LO}}$ stands for the partonic LO cross section with the incoming partons a and b , which is defined as follows,

$$\hat{\sigma}_{ab}^{\text{LO}}(p_a, p_b) = \int_m d\hat{\sigma}_{ab}^B(p_a, p_b). \quad (5.7)$$

The summation over all configurations with m final-state partons contributing to the observed process class is contained in the definition of the tree-level cross section,

$$d\hat{\sigma}_{ab}^B(p_a, p_b) = \sum_{\{m\}} d\Phi^{(m)}(p_a, p_b) F_{\text{jet}}^{(m)}(p_a, p_b; \dots, p_i) \times \overline{|\mathcal{M}_{ab}^{(m)}(p_a, p_b; \dots, p_i)|^2} . \quad (5.8)$$

In general, dimensional regularization is used for treating the divergences showing up in the NLO QCD calculations. Therefore, the definition in Eq. (5.8) and the following ones are understood as defined in $D = 4 - 2\varepsilon$ dimensions with a D -dimensional phase space. The generic derivations needed for the calculation of NLO QCD cross sections via dipole subtraction formalism are presented in great detail in Ref. [62] and shall not be repeated here. As demonstrated in the given reference, all tree-level matrix elements can—which is a huge advantage of this approach—be evaluated in four dimensions, whereas the D -dimensional definition is, of course, needed for the analytical integration of the dipole terms. Using the formulae derived in Ref. [62], the remaining situation where explicit calculations have to be performed in D space–time dimensions is the evaluation of loop integrals, which will be referred to in Section 5.3 when the virtual corrections are discussed. However, since the partonic cross section in Eq. (5.8) is finite in four dimensions, the limit $\varepsilon \rightarrow 0$ can be simply performed in the LO case.

The hadronic cross section at NLO QCD accuracy is defined in an analogous way, namely by

$$\begin{aligned} \sigma_{\text{pp/pp}}^{\text{NLO}}(p_1, p_2) &= \sum_{a,b} \int_0^1 dx_1 \int_0^1 dx_2 f_{a(\text{p})}^{\text{NLO}}(x_1, \mu_{\text{fact}}) f_{b(\text{p/p})}^{\text{NLO}}(x_2, \mu_{\text{fact}}) \\ &\quad \times (\hat{\sigma}_{ab}^{\text{LO}}(x_1 p_1, x_2 p_2) + \hat{\sigma}_{ab}^{\text{NLO}}(x_1 p_1, x_2 p_2, \mu_{\text{fact}})) , \end{aligned} \quad (5.9)$$

where NLO PDFs are to be used. The partonic NLO cross section receives three different contributions,

$$\hat{\sigma}_{ab}^{\text{NLO}}(p_a, p_b; \mu_{\text{fact}}) = \int_{m+1} d\hat{\sigma}_{ab}^{\text{R}}(p_a, p_b) + \int_m d\hat{\sigma}_{ab}^{\text{V}}(p_a, p_b) + \int_m d\hat{\sigma}_{ab}^{\text{C}}(p_a, p_b) . \quad (5.10)$$

The upper index 'R' labels the real corrections containing one further QCD parton in the final state. Its emission leads to soft or collinear singularities with respect to initial- and final-state partons. The soft singularities and those arising from collinear final-state particles cancel against analogous divergences appearing in the loop integrals of the virtual corrections, labelled by the index 'V', which is guaranteed by factorization theorems [60, 74]. The remaining collinear initial-state singularities are independent of the specific process considered and can therefore be absorbed into the description of the incoming hadron leading to collinear-subtraction counterterms, which are marked by the label 'C'. The whole NLO cross section is finite, but the separate parts are not, due to the cancellations of singularities taking place between them. These cancellations cannot simply be performed numerically, because the different contributions do not live on the same phase

spaces. Therefore, a D -dimensional description is used to regularize the singularities. The respective parts of Eq. (5.10) are

$$d\hat{\sigma}_{ab}^R(p_a, p_b) = \sum_{\{m+1\}} d\Phi^{(m+1)}(p_a, p_b) F_{\text{jet}}^{(m+1)}(p_a, p_b; \dots, p_i, p_j) \overline{|\mathcal{M}_{ab}^{(m+1)}(p_a, p_b; \dots, p_i, p_j)|^2}, \quad (5.11)$$

$$d\hat{\sigma}_{ab}^V(p_a, p_b) = \sum_{\{m\}} d\Phi^{(m)}(p_a, p_b) F_{\text{jet}}^{(m)}(p_a, p_b; \dots, p_i) \overline{\mathcal{M}_{ab,1\text{-loop}}^{(m)}(p_a, p_b; \dots, p_i)}^2, \quad (5.12)$$

$$\begin{aligned} d\hat{\sigma}_{ab}^C(p_a, p_b) = & -\frac{\alpha_s}{2\pi} \frac{1}{\Gamma(1-\varepsilon)} \sum_{a'} \int_0^1 dz_1 \left(-\frac{1}{\varepsilon} \left(\frac{4\pi\mu^2}{\mu_{\text{fact}}^2} \right)^\varepsilon P^{aa'}(z_1) \right) d\hat{\sigma}_{a'b}^B(z_1 p_a, p_b) \\ & -\frac{\alpha_s}{2\pi} \frac{1}{\Gamma(1-\varepsilon)} \sum_{b'} \int_0^1 dz_2 \left(-\frac{1}{\varepsilon} \left(\frac{4\pi\mu^2}{\mu_{\text{fact}}^2} \right)^\varepsilon P^{bb'}(z_2) \right) d\hat{\sigma}_{ab'}^B(p_a, z_2 p_b), \end{aligned} \quad (5.13)$$

which leads to divergent contributions if the four-dimensional limit is taken. The basic idea of the dipole subtraction formalism is now to add and subtract so-called dipole terms to the cross section, which are defined in D dimensions on the $(m+1)$ -parton phase space in such a way that, on the one hand, all infrared singularities of the real corrections are cancelled. On the other hand, these dipoles can be integrated analytically over the one-parton phase spaces leading to divergences showing up as poles $\frac{1}{\varepsilon}$ and $\frac{1}{\varepsilon^2}$. The resulting expressions can be re-added to the other contributions cancelling the singularities there. How the contributions from the integrated dipole terms are distributed between virtual corrections and collinear-subtraction counterterms can be found in the detailed description of Ref. [62].

In case of VV+jet production where only one outgoing parton is present in the LO subprocesses, the upper limit of contributing dipoles is ten for each real-correction subprocess, namely

$$\begin{aligned} d\hat{\sigma}_{ab}^A(p_a, p_b) = & \sum_{\{m+1\}} d\Phi^{(m+1)}(p_a, p_b) \\ & \times \left\{ F_{\text{jet}}^{(m)}(\tilde{p}_a, p_b; \dots, \tilde{p}_{ij}) \mathcal{D}_a^{ij} + F_{\text{jet}}^{(m)}(p_a, \tilde{p}_b; \dots, \tilde{p}_{ij}) \mathcal{D}_b^{ij} \right. \\ & + F_{\text{jet}}^{(m)}(\tilde{p}_{ai}, p_b; \dots, \tilde{p}_j) \mathcal{D}_{ai}^j + F_{\text{jet}}^{(m)}(p_a, \tilde{p}_{bi}; \dots, \tilde{p}_j) \mathcal{D}_{bi}^j \\ & + F_{\text{jet}}^{(m)}(\tilde{p}_{aj}, p_b; \dots, \tilde{p}_i) \mathcal{D}_{aj}^i + F_{\text{jet}}^{(m)}(p_a, \tilde{p}_{bj}; \dots, \tilde{p}_i) \mathcal{D}_{bj}^i \\ & + F_{\text{jet}}^{(m)}(\tilde{p}_{ai}, p_b; \dots, \tilde{p}_j) \mathcal{D}_{ai,b} + F_{\text{jet}}^{(m)}(p_a, \tilde{p}_{bi}; \dots, \tilde{p}_j) \mathcal{D}_{bi,a} \\ & \left. + F_{\text{jet}}^{(m)}(\tilde{p}_{aj}, p_b; \dots, \tilde{p}_i) \mathcal{D}_{aj,b} + F_{\text{jet}}^{(m)}(p_a, \tilde{p}_{bj}; \dots, \tilde{p}_i) \mathcal{D}_{bj,a} \right\}, \end{aligned} \quad (5.14)$$

where the arguments of all dipoles are

$$\mathcal{D}^{\dots} = \mathcal{D}^{\dots}(p_a, p_b; \dots, p_i, p_j). \quad (5.15)$$

Concrete definitions of these dipoles will be given in Section 5.2. That section also contains a summary of all non-vanishing dipoles contributing to the real-emission subprocesses of the four gauge-boson-pair assignments in $pp/p\bar{p} \rightarrow VV + \text{jet} + X$.

With the dipole terms subtracted from the real corrections and re-added in the integrated form partially to the virtual corrections and to the collinear-subtraction counterterm, the NLO cross section can again be written as a sum of three contributions, which are separately finite now in contrast to Eq. (5.10) if the four-dimensional limit is taken,

$$\hat{\sigma}_{ab}^{\text{NLO}}(p_a, p_b; \mu_{\text{fact}}) = \hat{\sigma}_{ab}^{R-A}(p_a, p_b) + \hat{\sigma}_{ab}^{V+A}(p_a, p_b) + \hat{\sigma}_{ab}^{C+A}(p_a, p_b) . \quad (5.16)$$

The first term labelled by ‘R – A’ contains the real corrections and the unintegrated dipole terms. Since the D -dimensional definitions only lead to terms of $\mathcal{O}(\varepsilon)$ in both parts, the limit $\varepsilon \rightarrow 0$ can be performed separately,

$$\begin{aligned} \hat{\sigma}_{ab}^{R-A}(p_a, p_b) &= \int_{m+1} \left[d\hat{\sigma}_{ab}^R(p_a, p_b) \Big|_{\varepsilon=0} - d\hat{\sigma}_{ab}^A(p_a, p_b) \Big|_{\varepsilon=0} \right] \\ &= \sum_{m+1} d\Phi^{(m+1)}(p_a, p_b) \left\{ F_{\text{jet}}^{(m+1)}(p_a, p_b; \dots, p_i, p_j) \overline{|\mathcal{M}_{ab}^{(m+1)}(p_a, p_b; \dots, p_i, p_j)|^2} \right. \\ &\quad \left. - \sum_{\text{dipoles}} (\mathcal{D} \cdot F^{(m)})(p_a, p_b; \dots, p_i, p_j) \right\} , \end{aligned} \quad (5.17)$$

where the shorthand in the last line stands for the expression in curly brackets of Eq. (5.14). The distribution of the integrated dipoles between virtual corrections and collinear-subtraction counterterm is indicated symbolically by $d\hat{\sigma}^A = d\hat{\sigma}^{Av} + d\hat{\sigma}^{Ac}$.

The term labelled by ‘V + A’ contains the virtual corrections and those parts of the integrated subtraction terms with LO kinematics. Since the poles $\frac{1}{\varepsilon}$ and $\frac{1}{\varepsilon^2}$ cancel between the two contributions, they have to be combined before the limit $\varepsilon \rightarrow 0$ is performed,

$$\hat{\sigma}_{ab}^{V+A}(p_a, p_b) = \int_m \left[d\hat{\sigma}_{ab}^V(p_a, p_b) + \int_1 d\hat{\sigma}_{ab}^{Av}(p_a, p_b) \right] \Big|_{\varepsilon=0} . \quad (5.18)$$

Details on the calculation of the virtual corrections and the contribution $d\hat{\sigma}_{ab}^{Av}(p_a, p_b)$ will be given in Section 5.3.

The remaining contribution with the label ‘C + A’ contains the collinear-subtraction counterterm and the remaining collinear singularities related to initial-state partons. Here, the integration over the one-parton phase space is not fully performed analytically, but only up to a momentum fraction of the incoming parton, which is in analogy to the definitions of the collinear-subtraction counterterm in Eq. (5.13). Since the singularities arising in terms of poles $\frac{1}{\varepsilon}$ are process-independent and cancel between the two contributions, the matrix elements of the specific subprocesses factorize and can be evaluated in four dimensions. Details on this part of the cross section, which can symbolically be written as

$$\hat{\sigma}_{ab}^{C+A}(p_a, p_b) = \int_m \left[d\hat{\sigma}_{ab}^C(p_a, p_b) + \int_1 d\hat{\sigma}_{ab}^{Ac}(p_a, p_b) \right] \Big|_{\varepsilon=0} , \quad (5.19)$$

will be given in Section 5.4.

5.2 Real-correction contributions

The real-emission subprocesses, whose matrix elements are calculated in the previous chapter, in general contain both soft and collinear singularities in phase-space regions where one of the outgoing partons has low momentum or is collinear to another initial- or final-state parton. If the process class $pp/p\bar{p} \rightarrow VV + 2\text{jets} + X$ is considered, the respective regions are cut away via phase-space constraints. This is justified from an experimental point of view, because neither partons with very low momentum nor such ones with momenta nearly parallel to other partons can be resolved in the detector. However, when considering the process class $pp/p\bar{p} \rightarrow VV + \text{jet} + X$, exactly these phase-space regions with only one resolvable jet are relevant, because their signature is just that of $VV + \text{jet}$ production, and their order in perturbation theory is that of the virtual corrections. Moreover, virtual and real corrections are each individually infrared divergent. Apart from process-independent divergences that can be absorbed into the PDFs of the incoming partons, the Kinoshita–Lee–Nauenberg theorem [75, 76] states that these singularities completely cancel for sufficiently inclusive quantities. As described in the previous section, a rearrangement of the infrared singularities is performed by application of the dipole subtraction formalism [62]. As shown there, the calculation of both real-correction matrix elements and dipole terms, which are discussed in this section, can be calculated in four dimensions.

5.2.1 Relevant dipole factorization formulae

All dipole factorization formulae used in this thesis are defined in Ref. [62]. Since only four external QCD partons are involved in the process class $pp/p\bar{p} \rightarrow VV + \text{jet} + X$, three different kinds of subtraction terms are relevant for the present calculation. A brief overview of these situations, namely that of final-state singularities with initial-state spectators and those of initial-state singularities with final- or initial-state spectators, is presented in the following paragraphs.

Final-state singularities with initial-state spectator

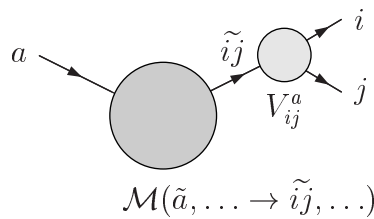


Figure 5.1: Effective diagram for the dipole formulae treating final-state singularities with initial-state spectators: The big circle stands for the LO matrix element—with all remaining external particles that do not contribute to the singularity omitted in the illustration, but indicated by dots in the labelling—, and the small one for the process-independent dipole. The emitter parton is labelled by (ij) and the spectator parton by a .

In case of final-state singularities, only initial-state spectators appear in the observed process class $pp/p\bar{p} \rightarrow VV + \text{jet} + X$, since there are no further final-state QCD partons. With the labelling of Figure 5.1, the momenta in the deformed subtraction-term phase space are defined as

$$\tilde{p}_a^\mu = x_{ij,a} p_a^\mu, \quad \tilde{p}_{ij}^\mu = p_i^\mu + p_j^\mu - (1 - x_{ij,a}) p_a^\mu, \quad x_{ij,a} = \frac{p_i p_a + p_j p_a - p_i p_j}{(p_i + p_j) p_a}, \quad (5.20)$$

while the remaining momenta remain unchanged. The redefinition of the momentum of the spectator parton is needed in order to guarantee both momentum conservation and the on-shellness of the emitter parton (ij). The evaluation of the LO amplitudes is performed with these deformed momenta of emitter and spectator partons in the whole section.

The dipole terms are given by

$$\begin{aligned} & \mathcal{D}_{ij}^a(a[p_a], b[p_b] \rightarrow V_1[k_1], V_2[k_2], i[p_i], j[p_j]) \\ &= -\frac{1}{2p_i \cdot p_j} \frac{1}{x_{ij,a}} \times \frac{f_{\text{sym}}}{N_{c_a} N_{\sigma_a} N_{c_b} N_{\sigma_b}} \sum_{\sigma_a, \sigma_b, \sigma_{ij}, \sigma_1, \sigma_2} \sum_{\sigma'_{ij}} \sum_{c_a, c_b, c_{ij}} \sum_{c'_a, c'_b, c'_{ij}} \\ & \quad \mathcal{M}^* \left(\tilde{a} \left[\begin{smallmatrix} c'_a \\ \tilde{p}_a \\ \sigma_a \end{smallmatrix} \right] b \left[\begin{smallmatrix} c'_b \\ p_b \\ \sigma_b \end{smallmatrix} \right] \rightarrow V_1 \left[\begin{smallmatrix} k_1 \\ \sigma_1 \end{smallmatrix} \right] V_2 \left[\begin{smallmatrix} k_2 \\ \sigma_2 \end{smallmatrix} \right] \tilde{ij} \left[\begin{smallmatrix} c'_{ij} \\ \tilde{p}_{ij} \\ \sigma'_{ij} \end{smallmatrix} \right] \right) \frac{(\mathbf{T}_a)_{c'_a c_a}^d (\mathbf{T}_{ij})_{c'_{ij} c_{ij}}^d}{\mathbf{T}_{ij}^2} \delta_{c'_b c_b} \\ & \quad \times \langle \sigma'_{ij} | \mathbf{V}_{ij}^a(\tilde{z}_i; x_{ij,a}) | \sigma_{ij} \rangle \mathcal{M} \left(\tilde{a} \left[\begin{smallmatrix} c_a \\ \tilde{p}_a \\ \sigma_a \end{smallmatrix} \right] b \left[\begin{smallmatrix} c_b \\ p_b \\ \sigma_b \end{smallmatrix} \right] \rightarrow V_1 \left[\begin{smallmatrix} k_1 \\ \sigma_1 \end{smallmatrix} \right] V_2 \left[\begin{smallmatrix} k_2 \\ \sigma_2 \end{smallmatrix} \right] \tilde{ij} \left[\begin{smallmatrix} c_{ij} \\ \tilde{p}_{ij} \\ \sigma_{ij} \end{smallmatrix} \right] \right) \\ & \equiv -\frac{1}{2p_i \cdot p_j} \frac{1}{x_{ij,a}} \left[\mathcal{M}^* \frac{\mathbf{T}_a \cdot \mathbf{T}_{ij}}{\mathbf{T}_{ij}^2} \mathbf{V}_{ij}^a \mathcal{M} \right] (\tilde{a}, b \rightarrow V_1, V_2, \tilde{ij}), \end{aligned} \quad (5.21)$$

where a, b, i, j denote any possible QCD partons, N_c and N_σ the averaging factors for colours and spins of initial-state particles, and f_{sym} the symmetry factor from identical outgoing particles in the real-correction subprocess. The last line introduces an abbreviation where the particle momenta, their colour and spin indices as well as sums including all additional factors are omitted. They are understood as automatically included if the short notation is used. A tilde set over a particle name means that the deformed momentum with a tilde has to be used in the evaluation of the amplitude. The definitions of the colour charge operators \mathbf{T} are collected in App. A.1. The splitting kernels \mathbf{V}_{ij}^a containing all final-state singularities are constructed in $D = 4 - 2\varepsilon$ dimensions. In the present calculation of the subtraction terms, where the integration over the dipole phase space is performed numerically, only their four-dimensional limit ($\varepsilon \rightarrow 0$) is needed, namely

$$\langle \sigma' | \mathbf{V}_{q_i g_j}^a(\tilde{z}_i; x_{ij,a}) | \sigma \rangle = 8\pi\alpha_s C_F \left[\frac{2}{1 - \tilde{z}_i + (1 - x_{ij,a})} - (1 + \tilde{z}_i) \right] \delta_{\sigma\sigma'}, \quad (5.22)$$

$$\begin{aligned} \langle \mu' | \mathbf{V}_{g_i g_j}^a(\tilde{z}_i; x_{ij,a}) | \mu \rangle &= 16\pi\alpha_s C_A \left[\frac{1}{p_i p_j} (\tilde{z}_i p_i^\mu - \tilde{z}_j p_j^\mu) (\tilde{z}_i p_i^{\mu'} - \tilde{z}_j p_j^{\mu'}) \right. \\ & \quad \left. - g^{\mu\mu'} \left(\frac{1}{1 - \tilde{z}_i + (1 - x_{ij,a})} + \frac{1}{1 - \tilde{z}_j + (1 - x_{ij,a})} - 2 \right) \right], \end{aligned} \quad (5.23)$$

$$\langle \mu' | \mathbf{V}_{q_i \bar{q}_j}^a(\tilde{z}_i; x_{ij,a}) | \mu \rangle = 8\pi\alpha_s T_R \left[-\frac{2}{p_i p_j} (\tilde{z}_i p_i^\mu - \tilde{z}_j p_j^\mu) (\tilde{z}_i p_i^{\mu'} - \tilde{z}_j p_j^{\mu'}) - g^{\mu\mu'} \right], \quad (5.24)$$

where

$$\tilde{z}_i = \frac{p_i p_a}{p_i p_a + p_j p_a} = \frac{p_i \tilde{p}_a}{\tilde{p}_{ij} \tilde{p}_a}, \quad \tilde{z}_j = \frac{p_j p_a}{p_i p_a + p_j p_a} = \frac{p_j \tilde{p}_a}{\tilde{p}_{ij} \tilde{p}_a}, \quad \tilde{z}_i + \tilde{z}_j = 1. \quad (5.25)$$

In Eq. (5.22), σ and σ' label the helicity of the emitter (anti-)quark (ij) that splits into the (anti-)quark i and the gluon j in the LO amplitude and its complex conjugate, respectively. In Eqs. (5.23) and (5.24), μ and μ' label the polarization vector of the emitter gluon (ij), i.e. the LO amplitude is understood as

$$\mathbb{M}(\lambda) = \mathcal{M}_\mu \varepsilon^{*\mu}(\lambda), \quad (5.26)$$

where $\varepsilon^{*\mu}(\lambda)$ is the polarization vector of the emitter gluon. In the calculation of the dipoles from the LO amplitudes, the product $\varepsilon^{*\mu}(\lambda) \varepsilon^{\mu'}(\lambda')$, which is split off the amplitude and its complex conjugate, is replaced by the expressions of Eqs. (5.23) and (5.24), respectively. However, the vector-valued amplitudes \mathcal{M}_μ do not have to be evaluated explicitly, but the resulting dipole can be expressed from the known helicity amplitudes via application of the polarization sum

$$\sum_{\lambda=+,-} \varepsilon^{*\mu}(k, \lambda) \varepsilon^{\mu'}(k, \lambda) = -g^{\mu\mu'} - \frac{k^\mu k^{\mu'} n^2}{(kn)^2} + \frac{n^\mu k^{\mu'} + n^{\mu'} k^\mu}{kn}, \quad (5.27)$$

where n is an arbitrary vector with $kn \neq 0$.

Using this identity, the term proportional to $-g^{\mu\mu'}$ can be written as

$$\begin{aligned} \mathcal{M}_\mu^*(-g^{\mu\mu'}) \mathcal{M}_{\mu'} &= \mathcal{M}_\mu^* \mathcal{M}_{\mu'} \left(\sum_{\lambda=+,-} \varepsilon^\mu(\tilde{p}_{ij}, \lambda) \varepsilon^{*\mu'}(\tilde{p}_{ij}, \lambda) + \frac{\tilde{p}_{ij}^\mu \tilde{p}_{ij}^{\mu'}}{(\tilde{p}_{ij} n)^2} - \frac{n^\mu \tilde{p}_{ij}^{\mu'} + n^{\mu'} \tilde{p}_{ij}^\mu}{\tilde{p}_{ij} n} \right) \\ &= \sum_{\lambda=+,-} \mathcal{M}_\mu^* \varepsilon^\mu(\tilde{p}_{ij}, \lambda) \mathcal{M}_{\mu'} \varepsilon^{*\mu'}(\tilde{p}_{ij}, \lambda) \\ &= \sum_{\lambda=+,-} |\mathcal{M}(\lambda)|^2, \end{aligned} \quad (5.28)$$

where \tilde{p}_{ij} is the momentum and λ the polarization of the emitter gluon, while the remaining arguments of the amplitude are suppressed. In the second equation, gauge invariance is used to eliminate all terms but those proportional to the polarisation vectors by the Ward identity

$$\mathcal{M}_\mu^{(*)} \tilde{p}_{ij}^\mu = 0. \quad (5.29)$$

The terms in Eqs. (5.23) and (5.24) that are not proportional to $g^{\mu\mu'}$ can also be expressed in terms of LO amplitudes: Inserting the four-dimensional metric tensor into the expressions

that are not proportional to $g^{\mu\mu'}$ and replacing it by means of the polarization sum from Eq. (5.27) gives

$$\begin{aligned}
& \mathcal{M}_\mu^*(\tilde{z}_i p_i^\mu - \tilde{z}_j p_j^\mu)(\tilde{z}_i p_i^{\mu'} - \tilde{z}_j p_j^{\mu'}) \mathcal{M}_{\mu'} \\
&= \mathcal{M}_\mu^* \left(\sum_{\lambda=+,-} \varepsilon^\mu(\tilde{p}_{ij}, \lambda) \varepsilon^{*\nu}(\tilde{p}_{ij}, \lambda) + \frac{\tilde{p}_{ij}^\mu \tilde{p}_{ij}^\nu}{(\tilde{p}_{ij} n)^2} - \frac{n^\mu \tilde{p}_{ij}^\nu + n^\nu \tilde{p}_{ij}^\mu}{\tilde{p}_{ij} n} \right) (\tilde{z}_i p_{i\nu} - \tilde{z}_j p_{j\nu}) \\
&\quad \times \mathcal{M}_{\mu'} \left(\sum_{\lambda'=+,-} \varepsilon^{*\mu'}(\tilde{p}_{ij}, \lambda') \varepsilon^{\nu'}(\tilde{p}_{ij}, \lambda') + \frac{\tilde{p}_{ij}^{\mu'} \tilde{p}_{ij}^{\nu'}}{(\tilde{p}_{ij} n)^2} - \frac{n^{\mu'} \tilde{p}_{ij}^{\nu'} + n^{\nu'} \tilde{p}_{ij}^{\mu'}}{\tilde{p}_{ij} n} \right) (\tilde{z}_i p_{i\nu'} - \tilde{z}_j p_{j\nu'}) \\
&= \sum_{\lambda=+,-} \mathcal{M}_\mu^* \varepsilon^\mu(\tilde{p}_{ij}, \lambda) (\tilde{z}_i p_{i\nu} - \tilde{z}_j p_{j\nu}) \varepsilon^{*\nu}(\tilde{p}_{ij}, \lambda) \\
&\quad \times \sum_{\lambda'=+,-} \mathcal{M}_{\mu'} \varepsilon^{*\mu'}(\tilde{p}_{ij}, \lambda') (\tilde{z}_i p_{i\nu'} - \tilde{z}_j p_{j\nu'}) \varepsilon^{\nu'}(\tilde{p}_{ij}, \lambda') \\
&= \sum_{\lambda=+,-} |\mathcal{M}(\lambda)|^2 |\varepsilon(\tilde{p}_{ij}, \lambda) \cdot (\tilde{z}_i p_i - \tilde{z}_j p_j)|^2 \\
&\quad + 2 \operatorname{Re} \left\{ \mathcal{M}^*(+) \mathcal{M}(-) [\varepsilon^*(\tilde{p}_{ij}, +) \cdot (\tilde{z}_i p_i - \tilde{z}_j p_j)] [\varepsilon(\tilde{p}_{ij}, -) \cdot (\tilde{z}_i p_i - \tilde{z}_j p_j)] \right\}. \quad (5.30)
\end{aligned}$$

Besides the Ward identity (5.29), the orthogonality relation

$$(\tilde{z}_i p_{i\mu} - \tilde{z}_j p_{j\mu}) \tilde{p}_{ij}^\mu = 0, \quad (5.31)$$

which follows from the construction of \tilde{p}_{ij} , is used in the second line of Eq. (5.30). Thus, only helicity amplitudes are needed, but their phase conventions must be known.

Initial-state singularities with final-state spectator

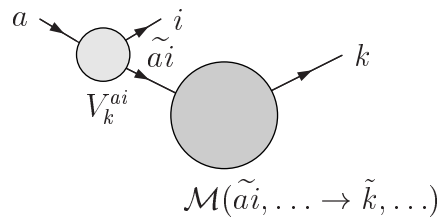


Figure 5.2: Effective diagram for the dipole formulae treating initial-state singularities with final-state spectators: The big circle stands for the LO matrix element, the small one for the process-independent dipole. The label (ai) stands for the emitter and k for the spectator parton. The remaining external particles are not explicitly shown, but indicated by dots in the labelling.

In case of initial-state singularities, both final-state and initial-state spectators appear in the process class $pp/p\bar{p} \rightarrow VV + \text{jet} + X$. In this paragraph the formulae for the case

of a final-state spectator are discussed. With the labelling of Figure 5.2 the momenta in the deformed subtraction-term phase space are defined as

$$\tilde{p}_{ai}^\mu = x_{ik,a} p_a^\mu, \quad \tilde{p}_k^\mu = p_k^\mu + p_i^\mu - (1 - x_{ik,a}) p_a^\mu, \quad x_{ik,a} = \frac{p_k p_a + p_i p_a - p_i p_k}{(p_k + p_i) p_a}, \quad (5.32)$$

with the remaining momenta unchanged. As in the situation discussed before, both momentum conservation and the on-shell relation for emitter and spectator are guaranteed by these momentum definitions. While the momentum of the emitter parton $p_{\tilde{ai}}$ is parallel to p_a , the momentum of the spectator parton \tilde{p}_k is not parallel to p_k in general. All LO amplitudes in this section are evaluated with these deformed momenta.

The dipole terms are given by

$$\begin{aligned} \mathcal{D}_k^{ai}(a[p_a], b[p_b] \rightarrow V_1[k_1], V_2[k_2], i[p_i], k[p_k]) \\ = -\frac{1}{2p_a \cdot p_i} \frac{1}{x_{ik,a}} \times \frac{f_{\text{sym}}}{N_{c_{ai}} N_{\sigma_{ai}} N_{c_b} N_{\sigma_b}} \sum_{\sigma_{ai}, \sigma_b, \sigma_k, \sigma_1, \sigma_2} \sum_{\sigma'_{ai}} \sum_{c_{ai}, c_b, c_k} \sum_{c'_{ai}, c'_b, c'_k} \\ \mathcal{M}^* \left(\tilde{\text{ai}} \left[\begin{smallmatrix} c'_{ai} \\ \tilde{p}_{ai} \\ \sigma'_{ai} \end{smallmatrix} \right] \text{b} \left[\begin{smallmatrix} c'_b \\ p_b \\ \sigma_b \end{smallmatrix} \right] \rightarrow V_1 \left[\begin{smallmatrix} k_1 \\ \sigma_1 \end{smallmatrix} \right] V_2 \left[\begin{smallmatrix} k_2 \\ \sigma_2 \end{smallmatrix} \right] \tilde{\text{k}} \left[\begin{smallmatrix} c'_k \\ \tilde{p}_k \\ \sigma_k \end{smallmatrix} \right] \right) \frac{(\mathbf{T}_{ai})_{c'_{ai} c_{ai}}^d (\mathbf{T}_k)_{c'_k c_k}^d}{\mathbf{T}_{ai}^2} \delta_{c'_b c_b} \\ \times \langle \sigma'_{ai} | \mathbf{V}_k^{ai}(\tilde{u}_i; x_{ik,a}) | \sigma_{ai} \rangle \mathcal{M} \left(\tilde{\text{ai}} \left[\begin{smallmatrix} c_{ai} \\ \tilde{p}_{ai} \\ \sigma_{ai} \end{smallmatrix} \right] \text{b} \left[\begin{smallmatrix} c_b \\ p_b \\ \sigma_b \end{smallmatrix} \right] \rightarrow V_1 \left[\begin{smallmatrix} k_1 \\ \sigma_1 \end{smallmatrix} \right] V_2 \left[\begin{smallmatrix} k_2 \\ \sigma_2 \end{smallmatrix} \right] \tilde{\text{k}} \left[\begin{smallmatrix} c_k \\ p_k \\ \sigma_k \end{smallmatrix} \right] \right) \\ = -\frac{1}{2p_a \cdot p_i} \frac{1}{x_{ik,a}} \left[\mathcal{M}^* \frac{\mathbf{T}_k \cdot \mathbf{T}_{ai}}{\mathbf{T}_{ai}^2} \mathbf{V}_k^{ai} \mathcal{M} \right] (\tilde{ai}, b \rightarrow V_1, V_2, \tilde{k}), \end{aligned} \quad (5.33)$$

where a, b, k, i denote any possible QCD partons. The same abbreviation as in the previous paragraph is used in the amplitudes on the right-hand side, and the colour charge operators \mathbf{T} are given in Section A.1. The splitting kernels \mathbf{V}_k^{ai} describing the initial-state singularities are formulated in $D = 4 - 2\epsilon$ dimensions. Again, the four-dimensional limit of the formulae can be taken in the present calculation, which results in

$$\langle \sigma' | \mathbf{V}_k^{\text{qag}_i}(x_{ik,a}; u_i) | \sigma \rangle = 8\pi\alpha_s C_F \left[\frac{2}{1 - x_{ik,a} + u_i} - (1 + x_{ik,a}) \right] \delta_{\sigma\sigma'}, \quad (5.34)$$

$$\langle \sigma' | \mathbf{V}_k^{\text{ga}\bar{\text{q}}_i}(x_{ik,a}) | \sigma \rangle = 8\pi\alpha_s T_R [1 - 2x_{ik,a}(1 - x_{ik,a})] \delta_{\sigma\sigma'}, \quad (5.35)$$

$$\begin{aligned} \langle \mu' | \mathbf{V}_k^{\text{qag}_i}(x_{ik,a}; u_i) | \mu \rangle = 8\pi\alpha_s C_F \left[-g^{\mu\mu'} x_{ik,a} \right. \\ \left. + \frac{1 - x_{ik,a}}{x_{ik,a}} \frac{2u_i(1 - u_i)}{p_i p_k} \left(\frac{p_i^\mu}{u_i} - \frac{p_k^\mu}{1 - u_i} \right) \left(\frac{p_i^{\mu'}}{u_i} - \frac{p_k^{\mu'}}{1 - u_i} \right) \right], \end{aligned} \quad (5.36)$$

$$\begin{aligned} \langle \mu' | \mathbf{V}_k^{\text{ga}\bar{\text{q}}_i}(x_{ik,a}; u_i) | \mu \rangle = 16\pi\alpha_s C_A \left[-g^{\mu\mu'} \left(\frac{1}{1 - x_{ik,a} + u_i} - 1 + x_{ik,a}(1 - x_{ik,a}) \right) \right. \\ \left. + \frac{1 - x_{ik,a}}{x_{ik,a}} \frac{u_i(1 - u_i)}{p_i p_k} \left(\frac{p_i^\mu}{u_i} - \frac{p_k^\mu}{1 - u_i} \right) \left(\frac{p_i^{\mu'}}{u_i} - \frac{p_k^{\mu'}}{1 - u_i} \right) \right], \end{aligned} \quad (5.37)$$

where

$$u_i = \frac{p_i p_a}{p_i p_a + p_k p_a}. \quad (5.38)$$

In Eqs. (5.34) and (5.35), σ and σ' label the helicity of the emitter (anti-)quark (ai) in the LO amplitude and its complex conjugate, respectively. In Eqs. (5.36) and (5.37), μ and μ' label the polarization vector of the emitter gluon (ai). Since this gluon is an incoming particle in the LO amplitude, the amplitude is defined by contraction of the vector-valued amplitude with the polarization vector of the incoming gluon, $\varepsilon^\mu(\lambda)$, namely

$$\mathbb{M}(\lambda) = \mathcal{M}_\mu \varepsilon^\mu(\lambda) . \quad (5.39)$$

As in the previous section, the vector-valued amplitudes are understood as LO amplitudes with the polarization vector of the emitter gluon extracted. The vector-valued amplitudes can again be eliminated by application of the polarization sum (5.27), the Ward identity (5.29), and an orthogonality relation similar to the one in Eq. (5.31) that reads

$$\left(\frac{p_{i\mu}}{u_i} - \frac{p_{k\mu}}{1-u_i} \right) \tilde{p}_{ij}^\mu = 0 . \quad (5.40)$$

Explicitly, the terms proportional to $g^{\mu\mu'}$ can be written as

$$\mathcal{M}_\mu^*(-g^{\mu\mu'})\mathcal{M}_{\mu'} = \sum_{\lambda=+,-} |\mathcal{M}(\lambda)|^2 , \quad (5.41)$$

in the dipole term, the remaining parts that are not proportional to $g^{\mu\mu'}$ give

$$\begin{aligned} & \mathcal{M}_\mu^* \left(\frac{p_i^\mu}{u_i} - \frac{p_k^\mu}{1-u_i} \right) \left(\frac{p_i^{\mu'}}{u_i} - \frac{p_k^{\mu'}}{1-u_i} \right) \mathcal{M}_{\mu'} \\ &= \sum_{\lambda=+,-} |\mathcal{M}(\lambda)|^2 \left| \varepsilon(\tilde{p}_{ij}, \lambda) \cdot \left(\frac{p_i}{u_i} - \frac{p_k}{1-u_i} \right) \right|^2 \\ & \quad + 2 \operatorname{Re} \left\{ \mathcal{M}^*(+) \mathcal{M}(-) \left[\varepsilon(\tilde{p}_{ij}, +) \cdot \left(\frac{p_i}{u_i} - \frac{p_k}{1-u_i} \right) \right] \left[\varepsilon^*(\tilde{p}_{ij}, -) \cdot \left(\frac{p_i}{u_i} - \frac{p_k}{1-u_i} \right) \right] \right\} . \end{aligned} \quad (5.42)$$

Initial-state singularities with initial-state spectator

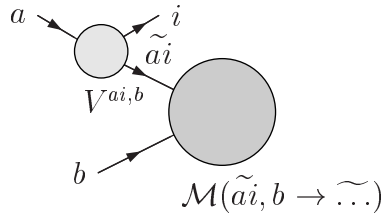


Figure 5.3: Effective diagram for the dipole formulae treating initial-state singularities with initial-state spectators: The big circle stands for the LO matrix element, the small one for the process-independent dipole. The emitter parton is labelled by (ai) and the spectator parton by b . The remaining outgoing particles are indicated by dots in the labelling.

The formulae for the case of initial-state singularities with an initial-state spectator, which is the remaining one needed for the real corrections of the process class $pp/p\bar{p} \rightarrow VV + \text{jet} + X$, are given in this paragraph. With the labelling of Figure 5.3, the momentum of the emitter parton in the deformed phase space is defined by

$$\tilde{p}_{ai}^\mu = x_{i,ab} p_a^\mu, \quad x_{i,ab} = \frac{p_a p_b + p_i p_a - p_i p_b}{p_a p_b}. \quad (5.43)$$

Differing from the two situations discussed before, the momentum of the incoming spectator parton is not deformed. Instead, the momenta of all outgoing particles—not only those of the QCD partons—are deformed in a way to guarantee both momentum conservation and on-shellness of all particles in the subtraction-term phase space. This deformation is described by a proper Lorentz transformation,

$$\begin{aligned} \tilde{k}_j^\mu &= \Lambda^\mu{}_\nu(K, \tilde{K}) k_j^\nu, \quad \Lambda^\mu{}_\nu(K, \tilde{K}) = g^\mu{}_\nu - \frac{2(K + \tilde{K})^\mu (K + \tilde{K})_\nu}{(K + \tilde{K})^2} + \frac{2\tilde{K}^\mu K_\nu}{K^2}, \\ K^\mu &= p_a^\mu + p_b^\mu - p_i^\mu, \quad \tilde{K}^\mu = \tilde{p}_{ai}^\mu + p_b^\mu. \end{aligned} \quad (5.44)$$

It is applied to all outgoing particles but the QCD parton i involved in the initial-state singularity.

The dipole terms are given by

$$\begin{aligned} &\mathcal{D}^{ai,b}(a[p_a], b[p_b] \rightarrow V_1[k_1], V_2[k_2], i[p_i], j[p_j]) \\ &= -\frac{1}{2p_a \cdot p_i} \frac{1}{x_{i,ab}} \times \frac{f_{\text{sym}}}{N_{c_{ai}} N_{\sigma_{ai}} N_{c_b} N_{\sigma_b}} \sum_{\sigma_{ai}, \sigma_b, \sigma_k, \sigma_1, \sigma_2} \sum_{\sigma'_{ai}} \sum_{c_{ai}, c_b, c_k} \sum_{c'_{ai}, c'_b, c'_k} \\ &\quad \mathcal{M}^* \left(\tilde{\text{ai}} \left[\begin{smallmatrix} c'_{ai} \\ \tilde{p}_{ai} \\ \sigma'_{ai} \end{smallmatrix} \right] \text{b} \left[\begin{smallmatrix} c'_b \\ p_b \\ \sigma_b \end{smallmatrix} \right] \rightarrow V_1 \left[\begin{smallmatrix} \tilde{k}_1 \\ \sigma_1 \end{smallmatrix} \right] V_2 \left[\begin{smallmatrix} \tilde{k}_2 \\ \sigma_2 \end{smallmatrix} \right] \text{k} \left[\begin{smallmatrix} c'_k \\ \tilde{p}_k \\ \sigma_k \end{smallmatrix} \right] \right) \frac{(\mathbf{T}_{ai})_{c'_{ai} c_{ai}}^d (\mathbf{T}_b)_{c'_b c_b}^d}{\mathbf{T}_{ai}^2} \delta_{c'_b c_b} \\ &\quad \times \langle \sigma'_{ai} | \mathbf{V}^{ai,b}(x_{i,ab}) | \sigma_{ai} \rangle \mathcal{M} \left(\tilde{\text{ai}} \left[\begin{smallmatrix} c_{ai} \\ \tilde{p}_{ai} \\ \sigma_{ai} \end{smallmatrix} \right] \text{b} \left[\begin{smallmatrix} c_b \\ p_b \\ \sigma_b \end{smallmatrix} \right] \rightarrow V_1 \left[\begin{smallmatrix} \tilde{k}_1 \\ \sigma_1 \end{smallmatrix} \right] V_2 \left[\begin{smallmatrix} \tilde{k}_2 \\ \sigma_2 \end{smallmatrix} \right] \tilde{\text{k}} \left[\begin{smallmatrix} c_k \\ \tilde{p}_k \\ \sigma_k \end{smallmatrix} \right] \right) \\ &= -\frac{1}{2p_a \cdot p_i} \frac{1}{x_{i,ab}} \left[\mathcal{M}^* \frac{\mathbf{T}_b \cdot \mathbf{T}_{ai}}{\mathbf{T}_{ai}^2} \mathbf{V}^{ai,b} \mathcal{M} \right] (\tilde{a}i, b \rightarrow \tilde{V}_1, \tilde{V}_2, j), \end{aligned} \quad (5.45)$$

where a, b, i, j stand for any possible QCD partons. The same abbreviations as in the previous paragraph are applied on the right-hand side of the equation, and all deformed momenta are marked by a tilde again. The colour charge operators \mathbf{T} are given in Section A.1. The splitting functions $\mathbf{V}^{ai,b}$ describing the initial-state singularities are presented after taking the four-dimensional limit of the $D = 4 - 2\varepsilon$ expressions, namely

$$\langle \sigma' | \mathbf{V}^{q_a g_i, b}(x_{i,ab}) | \sigma \rangle = 8\pi\alpha_s C_F \left[\frac{2}{1 - x_{i,ab}} - (1 + x_{i,ab}) \right] \delta_{\sigma\sigma'}, \quad (5.46)$$

$$\langle \sigma' | \mathbf{V}^{g_a \bar{q}_i, b}(x_{i,ab}) | \sigma \rangle = 8\pi\alpha_s T_R [1 - 2x_{i,ab}(1 - x_{i,ab})] \delta_{\sigma\sigma'}, \quad (5.47)$$

$$\begin{aligned} \langle \mu' | \mathbf{V}^{q_a \bar{q}_i, b}(x_{i,ab}) | \mu \rangle &= 8\pi\alpha_s C_F \left[-g^{\mu\mu'} x_{i,ab} \right. \\ &\quad \left. + \frac{1 - x_{i,ab}}{x_{i,ab}} \frac{2p_a \cdot p_b}{p_i \cdot p_a p_i \cdot p_b} \left(p_i^\mu - \frac{p_i p_a}{p_b p_a} p_b^\mu \right) \left(p_i^{\mu'} - \frac{p_i p_a}{p_b p_a} p_b^{\mu'} \right) \right], \end{aligned} \quad (5.48)$$

$$\begin{aligned} \langle \mu' | \mathbf{V}^{g_a g_i, b}(x_{i,ab}) | \mu \rangle = & 16\pi\alpha_s C_A \left[-g^{\mu\mu'} \left(\frac{x_{i,ab}}{1-x_{i,ab}} + x_{i,ab}(1-x_{i,ab}) \right) \right. \\ & \left. + \frac{1-x_{i,ab}}{x_{i,ab}} \frac{p_a \cdot p_b}{p_i \cdot p_a p_i \cdot p_b} \left(p_i^\mu - \frac{p_i p_a}{p_b p_a} p_b^\mu \right) \left(p_i^{\mu'} - \frac{p_i p_a}{p_b p_a} p_b^{\mu'} \right) \right]. \end{aligned} \quad (5.49)$$

In Eqs. (5.46) and (5.47), σ and σ' label the helicity of the emitter (anti-)quark (ai) in the LO amplitude and its complex conjugate, respectively. In Eqs. (5.48) and (5.49), μ and μ' label the polarization vector of the emitter gluon (ai). As in the previous paragraphs, the polarization vectors of emitter gluons are understood to be extracted from the LO amplitudes, and the resulting product of polarization vectors is replaced by the expressions in the respective splitting kernels. The remaining vector-valued amplitudes are defined in Eq. (5.39) for incoming gluon emitters. They can, however, be expressed in terms of the known LO amplitudes via application of the polarization sum (5.27), the Ward identity (5.29), and an orthogonality relation analogous to those in the previous cases,

$$\left(p_{i\mu} - \frac{p_i p_a}{p_b p_a} p_{b\mu} \right) \tilde{p}_{ij}^\mu = 0. \quad (5.50)$$

Explicitly, the terms proportional to $g^{\mu\mu'}$ yield

$$\mathcal{M}_\mu^*(-g^{\mu\mu'})\mathcal{M}_{\mu'} = \sum_{\lambda=+,-} |\mathcal{M}(\lambda)|^2 \quad (5.51)$$

in the dipole term. The expressions that are not proportional to $g^{\mu\mu'}$ read

$$\begin{aligned} & \mathcal{M}_\mu^* \left(p_i^\mu - \frac{p_i p_a}{p_b p_a} p_b^\mu \right) \left(p_i^{\mu'} - \frac{p_i p_a}{p_b p_a} p_b^{\mu'} \right) \mathcal{M}_{\mu'} \\ &= \sum_{\lambda=+,-} |\mathcal{M}(\lambda)|^2 \left| \varepsilon(\tilde{p}_{ij}, \lambda) \cdot \left(p_i - \frac{p_i p_a}{p_b p_a} p_b \right) \right|^2 \\ &+ 2 \operatorname{Re} \left\{ \mathcal{M}^*(+) \mathcal{M}(-) \left[\varepsilon(\tilde{p}_{ij}, +) \cdot \left(p_i - \frac{p_i p_a}{p_b p_a} p_b \right) \right] \left[\varepsilon^*(\tilde{p}_{ij}, -) \cdot \left(p_i - \frac{p_i p_a}{p_b p_a} p_b \right) \right] \right\}. \end{aligned} \quad (5.52)$$

5.2.2 Overview of the contributing subtraction counterterms

The diagrams shown in this paragraph give a representative set of real-emission diagrams in order to illustrate the different infrared singularities appearing in the various subprocesses. The kinematical limits leading to these divergences in the particular phase-space regions are the soft limit, i.e. the momentum of one parton approaches zero in the sense of $p_i = \lambda q$, $\lambda \rightarrow 0$, where q is an arbitrary light-like momentum and p_i the momentum of the soft parton, and the collinear limit, i.e. two partons become collinear, which is approached when $p_i \cdot p_j \rightarrow 0$ with the momenta p_i and p_j of the two collinear partons.

The filled circles indicate the phase-space regions leading to the divergences, which are to be cancelled against subtraction terms, the so-called dipoles. In this sense, the given diagrams can also be understood as illustrations of the subtraction terms themselves, where

the part of the diagram lying inside the filled circle stands for the universal splitting kernel and the part lying outside represents one diagram of the LO subprocess, whose matrix elements deliver the process-dependent component of the subtraction terms.

In the following, the dipoles for all real-emission subprocesses of the generic process class $pp/p\bar{p} \rightarrow VV + \text{jet} + X$ are given, where specific gauge-boson assignments are only used if the singularity structures differ between the different process classes. This is not the case for subprocesses with external gluons.

Real-emission subprocesses with external gluons

$q_1 \bar{q}_2 \rightarrow V_1 V_2 gg$ The matrix elements for the real-emission subprocesses with two outgoing gluons are given in Eqs. (4.76), (4.80), and (4.84) for all gauge-boson and (anti-)quark assignments. The singularity structure, which is illustrated in Figure 5.4, requires ten dipole terms due to the fact that each of the three diagrams accounts for two local subtraction terms from the two possible spectator partons. The central and the right one have to be taken into account for the two possible momentum assignments of the outgoing gluons. With the amplitude abbreviations introduced in Eq. (5.21), the dipole terms read

$$\mathcal{D}_{ij}^a = -\frac{1}{2p_i p_j} \frac{1}{x_{ij,a}} \left[\mathcal{M}^* \frac{\mathbf{T}_{q_a} \cdot \mathbf{T}_{g_{ij}}}{\mathbf{T}_{g_{ij}}^2} \mathbf{V}_{g_i g_j}^{q_a} \mathcal{M} \right] \left(\tilde{q}_1 \bar{q}_2 \rightarrow V_1 V_2 \tilde{g} \right), \quad (5.53a)$$

$$\mathcal{D}_{ij}^b = -\frac{1}{2p_i p_j} \frac{1}{x_{ij,b}} \left[\mathcal{M}^* \frac{\mathbf{T}_{\bar{q}_b} \cdot \mathbf{T}_{g_{ij}}}{\mathbf{T}_{g_{ij}}^2} \mathbf{V}_{g_i g_j}^{\bar{q}_b} \mathcal{M} \right] \left(q_1 \tilde{q}_2 \rightarrow V_1 V_2 \tilde{g} \right), \quad (5.53b)$$

$$\mathcal{D}_j^{ai} = -\frac{1}{2p_a p_i} \frac{1}{x_{ij,a}} \left[\mathcal{M}^* \frac{\mathbf{T}_{g_j} \cdot \mathbf{T}_{q_{ai}}}{\mathbf{T}_{q_{ai}}^2} \mathbf{V}_{g_j}^{q_a g_i} \mathcal{M} \right] \left(\tilde{q}_1 \bar{q}_2 \rightarrow V_1 V_2 \tilde{g} \right), \quad (5.53c)$$

$$\mathcal{D}^{ai,b} = -\frac{1}{2p_a p_i} \frac{1}{x_{i,ab}} \left[\mathcal{M}^* \frac{\mathbf{T}_{\bar{q}_b} \cdot \mathbf{T}_{q_{ai}}}{\mathbf{T}_{q_{ai}}^2} \mathbf{V}_{q_a g_i, \bar{q}_b} \mathcal{M} \right] \left(\tilde{q}_1 \bar{q}_2 \rightarrow \tilde{V}_1 \tilde{V}_2 \tilde{g} \right), \quad (5.53d)$$

$$\mathcal{D}_i^{aj} = -\frac{1}{2p_a p_j} \frac{1}{x_{ij,a}} \left[\mathcal{M}^* \frac{\mathbf{T}_{g_i} \cdot \mathbf{T}_{q_{aj}}}{\mathbf{T}_{q_{aj}}^2} \mathbf{V}_{g_i}^{q_a g_j} \mathcal{M} \right] \left(\tilde{q}_1 \bar{q}_2 \rightarrow V_1 V_2 \tilde{g} \right), \quad (5.53e)$$

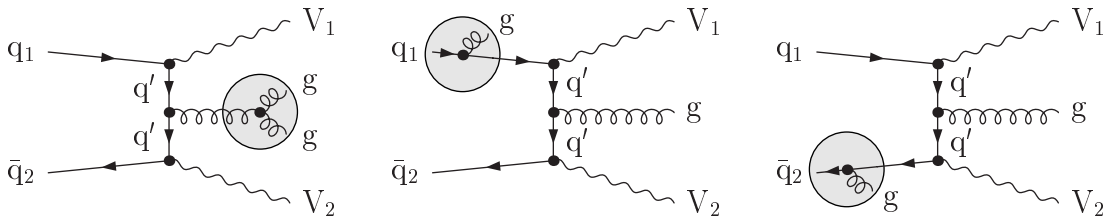


Figure 5.4: Representative diagrams illustrating the different infrared singularities appearing in the subprocesses $q_1 \bar{q}_2 \rightarrow V_1 V_2 gg$. The left diagram shows a final-state singularity, whereas the central diagram and the right one represent initial-state singularities.

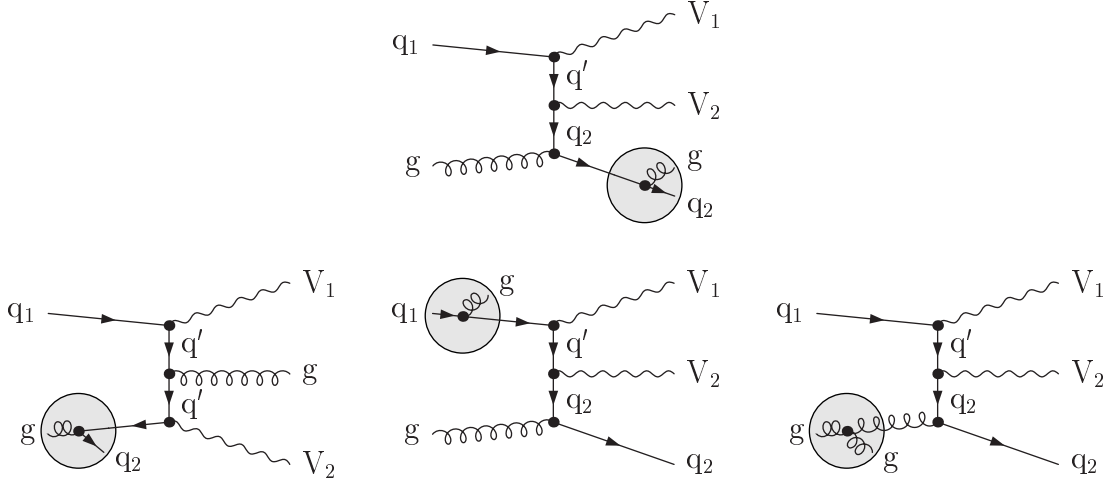


Figure 5.5: Representative diagrams illustrating the different infrared singularities appearing in the subprocesses $q_1 g \rightarrow V_1 V_2 q_2 g$. The upper diagram shows a final-state singularity, whereas the ones in the lower row represent initial-state singularities.

$$\mathcal{D}^{aj,b} = -\frac{1}{2p_a p_j} \frac{1}{x_{j,ab}} \left[\mathcal{M}^* \frac{\mathbf{T}_{\bar{q}_b} \cdot \mathbf{T}_{q_{aj}}}{\mathbf{T}_{q_{aj}}^2} \mathbf{V}^{q_a g_j, \bar{q}_b} \mathcal{M} \right] (\tilde{q}_1 \tilde{q}_2 \rightarrow \tilde{V}_1 \tilde{V}_2 \tilde{g}) , \quad (5.53f)$$

$$\mathcal{D}_j^{bi} = -\frac{1}{2p_b p_i} \frac{1}{x_{ij,b}} \left[\mathcal{M}^* \frac{\mathbf{T}_{g_j} \cdot \mathbf{T}_{\bar{q}_{bi}}}{\mathbf{T}_{\bar{q}_{bi}}^2} \mathbf{V}_{g_j}^{\bar{q}_b g_i} \mathcal{M} \right] (q_1 \tilde{q}_2 \rightarrow V_1 V_2 \tilde{g}) , \quad (5.53g)$$

$$\mathcal{D}^{bi,a} = -\frac{1}{2p_b p_i} \frac{1}{x_{i,ab}} \left[\mathcal{M}^* \frac{\mathbf{T}_{q_a} \cdot \mathbf{T}_{\bar{q}_{bi}}}{\mathbf{T}_{\bar{q}_{bi}}^2} \mathbf{V}^{\bar{q}_b g_i, q_a} \mathcal{M} \right] (q_1 \tilde{q}_2 \rightarrow \tilde{V}_1 \tilde{V}_2 \tilde{g}) , \quad (5.53h)$$

$$\mathcal{D}_i^{bj} = -\frac{1}{2p_b p_j} \frac{1}{x_{ij,b}} \left[\mathcal{M}^* \frac{\mathbf{T}_{g_i} \cdot \mathbf{T}_{\bar{q}_{bj}}}{\mathbf{T}_{\bar{q}_{bj}}^2} \mathbf{V}_{g_i}^{\bar{q}_b g_j} \mathcal{M} \right] (q_1 \tilde{q}_2 \rightarrow V_1 V_2 \tilde{g}) , \quad (5.53i)$$

$$\mathcal{D}^{bj,a} = -\frac{1}{2p_b p_j} \frac{1}{x_{j,ab}} \left[\mathcal{M}^* \frac{\mathbf{T}_{q_a} \cdot \mathbf{T}_{\bar{q}_{bj}}}{\mathbf{T}_{\bar{q}_{bj}}^2} \mathbf{V}^{\bar{q}_b g_j, q_a} \mathcal{M} \right] (q_1 \tilde{q}_2 \rightarrow \tilde{V}_1 \tilde{V}_2 \tilde{g}) , \quad (5.53j)$$

where the omitted arguments of the dipoles read

$$\mathcal{D}^{\dots} = \mathcal{D}^{\dots} (q_1 [p_a] \bar{q}_2 [p_b] \rightarrow V_1 [k_1] V_2 [k_2] g [p_i] g [p_j]) . \quad (5.54)$$

$q_1 g \rightarrow V_1 V_2 q_2 g$ The real-emission matrix elements of the subprocesses with a quark–gluon initial state can be taken from Eqs. (4.77), (4.81), and (4.85) for all gauge-boson and quark assignments. The singularity structure shown in Figure 5.5 causes eight non-vanishing local subtraction terms (two for each singularity from the two possible spectator partons in each case), namely

$$\mathcal{D}_{ij}^a = -\frac{1}{2p_i p_j} \frac{1}{x_{ij,a}} \left[\mathcal{M}^* \frac{\mathbf{T}_{q_a} \cdot \mathbf{T}_{q_{ij}}}{\mathbf{T}_{q_{ij}}^2} \mathbf{V}_{q_{ij}}^{q_a} \mathcal{M} \right] (\tilde{q}_1 g \rightarrow V_1 V_2 \tilde{q}_2) , \quad (5.55a)$$

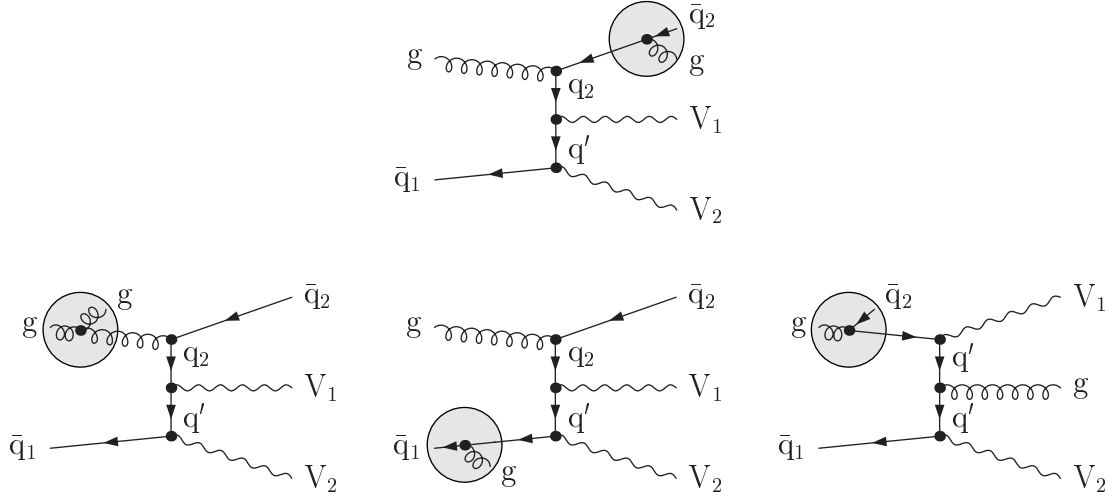


Figure 5.6: Representative diagrams illustrating the different infrared singularities appearing in the subprocesses $g\bar{q}_1 \rightarrow V_1 V_2 g\bar{q}_2$. The upper diagram shows a final-state singularity, whereas the ones in the lower row represent initial-state singularities.

$$\mathcal{D}_{ij}^b = -\frac{1}{2p_i p_j} \frac{1}{x_{ij,b}} \left[\mathcal{M}^* \frac{\mathbf{T}_{g_b} \cdot \mathbf{T}_{q_{ij}}}{\mathbf{T}_{q_{ij}}^2} \mathbf{V}_{q_{ij} g_j}^{g_b} \mathcal{M} \right] (q_1 \tilde{g} \rightarrow V_1 V_2 \tilde{q}_2) , \quad (5.55b)$$

$$\mathcal{D}_i^{aj} = -\frac{1}{2p_a p_j} \frac{1}{x_{ij,a}} \left[\mathcal{M}^* \frac{\mathbf{T}_{g_i} \cdot \mathbf{T}_{q_{aj}}}{\mathbf{T}_{q_{aj}}^2} \mathbf{V}_{q_{aj} g_j}^{q_a} \mathcal{M} \right] (\tilde{q}_1 g \rightarrow V_1 V_2 \tilde{q}_2) , \quad (5.55c)$$

$$\mathcal{D}^{aj,b} = -\frac{1}{2p_a p_j} \frac{1}{x_{j,ab}} \left[\mathcal{M}^* \frac{\mathbf{T}_{g_b} \cdot \mathbf{T}_{q_{aj}}}{\mathbf{T}_{q_{aj}}^2} \mathbf{V}_{q_{aj} g_j, g_b}^{q_a} \mathcal{M} \right] (\tilde{q}_1 g \rightarrow \tilde{V}_1 \tilde{V}_2 \tilde{q}_2) , \quad (5.55d)$$

$$\mathcal{D}_j^{bi} = -\frac{1}{2p_b p_i} \frac{1}{x_{ij,b}} \left[\mathcal{M}^* \frac{\mathbf{T}_{g_j} \cdot \mathbf{T}_{q_{bi}}}{\mathbf{T}_{q_{bi}}^2} \mathbf{V}_{g_j q_i}^{g_b} \mathcal{M} \right] (q_1 \tilde{q}_2 \rightarrow V_1 V_2 \tilde{g}) , \quad (5.55e)$$

$$\mathcal{D}_a^{bi} = -\frac{1}{2p_b p_i} \frac{1}{x_{i,ab}} \left[\mathcal{M}^* \frac{\mathbf{T}_{q_a} \cdot \mathbf{T}_{q_{bi}}}{\mathbf{T}_{q_{bi}}^2} \mathbf{V}_{g_i q_i, q_a}^{g_b} \mathcal{M} \right] (q_1 \tilde{q}_2 \rightarrow \tilde{V}_1 \tilde{V}_2 \tilde{g}) , \quad (5.55f)$$

$$\mathcal{D}_i^{bj} = -\frac{1}{2p_b p_j} \frac{1}{x_{ij,b}} \left[\mathcal{M}^* \frac{\mathbf{T}_{q_i} \cdot \mathbf{T}_{g_{bj}}}{\mathbf{T}_{g_{bj}}^2} \mathbf{V}_{q_i g_j}^{g_b} \mathcal{M} \right] (q_1 \tilde{g} \rightarrow V_1 V_2 \tilde{q}_2) , \quad (5.55g)$$

$$\mathcal{D}^{bj,a} = -\frac{1}{2p_b p_j} \frac{1}{x_{j,ab}} \left[\mathcal{M}^* \frac{\mathbf{T}_{q_a} \cdot \mathbf{T}_{g_{bj}}}{\mathbf{T}_{g_{bj}}^2} \mathbf{V}_{g_b g_j, q_a}^{g_b} \mathcal{M} \right] (q_1 \tilde{g} \rightarrow \tilde{V}_1 \tilde{V}_2 \tilde{q}_2) , \quad (5.55h)$$

where the omitted arguments of the dipoles are

$$\mathcal{D}^{\dots} = \mathcal{D}^{\dots}(q_1[p_a] g[p_b] \rightarrow V_1[k_1] V_2[k_2] q_2[p_i] g[p_j]) . \quad (5.56)$$

$g\bar{q}_1 \rightarrow V_1 V_2 g\bar{q}_2$ The matrix elements of the real-emission subprocesses with an initial state consisting of gluon–antiquark are given in Eqs. (4.78), (4.82), and (4.86) for all gauge-boson and antiquark assignments. The singularity structure shown in Figure 5.6 causes

eight non-vanishing local subtraction terms as in the previous paragraph. The resulting dipoles read

$$\mathcal{D}_{ij}^a = -\frac{1}{2p_i p_j} \frac{1}{x_{ij,a}} \left[\mathcal{M}^* \frac{\mathbf{T}_{g_a} \cdot \mathbf{T}_{\bar{q}_{ij}}}{\mathbf{T}_{\bar{q}_{ij}}^2} \mathbf{V}_{g_i \bar{q}_j}^{g_a} \mathcal{M} \right] \left(\tilde{g} \bar{q}_1 \rightarrow V_1 V_2 \tilde{q}_2 \right), \quad (5.57a)$$

$$\mathcal{D}_{ij}^b = -\frac{1}{2p_i p_j} \frac{1}{x_{ij,b}} \left[\mathcal{M}^* \frac{\mathbf{T}_{\bar{q}_b} \cdot \mathbf{T}_{\bar{q}_{ij}}}{\mathbf{T}_{\bar{q}_{ij}}^2} \mathbf{V}_{g_i \bar{q}_j}^{\bar{q}_b} \mathcal{M} \right] \left(g \tilde{q}_1 \rightarrow V_1 V_2 \tilde{q}_2 \right), \quad (5.57b)$$

$$\mathcal{D}_j^{ai} = -\frac{1}{2p_a p_i} \frac{1}{x_{ij,a}} \left[\mathcal{M}^* \frac{\mathbf{T}_{\bar{q}_j} \cdot \mathbf{T}_{g_{ai}}}{\mathbf{T}_{g_{ai}}^2} \mathbf{V}_{\bar{q}_j}^{g_{ai}} \mathcal{M} \right] \left(\tilde{g} \bar{q}_1 \rightarrow V_1 V_2 \tilde{q}_2 \right), \quad (5.57c)$$

$$\mathcal{D}^{ai,b} = -\frac{1}{2p_a p_i} \frac{1}{x_{i,ab}} \left[\mathcal{M}^* \frac{\mathbf{T}_{\bar{q}_b} \cdot \mathbf{T}_{g_{ai}}}{\mathbf{T}_{g_{ai}}^2} \mathbf{V}_{g_{ai}, \bar{q}_b}^{g_{ai}} \mathcal{M} \right] \left(\tilde{g} \bar{q}_1 \rightarrow \tilde{V}_1 \tilde{V}_2 \tilde{q}_2 \right), \quad (5.57d)$$

$$\mathcal{D}_i^{aj} = -\frac{1}{2p_a p_j} \frac{1}{x_{ij,a}} \left[\mathcal{M}^* \frac{\mathbf{T}_{g_i} \cdot \mathbf{T}_{q_{aj}}}{\mathbf{T}_{q_{aj}}^2} \mathbf{V}_{g_i}^{q_{aj}} \mathcal{M} \right] \left(\bar{q}_1 \bar{q}_2 \rightarrow V_1 V_2 \tilde{g} \right), \quad (5.57e)$$

$$\mathcal{D}^{aj,b} = -\frac{1}{2p_a p_j} \frac{1}{x_{j,ab}} \left[\mathcal{M}^* \frac{\mathbf{T}_{\bar{q}_b} \cdot \mathbf{T}_{q_{aj}}}{\mathbf{T}_{q_{aj}}^2} \mathbf{V}_{q_{aj}, \bar{q}_b}^{q_{aj}} \mathcal{M} \right] \left(\bar{q}_1 \bar{q}_2 \rightarrow \tilde{V}_1 \tilde{V}_2 \tilde{g} \right), \quad (5.57f)$$

$$\mathcal{D}_j^{bi} = -\frac{1}{2p_b p_i} \frac{1}{x_{ij,b}} \left[\mathcal{M}^* \frac{\mathbf{T}_{\bar{q}_j} \cdot \mathbf{T}_{\bar{q}_{bi}}}{\mathbf{T}_{\bar{q}_{bi}}^2} \mathbf{V}_{\bar{q}_j}^{\bar{q}_{bi}} \mathcal{M} \right] \left(g \tilde{q}_1 \rightarrow V_1 V_2 \tilde{q}_2 \right), \quad (5.57g)$$

$$\mathcal{D}^{bi,a} = -\frac{1}{2p_b p_i} \frac{1}{x_{i,ab}} \left[\mathcal{M}^* \frac{\mathbf{T}_{g_a} \cdot \mathbf{T}_{\bar{q}_{bi}}}{\mathbf{T}_{\bar{q}_{bi}}^2} \mathbf{V}_{\bar{q}_{bi}, g_a}^{\bar{q}_{bi}} \mathcal{M} \right] \left(g \tilde{q}_1 \rightarrow \tilde{V}_1 \tilde{V}_2 \tilde{q}_2 \right), \quad (5.57h)$$

where the omitted arguments of the dipoles read

$$\mathcal{D}^{\dots} = \mathcal{D}^{\dots} (g[p_a] \bar{q}_1[p_b] \rightarrow V_1[k_1] V_2[k_2] g[p_i] \bar{q}_2[p_j]). \quad (5.58)$$

$gg \rightarrow V_1 V_2 q_1 \bar{q}_2$ The matrix elements of the real-emission subprocesses with the gluon–gluon initial state can be found in Eqs. (4.79), (4.83), and (4.87) for all gauge-boson and (anti-)quark assignments. The initial-state singularities, which are the only ones to appear, are illustrated in Figure 5.7. They require the following eight local subtraction terms,

$$\mathcal{D}_j^{ai} = -\frac{1}{2p_a p_i} \frac{1}{x_{ij,a}} \left[\mathcal{M}^* \frac{\mathbf{T}_{\bar{q}_j} \cdot \mathbf{T}_{q_{ai}}}{\mathbf{T}_{q_{ai}}^2} \mathbf{V}_{\bar{q}_j}^{q_{ai}} \mathcal{M} \right] \left(\tilde{q}_1 g \rightarrow V_1 V_2 \tilde{q}_2 \right), \quad (5.59a)$$

$$\mathcal{D}^{ai,b} = -\frac{1}{2p_a p_i} \frac{1}{x_{i,ab}} \left[\mathcal{M}^* \frac{\mathbf{T}_{g_b} \cdot \mathbf{T}_{q_{ai}}}{\mathbf{T}_{q_{ai}}^2} \mathbf{V}_{g_{ai}, g_b}^{q_{ai}} \mathcal{M} \right] \left(\tilde{q}_1 g \rightarrow \tilde{V}_1 \tilde{V}_2 \tilde{q}_2 \right), \quad (5.59b)$$

$$\mathcal{D}_i^{aj} = -\frac{1}{2p_a p_j} \frac{1}{x_{ij,a}} \left[\mathcal{M}^* \frac{\mathbf{T}_{q_i} \cdot \mathbf{T}_{q_{aj}}}{\mathbf{T}_{q_{aj}}^2} \mathbf{V}_{q_i}^{q_{aj}} \mathcal{M} \right] \left(\tilde{q}_2 g \rightarrow V_1 V_2 \tilde{q}_1 \right), \quad (5.59c)$$

$$\mathcal{D}^{aj,b} = -\frac{1}{2p_a p_j} \frac{1}{x_{j,ab}} \left[\mathcal{M}^* \frac{\mathbf{T}_{g_b} \cdot \mathbf{T}_{q_{aj}}}{\mathbf{T}_{q_{aj}}^2} \mathbf{V}_{q_{aj}, g_b}^{q_{aj}} \mathcal{M} \right] \left(\tilde{q}_2 g \rightarrow \tilde{V}_1 \tilde{V}_2 \tilde{q}_1 \right), \quad (5.59d)$$

$$\mathcal{D}_j^{bi} = -\frac{1}{2p_b p_i} \frac{1}{x_{ij,b}} \left[\mathcal{M}^* \frac{\mathbf{T}_{\bar{q}_j} \cdot \mathbf{T}_{\bar{q}_{bi}}}{\mathbf{T}_{\bar{q}_{bi}}^2} \mathbf{V}_{\bar{q}_j}^{\bar{q}_{bi}} \mathcal{M} \right] \left(g \tilde{q}_1 \rightarrow V_1 V_2 \tilde{q}_2 \right), \quad (5.59e)$$

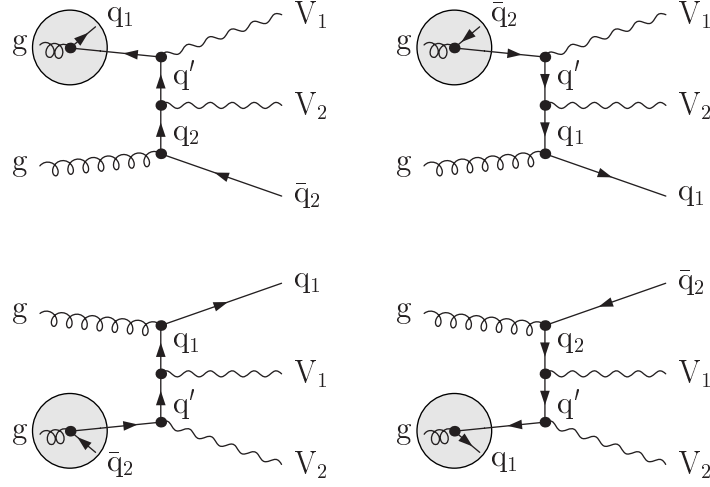


Figure 5.7: Representative diagrams illustrating the infrared singularities appearing in the subprocesses $gg \rightarrow V_1 V_2 q_1 \bar{q}_2$. All diagrams represent initial-state singularities.

$$\mathcal{D}^{bi,a} = -\frac{1}{2p_b p_i} \frac{1}{x_{i,ab}} \left[\mathcal{M}^* \frac{\mathbf{T}_{g_a} \cdot \mathbf{T}_{\bar{q}_{bi}}}{\mathbf{T}_{\bar{q}_{bi}}^2} \mathbf{V}^{g_b q_i, g_a} \mathcal{M} \right] \left(g \tilde{q}_1 \rightarrow \tilde{V}_1 \tilde{V}_2 \tilde{q}_2 \right), \quad (5.59f)$$

$$\mathcal{D}_i^{bj} = -\frac{1}{2p_b p_j} \frac{1}{x_{ij,b}} \left[\mathcal{M}^* \frac{\mathbf{T}_{q_i} \cdot \mathbf{T}_{q_{bj}}}{\mathbf{T}_{q_{bj}}^2} \mathbf{V}_{q_i}^{g_b \bar{q}_j} \mathcal{M} \right] \left(g \tilde{q}_2 \rightarrow V_1 V_2 \tilde{q}_1 \right), \quad (5.59g)$$

$$\mathcal{D}^{bj,a} = -\frac{1}{2p_b p_j} \frac{1}{x_{j,ab}} \left[\mathcal{M}^* \frac{\mathbf{T}_{g_a} \cdot \mathbf{T}_{q_{bj}}}{\mathbf{T}_{q_{bj}}^2} \mathbf{V}^{g_b \bar{q}_j, g_a} \mathcal{M} \right] \left(g \tilde{q}_2 \rightarrow \tilde{V}_1 \tilde{V}_2 \tilde{q}_1 \right), \quad (5.59h)$$

where again the omitted arguments of the dipoles are

$$\mathcal{D}^{\dots} = \mathcal{D}^{\dots} (g[p_a] g[p_b] \rightarrow V_1[k_1] V_2[k_2] q_1[p_i] \bar{q}_2[p_j]). \quad (5.60)$$

Real-emission subprocesses without external gluons: WW+jet and ZZ+jet

Considering the infrared singularities in the real-emission subprocesses without external gluons, all divergent configurations contain $g \rightarrow q\bar{q}$ splittings leading to final-state singularities or crossed variants of these splittings that cause initial-state singularities. The two process classes with a neutral gauge-boson pair—WW or ZZ—and those with a charged gauge-boson pair— W^+Z and W^-Z —have to be treated separately.

As far as the external partons are concerned, exactly the same subprocesses of WW+jet and ZZ+jet production contain infrared singularities. Therefore, these two process classes can be discussed simultaneously. The subprocesses of $pp/p\bar{p} \rightarrow WW + \text{jet} + X$ with contributions solely from diagrams with the two gauge bosons coupling to different fermion chains, do not show divergences in any region of phase space, since no $g \rightarrow q\bar{q}$ splittings arise.

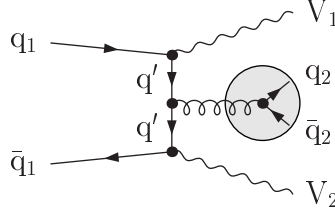


Figure 5.8: Representative diagram illustrating the final-state infrared singularity appearing in the subprocesses $q_1 \bar{q}_1 \rightarrow WW/ZZ q_2 \bar{q}_2$.

The subprocesses with quark–antiquark initial and final states show two kinds of divergences: For subprocesses of the type $q_1 \bar{q}_1 \rightarrow V_1 V_2 q_2 \bar{q}_2$, a final-state singularity appears due to a $g^* \rightarrow q \bar{q}$ splitting. In the $q_1 \bar{q}_2 \rightarrow V_1 V_2 q_1 \bar{q}_2$ situation, two initial-state singularities arise due to crossed variants of this splitting, namely $q \rightarrow q g^*$ and $\bar{q} \rightarrow \bar{q} g^*$, where g^* signals the off-shellness of the gluon in these splittings. If all (anti-)quarks belong to the same flavour both types of singularities appear in the same subprocess.

$q_1 \bar{q}_1 \rightarrow V_1 V_2 q_2 \bar{q}_2$ The matrix elements for this kind of subprocesses with $q_1 \neq q_2$ can be found in Eqs. (4.92), (4.96), and (4.97) for the respective parton assignments to WW+jet production and in Eq. (4.111) in case of ZZ+jet production. An illustration of the arising final-state singularity is given in Figure 5.8, the two resulting local subtraction terms are

$$\mathcal{D}_a^{ij} = -\frac{1}{2p_i p_j} \frac{1}{x_{ij,a}} \left[\mathcal{M}^* \frac{\mathbf{T}_{q_a} \cdot \mathbf{T}_{g_{ij}}}{\mathbf{T}_{g_{ij}}^2} \mathbf{V}_{q_i \bar{q}_j}^{q_a} \mathcal{M} \right] \left(\tilde{q}_1 \bar{q}_1 \rightarrow V_1 V_2 \tilde{g} \right), \quad (5.61a)$$

$$\mathcal{D}_b^{ij} = -\frac{1}{2p_i p_j} \frac{1}{x_{ij,b}} \left[\mathcal{M}^* \frac{\mathbf{T}_{\bar{q}_b} \cdot \mathbf{T}_{g_{ij}}}{\mathbf{T}_{g_{ij}}^2} \mathbf{V}_{q_i \bar{q}_j}^{\bar{q}_b} \mathcal{M} \right] \left(q_1 \tilde{q}_1 \rightarrow V_1 V_2 \tilde{g} \right), \quad (5.61b)$$

where the omitted arguments of the dipoles read

$$\mathcal{D}^{\dots} = \mathcal{D}^{\dots} (q_1 [p_a] \bar{q}_1 [p_b] \rightarrow V_1 [k_1] V_2 [k_2] q_2 [p_i] \bar{q}_2 [p_j]). \quad (5.62)$$

$q_1 \bar{q}_2 \rightarrow V_1 V_2 q_1 \bar{q}_2$ The matrix elements for this kind of subprocesses with $q_1 \neq q_2$ are given in Eqs. (4.93), (4.98), and (4.99) for the respective parton assignments to WW+jet production and in Eq. (4.112) for ZZ+jet production. The initial-state singularities of this subprocess class are illustrated in Figure 5.9, and the local subtraction terms are

$$\mathcal{D}_j^{ai} = -\frac{1}{2p_a p_i} \frac{1}{x_{ij,a}} \left[\mathcal{M}^* \frac{\mathbf{T}_{\bar{q}_j} \cdot \mathbf{T}_{g_{ai}}}{\mathbf{T}_{g_{ai}}^2} \mathbf{V}_{\bar{q}_j}^{q_a q_i} \mathcal{M} \right] \left(\tilde{g} \bar{q}_2 \rightarrow V_1 V_2 \tilde{q}_2 \right), \quad (5.63a)$$

$$\mathcal{D}^{ai,b} = -\frac{1}{2p_a p_i} \frac{1}{x_{i,ab}} \left[\mathcal{M}^* \frac{\mathbf{T}_{\bar{q}_b} \cdot \mathbf{T}_{g_{ai}}}{\mathbf{T}_{g_{ai}}^2} \mathbf{V}_{q_a q_i, \bar{q}_b} \mathcal{M} \right] \left(\tilde{g} \bar{q}_2 \rightarrow \tilde{V}_1 \tilde{V}_2 \tilde{q}_2 \right), \quad (5.63b)$$

$$\mathcal{D}_i^{bj} = -\frac{1}{2p_b p_j} \frac{1}{x_{ij,b}} \left[\mathcal{M}^* \frac{\mathbf{T}_{q_i} \cdot \mathbf{T}_{g_{bj}}}{\mathbf{T}_{g_{bj}}^2} \mathbf{V}_{q_i}^{\bar{q}_b \bar{q}_j} \mathcal{M} \right] \left(q_1 \tilde{g} \rightarrow V_1 V_2 \tilde{q}_1 \right), \quad (5.63c)$$

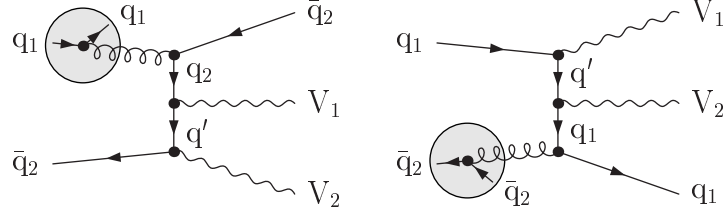


Figure 5.9: Representative diagram illustrating the initial-state infrared singularities appearing in the subprocesses $q_1 \bar{q}_2 \rightarrow WW/ZZ q_1 \bar{q}_2$.

$$\mathcal{D}^{bj,a} = -\frac{1}{2p_b p_j} \frac{1}{x_{j,ab}} \left[\mathcal{M}^* \frac{\mathbf{T}_{q_a} \cdot \mathbf{T}_{g_{bj}}}{\mathbf{T}_{g_{bj}}^2} \mathbf{V}^{\bar{q}_b \bar{q}_j, q_a} \mathcal{M} \right] (q_1 \tilde{g} \rightarrow \tilde{V}_1 \tilde{V}_2 \tilde{q}_1), \quad (5.63d)$$

where the omitted arguments of the dipoles are

$$\mathcal{D}^{\dots} = \mathcal{D}^{\dots} (q_1 [p_a] \bar{q}_2 [p_b] \rightarrow V_1 [k_1] V_2 [k_2] q_1 [p_i] \bar{q}_2 [p_j]). \quad (5.64)$$

$q\bar{q} \rightarrow V_1 V_2 q\bar{q}$ The matrix elements for the real-emission subprocesses with all external (anti-)quarks belonging to the same flavour can be taken from Eq. (4.89) for WW+jet production and from Eq. (4.108) for ZZ+jet production. In this case, both initial- and final-state singularities arise, since the subprocesses contain diagrams of the two types illustrated in Figures 5.8 and 5.9 with $q_1 = q_2 = q$, respectively. Therefore, the local subtraction terms are those of Eqs. (5.61) and (5.63), again with $q_1 = q_2 = q$, and the omitted arguments of the dipoles now are

$$\mathcal{D}^{\dots} = \mathcal{D}^{\dots} (q [p_a] \bar{q} [p_b] \rightarrow V_1 [k_1] V_2 [k_2] q [p_i] \bar{q} [p_j]). \quad (5.65)$$

In case of four external quarks or antiquarks, only initial-state singularities arise, since the configuration of a gluon splitting into two outgoing partons does not appear in these subprocesses. The two subprocess classes are charge conjugated to each other. Nevertheless, the needed dipoles are presented for both classes.

$q_1 q_2 \rightarrow V_1 V_2 q_2 q_1$ The matrix elements for this kind of subprocesses with $q_1 \neq q_2$ are given in Eqs. (4.94) and (4.100) for WW+jet production and in Eq. (4.113) in case of ZZ+jet production. The arising initial-state singularities are illustrated in Figure 5.10, and the corresponding four local subtraction terms read

$$\mathcal{D}_i^{aj} = -\frac{1}{2p_a p_j} \frac{1}{x_{ij,a}} \left[\mathcal{M}^* \frac{\mathbf{T}_{q_i} \cdot \mathbf{T}_{g_{aj}}}{\mathbf{T}_{g_{aj}}^2} \mathbf{V}^{q_a q_j} \mathcal{M} \right] (\tilde{g} q_2 \rightarrow V_1 V_2 \tilde{q}_2), \quad (5.66a)$$

$$\mathcal{D}^{aj,b} = -\frac{1}{2p_a p_j} \frac{1}{x_{j,ab}} \left[\mathcal{M}^* \frac{\mathbf{T}_{q_b} \cdot \mathbf{T}_{g_{aj}}}{\mathbf{T}_{g_{aj}}^2} \mathbf{V}^{q_a q_j, q_b} \mathcal{M} \right] (\tilde{g} q_2 \rightarrow \tilde{V}_1 \tilde{V}_2 \tilde{q}_2), \quad (5.66b)$$

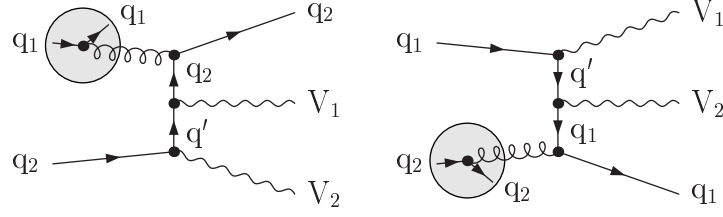


Figure 5.10: Representative diagram illustrating the initial-state infrared singularities appearing in the subprocesses $q_1 q_2 \rightarrow WW/ZZ q_2 q_1$.

$$\mathcal{D}_j^{bi} = -\frac{1}{2p_b p_i} \frac{1}{x_{ij,b}} \left[\mathcal{M}^* \frac{\mathbf{T}_{q_j} \cdot \mathbf{T}_{g_{bi}}}{\mathbf{T}_{g_{bi}}^2} \mathbf{V}_{q_b q_i} \mathcal{M} \right] (q_1 \tilde{g} \rightarrow V_1 V_2 \tilde{q}_1) , \quad (5.66c)$$

$$\mathcal{D}^{bi,a} = -\frac{1}{2p_b p_i} \frac{1}{x_{i,ab}} \left[\mathcal{M}^* \frac{\mathbf{T}_{q_a} \cdot \mathbf{T}_{g_{bi}}}{\mathbf{T}_{g_{bi}}^2} \mathbf{V}_{q_b q_i, q_a} \mathcal{M} \right] (q_1 \tilde{g} \rightarrow \tilde{V}_1 \tilde{V}_2 \tilde{q}_1) , \quad (5.66d)$$

where the omitted arguments of the dipoles read

$$\mathcal{D}^{\dots} = \mathcal{D}^{\dots} (q_1 [p_a] q_2 [p_b] \rightarrow V_1 [k_1] V_2 [k_2] q_2 [p_i] q_1 [p_j]) . \quad (5.67)$$

$q\bar{q} \rightarrow V_1 V_2 q\bar{q}$ The real-emission matrix elements of the subprocesses with four identically flavoured quarks can be taken from Eq. (4.90) in case of WW +jet-production and from Eq. (4.109) for ZZ +jet production. The appearing singularities are those illustrated in Figure 5.10 with $q_1 = q_2 = q$. Each of the singularities has to be taken into account with the two possible momentum assignments of the identical outgoing quarks. This leads to four more local subtraction terms in addition to those given in Eq. (5.66) with $q = q_1 = q_2$, namely

$$\mathcal{D}_j^{ai} = -\frac{1}{2p_a p_i} \frac{1}{x_{ij,a}} \left[\mathcal{M}^* \frac{\mathbf{T}_{q_j} \cdot \mathbf{T}_{g_{ai}}}{\mathbf{T}_{g_{ai}}^2} \mathbf{V}_{q_a q_i} \mathcal{M} \right] (\tilde{g} q \rightarrow V_1 V_2 \tilde{q}) , \quad (5.68a)$$

$$\mathcal{D}^{ai,b} = -\frac{1}{2p_a p_i} \frac{1}{x_{i,ab}} \left[\mathcal{M}^* \frac{\mathbf{T}_{q_b} \cdot \mathbf{T}_{g_{ai}}}{\mathbf{T}_{g_{ai}}^2} \mathbf{V}_{q_a q_i, q_b} \mathcal{M} \right] (\tilde{g} q \rightarrow \tilde{V}_1 \tilde{V}_2 \tilde{q}) , \quad (5.68b)$$

$$\mathcal{D}_i^{bj} = -\frac{1}{2p_b p_j} \frac{1}{x_{ij,b}} \left[\mathcal{M}^* \frac{\mathbf{T}_{q_i} \cdot \mathbf{T}_{g_{bj}}}{\mathbf{T}_{g_{bj}}^2} \mathbf{V}_{q_b q_j} \mathcal{M} \right] (q \tilde{g} \rightarrow V_1 V_2 \tilde{q}) , \quad (5.68c)$$

$$\mathcal{D}^{bj,a} = -\frac{1}{2p_b p_j} \frac{1}{x_{j,ab}} \left[\mathcal{M}^* \frac{\mathbf{T}_{q_a} \cdot \mathbf{T}_{g_{bj}}}{\mathbf{T}_{g_{bj}}^2} \mathbf{V}_{q_b q_j, q_a} \mathcal{M} \right] (q \tilde{g} \rightarrow \tilde{V}_1 \tilde{V}_2 \tilde{q}) , \quad (5.68d)$$

where the omitted arguments of all eight dipoles are

$$\mathcal{D}^{\dots} = \mathcal{D}^{\dots} (q [p_a] q [p_b] \rightarrow V_1 [k_1] V_2 [k_2] q [p_i] q [p_j]) . \quad (5.69)$$

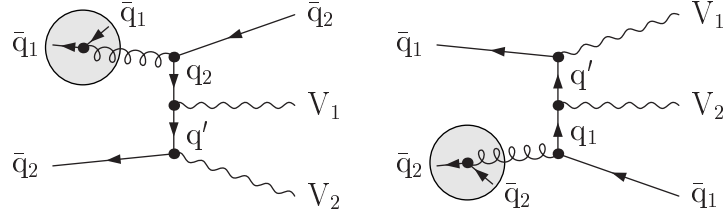


Figure 5.11: Representative diagram illustrating the initial-state infrared singularities appearing in the subprocesses $\bar{q}_1 \bar{q}_2 \rightarrow WW/ZZ \bar{q}_2 \bar{q}_1$.

$\bar{q}_1 \bar{q}_2 \rightarrow V_1 V_2 \bar{q}_2 \bar{q}_1$ The matrix elements for this kind of subprocesses with $q_1 \neq q_2$ are given in Eqs. (4.95) and (4.101) for WW+jet production and in Eq. (4.114) for ZZ+jet production. The arising initial-state singularities are illustrated in Figure 5.11, and the corresponding local subtraction terms read

$$\mathcal{D}_i^{aj} = -\frac{1}{2p_a p_j} \frac{1}{x_{ij,a}} \left[\mathcal{M}^* \frac{\mathbf{T}_{\bar{q}_i} \cdot \mathbf{T}_{g_{aj}}}{\mathbf{T}_{g_{aj}}^2} \mathbf{V}_{\bar{q}_i}^{\bar{q}_a q_j} \mathcal{M} \right] \left(\tilde{g} \bar{q}_1 \rightarrow V_1 V_2 \tilde{q}_2 \right), \quad (5.70a)$$

$$\mathcal{D}^{aj,b} = -\frac{1}{2p_a p_j} \frac{1}{x_{j,ab}} \left[\mathcal{M}^* \frac{\mathbf{T}_{\bar{q}_b} \cdot \mathbf{T}_{g_{aj}}}{\mathbf{T}_{g_{aj}}^2} \mathbf{V}_{\bar{q}_b}^{\bar{q}_a q_j, \bar{q}_b} \mathcal{M} \right] \left(\tilde{g} \bar{q}_1 \rightarrow \tilde{V}_1 \tilde{V}_2 \tilde{q}_2 \right), \quad (5.70b)$$

$$\mathcal{D}_j^{bi} = -\frac{1}{2p_b p_i} \frac{1}{x_{ij,b}} \left[\mathcal{M}^* \frac{\mathbf{T}_{q_j} \cdot \mathbf{T}_{g_{bi}}}{\mathbf{T}_{g_{bi}}^2} \mathbf{V}_{q_j}^{\bar{q}_b \bar{q}_i} \mathcal{M} \right] \left(\bar{q}_1 \tilde{g} \rightarrow V_1 V_2 \tilde{q}_2 \right), \quad (5.70c)$$

$$\mathcal{D}^{bi,a} = -\frac{1}{2p_b p_i} \frac{1}{x_{i,ab}} \left[\mathcal{M}^* \frac{\mathbf{T}_{q_a} \cdot \mathbf{T}_{g_{bi}}}{\mathbf{T}_{g_{bi}}^2} \mathbf{V}_{q_a}^{\bar{q}_b \bar{q}_i, q_a} \mathcal{M} \right] \left(\bar{q}_1 \tilde{g} \rightarrow \tilde{V}_1 \tilde{V}_2 \tilde{q}_2 \right), \quad (5.70d)$$

where the omitted arguments of the dipoles read

$$\mathcal{D}^{\dots} = \mathcal{D}^{\dots} (\bar{q}_1 [p_a] \bar{q}_2 [p_b] \rightarrow V_1 [k_1] V_2 [k_2] \bar{q}_2 [p_i] \bar{q}_1 [p_j]). \quad (5.71)$$

$\bar{q} \bar{q} \rightarrow V_1 V_2 \bar{q} \bar{q}$ The matrix elements of the subprocesses with four identically flavoured antiquarks are given in Eq. (4.91) in case of WW+jet-production and in Eq. (4.110) for ZZ+jet production. The arising initial-state singularities are those of Figure 5.11 with $q_1 = q_2 = q$, again with two different momentum assignments due to the identical outgoing antiquarks. In addition to the dipoles of Eq. (5.70), four further local subtraction terms contribute, namely

$$\mathcal{D}_j^{ai} = -\frac{1}{2p_a p_i} \frac{1}{x_{ij,a}} \left[\mathcal{M}^* \frac{\mathbf{T}_{q_j} \cdot \mathbf{T}_{g_{ai}}}{\mathbf{T}_{g_{ai}}^2} \mathbf{V}_{q_j}^{\bar{q}_a \bar{q}_i} \mathcal{M} \right] \left(\tilde{g} \bar{q} \rightarrow V_1 V_2 \tilde{q} \right), \quad (5.72a)$$

$$\mathcal{D}^{ai,b} = -\frac{1}{2p_a p_i} \frac{1}{x_{i,ab}} \left[\mathcal{M}^* \frac{\mathbf{T}_{q_b} \cdot \mathbf{T}_{g_{ai}}}{\mathbf{T}_{g_{ai}}^2} \mathbf{V}_{q_b}^{\bar{q}_a \bar{q}_i, q_b} \mathcal{M} \right] \left(\tilde{g} \bar{q} \rightarrow \tilde{V}_1 \tilde{V}_2 \tilde{q} \right), \quad (5.72b)$$

$$\mathcal{D}_i^{bj} = -\frac{1}{2p_b p_j} \frac{1}{x_{ij,b}} \left[\mathcal{M}^* \frac{\mathbf{T}_{q_i} \cdot \mathbf{T}_{g_{bj}}}{\mathbf{T}_{g_{bj}}^2} \mathbf{V}_{q_i}^{\bar{q}_b \bar{q}_j} \mathcal{M} \right] \left(\bar{q} \tilde{g} \rightarrow V_1 V_2 \tilde{q} \right), \quad (5.72c)$$

$$\mathcal{D}^{bj,a} = -\frac{1}{2p_b p_j} \frac{1}{x_{j,ab}} \left[\mathcal{M}^* \frac{\mathbf{T}_{\bar{q}_a} \cdot \mathbf{T}_{g_{bj}}}{\mathbf{T}_{g_{bj}}^2} \mathbf{V}^{\bar{q}_b \bar{q}_j, \bar{q}_a} \mathcal{M} \right] (\bar{q} \tilde{g} \rightarrow \tilde{V}_1 \tilde{V}_2 \tilde{q}) , \quad (5.72d)$$

where the omitted arguments of all eight dipoles are

$$\mathcal{D}^{\dots} = \mathcal{D}^{\dots} (\bar{q}[p_a] \bar{q}[p_b] \rightarrow V_1[k_1] V_2[k_2] \bar{q}[p_i] \bar{q}[p_j]) . \quad (5.73)$$

Real-emission subprocesses without external gluons: WZ+jet

Since each subprocess of $pp/p\bar{p} \rightarrow W^\pm Z + \text{jet} + X$ has its charge-conjugate counterpart in $pp/p\bar{p} \rightarrow W^\mp Z + \text{jet} + X$, both process classes show the same singularity structure. Again, all singularities in the real-emission subprocesses without external gluons arise from $g \rightarrow q\bar{q}$ splittings or crossed versions. Consequently, fermion chains with the W boson attached do not cause divergences, which leads to at most four dipole terms per subprocess.

In the subprocesses with quark–antiquark initial and final states, both final- and initial-state singularities arise depending on the respective parton assignments. The discussion starts with the subprocesses showing only one singular phase-space region, which all contain (anti-)quarks of three different flavours or an identically flavoured quark–antiquark pair in the initial state.

$q_1 \bar{q}_2 \rightarrow W Z q_3 \bar{q}_3$ The matrix elements of this kind of subprocesses with $q_3 \neq q_1$ and $q_3 \neq q_2$ are given in Eq. (4.123). The initial-state singularity is illustrated in Figure 5.12, and the corresponding local subtraction terms are

$$\mathcal{D}_{ij}^a = -\frac{1}{2p_i p_j} \frac{1}{x_{ij,a}} \left[\mathcal{M}^* \frac{\mathbf{T}_{q_a} \cdot \mathbf{T}_{g_{ij}}}{\mathbf{T}_{g_{ij}}^2} \mathbf{V}_{q_i \bar{q}_j}^{q_a} \mathcal{M} \right] (\tilde{q}_1 \bar{q}_2 \rightarrow W Z \tilde{g}) , \quad (5.74a)$$

$$\mathcal{D}_{ij}^b = -\frac{1}{2p_i p_j} \frac{1}{x_{ij,b}} \left[\mathcal{M}^* \frac{\mathbf{T}_{\bar{q}_b} \cdot \mathbf{T}_{g_{ij}}}{\mathbf{T}_{g_{ij}}^2} \mathbf{V}_{q_i \bar{q}_j}^{\bar{q}_b} \mathcal{M} \right] (q_1 \tilde{q}_2 \rightarrow W Z \tilde{g}) , \quad (5.74b)$$

where the omitted arguments of the dipoles are

$$\mathcal{D}^{\dots} = \mathcal{D}^{\dots} (q_1[p_a] \bar{q}_2[p_b] \rightarrow W[k_1] Z[k_2] q_3[p_i] \bar{q}_3[p_j]) . \quad (5.75)$$

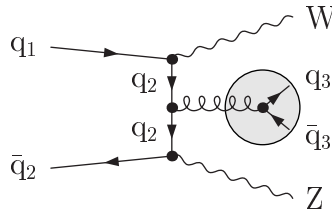


Figure 5.12: Representative diagram illustrating the final-state infrared singularity appearing in the subprocesses $q_1 \bar{q}_2 \rightarrow W Z q_3 \bar{q}_3$.

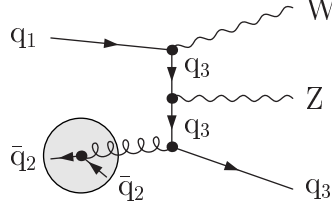


Figure 5.13: Representative diagram illustrating the initial-state infrared singularity appearing in the subprocesses $q_1 \bar{q}_2 \rightarrow WZ q_3 \bar{q}_2$.

$q_1 \bar{q}_2 \rightarrow WZ q_3 \bar{q}_2$ The matrix elements of this kind of subprocesses with $q_3 \neq q_1$ and $q_3 \neq q_2$ can be obtained from Eqs. (4.116) and (4.125) for $q_1 = q_2$ and $q_1 \neq q_2$, respectively. The arising initial-state singularity is illustrated in Figure 5.13, and the two corresponding local subtraction terms are

$$\mathcal{D}_i^{bj} = -\frac{1}{2p_b p_j} \frac{1}{x_{ij,b}} \left[\mathcal{M}^* \frac{\mathbf{T}_{q_i} \cdot \mathbf{T}_{g_{bj}}}{\mathbf{T}_{g_{bj}}^2} \mathbf{V}_{q_i}^{\bar{q}_b \bar{q}_j} \mathcal{M} \right] (q_1 \tilde{g} \rightarrow WZ \tilde{q}_3), \quad (5.76a)$$

$$\mathcal{D}^{bj,a} = -\frac{1}{2p_b p_j} \frac{1}{x_{j,ab}} \left[\mathcal{M}^* \frac{\mathbf{T}_{q_a} \cdot \mathbf{T}_{g_{bj}}}{\mathbf{T}_{g_{bj}}^2} \mathbf{V}_{q_b \bar{q}_j, q_a} \mathcal{M} \right] (q_1 \tilde{g} \rightarrow \tilde{W} \tilde{Z} \tilde{q}_3), \quad (5.76b)$$

where the omitted arguments of the dipoles are

$$\mathcal{D}^{\dots} = \mathcal{D}^{\dots} (q_1 [p_a] \bar{q}_2 [p_b] \rightarrow W[k_1] Z[k_2] q_3 [p_i] \bar{q}_2 [p_j]). \quad (5.77)$$

$q_1 \bar{q}_2 \rightarrow WZ q_1 \bar{q}_3$ The matrix elements of these subprocesses with $q_3 \neq q_1$ and $q_3 \neq q_2$ are given in Eqs. (4.120) and (4.126) for $q_1 = q_2$ and $q_1 \neq q_2$, respectively. Analogously to the previous case, an initial-state singularity arises, which is illustrated in Figure 5.14, and the two corresponding local subtraction terms are

$$\mathcal{D}_j^{ai} = -\frac{1}{2p_a p_i} \frac{1}{x_{ij,a}} \left[\mathcal{M}^* \frac{\mathbf{T}_{\bar{q}_j} \cdot \mathbf{T}_{g_{ai}}}{\mathbf{T}_{g_{ai}}^2} \mathbf{V}_{\bar{q}_j}^{q_a q_i} \mathcal{M} \right] (\tilde{q}_2 \rightarrow WZ \tilde{q}_3), \quad (5.78a)$$

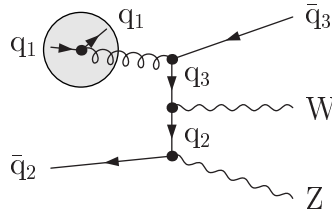


Figure 5.14: Representative diagram illustrating the initial-state infrared singularity appearing in the subprocesses $q_1 \bar{q}_2 \rightarrow WZ q_1 \bar{q}_3$.

$$\mathcal{D}^{ai,b} = -\frac{1}{2p_a p_i} \frac{1}{x_{i,ab}} \left[\mathcal{M}^* \frac{\mathbf{T}_{\bar{q}_b} \cdot \mathbf{T}_{g_{ai}}}{\mathbf{T}_{g_{ai}}^2} \mathbf{V}^{q_a q_i, \bar{q}_b} \mathcal{M} \right] \left(\tilde{g}_{\bar{q}_2} \rightarrow \tilde{W} \tilde{Z} \tilde{q}_3 \right). \quad (5.78b)$$

The omitted arguments of the dipoles read

$$\mathcal{D}^{\dots} = \mathcal{D}^{\dots} (q_1 [p_a] \bar{q}_2 [p_b] \rightarrow W [k_1] Z [k_2] q_1 [p_i] \bar{q}_3 [p_j]). \quad (5.79)$$

$q_1 \bar{q}_2 \rightarrow W Z q_2 \bar{q}_2$ The matrix elements of this kind of subprocesses are provided in Eq. (4.119). Since this subprocess class contains diagrams like those shown in Figures 5.12 and 5.13 with $q_3 = q_2$, both final- and initial-state singularities arise. The four corresponding local subtraction terms are given in Eqs. (5.74) and (5.76), again with $q_3 = q_2$, where the arguments of the dipoles are

$$\mathcal{D}^{\dots} = \mathcal{D}^{\dots} (q_1 [p_a] \bar{q}_2 [p_b] \rightarrow W [k_1] Z [k_2] q_2 [p_i] \bar{q}_2 [p_j]). \quad (5.80)$$

$q_1 \bar{q}_2 \rightarrow W Z q_1 \bar{q}_1$ The matrix elements of these real-emission subprocesses are taken from Eq. (4.115). Analogously to the previously discussed case, diagrams leading to two different types of singularities are contained in this subprocess class, namely those illustrated in Figures 5.12 and 5.14 with $q_3 = q_1$. The resulting final- and initial-state singularities require four local subtraction terms, which are known from Eqs. (5.74) and (5.78), again with $q_3 = q_1$ and the arguments of the dipoles as follows,

$$\mathcal{D}^{\dots} = \mathcal{D}^{\dots} (q_1 [p_a] \bar{q}_2 [p_b] \rightarrow W [k_1] Z [k_2] q_1 [p_i] \bar{q}_1 [p_j]). \quad (5.81)$$

In the subprocesses with only external quarks or antiquarks, only initial-state singularities can show up, as in the case of WW+jet and ZZ+jet production. The external parton content is three up-type and one down-type (anti-)quark (or vice versa) in each subprocess. The W boson always couples to the fermion chain with the down-type (up-type) (anti-)quark. Therefore, only one generic divergence type arises in each subprocess, namely from diagrams with both gauge bosons coupling to that fermion chain. If only two external flavours are involved, this singularity shows up in two different phase-space regions due to the two possibilities to close the fermion chains.

$q_1 q_3 \rightarrow W Z q_3 q_2$ The matrix elements of this kind of subprocesses with $q_3 \neq q_1$ and $q_3 \neq q_2$ are given in Eq. (4.127). The appearing initial-state singularity is depicted in Figure 5.15, and the corresponding local subtraction terms read

$$\mathcal{D}_j^{bi} = -\frac{1}{2p_b p_i} \frac{1}{x_{ij,b}} \left[\mathcal{M}^* \frac{\mathbf{T}_{q_j} \cdot \mathbf{T}_{g_{bi}}}{\mathbf{T}_{g_{bi}}^2} \mathbf{V}^{q_b q_i, q_j} \mathcal{M} \right] \left(q_1 \tilde{g} \rightarrow W Z \tilde{q}_2 \right), \quad (5.82a)$$

$$\mathcal{D}^{bi,a} = -\frac{1}{2p_b p_i} \frac{1}{x_{i,ab}} \left[\mathcal{M}^* \frac{\mathbf{T}_{q_a} \cdot \mathbf{T}_{g_{bi}}}{\mathbf{T}_{g_{bi}}^2} \mathbf{V}^{q_b q_i, q_a} \mathcal{M} \right] \left(q_1 \tilde{g} \rightarrow \tilde{W} \tilde{Z} \tilde{q}_2 \right), \quad (5.82b)$$

where the omitted arguments of the dipoles are

$$\mathcal{D}^{\dots} = \mathcal{D}^{\dots} (q_1 [p_a] q_3 [p_b] \rightarrow W [k_1] Z [k_2] q_3 [p_i] q_2 [p_j]). \quad (5.83)$$

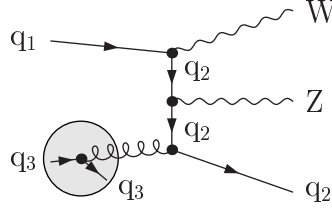


Figure 5.15: Representative diagram illustrating the initial-state infrared singularity appearing in the subprocesses $q_1 q_3 \rightarrow W Z q_3 q_2$.

$q_1 q_2 \rightarrow W Z q_2 q_2$ The real-emission matrix elements of the subprocesses with two identical quarks in the final state are provided in Eq. (4.121). The initial-state singularities showing up are those of Figure 5.15 with $q_3 = q_2$, where two possible momentum assignments for the identical outgoing quarks have to be taken into account. In addition to the two dipoles of Eq. (5.82), the following two local subtraction terms contribute,

$$\mathcal{D}_i^{bj} = -\frac{1}{2p_b p_j} \frac{1}{x_{ij,b}} \left[\mathcal{M}^* \frac{\mathbf{T}_{q_i} \cdot \mathbf{T}_{g_{bj}}}{\mathbf{T}_{g_{bj}}^2} \mathbf{V}_{q_b q_j} \mathcal{M} \right] (q_1 \tilde{g} \rightarrow W Z \tilde{q}_2), \quad (5.84a)$$

$$\mathcal{D}^{bj,a} = -\frac{1}{2p_b p_j} \frac{1}{x_{j,ab}} \left[\mathcal{M}^* \frac{\mathbf{T}_{q_a} \cdot \mathbf{T}_{g_{bj}}}{\mathbf{T}_{g_{bj}}^2} \mathbf{V}_{q_b q_j, q_a} \mathcal{M} \right] (q_1 \tilde{g} \rightarrow \tilde{W} \tilde{Z} \tilde{q}_2), \quad (5.84b)$$

where the arguments of all four dipoles are

$$\mathcal{D}^{\dots} = \mathcal{D}^{\dots} (q_1 [p_a] q_2 [p_b] \rightarrow W [k_1] Z [k_2] q_2 [p_i] q_2 [p_j]). \quad (5.85)$$

$q_1 q_1 \rightarrow W Z q_1 q_2$ The matrix elements of the real-emission subprocesses with two identical quarks in the initial state are taken from Eq. (4.117). The arising initial-state singularities are illustrated in Figure 5.15 with $q_3 = q_1$. In this subprocess class, divergences related to the two identical initial-state quarks appear, which leads to further dipoles in addition to those of Eq. (5.82), namely

$$\mathcal{D}_j^{ai} = -\frac{1}{2p_a p_i} \frac{1}{x_{ij,a}} \left[\mathcal{M}^* \frac{\mathbf{T}_{q_j} \cdot \mathbf{T}_{g_{ai}}}{\mathbf{T}_{g_{ai}}^2} \mathbf{V}_{q_a q_i} \mathcal{M} \right] (q_1 \tilde{g} \rightarrow W Z \tilde{q}_2), \quad (5.86a)$$

$$\mathcal{D}^{ai,b} = -\frac{1}{2p_a p_i} \frac{1}{x_{i,ab}} \left[\mathcal{M}^* \frac{\mathbf{T}_{q_b} \cdot \mathbf{T}_{g_{ai}}}{\mathbf{T}_{g_{ai}}^2} \mathbf{V}_{q_a q_i, q_b} \mathcal{M} \right] (q_1 \tilde{g} \rightarrow \tilde{W} \tilde{Z} \tilde{q}_2), \quad (5.86b)$$

where the arguments of all four dipoles are

$$\mathcal{D}^{\dots} = \mathcal{D}^{\dots} (q_1 [p_a] q_1 [p_b] \rightarrow W [k_1] Z [k_2] q_1 [p_i] q_2 [p_j]). \quad (5.87)$$

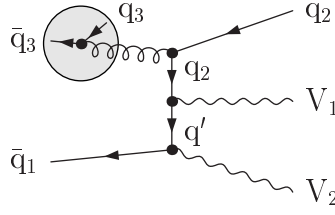


Figure 5.16: Representative diagram illustrating the initial-state infrared singularity appearing in the subprocesses $\bar{q}_3 \bar{q}_1 \rightarrow WZ \bar{q}_2 \bar{q}_3$.

$\bar{q}_3 \bar{q}_1 \rightarrow WZ \bar{q}_2 \bar{q}_3$ The matrix elements of this kind of subprocesses with $q_3 \neq q_1$ and $q_3 \neq q_2$ can be found in Eq. (4.128). The appearing initial-state singularity is illustrated in Figure 5.16. The corresponding local subtraction terms are

$$\mathcal{D}_i^{aj} = -\frac{1}{2p_a p_j} \frac{1}{x_{ij,a}} \left[\mathcal{M}^* \frac{\mathbf{T}_{\bar{q}_i} \cdot \mathbf{T}_{g_{aj}}}{\mathbf{T}_{g_{aj}}^2} \mathbf{V}_{\bar{q}_i}^{\bar{q}_a \bar{q}_j} \mathcal{M} \right] \left(\tilde{g} \bar{q}_1 \rightarrow WZ \tilde{\bar{q}}_2 \right), \quad (5.88a)$$

$$\mathcal{D}^{aj,b} = -\frac{1}{2p_a p_j} \frac{1}{x_{j,ab}} \left[\mathcal{M}^* \frac{\mathbf{T}_{\bar{q}_b} \cdot \mathbf{T}_{g_{aj}}}{\mathbf{T}_{g_{aj}}^2} \mathbf{V}_{\bar{q}_a \bar{q}_j, \bar{q}_b} \mathcal{M} \right] \left(\tilde{g} \bar{q}_1 \rightarrow \tilde{W} \tilde{Z} \tilde{\bar{q}}_2 \right), \quad (5.88b)$$

where the omitted arguments of the dipoles are

$$\mathcal{D}^{\dots} = \mathcal{D}^{\dots}(\bar{q}_3[p_a] \bar{q}_1[p_b] \rightarrow W[k_1] Z[k_2] \bar{q}_2[p_i] \bar{q}_3[p_j]). \quad (5.89)$$

$\bar{q}_2 \bar{q}_1 \rightarrow WZ \bar{q}_2 \bar{q}_2$ The real-emission matrix elements of the subprocesses with two identical antiquarks in the final state are obtained from Eq. (4.118). The arising initial-state singularities are already given in Figure 5.16 with $q_3 = q_2$. As in the analogous case with four external quarks, two possible momentum assignments for the identical outgoing antiquarks have to be taken into account. This leads to two further local subtraction terms in addition to those of Eq. (5.88), namely

$$\mathcal{D}_j^{ai} = -\frac{1}{2p_a p_i} \frac{1}{x_{ij,a}} \left[\mathcal{M}^* \frac{\mathbf{T}_{\bar{q}_j} \cdot \mathbf{T}_{g_{ai}}}{\mathbf{T}_{g_{ai}}^2} \mathbf{V}_{\bar{q}_j}^{\bar{q}_a \bar{q}_i} \mathcal{M} \right] \left(\tilde{g} \bar{q}_1 \rightarrow WZ \tilde{\bar{q}}_2 \right), \quad (5.90a)$$

$$\mathcal{D}^{ai,b} = -\frac{1}{2p_a p_i} \frac{1}{x_{i,ab}} \left[\mathcal{M}^* \frac{\mathbf{T}_{\bar{q}_b} \cdot \mathbf{T}_{g_{ai}}}{\mathbf{T}_{g_{ai}}^2} \mathbf{V}_{\bar{q}_a \bar{q}_i, \bar{q}_b} \mathcal{M} \right] \left(\tilde{g} \bar{q}_1 \rightarrow \tilde{W} \tilde{Z} \tilde{\bar{q}}_2 \right), \quad (5.90b)$$

where the arguments of all four dipoles are

$$\mathcal{D}^{\dots} = \mathcal{D}^{\dots}(\bar{q}_2[p_a] \bar{q}_1[p_b] \rightarrow W[k_1] Z[k_2] \bar{q}_2[p_i] \bar{q}_2[p_j]). \quad (5.91)$$

$\bar{q}_1 \bar{q}_1 \rightarrow WZ \bar{q}_2 \bar{q}_1$ The matrix elements of the real-emission subprocesses with two identical antiquarks in the initial state are given in Eq. (4.122). The appearing initial-state

singularities are shown in Figure 5.16 with $q_3 = q_1$. This subprocess class shows divergences related to both identical initial-state antiquarks, leading to the following additional dipoles besides those of Eq. (5.88),

$$\mathcal{D}_i^{bj} = -\frac{1}{2p_b p_j} \frac{1}{x_{ij,b}} \left[\mathcal{M}^* \frac{\mathbf{T}_{\bar{q}_i} \cdot \mathbf{T}_{g_{bj}}}{\mathbf{T}_{g_{bj}}^2} \mathbf{V}_{\bar{q}_i}^{\bar{q}_b \bar{q}_j} \mathcal{M} \right] \left(\bar{q}_1 \tilde{g} \rightarrow W Z \tilde{q}_2 \right), \quad (5.92a)$$

$$\mathcal{D}^{bj,a} = -\frac{1}{2p_b p_j} \frac{1}{x_{j,ab}} \left[\mathcal{M}^* \frac{\mathbf{T}_{\bar{q}_a} \cdot \mathbf{T}_{g_{bj}}}{\mathbf{T}_{g_{bj}}^2} \mathbf{V}_{\bar{q}_b \bar{q}_j, \bar{q}_a} \mathcal{M} \right] \left(\bar{q}_1 \tilde{g} \rightarrow \tilde{W} \tilde{Z} \tilde{q}_2 \right), \quad (5.92b)$$

where the arguments of all four dipoles are

$$\mathcal{D}^{\dots} = \mathcal{D}^{\dots}(\bar{q}_1[p_a] \bar{q}_1[p_b] \rightarrow W[k_1] Z[k_2] \bar{q}_2[p_i] \bar{q}_1[p_j]). \quad (5.93)$$

5.3 Virtual corrections to VV+jet production

5.3.1 Evaluation with FORMCALC/LOOPTOOLS

In this thesis, the one-loop diagrams are evaluated by means of the FORMCALC/ LOOPTOOLS package [78]. More precisely, the generation of all loop diagrams is performed with FEYNARTS 3.2 [79]. The output is further manipulated by means of FORMCALC 5.2 [78] leading to FORTRAN code for the amplitude calculation. FORMCALC neglects rational terms of IR origin, because a mass regularization is assumed for IR divergences. This approach is justified also in case of dimensional regularization, since no such rational terms of IR origin arise from the $(D - 4)$ -dimensional part, as shown in Ref. [80]. Rational terms arising from UV divergences are properly calculated by FORMCALC. The whole tensor reduction is done by means of the LOOPTOOLS library [78], which employs the Denner–Dittmaier reduction scheme of Ref. [81] for five-point functions and Passarino–Veltmann reduction [82] for the lower-point tensors. For the evaluation of regular scalar integrals, the FF package [83, 84] is applied. The dimensionally regularized IR-divergent integrals are linked to this library. All the divergent integrals needed for the calculations to $pp/p\bar{p} \rightarrow VV + \text{jet} + X$ are collected in App. B. Which scalar one-loop diagrams actually contain IR singularities is explained in Ref. [76]: Collinear singularities appear if a massless external particle splits into two massless internal particles of a loop diagram, and soft singularities arise if two external particles exchange a massless boson. All IR-divergent parts of integrals can be expressed in terms of three-point functions only, which is spelled out in Ref. [85].

In dimensional regularization, γ_5 is treated as implemented in FORMCALC, i.e. with the pure anticommutation relation $\{\gamma_5, \gamma_\mu\} = 0$ as in four space–time dimensions and keeping the four-dimensional expression for $\text{Tr}\{\gamma_\alpha \gamma_\beta \gamma_\gamma \gamma_\delta \gamma_5\}$ which is proportional to $\epsilon_{\alpha\beta\gamma\delta}$. The expressions containing γ_5 show up in identically ordered fermion chains both in the virtual and the real corrections, between which the IR divergences cancel. This situation is illustrated in Figure 5.17 where two related interference diagrams are depicted that only differ in the position of the cut indicated by the dashed lines. In the calculation it must

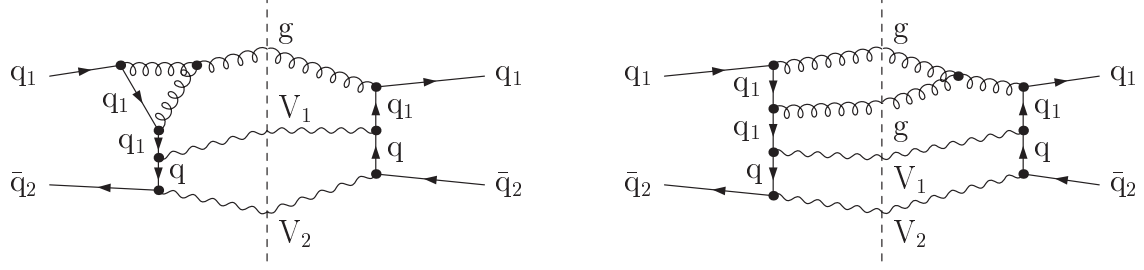


Figure 5.17: Interference diagrams illustrating the cancellation of IR divergences: The left-hand side shows a virtual×born diagram contributing at NLO, the right-hand side a real×real diagram. The two diagrams are obtained from each other by a shift of the cut.

be guaranteed that γ_5 is treated identically in both cases, i.e. with the same terms arising if γ_5 is shifted in the evaluation of fermion chains. One way to do so is using the four-dimensional anticommutation relation with no extra terms arising at all. For UV divergences, the FORMCALC approach is justified in Ref. [86]. An alternative procedure with anticommutation relations for the four-dimensional part of γ_5 , but commutation relations for a split-off $(D-4)$ -dimensional part is suggested in Ref. [87, 88]. At NLO, however, this method and the simpler approach applied in this thesis can be shown to deliver identical results. This agreement between the results is numerically confirmed in the comparison of virtual corrections to WW+jet production in Ref. [40].

The virtual corrections to the subprocesses of VV+jet can in general be subdivided into two parts, which are the bosonic corrections with all one-loop diagrams containing at least one additional virtual gluon and the fermionic corrections containing a closed quark loop. The counterterm contribution, which can also be decomposed into a bosonic and a fermionic part, stems from the renormalization procedure and cancels the ultraviolet singularities in the loop diagrams.

5.3.2 Bosonic corrections from virtual-gluon exchange

For all gauge-boson assignments of $pp/p\bar{p} \rightarrow VV + \text{jet} + X$, the bosonic diagrams can—as in the LO case—be subdivided into a group of diagrams with the two weak gauge bosons coupling directly to the fermion chain and another group containing an intermediate gauge boson and a three-vector-boson vertex. The latter does again not contribute to the ZZ+jet case, because no three-gauge-boson vertex with two Z bosons attached exists in the SM.

As in the previous chapters, exemplary diagrams are given only for the quark–antiquark initial state, because all other diagrams can be obtained by crossing the outgoing gluon with one of the incoming partons.

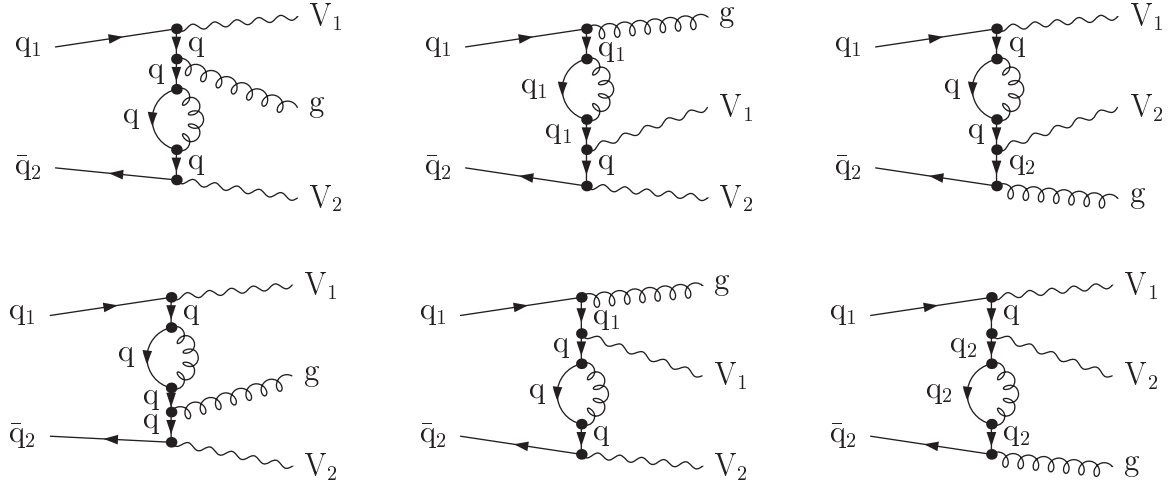


Figure 5.18: Self-energy diagrams with the two weak gauge bosons coupling directly to the fermion chain.

Diagrams without intermediate electroweak gauge bosons

The self-energy diagrams without intermediate electroweak gauge bosons are depicted in Figure 5.18. As for all other bosonic corrections with direct gauge-boson coupling to the fermion chain, each diagram contributing to ZZ+jet and WZ+jet production has to be taken into account for the two possible orders of the weak gauge bosons. In case of WW+jet production, the order of the two W bosons is determined by the charges of the external (anti-)quarks in the same way as in the LO diagrams.

Self-energy contributions to external partons can be omitted, since the renormalization conditions in the applied on-shell scheme for the wave functions are chosen in such a way that these contributions exactly cancel against the respective counterterm diagrams, which are consequently left out as well.

The vertex-correction diagrams are shown in Figure 5.19. Here, the vertices of both the massive gauge bosons and the gluon to the fermion chain receive NLO QCD corrections. The quark–gluon vertex receives further contributions involving a three-gluon-vertex due to the non-Abelian structure of QCD.

Also the box corrections contain diagrams with an exchange of a virtual gluon between two points on the fermion chain and further diagrams with a three-gluon vertex. These diagrams are depicted in Figure 5.20.

The same is true for the pentagon diagrams contributing to VV+jet production, which are shown in Figure 5.21.

Apart from the case of external bottom (anti-)quarks in WW+jet production, all internal masses appearing in the loop integrals vanish. On the one hand, this significantly simplifies the evaluation of the respective integrals. On the other side, the integrals show more infrared divergences, which are treated in dimensional regularization. All necessary

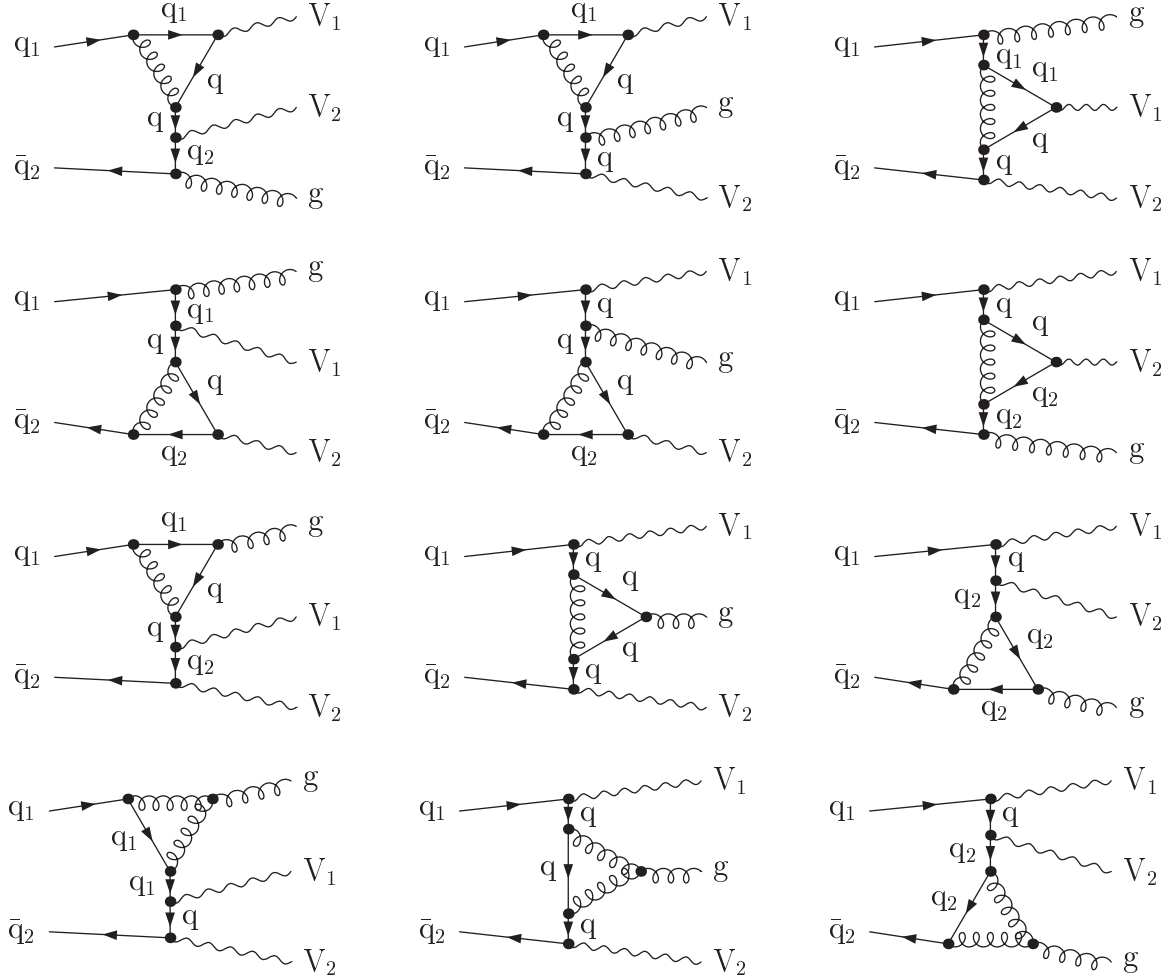


Figure 5.19: Vertex-correction diagrams with the two weak gauge bosons coupling directly to the fermion chain.

scalar integrals containing infrared singularities are collected in App. B.1 for vanishing internal masses. In case of external bottom (anti-)quarks, top propagators appear in the loops of some diagrams. However, due to the fact that the electroweak gauge bosons do not couple to gluons, the number of massive quark propagators in each loop is limited to no more than two neighbouring ones in all contributions up to pentagon diagrams. For the situation of an incoming $b\bar{b}$ pair, the needed divergent integrals with external masses are provided in App. B.2. Since the internal top quark does not show up in resonant propagators, no decay width has to be introduced, and hence all masses showing up in the loop integrals are real. This situation changes if a bottom–gluon or gluon–antibottom initial state is considered, where internal top-quark resonances arise making the introduction of a top width necessary. As a consequence, scalar integrals with up to two internal complex masses would be needed. Since the respective subprocesses are excluded in the analysis

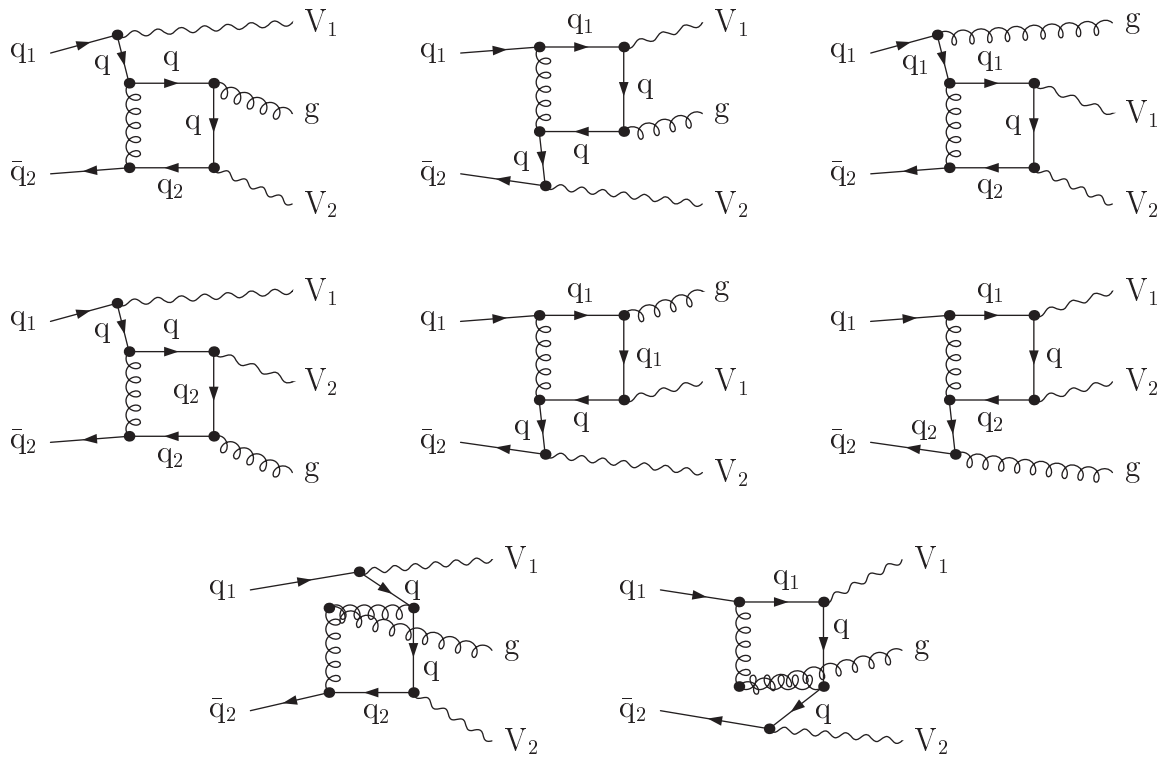


Figure 5.20: Box diagrams with the two weak gauge bosons coupling directly to the fermion chain.

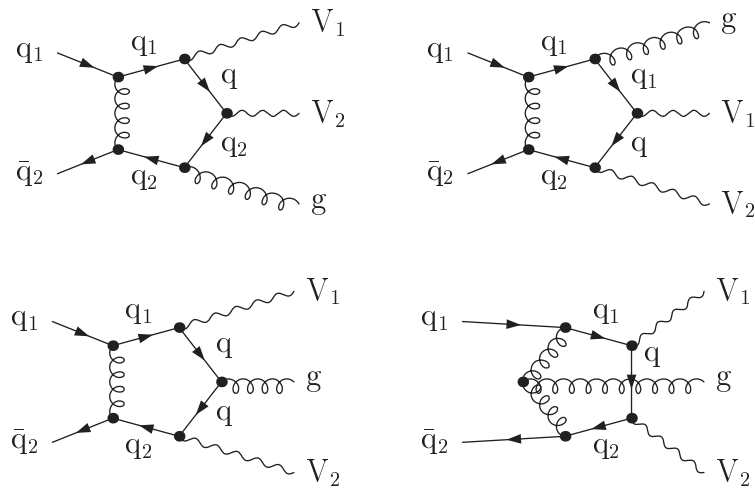


Figure 5.21: Pentagon diagrams.

of this thesis, because they actually contribute to the off-shell continuation of $W^+\bar{t}$ or W^-t production with a decaying top (anti-)quark, these integrals are not given here. If, however, these processes should be added to the $WW+\text{jet}$ analysis later on, the respective scalar integrals with complex internal masses have to be used.

Diagrams with an intermediate electroweak gauge boson

In the group of diagrams with the two outgoing gauge bosons coupling to the fermion chain by means of an intermediate vector boson and a three-gauge-boson vertex, only self-energy, vertex, and box corrections are present, because the virtual gluon does not couple to the electroweak gauge bosons. Since all internal masses vanish in the relevant loop integrals, the same scalar integrals as in the previous paragraph are needed.

As before, all self-energy corrections with respect to external particles are omitted due to the renormalization conditions. The remaining ones are presented in Figure 5.22.

The vertex diagrams, shown in Figure 5.23, deliver corrections to the couplings of both the electroweak gauge boson and the gluon to the quark chain. In the latter case, three-gluon vertices arise due to the non-Abelian structure of QCD.

Also the box corrections, which are depicted in Figure 5.24, receive contributions from simple gluon exchange between two points on the quark chain and from diagrams with a three-gluon vertex.

5.3.3 Fermionic corrections from closed quark loops

In the fermionic contributions, the major differences show up between the four gauge-boson assignments in $pp/p\bar{p} \rightarrow VV + \text{jet} + X$, which is mainly due to the gauge-boson charges.

Independent of these charges, for all gauge-boson assignments self-energy corrections to external gluons may be omitted, since the renormalization conditions are chosen to compensate these corrections of external wave functions.

$WW+\text{jet}$

The only fermionic vertex corrections arise from diagrams with an intermediate electroweak gauge boson, which are depicted in Figure 5.25. Diagrams with both W bosons attached directly to the loop are excluded by colour-charge conservation, such with only one W boson by electric charge conservation.

The box corrections containing both W bosons coupling directly to the quark loop are shown in Figure 5.26, where all diagrams contribute for the three quark generations. Both up- and down-type quarks are present in each loop, due to the two charged W bosons, and their order is again determined by the W charges. As in all previous cases with two W bosons coupling to the same fermionic chain, the CKM matrix can be treated as diagonal according to the unitarity argument in Eq. (3.2), which holds at least in the applied approximation of vanishing mixing between the two light quark generations and the third one.

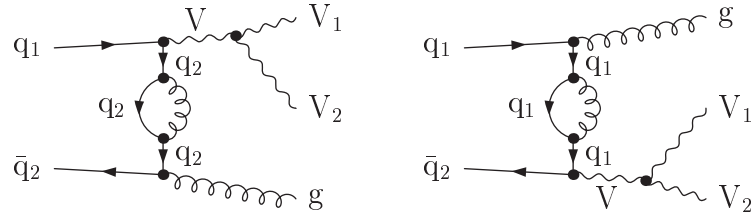


Figure 5.22: Self-energy diagrams with an intermediate electroweak gauge boson.

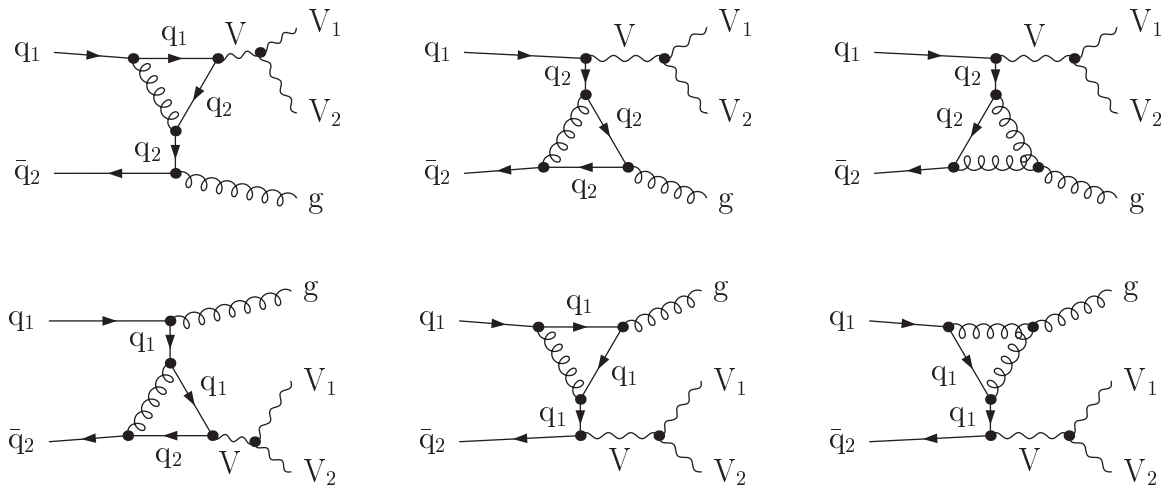


Figure 5.23: Vertex-correction diagrams with an intermediate electroweak gauge boson.

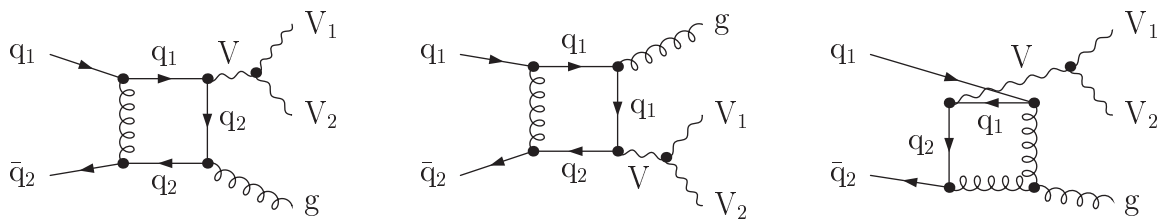


Figure 5.24: Box diagrams with an intermediate electroweak gauge boson.

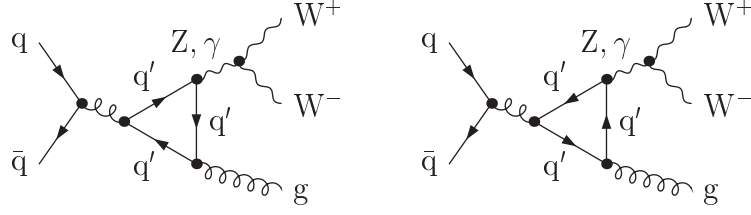


Figure 5.25: Fermionic vertex-correction diagrams to WW +jet production involving an intermediate Z boson/photon.

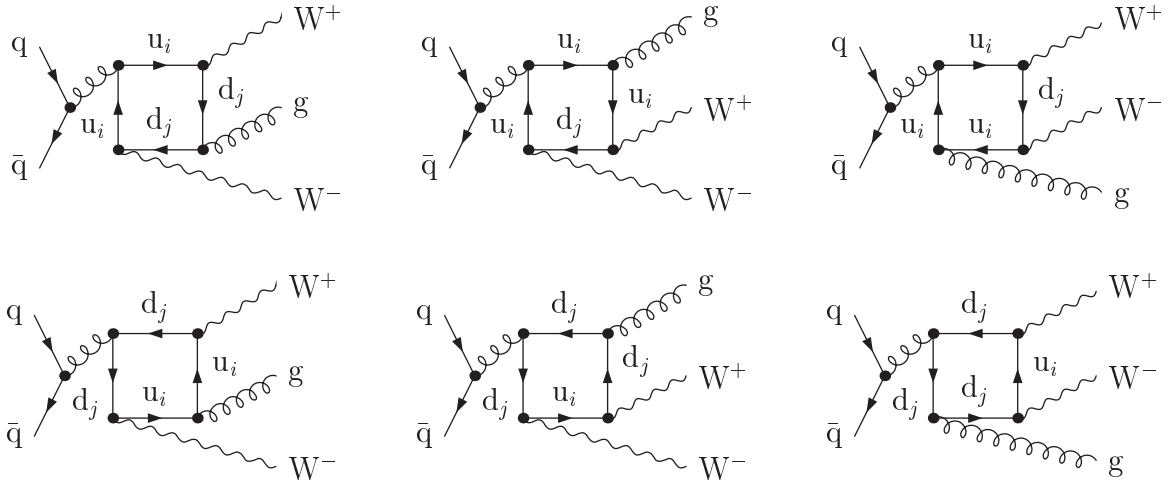


Figure 5.26: Fermionic box diagrams in WW +jet-production.

While the massive-quark loops in the vertex corrections do not lead to singular diagrams, those in the boxes do in case of a five-flavour calculation, where the mass of the bottom quark is set to zero. The resulting infrared-divergent scalar 4-point integrals with one or two neighbouring internal masses—those with more than two internal masses do not contain divergences—are collected in App. B.2 as well as the divergent lower-point functions arising in the tensor reduction of the boxes.

ZZ +jet

Since both gauge bosons are neutral in case of ZZ +jet production, the vertex corrections have one of the outgoing Z bosons and the external gluon attached. The respective diagrams are given in Figure 5.27. All six quark insertions contribute to the loops. Diagrams with both Z bosons coupling to the quark loop, which are allowed by electric charge conservation, have to vanish due to colour-charge conservation, since the intermediate gluon cannot decay into colourless particles only.

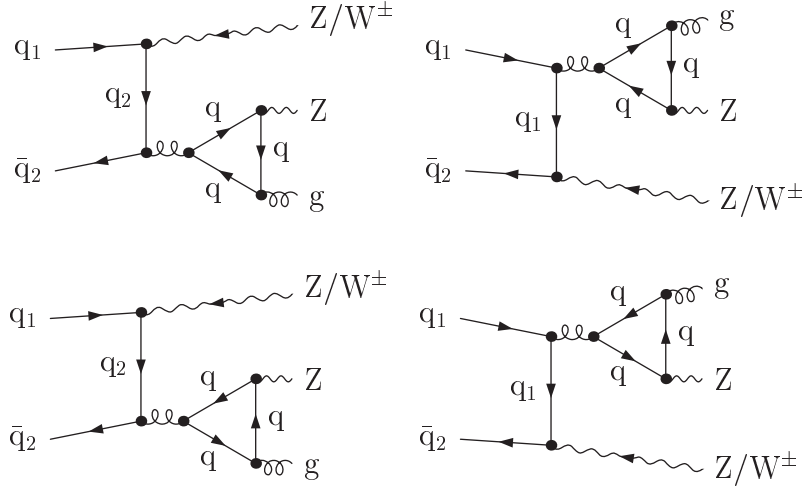


Figure 5.27: Fermionic vertex-correction diagrams contributing to ZZ+jet and WZ+jet production for the respective gauge-boson assignments.

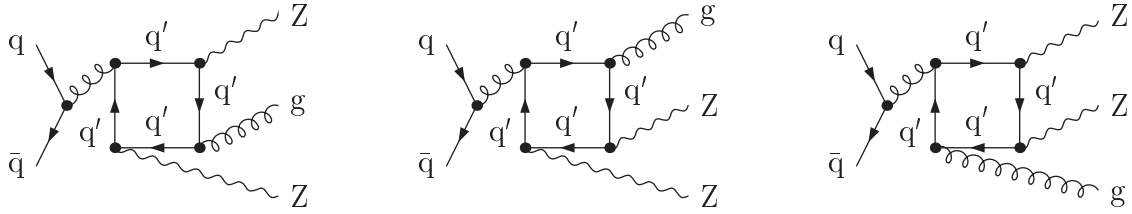


Figure 5.28: Fermionic box diagrams in ZZ+jet-production.

The box diagrams contributing to ZZ+jet production are depicted in Figure 5.28, where each diagram has to be taken into account for the two possible permutations of the Z bosons. Again, all six quark insertions have to be included for each diagram. Care has to be taken with respect to double-counting of diagrams, since an exchange of the direction of the fermion chain in the loop leads to exactly the same diagrams as exchanging the momentum assignments of the Z bosons. Consequently, only six instead of twelve diagrams contribute for each internal quark flavour.

The virtual corrections of both WW+jet and ZZ+jet production receive a further contribution including a heavy-quark loop and the weak-gauge-boson pair coupling by an intermediate Higgs boson, which are shown in Figure 5.29. In the five-flavour-scheme calculation, only the top-quark loop contributes, whereas in the four-flavour case with the bottom quark treated as a massive particle both quark loops of third-generation quarks show non-vanishing couplings to the Higgs boson. One could argue that these contributions should not be taken into account for WW+jet and ZZ+jet production, since these are

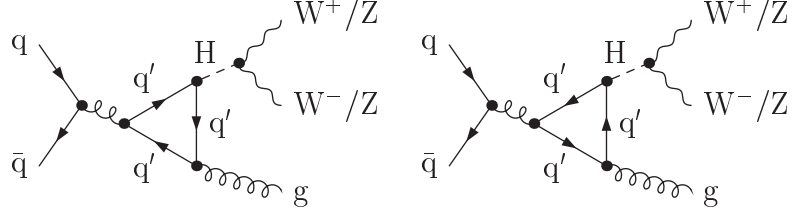


Figure 5.29: Fermionic vertex-correction diagrams with an intermediate Higgs boson contributing to $WW+\text{jet}$ and $ZZ+\text{jet}$ production, respectively.

both relevant as background processes to $H+\text{jet}$ production with a subsequent decay of the Higgs boson to the respective gauge-boson pair. Therefore, the diagrams of Figure 5.29 should better be assigned to the signal process in this case. However, their numerical impact turns out to be so small that the distinction is of no phenomenological meaning anyway.

WZ+jet

Due to the non-vanishing charge of the gauge-boson pair in $WZ+\text{jet}$ production, only diagrams with the Z boson attached to the closed quark loop and the W boson coupling to the external fermion chain contribute. These diagrams are depicted in Figure 5.27. The non-zero charge of the gauge-boson pair naturally forbids contributions with an intermediate Higgs boson.

5.3.4 Counterterm contribution

The counterterm contributions resulting from the renormalization procedure deliver a further contribution to the virtual corrections. Since the renormalization conditions are chosen in such a way that external self-energy and counterterm diagrams cancel, the respective contributions are omitted—as in the self-energy corrections described in the two previous subsections. The remaining diagrams can again be subdivided into diagrams with and without an intermediate gauge-boson and a three-gauge-boson vertex, whereat the former are not present in $ZZ+\text{jet}$ production. In both groups, counterterms contribute to the quark propagators, which are depicted in Figures 5.30 and 5.32, respectively. Further on, the vertices for massive gauge bosons and gluons coupling to a quark chain are renormalized leading to vertex counterterms, which are shown in Figures 5.31 and 5.33, respectively. As the virtual corrections, the counterterm contributions can be subdivided into bosonic and fermionic parts. However, not each diagram can be assigned to the bosonic or the fermionic corrections: Whereas the propagator-counterterm diagrams and the vertex-counterterm diagrams of the electroweak couplings contain only bosonic corrections, the vertex-counterterm diagrams of the strong couplings receive both bosonic and fermionic contributions.

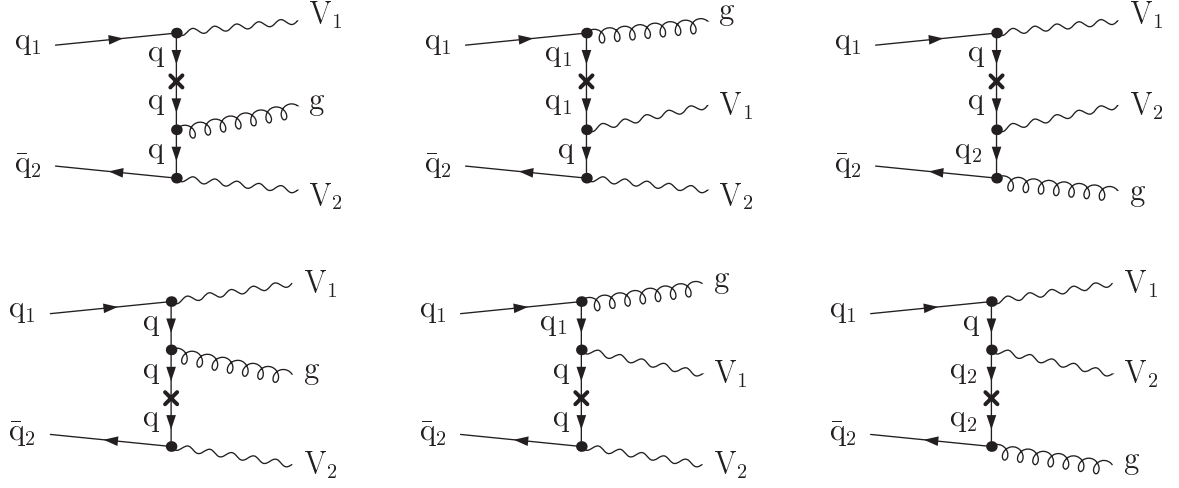


Figure 5.30: Propagator-counterterm diagrams without three-gauge-boson vertex.

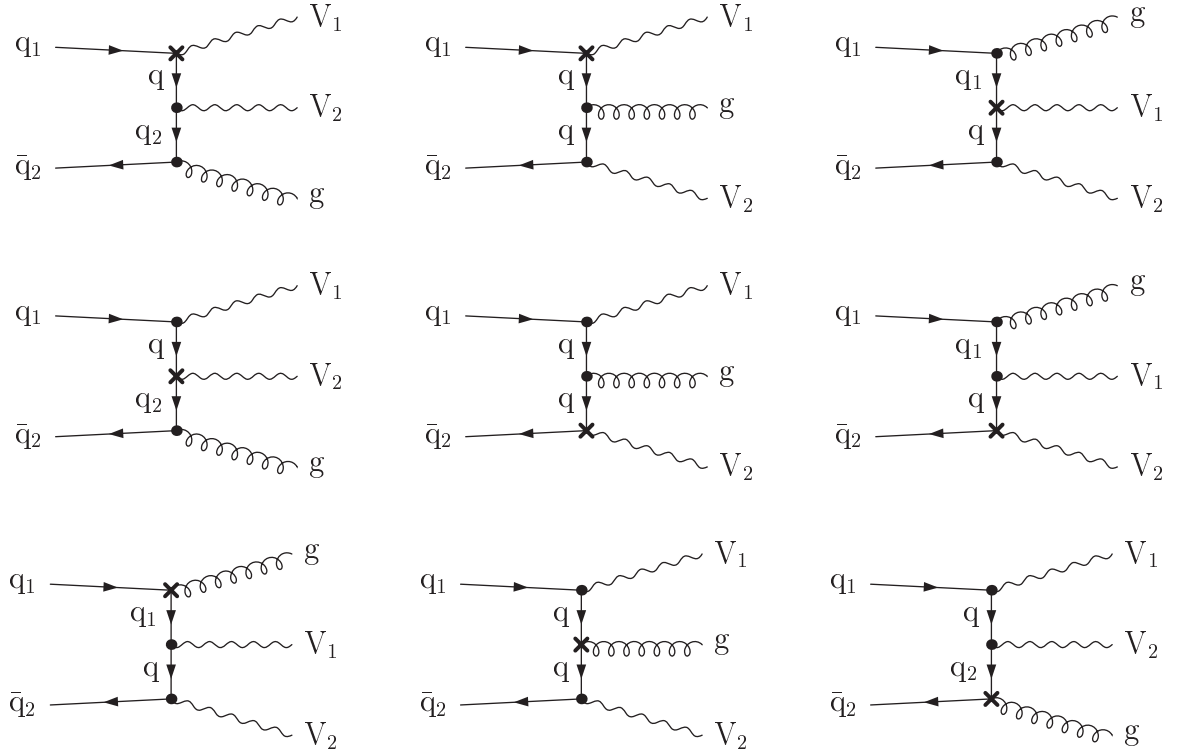


Figure 5.31: Vertex-counterterm diagrams without three-gauge-boson vertex.

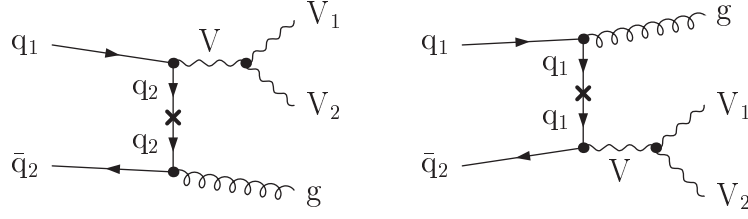


Figure 5.32: Propagator-counterterm diagrams with three-gauge-boson vertex.

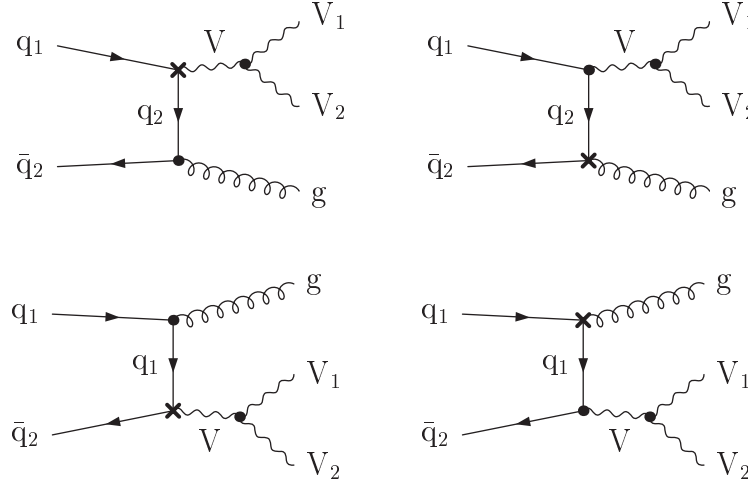


Figure 5.33: Vertex-counterterm diagrams with three-gauge-boson vertex.

If only massless quarks are involved, each counterterm diagram can be written as a factor times the respective LO diagram. If the sum is taken over all counterterm diagrams based on the same LO diagram, the resulting prefactor depends only on the external particles and the number of strong couplings, which are identical for all diagrams. (This selection corresponds to embracing the five diagrams in each column of Figures 5.30 and 5.31 for the case of direct gauge-boson coupling and the three diagrams in each column of Figures 5.32 and 5.33 for the contributions involving a three-gauge-boson vertex.) Therefore, the whole counterterm amplitude can be expressed as

$$\mathcal{M}_{ab,ct}(p_a, p_b; \dots p_i) = \left(\delta Z_q + \frac{1}{2} \delta Z_A + \delta Z_{g_s} \right) \mathcal{M}_{ab,LO}(p_a, p_b; \dots p_i) . \quad (5.94)$$

The renormalization constants are calculated as follows,

$$\delta Z_q = -\frac{C_F \alpha_s}{4\pi} (\Delta^{\text{UV}}(\mu) - \Delta_1^{\text{IR}}(\mu)) , \quad (5.95)$$

$$\delta Z_A = -\frac{\alpha_s}{2\pi} \left[\left(\frac{N_f}{3} - \frac{5}{2} \right) (\Delta^{\text{UV}}(\mu) - \Delta_1^{\text{IR}}(\mu)) + \frac{1}{3} \sum_{\substack{q \\ m_q \neq 0}} \left(\Delta_1^{\text{IR}}(\mu) + \ln \frac{M_W^2}{m_q^2} \right) \right] , \quad (5.96)$$

$$\delta Z_{g_s} = \frac{\alpha_s}{4\pi} \left[\left(\frac{N_f}{3} - \frac{11}{2} \right) \left(\Delta^{\text{UV}}(\mu) - \ln \frac{\mu_{\text{ren}}^2}{M_W^2} \right) + \frac{1}{3} \sum_{\substack{q \\ m_q \neq 0}} \left(\Delta_1^{\text{IR}}(\mu) + \ln \frac{M_W^2}{m_q^2} \right) \right]. \quad (5.97)$$

I.e., an on-shell renormalization of the wave functions of the external QCD partons and a $\overline{\text{MS}}$ renormalization for the strong coupling is performed with the massive-quark loops in the gluon self-energy subtracted at zero momentum. Hence, the sum over q runs over all massive quarks, namely $q = t$ in the five-flavour scheme and $q = b, t$ in the four-flavour scheme. In contrast to the usual dimensional regularization scheme, IR and UV divergences are distinguished in the scheme applied in this thesis. Otherwise, the renormalization constant of the quark wave function (5.95) would be zero.

If massive quarks are involved as internal particles, as the top quark is for WW+jet subprocesses with external bottom (anti-)quarks, the LO amplitude does not simply factorize. Instead, additional contributions arise from all diagrams involving a top-mass counterterm, which are shown in Figure 5.30 for $q = t$. With the contribution proportional to δZ_t omitted, because it always cancels against the respective vertex-counterterm diagrams, this additional term reads

$$\begin{aligned} & \mathcal{M}_{ab, \delta m_t}(p_a, p_b; \dots p_i) \\ &= \frac{\delta m_t}{m_t} \times \left(\frac{2m_t^2}{k_t^2 - m_t^2} \mathcal{M}_{ab, \text{LO } t\text{-diag}}(p_a, p_b; \dots p_i) + \mathcal{M}_{ab, \text{LO } t\text{-diag}}(p_a, p_b; \dots p_i) \Big|_{\propto m_t} \right), \end{aligned} \quad (5.98)$$

where k_t denotes the momentum of the top propagator and $\mathcal{M}_{\text{LO } t\text{-diag}}$ the amplitude of the respective LO diagram. The second term in brackets means only the part of the LO amplitude that is proportional to m_t from the top propagator, which arises—in terms of the WvdW formalism—from the diagonal elements of the fermionic propagator given in Table 4.3. This term turns out to contribute only in diagrams with two top propagators, namely those in the left column of Figure 5.30, because the contribution proportional to m_t vanishes otherwise. The top-mass counterterm is given by

$$\frac{\delta m_t}{m_t} = -\frac{\alpha_s}{3\pi} (3\Delta^{\text{UV}}(\mu) + 4). \quad (5.99)$$

With the results from the two previous sections, the one-loop matrix elements in Eq. (5.18) can be evaluated via

$$\begin{aligned} |\overline{\mathcal{M}_{ab, 1\text{-loop}}(p_a, p_b; \dots p_i)}|^2 &= \frac{f_{\text{sym}}}{N_{c_a} N_{\sigma_a} N_{c_b} N_{\sigma_b}} \sum_{\sigma_a, \sigma_b, \dots, \sigma_i} \sum_{c_a, c_b, c_i} 2 \text{Re} \{ \mathcal{M}_{\text{LO}}^*(p_a, p_b; \dots p_i) \\ &\quad \times (\mathcal{M}_{ab, \text{virt}}(p_a, p_b; \dots p_i) + \mathcal{M}_{ab, \text{ct}}(p_a, p_b; \dots p_i)) \}, \end{aligned} \quad (5.100)$$

where $\sigma_a, \sigma_b, \dots, \sigma_i$ are the spins of all external particles and c_a, c_b, c_i the colours of the QCD partons. N_σ and N_c are spin- and colour-averaging factors of the initial-state partons, and f_{sym} is the symmetry factor for identical outgoing particles, which are all identical to those in the LO matrix elements.

5.3.5 Contribution from integrated subtraction counterterms

The infrared divergences contained in Eq. (5.100) in terms of poles $\frac{1}{\varepsilon}$ and $\frac{1}{\varepsilon^2}$ cancel against the respective parts of the dipole terms integrated over the one-particle phase space. This dipole contribution can be written as the averaged LO matrix element times a factor containing the infrared poles, which can be determined from the general formulae in Ref. [62]. The symbolic term in Eq. (5.18) then reads

$$\begin{aligned}
\int_1 d\hat{\sigma}_{ab}^{\text{AV}}(p_a, p_b; \dots p_i) &= -\frac{\alpha_s}{2\pi} \sum_{\{m\}} \frac{1}{4} \overline{|\mathcal{M}_{ab}^{\text{LO}}(p_a, p_b; \dots, p_i)|^2} \\
&\times \left\{ -2 C_A \left[2\Delta_2^{\text{IR}}(\mu) + \Delta_1^{\text{IR}}(\mu) \left(\frac{11}{3} - \ln \frac{2p_a p_i}{M_W^2} - \ln \frac{2p_b p_i}{M_W^2} \right) \right. \right. \\
&\quad \left. \left. + \frac{1}{2} \left(\ln^2 \frac{2p_a p_i}{M_W^2} - \ln^2 \frac{2p_b p_i}{M_W^2} \right) - \frac{11}{6} \left(\ln \frac{2p_a p_i}{M_W^2} + \ln \frac{2p_b p_i}{M_W^2} \right) + \frac{100}{9} - \frac{4\pi^2}{3} \right] \right. \\
&\quad \left. - \frac{9}{2} C_F \left[2\Delta_2^{\text{IR}}(\mu) + \Delta_1^{\text{IR}}(\mu) \left(3 - \ln \frac{2p_a p_i}{M_W^2} - \ln \frac{2p_b p_i}{M_W^2} \right) \right. \right. \\
&\quad \left. \left. + \frac{1}{2} \left(\ln^2 \frac{2p_a p_i}{M_W^2} - \ln^2 \frac{2p_b p_i}{M_W^2} \right) - \frac{3}{2} \left(\ln \frac{2p_a p_i}{M_W^2} + \ln \frac{2p_b p_i}{M_W^2} \right) + 10 - \frac{4\pi^2}{3} \right] \right. \\
&\quad \left. + \frac{1}{2} C_F \left[2\Delta_2^{\text{IR}}(\mu) + \Delta_1^{\text{IR}}(\mu) \left(3 - 2 \ln \frac{2p_a p_b}{M_W^2} \right) + \ln^2 \frac{2p_a p_b}{M_W^2} - 3 \ln \frac{2p_a p_b}{M_W^2} + 10 - \frac{4\pi^2}{3} \right] \right. \\
&\quad \left. - 2 N_f T_R \left[-\frac{4}{3} \Delta_1^{\text{IR}}(\mu) + \frac{2}{3} \left(\ln \frac{2p_a p_i}{M_W^2} + \ln \frac{2p_b p_i}{M_W^2} \right) - \frac{32}{9} \right] \right\} + \mathcal{O}(\varepsilon), \tag{5.101}
\end{aligned}$$

where simplifications between different contributions are not performed in order not to hide the origin of the respective terms. The factor $\frac{1}{4}$ in front of the LO matrix element compensates the colour factor contained in Eq. (4.58). This factor must not appear here, because the $\text{SU}(3)_C$ generators from the LO amplitudes are to be combined with those arising from the dipole terms, leading to the numerical factors in front of each colour charge in Eq. (5.101). The divergences $\Delta_1^{\text{IR}}(\mu)$ and $\Delta_2^{\text{IR}}(\mu)$ are defined in App. B.

The sum of the expressions in Eqs. (5.100) and (5.101) is both ultraviolet and infrared finite. Therefore, the four-dimensional limit can be taken in Eq. (5.18) after cancelling the divergences, which is done either analytically or numerically, where the latter means setting the divergences technically to an arbitrary value. Since the result must be independent of this value, its variation can be used as a numerical check on the finiteness of the result.

Since initial and final states of the virtual-correction subprocesses are identical to those in the LO case, the numerical phase-space integration can be performed in the same way, as described in Chapter 7.

5.4 Collinear-subtraction counterterms

The collinear-subtraction counterterm accounts for contributions from collinear emission off one of the incoming partons before entering the hard scattering process. Such emissions are included in the real corrections in a perturbative way, leading to initial-state singularities that actually originate from the non-applicability of perturbation theory for low momentum transfers. The factorization scale denotes the scale up to which such an emission is understood as collinear and, therefore, is assigned to the non-perturbatively described hadron structure. This contribution can be written in terms of a PDF redefinition to compensate for the divergences, as described in the following subsection. The PDF, however, receives an additional dependence on the factorization scale. Since its value is chosen arbitrarily, the dependence on it is artificial and must decrease when going to higher orders in perturbation theory.

5.4.1 Redefinition of PDFs

As mentioned in the beginning of this chapter, the remaining infrared divergences, which do not cancel between virtual and real corrections, are process independent and can therefore be absorbed into the structure of the incoming hadrons, which is described non-perturbatively via PDFs. How this absorption can be understood as a redefinition of PDFs is illustrated by considering the contribution of the first term in Eq. (5.13) to the NLO cross section, which is—taken alone—infrared divergent and correspondingly contains poles $\frac{1}{\varepsilon}$ in $D = 4 - 2\varepsilon$ dimensions. As shown in Ref. [62], this contribution can—up to terms of $\mathcal{O}(\varepsilon)$ —be written as

$$\begin{aligned}
& \sum_a \int_0^1 dx_1 f_a(x_1, \mu_{\text{fact}}) d\hat{\sigma}_{ab}^{\text{C}}(p_a, p_b) \Big|_{a \rightarrow a'} \\
&= \sum_a \int_0^1 dx_1 \int_0^1 dz_1 f_a(x_1, \mu_{\text{fact}}) \sum_{a'} P^{aa'}(z_1) \frac{\alpha_s}{2\pi} \frac{\Gamma(1+\varepsilon)}{\varepsilon} \left(\frac{4\pi\mu^2}{\mu_{\text{fact}}^2} \right)^\varepsilon d\hat{\sigma}_{a'b}^{\text{B}}(z_1 x_1 p_a, x_2 p_b) \\
&= \sum_{a,a'} \int_0^1 d\xi_1 \int_{\xi_1}^1 \frac{dz_1}{z_1} f_a\left(\frac{\xi_1}{z_1}, \mu_{\text{fact}}\right) P^{aa'}(z_1) \frac{\alpha_s}{2\pi} \frac{\Gamma(1+\varepsilon)}{\varepsilon} \left(\frac{4\pi\mu^2}{\mu_{\text{fact}}^2} \right)^\varepsilon d\hat{\sigma}_{a'b}^{\text{B}}(\xi_1 p_a, x_2 p_b) \\
&= \sum_a \int_0^1 dx_1 f_a^{\text{C}}(x_1, \mu_{\text{fact}}; \varepsilon) d\hat{\sigma}_{ab}^{\text{B}}(x_1 p_a, x_2 p_b) , \\
& f_a^{\text{C}}(x_1, \mu_{\text{fact}}; \varepsilon) = \int_{x_1}^1 \frac{dz_1}{z_1} \sum_{a'} f_{a'}\left(\frac{x_1}{z_1}, \mu_{\text{fact}}\right) P^{a'a}(z_1) \frac{\alpha_s}{2\pi} \frac{\Gamma(1+\varepsilon)}{\varepsilon} \left(\frac{4\pi\mu^2}{\mu_{\text{fact}}^2} \right)^\varepsilon , \quad (5.102)
\end{aligned}$$

where the first equation just repeats the definition, and a transformation of the integration variables is performed in the second equation. In the third equation, the sums over a and a' are interchanged, and a definition for the NLO correction to the PDF is introduced, accompanied by a renaming of summation indices and integration variables. The functions $P^{aa'}$ are the Altarelli–Parisi splitting functions, which are given in App. A.2, and μ_{fact} denotes the factorization scale.

5.4.2 Combined contribution of collinear terms and integrated dipoles

The cancellation of divergences between the collinear-subtraction counterterms and the second part of the re-added subtraction terms, where the integration over the longitudinal momentum fraction carried by one of the incoming partons is not performed analytically, can be performed generically as discussed in Ref. [62]. The result for the sum of both contributions on the right-hand side of Eq. (5.19), which is finite and can therefore be evaluated in four dimensions, is given by

$$\begin{aligned}
\hat{\sigma}_{ab}^{\text{C+A}}(p_a, p_b) = & \frac{f_{\text{sym}}}{N_{c_a} N_{\sigma_a} N_{c_b} N_{\sigma_b}} \sum_{\sigma_a, \sigma_b, \dots, \sigma_i} \sum_{c_a, c_b, c_i} \sum_c \int_0^1 dz \\
& \times \left\{ d\Phi^{(m)}(zp_a, p_b) F_{\text{jet}}^{(m)}(zp_a, p_b; \dots, p_i) \mathcal{M}_{cb, \text{LO}}^*(zp_a, p_b; \dots p_i) \right. \\
& \quad \times (\mathbf{K}^{a,c}(z) + \mathbf{P}^{a,c}(zp_a, z; \mu_{\text{fact}}^2)) \mathcal{M}_{cb, \text{LO}}(zp_a, p_b; \dots p_i) \\
& \quad + d\Phi^{(m)}(p_a, zp_b) F_{\text{jet}}^{(m)}(p_a, zp_b; \dots, p_i) \mathcal{M}_{ac, \text{LO}}^*(p_a, zp_b; \dots p_i) \\
& \quad \left. \times (\mathbf{K}^{b,c}(z) + \mathbf{P}^{b,c}(zp_b, z; \mu_{\text{fact}}^2)) \mathcal{M}_{ac, \text{LO}}(p_a, zp_b; \dots p_i) \right\}, \quad (5.103)
\end{aligned}$$

where $\sigma_a, \sigma_b, \dots, \sigma_i$ are the spins of the external particles, c_a, c_b, c_i the colour indices of the QCD partons, N_σ and N_c the averaging factors for initial-state partons and f_{sym} the symmetry factor for identical final-state particles. The colour-charge operators \mathbf{K} and \mathbf{P} are collected in Section A.2.

The numerical integration of this contribution is performed as for the LO subprocesses in general, but with an additional integration over the longitudinal momentum fraction carried by one of the incoming partons, which is denoted by z in Eq. (5.103). Since some of the colour-charge operators \mathbf{K} and \mathbf{P} contain both δ -functions and $+$ -distributions, namely those containing gg, qq, or $\bar{q}q$ splittings, the numerical integration becomes more involved. The treatment of the arising complications is shifted to Chapter 7.

Chapter 6

Inclusion of gauge-boson decays

In the previous chapter, the calculation of $pp/p\bar{p} \rightarrow VV + \text{jet} + X$ at NLO QCD accuracy is described with the respective gauge bosons treated as stable particles. Naturally, this is not the situation in real experiments, so the inclusion of gauge-boson decays has to be considered.

In Section 6.1, different strategies for the description of gauge-boson decays are discussed. First, the full calculation with intermediate off-shell gauge bosons is considered. Consequently, further diagrams contributing to the same leptonic final state, which only contain one resonant gauge-boson propagator, have to be taken into account for reasons of gauge invariance. Since all diagrams without a doubly-resonant structure should be significantly suppressed and also off-shell effects are not expected to play a decisive role, two approximations are applied to simplify the calculation: In the so-called “narrow width approximation” (NWA), unpolarized gauge bosons are produced as on-shell particles, which then decay isotropically in their respective rest frames. Afterwards, an improved version of the NWA is introduced, where the spin information of the produced gauge bosons is kept for the description of the decays, but the gauge bosons are still treated as on-shell particles.

In Section 6.2, the additional building blocks needed for the evaluation of helicity amplitudes including gauge-boson decays are presented both for the improved NWA and for the full calculation. For performing the simple NWA, no further calculations are needed.

In Section 6.3, the generic way how to implement the building blocks describing the gauge-boson decays into the matrix-element calculation of Chapter 4 is explained. In the improved NWA, the NLO QCD calculation of Chapter 5 is not affected at all apart from some trivial changes. In the full calculation, a number of additional singly-resonant diagrams has to be introduced, which does, however, not lead to a significant complication of the singularity structure.

6.1 Strategies for the description of leptonic gauge-boson decays

Since the massive gauge bosons are unstable particles, their decays should be included into the analysis. In this context, especially the cases of both gauge bosons decaying into as many charged leptons as possible—i.e. W bosons decay to lepton–neutrino pairs, Z bosons to two charged leptons—is of interest due to its clean signature in the detector. Besides, the appearance of quarks and antiquarks in case of a semileptonic or even purely hadronic decay of the gauge-boson pair would render the calculation of NLO QCD corrections much more complicated, since the decay products would have to be implicated into the NLO calculation leading, e.g., to hexagon or even heptagon diagrams in the virtual corrections. From a phenomenological point of view, those processes whose signature would be $V(\rightarrow 2\text{leptons}) + 3\text{jets}$ in the semi-leptonic case and only 5jets in the purely hadronic case are dominated by large backgrounds from jet production via pure QCD processes.

For these reasons, only leptonic gauge-boson decays are considered in this thesis. The inclusion of the decays is performed by means of three different strategies for the LO processes, which are presented in the following paragraphs. From a comparison of these LO results, which will be presented in Section 8.5, the improved NWA turns out to be an appropriate compromise between complexity of the calculations and accuracy of the results. Therefore, the NLO calculation is performed by means of the improved NWA.

6.1.1 Full calculation with off-shell gauge bosons

In the calculation of full amplitudes for the processes of $pp/p\bar{p} \rightarrow VV + \text{jet} + X$, the diagrams contributing to the subprocesses can be subdivided into two classes, namely diagrams showing two gauge-boson propagators that can become resonant and other diagrams containing less resonances.

The generic doubly-resonant diagrams are presented in Figure 6.1 for one generic LO subprocess. All other subprocesses can be obtained from this by means of crossing symmetry. The doubly-resonant diagrams contain all the VV +jet-production diagrams of Figures 3.6 and 3.7 with the two massive gauge bosons decaying to leptons. Moreover, further diagrams showing the same structure contribute in case of WZ +jet and ZZ +jet production, since each intermediate Z boson can be replaced by a photon. The resulting diagrams even show divergences if the virtuality of an intermediate photon approaches zero. These phase-space regions are, however, excluded by cuts on the invariant masses of lepton–antilepton pairs. Such cuts are justified experimentally, since both the lepton and the antilepton are detected. It is convenient to restrict these invariant masses to the region around the mass of the Z boson, since the phase-space region where the process is actually interesting—e.g. as a background process for $H(\rightarrow ZZ^*) + \text{jet}$ production—contains only outgoing leptons from resonant Z bosons.

Aside from this doubly-resonant group, a number of diagrams that in general contain only one or even no resonant gauge-boson propagator contribute to the subprocesses.

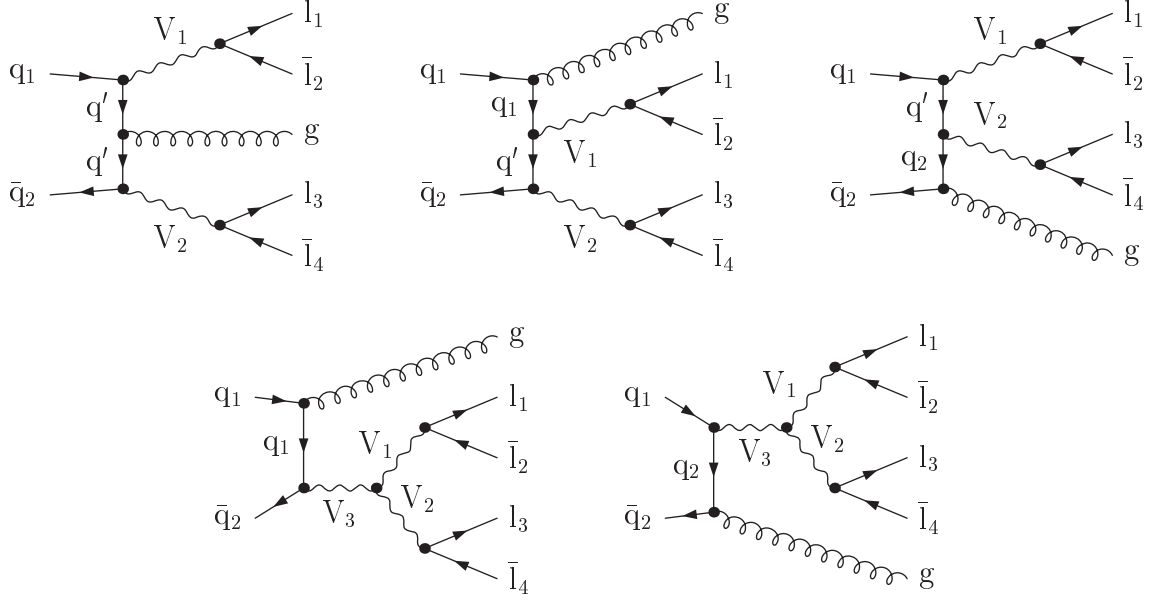


Figure 6.1: Generic diagrams with two resonant gauge-boson propagators (referred to as “doubly-resonant” diagrams) contributing to the partonic process $q_1 \bar{q}_2 \rightarrow l_1 \bar{l}_2 l_3 \bar{l}_4 g$ at LO. The second row only contributes if a non-vanishing three-gauge-boson vertex exists. Diagrams for all possible assignments of (anti-)leptons and gauge bosons leading to the same final state contribute.

Their topologies are characterized by the situation that one gauge boson decays to a lepton–antilepton pair with the second pair attached to this leptonic fermion chain by means of a second gauge boson. Generic diagrams illustrating this situation are given in Figure 6.2. For WZ+jet and ZZ+jet with leptonic decays, infrared singularities show up from $\gamma \rightarrow l^- l^+$ splittings, which are again cut away by restricting the invariant mass of the lepton–antilepton pair to the region around the Z-boson mass.

The singularities appearing at the poles of the LO gauge-boson propagators are treated by introduction of a decay width arising from a partial Dyson resummation of self-energy contributions to the propagator. The gauge-boson widths are introduced in terms of complex gauge-boson masses according to the complex-mass scheme at LO, which is described in Ref. [69]. For the LO amplitudes considered here, this means replacing

$$M_W^2 \rightarrow M_W^2 - i\Gamma_W M_W, \quad M_Z^2 \rightarrow M_Z^2 - i\Gamma_Z M_Z. \quad (6.1)$$

To preserve gauge invariance, the gauge-boson masses have to be treated as complex quantities everywhere, in particular in the definition of the weak mixing angle,

$$\cos \theta_W = \frac{M_W^2}{M_Z^2} \rightarrow \frac{M_W^2 - i\Gamma_W M_W}{M_Z^2 - i\Gamma_Z M_Z}, \quad (6.2)$$

and all couplings derived from this quantity. The values of the gauge-boson widths are

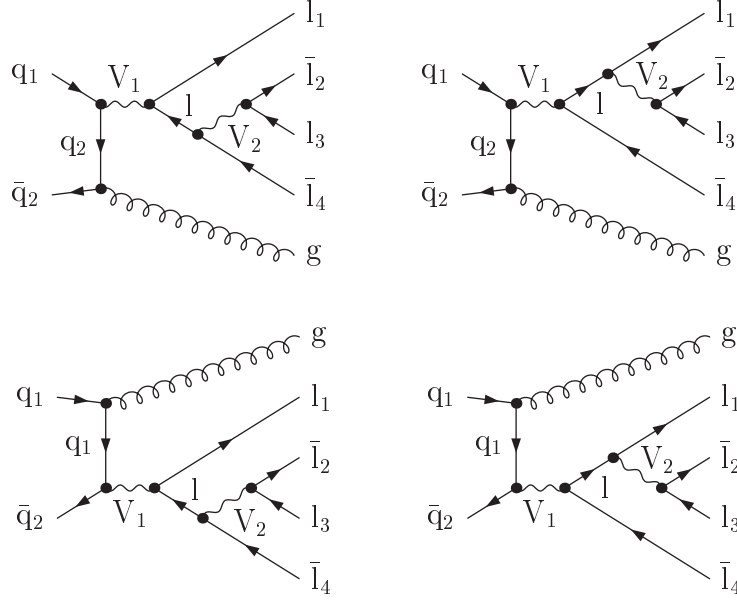


Figure 6.2: Generic diagrams with only one resonant gauge-boson propagator (referred to as "singly-resonant" diagrams) contributing to the generic partonic process $q_1 \bar{q}_2 \rightarrow l_1 \bar{l}_2 l_3 \bar{l}_4 g$ at LO. Further permutations of the leptons l_1, l_3 and antileptons \bar{l}_2, \bar{l}_4 contribute depending on the specific lepton and gauge-boson assignments. All intermediate particles have to be summed over all possible insertions.

calculated at NLO QCD level with vanishing fermion masses,

$$\Gamma_W = \frac{\alpha}{6} M_W \left[\sum_l (C_{Wl}^-)^2 + \sum_{u,d} (C_{Wud}^-)^2 \left(1 + \frac{\alpha_s(M_Z)}{\pi} \right) \right], \quad (6.3)$$

$$\Gamma_Z = \frac{\alpha}{6} M_Z \left[\sum_l ((C_{Zl}^+)^2 + (C_{Zl}^-)^2) + \sum_{q \neq t} ((C_{Zq}^+)^2 + (C_{Zq}^-)^2) \left(1 + \frac{\alpha_s(M_Z)}{\pi} \right) \right]. \quad (6.4)$$

In Eq. (6.3), the sums run over all three lepton generations and the two light-quark families, in Eq. (6.4) over the three charged leptons and neutrinos and the five light quarks.

The rules for a consistent treatment of unstable particles in the complex-mass scheme at NLO are collected in Refs. [70, 71]. They are not presented in detail in this thesis, since an NLO calculation using full amplitudes is not necessary for obtaining hadron-collider accuracy, since the improved NWA turns out to be an appropriate approximation.

6.1.2 Narrow-width approximation

In the NWA, the produced gauge bosons are treated as on-shell particles in the production process. The leptonic decays are understood as isotropic in the rest frames of the respective gauge bosons, because their spin information from the production process is dropped. Therefore, the matrix elements of the VV+jet-production subprocesses can be used without

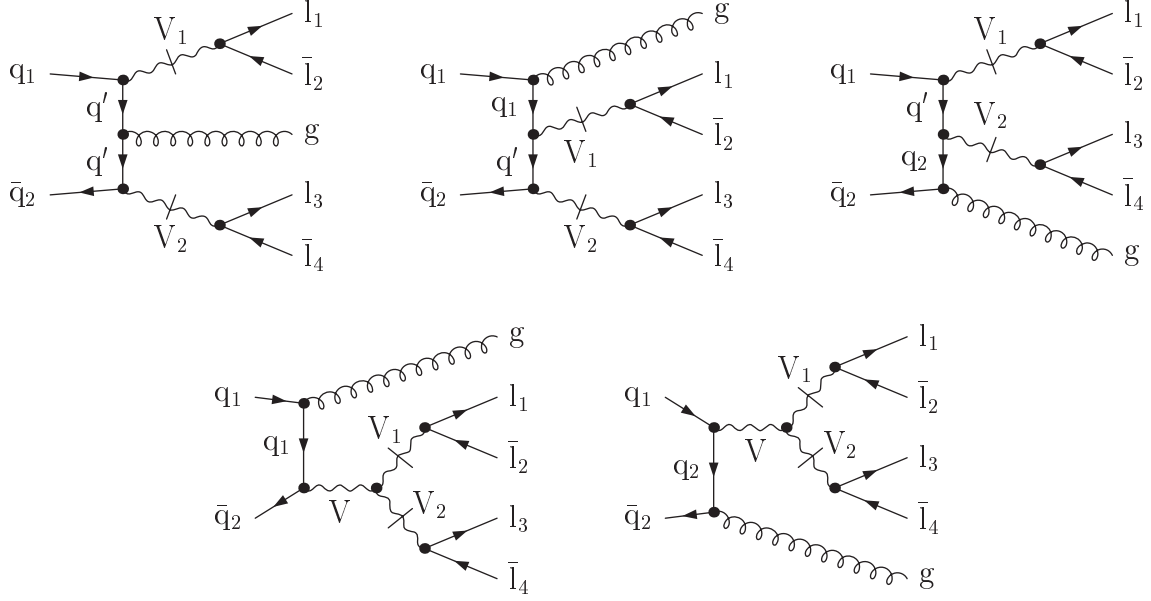


Figure 6.3: NWA diagrams with two on-shell gauge-boson propagators for the generic partonic process $q_1 \bar{q}_2 \rightarrow V_1(\rightarrow l_1 \bar{l}_2) V_2(\rightarrow l_3 \bar{l}_4) g$ at LO. The on-shell propagators are denoted by the dash perpendicular to the propagator line. In the first row, the order of gauge bosons is prescribed by the charges of the external quark–antiquark pair in WW+jet production. In WZ+jet and ZZ+jet production, the diagrams also contribute for V_1 and V_2 with their respective decay leptons interchanged.

modifications by only introducing the respective branching ratios for the Z- and W-boson decays, which are given by

$$\text{BR}_{W^+ \rightarrow \nu_l l^+} = \frac{\Gamma_{W^+ \rightarrow \nu_l l^+}}{\Gamma_W}, \quad \text{BR}_{W^- \rightarrow l^- \bar{\nu}_l} = \frac{\Gamma_{W^- \rightarrow l^- \bar{\nu}_l}}{\Gamma_W}, \quad \text{BR}_{Z \rightarrow l^- l^+} = \frac{\Gamma_{Z \rightarrow l^- l^+}}{\Gamma_Z}. \quad (6.5)$$

The partial widths for leptonic gauge-boson decays are

$$\Gamma_{W^+ \rightarrow \nu_l l^+} = \Gamma_{W^- \rightarrow l^- \bar{\nu}_l} = \frac{\alpha}{6} M_W (C_{W \bar{\nu}_l l}^-)^2, \quad (6.6)$$

$$\Gamma_{Z \rightarrow l^- l^+} = \frac{\alpha}{6} M_Z ((C_{Z l^+ l^-}^+)^2 + (C_{Z l^+ l^-}^-)^2), \quad (6.7)$$

since the leptonic gauge-boson decays do not receive NLO QCD corrections.

Consequently, the approximation of on-shell gauge bosons restricts the diagrams contributing to the respective subprocesses of $pp/p\bar{p} \rightarrow VV + \text{jet} + X$ to those containing two resonant gauge-boson propagators, which stand in one-to-one correspondence to the pure gauge-boson pair production diagrams in Figures 3.6 and 3.7. The analogous NWA diagrams are collected in Figure 6.3 for one LO subprocess.

6.1.3 Improved narrow-width approximation

In the comparison that will be presented in Section 8.5 for LO calculations, the simple NWA turns out to deliver only a rough approximation of the full evaluation. Whereas the integrated cross sections show modest deviations between the full amplitude calculation and the simple NWA, discrepancies of up to 20% arise in some phase-space regions if differential cross sections are considered.

An appropriate compromise between full calculation and naive NWA is yielded by an improved version of the NWA. Here, the gauge bosons are still treated as on-shell particles, but their spin information is kept. This information is known from the fact that helicity amplitudes have been used for calculating the production amplitudes. It is used to improve the description of the leptonic gauge-boson decays, which are not isotropic in the respective gauge-boson rest frames anymore.

The diagrams contributing to the LO subprocesses are again given by Figure 6.3 for one specific channel, while the others can be obtained from this by application of crossing symmetry. The modification of amplitudes is essentially the same for LO subprocesses and all contributions to the NLO QCD cross section: the polarization vector/bispinor of each of the outgoing gauge bosons is replaced by the leptonic currents of its decay products. For the rest of the amplitude, the momenta of the gauge bosons are set on shell. The Breit–Wigner propagators arising in the absolute square of the amplitudes are separated. They are replaced by delta functions with an appropriate normalization obtained by integrating over the Breit–Wigner propagator in the limit $\Gamma_V \rightarrow 0$. Details on this procedure will be given in the following section and in Section 7.2.

Since the improved NWA turns out to reproduce the full calculation to sufficient accuracy in the LO comparison of Section 8.5, this strategy for describing the leptonic decays is applied for the NLO QCD calculations in this thesis.

6.2 Building blocks for leptonic gauge-boson decays

Analogously to Section 4.2, the building blocks needed for the extension of the helicity amplitudes in the WvdW formalism to decaying gauge bosons are provided. In addition to the assignments of Tables 4.5 and 4.6, the definitions of Table 6.1 are used in the description of the outgoing leptons.

(Anti-)lepton	momentum vector	spinor	momentum bispinor
outgoing lepton	l_1^μ	λ_A	$L_{1,\dot{A}B}$
outgoing antilepton	l_2^μ	λ'_A	$L_{2,\dot{A}B}$
outgoing lepton	l_3^μ	ξ_A	$L_{3,\dot{A}B}$
outgoing antilepton	l_4^μ	ξ'_A	$L_{4,\dot{A}B}$

Table 6.1: Notation of momenta, spinors and bispinors of the outgoing (anti-)leptons.

For calculating the doubly-resonant amplitudes shown in Figure 6.1, only the following block is needed to describe the decay of a gauge boson into two leptons, which is—apart from the colour structure—identical to the subdiagram described in Eq. (4.19), namely

$$\mathcal{A}\left(V\left[\begin{smallmatrix} a \\ l_1+l_2 \\ v \end{smallmatrix}\right] \rightarrow l_1\left[\begin{smallmatrix} l_1 \\ \lambda \end{smallmatrix}\right] \bar{l}_2\left[\begin{smallmatrix} l_2 \\ \lambda' \end{smallmatrix}\right]\right) = V \bullet \text{---} \text{---} \bullet \begin{array}{l} \nearrow l_1 \\ \searrow \bar{l}_2 \end{array}$$

$$= \begin{cases} \frac{2eC_{V\bar{l}_1l_2}^- \lambda'_A \lambda_B}{(l_1+l_2)^2 - M_V^2} & \text{for } \lambda = L, \lambda' = R, \\ \frac{2eC_{V\bar{l}_1l_2}^+ \lambda_A \lambda'_B}{(l_1+l_2)^2 - M_V^2} & \text{for } \lambda = R, \lambda' = L. \end{cases} \quad (6.8)$$

Since these subdiagrams show up in the evaluation of full decay amplitudes with intermediate off-shell gauge bosons, the pole of the gauge-boson propagator is treated as prescribed by the complex-mass scheme explained above, i.e. the gauge-boson mass and also the electroweak coupling are treated as complex quantities according to Eqs. (6.1) and (6.2).

The only additional subdiagrams needed for the improved NWA are the currents of the decay leptons. The resulting expression is

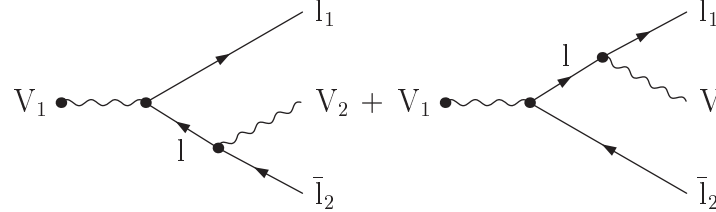
$$\mathcal{A}_{\text{NW}}\left(V\left[\begin{smallmatrix} a \\ l_1+l_2 \\ v \end{smallmatrix}\right] \rightarrow l_1\left[\begin{smallmatrix} l_1 \\ \lambda \end{smallmatrix}\right] \bar{l}_2\left[\begin{smallmatrix} l_2 \\ \lambda' \end{smallmatrix}\right]\right) = V \bullet \text{---} \text{---} \bullet \begin{array}{l} \nearrow l_1 \\ \searrow \bar{l}_2 \end{array}$$

$$= \begin{cases} 2eC_{V\bar{l}_1l_2}^- \lambda'_A \lambda_B & \text{for } \lambda = L, \lambda' = R, \\ 2eC_{V\bar{l}_1l_2}^+ \lambda_A \lambda'_B & \text{for } \lambda = R, \lambda' = L, \end{cases} \quad (6.9)$$

which replaces the polarization bispinors of the weak gauge bosons in the improved NWA amplitudes. The amplitudes are evaluated in the limit $\Gamma_V \rightarrow 0$, i.e. all masses and couplings can be treated as real quantities in the improved NWA, apart from the gauge-boson mass in the propagator. Taking the limit naively here would lead to the well-known divergence if the gauge boson becomes on shell. Therefore, the propagator is extracted from the amplitude. Its treatment will be discussed in Section 7.2.

Also for the calculation of singly-resonant diagrams, only building blocks regarding the decay leptons have to be evaluated anew. The necessary subdiagrams for the production of a single gauge-boson in association with one or two jets are already known from the subdiagrams involving an intermediate electroweak gauge boson, namely in the building blocks in Eqs. (4.21) and (4.24). Instead of a three-gauge-boson vertex, a gauge-boson decay to four leptons with their fermion chains connected by a second intermediate gauge boson is needed for the singly-resonant diagrams. To this end, the following building block

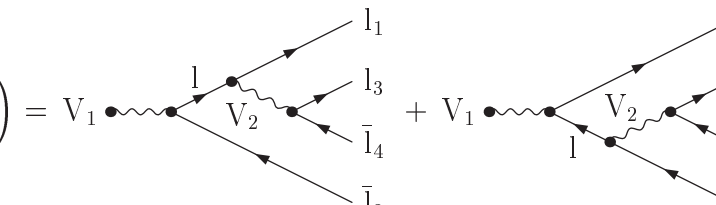
describing the decay of a gauge boson to a lepton–antilepton pair and a second gauge boson is calculated,

$$\mathcal{A}\left(V\left[\begin{smallmatrix} y \\ v_1 \end{smallmatrix}\right] \rightarrow V_2\left[\begin{smallmatrix} k_2 \\ v_2^* \end{smallmatrix}\right] l_1\left[\begin{smallmatrix} l_1 \\ \lambda \end{smallmatrix}\right] \bar{l}_2\left[\begin{smallmatrix} l_2 \\ \lambda' \end{smallmatrix}\right]\right) = V_1 \text{ (diagram)} + V_1 \text{ (diagram)}, \quad (6.10)$$


$$\mathcal{A}\left(V_1\left[\begin{smallmatrix} y \\ v_1 \end{smallmatrix}\right] \rightarrow V_2\left[\begin{smallmatrix} k_2 \\ v_2^* \end{smallmatrix}\right] l_1\left[\begin{smallmatrix} l_1 \\ L \end{smallmatrix}\right] \bar{l}_2\left[\begin{smallmatrix} l_2 \\ R \end{smallmatrix}\right]\right) = \frac{2e^2 v_{2,\dot{G}H}^*}{(l_1 + l_2 + k_2)^2 - M_{V_1}^2} \times \left[-\frac{C_{V_1\bar{l}_2}^- C_{V_2\bar{l}_1}^-}{(l_1 + k_2)^2} \lambda'_{\dot{K}} (L_1 + K_2)^{\dot{G}V} \epsilon_{VL} \lambda^H + \frac{C_{V_1\bar{l}_1}^- C_{V_2\bar{l}_2}^-}{(l_2 + k_2)^2} \lambda'^{\dot{G}} (L_2 + K_2)^{\dot{U}H} \epsilon_{\dot{U}\dot{K}} \lambda_L \right], \quad (6.10a)$$

$$\mathcal{A}\left(V_1\left[\begin{smallmatrix} y \\ v_1 \end{smallmatrix}\right] \rightarrow V_2\left[\begin{smallmatrix} k_2 \\ v_2^* \end{smallmatrix}\right] l_1\left[\begin{smallmatrix} l_1 \\ R \end{smallmatrix}\right] \bar{l}_2\left[\begin{smallmatrix} l_2 \\ L \end{smallmatrix}\right]\right) = \frac{2e^2 v_{2,\dot{G}H}^*}{(l_1 + l_2 + k_2)^2 - M_{V_1}^2} \times \left[-\frac{C_{V_1\bar{l}_2}^+ C_{V_2\bar{l}_1}^+}{(l_1 + k_2)^2} \lambda_{\dot{K}} (L_1 + K_2)^{\dot{U}H} \epsilon_{\dot{U}\dot{K}} \lambda'_L + \frac{C_{V_1\bar{l}_1}^+ C_{V_2\bar{l}_2}^+}{(l_2 + k_2)^2} \lambda_{\dot{K}} (L_2 + K_2)^{\dot{G}V} \epsilon_{VL} \lambda'^H \right]. \quad (6.10b)$$

Contracting Eq. (6.10) with Eq. (6.8) for a second lepton–antilepton pair leads to the needed four-lepton decay of a gauge boson. Which of the two outgoing lepton–antilepton pairs couples to the primary gauge boson is not prescribed in general by the respective VV+jet-production subprocess, so permutations of the two outgoing lepton–antilepton pairs have to be taken into account. In case of two identical (anti-)leptons, further contributions arise from interchanging the two (anti-)leptons. In the latter case, relative minus signs result from the changed fermion-number flow. The generic subamplitudes read

$$\mathcal{A}_{\text{SR}}\left(V\left[\begin{smallmatrix} y \\ v_1 \end{smallmatrix}\right] \rightarrow l_1\left[\begin{smallmatrix} l_1 \\ \lambda \end{smallmatrix}\right] \bar{l}_2\left[\begin{smallmatrix} l_2 \\ \lambda' \end{smallmatrix}\right] l_3\left[\begin{smallmatrix} l_3 \\ \xi \end{smallmatrix}\right] \bar{l}_4\left[\begin{smallmatrix} l_4 \\ \xi' \end{smallmatrix}\right]\right) = V_1 \text{ (diagram)} + V_1 \text{ (diagram)} + \left(\mathcal{X}\left[\begin{smallmatrix} l_1 \leftrightarrow l_3 \\ l_2 \leftrightarrow l_4 \end{smallmatrix}\right] - \mathcal{X}[l_1 \leftrightarrow l_3] - \mathcal{X}[l_2 \leftrightarrow l_4] \right) \{ \dots \} \\ = \sum_{V_2} \hat{\mathcal{A}}\left(V_1\left[\begin{smallmatrix} y \\ v_1 \end{smallmatrix}\right] \rightarrow V_2\left[\begin{smallmatrix} k_2 \\ v_2^* \end{smallmatrix}\right] l_1\left[\begin{smallmatrix} l_1 \\ \lambda \end{smallmatrix}\right] \bar{l}_2\left[\begin{smallmatrix} l_2 \\ \lambda' \end{smallmatrix}\right]\right) \mathcal{A}\left(V_2\left[\begin{smallmatrix} k_2 \\ v_2 \end{smallmatrix}\right] \rightarrow l_3\left[\begin{smallmatrix} l_3 \\ \xi \end{smallmatrix}\right] \bar{l}_4\left[\begin{smallmatrix} l_4 \\ \xi' \end{smallmatrix}\right]\right) + \left(\mathcal{X}\left[\begin{smallmatrix} l_1 \leftrightarrow l_3 \\ l_2 \leftrightarrow l_4 \end{smallmatrix}\right] - \mathcal{X}[l_1 \leftrightarrow l_3] - \mathcal{X}[l_2 \leftrightarrow l_4] \right) \{ \dots \}, \quad (6.11)$$


$$\begin{aligned}
\mathcal{A}_{\text{SR}}\left(V_1\left[\begin{smallmatrix} y \\ v_1 \end{smallmatrix}\right] \rightarrow l_1\left[\begin{smallmatrix} l_1 \\ L \end{smallmatrix}\right] \bar{l}_2\left[\begin{smallmatrix} l_2 \\ L \end{smallmatrix}\right] l_3\left[\begin{smallmatrix} l_3 \\ L \end{smallmatrix}\right] \bar{l}_4\left[\begin{smallmatrix} l_4 \\ R \end{smallmatrix}\right]\right) &= \frac{4e^3}{y^2 - M_{V_1}^2} \sum_{V_2} \sum_l \frac{C_{V_2 \bar{l}_3 l_4}^-}{(l_3 + l_4)^2 - M_{V_2}^2} \\
&\times \left(\frac{C_{V_1 \bar{l}_2}^- C_{V_2 \bar{l}_1 l}^-}{(y - l_2)^2} \langle \xi \lambda \rangle \lambda'_{\dot{K}} (Y - L_2)_{\dot{U}L} \xi'^{\dot{U}} - \frac{C_{V_1 \bar{l}_1 l}^- C_{V_2 \bar{l}_2}^-}{(y - l_1)^2} \langle \xi' \lambda' \rangle^* (Y - L_1)_{\dot{K}V} \xi^V \lambda_L \right) \\
&+ \left(\mathcal{X}\left[\begin{smallmatrix} l_1 \leftrightarrow l_3 \\ l_2 \leftrightarrow l_4 \end{smallmatrix}\right] - \mathcal{X}[l_1 \leftrightarrow l_3] - \mathcal{X}[l_2 \leftrightarrow l_4] \right) \left\{ \dots \right\}, \tag{6.11a}
\end{aligned}$$

$$\begin{aligned}
\mathcal{A}_{\text{SR}}\left(V_1\left[\begin{smallmatrix} y \\ v_1 \end{smallmatrix}\right] \rightarrow l_1\left[\begin{smallmatrix} l_1 \\ R \end{smallmatrix}\right] \bar{l}_2\left[\begin{smallmatrix} l_2 \\ L \end{smallmatrix}\right] l_3\left[\begin{smallmatrix} l_3 \\ R \end{smallmatrix}\right] \bar{l}_4\left[\begin{smallmatrix} l_4 \\ L \end{smallmatrix}\right]\right) &= \frac{4e^3}{y^2 - M_{V_1}^2} \sum_{V_2} \sum_l \frac{C_{V_2 \bar{l}_3 l_4}^+}{(l_3 + l_4)^2 - M_{V_2}^2} \\
&\times \left(\frac{C_{V_1 \bar{l}_2}^+ C_{V_2 \bar{l}_1 l}^+}{(y - l_2)^2} \langle \xi \lambda \rangle^* (Y - L_2)_{\dot{K}V} \xi'^V \lambda'_L - \frac{C_{V_1 \bar{l}_1 l}^+ C_{V_2 \bar{l}_2}^+}{(y - l_1)^2} \langle \xi' \lambda' \rangle \lambda_{\dot{K}} (Y - L_1)_{\dot{U}L} \xi'^{\dot{U}} \right) \\
&+ \left(\mathcal{X}\left[\begin{smallmatrix} l_1 \leftrightarrow l_3 \\ l_2 \leftrightarrow l_4 \end{smallmatrix}\right] - \mathcal{X}[l_1 \leftrightarrow l_3] - \mathcal{X}[l_2 \leftrightarrow l_4] \right) \left\{ \dots \right\}, \tag{6.11b}
\end{aligned}$$

$$\begin{aligned}
\mathcal{A}_{\text{SR}}\left(V_1\left[\begin{smallmatrix} y \\ v_1 \end{smallmatrix}\right] \rightarrow l_1\left[\begin{smallmatrix} l_1 \\ L \end{smallmatrix}\right] \bar{l}_2\left[\begin{smallmatrix} l_2 \\ R \end{smallmatrix}\right] l_3\left[\begin{smallmatrix} l_3 \\ R \end{smallmatrix}\right] \bar{l}_4\left[\begin{smallmatrix} l_4 \\ L \end{smallmatrix}\right]\right) &= \frac{4e^3}{y^2 - M_{V_1}^2} \sum_{V_2} \sum_l \frac{C_{V_2 \bar{l}_3 l_4}^+}{(l_3 + l_4)^2 - M_{V_2}^2} \\
&\times \left(\frac{C_{V_1 \bar{l}_2}^- C_{V_2 \bar{l}_1 l}^-}{(y - l_2)^2} \langle \xi' \lambda \rangle \lambda'_{\dot{K}} (Y - L_2)_{\dot{U}L} \xi'^{\dot{U}} - \frac{C_{V_1 \bar{l}_1 l}^- C_{V_2 \bar{l}_2}^-}{(y - l_1)^2} \langle \xi \lambda' \rangle^* (Y - L_1)_{\dot{K}V} \xi'^V \lambda_L \right) \\
&+ \mathcal{X}\left[\begin{smallmatrix} l_1 \leftrightarrow l_3 \\ l_2 \leftrightarrow l_4 \end{smallmatrix}\right] \left\{ \dots \right\}, \tag{6.11c}
\end{aligned}$$

$$\begin{aligned}
\mathcal{A}_{\text{SR}}\left(V_1\left[\begin{smallmatrix} y \\ v_1 \end{smallmatrix}\right] \rightarrow l_1\left[\begin{smallmatrix} l_1 \\ R \end{smallmatrix}\right] \bar{l}_2\left[\begin{smallmatrix} l_2 \\ L \end{smallmatrix}\right] l_3\left[\begin{smallmatrix} l_3 \\ L \end{smallmatrix}\right] \bar{l}_4\left[\begin{smallmatrix} l_4 \\ R \end{smallmatrix}\right]\right) &= \frac{4e^3}{y^2 - M_{V_1}^2} \sum_{V_2} \sum_l \frac{C_{V_2 \bar{l}_3 l_4}^-}{(l_3 + l_4)^2 - M_{V_2}^2} \\
&\times \left[\frac{C_{V_1 \bar{l}_2}^+ C_{V_2 \bar{l}_1 l}^+}{(y - l_2)^2} \langle \xi' \lambda \rangle^* (Y - L_2)_{\dot{K}V} \xi^V \lambda'_L - \frac{C_{V_1 \bar{l}_1 l}^+ C_{V_2 \bar{l}_2}^+}{(y - l_1)^2} \langle \xi \lambda' \rangle \lambda_{\dot{K}} (Y - L_1)_{\dot{U}L} \xi'^{\dot{U}} \right] \\
&+ \mathcal{X}\left[\begin{smallmatrix} l_1 \leftrightarrow l_3 \\ l_2 \leftrightarrow l_4 \end{smallmatrix}\right] \left\{ \dots \right\}, \tag{6.11d}
\end{aligned}$$

$$\mathcal{A}_{\text{SR}}\left(V_1\left[\begin{smallmatrix} y \\ v_1 \end{smallmatrix}\right] \rightarrow l_1\left[\begin{smallmatrix} l_1 \\ L \end{smallmatrix}\right] \bar{l}_2\left[\begin{smallmatrix} l_2 \\ L \end{smallmatrix}\right] l_3\left[\begin{smallmatrix} l_3 \\ R \end{smallmatrix}\right] \bar{l}_4\left[\begin{smallmatrix} l_4 \\ R \end{smallmatrix}\right]\right) = -\mathcal{X}[l_2 \leftrightarrow l_4] \left\{ \mathcal{A}_{\text{SR}}\left(V_1\left[\begin{smallmatrix} y \\ v_1 \end{smallmatrix}\right] \rightarrow l_1\left[\begin{smallmatrix} l_1 \\ L \end{smallmatrix}\right] \bar{l}_2\left[\begin{smallmatrix} l_2 \\ R \end{smallmatrix}\right] l_3\left[\begin{smallmatrix} l_3 \\ R \end{smallmatrix}\right] \bar{l}_4\left[\begin{smallmatrix} l_4 \\ L \end{smallmatrix}\right]\right) \right\}, \tag{6.11e}$$

$$\mathcal{A}_{\text{SR}}\left(V_1\left[\begin{smallmatrix} y \\ v_1 \end{smallmatrix}\right] \rightarrow l_1\left[\begin{smallmatrix} l_1 \\ R \end{smallmatrix}\right] \bar{l}_2\left[\begin{smallmatrix} l_2 \\ R \end{smallmatrix}\right] l_3\left[\begin{smallmatrix} l_3 \\ L \end{smallmatrix}\right] \bar{l}_4\left[\begin{smallmatrix} l_4 \\ L \end{smallmatrix}\right]\right) = -\mathcal{X}[l_1 \leftrightarrow l_3] \left\{ \mathcal{A}_{\text{SR}}\left(V_1\left[\begin{smallmatrix} y \\ v_1 \end{smallmatrix}\right] \rightarrow l_1\left[\begin{smallmatrix} l_1 \\ L \end{smallmatrix}\right] \bar{l}_2\left[\begin{smallmatrix} l_2 \\ R \end{smallmatrix}\right] l_3\left[\begin{smallmatrix} l_3 \\ R \end{smallmatrix}\right] \bar{l}_4\left[\begin{smallmatrix} l_4 \\ L \end{smallmatrix}\right]\right) \right\}. \tag{6.11f}$$

The expression $\{\dots\}$ always refers to the whole term given ahead. For most assignments of (anti-)leptons only some of the terms deliver non-vanishing contributions, since a large number of coupling constants $C_{V\bar{l}l'}^\sigma$ is zero. This holds in particular in any case where l and l' do not belong to the same lepton family.

6.3 Implementation of decays into the production matrix elements

By means of the VV+jet production building blocks taken from Section 4.2 and those describing the leptonic decays, which are calculated in the previous section, the matrix elements for all subprocesses including leptonic gauge-boson decays can be easily constructed by some replacements that are discussed in this section. Including leptonic decays into the NLO QCD calculation does not change the structure of singularities. Therefore, the dipole subtraction formalism can be applied as described in Chapter 5 with the necessary replacements in the amplitudes explained in this section.

6.3.1 Full calculation with off-shell gauge bosons

In the approach with full off-shell decays of the gauge bosons, the arising poles in the gauge-boson propagators are treated as explained in Section 6.1.1 by means of the complex-mass scheme. The respective replacements of masses and couplings according to Eqs. (6.1) and (6.2) are to be performed. No new symbols for the resulting complex quantities are introduced here.

The amplitudes for the full calculations receive two different kinds of contributions, namely the doubly-resonant diagrams, where both gauge-boson propagators can become resonant at the same time, and the singly-resonant diagrams, where only one resonant propagator appears. If all four outgoing leptons and antileptons belong to the same generation, a larger amount of diagrams contributes. For WZ+jet and ZZ+jet, these diagrams are obtained by adding the particular amplitudes with the identical (anti-)leptons crossed. In the case of WW+jet, no such crossed contributions arise. However, the final state $l^-l^+\nu_l\bar{\nu}_l$ +jet can also result from ZZ+jet production with one Z boson decaying to a charged lepton–antilepton pair, and the other one to a neutrino–antineutrino pair. These diagrams have to be included as well for gauge-invariance reasons. However, the interference of WW+jet and ZZ+jet is a pure off-shell effect and thus suppressed. Moreover, the signature “2leptons + $p_{T,\text{miss}}$ + jet” is also received if the neutrino pair belongs to a different generation as the charged leptons. For completeness, also these processes should be added. However, the numerical calculations discussed in this thesis are only performed for leptons of different generations. Therefore, no specific results are provided for the others if they cannot be produced as a simple byproduct.

Doubly-resonant contributions

The doubly-resonant diagrams to WW+jet, ZZ+jet, and WZ+jet production are illustrated in Figures 6.4, 6.5, and 6.6, respectively, for one specific LO channel with a quark–antiquark initial state and the two lepton–antilepton pairs belonging to different families.

The doubly-resonant contributions are directly derived from the contributions already present in VV+jet production by replacing the polarization bispinors of the outgoing gauge bosons by a gauge-boson propagator and the leptonic current of their decay products. In

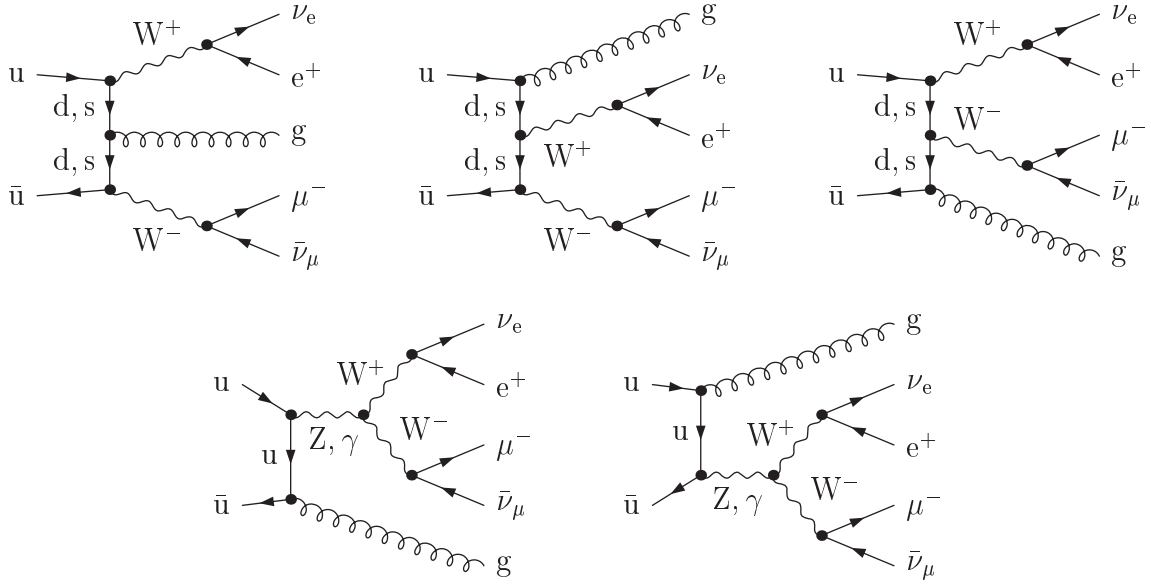


Figure 6.4: Diagrams with two simultaneously resonant W propagators of the partonic subprocess $u\bar{u} \rightarrow \nu_e e^+ \mu^- \bar{\nu}_\mu g$ contributing to $pp/p\bar{p} \rightarrow \nu_e e^+ \mu^- \bar{\nu}_\mu + \text{jet} + X$.

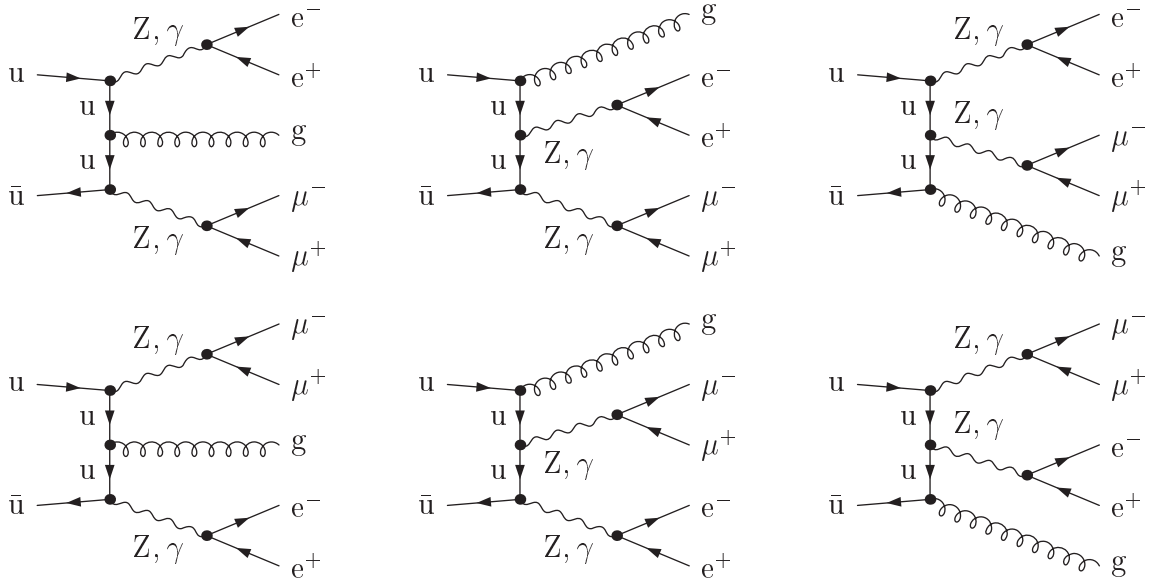


Figure 6.5: Diagrams with two resonant Z propagators of the subprocess $u\bar{u} \rightarrow e^- e^+ \mu^- \mu^+ g$ contributing to $pp/p\bar{p} \rightarrow e^- e^+ \mu^- \mu^+ + \text{jet} + X$. One or both Z bosons can be replaced by photons leading to the same final state.

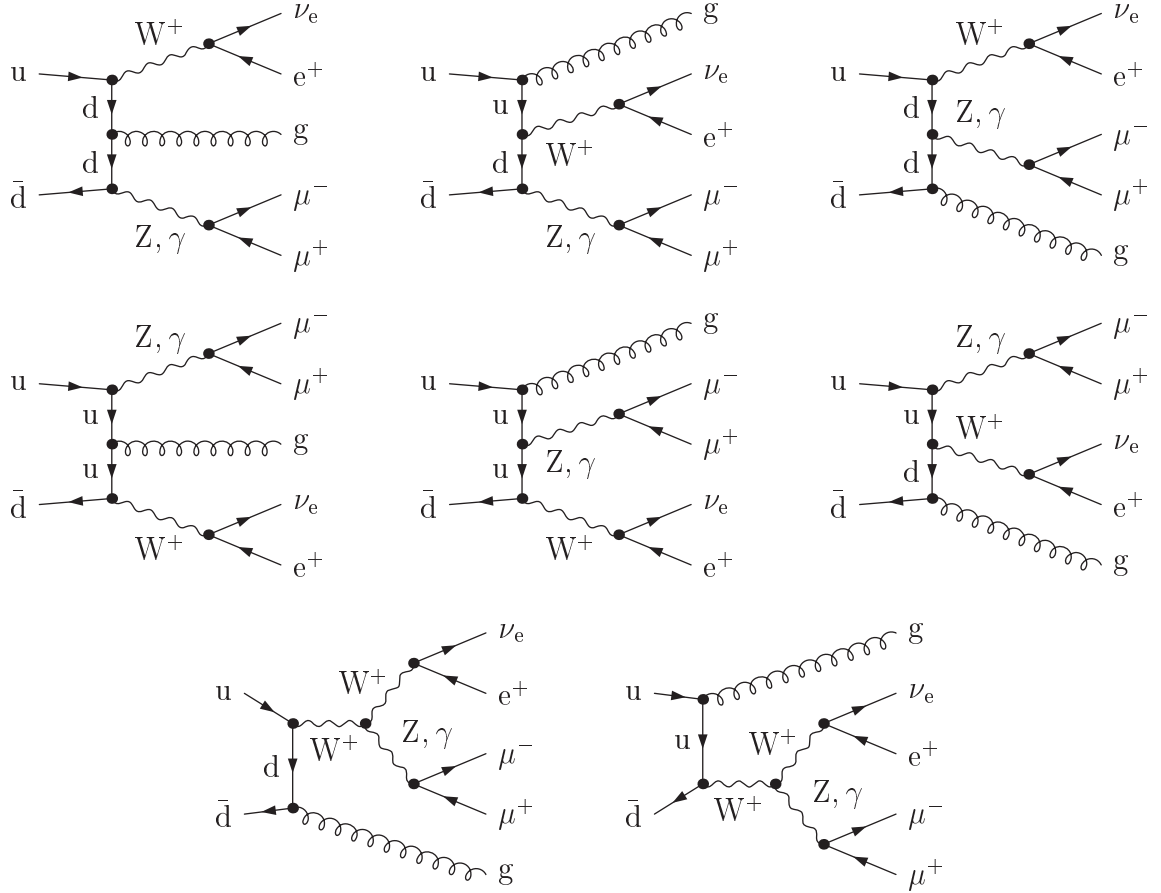


Figure 6.6: Diagrams with a resonant W propagator and a resonant Z propagator of the subprocess $u\bar{d} \rightarrow \nu_e e^+ \mu^- \mu^+ g$, which contributes to $pp/p\bar{p} \rightarrow \nu_e e^+ \mu^- \mu^+ + \text{jet} + X$. The subprocess gets also contributions from diagrams with the intermediate Z bosons replaced by photons. The diagrams for the respective subprocess contributing to $pp/p\bar{p} \rightarrow e^- \bar{\nu}_e \mu^- \mu^+ + \text{jet} + X$ can be obtained by exchanging all particles by the corresponding antiparticles and vice versa.

the process classes $WZ+\text{jet}$ and $ZZ+\text{jet}$, further contributions arise from replacing the Z boson by an intermediate photon, which are actually not doubly-resonant but show the same topology and are therefore also calculated here. The corresponding amplitudes are constructed as follows, where the sum over the intermediate gauge bosons $V_{1,2}$ refers to the Z -boson-photon replacements described before,

$$\begin{aligned}
& \mathcal{M}_X^{\text{DR}} \left(q_1 \begin{bmatrix} i \\ p \\ \sigma \end{bmatrix} \bar{q}_2 \begin{bmatrix} j \\ p' \\ \sigma' \end{bmatrix} \rightarrow l_1 \begin{bmatrix} l_1 \\ \lambda \end{bmatrix} \bar{l}_2 \begin{bmatrix} l_2 \\ \lambda' \end{bmatrix} l_3 \begin{bmatrix} l_3 \\ \xi \end{bmatrix} \bar{l}_4 \begin{bmatrix} l_4 \\ \xi' \end{bmatrix} + X \right) \\
&= \sum_{V_1} \sum_{V_2} \hat{\mathcal{M}}_X \left(q_1 \begin{bmatrix} i \\ p \\ \sigma \end{bmatrix} \bar{q}_2 \begin{bmatrix} j \\ p' \\ \sigma' \end{bmatrix} \rightarrow V_1 \begin{bmatrix} k_1 \\ v_1^* \end{bmatrix} V_2 \begin{bmatrix} k_2 \\ v_2^* \end{bmatrix} + X \right) \\
&\quad \times \left\{ \mathcal{A} \left(V_1 \begin{bmatrix} k_1 \\ v_1^* \end{bmatrix} \rightarrow l_1 \begin{bmatrix} l_1 \\ \lambda \end{bmatrix} \bar{l}_2 \begin{bmatrix} l_2 \\ \lambda' \end{bmatrix} \right) \mathcal{A} \left(V_2 \begin{bmatrix} k_2 \\ v_2^* \end{bmatrix} \rightarrow l_3 \begin{bmatrix} l_3 \\ \xi \end{bmatrix} \bar{l}_4 \begin{bmatrix} l_4 \\ \xi' \end{bmatrix} \right) - \mathcal{X} [l_2 \leftrightarrow l_4] \{ \dots \} \right\}, \quad (6.12)
\end{aligned}$$

with the building blocks for the leptonic gauge-boson decay defined in Eq. (6.10). The expression $\{\dots\}$ again refers to the convenient expression with the minus sign arising from the changed fermion-number flow. The crossed term only contributes to WZ+jet and ZZ+jet subamplitudes if all (anti-)leptons belong to the same generation. The expression '+X' in the particle content refers to all possible insertions of QCD partons, which are used for the evaluation of the LO and real-emission subamplitudes \mathcal{M}_X , $X = Q, V, F$, collected in Section 4.3. Analogous replacement rules also hold for the evaluation of the remaining NLO QCD contributions in Chapter 5, which is due to the fact that the outgoing leptons do not affect the structure of singularities that has to be controlled there.

Singly-resonant contributions

Since the selection of contributing diagrams is not very transparent for specified lepton assignments in the generic form used in the definition of Eq. (6.11), the singly-resonant contributions to the off-shell continuations of WW+jet, ZZ+jet, and WZ+jet production with leptonic decays are shown in Figures 6.7, 6.8, and 6.9, respectively, for the quark–antiquark initial state and lepton–antilepton pairs of different generations in the final state.

For WW+jet subprocesses, the configuration with both the Z and the W propagator being resonant is kinematically allowed, but does not significantly contribute because the corresponding phase-space region is too small. Since in all cases a W boson couples to the quark chain in WZ+jet subprocesses, not even small phase-space regions with both W and Z propagators being resonant simultaneously can arise.

The singly-resonant contributions to the process classes WW+jet and WZ+jet are obtained from the known production subamplitudes by only considering those containing an intermediate electroweak gauge boson. The respective gauge-boson propagator and the three-vector-boson vertex with polarization bispinors attached is replaced by the polarization bispinor of the intermediate gauge boson. This defines subamplitudes actually corresponding to V+jet production, namely

$$\mathcal{M}_V\left(q_1\begin{bmatrix}i\\p\\p_\sigma\end{bmatrix}\bar{q}_2\begin{bmatrix}j\\p'\\p'_{\sigma'}\end{bmatrix}\rightarrow V_1\begin{bmatrix}k_1\\v_1^*\end{bmatrix}V_2\begin{bmatrix}k_2\\v_2^*\end{bmatrix}+X\right)\rightarrow\mathcal{M}\left(q_1\begin{bmatrix}i\\p\\p_\sigma\end{bmatrix}\bar{q}_2\begin{bmatrix}j\\p'\\p'_{\sigma'}\end{bmatrix}\rightarrow V\begin{bmatrix}y\\v^*\end{bmatrix}+X\right), \quad (6.13)$$

by the replacement

$$e\sum_V\frac{C_{V\bar{V}_1\bar{V}_2}}{y^2-M_V^2}\mathcal{V}_{\dot{K}L}\rightarrow v_{\dot{K}L}^*. \quad (6.14)$$

With the V+jet subamplitude defined in Eq. (6.13) and the building block for the description of a gauge-boson decay into four fermions without a three-gauge-boson vertex given in Eq. (6.11), the subamplitudes describing the singly-resonant contributions read

$$\begin{aligned} &\mathcal{M}_V^{\text{SR}}\left(q_1\begin{bmatrix}i\\p\\p_\sigma\end{bmatrix}\bar{q}_2\begin{bmatrix}j\\p'\\p'_{\sigma'}\end{bmatrix}\rightarrow l_1\begin{bmatrix}l_1\\\lambda\end{bmatrix}\bar{l}_2\begin{bmatrix}l_2\\\lambda'\end{bmatrix}l_3\begin{bmatrix}l_3\\\xi\end{bmatrix}\bar{l}_4\begin{bmatrix}l_4\\\xi'\end{bmatrix}+X\right) \\ &= \sum_V\hat{\mathcal{M}}\left(q_1\begin{bmatrix}i\\p\\p_\sigma\end{bmatrix}\bar{q}_2\begin{bmatrix}j\\p'\\p'_{\sigma'}\end{bmatrix}\rightarrow V\begin{bmatrix}y\\v^*\end{bmatrix}+X\right)\mathcal{A}\left(V\begin{bmatrix}y\\v\end{bmatrix}\rightarrow l_1\begin{bmatrix}l_1\\\lambda\end{bmatrix}\bar{l}_2\begin{bmatrix}l_2\\\lambda'\end{bmatrix}l_3\begin{bmatrix}l_3\\\xi\end{bmatrix}\bar{l}_4\begin{bmatrix}l_4\\\xi'\end{bmatrix}\right), \end{aligned} \quad (6.15)$$

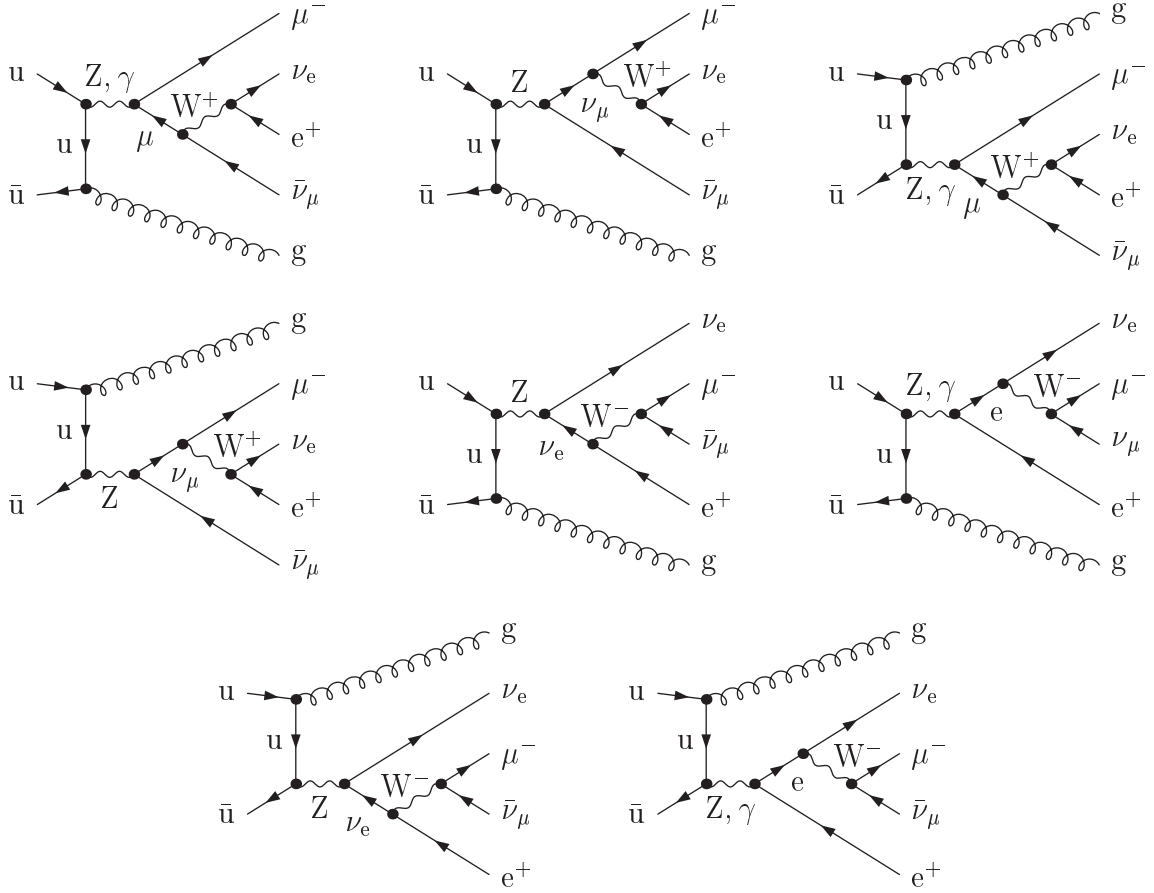


Figure 6.7: Diagrams with only one resonant W propagator of the partonic subprocess $u\bar{u} \rightarrow \nu_e e^+ \mu^- \bar{\nu}_\mu g$ contributing to $pp/p\bar{p} \rightarrow \nu_e e^+ \mu^- \bar{\nu}_\mu + \text{jet} + X$.

where ‘+X’ again denotes all relevant parton configurations for LO and real-emission subamplitudes.

For ZZ +jet production, this procedure does not work, because no contributions with an intermediate gauge-boson arise there due to the absence of a respective three-gauge-boson vertex with two Z bosons attached. Singly-resonant contributions, however, exist. They are identical to those contributing to WW +jet production apart from exchanging the outgoing leptons.

The calculation of matrix elements for LO and real-emission subprocesses, which are described in Section 4.4, is performed by replacing each subamplitude there with the respective doubly-resonant subamplitude from Eq. (6.12). Each subamplitude containing an intermediate gauge boson, denoted by \mathcal{M}_V , gets an additional contribution from a respective singly-resonant amplitude in the WW +jet and WZ +jet contributions. The absence of such subamplitudes in ZZ +jet contribution requires a different proceeding. Here, the singly-resonant amplitudes are to be added to Eq. (4.38) for the case of external gluons and to the abbreviation in Eq. (4.49) for the subprocesses with two fermion chains. When

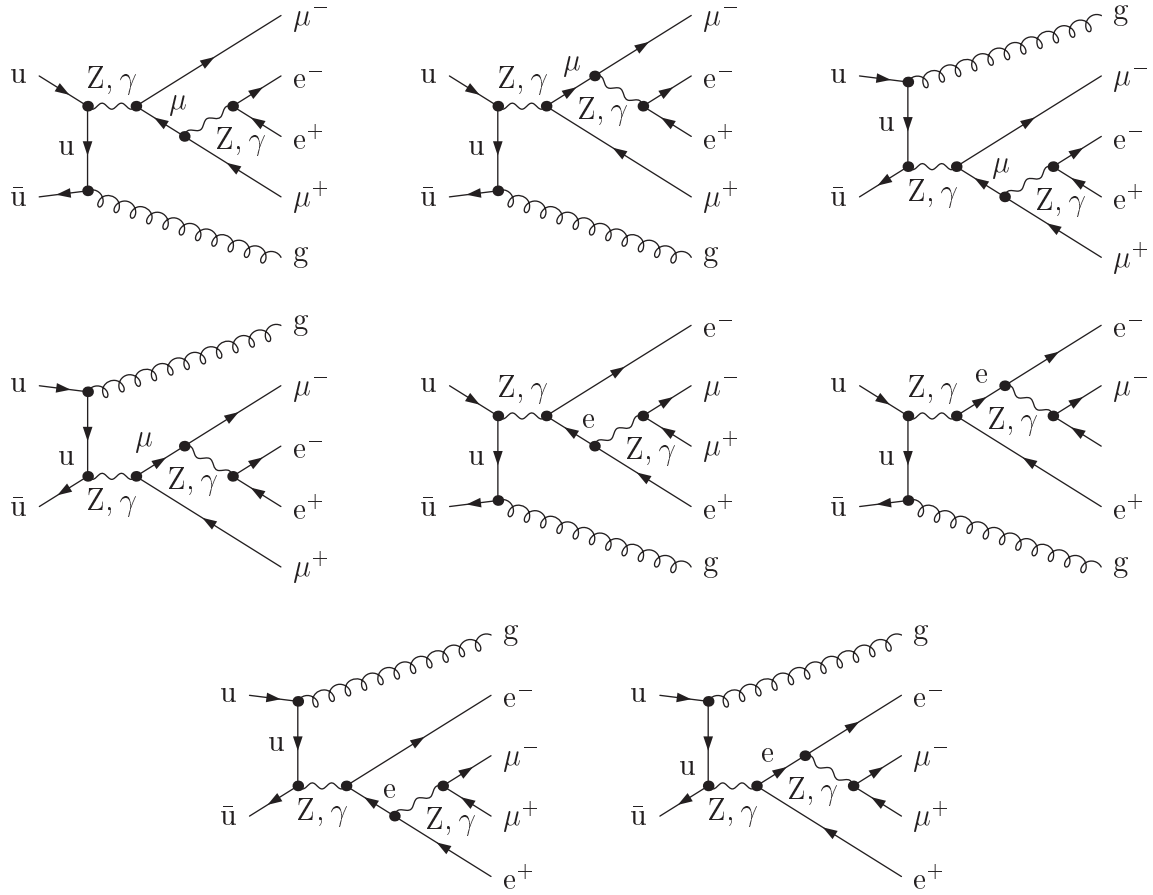


Figure 6.8: Diagrams with only one resonant Z propagator of the subprocess $u\bar{u} \rightarrow e^-e^+\mu^-\mu^+g$ contributing to $pp/p\bar{p} \rightarrow e^-e^+\mu^-\mu^+ + \text{jet} + X$. As in the doubly-resonant case, also diagrams with one or both intermediate Z bosons replaced by photons contribute.

summing over the spins of external particles, the sum over the polarizations of the two gauge bosons is replaced by a sum over the helicities of the outgoing (anti-)leptons. The number of non-vanishing helicity configuration is reduced by the fact that all (anti-)leptons are treated as massless particles. Besides, lepton–antilepton pairs coupling to intermediate W bosons only contribute in the channel with left-handed leptons and right-handed antileptons. The symmetry factor $\frac{1}{2}$ due to the two identical outgoing gauge bosons in $ZZ + \text{jet}$ production is to be removed from the amplitudes. If the two lepton–antilepton pairs belong to different generations, no new symmetry factors arise from the leptonic part of the final state. If they belong to the same generation, a factor $\frac{1}{2}$ has to be added for $WZ + \text{jet}$ and a factor $\frac{1}{4}$ in the $ZZ + \text{jet}$ case due to two pairs of identical particles.

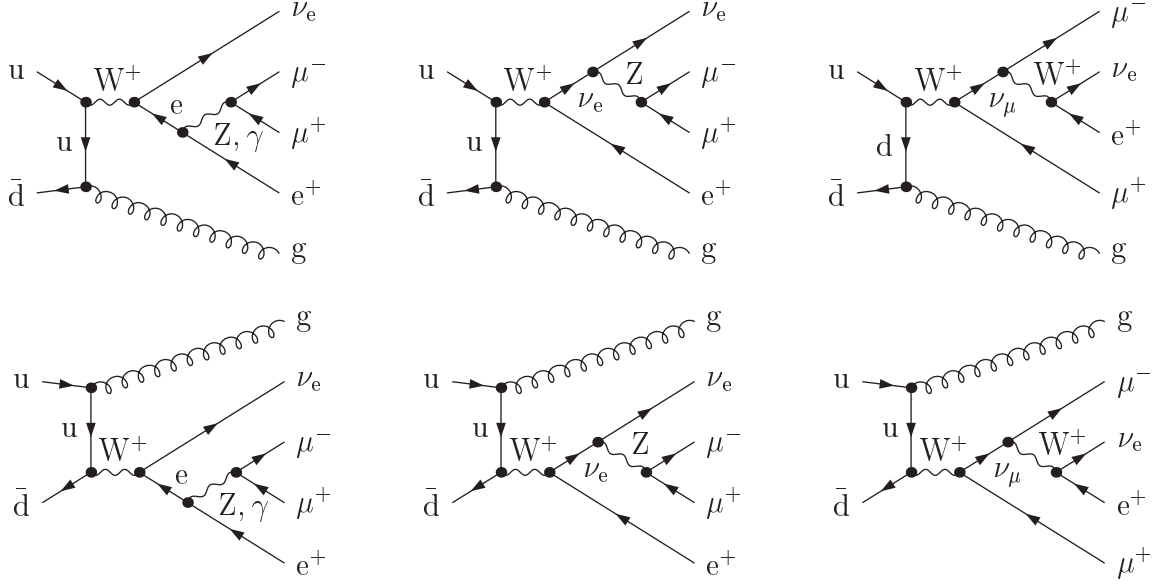


Figure 6.9: Diagrams with at most one resonant W or Z propagator of the subprocess $u\bar{d} \rightarrow \nu_e e^+ \mu^- \mu^+ g$ contributing to $pp/p\bar{p} \rightarrow \nu_e e^+ \mu^- \mu^+ + \text{jet} + X$.

6.3.2 Improved narrow-width approximation

The amplitudes contributing in the improved NWA correspond to the doubly-resonant ones of the full amplitude calculation discussed in the previous subsection. In all subamplitudes contributing to the LO and real-emission subprocesses in Section 4.3, the gauge-boson polarization bispinors are replaced by the currents of the decay leptons. The Breit–Wigner propagator is extracted and integrated over. It is replaced by a suitably normalized δ -function. Details on this will be explained in Section 7.2. The remainder of the amplitude reads

$$\begin{aligned} \mathcal{M}_X^{\text{NW}} \left(q_1 \begin{bmatrix} i \\ p \\ \sigma \end{bmatrix} \bar{q}_2 \begin{bmatrix} j \\ p' \\ \sigma' \end{bmatrix} \rightarrow l_1 \begin{bmatrix} l_1 \\ \lambda \end{bmatrix} \bar{l}_2 \begin{bmatrix} l_2 \\ \lambda' \end{bmatrix} l_3 \begin{bmatrix} l_3 \\ \xi \end{bmatrix} \bar{l}_4 \begin{bmatrix} l_4 \\ \xi' \end{bmatrix} + X \right) &= \hat{\mathcal{M}}_X \left(q_1 \begin{bmatrix} i \\ p \\ \sigma \end{bmatrix} \bar{q}_2 \begin{bmatrix} j \\ p' \\ \sigma' \end{bmatrix} \rightarrow V_1 \begin{bmatrix} k_1 \\ v_1^* \end{bmatrix} V_2 \begin{bmatrix} k_2 \\ v_2^* \end{bmatrix} + X \right) \\ &\times \mathcal{A}_{\text{NW}} \left(V_1 \begin{bmatrix} k_1 \\ v_1^* \end{bmatrix} \rightarrow l_1 \begin{bmatrix} l_1 \\ \lambda \end{bmatrix} \bar{l}_2 \begin{bmatrix} l_2 \\ \lambda' \end{bmatrix} \right) \mathcal{A}_{\text{NW}} \left(V_2 \begin{bmatrix} k_2 \\ v_2^* \end{bmatrix} \rightarrow l_3 \begin{bmatrix} l_3 \\ \xi \end{bmatrix} \bar{l}_4 \begin{bmatrix} l_4 \\ \xi' \end{bmatrix} \right), \end{aligned} \quad (6.16)$$

with the building block describing the gauge-boson decays in improved NWA defined in Eq. (6.9). Differing from the full amplitude calculation, no sum is taken over intermediate gauge-boson states because only the contributions from resonant massive gauge bosons are taken into account in this approximation. In the NLO QCD calculations in Chapter 5, the analogous replacement rules are applied.

As in the full amplitude calculation, the sum over external spins in the calculation of matrix elements runs over the (anti-)lepton helicities here instead of the gauge-boson polarizations.

The symmetry factor $\frac{1}{2}$ arising from the two identical gauge bosons in the final state of $ZZ + \text{jet}$ production has to be dropped as in the full amplitude calculation. However, care

has to be taken if both lepton–antilepton pairs from the decays belong to the same generation. Naively, a symmetry factor $\frac{1}{2}$ in the WZ+jet case and a factor $\frac{1}{4}$ for ZZ+jet would be introduced. This is, however, in contradiction to the fact that the indistinguishability of the (anti-)leptons is spoiled by the on-shell condition of the intermediate gauge bosons. Assuming that \bar{l}_2 and \bar{l}_4 are identical antileptons, the preselection that the leptons l_1 and \bar{l}_2 stem from the decay of Z_1 and not, for instance, l_1 and \bar{l}_4 , has to be taken into account in the determination of symmetry factors. This leads to the situation that symmetry factors may not be introduced for each pair of identical particles, but only for each identical lepton–antilepton pair. The resulting symmetry factors are 1 for WZ+jet and $\frac{1}{2}$ in the ZZ+jet case, which are the same factors as in the VV+jet-production processes without decays.

In the full amplitude calculation, this factor 2 can be assigned to the two terms in brackets in Eq. (6.12). Assuming again that \bar{l}_2 and \bar{l}_4 are identical antileptons, the first term therein dominates if the gauge-boson propagator related to l_1 and \bar{l}_2 and simultaneously that one related to l_3 and \bar{l}_4 are resonant. The second term does if the roles of \bar{l}_2 and \bar{l}_4 are interchanged. Since the overlap between the two resonant phase-space regions is small, interferences between the two terms are negligible. Thus, the integration over the whole phase space leads to roughly twice the cross section one would obtain if one of the terms was absent.

Chapter 7

Numerical phase-space integration

In the previous chapters, analytic formulae for the LO and NLO cross sections are evaluated. The phase-space integrations therein are, however, by far too complicated to be performed analytically. Furthermore, a numerical calculation is even more convenient for the implementation of phase-space cuts, and also the evaluation of differential cross sections is simplified by this approach.

In Section 7.1, the multi-channel Monte Carlo method for performing a numerical phase-space integration is introduced.

A generic way how to construct an n -particle phase space from three generic building blocks is discussed in Section 7.2.

Section 7.3 provides some improvements of the LO phase-space generator to face the challenges of a numerical integration of NLO contributions in the dipole subtraction method.

7.1 Multi-channel Monte Carlo integration

The phase-space volume applied in the cross sections of Section 5.1 is defined as

$$d\Phi^{(n)}(p_a, p_b; k_1, \dots, k_n) = \frac{(2\pi)^{4-3n}}{2\sqrt{(p_a + p_b)^2}} d\phi^{(n)}(p_a, p_b; k_1, \dots, k_n), \quad (7.1)$$

$$d\phi^{(n)}(p_a, p_b; k_1, \dots, k_n) = \left[\prod_{i=1}^n d^4 k_i \delta(k_i^2 - m_i^2) \theta(k_i^0) \right] \delta^{(4)} \left(p_a + p_b - \sum_{i=1}^n k_i \right), \quad (7.2)$$

for an n -particle phase space with outgoing momenta k_i , $i = 1, \dots, n$. Generic properties of phase spaces are discussed in Ref. [89]. The quantities to be evaluated are cross sections,

$$\sigma_{ab}(p_a, p_b) = \int_n d\Phi^{(n)}(p_a, p_b) f(p_a, p_b, k_1, \dots, k_n), \quad (7.3)$$

where f collects both θ -functions in order to realize phase-space cuts applied on the outgoing particles and the transition matrix elements of the respective subprocesses. In the NLO calculations, the function f in general contains additional contributions from dipole terms which are, however, also built from LO matrix elements.

The functions f in general show—already in LO cross sections—a complicated peak behaviour mainly due to the propagator structure of squared diagrams, which are contained in the matrix elements. To improve the performance of the numerical integration, phase-space mappings according to this propagator structure are introduced,

$$\sigma_{ab}(p_a, p_b) = \int d\mathbf{r}^{3n-4} \frac{f_{ab}(k_i(\Phi(\mathbf{r})))}{g(\Phi(\mathbf{r}))}, \quad \frac{1}{g(\Phi(\mathbf{r}))} = \rho(k_i(\Phi(\mathbf{r}))) \left| \frac{\partial \Phi(\mathbf{r})}{\partial \mathbf{r}} \right|, \quad (7.4)$$

where f_{ab} delivers a brief notation of the former function f with the phase-space prefactor absorbed into it. Φ denotes the mapping between appropriate phase-space variables and the momenta of the outgoing particles, and ρ is the respective phase-space density. For a random generation of phase-space points, it is convenient to express these phase-space variables, which can be selected in a generic way as discussed in Section 7.2, in terms of uniform integration variables $\mathbf{r} = (r_1, \dots, r_{3n-4})$ defined on the unit hypercube, i.e. $r_i \in (0, 1)$. These mappings $\mathbf{r} \mapsto \Phi(\mathbf{r})$ can be chosen in such a way that the probability density $g(\Phi(\mathbf{r}))$ mimics the peak behaviour of the integrand, which is called “importance sampling”.

Using one phase-space mapping only facilitates the treatment of one or at most a small group of diagrams showing similar structures. A more sophisticated approach is provided by the multi-channel Monte Carlo method [90, 91]. This method allows the combination of different mappings—the so-called channels—in one probability density g_{tot} and therefore to smooth the integrand simultaneously in the whole integration region. Which of the M channels is used for the determination of a specific phase-space point in the numerical integration is chosen randomly. By introducing so-called “a-priori weights” $\alpha_k, k = 1, \dots, M$ ($\alpha_k \geq 0, \sum_{k=1}^M \alpha_k = 1$), the probability of choosing an individual channel k can be adapted to further improve the integrator performance. Introducing these extensions, the integral of Eq. (7.4) can be written as

$$\sigma_{ab}(p_a, p_b) = \int_0^1 dr \sum_{l=1}^M \theta(r - \beta_{l-1}) \theta(\beta_l - r) \int_0^1 d^{3n-4} \mathbf{r} \frac{f_{ab}(k_i(\Phi_{k(r)}(\mathbf{r})))}{g_{\text{tot}}(\Phi_{k(r)}(\mathbf{r}))}, \quad (7.5)$$

$$g_{\text{tot}}(\Phi_{k(r)}(\mathbf{r})) = \sum_{l=1}^M \alpha_l g_l(\Phi_{k(r)}(\mathbf{r})), \quad (7.6)$$

where β_l is a partition of unity,

$$\beta_0 = 0, \quad \beta_l = \sum_{j=1}^l \alpha_j, \quad l = 1, \dots, M-1, \quad \beta_M = \sum_{l=1}^M \alpha_l = 1, \quad (7.7)$$

and $k(r)$ denotes the channel that is used to determine the respective phase-space point. It is selected by the sum over θ -functions in a way that is appropriate for the numeric realization of the integral. $g_l(\Phi_{k(r)}(\mathbf{r}))$ is the probability density of the specific channel l , evaluated at the phase-space point delivered from the mapping of channel $k(r)$. For a more detailed derivation of these formulae, the reader is referred, e.g., to Refs. [73, 92].

The numerical evaluation of Eq. (7.5) is performed by randomly choosing the values of the integration variables r and \mathbf{r} , which are all defined on the interval $(0, 1)$, to first select one channel and then determine one phase-space point where the integrand is evaluated according to the respective mapping. Repeating this N times delivers an approximation of the cross section by averaging over the obtained results,

$$\sigma_{ab}(p_a, p_b) \approx \frac{1}{N} \sum_{j=1}^N \hat{\omega}_j, \quad \hat{\omega}_j = \frac{f_{ab}(k_i(\Phi_{k(r_j)}(\mathbf{r}_j)))}{g_{\text{tot}}(\Phi_{k(r_j)}(\mathbf{r}_j))}. \quad (7.8)$$

The standard deviation of the integral is given by

$$\delta\sigma_{ab}(p_a, p_b) = \sqrt{\frac{\sum_{j=1}^N \hat{\omega}_j^2 - \left(\sum_{j=1}^N \hat{\omega}_j\right)^2}{N(N-1)}}. \quad (7.9)$$

In the beginning of an integration, the a-priori weights are chosen to be equal for all channels. It is, however, sometimes convenient to modify them in order to minimize the Monte Carlo error. For improving the set of new weights, the adaptive optimization method presented in Ref. [93] is applied. This method suggests to calculate a new set of weights after N_{wo} evaluated phase-space points via

$$\alpha_k^{\text{new}} \propto \alpha_k \sqrt{W_k(\boldsymbol{\alpha})}, \quad W_k(\boldsymbol{\alpha}) = \frac{1}{N_{\text{wo}}} \sum_{j=1}^{N_{\text{wo}}} \frac{g_l(\Phi_{k(r_j)}(\mathbf{r}_j))}{g_{\text{tot}}(\Phi_{k(r_j)}(\mathbf{r}_j))} \hat{\omega}_j^2, \quad \sum_{k=1}^M \alpha_k^{\text{new}} = 1. \quad (7.10)$$

This procedure is repeated several times using the respective new sets of weights in every optimization step. Since—as shown in Ref. [93]—the theoretically optimal set of α_k obeys the condition $W_k(\boldsymbol{\alpha}) = W_l(\boldsymbol{\alpha})$ for all channels $k, l = 1, \dots, M$, the quality of weights used in each optimization step is measured by the variable

$$D = \max_{k,l} |W_k(\boldsymbol{\alpha}) - W_l(\boldsymbol{\alpha})|. \quad (7.11)$$

After a reasonable number of steps—which is in general reached if the weights do not differ considerably between succeeding ones—the set of weights from the optimization step leading to the minimal value of D in Eq. (7.11) is kept for the rest of the integration.

It is convenient to introduce a lower limit on the size of these weights, because too small weights for single channels might spoil the numerical stability of the integration. If a weight calculated according to Eq. (7.10) becomes smaller than the limit, it is set onto the value of this limit by hand. The remaining weights are rescaled in order to obey the fundamental normalization $\sum_{k=1}^M \alpha_k^{\text{new}} = 1$.

7.2 Generic phase-space construction

Each n -particle phase space can be composed from three different building blocks, namely

- integration over time-like invariants,

- phase spaces of two-particle decays, and
- phase spaces for t -channel-like $2 \rightarrow 2$ scattering processes,

which can be described generically. The decomposition of the phase space in Eq. (7.1) is performed by expressing the δ -function therein as an integration over a momentum introduced anew. This momentum is fixed as the sum over outgoing momenta by δ -functions, e.g.

$$\delta^{(4)}\left(p + p' - \sum_{i=1}^n k_i\right) = \int d^4 k_{2\dots n} \delta^{(4)}(p + p' - k_1 - k_{2\dots n}) \delta^{(4)}\left(k_{2\dots n} - \sum_{i=2}^n k_i\right). \quad (7.12)$$

The non-negativity of its energy component is trivially guaranteed by construction,

$$\theta(k_2^0) \cdots \theta(k_n^0) = \theta(k_2^0) \cdots \theta(k_n^0) \times \theta(k_{2\dots n}^0). \quad (7.13)$$

In a last step, a time-like invariant is introduced as an integration variable that determines the square of the new integration momentum,

$$\int_{s_{2\dots n, \min}}^{s_{2\dots n, \max}} ds_{2\dots n} \delta(s_{2\dots n} - k_{2\dots n}^2). \quad (7.14)$$

This procedure is repeated $(n - 2)$ times, resulting in the phase-space decomposition suggested before. Here, the phase space of a 2-particle decay $D(p_{ab}) \rightarrow A(k_a) + B(k_b)$ is defined by

$$\int d\Omega_d(s_{ab}, s_a, s_b) = \int d^4 k_a d^4 k_b \delta(k_a^2 - s_a) \theta(k_a^0) \delta(k_b^2 - s_b) \theta(k_b^0) \delta^{(4)}(p_{ab} - k_a - k_b), \quad (7.15)$$

with $s_{ab} = p_{ab}^2$, and the t -channel phase space for $C(p_a) + D(p_b) \rightarrow A(k_a) + B(k_b)$ by

$$\int d\Omega_p(p_a, p_b, s_a, s_b) = \int d^4 k_a d^4 k_b \delta(k_a^2 - s_a) \theta(k_a^0) \delta(k_b^2 - s_b) \theta(k_b^0) \delta^{(4)}(p_a + p_b - k_a - k_b), \quad (7.16)$$

where $s_i = m_i^2$ for external particles in both definitions. The respective mappings applied to the two phase spaces, which can be evaluated in the rest frame of the total incoming momentum, and all rotations and boosts needed to build the whole phase space are explained in Refs. [73, 92, 94]. At this point, only the mapping of time-like invariants is explained in more detail, because the peak structure of the integrand mainly arises from the respective propagators. (The mappings introduced here can also be used for smoothing the Mandelstam variable t in $2 \rightarrow 2$ scattering phase spaces with adequate sign changes.) The integral over the time-like invariant is mapped via

$$\int_{s_{\min}}^{s_{\max}} ds = \int_0^1 \frac{dr}{g_s(s(r), m^2, \nu, s_{\min}, s_{\max})}, \quad s(r) = h(r, m^2, \nu, s_{\min}, s_{\max}), \quad (7.17)$$

$$g_s(s(r), m^2, \nu, s_{\min}, s_{\max}) = \frac{dh(r, m^2, \nu, s_{\min}, s_{\max})}{dr}, \quad (7.18)$$

with the functions h and g_s defined according to the diagram to be smoothed. If the mapped time-like invariant corresponds to a propagator in the particular diagram, the following mappings are used with respect to the propagator type.

Propagator with vanishing width: $f \propto 1/(s - m^2)^2$

Propagators for stable particles or particles that are non-resonant and therefore their widths are treated as zero—like the intermediate gauge-boson propagators in case of the production of stable gauge bosons—are mapped via

$$\begin{aligned} h(r, m^2, \nu, s_{\min}, s_{\max}) &= \left[r (s_{\max} - m^2)^{1-\nu} + (1-r) (s_{\min} - m^2)^{1-\nu} \right]^{\frac{1}{1-\nu}} + m^2, \\ g_s(s, m^2, \nu, s_{\min}, s_{\max}) &= \frac{1-\nu}{\left[(s_{\max} - m^2)^{1-\nu} - (s_{\min} - m^2)^{1-\nu} \right] (s - m^2)^\nu}, \end{aligned} \quad (7.19)$$

for $\nu \neq 1$. In the actual calculations, $\nu = 1.1$ turns out to be an appropriate choice. As suggested in Ref. [92], a small negative value of m^2 is introduced for massless propagators to avoid numerical instabilities. For the Mandelstam variable t arising in the $2 \rightarrow 2$ scattering phase spaces, this mapping is used with the respective sign changes,

$$t = -h(r, -m^2, \nu, -t_{\min}, -t_{\max}). \quad (7.20)$$

Breit–Wigner propagator: $f \propto 1/((s - m^2)^2 + m^2\Gamma^2)$

For resonant propagators showing the Breit–Wigner form, the mapping

$$\begin{aligned} h(r, m^2 - im\Gamma, 2, s_{\min}, s_{\max}) &= m^2 + m\Gamma \tan[y_1 + (y_2 - y_1)r], \\ g_s(s, m^2 - im\Gamma, 2, s_{\min}, s_{\max}) &= \frac{m\Gamma}{(y_2 - y_1) [(s - m^2)^2 + m^2\Gamma^2]}, \end{aligned} \quad (7.21)$$

with

$$y_{1,2} = \arctan\left(\frac{s_{\min, \max} - m^2}{m\Gamma}\right) \quad (7.22)$$

is applied. Such propagators arise both for gauge bosons in the full amplitude calculations including decays and for top resonances.

In case of the NWA used for the description of massive gauge-boson decays, these propagators are replaced by δ -functions with the respective trivial integration performed analytically. The appropriate normalization results from integrating over the Breit–Wigner propagator with the limit $\Gamma_V \rightarrow 0$ taken wherever possible,

$$\int_{s_{\min}}^{s_{\max}} \frac{ds}{(s - M_V^2)^2 + M_V^2\Gamma_V^2} \xrightarrow{\Gamma_V \rightarrow 0} \frac{\pi}{M_V\Gamma_V}. \quad (7.23)$$

In order to implement this approximation into the generic framework for the phase-space generation, a “pseudo-mapping” is defined, where g_s should not be understood as the Jacobi determinant of the mapping here, contrary to Eq. (7.18),

$$s(r) = M_V^2, \quad g_s(s(r)) = \frac{M_V\Gamma_V}{\pi}. \quad (7.24)$$

For all time-like invariants that do not correspond to propagators in a diagram and all angles, which are calculated in the rest frames of the respective two-particle phase spaces, linear mappings are applied,

$$s = s_{\max}r + s_{\min}(1 - r) , \quad \phi = 2\pi r , \quad \cos \theta = 2r - 1 . \quad (7.25)$$

By the approach discussed in this section, the integral over each n -particle phase space can in general be decomposed as follows,

$$\int d\phi^{(n)}(p_a, p_b) = \prod_{i=1}^{n-2} \int ds^{(i)} \prod_{j=1}^{n_d} \int d\Omega_d^{(j)} \prod_{k=1}^{n-n_d-1} \int d\Omega_p^{(k)} , \quad (7.26)$$

where $n_d \leq n - 1$ is the number of two-particle decays arising in the described channel. The arguments of the respective elements are to be restored according to the specific phase-space decomposition.

7.3 Improvements of the integrator performance

While the methods described in the foregoing sections are generally appropriate for the numerical evaluation of any $2 \rightarrow n$ scattering cross sections at LO, the NLO contributions to cross sections—in particular the real corrections—require some improvements. The virtual part does not lead to numerical instabilities arising from the phase-space integration, since the cancellation of singularities is performed analytically. The problems to be solved in the integration of virtual corrections are related to a stable evaluation of loop integrals in exceptional phase-space regions. Apart from a few events, this problem is solved by using the Denner–Dittmaier reduction scheme [81] for five-point functions. The remaining events that are not evaluated in a stable way are thrown away by applying a technical cut. Since only a handful out of a million events are thrown away in each channel, the results are not significantly influenced by this action.

7.3.1 Extra channels for subtraction terms in the real corrections

In the real-correction contributions, the function f in Eq. (7.3) contains both matrix elements and dipole terms, whereas the phase-space parametrizations described so far are only adapted to the first. The multi-channel approach, however, provides a convenient way to extend the procedure by simply adding additional channels adapted to the peak structure of the dipole terms. The $(m + 1)$ -particle phase space of the real corrections can be decomposed into an m -particle phase space and a description of the remaining parton, which can be used for the phase-space generation.

For the dipoles describing final-state singularities with an initial-state spectator, such

a decomposition can be achieved via

$$\begin{aligned} \int d\phi^{(m+1)}(p_a, p_b; k_1, \dots, k_{m-1}, p_i, p_j) &= \int_0^1 dx_{12,a} \int d\phi^{(m)}(\tilde{p}_a, p_b; k_1, \dots, k_{m+1}, \tilde{p}_{ij}) \\ &\times \int d\phi^{(2)}(p_i + p_j; p_i, p_j) \times 2 p_a(p_i + p_j) , \end{aligned} \quad (7.27)$$

where the relations between the momenta of real-correction and dipole phase spaces are given in Eq. (5.43). The situation of initial-state singularities with a final-state spectator can be treated analogously with $\tilde{p}_a \rightarrow \tilde{p}_{ai}$, $\tilde{p}_j \rightarrow \tilde{p}_k$, and the momentum relations of Eq. (5.32). It turns out, however, to be convenient to use different mappings for the two-parton phase space $d\phi^{(2)}$, which is discussed at the end of this subsection.

For the dipoles describing initial-state singularities with an initial-state spectator, a different decomposition is used,

$$\begin{aligned} \int d\phi^{(m+1)}(p_a, p_b; k_1, \dots, k_{m-1}, p_i, p_j) &= \int_0^1 dx_{1,ab} \int d\Omega_i(p_i) \times \frac{1}{4} p_i^0 \sqrt{(p_a + p_b)^2} \\ &\times \int d\phi^{(m)}(\tilde{p}_{ai}, p_b; \tilde{k}_1, \dots, \tilde{k}_{m-1}, \tilde{p}_j) , \end{aligned} \quad (7.28)$$

with the momenta of the two phase spaces related via Eq. (5.43). The solid angle of the momentum p_i is denoted by $d\Omega_i(p_i)$, and p_i^0 is its energy component in the rest frame of the incoming momenta p_a and p_b .

In general, the lower integration limit of the variables $x_{ij,a}$ and $x_{i,ab}$ can be chosen as $x_{\min} > 0$ from kinematical constraints. For the variable transformation of the respective integral,

$$\int_{x_{\min}}^1 dx = \int_0^1 \frac{dr}{g_x(x(r))} , \quad (7.29)$$

the following mappings turn out to be convenient,

$$x(r) = 1 + x_{\min} - \exp(r \ln x_{\min}) , \quad g_x(x(r)) = \frac{1}{(x(r) - (x_{\min} + 1)) \ln x_{\min}} , \quad (7.30)$$

and

$$x(r) = (1 - x_{\min})(1 - r)^n + x_{\min} , \quad g_x(x(r)) = \frac{1}{(x(r) - x_{\min})^{1-\frac{1}{n}} n (1 - x_{\min})^{\frac{1}{n}}} . \quad (7.31)$$

In the case of Eq. (7.27), the mapping in Eq. (7.30) is applied, for Eq. (7.28) the one in Eq. (7.31) with $n = 4$. In principle, the variables \tilde{z}_i or u_i defined in Eqs. (5.25) and (5.38), respectively, could be used in the mapping of $d\phi^{(2)}$ in Eq. (7.27), and an analogously defined quantity for $d\Omega_i(p_i)$ in Eq. (7.28). In the numerical calculations of this thesis, they are, however, not used. These quantities would mainly be useful to construct mappings that populate the regions around the singularities described by the dipoles. Exactly these regions, however, do not deliver large contributions in the sum over real corrections and dipoles, since the singularities cancel between the two contributions. Instead, angles are used for the mappings of $d\phi^{(2)}$ in Eq. (7.27) and $d\Omega_i^{(2)}$ in Eq. (7.28).

7.3.2 Improving numerics in critical phase-space regions

The main problems concerning the stability of the phase-space integration arise where numerical cancellations take place between contributions that are defined on different phase spaces. This is obviously the case for the real-correction contributions, but also in the collinear-subtraction terms. Since the cuts on outgoing momenta, which are included in the jet functions defined in Section 5.1, are to be applied to the respective phase spaces, large integrands can result from single phase-space points if some contributions are cut away while the others pass the cuts. Improvements can be achieved here in the range of the transverse-momentum cut on the hadronic jet, since it is present in all calculated cross sections and quite easily accessible via mappings.

To this end, further channels are added to the multi-channel integrator. These are constructed according to diagrams containing a t -channel propagator with the two incoming partons and an outgoing parton involved. The usual t -channel mapping for this propagator is replaced by a new mapping that is constructed to populate the phase-space region where the transverse momentum of the outgoing parton is roughly equal to the transverse-momentum cut imposed on the jet. Mainly phase-space points with this property, namely $p_{T,i} \approx p_{T,\text{jet,cut}}$ if i is an outgoing parton, turn out to cause instabilities if numerical cancellations take place between contributions evaluated at different phase-space points. For this purpose, the t -channel phase space is decomposed as follows,

$$\begin{aligned} \int d\Omega_p(p_a, p_b; p_i^2 = 0, s_{\text{rest}}) &= \int_{-|\mathbf{p}_i|}^{|\mathbf{p}_i|} dp_i^3 \int_0^{2\pi} d\varphi_i \frac{1}{4\sqrt{(p_a + p_b)^2}} , \quad |\mathbf{p}_i| = \frac{(p_a + p_b)^2 - s_{\text{rest}}}{2\sqrt{(p_a + p_b)^2}} , \\ &= \int_0^1 dr_1 \int_0^1 dr_2 \frac{\pi}{2\sqrt{(p_a + p_b)^2} g_z(p_i^3(r_1))} , \end{aligned} \quad (7.32)$$

where p_i is the light-like momentum of the outgoing parton, p_i^3 its component in beam direction, and s_{rest} the squared momentum of the remaining outgoing particles. For the mapping of $p_i^3(r)$, the following composition of rational functions is used if $|\mathbf{p}_i| > p_{T,\text{jet,cut}}$,

$$p_i^3(r) = \begin{cases} -\frac{|\mathbf{p}_i| - a_T}{a^n} (a - r)^n - a_T & \text{for } r < a , \\ \frac{a_T}{(0.5 - a)^n} (r - a)^n - a_T & \text{for } a < r < 0.5 , \\ -\frac{a_T}{(0.5 - a)^n} ((1 - a) - r)^n + a_T & \text{for } 0.5 < r < 1 - a , \\ \frac{|\mathbf{p}_i| - a_T}{a^n} (r - (1 - a))^n + a_T & \text{for } r > 1 - a , \end{cases} \quad (7.33)$$

$$g_z(p_i^3(r)) = \begin{cases} \frac{a}{n(|\mathbf{p}_i| - a_T)^{\frac{1}{n}} (-(p_i^3 + a_T))^{1 - \frac{1}{n}}} & \text{for } r < a , \\ \frac{0.5 - a}{n(a_T)^{\frac{1}{n}} (p_i^3 + a_T)^{1 - \frac{1}{n}}} & \text{for } a < r < 0.5 , \\ \frac{0.5 - a}{n(a_T)^{\frac{1}{n}} (-(p_i^3 - a_T))^{1 - \frac{1}{n}}} & \text{for } 0.5 < r < 1 - a , \\ \frac{a}{n(|\mathbf{p}_i| - a_T)^{\frac{1}{n}} (p_i^3 - a_T)^{1 - \frac{1}{n}}} & \text{for } r > 1 - a , \end{cases} \quad (7.34)$$

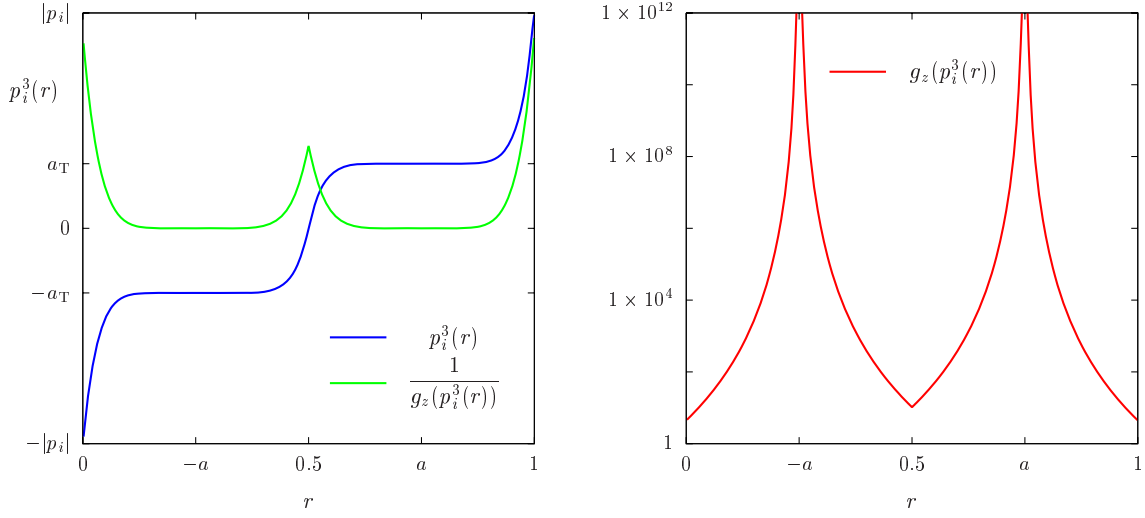


Figure 7.1: Illustration of the mapping for $p_i^3(r)$ if $|\mathbf{p}_i| > p_{\text{T,jet,cut}}$ as defined in Eq. (7.33). The units for $1/g_z(p_i^3(r))$ (left-hand plot) and $g_z(p_i^3(r))$ (right-hand plot) are arbitrary. The choice of parameter values is given in the text.

where

$$a_{\text{T}} = \sqrt{|\mathbf{p}_i|^2 - p_{\text{T,jet,cut}}^2} . \quad (7.35)$$

The parameters $n > 0$ and $0 \leq a_r \leq 0.5$ can be chosen arbitrarily. For the actual calculations and in the illustration shown in Figure 7.1, we set $n = 8$ and $a_r = 0.25$, which turns out to be an appropriate choice by trial and error. For $|\mathbf{p}_i| \leq p_{\text{T,jet,cut}}$, a_{T} is set to zero and $a_r = 0.5$, so only the first and the last line in the definition of the mapping are applied in this case. From Eq. (7.35) it is straightforward to see that $|p_i^3| \approx a_{\text{T}}$ corresponds to $p_{i,\text{T}} \approx p_{\text{T,jet,cut}}$. Hence, the described mapping is useful to populate this critical region.

In the ‘C + A’ contributions to the NLO cross section, which is discussed in Section 5.4, this mapping is used for all subprocesses with gg, qq, or $\bar{q}q$ splittings. These subprocesses contain plus-distributions with respect to the momentum fraction z that one of the incoming partons carries, leading to two different phase-space points contributing, the one with the CM energy $\sqrt{z\hat{s}}$ and the other with $\sqrt{\hat{s}}$. The mappings for both points, which are generated simultaneously, are chosen to match in the limit $z \rightarrow 1$, where both contributions tend to infinity, but with a finite value of their sum. Away from that limit, a numerical cancellation takes place. This cancellation is, however, spoiled if one of the two contributions is cut away and the other one passes the cuts, leading to very large weights of single events. These events can be identified as the jumps in the evolution of the integration error on the left-hand side of Figure 7.2. A remarkable improvement is achieved by adding some extra channels including the mapping of Eq. (7.33), which can be seen on the right-hand side of Figure 7.2.

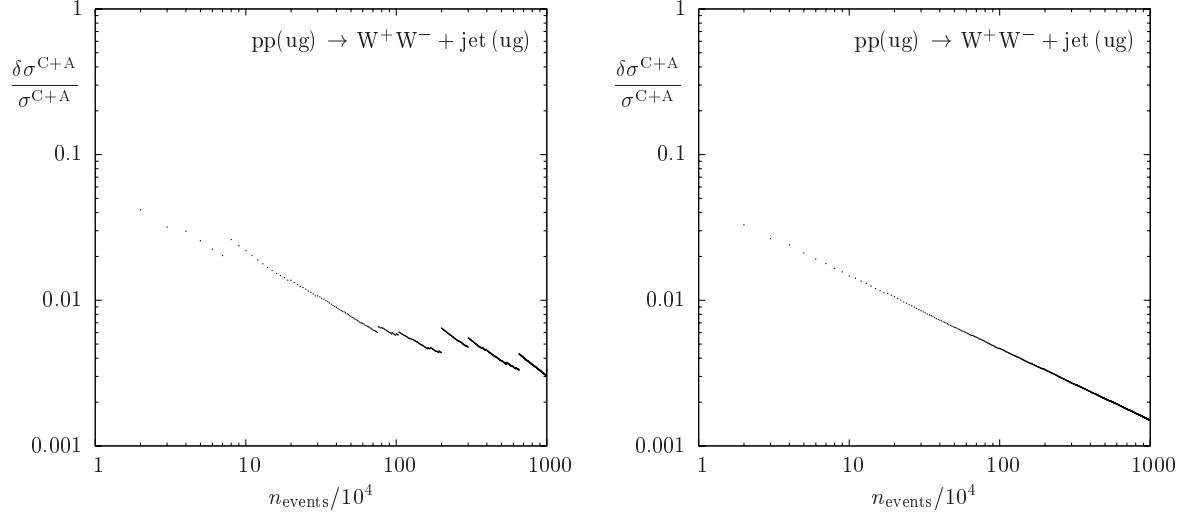


Figure 7.2: Performance of the numerical integration: The evolution of the relative integration error $\delta\sigma/\sigma$ with the number of evaluated events is depicted. As an example, a set of subprocesses of the C+A contribution to the hadronic cross section for WW+jet production is shown, namely those with an up-quark–gluon initial state. Extra channels as explained in the text are only implemented in the integration that corresponds to the error evolution in the right-hand plot.

In the ‘R – A’ contributions to the NLO cross section, a similar problem arises for all real-correction subprocesses containing singularities, which are defined on an $(m + 1)$ -particle phase space. The singularities are cured numerically by means of the dipole terms defined on m -particle phase spaces, where the different phase spaces are degenerate again only if the respective limits—collinear or soft—are taken. Away from these limits, as in the case discussed before, the cancellation is spoiled if at least one of the relevant contributions is cut away, whereas the others pass all cuts. The additional channels to improve the stability of the numerical integration are constructed by using the phase-space decomposition of Eq. (7.27). For all diagrams involving t -channel-like situations with both initial-state partons and a final-state parton, the usual t -channel mapping is replaced by the mapping of Eqs. (7.32) – (7.35), which refers to the outgoing parton in the dipole phase space here. Its transverse momentum coincides with the transverse part of the summed momenta of the two outgoing partons in the respective real-correction phase space. The improvement resulting from this procedure is in general not as strong as in the ‘C + A’ case, but the achieved numerical stability is already acceptable.

For all these contributions with numerical cancellations between different phase spaces, it turns out to be convenient not to apply the adaptive weight optimization described in Section 7.1. The reason is that single events with high weights—which can still show up despite all improvements—would possibly disturb the optimization procedure. Therefore, the weights of all channels remain unchanged in the whole integration.

Chapter 8

Numerical results

In this chapter, numerical results are presented for the generic process class $pp/p\bar{p} \rightarrow VV + \text{jet} + X$. In Section 8.1, the values of the input parameters and the setup used for all calculations are given.

Section 8.2 describes the numerical checks applied to ensure the correctness of the given results. Moreover, for WW+jet production comparisons with the calculations of two independent groups have been performed, which is briefly reported on.

In Section 8.3, the scale dependence of all partonic subprocesses to the LO cross sections for the four weak-gauge-boson assignments are presented in order to give an overview which partonic channels yield the main contributions in the respective process classes.

As discussed in Section 3.3, the cross-section calculations are performed using the four- and the five-flavour schemes. In Section 8.4, both LO and NLO cross sections are compared between the two approaches, showing good agreement within the expected errors. Therefore, all further numerics are discussed only in the five-flavour approach. Moreover, the scale variations of the cross sections are considered for LHC and Tevatron. Finally, the influence of a variation of the transverse-momentum cut applied on the jet is discussed for the VV+jet production cross sections.

Corresponding to Section 6.1, the inclusion of gauge-boson decays is considered by a full amplitude calculation, in the NWA, and in an improved version of the NWA. In Section 8.5, the cross sections for all gauge-boson assignments are presented at LO. Especially if distributions are taken into account, the improved NWA turns out to provide a significantly better approximation of the full results than the simple one.

Therefore, the improved NWA is applied for the NLO QCD calculations presented in Section 8.6. First, an overview is given over the size of the VV+jet cross sections including decays and additional cuts on the outgoing leptons. Afterwards, differential cross sections are presented for WW+jet at the LHC and the Tevatron. Since the cross sections for WZ+jet and ZZ+jet are quite small at the Tevatron, distributions are only discussed here for the LHC.

8.1 Setup and input parameters

For the numerical calculations, the following SM parameters [95] are used,

$$M_W = 80.425 \text{ GeV} , \quad M_Z = 91.1876 \text{ GeV} , \quad G_F = 1.16637 \times 10^{-5} \text{ GeV}^{-2} . \quad (8.1)$$

The electromagnetic coupling α is evaluated from these via

$$\alpha = \alpha_{G_\mu} = \frac{\sqrt{2} G_F M_W^2 \sin^2 \theta_W}{\pi} , \quad (8.2)$$

where θ_W is the electroweak mixing angle defined in Eq. (2.14). This choice of α already respects basic corrections to the electroweak coupling from higher orders of perturbation theory, which is explained, e.g., in Ref. [96]. The widths of the weak gauge bosons are calculated—in case of the production of stable weak gauge bosons they are, of course, set to zero—from all decay channels at NLO QCD with the fermion masses neglected, according to Eqs. (6.3) and (6.4). With the value of the strong coupling at the scale M_Z taken from Ref. [97],

$$\alpha_s(M_Z) = 0.1176 , \quad (8.3)$$

the calculated widths are

$$\Gamma_W = 2.0996 \text{ GeV} , \quad \Gamma_Z = 2.5097 \text{ GeV} . \quad (8.4)$$

The SM parameters already used in the publications on WW+jet production (see Refs. [40, 98, 99, 100]) are not replaced by the more recent values [97] in order to facilitate comparisons; the numerical impact of the slightly changed central value of M_W is, however, negligible anyway at the required accuracy.

The values for the strong coupling in the amplitude calculation are evaluated according to a 1-loop-running at LO and a 2-loop-running at NLO as described in Ref. [60],

$$\alpha_{s,1\text{-loop}}(\mu_{\text{ren}}) = \frac{1}{\frac{33-2N_f}{12\pi} \ln \frac{\mu_{\text{ren}}^2}{\Lambda_{\text{QCD}}^2}} , \quad (8.5)$$

$$\alpha_{s,2\text{-loop}}(\mu_{\text{ren}}) = \alpha_{s,1\text{-loop}}(\mu_{\text{ren}}) \left(1 - \frac{6(153 - 19N_f)}{(33 - 2N_f)^2} \frac{\ln \left(\ln \frac{\mu_{\text{ren}}^2}{\Lambda_{\text{QCD}}^2} \right)}{\ln \frac{\mu_{\text{ren}}^2}{\Lambda_{\text{QCD}}^2}} \right) , \quad (8.6)$$

where μ_{ren} is the renormalization scale, N_f the number of active light quark flavours and Λ_{QCD} the QCD scale parameter. The values of Λ_{QCD} are chosen as prescribed by the applied PDF sets: In the five-flavour scheme, the PDFs of CTEQ6 [101, 102] are used with $N_f = 5$, namely CTEQ6L1 with $\Lambda_{\text{QCD}} = 165 \text{ MeV}$ at LO and CTEQ6M with $\Lambda_{\text{QCD}} = 226 \text{ MeV}$ at NLO. In the four-flavour scheme, the PDFs of MRST2004 (see Ref. [103]) with $N_f = 4$ are taken, namely MRST2004F4LO with $\Lambda_{\text{QCD}} = 220 \text{ MeV}$ at LO and MRST2004F4NLO with $\Lambda_{\text{QCD}} = 347 \text{ MeV}$ at NLO. The renormalization of α_s is performed as described in Section 5.3.4, i.e. with the heavy-quark loops in the gluon self-energy decoupled: In the

five-flavour scheme only the top loop is decoupled, in the five-flavour scheme both the top and the bottom loop.

The Cabbibo angle in the applied approximation for the CKM matrix is set to

$$\theta_C = 0.227 , \quad (8.7)$$

the explicit entries are calculated from this according to Eq. (3.1).

In the calculations of VV+jet production, only a cut on the transverse momentum of the hadronic jet is applied, which is necessary since the cross sections would diverge without such a restriction already at LO. Different values are used for $p_{T,\text{jet,cut}}$ which are explicitly given for the respective results. In this thesis, the successive combination jet algorithm of Ref. [77] with $R = 1$ is applied to decide whether two final-state partons can be resolved as two separated jets or whether they have to be combined to only one jet. For VV+jet production, a dependence on the specific jet algorithm only arises in the real-emission subprocesses because the LO and all other NLO contributions contain only one parton in the final state.

If the weak-gauge-boson decays are included, a set of further cuts is applied which is in general not necessary for the finiteness of cross sections, but provides results which are closer to the experimental situation. These additional cuts are

$$|\eta_{\text{jet}}| < 4.5 , \quad p_{T,\text{lepton}} > 25 \text{ GeV} , \quad |\eta_{\text{lepton}}| < 2.5 , \quad (8.8)$$

where η is the rapidity and p_T the transverse momentum of the respective particle. All leptonic cuts are applied only to charged leptons, of course. In the process classes with outgoing neutrinos, which are WW+jet and WZ+jet production with the considered decays, as an additional condition the missing transverse momentum is required to obey

$$p_{T,\text{miss}} > 25 \text{ GeV} . \quad (8.9)$$

The missing transverse momentum is particularly of interest if WW+jet or WZ+jet are considered as background processes for SUSY searches. Here, the missing transverse momentum is due to the LSP that also leaves the detector unseen.

Furthermore, isolation cuts in order to separate all visible leptons from each other and from hadronic jets are applied,

$$R_{\text{lepton,jet}} > 0.4 , \quad R_{\text{lepton,lepton}} > 0.2 , \quad (8.10)$$

where $R = \sqrt{(\Delta\varphi)^2 + (\Delta\eta)^2}$. The angle between the two particles in the transverse plane is denoted by $\Delta\varphi$, and $\Delta\eta$ is the difference of their rapidities.

In the full amplitude calculations of WZ+jet or ZZ+jet production, a further cut is applied to the two leptons resulting from Z decays. Since the processes we are actually interested in contain resonant Z bosons, the invariant mass of the lepton–antilepton pair is restricted to the region around M_Z ,

$$|M_{l-l^+} - M_Z| < x \Gamma_Z , \quad (8.11)$$

where x can be adapted. From diagrams with the intermediate Z boson replaced by a photon, infrared singularities might arise due to $\gamma \rightarrow l-l^+$ splittings in the limit of vanishing photon virtualities. By the invariant-mass cut, however, such singularities are excluded.

8.2 Survey of numerical checks

8.2.1 Comparison with available tools

In order to ensure the correctness of the results calculated in this thesis, a number of checks has been performed using publicly available tools: All LO and real-emission matrix elements are checked against the package MADGRAPH [104] which is based on the HELAS library [105] for the evaluation of helicity amplitudes. Since the applied version of MADGRAPH does not support a non-trivial CKM matrix, the checks are done with a trivial one, leading in general to an agreement of more than 13 digits.

To provide a check also for integrated cross sections, a detailed comparison with WHIZARD 1.50 [106] and SHERPA 1.0.8 [107] has been performed for WW+jet, both for the LO and the real-emission subprocesses. The latter are made finite by demanding a minimal invariant mass of the two jets, i.e. the checks are actually performed for the LO subprocesses of $pp/p\bar{p} \rightarrow WW + 2\text{jets} + X$. All these comparisons lead to full agreement in the range of the integration errors. A detailed survey of the individual subprocesses is provided in Ref. [73]. In the remaining process classes of VV+jet production, only comparisons of the LO cross sections are performed, leading again to full numerical agreement in the range of the integration errors.

8.2.2 Independent NLO QCD calculations for WW+jet

For WW+jet production, a second full NLO QCD calculation based on, as far as possible, different techniques or at least different implementations has been performed, leading to full numerical agreement with the calculation provided in this thesis. Some results on WW+jet production are presented in Ref. [98]. The evaluation of the virtual corrections of this second version is performed essentially in the same way as described in Refs. [108, 109] where the processes of $t\bar{t}H$ and $t\bar{t}$ +jet production are discussed, respectively. Point-wise comparisons between the two calculations are performed for the different subprocesses at some phase-space points, leading to an agreement of at least 7 digits for all compared events, which is acceptable since numerical cancellations occur in the complex evaluation of the loop integrals. The real-emission subprocesses and the collinear-subtraction counterterms are also compared with a second version, which is based on MADGRAPH matrix elements extended to support a non-trivial CKM matrix and a dipole library developed for the $t\bar{t}$ +jet calculation [109]. Again, the results at individual phase-space points turn out to be consistent at the level of the computational accuracy. For all integrated contributions to the cross section, an agreement typically in the range of one or two standard deviations is obtained as expected from statistics.

Independently of the calculations of Ref. [98], two further groups have performed NLO QCD calculations on WW+jet production. The results of one of these groups are given in Ref. [110], whereas those of the second group are not published yet. In Ref. [40], a tuned comparison of the three calculations is provided for the integrated LO cross section, which agree again within statistical errors, and of the virtual corrections at one specific phase-

space point. Here, the renormalized matrix elements are subdivided to bosonic corrections and fermionic corrections with only the two light generations included. They are given in terms of the coefficients to the poles $\frac{1}{\varepsilon^2}$ and $\frac{1}{\varepsilon}$, and the constant part, i.e. in a way that is independent of the specific treatment of the infrared singularities. (An external comparison of our results for the third-generation loops could unfortunately not be performed so far.) Agreement is achieved between all three results at an accuracy level comparable to the internal checks of our group.

8.3 Discussion of VV+jet cross sections at LO

The LO cross sections for all weak-gauge-boson assignments get contributions from $q\bar{q}$, qg , and $g\bar{q}$ initial states. In this section, the relevance of the respective partonic channels is discussed both for results of proton–proton collisions at $\sqrt{s} = 14$ TeV (LHC setup) and of proton–antiproton collisions at $\sqrt{s} = 1.96$ TeV (Tevatron setup). Scale variations of a factor 10 around the central scale, which is chosen to be M_W for WW+jet and WZ+jet production and M_Z for ZZ+jet production, are considered. Here and in the following sections, the common scale $\mu = \mu_{\text{ren}} = \mu_{\text{fact}}$ is used, i.e. renormalization and factorization scale are set equal and are varied simultaneously.

Without specifying the weak-gauge-boson assignments, some general remarks can be made about the relevance of the specific channels. At the LHC, each partonic process involves at most one valence quark from one of the protons. Therefore, the gluon flux, which is essentially larger at the LHC compared to Tevatron, leads to in general larger contributions from qg channels compared to $q\bar{q}$ channels, whereas the $g\bar{q}$ initial states contribute significantly less since no valence partons are involved here. The situation at Tevatron is essentially different because the proton–antiproton collisions provide $q\bar{q}$ contributions with two valence partons that dominate the cross sections. The scale dependence of the cross sections turns out to be stronger at Tevatron than at LHC, which is due to the factorization-scale variation. While the renormalization-scale variation only reflects the running of the strong coupling α_s , which is the same in both cases, the factorization scale dependence is quite flat for nearly all channels at LHC in the considered range. At Tevatron, however, an increase of roughly the same order as the one arising from the renormalization-scale dependence is found in the direction of lower scales. A detailed analysis of the scale dependence of LO cross sections to WW+jet production is provided in Ref. [73].

Figure 8.1 shows the results for WW+jet production. In case of the LHC, the partonic contributions with up-type quarks prevail those with down-type quarks, which can be understood by comparing the valence-quark PDFs in the protons. The antiquark PDFs of the lightest generation result in an inverted order of the $g\bar{q}$ channels at the LHC where the $g\bar{d}$ channel prevails the $g\bar{u}$ contribution. For Tevatron, the described valence-PDF effect occurs twice in the $q\bar{q}$ channel, leading roughly to a factor 4 between $u\bar{u}$ and $d\bar{d}$. The channels qg and $g\bar{q}$ deliver exactly the same contribution to the integrated cross sections due to the charge-conjugation-invariant hadronic initial state. Naturally, the channels

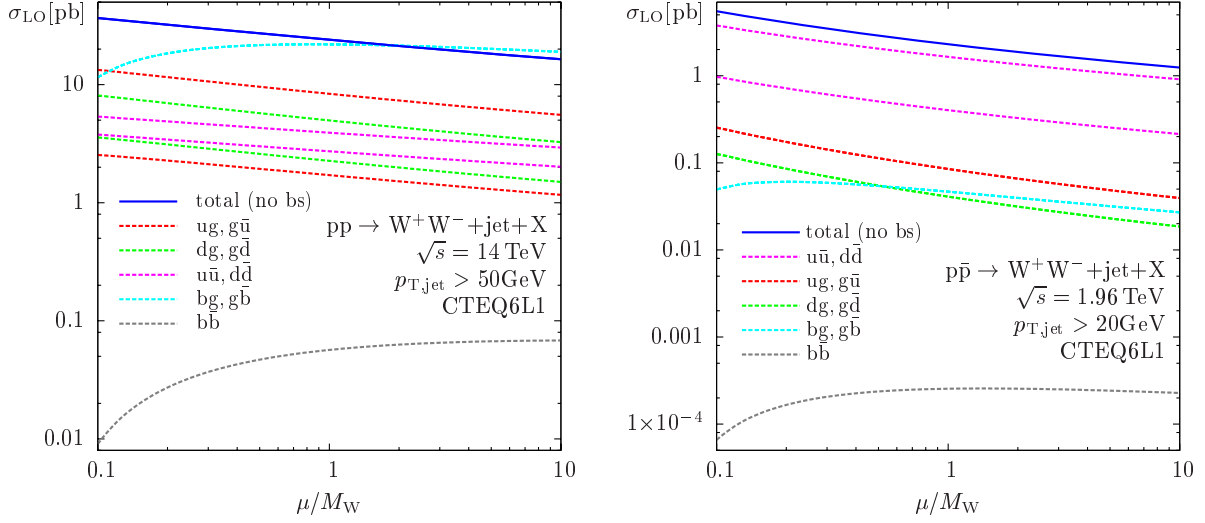


Figure 8.1: Partonic contributions to the LO cross section of $WW+\text{jet}$ at the LHC (left-hand side) and the Tevatron (right-hand side): A scale variation with $\mu = \mu_{\text{fact}} = \mu_{\text{ren}}$ is shown for all channels. If more than one curve with identical colours is given, the first one mentioned in the key corresponds to the upper curve. The contribution named ‘total’ does not contain bottom contributions.

involving valence-(anti-)quarks dominate, and therefore the described PDF effect leads again to larger contributions from $ug/g\bar{u}$ compared to $dg/g\bar{d}$.

In addition, for both colliders the channels involving bottom flavours are shown in the plots. As expected, $b\bar{b}$ is numerically negligible in both cases, whereas the bg channel and the $g\bar{b}$ channel—whose contributions to the integrated cross section are the same—each account roughly for the same amount as all the subprocesses involving (anti-)quarks of the two light generations at LHC. As already explained in Section 3.2, this is due to the fact that these subprocesses actually describe resonant and non-resonant tW^- and $\bar{t}W^+$ production, respectively, with the top decays included. Therefore, these channels—and the respective NLO corrections concerning these channels containing top resonances—are not taken into account in the following sections. For Tevatron, their numerical impact is not that large, since the energy to produce top resonances in addition to a W boson is rarely available. The respective channels are, however, treated in the same way here as for the LHC. The different shapes of the scale-variation curves with bottom flavours result from a strong decrease of the bottom PDFs for smaller values of the factorization scale.

For $ZZ+\text{jet}$ production, the PDF effects explained in the previous passage still hold, but are overcompensated by the coupling strength of the Z bosons to quark chains that favours down-type (anti-)quarks in general, as depicted in Figure 8.2. For the LHC, this results in an inverted order of the channels involving valence quarks, with the down-type subprocesses contributing more now. In the case of Tevatron, this effect is not strong enough to invert the order, but the dominance of the $u\bar{u}$ channel over the $d\bar{d}$ channel is weakened, whereas the subprocesses $ug/g\bar{u}$ and $dg/g\bar{d}$ contribute roughly the same to

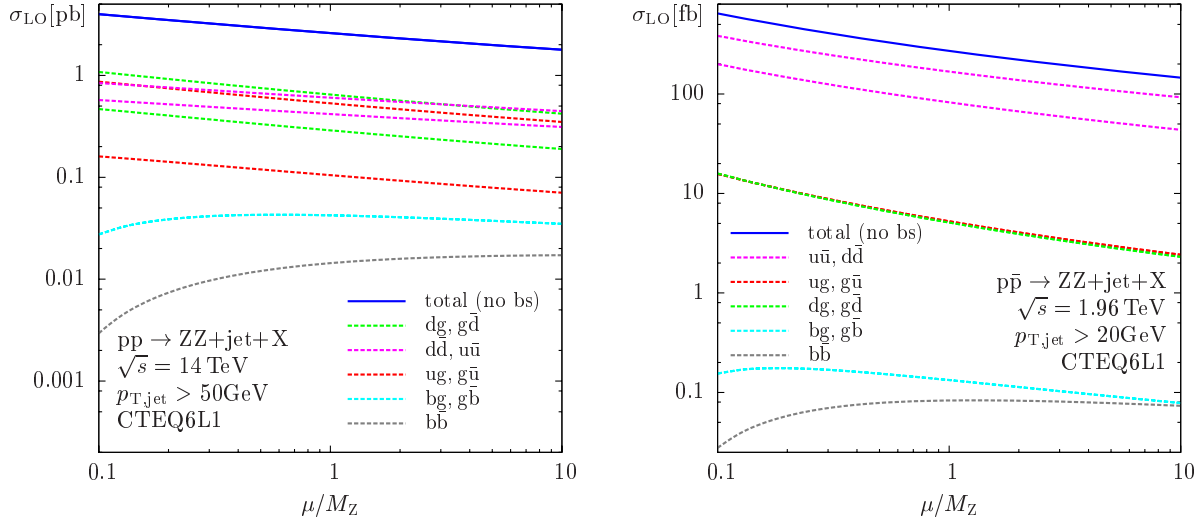


Figure 8.2: As in Figure 8.1, but for ZZ+jet production.

the LO cross section. The channels involving bottom flavours are not enhanced by top resonances in ZZ+jet production. For LHC, their sum accounts for about 4% of the LO cross section only involving the two other generations. Therefore, an LO calculation for the external bottom flavours would be enough for the required level of accuracy. Since the NLO corrections to these channels are essentially the same as for the other light flavours, the NLO calculations could also be simply performed. However, taking into account a further suppression of bottom channels via anti-b-tagging justifies to omit all external bottom contributions in the following NLO calculations. For Tevatron, the respective contributions are beneath the per-mille level and can therefore be neglected anyway.

The respective results for WZ+jet production are collected in Figure 8.3. The partonic initial states shown there contribute either to W^+Z +jet or W^-Z +jet, depending on their charge. The PDF effects discussed for WW+jet explain the situation that the contributions to W^+Z +jet are larger than the respective ones to W^-Z +jet at LHC, since both up-quark and down-antiquark initial states are favoured in proton-proton collisions. Both are only present in the W^+Z +jet case, which simply results from charge conservation. For proton-antiproton collisions at Tevatron, the two processes are connected by \mathcal{CP} symmetry on the hadronic level, yielding the same integrated cross sections for the two process classes. The dominance of the $u\bar{d}/d\bar{u}$ channel as well as the predominance of $ug/g\bar{u}$ over $dg/g\bar{d}$ is again understood from the PDFs. Bottom flavours do not contribute at all in the applied approximation for the CKM matrix.

8.4 NLO QCD cross sections for VV+jet production

After analyzing the individual contributions to the LO cross section in the previous section, the effects of NLO QCD corrections on the VV+jet cross sections are discussed here. For

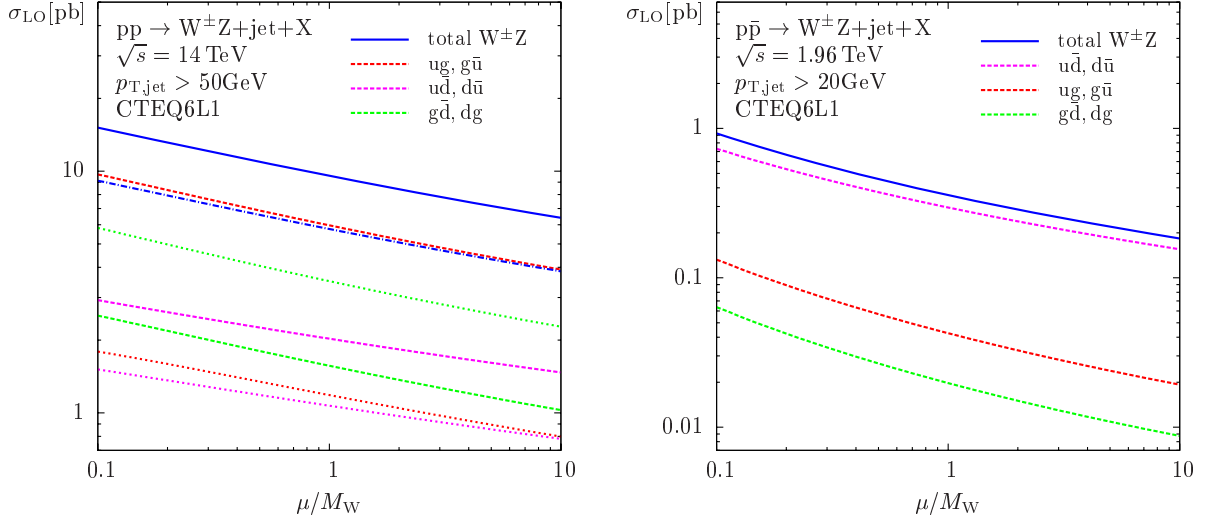


Figure 8.3: As in Figure 8.1, but for WZ+jet production. In the key, the first entry refers to $W^+Z+\text{jet}$, the second one to $W^-Z+\text{jet}$, where the latter channels are in addition marked by dotted lines for LHC.

most of the numerical results of this and the following sections, two different definitions of the NLO observables are used. The one observable is defined more inclusively by only requiring at least one hard jet with a minimum transverse momentum after application of a jet algorithm. The more exclusively defined observable applies a veto on a second separable hard jet and describes therefore genuine VV+jet production. To this end, real-correction events with two jets fulfilling the $p_{T,\text{jet,cut}}$ condition that are not combined by the jet algorithm are not counted in the more exclusive observable. The phase-space regions in the real-correction subprocesses that are relevant for curing infrared singularities from the virtual corrections are not influenced, since the applied restriction only refers to genuine VV+2jets events. Therefore, the difference between the results for the two NLO observables is precisely given by the respective LO observable of VV+2jets production—evaluated, however, with NLO PDFs.

8.4.1 Four-flavour versus five-flavour scheme

Before the scale dependence of the NLO cross sections is discussed in the next paragraph, a comparison between the results obtained in the four-flavour and the five-flavour scheme, respectively, as described in Section 3.3, is provided. The NLO QCD cross sections for all four gauge-boson assignments to VV+jet production are presented in Figure 8.4 for the LHC setup with $p_{T,\text{jet,cut}} = 50 \text{ GeV}$ and in Figure 8.5 for the Tevatron setup with $p_{T,\text{jet,cut}} = 20 \text{ GeV}$, both for the four-flavour calculations with MRST2004F4 PDFs and the five-flavour calculations with CTEQ6 PDFs.

In case of the LHC, the relative deviations between the two approaches show a qualitatively similar behaviour: whereas the deviation significantly increases in direction of lower

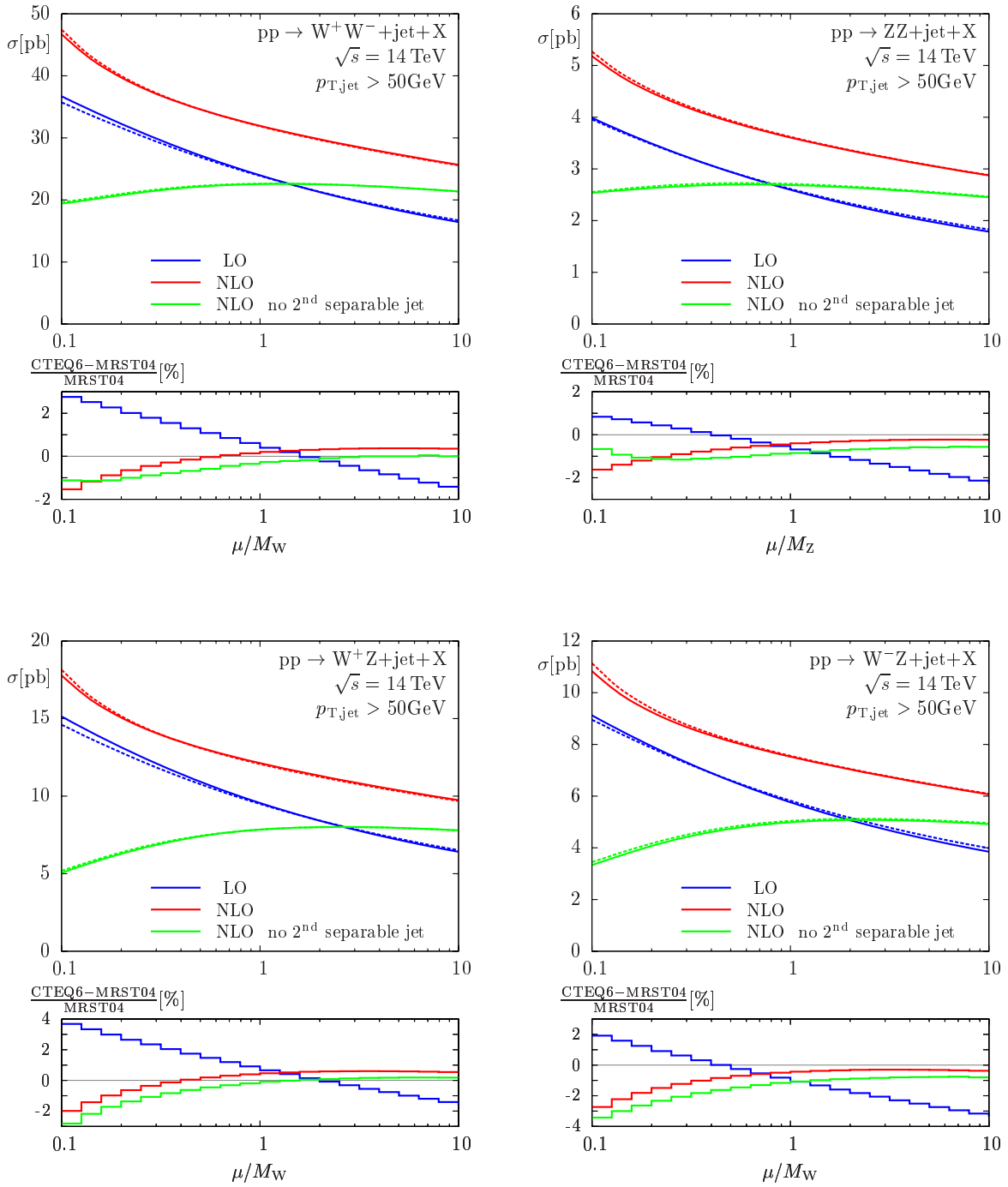


Figure 8.4: Comparison of VV+jet-production cross sections at the LHC: The straight lines show the results calculated with the five-flavour PDFs CTEQ6—namely CTEQ6L1 in LO cross sections and CTEQ6M in NLO—, the dashed lines those calculated with the respective LO and NLO four-flavour PDFs of MRST2004. Contributions from external bottom (anti-)quarks are omitted in the CTEQ6 case, as described in Section 3.3.

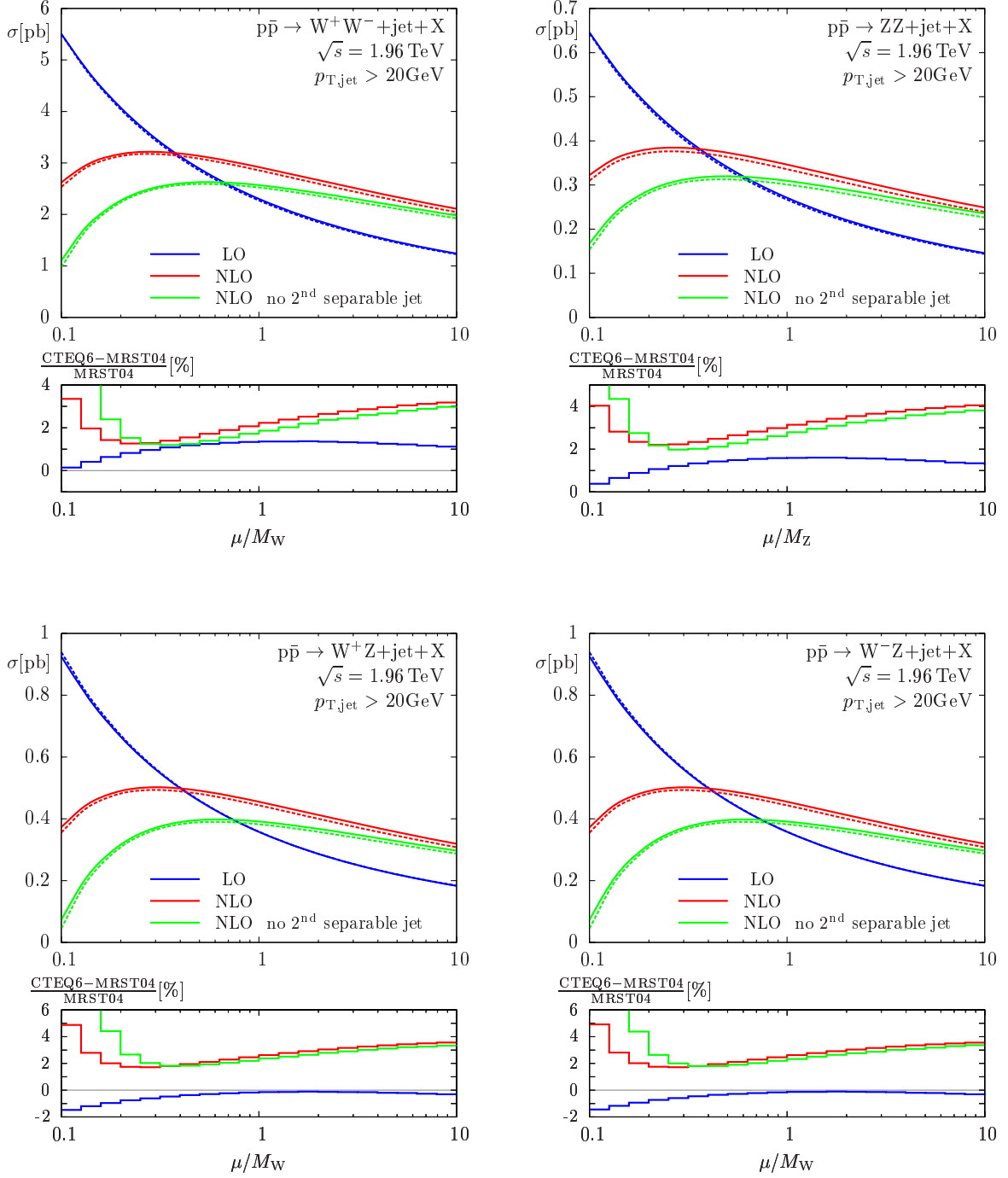


Figure 8.5: As in Figure 8.4, but for the Tevatron setup.

scales at LO, which leads, however, to relative deviations of less than 4% in the whole range, it is nearly flat for both NLO observables where the results deviate by less than 2% for all process classes. For the Tevatron, the comparison between the two approaches delivers deviations of less than 2% at LO over the full scaling range. The NLO cross sections turn out to be slightly larger in the CTEQ6 approach, but on a level of less than 4% for the whole range of interest. The smallest scales depicted may be ignored, because they obviously describe a region where the NLO calculation is not a good approximation any more, as one can see from the steep decline of the absolute values for the NLO cross sections in that range of scales.

Since the results evaluated with different PDF sets can in general not be expected to agree exactly—not only in the present case where different descriptions of the bottom (anti-)quark are applied—this analysis can be seen as a confirmation that the approximation that is applied in the five-flavour calculation delivers fully acceptable results. Moreover, the deviations between the two approaches are far below the expected experimental errors. The good agreement has been further confirmed by performing the same comparison for $p_{T,\text{jet,cut}} = 100$ GeV at LHC and $p_{T,\text{jet,cut}} = 50$ GeV at Tevatron, yielding the same results qualitatively. In addition, also differential cross sections have been compared with no significant deviations showing up in any phase-space regions. Numerical results of these further comparisons are omitted here, because they are not supposed to provide new insight.

8.4.2 Scale dependence of NLO QCD cross sections

Considering the scale dependence in the transition from LO to NLO at the LHC (see Figure 8.4), only a modest reduction is observed if gauge-boson pairs in association with two hard jets are taken into account. This large residual scale dependence is mainly due to the qg channels, followed by contributions with two valence quarks in the initial state, which are present in the real corrections, but not at LO. The scale dependence can be significantly suppressed upon applying the veto of having “no 2nd separable jet”. The relevance of a jet veto in order to suppress the scale dependence at NLO was also realized for genuine W -pair production at hadron colliders [111]. A reduction of the difference between the two curves, which represents—as mentioned in the beginning of this section—the contribution of genuine VV+2jets events, is also achieved by increasing the value of the cut on $p_{T,\text{jet}}$, which is illustrated in Figure 8.6 for WW +jet production with $p_{T,\text{jet,cut}} > 100$ GeV in the LHC setup and $p_{T,\text{jet,cut}} > 50$ GeV for the Tevatron.

In general, the influence of the restriction on genuine VV+jet production via the described jet veto is not that large in the Tevatron setup (see Figure 8.5). This can be understood from the lower CM energy at Tevatron: The energy for producing a second hard jet is available more rarely here, so a stronger suppression of VV+2jets events is obtained. The fact that the difference between the two NLO observables strongly decreases when going to higher $p_{T,\text{jet,cut}}$ values—as shown on the right-hand side of Figure 8.6—confirms this interpretation.

For all VV+jet-production processes, a significant reduction of the scale dependence is

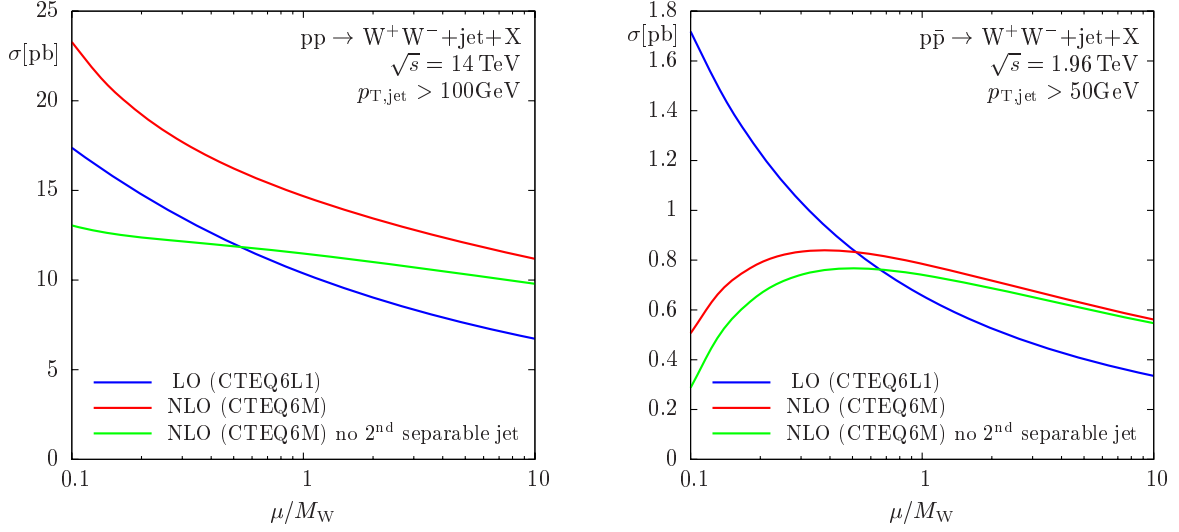


Figure 8.6: Scale dependence of the WW+jet cross sections with $\mu = \mu_{\text{fact}} = \mu_{\text{ren}}$, where $p_{T,\text{jet}} > 100$ GeV is applied for the LHC, and $p_{T,\text{jet}} > 50$ GeV for the Tevatron.

achieved by calculating the NLO corrections to the respective cross sections—at the LHC, however, only if a veto on a second hard jet is applied. Therefore, a summary plot for the scale dependence of all four gauge-boson-pair assignments is provided in Figure 8.7 for the LO and the more exclusive NLO cross sections, with two different $p_{T,\text{jet,cut}}$ values, respectively, both for the LHC and Tevatron.

8.4.3 Dependence on the transverse-momentum cut on the jet

To close the discussion of the NLO cross sections for VV+jet with stable weak gauge bosons, their dependence on the cut applied to the transverse momentum of the jet is considered here. In Figures 8.8 and 8.9, the $p_{T,\text{jet,cut}}$ dependence is shown for all four gauge-boson assignments in the LHC and the Tevatron setup, respectively. In order to introduce a measure for the scale uncertainties of the cross sections, bands are depicted that correspond to a variation of $\mu = \mu_{\text{ren}} = \mu_{\text{fact}}$ by a factor 2 around the central scale. A crossing of the curves for differing scale values leads to vanishing band widths at some points, which is an artifact of how the results are depicted and should not be misinterpreted as a vanishing scale uncertainty. In the plots of Figure 8.9, the band corresponding to the more inclusive cross section is partially covered by the more exclusive one. Both curves are, however, shown here in order to confirm the statement that the effect of genuine VV+2jets events decreases with an increasing value of $p_{T,\text{jet,cut}}$. This becomes manifest in the overlap of the two bands especially for large cut values at the Tevatron, but is also evident in the plots for the LHC setup (see Figure 8.8) from the convergence of the two NLO bands when going to larger values for $p_{T,\text{jet,cut}}$. Eventually, the $p_{T,\text{jet,cut}}$ variation reflects the behaviour discussed in the previous paragraph: For Tevatron, a considerable reduction of the scale

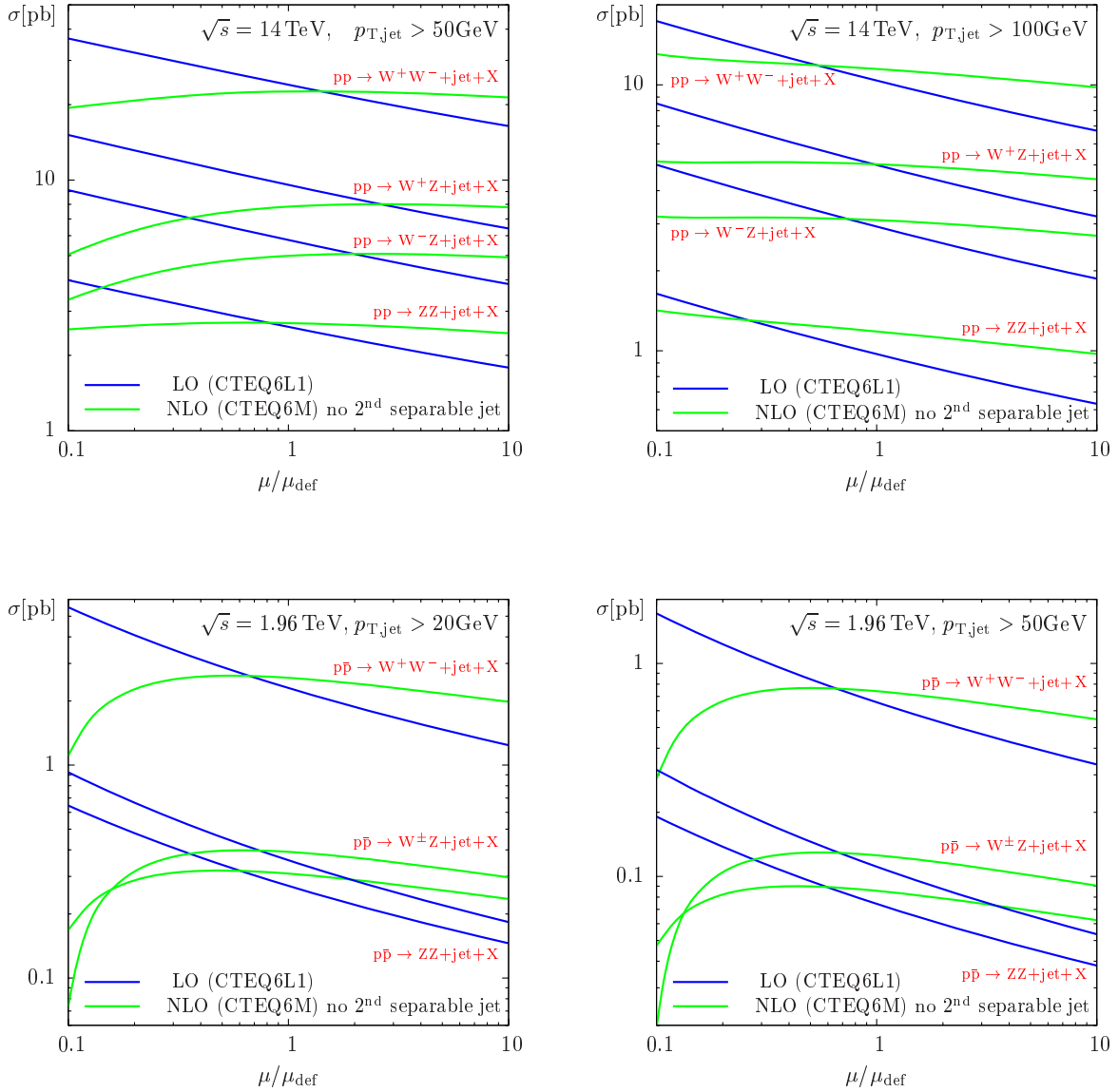


Figure 8.7: Scale dependence of the VV+jet cross sections with $\mu = \mu_{\text{fact}} = \mu_{\text{ren}}$: The upper plots show LHC results for $p_{T,\text{jet}} > 50, 100 \text{ GeV}$, the lower ones contain Tevatron results for $p_{T,\text{jet}} > 20, 50 \text{ GeV}$. At NLO, only the curves for genuine VV+jet production are shown. The scale μ_{def} is set to M_W for WW+jet and WZ+jet, and to M_Z for ZZ+jet.

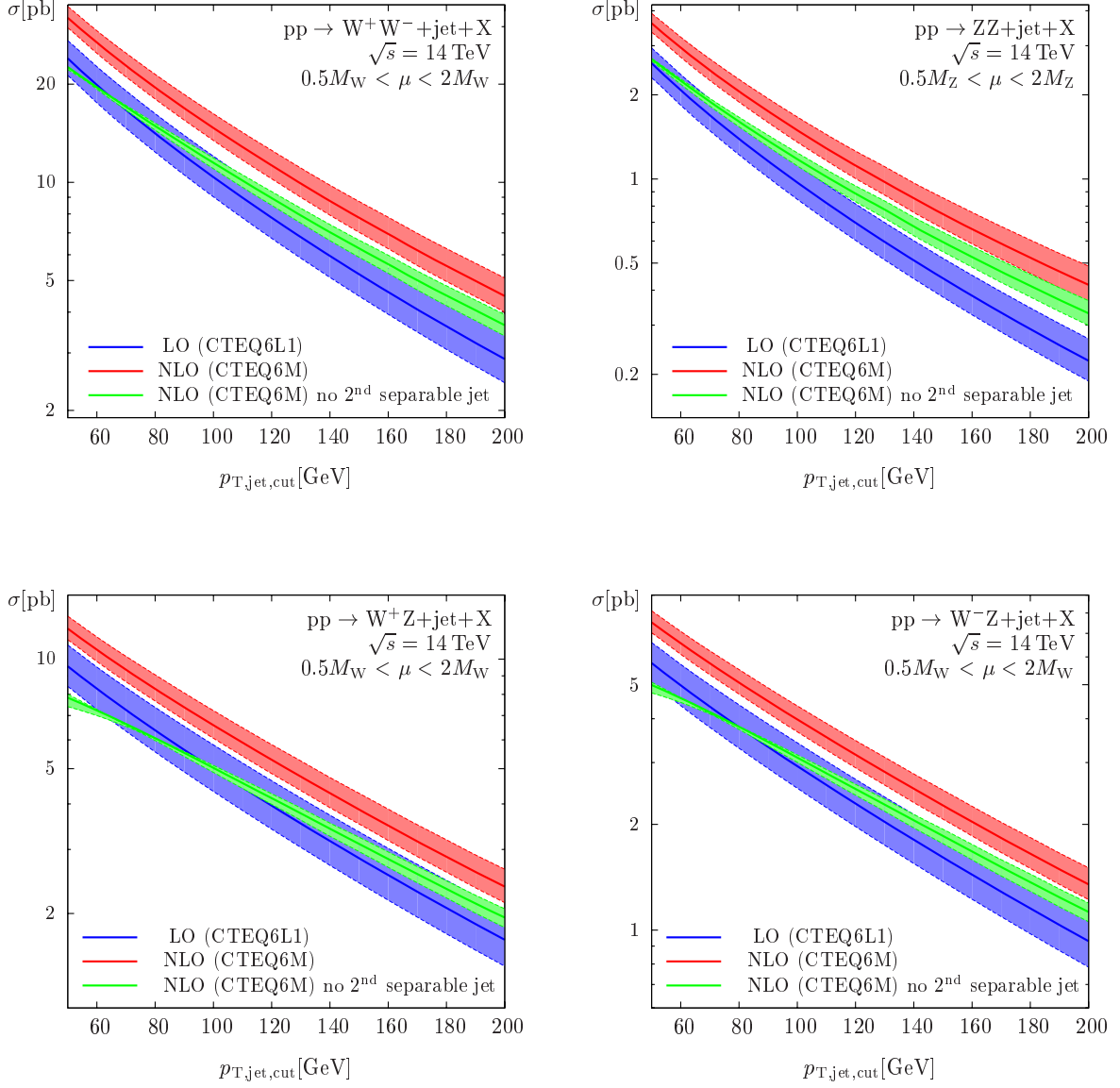


Figure 8.8: Variation of the VV+jet cross sections with $p_{T,jet,cut}$ at the LHC: The bands correspond to a scale variation, again with $\mu = \mu_{fact} = \mu_{ren}$, by a factor 2 around the central scale. The red and the green curves correspond to the different definitions of the NLO observable, where the red one depicts the more inclusive quantity.

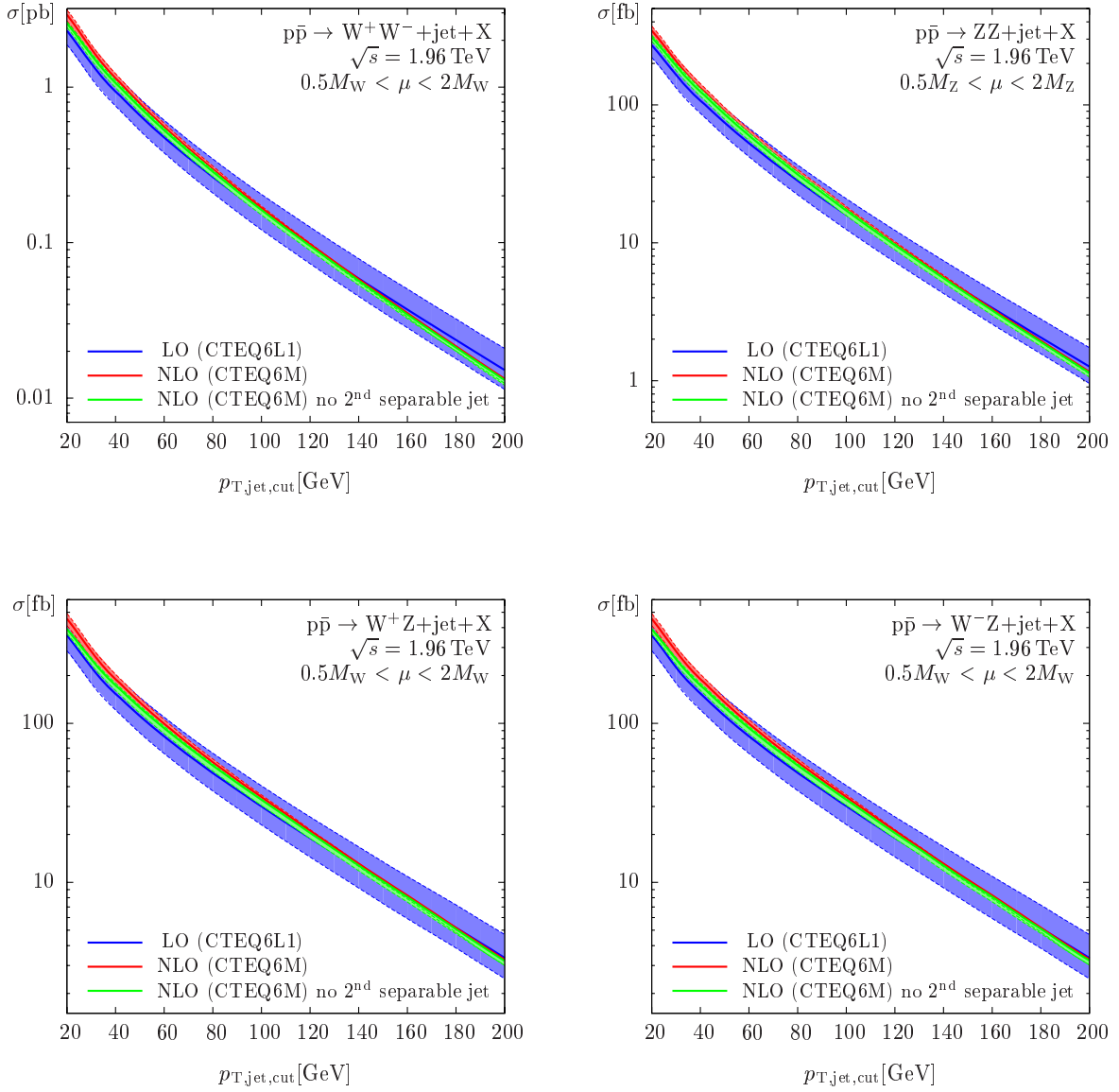


Figure 8.9: As in Figure 8.8, but for the Tevatron setup.

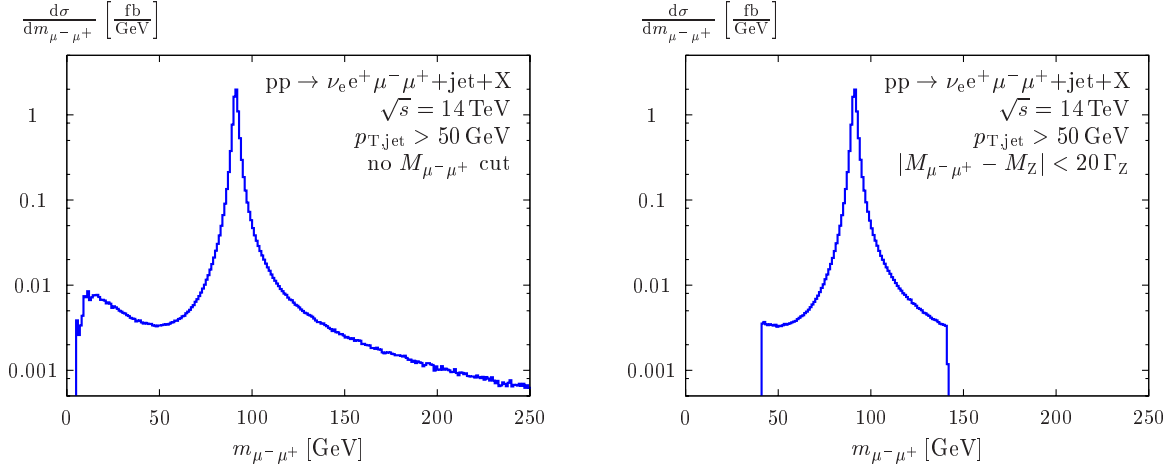


Figure 8.10: Differential cross section with respect to the invariant mass of the decay leptons for W^+Z +jet. No cut is applied on their invariant mass in the left-hand plot. The invariant-mass cut applied in the right-hand plot is chosen such that the Z peak is included, but the contribution of photons with low virtuality is cut away.

uncertainty is achieved when going from LO to NLO, whereas this reduction is only mild for LHC unless $VV+2$ jets events are vetoed.

8.5 LO analysis of the different decay descriptions

Up to now, the massive gauge bosons are treated as stable particles, which is, of course, not the actual situation in experiment. An inclusion of leptonic decays into the calculation of VV +jet production can be performed in different ways. In this section, a comparison of LO results for the three strategies discussed in Section 6.1 is performed, which are a full amplitude calculation, the simple NWA, and an improved version of the NWA that treats the weak gauge bosons as on-shell particles, but keeps spin correlations. The aim of this discussion is to find an adequate approximation in order to avoid performing the full amplitude calculation but still to obtain an appropriate description of the decays. In the processes ZZ +jet and WZ +jet, a cut is applied on the invariant mass of the leptons from the Z decays, which is illustrated in Figure 8.10. The right-hand plot indicates that the cut value is chosen such that the main part of the Z peak is included. The increase for low invariant masses, however, which is due to photons with small invariant masses, is cut away. The cut value used for the calculation corresponds to $x = 20$ in Eq. (8.11). If no lepton-separation cut was applied, the cross section would even be divergent in the limit of a vanishing invariant mass of the lepton-antilepton pair. If a smaller region around the Z peak is considered, i.e. a more typical cut, e.g. $x = 5$ is applied, the NWAs systematically overestimate the cross sections compared to the respective full amplitude calculation. This is due to the fact that the normalization of the δ -function replacing the Breit–Wigner propagator in the improved NWA is calculated in the limit $\Gamma_V \rightarrow 0$, i.e. for an infinite range of Z virtualities. Using finite limits in the evaluation of the normalization factor

yields corrections of roughly 7% for each Z propagator if the limits corresponding to $x = 5$ are inserted. The corrections corresponding to $x = 20$, however, are in the per-cent region and can thus be neglected. If an experimental cut on the invariant mass of the leptons should be applied, such a correction factor would have to be included in the improved NWA, and the branching ratios that are used for the simple NWA would have to be modified by such a correction factor as well.

In Figure 8.11, the cross-section results are shown for the full amplitude calculation and the two approximations in the LHC setup with $p_{T,\text{jet,cut}} > 50$ GeV. Considering only integrated cross sections, both approximations reproduce the full results at the expected accuracy of $\mathcal{O}(\Gamma_V/M_V)$. For WW+jet production, we find a deviation of about +3% for the simple NWA and of +1% for the improved version. For the process classes with Z-boson decays involved, the full amplitude calculation depends on the invariant-mass cut, as discussed above. By using $x = 20$ in this comparison, it is justified not to include a correction factor into the NWA calculations. For ZZ+jet production, the deviation is roughly +2% for the simple NWA and -1% for the improved NWA. For WZ+jet production, it accounts for +4% and +6% for the simple NWA in W^+Z +jet and W^-Z +jet, respectively, whereas the improved NWA reproduces the full amplitude calculation better than on the 1% level for both charge assignments. The differences between the two approximations are due to the ignored spin correlations in the simple NWA, which leads to different distributions of the decay leptons over the phase space. These changes become manifest in the integrated cross sections if cuts are applied. For the calculations depicted in Figure 8.11, the cuts described in Eqs. (8.8) – (8.11) are used with $x = 20$. In general, both the simple and the improved version of the NWA would give the same integrated cross sections if no leptonic cuts were applied. This is due to the fact that taking the spin correlations into account only causes a redistribution between the contributions arising from different gauge-boson polarizations, which does not influence the integrated result.

Distributions in specific variables are, however, strongly affected, which can be seen from the differential cross sections given in Figures 8.12 and 8.13 for WW+jet. Only the distributions for decay leptons are shown there because these are, naturally, mainly affected by the different decay descriptions. Considering the distributions of transverse momentum p_T and rapidity η of each of the two decay leptons, the improved NWA delivers a very accurate reproduction of the full calculation, whereas the simple version deviates by up to 15% in some phase-space regions. The distributions of the angles between the two leptons— φ denotes the angle in the transverse plane and $\cos\theta$ the solid angle between the two leptons—resulting from the full amplitude calculation are also in general reproduced more precisely by the improved NWA. No explicit distributions are shown for the other gauge-boson assignments, but the general statement holds also for these.

The analysis of this section motivates the application of the improved NWA for the NLO QCD calculations to $pp/p\bar{p} \rightarrow VV + \text{jet} + X$ with leptonic decays, at least in a first step. To include an experimental cut on the invariant mass of the leptons from a Z decay into the calculation, a respective factor could be used to rescale the improved NWA results, as discussed in this section. Such a factor is, however, not implemented in the results presented in the following.

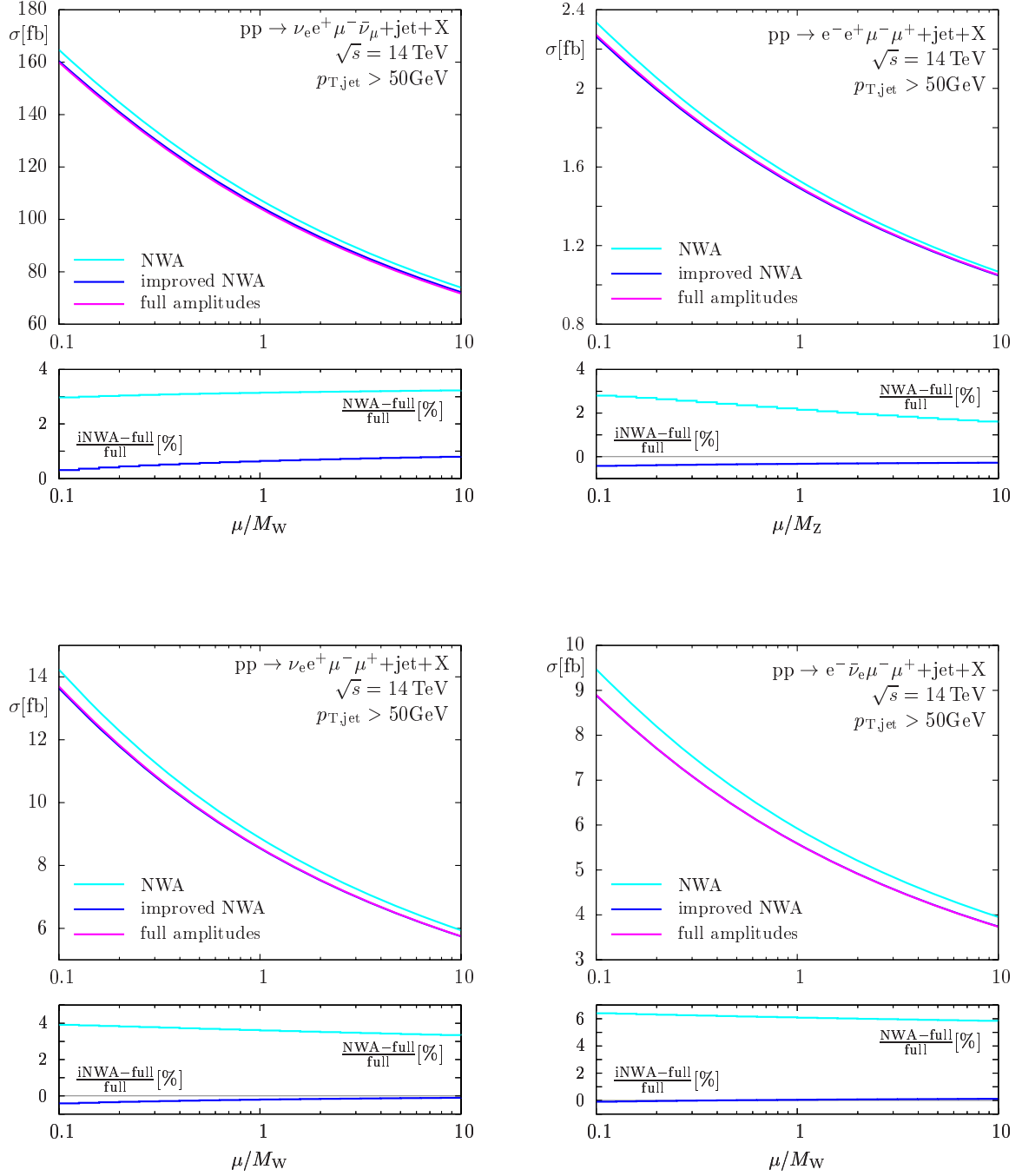


Figure 8.11: Comparison of different decay descriptions for VV+jet at LO in the LHC setup: Scale variations with $\mu = \mu_{\text{fact}} = \mu_{\text{ren}}$ are depicted for the full amplitude calculation, the simple NWA, and the improved NWA (iNWA). The iNWA curve is sometimes covered by the curve representing the full calculation if the relative deviation is very small.

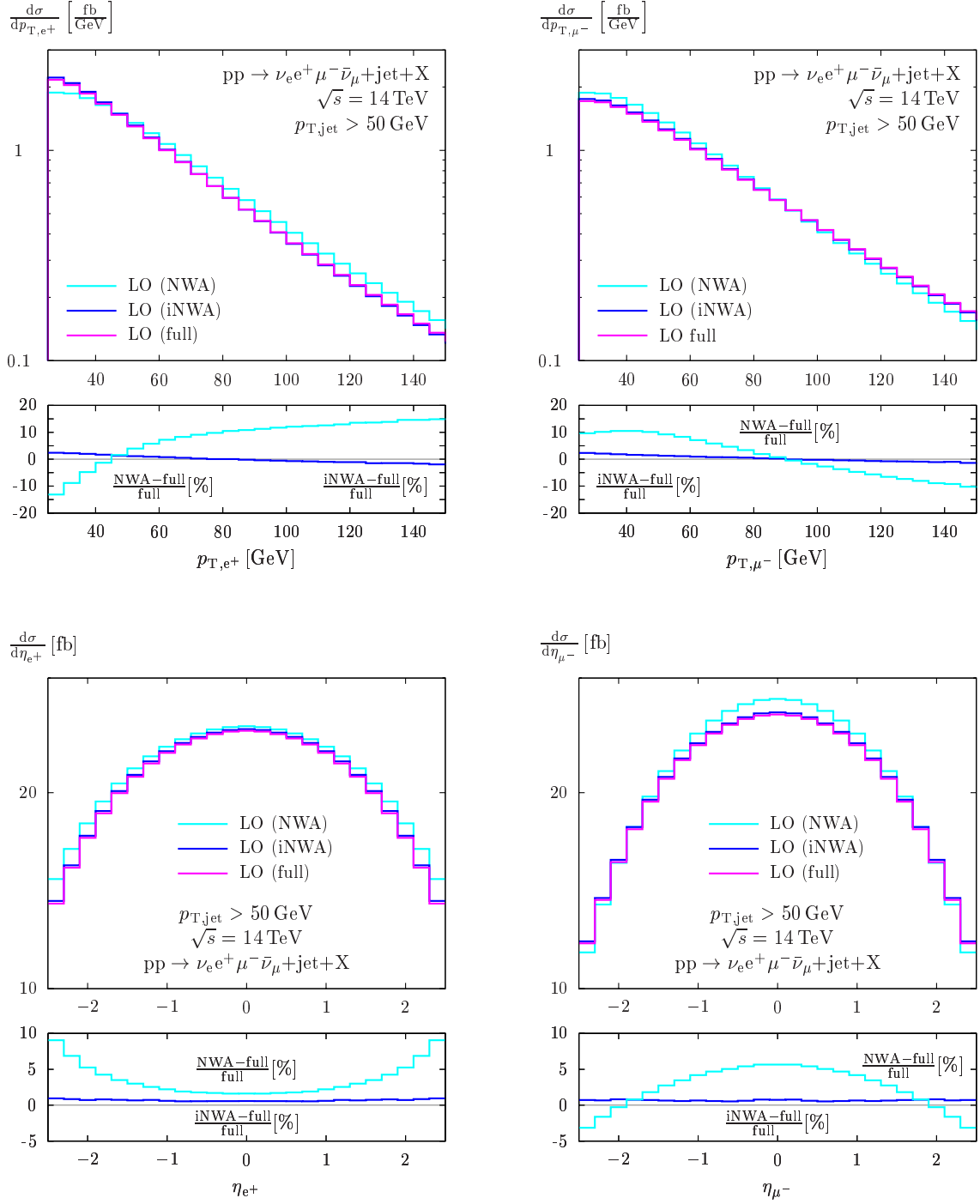


Figure 8.12: Comparison of different decay descriptions for differential cross sections to WW+jet: All observables are evaluated at $\mu = \mu_{\text{fact}} = \mu_{\text{ren}} = M_W$ for the full amplitude calculation, the simple NWA, and the improved NWA. The upper plots show the p_T distributions of each of the two decay leptons, the lower ones the respective η distributions.

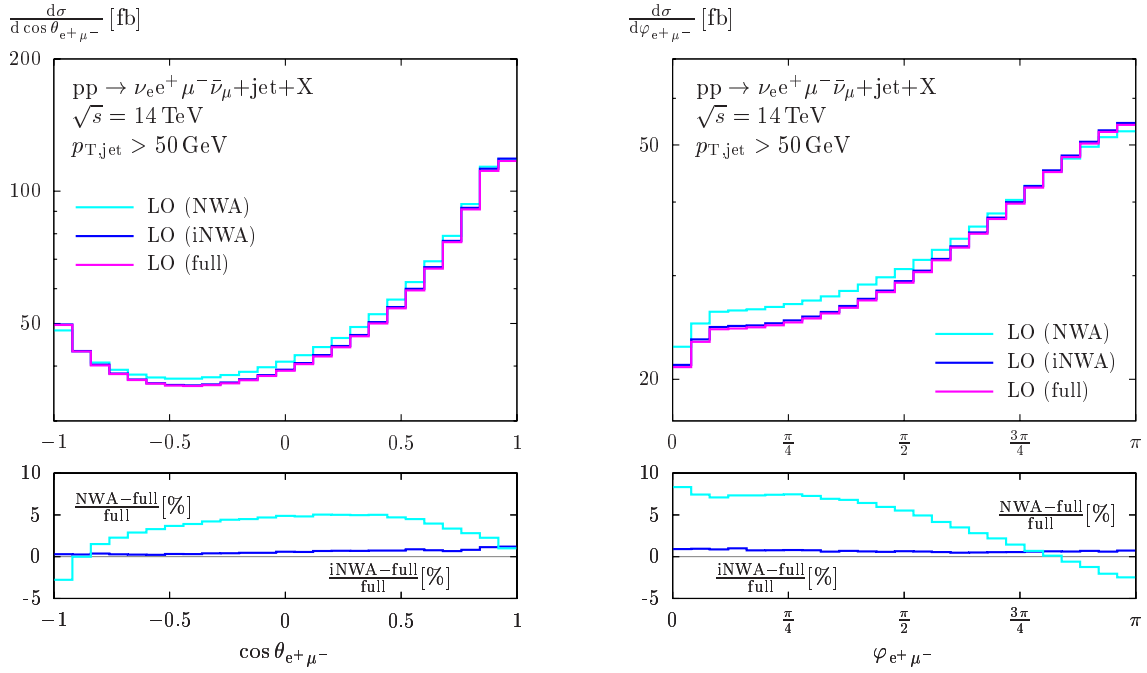


Figure 8.13: As in Figure 8.12, but for the cosine of the solid angle $\cos\theta$ and the angle φ in the transverse plane between the two leptons.

8.6 VV+jet with decays in improved NWA at NLO QCD

After proving the applicability of the improved NWA to approximate the full amplitude calculation results at LO in the previous section, the NLO QCD corrections are discussed here in this framework.

8.6.1 Integrated NLO QCD cross sections

In Figure 8.14, the analogous scale variations as in Figure 8.7 for stable gauge bosons are depicted for VV+jet with leptonic decays included. As described in Chapter 6, the decay channels with as many charged leptons as possible are considered, i.e. all W bosons decay leptonically and the Z bosons decay into a charged lepton–antilepton pair. The analysis given here is restricted to the case that both gauge bosons decay to leptons of different generations. For a simplified notation, the first gauge boson mentioned decays to leptons of the first generation and the second one to those of the second. Since all lepton masses are neglected, exchanging the generations yields identical results. In the NWA, the integrated cross sections would not even change if all decay leptons belong to the same generation apart from a symmetry factor $\frac{1}{2}$ in the ZZ+jet case, which is explained in Section 6.3 in detail. For leptonic distributions, however, the distinction of identical particles would

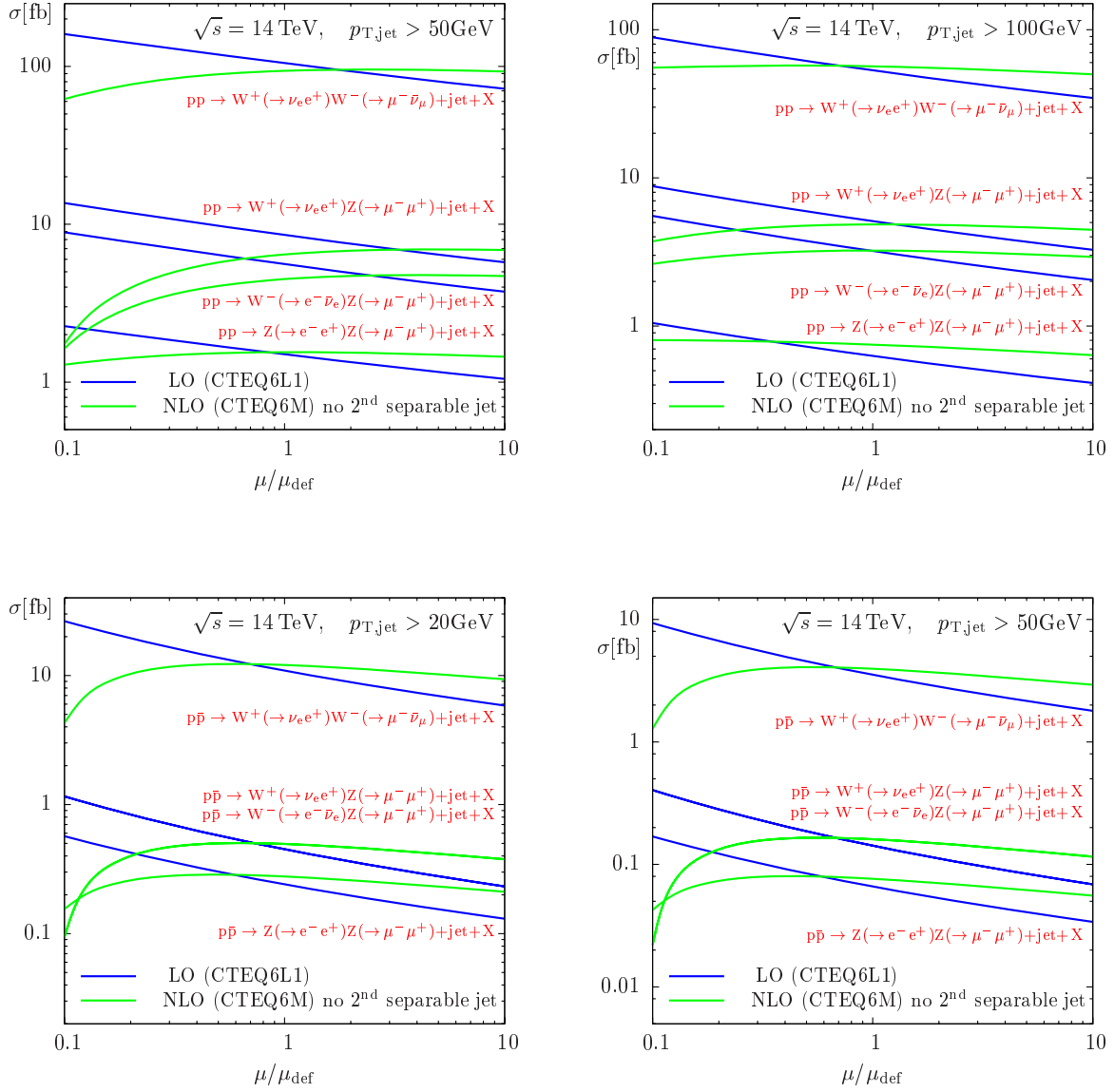


Figure 8.14: As in Figure 8.7, but for VV+jet production with leptonic gauge-boson decays included by application of the improved NWA.

require an ordering of the identical leptons, e.g. by their transverse momenta. This is due to the fact, that the assignment of leptons to the decaying gauge bosons is artificially determined in the NWA by their on-shell condition, which is no more fixed for the full amplitude calculation. Therefore, the discussion here is restricted to leptons of different generations from each decay.

Considering the scale dependence for the various process classes, the results obtained from pure VV+jet production analysis are confirmed: The scale dependence of the cross sections for all process classes is significantly reduced when going from LO to NLO if—at least in the LHC setup—a second hard jet is vetoed. Whereas for the production processes the WW+jet cross section exceeds that one of ZZ+jet by roughly one order of magnitude, this difference is amplified by another order of magnitude when leptonic decays are considered. This is mainly due to the fact that the branching ratios of $W^+ \rightarrow \nu l^+$ and $W^- \rightarrow l^- \bar{\nu}$ exceed that of $Z \rightarrow l^- l^+$ by more than a factor 3. The integrated cross sections for WZ+jet and ZZ+jet at the Tevatron turn out to be significantly below 1 fb for each leptonic channel for the applied set of cuts. A factor 9 for WZ+jet and $\frac{9}{2}$ for ZZ+jet, respectively, can be obtained by summing over all three lepton generations, but still not enough statistics is expected for these channels from Tevatron data. Therefore, a detailed investigation of differential cross sections for these process classes is dropped.

8.6.2 Differential cross sections at NLO QCD

After giving an overview over the integrated cross sections of VV+jet production with leptonic decays in Figure 8.14, the step from LO to NLO in differential cross sections is considered in this section.

WW+jet

A survey of distributions for differential WW+jet cross sections with leptonic decays is given in Figures 8.15 – 8.17 for the LHC setup with $p_{T,\text{jet,cut}} = 50 \text{ GeV}$ and $\mu = \mu_{\text{ren}} = \mu_{\text{fact}} = M_W$. In general, the jet distributions are understood as distributions of the harder jet in the more inclusive definition of the NLO observables. Figure 8.15 provides transverse-momentum distributions for the hadronic jet and the missing transverse momentum due to (anti-)neutrinos leaving the detector unseen (upper plots) and for the two charged decay leptons (lower plots). For all p_T distributions, a tendency of the more exclusive NLO cross section to decrease faster than the LO cross section when going to higher values is evident. This can be understood from the fact that a fixed value is used for the renormalization scale in the running of the strong coupling. If, instead, the transverse momentum of the jet is understood as the relevant scale of the considered process, which might be a good choice since the only arising strong coupling concerns this jet, using $\alpha_s(M_W)$ in the LO calculation overestimates the contributions for large $p_{T,\text{jet}}$ values due to the ignored decrease of the QCD coupling. Besides, an underestimation for lower $p_{T,\text{jet}}$ values follows from the same arguments, which can explain the behaviour observed in the respective plots of Figure 8.15. Since the remaining transverse momenta are connected to $p_{T,\text{jet}}$ by

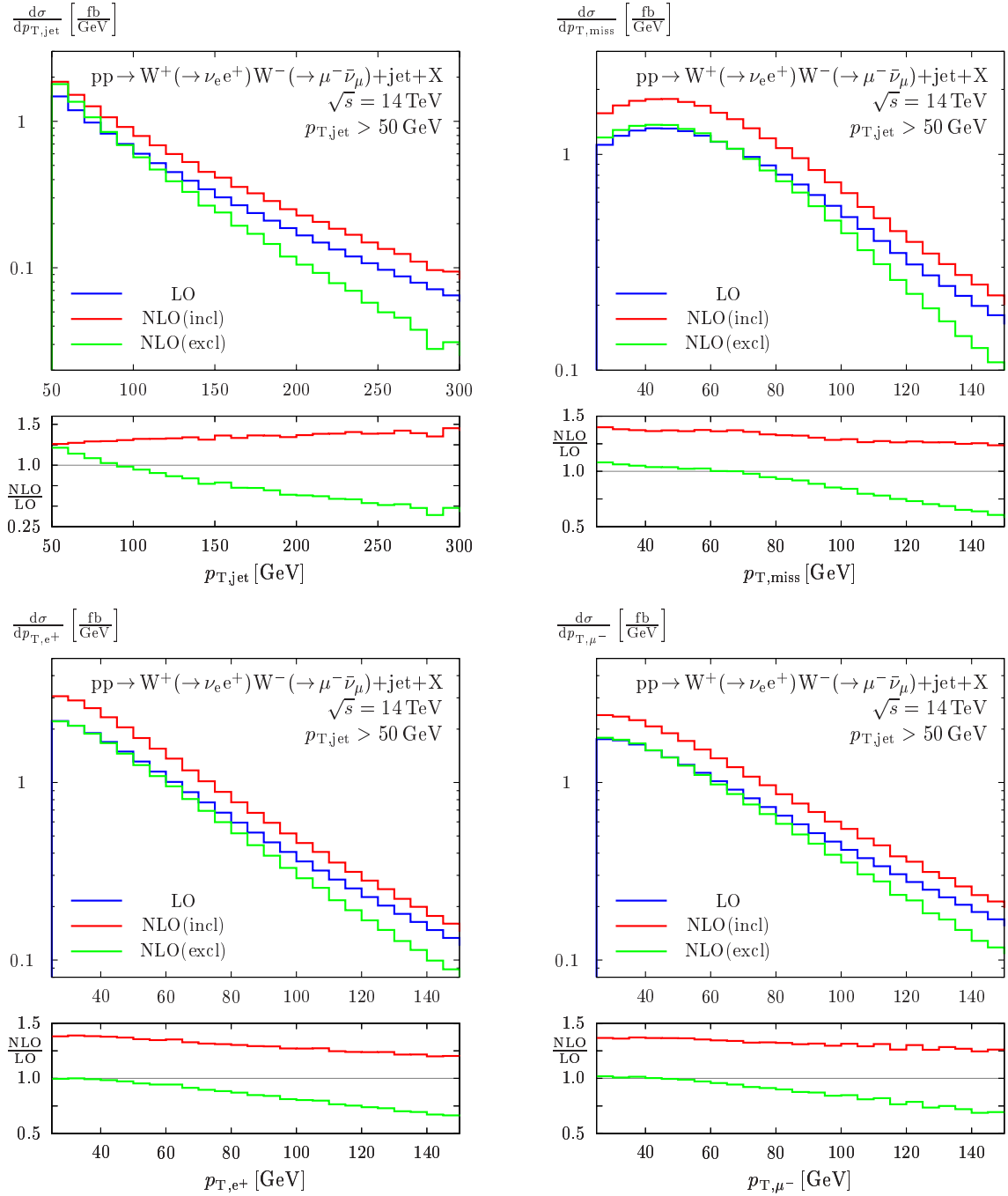


Figure 8.15: Differential cross sections for WW+jet with decays included in the improved NWA at the LHC: The LO and NLO distributions are shown for $\mu = \mu_{\text{fact}} = \mu_{\text{ren}} = M_W$. The two different NLO observables are defined as before. The distributions for the transverse momenta p_T of the jet and of the decay leptons, and for the missing transverse momentum $p_{T,\text{miss}}$ are depicted. The start p_T 's are determined by the respective cuts.

momentum conservation, the same argumentation also holds for these distributions. The effect is, however, much stronger for the jet compared to the leptons due to the tendency of coloured particles to radiate further QCD partons. For the more inclusive NLO observable, this effect is overcompensated by genuine $WW+2\text{jets}$ events which are—being actually LO contributions—also influenced by the same effect. In the p_T distributions for the two decay leptons, a slight tendency to harder jets can be found for the lepton. That a difference arises at all can be understood from the defined order of the W bosons coupling to the fermion chain, because t -channel-like emissions of the W bosons cause large contributions. Whereas a t -channel-like emission of a W^+ can only arise in case of an incoming up quark or down antiquark, an analogous emission of a W^- always stems from an incoming down quark or up antiquark. The antilepton always results from the W^+ decay and the lepton from the W^- decay. Since especially the subprocesses initiated by an incoming up-quark are boosted in the direction of the up quarks, the different PDFs of the incoming partons are expected to cause the observed difference.

This boost effect can also be seen in the upper plots of Figure 8.16 where distributions of the rapidities of the leptons are depicted. Here, the antilepton shows a slightly larger tendency to small angles against the beam axes than the lepton. Naturally, due to the symmetric hadronic initial state in proton–proton collisions the rapidity distributions are symmetric. The size of the relative NLO corrections turns out to be nearly independent of these quantities. The symmetry property still holds for the rapidity of the hadronic jet, which is shown in the lower plot of Figure 8.16. The NLO corrections to this quantity, however, become large for very small angles against the beam axes. Apart from this small phase-space region, which is negligible anyway if the total amount of events is considered, the NLO corrections turn out to be nearly independent of the jet rapidity as well.

The two distributions in Figure 8.17 depict the angle correlations between the two decay leptons. The angle between the two leptons in the transverse plane is represented by φ , which is a quantity invariant under boosts in the beam direction. By $\cos\theta$ the opening angle between these two leptons in the laboratory frame is denoted. Considering the φ distribution, i.e. ignoring the boost effect along the beam axes, the two charged leptons turn out to fly preferentially into opposite directions. This is not surprising, since momentum conservation forces the two W bosons at least to show a tendency to opposite directions which is mediated to their decay products by boost effects. This angle between the leptons is, however, important for the distinction of the background process $WW+\text{jet}$ from the signal process $H(\rightarrow WW^*)+\text{jet}$ in Higgs searches. This is due to the fact that the decay leptons of a W -boson pair arising from the decay of a scalar Higgs particle show the—on the first view non-intuitive—tendency to fly into the same direction. This property results from the spin correlation of the W^+W^- system, which is discussed in detail in Ref. [112]: Since, in the rest frame of the Higgs boson, the spins of the W bosons are anti-correlated, and only a left-handed charged lepton and a right-handed charged antilepton can arise from the decays, their emission in the same direction is favoured. This correlation effect is, of course, smeared in $H(\rightarrow WW^*)+\text{jet}$, since the Higgs boson is not only boosted in direction of the beam axes here due to the emitted jet, but a remainder of the effect should still be measurable. For $WW+\text{jet}$ production, however, the spins of the two W bosons are

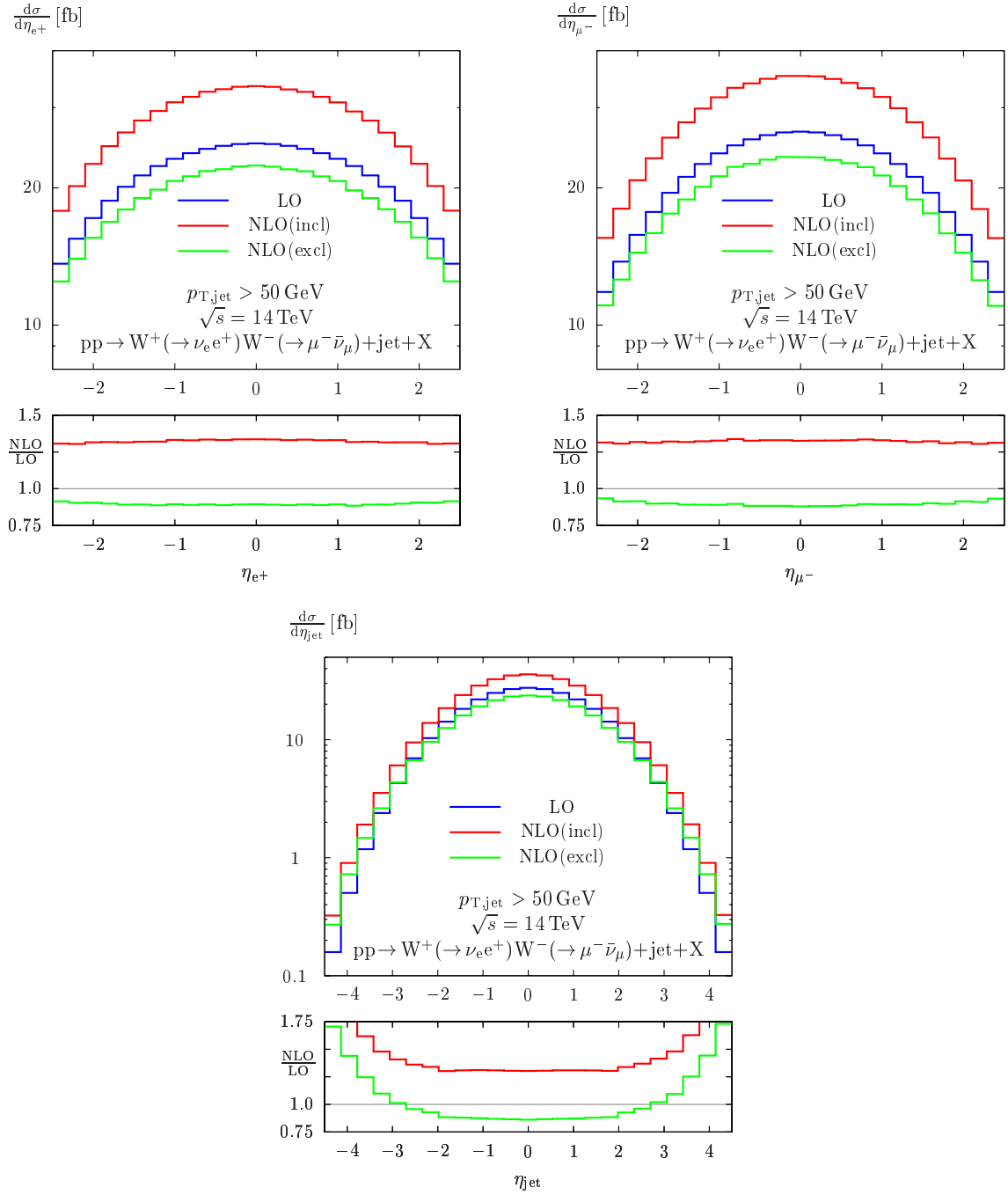


Figure 8.16: As in Figure 8.15, but for the rapidity η of the charged decay leptons (upper plots) and the rapidity of the jet (lower plot).

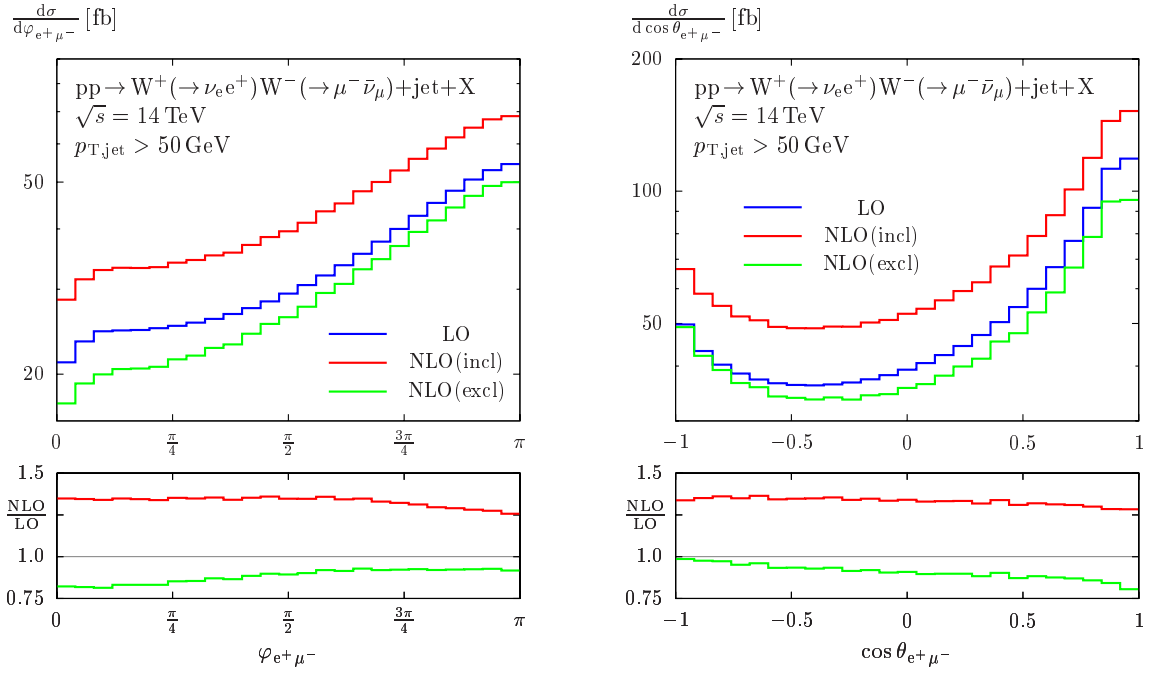


Figure 8.17: As in Figure 8.15, but for the angle φ in the transverse plane and the cosine of the solid angle $\cos\theta$ between the two leptons.

not correlated in such a way, as depicted in Figure 8.17, but tend to opposite directions. In the $\cos\theta$ distribution, this preference is overcompensated by the boost effect along the beam axes, leading to a tendency in direction of small opening angles. The dependence of the size of NLO corrections on both angles turns out, however, to be modest.

Considering the same quantities for WW+jet production in the Tevatron setup, most of the effects can be explained by the fact that proton–antiproton collisions take place here instead of proton–proton collisions. Besides, the lower CM energy compared to the LHC plays an important role. We start again with the discussion of transverse-momentum distributions of the hard jet, the decay leptons, and the missing transverse momentum, which are shown in Figure 8.18. Here, the behaviour of the more exclusive NLO observables can in principle be explained in the same way as for LHC: The LO results overestimate the cross section at high scales and underestimate it at low scales due to the fixed renormalization scale used in the calculation. As already observed when considering integrated cross sections, the difference between the two NLO observables is quite small at the Tevatron, which can be understood from the smaller CM energy: In most cases, not enough energy is available for the production of a second hard jet. Therefore, the LO contributions of $p\bar{p} \rightarrow WW + 2\text{jets} + X$ contained in the more inclusive NLO observable only weaken this effect, but do not overcompensate it as for the LHC setup. The p_T distributions of the two decay leptons are identical up to numerical fluctuations. This results from the fact that the hadronic process $p\bar{p} \rightarrow WW + \text{jet} + X$ is invariant under \mathcal{CP} transformations. Thus,

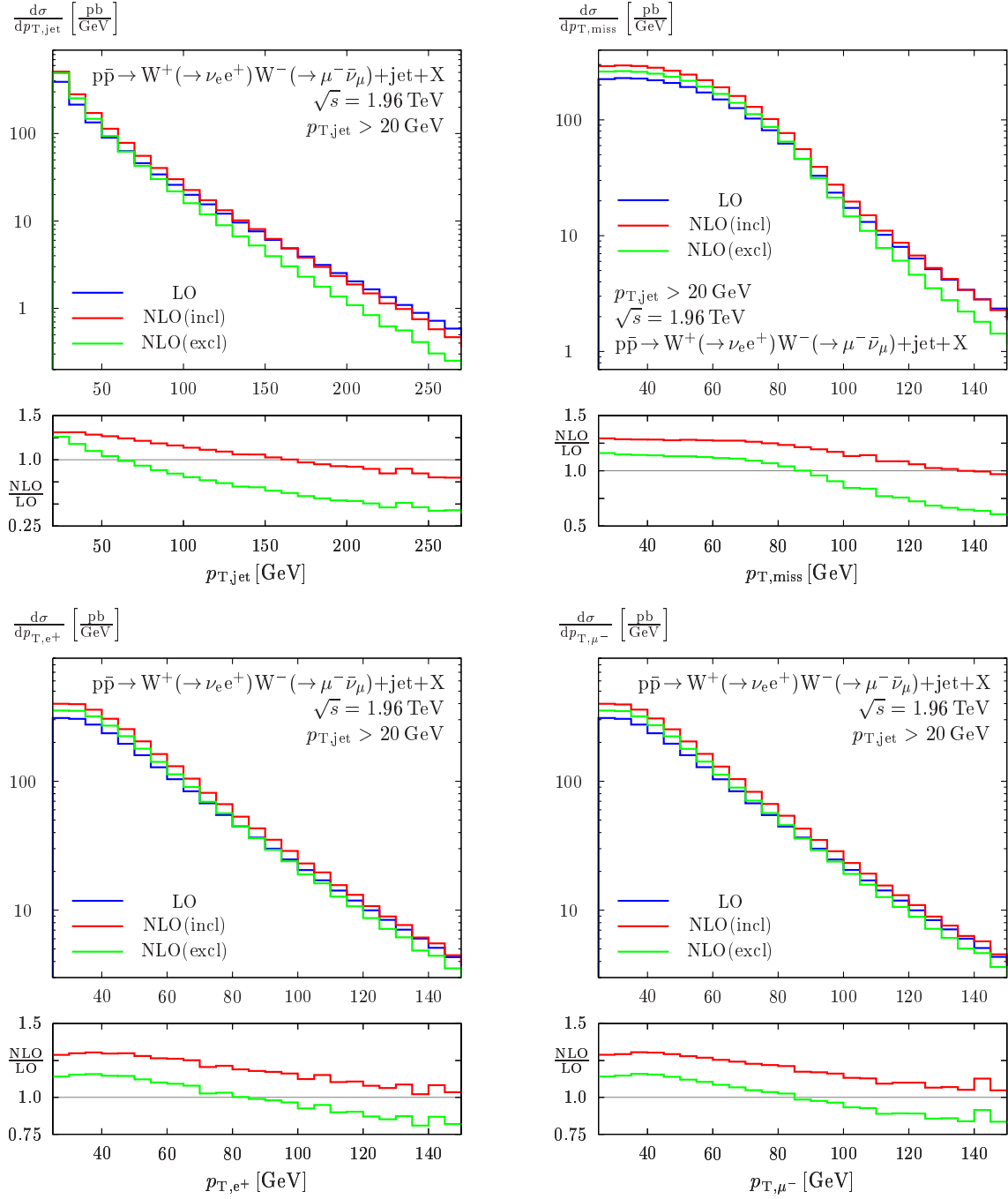


Figure 8.18: As in Figure 8.15, but for the Tevatron setup.

in contrast to proton–proton collisions, PDF effects do not cause differences between the p_T distributions of the leptons, since the quark PDFs of the proton equal the antiquark PDFs of the antiproton, and vice versa.

The distributions of the rapidities η of the leptons, which are depicted in Figure 8.19, are not symmetric with respect to $\eta = 0$ due to the different hadronic initial states. Instead, the distributions of the lepton and the antilepton are identical if one of the distributions is mirrored around the $\eta = 0$ axis. In the Tevatron setup, the positive beam axis corresponds to the direction of the proton beam, and the negative axis to the antiproton beam. Correspondingly, positive η values describe momenta tending in the direction of the proton beam and vice versa.

The difference between proton–proton and proton–antiproton collisions in the leptonic distributions is explained as follows: In the proton–proton case, each partonic subprocess with a non-symmetric initial state has its counterpart yielding exactly the same contribution in opposite direction, e.g. the initial states $u_p(p_1)g_p(p_2)$ and $g_p(p_1)u_p(p_2)$ with p_1 and p_2 labelling the proton momenta in positive and negative beam directions, respectively. (Symmetric initial states as e.g. $u_p(p_1)u_p(p_2)$ deliver symmetric cross sections, anyway.) Thus, the sum over all contributions is symmetric with respect to $\eta = 0$. In proton–antiproton collisions, however, the corresponding subprocesses $u_p(p_1)g_{\bar{p}}(p_2)$ and $g_p(p_1)u_{\bar{p}}(p_2)$ do not yield symmetric contributions due to the different PDFs of proton and antiproton. Instead, each partonic initial state has a counterpart due to the \mathcal{CP} symmetry of the hadronic process. Hence, pairs of subprocesses as e.g. $u_p(p_1)g_{\bar{p}}(p_2)$ and $g_p(p_1)\bar{u}_{\bar{p}}(p_2)$ deliver identical contributions to integrated cross sections. The pair-wise appearance of \mathcal{CP} symmetric subprocesses, however, results in identical distributions for charge-conjugate particles if in addition a space inversion is performed.

Applied to the present case, this explains that the rapidity distributions of the lepton and the antilepton are the same up to a space inversion. Their transverse momenta are, however, invariant under a space inversion. Thus, the corresponding distributions are identical.

Considering the non-symmetric rapidity distributions, a tendency of the antilepton to the positive beam direction and, correspondingly, of the lepton to the negative beam direction is evident. To explain this, the argument of t -channel-like emission of W bosons can again be applied. As discussed in the LHC case, the W^+ boson, and consequently the antilepton, can only be emitted in this way from an up quark or a down antiquark. Since the $q\bar{q}$ channels dominate at the Tevatron, only these have to be taken into account for a qualitative discussion. In the average, these subprocesses do not produce boosted events in a distinguished direction due to the fact that the quark PDFs in the proton are equal to the respective antiquark PDFs in the antiproton. The contributions $u_p(p_1)\bar{u}_{\bar{p}}(p_2)$ and $d_p(p_1)\bar{d}_{\bar{p}}(p_2)$ dominate over the contributions $\bar{u}_p(p_1)u_{\bar{p}}(p_2)$ and $\bar{d}_p(p_1)d_{\bar{p}}(p_2)$. Due to the effect of t -channel-like W^+ emission, the first tends to antilepton emission in the positive beam direction, the latter to the negative direction, as depicted in Figure 8.20. Since the $u\bar{u}$ channel exceeds the $d\bar{d}$ channel roughly by a factor 4 in total, a tendency to the positive beam direction results. The same argumentation holds, *mutatis mutandis*, for the lepton and the W^- boson.

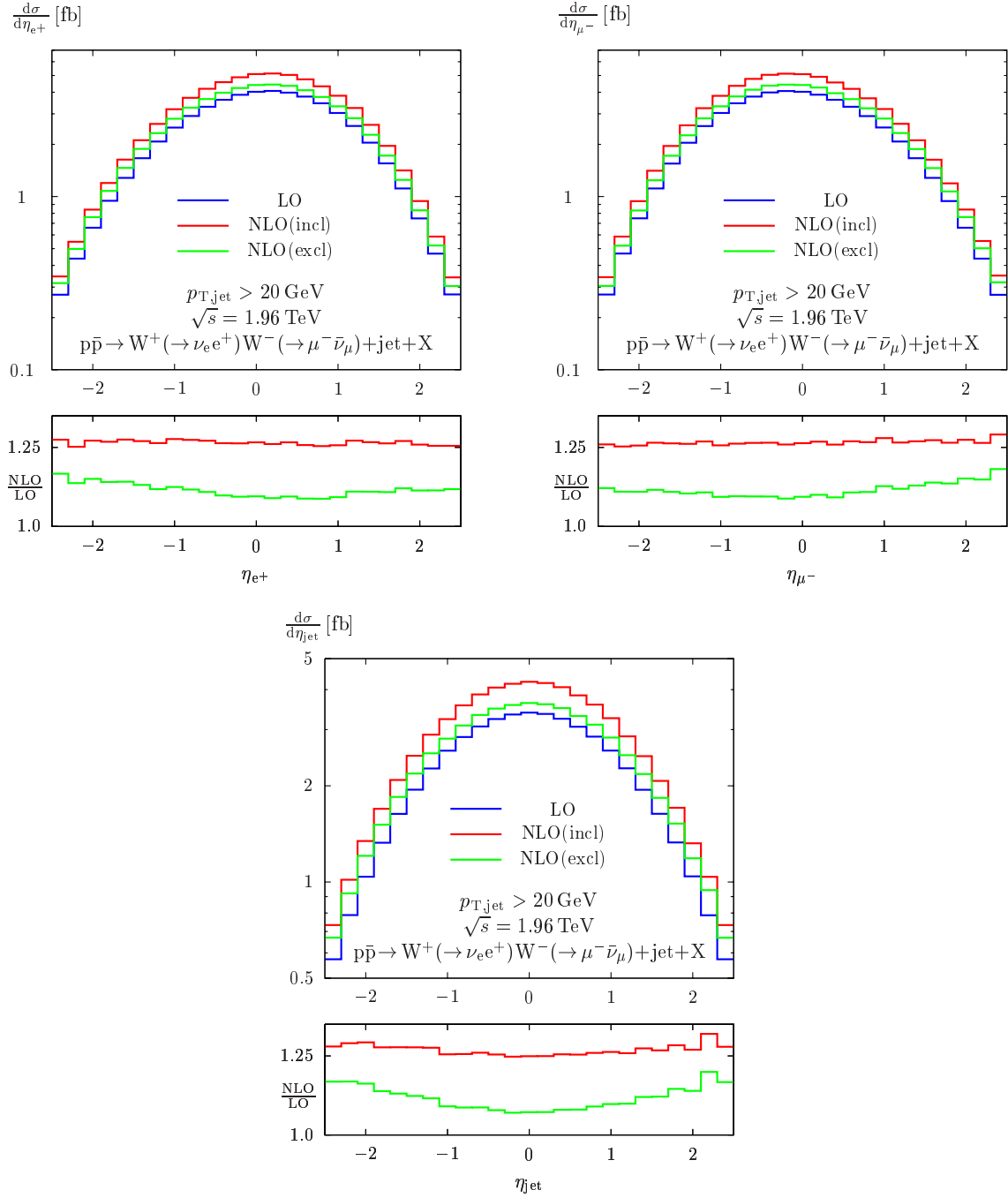


Figure 8.19: As in Figure 8.16, but for the Tevatron setup.

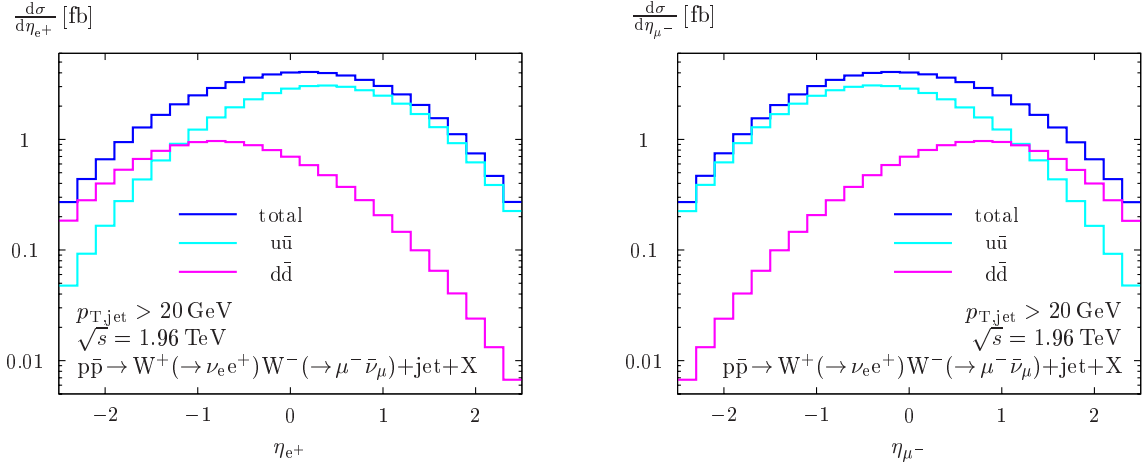


Figure 8.20: As in Figure 8.19, but only the LO distributions for the rapidities η of the lepton and the antilepton are depicted. In addition, the two dominating partonic contributions $u\bar{u}$ and $d\bar{d}$ to the hadronic cross section are shown.

The rapidity of the jet, which is depicted in the lower plot of Figure 8.19, is symmetric with respect to $\eta = 0$. This is due to the fact that no distinction can be made between hadronic jets arising from gluons, quarks, or antiquarks. Therefore, the sum over all contributions, which are \mathcal{CP} symmetric in pairs, yields a symmetric distribution. As in the case of LHC, the size of NLO corrections turns out to be only slightly dependent on the rapidities both of the jet and the leptons. Considering the absolute rapidity dependence of the cross sections, a tendency to events that are not strongly boosted in the direction of the beam axes is observed. This can be understood from the fact that the dominating partonic channels with initial states of valence quark and valence antiquark are not strongly boosted in general.

Finally, the angle correlations between the two decay leptons are considered. The angle in the transverse plane is again labelled by φ , $\cos\theta$ is the solid angle between the two leptons. The corresponding distributions are depicted in Figure 8.21. These angle correlations are very important also at Tevatron to distinguish the background process $WW+\text{jet}$ from the signal process $H(\rightarrow WW^*)+\text{jet}$. Details on this topic are given in the discussion of the respective LHC distributions. Also in the Tevatron setup, the two leptons tend to fly into opposite directions in the transverse plane. In contrast to the situation at the LHC, this tendency is still observed if boost effects are taken into account, which can be read off the distribution of the opening angle $\cos\theta$. This is again understood from the fact that no tendency to strongly boosted events arises in the dominantly contributing partonic channels.

ZZ+jet

A survey of distributions for differential ZZ+jet cross sections with decays to charged leptons is given in Figures 8.22 – 8.25 for the LHC setup with $p_{T,\text{jet,cut}} = 50 \text{ GeV}$ and $\mu = \mu_{\text{ren}} = \mu_{\text{fact}} = M_Z$. In Figure 8.22, the transverse-momentum distribution of the hadronic

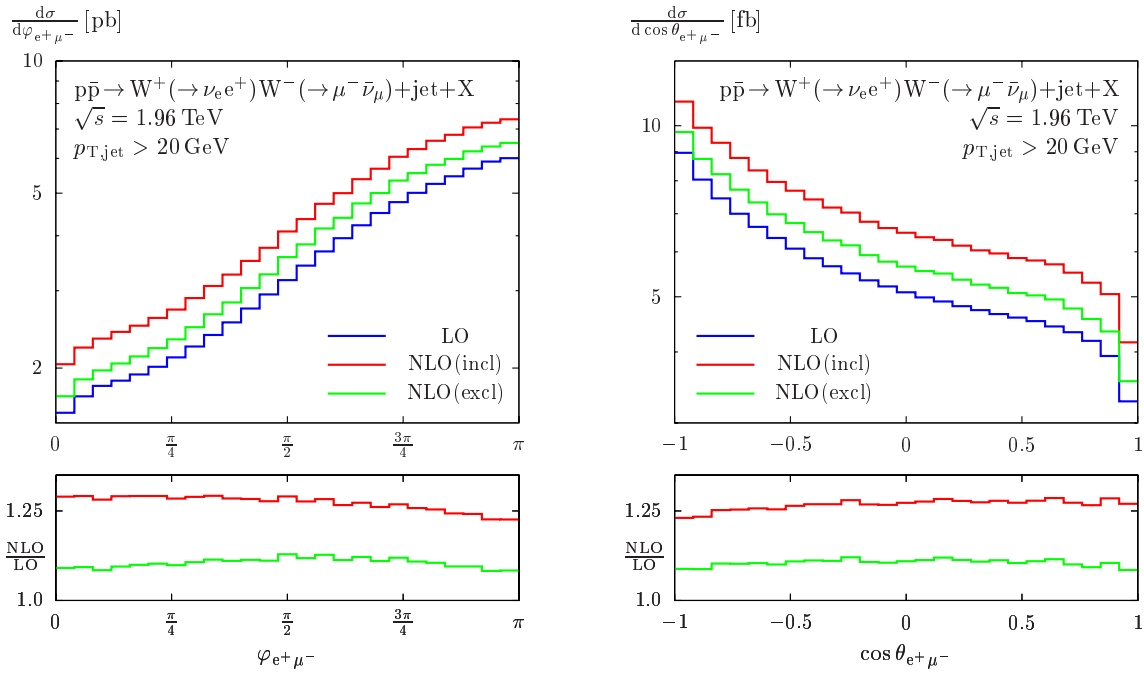


Figure 8.21: As in Figure 8.17, but for the Tevatron setup.

jet and its rapidity η are depicted. As discussed for WW+jet production, the quantities with respect to the harder jet are taken into account in the case of the more inclusive NLO observable. The shape of the $p_{T,jet}$ distribution reflects that of the corresponding WW+jet distribution. The influence of the NLO corrections is already explained in that context as well.

The effect of the NLO corrections on the rapidity distribution of the jet is also similar to the situation of WW+jet production: The relative correction is nearly flat for low rapidities and becomes larger if the jet is boosted more strongly in the direction of the beam axes. These large positive corrections in the region of large rapidities can be understood by a simple statistical effect: NLO corrections in general redistribute events. Since most events show jets in the region of lower rapidities, it is just more likely to redistribute events from the low-rapidity region to the high-rapidity region than the other way round.

The differential cross sections with respect to the momenta of the decay leptons are, naturally, the same for e^-, μ^- on the one side and e^+, μ^+ on the other side. The distributions for transverse momenta and rapidities of the leptons are presented in Figure 8.23. Size and direction of the NLO corrections to the p_T distributions can again be explained by the fixed scale of the strong coupling, as described in the previous paragraph on WW+jet production. The NLO corrections turn out to be independent of the leptonic rapidities. At first sight, the distributions for leptons and antileptons seem to be identical. This is, however, not exactly true, but the deviations are extremely small and hardly noticeable. The hadronic process does not provide a symmetry to produce identical distributions for the leptons and the antileptons arising from the Z decays.

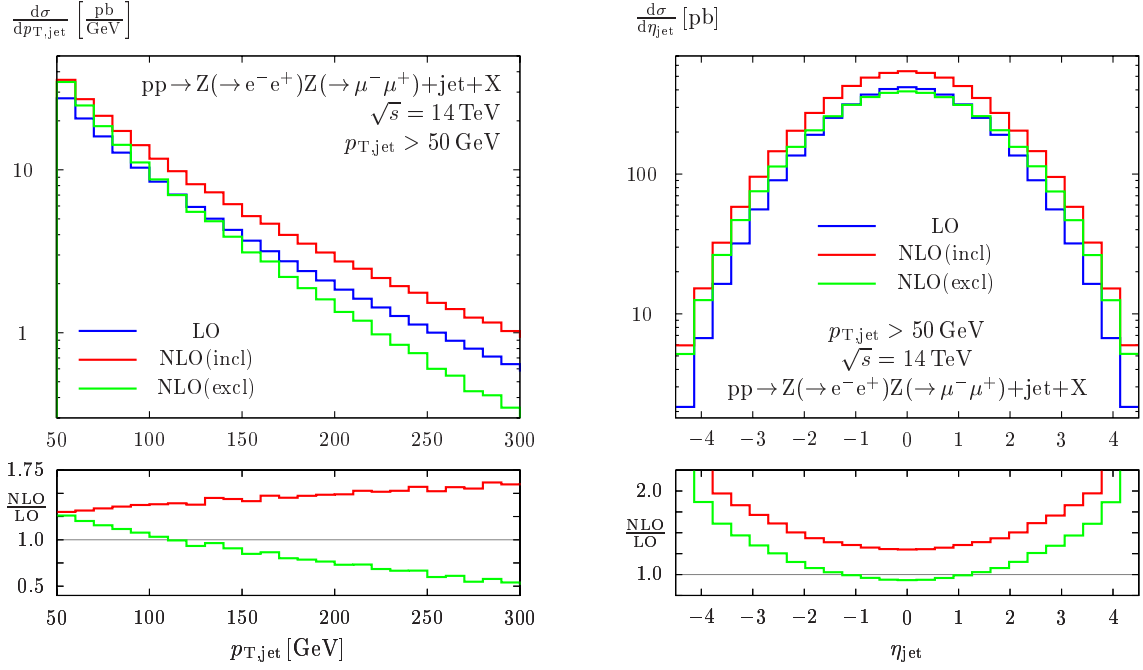


Figure 8.22: As in Figure 8.15, but for $ZZ+jet$ with $\mu = \mu_{fact} = \mu_{ren} = M_Z$. The distributions for the transverse momentum p_T and the rapidity η of the jet are depicted. The start p_T is determined by the applied cut.

For proton–antiproton collisions, however, the respective distributions are identical, because the hadronic process is \mathcal{CP} symmetric in this case. Analogously to $WW+jet$, one finds also identical rapidity contributions for leptons and antileptons if one of the two distributions is mirrored with respect to the $\eta = 0$ axis for the Tevatron setup.

In Figures 8.24 and 8.25, the angles between the decay leptons are depicted, namely both the angle φ in the transverse plane and the cosine of the opening angle in the laboratory frame, $\cos \theta$. In all distributions, a decline is observed if the angles between the leptons become very small. This is simply explained by the applied lepton-separation cuts. Of course, the angles between lepton pairs from one and the same Z boson are quite different compared to the angles between leptons arising from the decays of two different Z bosons. We start with the first case that is shown in the upper plots of Figure 8.24. Since both leptons result from the two-particle decay of one Z boson, the angle between the leptons in the transverse plane is always equal to π if the momentum of the decaying lepton is parallel to the beam axis. The larger the angle between the decaying Z boson and the beam axis is, the more probable are events with a small angle φ between the decay leptons. Therefore, small transverse angles between the decay leptons correspond to Z bosons with large transverse momenta and vice versa. This correlation delivers a possible explanation for the observation that the NLO corrections are negative in the region of small angles in the transverse plane and positive for large ones. The shape of the relative correction in the more inclusive NLO observable is roughly the same as for the more exclusive one. The

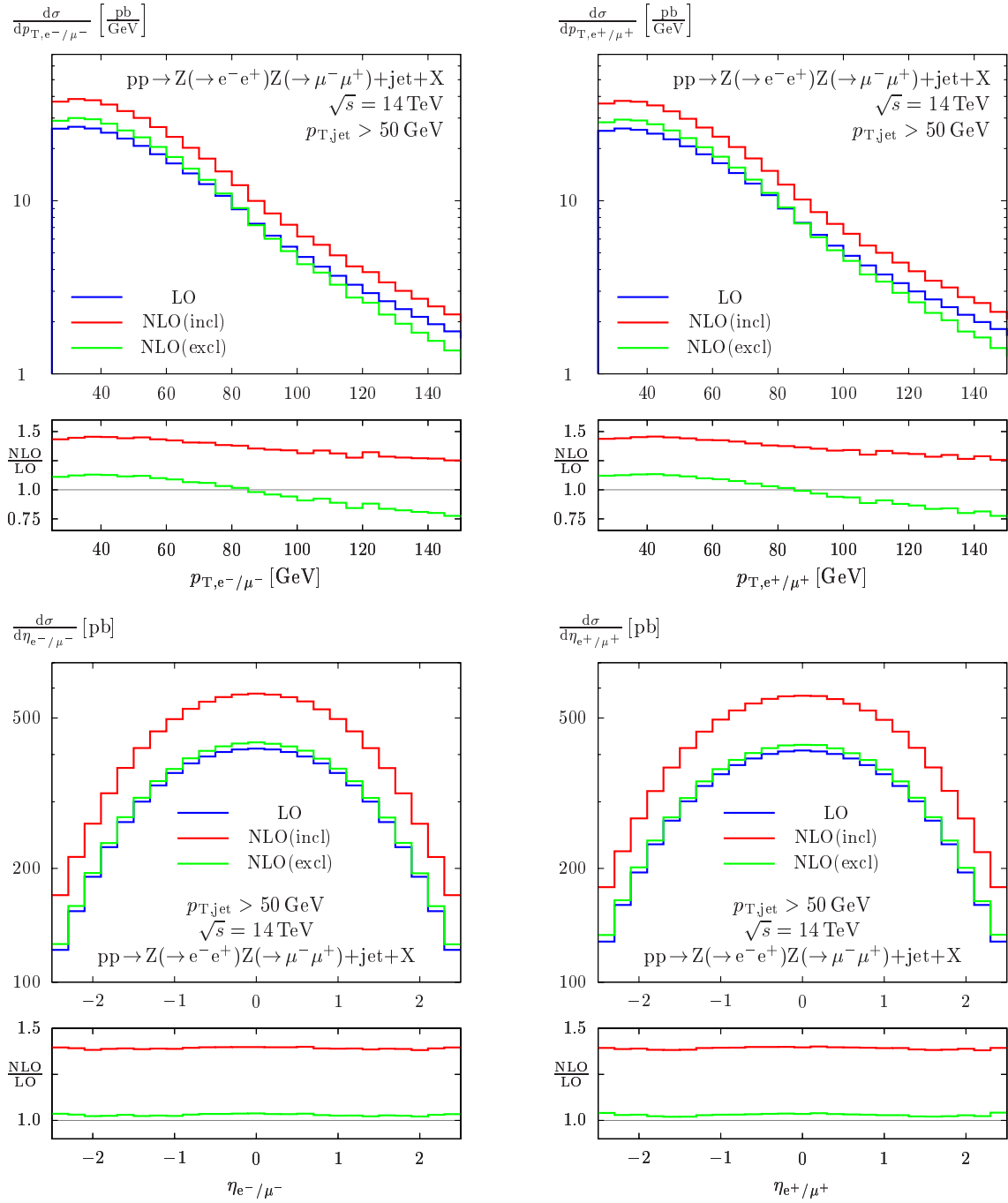


Figure 8.23: As in Figure 8.22, but the distributions for the transverse momenta p_T and the rapidities η of the leptons are shown.

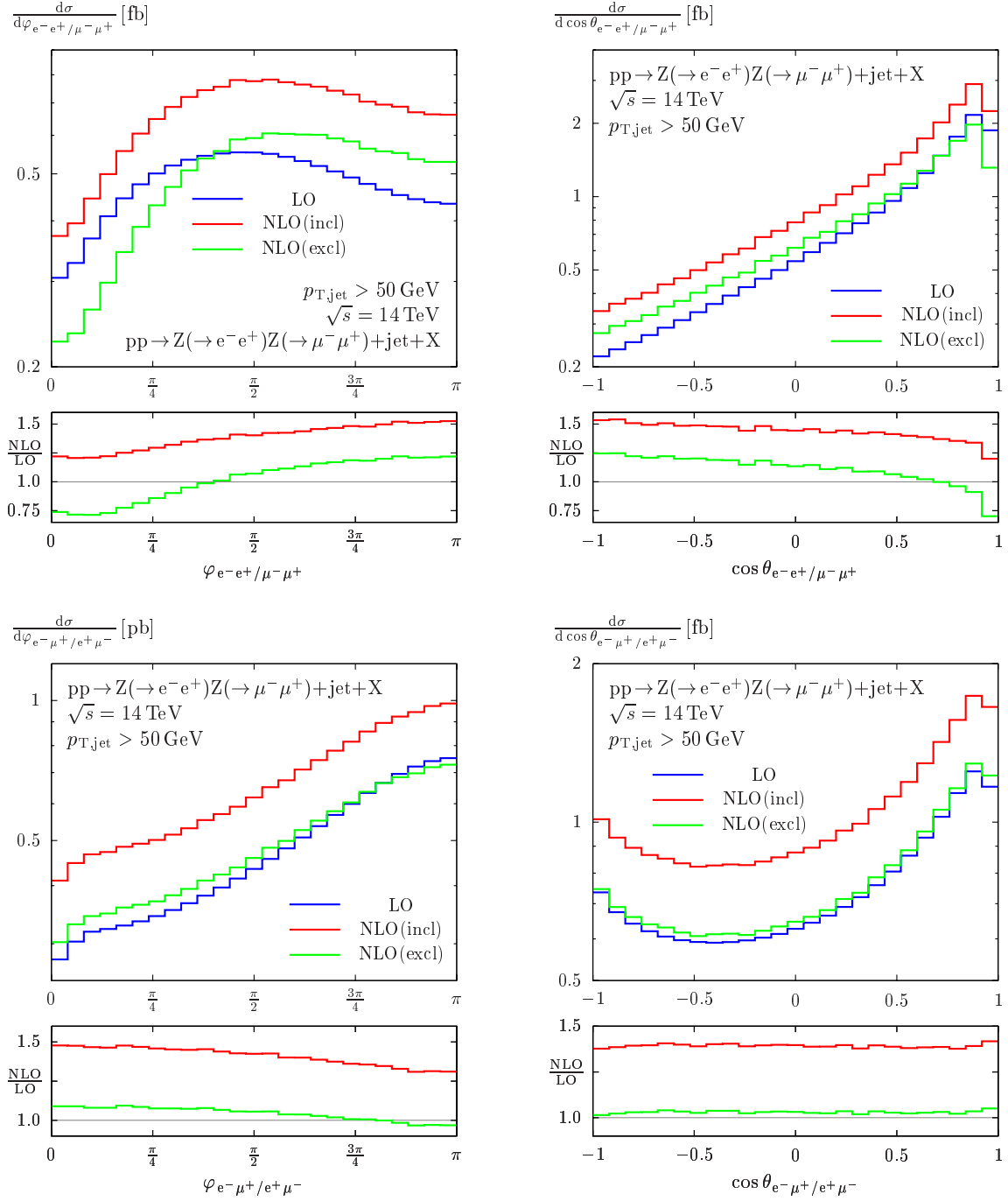


Figure 8.24: As in Figure 8.22, but the angle φ in the transverse plane and the cosine of the solid angle $\cos\theta$ between lepton and antilepton are depicted. The upper plots show the angles for leptons from the same Z decay. In the lower plots, the angles between a lepton and an antilepton stemming from different Z decays are given.

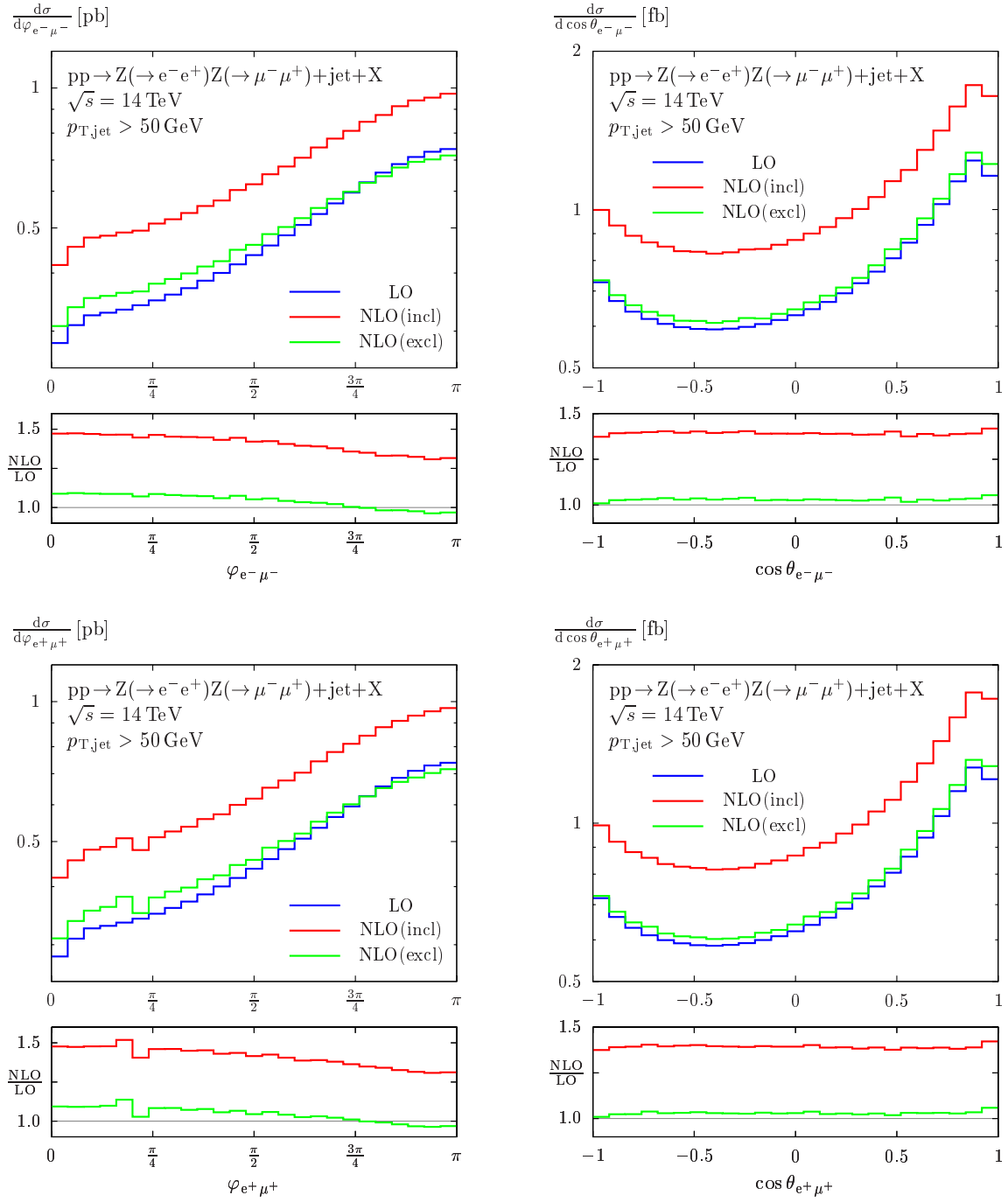


Figure 8.25: As in Figure 8.24, but the respective angles between two leptons (upper plots) and two antileptons (lower plots) are shown.

described effect is, however, smoothed a bit. This could again be explained by the fact that the difference between the two NLO observables is an LO contribution itself. Thus, it also tends to mimic the behaviour of the LO approximation to overestimate low- p_T regions and vice versa. The distribution of the solid angle in the laboratory frame, $\cos\theta$, also shows the tendency to be overestimated for small angles between the decay leptons, and to be underestimated for large angles.

In contrast to this, the angles between leptons from different Z decays reflect the behaviour already observed in the discussion of WW+jet production: Due to momentum conservation, the two Z bosons show a tendency to fly into opposite directions. This tendency is carried over to their decay leptons due to boost effects. Therefore, the φ distributions on the left-hand side of Figure 8.24 (lower plot) and Figure 8.25 have their maxima at $\varphi = \pi$. Deviations are found here between the distribution for the angles between a lepton and an antilepton on the one side, and the distributions for the angles between two leptons or two antileptons on the other side. A slight tendency to lower angles is observed for the latter situation, which might originate from the spin correlations between the two Z decays. It is, however, not evident, how the direction of this deviation could be explained. For the distributions of angles between two leptons on the one hand and two antileptons on the other hand, no evidence to be different is found. However, we do not have a good reason for them to be identical. The distributions for the cosine of the solid angle $\cos\theta$ reflect again the behaviour observed for WW+jet: The tendency of the two leptons to fly into opposite directions is overcompensated by boost effects. Finally, the dependence of the NLO corrections on all angles between leptons from different Z-boson decays turns out to be only modest.

WZ+jet

The discussion of differential cross sections for WZ+jet is performed for both charge assignments of the W boson simultaneously. All distributions for W^+Z +jet are provided in the plots on the left-hand side of Figures 8.26 – 8.33. On the right-hand side, the respective differential cross sections for W^-Z +jet are depicted. The pairs of plots shown side by side are combined in order to compare the corresponding quantities of the two processes, e.g. the charged leptons resulting from the W bosons, etc. As discussed before, the cross sections for the two processes are not about the same size in proton–proton collisions, because different partonic initial states contribute. Therefore, the comparison is not so much based on the absolute size of the cross sections, but on the shapes of the distributions.

For the transverse momenta, which are shown in Figures 8.26 – 8.28, we find a similar behaviour as already observed in WW+jet and ZZ+jet production: The LO approximations tend to overestimate the cross sections at high transverse momenta and to underestimate it for low momenta, as discussed for the other VV+jet processes. Considering the transverse momenta of the leptons arising from the W decays in Figure 8.27—the missing transverse momentum represents the neutrino resulting from this decay—a tendency to lower values is found for the antilepton in W^+Z +jet and for the antineutrino in W^-Z +jet. In comparison to that, the lepton in W^+Z +jet and the neutrino in W^-Z +jet tend to

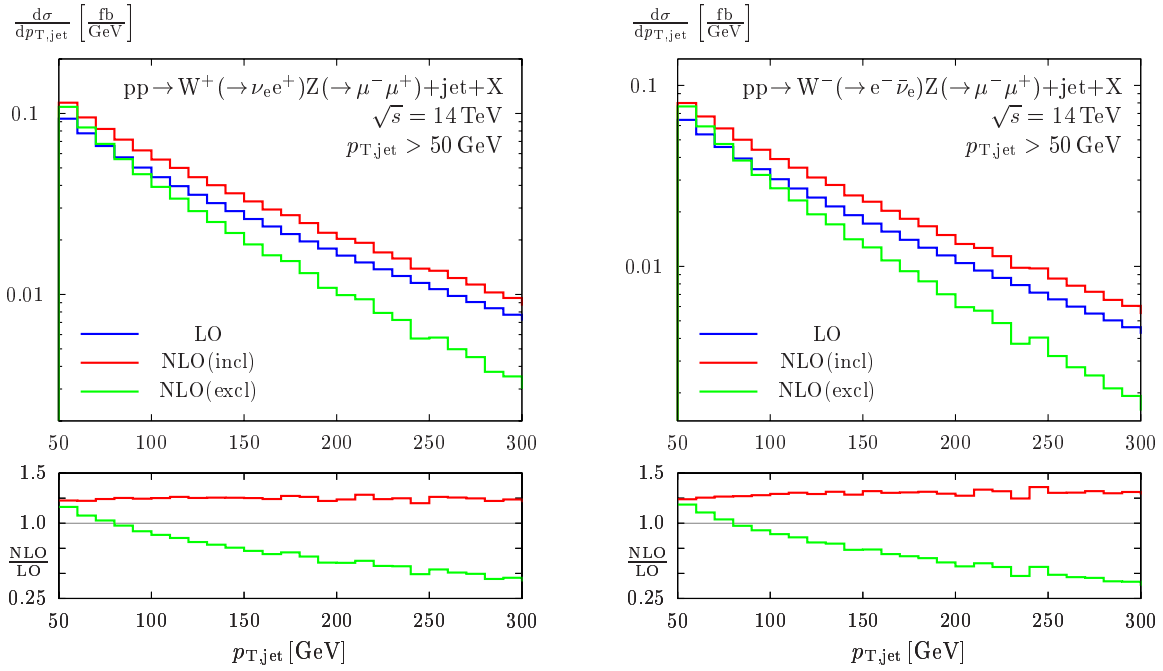


Figure 8.26: As in Figure 8.15, but for $W^+Z+\text{jet}$ (left-hand plot) and $W^-Z+\text{jet}$ (right-hand plot) with $\mu = \mu_{\text{fact}} = \mu_{\text{ren}} = M_W$. The distributions for the transverse momenta p_T of the jet are depicted.

higher transverse momenta. If the analogous distributions for proton–antiproton collisions are considered, we find identical results for neutrino and antineutrino, and for charged lepton and antilepton, respectively. This is due to the fact that the hadronic processes $p\bar{p} \rightarrow W^+Z + \text{jet} + X$ and $p\bar{p} \rightarrow W^-Z + \text{jet} + X$ are charge conjugated to each other, which is not the case for $WZ+\text{jet}$ in proton–proton collisions.

For the decay leptons stemming from the Z decays, which are shown in Figure 8.28, again slight differences arise between leptons and antileptons, as already observed for $ZZ+\text{jet}$.

The rapidity distributions of the jet and the decay leptons are depicted in Figures 8.29 and 8.30. As for the previously discussed $VV+\text{jet}$ processes, the NLO corrections to the cross sections are nearly independent of these rapidities. Again, a strong overestimation of the LO predictions for strongly boosted jets is observed. This is, however, the same situation as for the other $VV+\text{jet}$ processes and can be understood from statistics again.

The most obvious discrepancy between $W^+Z+\text{jet}$ and $W^-Z+\text{jet}$ in the rapidity distributions is observed for the charged leptons from the W decays. Here, the antilepton in the $W^+Z+\text{jet}$ case shows the strong tendency to be boosted in direction of the beam axis, whereas the respective lepton in the $W^-Z+\text{jet}$ case tends to populate the central region. This situation can again—as for $WW+\text{jet}$ —be explained by large contributions arising from t -channel-like emission of the W boson: For $W^+Z+\text{jet}$, the partonic channels yielding the main part to the cross sections contain an initial-state up quark. Due to its

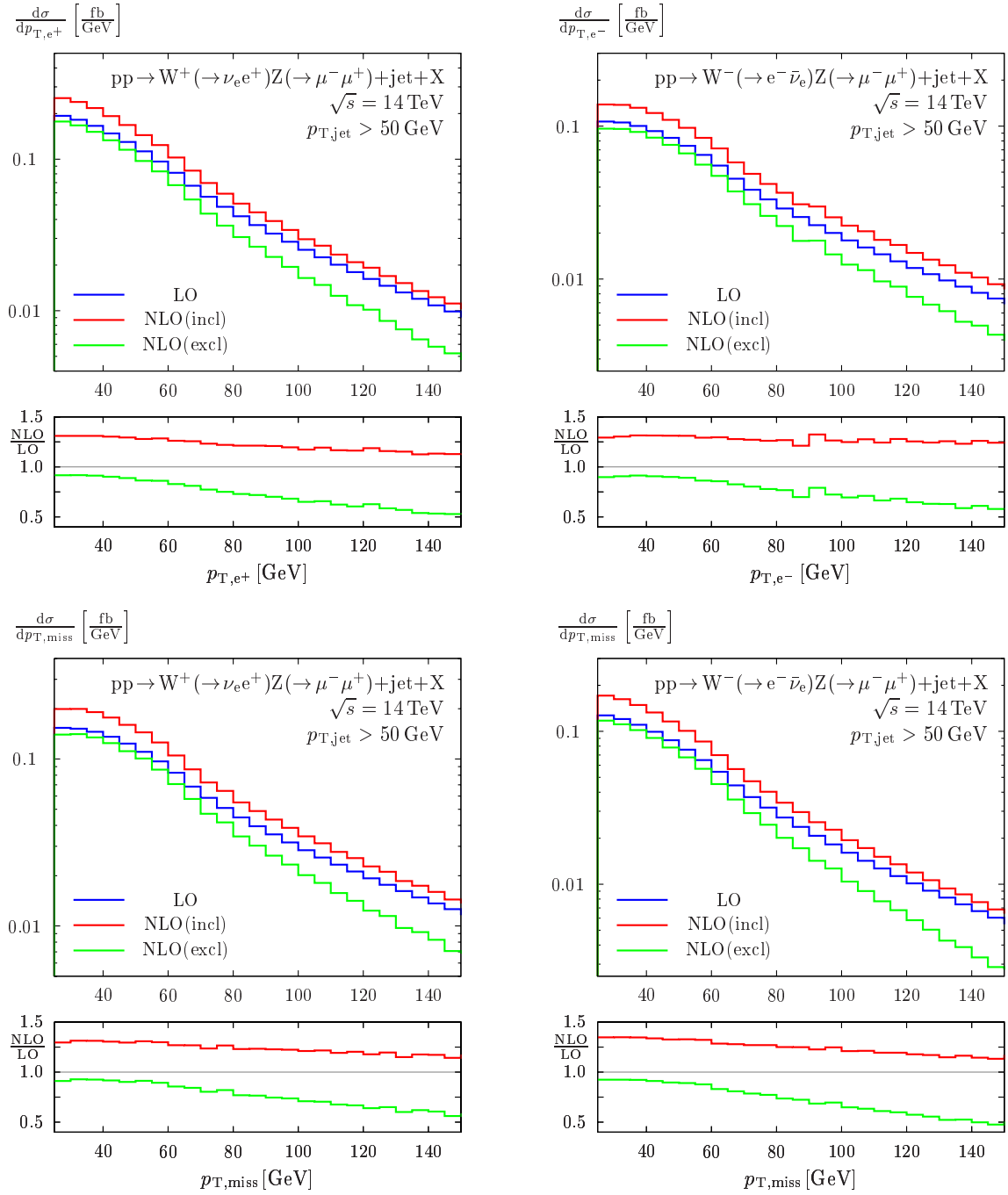


Figure 8.27: As in Figure 8.26, but for the distributions of the transverse momenta of the lepton from the W decay (upper plots) and the missing transverse momenta (lower plots).

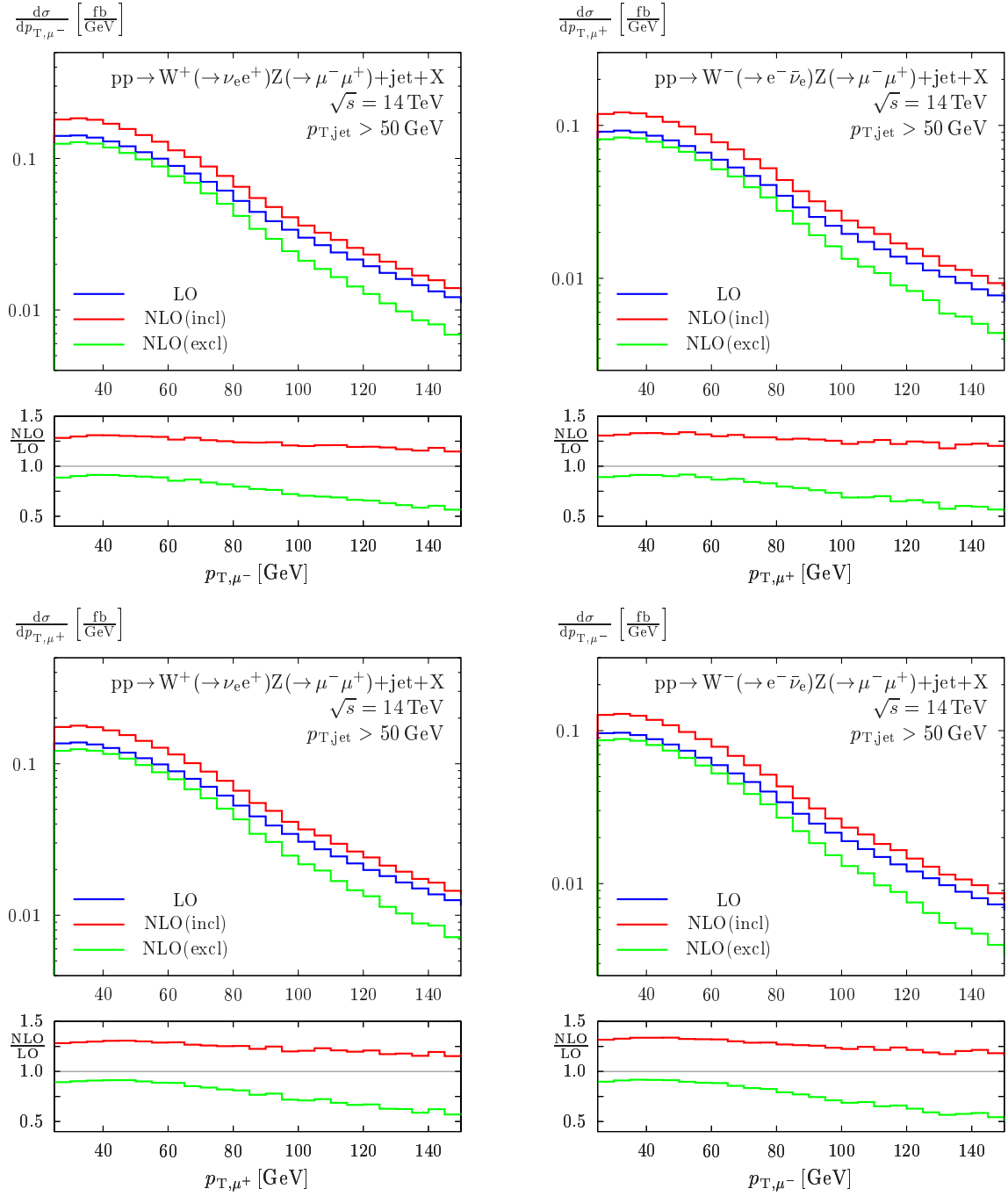


Figure 8.28: As in Figure 8.26, but the transverse momenta of the leptons from the Z decay are shown.

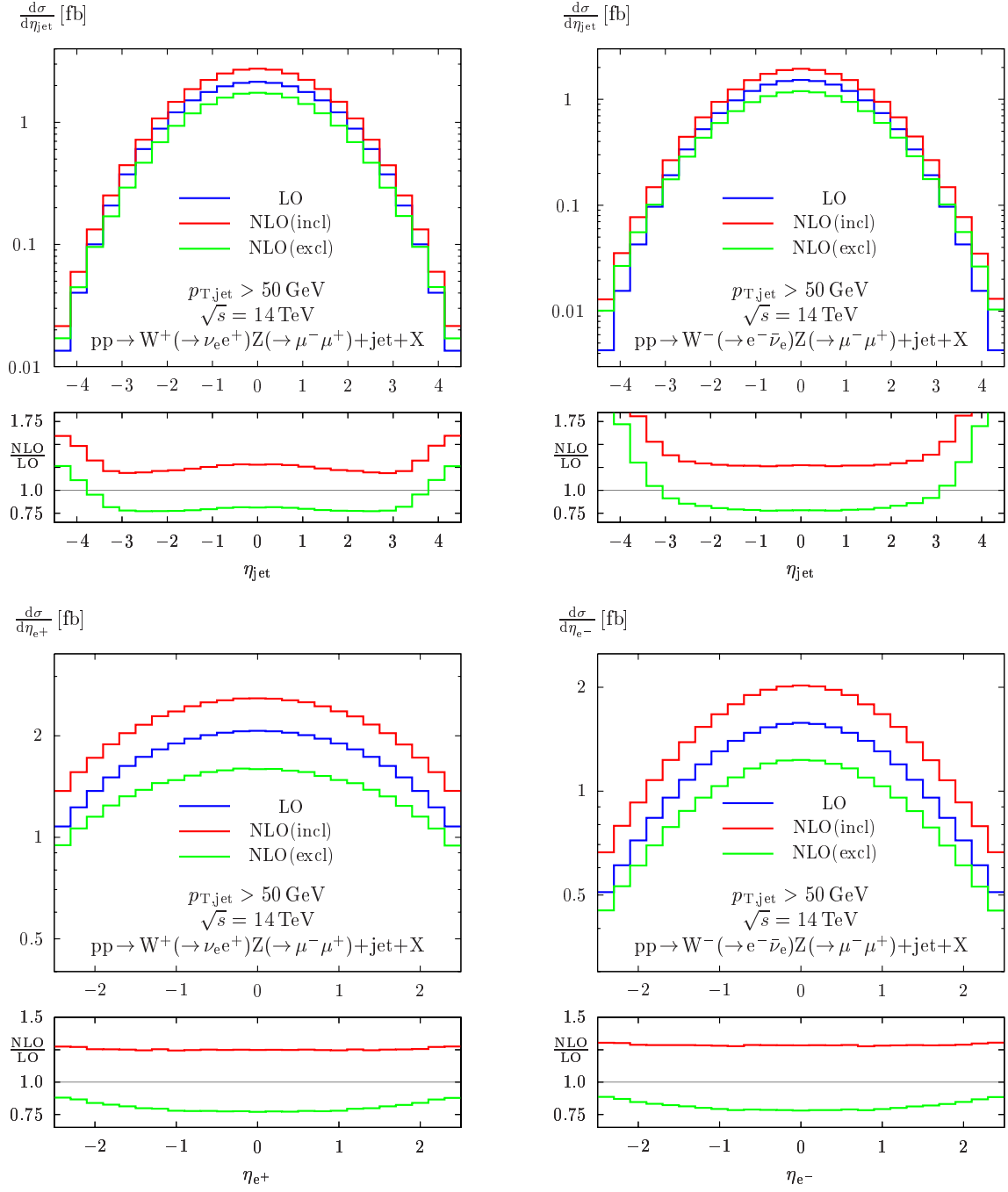


Figure 8.29: As in Figure 8.26, but for the rapidity distributions of the jet (upper plots) and of the lepton from the W decay (lower plots).

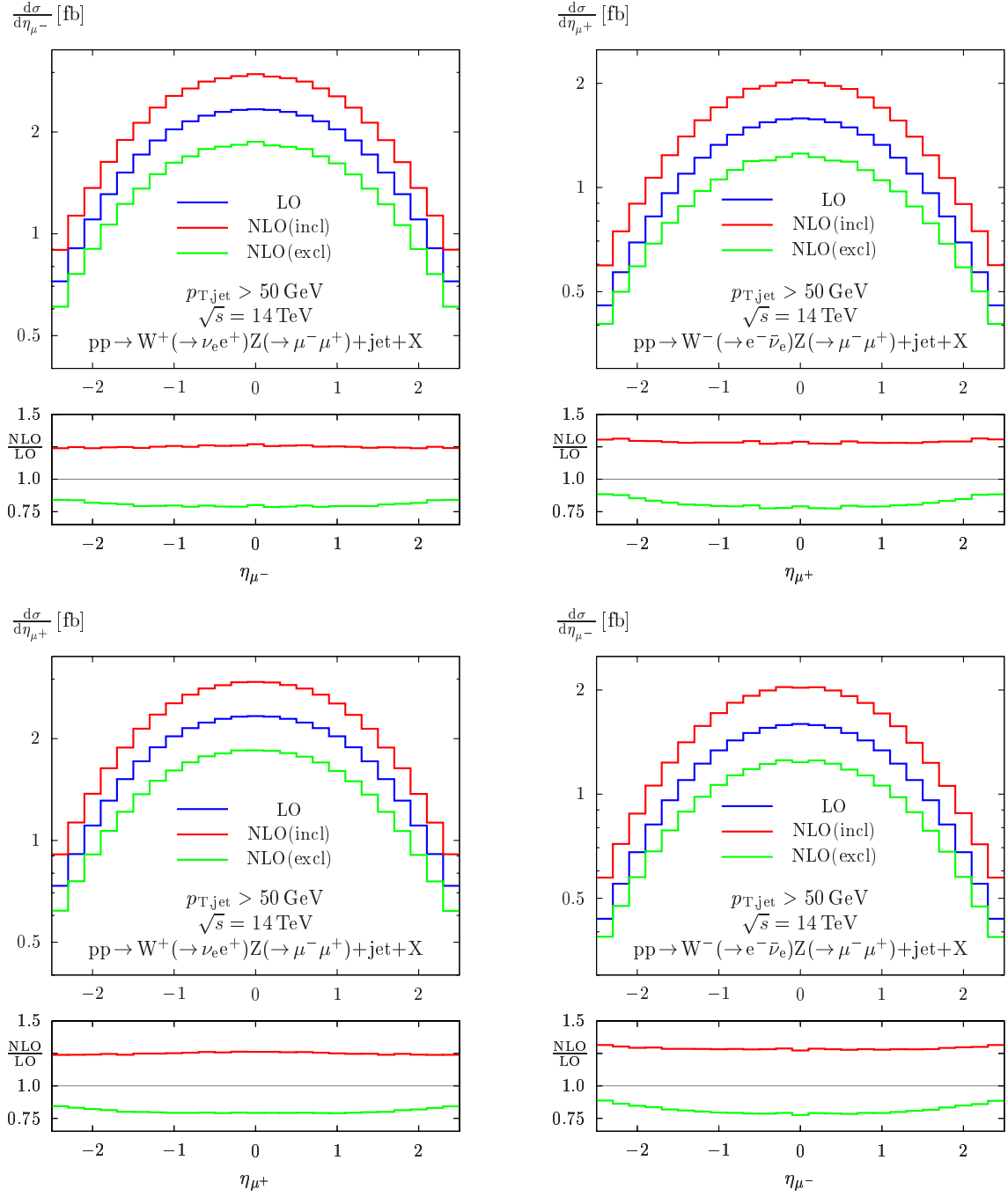


Figure 8.30: As in Figure 8.26, but the rapidities of the leptons from the Z decay are depicted.

large PDF at high momenta, the resulting events are strongly boosted. By means of the t -channel-like emission of the W boson, this boost is carried over to the antilepton from the W decay. For W^-Z +jet, however, no up-quark initial states contribute due to charge conservation. The partonic channels with an incoming down quark are not that strongly boosted. Thus, t -channel-like W emission off this quark leads to decay leptons that show preferentially larger angles against the beam axes.

The correlations between the decay leptons are presented in Figures 8.31 – 8.33, where the angles in the transverse plane and the cosines of the solid angles between pairs of decay leptons are given. The angles between the leptons arising from the same Z boson decay, which are depicted in Figure 8.31, show similar shapes of the differential cross sections compared to the respective case in ZZ +jet production. Since this statement holds for both gauge-boson assignments considered here, we refer to the explanations for these distributions and the role of the NLO corrections provided in the context of ZZ +jet production.

The angles between leptons resulting from different gauge-boson decays also lead to distributions with similar shapes as observed for the respective quantities in WW +jet and ZZ +jet production. These distributions are given in Figures 8.32 and 8.33: The tendency of pairs of such decay leptons to fly into opposite directions in the transverse plane is overcompensated by boost effects. Therefore, the distributions of the solid angle between two such decay leptons show maxima at small opening angles. A slightly stronger boost effect can be observed for W^+Z +jet. This can again be understood from the involved partonic channels: The contributions with initial-state up quarks show the strongest tendency to events boosted in direction of the beam axes. Such channels are, however, only present in W^+Z +jet production, but not for W^-Z +jet. Finally, we compare the angle correlations between two leptons or two antileptons for W^-Z +jet and W^+Z +jet, respectively, with those between a lepton from one gauge-boson decay and an antilepton from the other. In both process classes, a slight tendency to small opening angles is found for the angles between two identically charged leptons. Such a tendency is also observed in the discussion of the ZZ +jet production process. The reason for this effect might be found in the spin correlations of the leptons again.

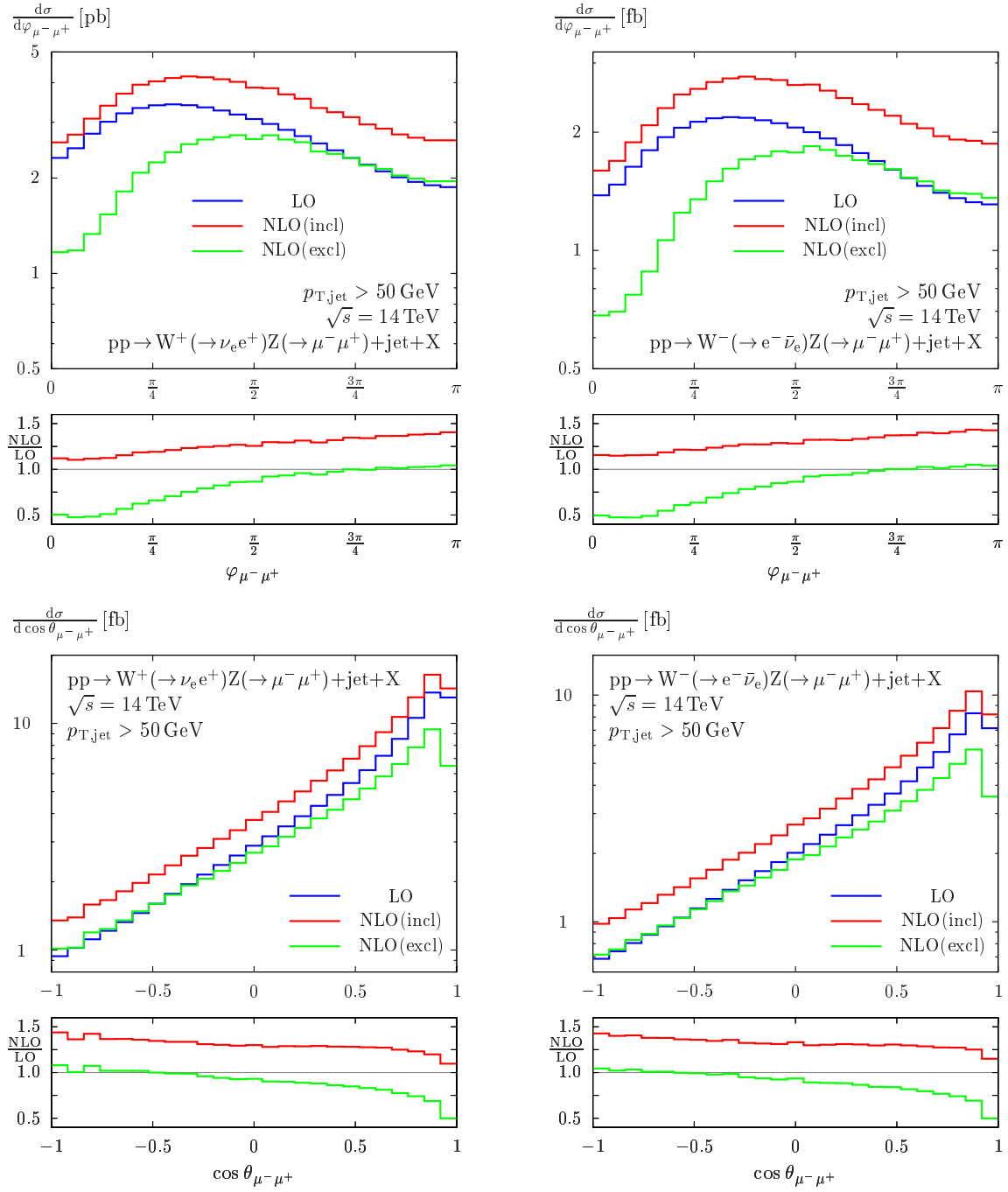


Figure 8.31: As in Figure 8.26, but the angle φ in the transverse plane (upper plots) and the cosine of the solid angle $\cos \theta$ (lower plots) between the leptons from the Z decay are given.

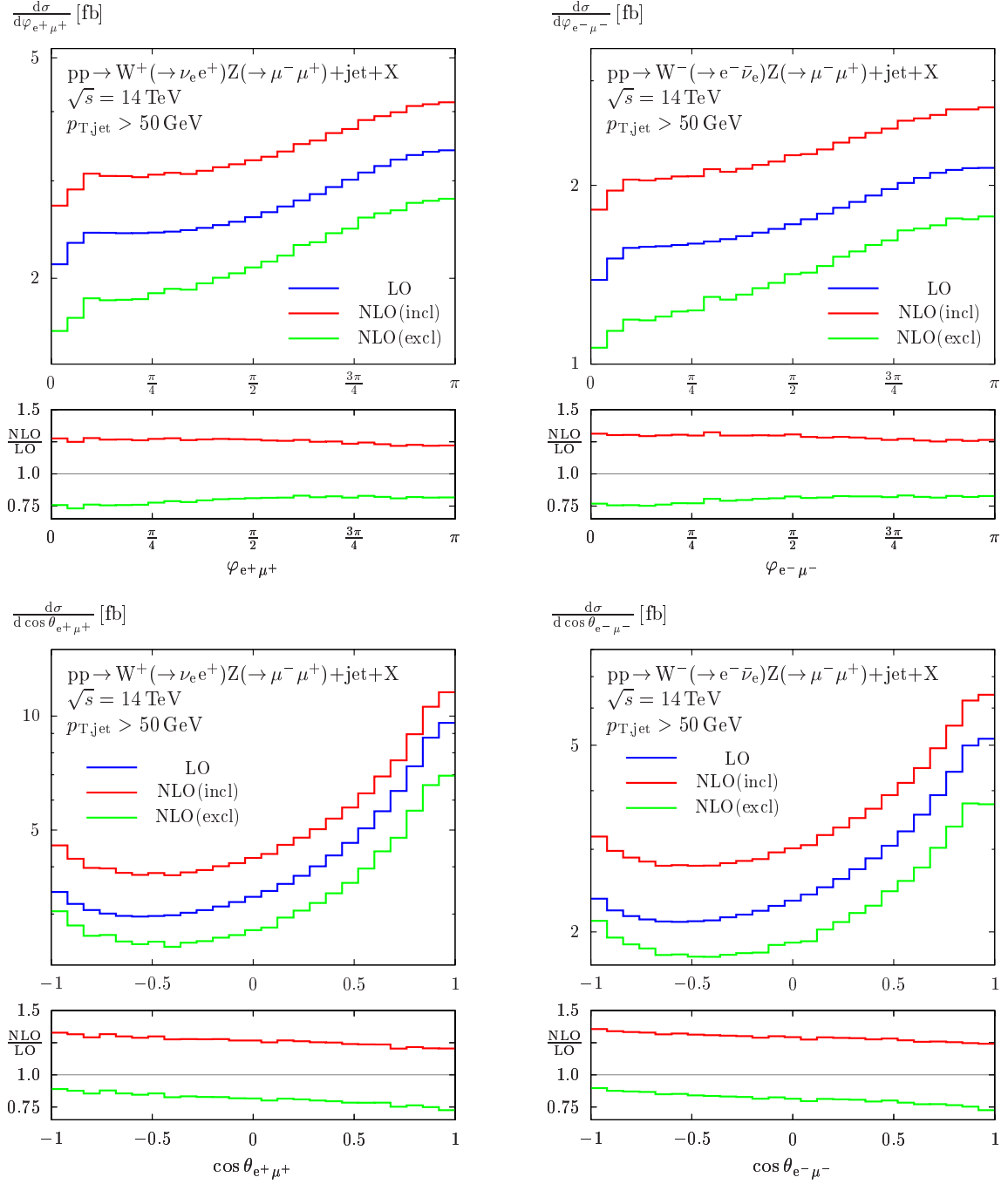


Figure 8.32: As in Figure 8.31, but for the angles between the two antileptons (left-hand plots) and the two leptons (right-hand plots) from different gauge-boson decays.

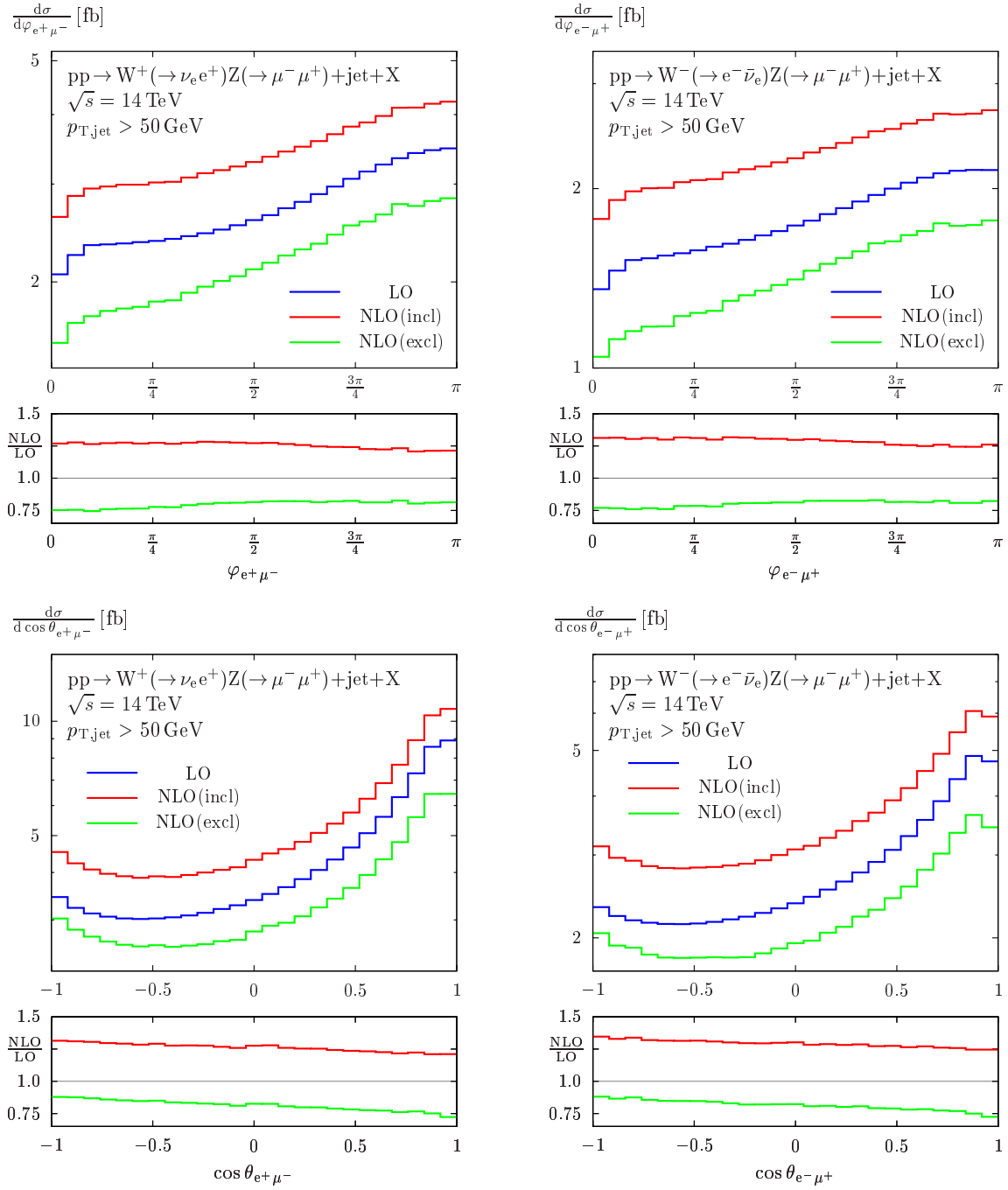


Figure 8.33: As in Figure 8.31, but for the angles between the lepton and the antilepton from different gauge-boson decays.

Chapter 9

Summary and outlook

In this thesis, the NLO QCD cross sections for the process classes $pp/p\bar{p} \rightarrow VV + \text{jet} + X$ are evaluated. The Catani–Seymour dipole subtraction formalism is applied to control the IR divergences, which cancel between the different contributions. The matrix elements for the real corrections are evaluated in terms of helicity amplitudes by applying the Weyl–van-der-Waerden formalism. The loop integrals in the virtual corrections are calculated by means of the FORMCALC/LOOPTOOLS package with the regular scalar integrals taken from the FF library. The needed IR-divergent scalar integrals in dimensional regularization are linked to this library. The phase-space integration is performed by a multi-channel Monte Carlo integrator with weight optimization written in C++. In order to improve the integration, additional channels are included for the integration of the difference of the real-emission matrix elements and the subtraction terms.

For all allowed assignments of the weak-gauge-boson pair, namely W^+W^- , ZZ , W^+Z , and W^-Z , the NLO corrections to the integrated cross sections stabilize the dependence on renormalization and factorization scales significantly. For proton–proton collisions at the LHC, this reduction is only modest if inclusive $VV + \text{jet}$ production is considered. This is due to the fact that additional $VV + 2\text{jets}$ events contribute here. These are LO processes by themselves and, thus, suffer from the strong scale dependence that is in general present in LO QCD calculations. Applying a veto on a second hard jet improves the situation remarkably and, hence, leads to a considerable stabilization of the scale dependence. For proton–antiproton collisions at the CM energy of Tevatron, the influence of genuine $VV + 2\text{jets}$ events is modest. Therefore, the scale dependence is strongly improved here with or without a veto on a second hard jet.

The cross-section calculations are performed both in the five-flavour scheme and in the four-flavour scheme, where the PDF sets of CTEQ6 are applied in the first case, and those of MRST2004 in the latter case. The deviations between the two evaluations are typically of the order of some per cent, as it is expected for different PDF sets. Besides, this comparison is performed to show the validity of the approximation concerning bottom (anti-)quarks applied in the five-flavour calculation: Only their infrared-divergent part is included in the calculation, whereas contributions with top resonances are neglected, because they should be assigned to distinguished process classes, namely $t\bar{t}$, tW^- , or $\bar{t}W^+$.

with off-shell effects of the top (anti-)quark. The good agreement with the four-flavour calculation, where no external bottom quarks are taken into account at all, confirms the validity of the applied approximation. However, contributions from these process classes with off-shell top quarks could be taken into account in an advanced study of WW+jet production. A reason to do so might be that, for leptonic W decays, an invariant-mass cut on the decay products of the top could not be applied due to the decay neutrinos leaving the detector unseen. Assuming that anti-b-tagging only works with an efficiency of about 50%, sizeable $\bar{t}W^+$ and tW^- contributions show up that can not easily be distinguished from WW+jet events. To take this into account, it should be useful to have a five-flavour calculation that includes external bottom (anti-)quarks and also provides PDFs for them. In the remaining process classes of VV+jet, no top resonances show up at all. The good agreement of the two calculations also confirms the validity of the approximation to omit external bottom (anti-)quarks here.

Beyond the VV+jet production processes, leptonic decays are included to improve the analysis. A full amplitude calculation including resonant and non-resonant diagrams is performed at LO. In a comparison of LO results, an improved version of the NWA that takes spin correlations into account is proven to deliver a good approximation of the full amplitude calculation. Thus, the NLO QCD calculation with leptonic gauge-boson decays is performed by application of the improved NWA. The analysis of differential cross sections in this framework suggests that the main effect of the NLO corrections could probably be used to improve the LO predictions by evaluating the strong coupling at a phase-space dependent scale. The choice of this scale could be fine-tuned by means of the NLO distributions provided here.

Although a full amplitude calculation for VV+jet with leptonic decays is not performed at NLO QCD in this thesis, the necessary building blocks are provided. Whether such a calculation makes sense has to be decided from an experimental point of view. There are, however, no theoretical obstacles to extending the presented calculations to an NLO QCD calculation using full amplitudes instead of the improved NWA.

Moreover, a number of building blocks is provided for more complicated NLO QCD calculations, especially also for $2 \rightarrow 4$ processes. These are, in particular, $pp/p\bar{p} \rightarrow VV + 2\text{jets} + X$ and $pp/p\bar{p} \rightarrow W^+W^-b\bar{b}+X$, where the latter is especially interesting as the off-shell continuation of $t\bar{t}$ production at hadron colliders. The amplitudes for all necessary LO subprocesses are already provided, as well as a set of building blocks that can be used to calculate also the real-correction amplitudes. Besides, the methods used to implement gauge-boson decays could be applied in the same way. Moreover, a phase-space generator has been written that is easily extendable to these process classes and provides a method for a stable numerical integration of NLO cross sections. The bottleneck in this kind of calculations are still the virtual corrections with up to hexagon integrals that have to be evaluated—both in a numerically stable way and in reasonable time. However, lots of progress has been achieved on this in the last time [80], so that NLO QCD calculations for $2 \rightarrow 4$ processes seem definitely feasible.

Appendix A

Definitions used in the dipole subtraction formalism

All definitions provided in this appendix are taken from Ref. [62]. Here, only quantities that are not given in the main text are collected.

A.1 Colour charges

The definition of the matrix-valued colour-charge operators \mathbf{T} describing gluon emission is given in the following. For an outgoing parton i , the colour-charge operator is defined as

$$\mathbf{T}_i \rightarrow (\mathbf{T}_i)_{c_i b_i}^d = \begin{cases} i f_{c_i d b_i} & \text{if } i = \text{gluon} , \\ \mathbf{T}_{c_i b_i}^d & \text{if } i = \text{quark} , \\ -\mathbf{T}_{c_i b_i}^d & \text{if } i = \text{antiquark} , \end{cases} \quad (\text{A.1})$$

and for an incoming parton a as

$$\mathbf{T}_a \rightarrow (\mathbf{T}_a)_{c_a b_a}^d = \begin{cases} i f_{c_a d b_a} & \text{if } a = \text{gluon} , \\ -\mathbf{T}_{c_a b_a}^d & \text{if } a = \text{quark} , \\ \mathbf{T}_{c_a b_a}^d & \text{if } a = \text{antiquark} . \end{cases} \quad (\text{A.2})$$

The $\text{SU}(3)_C$ generators T^a can be chosen as the Gell-Mann matrices, $T^a = \frac{\lambda^a}{2}$, f_{abc} are the totally antisymmetric structure constants of $\text{SU}(3)_C$. The squares of these operators applied to a parton i are the respective Casimir operators,

$$\mathbf{T}_i^2 = C_i = \begin{cases} N_c = C_A = 3 & \text{if } i = \text{gluon} , \\ \frac{N_c^2 - 1}{2N_c} = C_F = \frac{4}{3} & \text{if } i = (\text{anti-})\text{quark} , \end{cases} \quad (\text{A.3})$$

where N_c stands for the number of colours. The $\text{SU}(3)_C$ generators are normalized according to

$$\text{Tr} \{T^a T^b\} = T_R \delta^{ab} , \quad T_R = \frac{1}{2} . \quad (\text{A.4})$$

A.2 Operators in the collinear-subtraction counter-terms

In the $\overline{\text{MS}}$ scheme, the insertion operators $\mathbf{K}^{a,a'}(x)$ and $\mathbf{P}^{a,a'}(xp, x, \mu_{\text{fact}})$ in the relevant case with two incoming partons a, b and only one outgoing parton i are

$$\mathbf{K}^{a,a'}(x) = \frac{\alpha_S}{2\pi} \left\{ \overline{K}^{aa'}(x) + \delta^{aa'} \gamma_i \frac{\mathbf{T}_i \cdot \mathbf{T}_a}{\mathbf{T}_i^2} \left[\left(\frac{1}{1-x} \right)_+ + \delta(1-x) \right] - \frac{\mathbf{T}_b \cdot \mathbf{T}_{a'}}{\mathbf{T}_{a'}^2} \tilde{K}^{aa'}(x) \right\}, \quad (\text{A.5})$$

$$\mathbf{P}^{a,a'}(p_b, p_i; xp, x, \mu_{\text{fact}}) = \frac{\alpha_S}{2\pi} P^{aa'}(x) \left[\frac{\mathbf{T}_i \cdot \mathbf{T}_{a'}}{\mathbf{T}_{a'}^2} \ln \frac{\mu_{\text{fact}}^2}{2xp_a p_i} + \frac{\mathbf{T}_b \cdot \mathbf{T}_{a'}}{\mathbf{T}_{a'}^2} \ln \frac{\mu_{\text{fact}}^2}{2xp_a p_b} \right]. \quad (\text{A.6})$$

These definitions are taken from Eqs. (10.24) and (10.25) in Ref. [62], respectively. The colour operators are defined in the previous section, and the constants γ_i are

$$\gamma_i = \begin{cases} \frac{11}{6} C_A - \frac{2}{3} T_R N_f & \text{if } i = (\text{anti-})\text{quark}, \\ \frac{3}{2} C_F & \text{if } i = \text{gluon}. \end{cases} \quad (\text{A.7})$$

The regularized Altarelli–Parisi splitting functions [61] in four dimensions read

$$P^{\text{qg}}(x) = P^{\text{q}\bar{\text{g}}}(x) = C_F \frac{1 + (1-x)^2}{x}, \quad (\text{A.8})$$

$$P^{\text{gq}}(x) = P^{\text{g}\bar{\text{q}}}(x) = T_R [x^2 + (1-x)^2], \quad (\text{A.9})$$

$$P^{\text{qq}}(x) = P^{\text{q}\bar{\text{q}}}(x) = C_F \left(\frac{1+x^2}{1-x} \right)_+ = C_F \left(-(1+x) + \left(\frac{2}{1-x} \right)_+ + \frac{3}{2} \delta(1-x) \right), \quad (\text{A.10})$$

$$P^{\text{gg}}(x) = 2C_A \left[\left(\frac{1}{1-x} \right)_+ + \frac{1-x}{x} - 1 + x(1-x) \right] \quad (\text{A.11})$$

$$+ \delta(1-x) \left(\frac{11}{6} C_A - \frac{2}{3} N_f T_R \right), \quad (\text{A.12})$$

$$P^{\text{q}\bar{\text{q}}}(x) = P^{\text{q}\bar{\text{q}}}(x) = 0. \quad (\text{A.13})$$

It is also convenient to introduce the regular parts P_{reg}^{ab} of the Altarelli–Parisi splitting functions. Their regular parts are obtained as follows,

$$P_{\text{reg}}^{ab} \equiv P^{ab}(x) - \delta^{ab} \left[2\mathbf{T}_a^2 \left(\frac{1}{1-x} \right)_+ + \gamma_a \delta(1-x) \right], \quad (\text{A.14})$$

where the colour operators are provided in the previous section and γ_i in Eq. (A.7). In the non-trivial case $a = b$, the explicit results read

$$P_{\text{reg}}^{\text{qq}}(x) = P_{\text{reg}}^{\text{q}\bar{\text{q}}}(x) = -C_F (1+x), \quad (\text{A.15})$$

$$P_{\text{reg}}^{\text{gg}}(x) = 2 C_A \left[\frac{1-x}{x} - 1 + x(1-x) \right]. \quad (\text{A.16})$$

The flavour kernels $\overline{K}^{aa'}(x)$ arising in Eq. (A.5) are given by the following expressions for explicit flavour assignments,

$$\overline{K}^{\text{qg}}(x) = \overline{K}^{\bar{\text{q}}\text{g}}(x) = P^{\text{qg}}(x) \ln \frac{1-x}{x} + C_F x, \quad (\text{A.17})$$

$$\overline{K}^{\text{gq}}(x) = \overline{K}^{\text{g}\bar{\text{q}}}(x) = P^{\text{gq}}(x) \ln \frac{1-x}{x} + T_R 2x(1-x), \quad (\text{A.18})$$

$$\begin{aligned} \overline{K}^{\text{qq}}(x) = \overline{K}^{\bar{\text{q}}\bar{\text{q}}}(x) = C_F \left[\left(\frac{2}{1-x} \ln \frac{1-x}{x} \right)_+ - (1+x) \ln \frac{1-x}{x} + (1-x) \right] \\ - \delta(1-x) (5 - \pi^2) C_F, \end{aligned} \quad (\text{A.19})$$

$$\begin{aligned} \overline{K}^{\text{gg}}(x) = 2 C_A \left[\left(\frac{1}{1-x} \ln \frac{1-x}{x} \right)_+ + \left(\frac{1-x}{x} - 1 + x(1-x) \right) \ln \frac{1-x}{x} \right] \\ - \delta(1-x) \left[\left(\frac{50}{9} - \pi^2 \right) C_A - \frac{16}{9} T_R N_f \right], \end{aligned} \quad (\text{A.20})$$

$$\overline{K}^{\text{qq}}(x) = \overline{K}^{\bar{\text{q}}\bar{\text{q}}}(x) = 0. \quad (\text{A.21})$$

The correlation terms $\tilde{K}^{aa'}(x)$ arise due to the parton-parton correlations in the initial state. These functions are given by

$$\tilde{K}^{ab}(x) = P_{\text{reg}}^{ab}(x) \ln(1-x) + \delta^{ab} \mathbf{T}_a^2 \left[\left(\frac{2}{1-x} \ln(1-x) \right)_+ - \frac{\pi^2}{3} \delta(1-x) \right]. \quad (\text{A.22})$$

The plus-distribution $[\dots]_+$ is defined by its action on a generic test function $g(x)$,

$$\int_0^1 dx g(x) [\mathcal{V}(x)]_+ \equiv \int_0^1 dx [g(x) - g(1)] \mathcal{V}(x). \quad (\text{A.23})$$

Appendix B

Dimensionally regularized scalar integrals

The IR-divergent integrals are treated by mass regularization in the FF package that is implemented in LOOPTOOLS. However, for the NLO QCD calculations performed here, dimensionally regularized scalar integrals are needed. To this end, all divergent integrals used in the calculations are collected, where the UV and IR divergences are distinguished. The following parametrization of the divergences is chosen,

$$\begin{aligned}\Delta^{\text{UV}}(\mu) &= \left(\frac{4\pi\mu^2}{M_W^2}\right)^\varepsilon \frac{\Gamma(1+\varepsilon)}{\varepsilon}, \\ \Delta_1^{\text{IR}}(\mu) &= \left(\frac{4\pi\mu^2}{M_W^2}\right)^\varepsilon \frac{\Gamma(1+\varepsilon)}{\varepsilon}, \quad \Delta_2^{\text{IR}}(\mu) = \left(\frac{4\pi\mu^2}{M_W^2}\right)^\varepsilon \frac{\Gamma(1+\varepsilon)}{\varepsilon^2}.\end{aligned}$$

The following definition for the scalar two-, three-, and four-point functions, which are denoted as B_0 , C_0 , and D_0 , respectively, is applied,

$$B_0(s_1 = k_1^2; m_1, m_2) = \frac{(2\pi\mu)^{4-D}}{i\pi^2} \int d^D q \left\{ (q^2 - m_1^2 + i0)((q + k_1)^2 - m_2^2 + i0) \right\}^{-1}, \quad (\text{B.1})$$

$$\begin{aligned}C_0(s_1, s_2, s_3; m_1, m_2, m_3) &= \frac{(2\pi\mu)^{4-D}}{i\pi^2} \\ &\times \int d^D q \left\{ (q^2 - m_1^2 + i0) ((q + k_1)^2 - m_2^2 + i0) ((q + k_2)^2 - m_3^2 + i0) \right\}^{-1}, \quad (\text{B.2})\end{aligned}$$

$$\begin{aligned}D_0(s_1, s_2, s_3, s_4; s, t; m_1, m_2, m_3, m_4) &= \frac{(2\pi\mu)^{4-D}}{i\pi^2} \int d^D q \left\{ (q^2 - m_1^2 + i0) \right. \\ &\times ((q + k_1)^2 - m_2^2 + i0) ((q + k_2)^2 - m_3^2 + i0) ((q + k_3)^2 - m_4^2 + i0) \left. \right\}^{-1}, \quad (\text{B.3})\end{aligned}$$

where all quantities in use are defined in Figure B.1, and $D = 4 - 2\varepsilon$.

In Section B.1, the needed integrals with vanishing internal masses are collected. In Section B.2, we provide all the integrals with internal masses arising in closed fermion loops

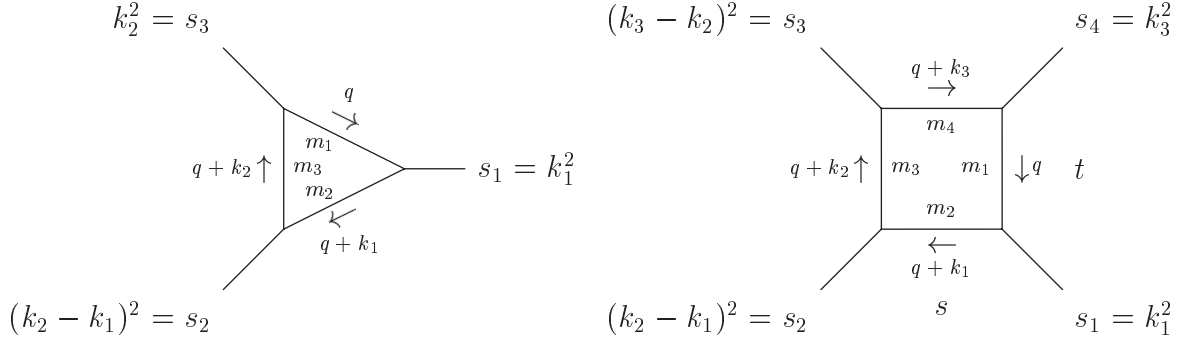


Figure B.1: Notation applied to three-point integrals (left-hand side) and four-point integrals (right-hand side).

with third-generation quarks and in contributions with incoming bottom (anti-)quarks. Note that the given integrals are only valid for real masses in general.

Overlined virtualities are understood to obtain an infinitesimal imaginary part, i.e. $\bar{s} = s + i0$, etc. Overlined mass squares arising in App. B.2 get a negative imaginary part, $\bar{m}^2 = m^2 - i0$. For logarithms and dilogarithms one has to guarantee that continuations over all possible cuts are continuous. Therefore, a proper analytic continuation is performed.

B.1 Integrals with vanishing internal masses

In the notation used for the massless integrals, the arguments concerning internal masses are dropped, since they are trivially zero.

B.1.1 Two-point functions

In terms of the massless two-point functions, two cases have to be discussed: For a vanishing incoming virtuality, a scaleless integral results, which is defined to be zero in dimensional regularization. It makes sense, however, to distinguish between IR and UV divergences here, since this zero arises from a cancellation between the two here,

$$B_0(0) = \Delta^{\text{UV}}(\mu) - \Delta_1^{\text{IR}}(\mu) . \quad (\text{B.4})$$

The integral with a non-vanishing scale is only UV divergent,

$$B_0(s) = \Delta^{\text{UV}}(\mu) - \ln \left(\frac{-\bar{s}}{M_W^2} \right) + 2 + \mathcal{O}(\varepsilon) . \quad (\text{B.5})$$

B.1.2 Three-point functions

The three-point functions with vanishing masses contain two divergent cases, namely those with one or two incoming virtualities equal to zero. The results for these IR-divergent

integrals, which can be found, e.g., in Ref. [85], read

$$C_0(0, 0, s_3) = \frac{1}{s} \left\{ \Delta_2^{\text{IR}}(\mu) - \Delta_1^{\text{IR}}(\mu) \ln \left(\frac{-\bar{s}_3}{M_W^2} \right) + \frac{1}{2} \ln^2 \left(\frac{-\bar{s}_3}{M_W^2} \right) - \frac{\pi^2}{6} + \mathcal{O}(\varepsilon) \right\}, \quad (\text{B.6})$$

$$C_0(0, s_2, s_3) = \frac{1}{s_2 - s_3} \left\{ \Delta_1^{\text{IR}}(\mu) \ln \left(\frac{\bar{s}_3}{\bar{s}_2} \right) + \frac{1}{2} \left[\ln^2 \left(\frac{-\bar{s}_2}{M_W^2} \right) - \ln^2 \left(\frac{-\bar{s}_3}{M_W^2} \right) \right] + \mathcal{O}(\varepsilon) \right\}. \quad (\text{B.7})$$

B.1.3 Four-point functions

All divergent four-point functions with vanishing internal masses are taken from Ref. [114] with appropriate analytical continuations,

$$D_0(0, 0, 0, 0; s, t) = \frac{1}{st} \left\{ 4\Delta_2^{\text{IR}}(\mu) - 2\Delta_1^{\text{IR}}(\mu) \left(\ln \left(\frac{-\bar{s}}{M_W^2} \right) + \ln \left(\frac{-\bar{t}}{M_W^2} \right) \right) + \ln^2 \left(\frac{-\bar{s}}{M_W^2} \right) + \ln^2 \left(\frac{-\bar{t}}{M_W^2} \right) - \ln^2 \left(\frac{\bar{s}}{\bar{t}} \right) - \frac{5}{3}\pi^2 + \mathcal{O}(\varepsilon) \right\}, \quad (\text{B.8})$$

$$D_0(0, 0, 0, s_4; s, t) = \frac{1}{st} \left\{ 2\Delta_2^{\text{IR}}(\mu) + 2\Delta_1^{\text{IR}}(\mu) \left[\ln \left(\frac{-\bar{s}_4}{M_W^2} \right) - \ln \left(\frac{-\bar{s}}{M_W^2} \right) - \ln \left(\frac{-\bar{t}}{M_W^2} \right) \right] - \ln^2 \left(\frac{-\bar{s}_4}{M_W^2} \right) + 2 \ln \left(\frac{-\bar{s}}{M_W^2} \right) \ln \left(\frac{-\bar{t}}{M_W^2} \right) - 2\text{Li}_2 \left(1 - \frac{\bar{s}_4}{\bar{s}} \right) - 2\text{Li}_2 \left(1 - \frac{\bar{s}_4}{\bar{t}} \right) - \frac{2}{3}\pi^2 + \mathcal{O}(\varepsilon) \right\}, \quad (\text{B.9})$$

$$D_0(s_1, 0, s_3, 0; s, t) = \frac{2}{st - s_1 s_3} \left\{ \Delta_1^{\text{IR}}(\mu) \left[\ln \left(\frac{\bar{s}_1}{\bar{s}} \right) + \ln \left(\frac{\bar{s}_3}{\bar{t}} \right) \right] + \ln \left(\frac{-\bar{s}}{M_W^2} \right) \ln \left(\frac{\bar{t}}{M_W^2} \right) - \frac{1}{2} \left[\ln^2 \left(\frac{-\bar{s}_1}{M_W^2} \right) + \ln^2 \left(\frac{-\bar{s}_3}{M_W^2} \right) \right] + \mathcal{L}i_2 \left(\frac{\bar{s}_1}{\bar{s}}, \frac{\bar{s}_3}{\bar{t}} \right) - \left[\text{Li}_2 \left(1 - \frac{\bar{s}_1}{\bar{s}} \right) + \text{Li}_2 \left(1 - \frac{\bar{s}_1}{\bar{t}} \right) + \text{Li}_2 \left(1 - \frac{\bar{s}_3}{\bar{s}} \right) + \text{Li}_2 \left(1 - \frac{\bar{s}_3}{\bar{t}} \right) \right] + \mathcal{O}(\varepsilon) \right\}, \quad (\text{B.10})$$

$$D_0(0, 0, s_3, s_4; s, t) = \frac{1}{st} \left\{ \Delta_2^{\text{IR}}(\mu) + \Delta_1^{\text{IR}}(\mu) \left[\ln \left(\frac{\bar{s}_3}{\bar{t}} \right) + \ln \left(\frac{\bar{s}_4}{\bar{t}} \right) - \ln \left(\frac{-\bar{s}}{M_W^2} \right) \right] + \frac{1}{2} \left[\ln^2 \left(\frac{-\bar{s}}{M_W^2} \right) - \ln^2 \left(\frac{\bar{s}_3}{\bar{s}_4} \right) \right] - \ln \left(\frac{-\bar{s}}{M_W^2} \right) \left[\ln \left(\frac{\bar{s}_3}{\bar{t}} \right) + \ln \left(\frac{\bar{s}_4}{\bar{t}} \right) \right] - 2 \left[\text{Li}_2 \left(1 - \frac{\bar{s}_3}{\bar{t}} \right) + \text{Li}_2 \left(1 - \frac{\bar{s}_4}{\bar{t}} \right) \right] - \frac{1}{6}\pi^2 + \mathcal{O}(\varepsilon) \right\}, \quad (\text{B.11})$$

$$D_0(0, s_2, s_3, s_4; s, t) = \frac{1}{st - s_2 s_4} \left\{ \Delta_1^{\text{IR}}(\mu) \left[\ln \left(\frac{\bar{s}_2}{\bar{s}} \right) + \ln \left(\frac{\bar{s}_4}{\bar{t}} \right) \right] - \frac{1}{2} \left[\ln^2 \left(\frac{-\bar{s}_2}{M_W^2} \right) + \ln^2 \left(\frac{-\bar{s}_4}{M_W^2} \right) \right] + \left[\ln \left(\frac{\bar{s}_2}{\bar{s}} \right) + \ln \left(\frac{\bar{s}_4}{\bar{t}} \right) \right] \left[\ln \left(\frac{\bar{s}_3}{\bar{s}_2} \right) - \ln \left(\frac{\bar{s}_4}{M_W^2} \right) \right] - 2 \left[\mathcal{L}i_2 \left(\frac{\bar{s}}{\bar{s}_2}, \frac{\bar{t}}{\bar{s}_4} \right) + \text{Li}_2 \left(1 - \frac{\bar{s}_2}{\bar{s}} \right) + \text{Li}_2 \left(1 - \frac{\bar{s}_4}{\bar{t}} \right) \right] + \mathcal{O}(\varepsilon) \right\}. \quad (\text{B.12})$$

The dilogarithm with two arguments arising in Eqs. (B.10) and (B.12) is defined as follows,

$$\mathcal{Li}_2(x, y) = \text{Li}_2(1 - xy) + \ln(1 - xy) [\ln(xy) - \ln(x) - \ln(y)] . \quad (\text{B.13})$$

B.2 Integrals with internal masses

B.2.1 Two-point functions

Since the massive two-point functions do not contain IR divergences, those implemented in the FF package [83, 84] are used.

B.2.2 Three-point functions

The only IR-divergent three-point function with a non-vanishing mass that is needed in this thesis can be obtained again, e.g., from Ref. [85],

$$\begin{aligned} C_0(0, s_2, s_3; 0, 0, m^2) = & \frac{1}{s_2 - s_3} \left\{ \Delta_1^{\text{IR}}(\mu) \ln \left(\frac{\bar{m}^2 - \bar{s}_3}{\bar{m}^2 - \bar{s}_2} \right) - \ln \left(\frac{\bar{m}^2}{M_W^2} \right) \ln \left(\frac{\bar{m}^2 - \bar{s}_3}{\bar{m}^2 - \bar{s}_2} \right) \right. \\ & + \ln^2 \left(\frac{\bar{m}^2 - \bar{s}_2}{\bar{m}^2} \right) - \ln^2 \left(\frac{\bar{m}^2 - \bar{s}_3}{\bar{m}^2} \right) \\ & \left. + \text{Li}_2 \left(1 - \frac{\bar{m}^2 - \bar{s}_2}{\bar{m}^2} \right) - \text{Li}_2 \left(1 - \frac{\bar{m}^2 - \bar{s}_3}{\bar{m}^2} \right) + \mathcal{O}(\varepsilon) \right\} . \quad (\text{B.14}) \end{aligned}$$

B.2.3 Four-point functions

The divergent four-point integrals with real internal masses are taken from Ref. [115]. Numerical checks have been performed with Ref. [116]. The following integrals are used in the calculation,

$$D_0(0, 0, s_3, s_4; s, t; 0, 0, 0, m^2) = \frac{1}{s(t - m^2)} \quad (\text{B.15})$$

$$\begin{aligned} \times \left\{ \Delta_2^{\text{IR}}(\mu) + \Delta_1^{\text{IR}}(\mu) \left[\ln \left(\frac{-\bar{s}}{M_W^2} \right) + \ln \frac{(\bar{m}^2 - \bar{t})^2}{(\bar{m}^2 - \bar{s}_3)(\bar{m}^2 - \bar{s}_4)} \right] \right. \\ - 2 \text{Li} \left(1 - \frac{\bar{m}^2 - \bar{s}_3}{\bar{m}^2 - \bar{t}} \right) - 2 \text{Li} \left(1 - \frac{\bar{m}^2 - \bar{s}_4}{\bar{m}^2 - \bar{t}} \right) - \text{Li} \left(1 - \frac{\bar{m}^2 - \bar{s}_3}{-\bar{s}} \frac{\bar{m}^2 - \bar{s}_4}{\bar{m}^2} \right) \\ + \frac{1}{2} \ln^2 \left(\frac{-\bar{s}}{M_W^2} \right) - \frac{1}{2} \ln^2 \left(\frac{-\bar{s}}{\bar{m}^2} \right) + 2 \ln \left(\frac{\bar{m}^2 - \bar{t}}{\bar{m}^2} \right) \ln \left(\frac{-\bar{s}}{\bar{m}^2} \right) \\ \left. - \ln \left(\frac{\bar{m}^2 - \bar{s}_3}{\bar{m}^2} \right) \ln \left(\frac{\bar{m}^2 - \bar{s}_3}{M_W^2} \right) - \ln \left(\frac{\bar{m}^2 - \bar{s}_4}{\bar{m}^2} \right) \ln \left(\frac{\bar{m}^2 - \bar{s}_4}{M_W^2} \right) - \frac{\pi^2}{3} + \mathcal{O}(\varepsilon) \right\} , \end{aligned}$$

$$D_0(0, s_2, s_3, s_4; s, t; 0, 0, 0, m^2) = \frac{1}{st - m^2 s - s_2 s_4 + m^2 s_2} \quad (\text{B.16})$$

$$\times \left\{ \Delta_1^{\text{IR}}(\mu) \ln \frac{(\bar{m}^2 - \bar{s}_4) \bar{s}_2}{(\bar{m}^2 - \bar{t}) \bar{t}} + \text{Li} \left(1 - \frac{\bar{m}^2 - \bar{s}_3}{-\bar{s}_2} \frac{\bar{m}^2 - \bar{t}}{\bar{m}^2} \right) - \text{Li} \left(1 - \frac{\bar{m}^2 - \bar{s}_3}{-\bar{s}} \frac{\bar{m}^2 - \bar{s}_4}{\bar{m}^2} \right) \right\}$$

$$\begin{aligned}
& +2 \operatorname{Li}\left(1 - \frac{\bar{m}^2 - \bar{t}}{\bar{m}^2 - \bar{s}_4}\right) - 2 \operatorname{Li}\left(1 - \frac{\bar{s}_2}{\bar{s}}\right) + 2 \operatorname{Li}\left(1 - \frac{\bar{s}_2 \bar{m}^2 - \bar{s}_4}{\bar{s} \bar{m}^2 - \bar{t}}\right) \\
& + 2 \ln\left(\frac{M_W \bar{m}}{\bar{m}^2 - \bar{t}}\right) \ln\left(\frac{(\bar{m}^2 - \bar{s}_4) \bar{s}_2}{(\bar{m}^2 - \bar{t}) \bar{s}}\right) + \mathcal{O}(\varepsilon) \Big\} .
\end{aligned}$$

$$D_0(0, s_2, s_3, s_4; s, t; 0, 0, m_3^2, m_4^2) = \frac{1}{(m_3^2 - s)(m_4^2 - t) - (m_3^2 - s_2)(m_4^2 - s_4)} \quad (\text{B.17})$$

$$\begin{aligned}
& \times \left\{ \Delta_1^{\text{IR}}(\mu) \ln\left(\frac{(\bar{m}_3^2 - \bar{s}_2)(\bar{m}_4^2 - \bar{s}_4)}{(\bar{m}_3^2 - \bar{s}_2)(\bar{m}_4^2 - \bar{t})}\right) - 2 \operatorname{Li}\left(1 - \frac{\bar{m}_3^2 - \bar{s}_2}{\bar{m}_3^2 - \bar{s}}\right) - 2 \operatorname{Li}\left(1 - \frac{\bar{m}_4^2 - \bar{s}_4}{\bar{m}_4^2 - \bar{t}}\right) \right. \\
& - \operatorname{Li}\left(1 - \frac{\bar{m}_3^2 - \bar{s}_2}{\bar{m}_4^2 - \bar{t}} \frac{\gamma_{34}^+}{\gamma_{34}^+ - 1}\right) - \operatorname{Li}\left(1 - \frac{\bar{m}_4^2 - \bar{s}_4}{\bar{m}_3^2 - \bar{s}} \frac{\gamma_{43}^+}{\gamma_{43}^+ - 1}\right) - \frac{1}{2} \ln^2\left(\frac{\gamma_{34}^+}{\gamma_{34}^+ - 1}\right) \\
& - \operatorname{Li}\left(1 - \frac{\bar{m}_3^2 - \bar{s}_2}{\bar{m}_4^2 - \bar{t}} \frac{\gamma_{34}^-}{\gamma_{34}^- - 1}\right) - \operatorname{Li}\left(1 - \frac{\bar{m}_4^2 - \bar{s}_4}{\bar{m}_3^2 - \bar{s}} \frac{\gamma_{43}^-}{\gamma_{43}^- - 1}\right) - \frac{1}{2} \ln^2\left(\frac{\gamma_{34}^-}{\gamma_{34}^- - 1}\right) \\
& + 2 \operatorname{Li}\left(1 - \frac{\bar{m}_3^2 - \bar{s}_2}{\bar{m}_3^2 - \bar{s}} \frac{\bar{m}_4^2 - \bar{s}_4}{\bar{m}_4^2 - \bar{t}}\right) + 2 \ln\left(\frac{\bar{m}_3^2 - \bar{s}}{M_W^2}\right) \ln\left(\frac{\bar{m}_4^2 - \bar{t}}{M_W^2}\right) - \ln^2\left(\frac{\bar{m}_3^2 - \bar{s}_2}{M_W^2}\right) \\
& \left. - \ln^2\left(\frac{\bar{m}_4^2 - \bar{s}_4}{M_W^2}\right) + \ln\left(\frac{\bar{m}_3^2 - \bar{s}_2}{\bar{m}_4^2 - \bar{t}}\right) \ln\left(\frac{\bar{m}_3^2}{M_W^2}\right) + \ln\left(\frac{\bar{m}_4^2 - \bar{s}_4}{\bar{m}_3^2 - \bar{s}}\right) \ln\left(\frac{\bar{m}_4^2}{M_W^2}\right) + \mathcal{O}(\varepsilon) \right\} ,
\end{aligned}$$

$$\text{where } \gamma_{ij}^\pm = \frac{1}{2} \left[1 - \frac{m_i^2 - m_j^2}{s_3} \pm \sqrt{\left(1 - \frac{m_i^2 - m_j^2}{s_3}\right)^2 - \frac{4m_j^2}{s_3}} \right] , \quad (\text{B.18})$$

$$D_0(0, s_2, 0, s_4; s, t; 0, 0, m_3^2, m_4^2) = \frac{1}{(m_3^2 - s)(m_4^2 - t) - (m_3^2 - s_2)(m_4^2 - s_4)} \quad (\text{B.19})$$

$$\begin{aligned}
& \times \left\{ \Delta_1^{\text{IR}}(\mu) \ln\left(\frac{(\bar{m}_3^2 - \bar{s}_2)(\bar{m}_4^2 - \bar{s}_4)}{(\bar{m}_3^2 - \bar{s}_2)(\bar{m}_4^2 - \bar{t})}\right) - 2 \operatorname{Li}\left(1 - \frac{\bar{m}_3^2 - \bar{s}_2}{\bar{m}_3^2 - \bar{s}}\right) - 2 \operatorname{Li}\left(1 - \frac{\bar{m}_4^2 - \bar{s}_4}{\bar{m}_4^2 - \bar{t}}\right) \right. \\
& - \operatorname{Li}\left(1 - \frac{\bar{m}_3^2 - \bar{s}_2}{\bar{m}_4^2 - \bar{t}}\right) - \operatorname{Li}\left(1 - \frac{\bar{m}_4^2 - \bar{s}_4}{\bar{m}_3^2 - \bar{s}}\right) \\
& - \operatorname{Li}\left(1 - \frac{\bar{m}_4^2}{\bar{m}_3^2} \frac{\bar{m}_3^2 - \bar{s}_2}{\bar{m}_4^2 - \bar{t}}\right) - \operatorname{Li}\left(1 - \frac{\bar{m}_3^2}{\bar{m}_4^2} \frac{\bar{m}_4^2 - \bar{s}_4}{\bar{m}_3^2 - \bar{s}}\right) - \frac{1}{2} \ln^2\left(\frac{\bar{m}_4^2}{\bar{m}_3^2}\right) \\
& + 2 \operatorname{Li}\left(1 - \frac{\bar{m}_3^2 - \bar{s}_2}{\bar{m}_3^2 - \bar{s}} \frac{\bar{m}_4^2 - \bar{s}_4}{\bar{m}_4^2 - \bar{t}}\right) + 2 \ln\left(\frac{\bar{m}_3^2 - \bar{s}}{M_W^2}\right) \ln\left(\frac{\bar{m}_4^2 - \bar{t}}{M_W^2}\right) - \ln^2\left(\frac{\bar{m}_3^2 - \bar{s}_2}{M_W^2}\right) \\
& \left. - \ln^2\left(\frac{\bar{m}_4^2 - \bar{s}_4}{M_W^2}\right) + \ln\left(\frac{\bar{m}_3^2 - \bar{s}_2}{\bar{m}_4^2 - \bar{t}}\right) \ln\left(\frac{\bar{m}_3^2}{M_W^2}\right) + \ln\left(\frac{\bar{m}_4^2 - \bar{s}_4}{\bar{m}_3^2 - \bar{s}}\right) \ln\left(\frac{\bar{m}_4^2}{M_W^2}\right) + \mathcal{O}(\varepsilon) \right\} ,
\end{aligned}$$

where (B.19) is obtained from (B.17) by taking the limit $s_3 \rightarrow 0$.

Bibliography

- [1] J. S. Schwinger, Phys. Rev. **73** (1948) 416.
- [2] H. Suura and E. H. Wichmann, Phys. Rev. **105** (1957) 1930.
- [3] A. Petermann, Phys. Rev. **105** (1957) 1931.
- [4] J. Bailey *et al.* [CERN-Mainz-Daresbury Collaboration], Nucl. Phys. B **150**, 1 (1979).
- [5] S. L. Glashow, Nucl. Phys. **22**, 579 (1961).
- [6] S. Weinberg, Phys. Rev. Lett. **19** (1967) 1264.
- [7] A. Salam, in “Elementary Particle Theory, Proc. 8th Nobel Symp.,” ed. N. Svartholm, *Wiley-Interscience, New York, 1968*.
- [8] G. Arnison *et al.* [UA1 Collaboration], Phys. Lett. B **122**, 103 (1983).
- [9] G. Arnison *et al.* [UA1 Collaboration], Phys. Lett. B **126**, 398 (1983).
- [10] G. Arnison *et al.* [UA1 Collaboration], Phys. Lett. B **129**, 273 (1983).
- [11] G. Arnison *et al.* [UA1 Collaboration], Phys. Lett. B **134**, 469 (1984).
- [12] G. Arnison *et al.* [UA1 Collaboration], Phys. Lett. B **147**, 241 (1984).
- [13] P. W. Higgs, Phys. Rev. Lett. **13** (1964) 508.
- [14] P. W. Higgs, Phys. Rev. **145** (1966) 1156.
- [15] F. Englert and R. Brout, Phys. Rev. Lett. **13** (1964) 321.
- [16] G. S. Guralnik, C. R. Hagen and T. W. B. Kibble, Phys. Rev. Lett. **13** (1964) 585.
- [17] T. W. B. Kibble, Phys. Rev. **155** (1967) 1554.
- [18] S. Weinberg, Phys. Rev. Lett. **18** (1967) 507.
- [19] O. W. Greenberg, Phys. Rev. Lett. **13**, 598 (1964).
- [20] M. Y. Han and Y. Nambu, Phys. Rev. **139**, B1006 (1965).

- [21] A. Salam, in “Scale and Conformal Invariance in Hadron Physics” ed. R. Gatto, *Wiley, New York, 1973*.
- [22] M. Gell-Mann, *Phys. Lett.* **8**, 214 (1964).
- [23] G. Zweig, CERN-TH-401.
- [24] D. J. Gross and F. Wilczek, *Phys. Rev. Lett.* **30**, 1343 (1973).
- [25] H. D. Politzer, *Phys. Rev. Lett.* **30**, 1346 (1973).
- [26] R. P. Feynman, *Phys. Rev. Lett.* **23** (1969) 1415.
- [27] R. P. Feynman, “Photon–Hadron Interactions,” *Benjamin, New York, 1972*.
- [28] S. Weinberg, *Phys. Rev. Lett.* **31**, 494 (1973).
- [29] D. P. Barber *et al.*, *Phys. Rev. Lett.* **43** (1979) 830.
- [30] G. 't Hooft, *Nucl. Phys. B* **33** (1971) 173.
- [31] F. Abe *et al.* [CDF Collaboration], *Phys. Rev. Lett.* **74** (1995) 2626 [arXiv:hep-ex/9503002].
- [32] S. Abachi *et al.* [D0 Collaboration], *Phys. Rev. Lett.* **74** (1995) 2632 [arXiv:hep-ex/9503003].
- [33] K. Hoshino [DONUT Collaboration], *Prepared for 8th Asia Pacific Physics Conference (APPC 2000), Taipei, Taiwan, 7-10 Aug 2000*
- [34] R. Barate *et al.* [LEP Working Group for Higgs boson searches and ALEPH Collaboration], *Phys. Lett. B* **565** (2003) 61 [arXiv:hep-ex/0306033].
- [35] ALEPH Collaboration and DELPHI Collaboration and L3 Collaboration, arXiv:hep-ex/0212036.
- [36] O. Bruning, P. Collier, P. Lebrun, S. Myers, R. Ostojic, J. Poole and P. Proudlock, “LHC design report. Vol. 1: The LHC main ring, Vol. 2: The LHC infrastructure and general services, Vol. 3: The LHC injector chain.”
- [37] J. Brau *et al.*, “International Linear Collider reference design report. Vol. 1: Executive summary, Vol. 2: Physics at the ILC, Vol. 3: Accelerator, Vol. 4: Detectors.”
- [38] A. Del Popolo, arXiv:0801.1091 [astro-ph].
- [39] C. Buttar *et al.*, arXiv:hep-ph/0604120.
- [40] Z. Bern *et al.* [NLO Multileg Working Group], arXiv:0803.0494 [hep-ph].

- [41] E. W. N. Glover, J. Ohnemus and S. S. D. Willenbrock, Phys. Lett. B **206** (1988) 696.
- [42] V. D. Barger, G. Bhattacharya, T. Han and B. A. Kniehl, Phys. Rev. D **43** (1991) 779.
- [43] M. Dittmar and H. K. Dreiner, Phys. Rev. D **55**, 167 (1997) [arXiv:hep-ph/9608317].
- [44] D. L. Rainwater and D. Zeppenfeld, Phys. Rev. D **60**, 113004 (1999) [Erratum-ibid. D **61**, 099901 (2000)] [arXiv:hep-ph/9906218].
- [45] N. Kauer, T. Plehn, D. L. Rainwater and D. Zeppenfeld, Phys. Lett. B **503**, 113 (2001) [arXiv:hep-ph/0012351].
- [46] S. Asai *et al.*, Eur. Phys. J. C **32S2** (2004) 19 [arXiv:hep-ph/0402254].
- [47] S. Abdullin *et al.*, Eur. Phys. J. C **39S2** (2005) 41.
- [48] L. Zivkovic, Czech. J. Phys. **54** (2004) A73.
- [49] B. Mellado, W. Quayle and S. L. Wu, Phys. Rev. D **76** (2007) 093007 [arXiv:0708.2507 [hep-ph]].
- [50] “ATLAS Collaboration, Technical Design Report Vol. 2,” CERN-LHCC 99-15 (May 1999).
- [51] “CMS Collaboration, Technical Design Report Vol. 2: Physical Performance, Technical Proposal,” CERN-LHCC 99-15 (May 1999).
- [52] G. Chachamis, M. Czakon and D. Eiras, arXiv:0802.4028 [hep-ph].
- [53] G. Chachamis, M. Czakon and D. Eiras, arXiv:0806.3043 [hep-ph].
- [54] M. Böhm, A. Denner, H. Joos, “Gauge Theories of the Strong and Electroweak Interaction,” *B.G.Teubner, Stuttgart·Leipzig·Wiesbaden, 2001*.
- [55] M. E. Peskin, D. V. Schroeder, “An Introduction to Quantum Field Theory,” *Addison-Wesley Publishing Company, 1995*.
- [56] S. Weinberg, “The Quantum Field Theory. Vol. 1: Foundations,” “The Quantum Field Theory. Vol. 2: Modern Applications,” *Cambridge University Press, 1995/1996*.
- [57] G. 't Hooft, Nucl. Phys. B **35** (1971) 167.
- [58] T. Kobayashi, Prog. Theor. Phys. **49** (1973) 282.
- [59] A. Denner, Fortsch. Phys. **41** (1993) 307 [arXiv:0709.1075 [hep-ph]].
- [60] R. K. Ellis, W. J. Stirling, B. R. Webber, “QCD and Collider Physics,” *Cambridge University Press, 1996*.

- [61] G. Altarelli and G. Parisi, Nucl. Phys. B **126** (1977) 298.
- [62] S. Catani and M. H. Seymour, Nucl. Phys. B **485** (1997) 291 [Erratum-ibid. B **510** (1998) 503] [arXiv:hep-ph/9605323].
- [63] N. Cabibbo, Phys. Rev. Lett. **10** (1963) 531.
- [64] C. Neu [CDF Collaboration], FERMILAB-CONF-06-162-E.
- [65] K. Hanagaki [D0 Collaboration], FERMILAB-CONF-05-647-E.
- [66] T. Wright [CDF and D0 Collaboration], arXiv:0707.1712 [hep-ex].
- [67] A. Wildauer and F. Akesson, in “Interlaken 2004, Computing in high energy physics and nuclear physics,” 419-422.
- [68] M. Lehmacher, arXiv:0809.4896 [hep-ex].
- [69] A. Denner, S. Dittmaier, M. Roth and D. Wackeroth, Nucl. Phys. B **560** (1999) 33 [arXiv:hep-ph/9904472].
- [70] A. Denner, S. Dittmaier, M. Roth and L. H. Wieders, Nucl. Phys. B **724** (2005) 247 [arXiv:hep-ph/0505042].
- [71] A. Denner and S. Dittmaier, Nucl. Phys. Proc. Suppl. **160** (2006) 22 [arXiv:hep-ph/0605312].
- [72] S. Dittmaier, Phys. Rev. D **59** (1999) 016007 [arXiv:hep-ph/9805445].
- [73] S. Kallweit, diploma thesis (in German), LMU Munich, 2006.
- [74] G. Sterman, “An Introduction to Quantum Field Theory ,” *Cambridge University Press, 1993*.
- [75] T. D. Lee and M. Nauenberg, Phys. Rev. **133** (1964) B1549
- [76] T. Kinoshita, J. Math. Phys. **3** (1962) 650.
- [77] S. D. Ellis and D. E. Soper, Phys. Rev. D **48** (1993) 3160 [arXiv:hep-ph/9305266].
- [78] T. Hahn and M. Perez-Victoria, Comput. Phys. Commun. **118** (1999) 153 [arXiv:hep-ph/9807565].
- [79] T. Hahn, Comput. Phys. Commun. **140** (2001) 418 [arXiv:hep-ph/0012260].
- [80] A. Bredenstein, A. Denner, S. Dittmaier and S. Pozzorini, JHEP **0808** (2008) 108 [arXiv:0807.1248 [hep-ph]].
- [81] A. Denner and S. Dittmaier, Nucl. Phys. B **658** (2003) 175 [arXiv:hep-ph/0212259].

- [82] G. Passarino and M. J. G. Veltman, Nucl. Phys. B **160** (1979) 151.
- [83] G. J. van Oldenborgh and J. A. M. Vermaseren, Z. Phys. C **46** (1990) 425.
- [84] G. J. van Oldenborgh, Comput. Phys. Commun. **66** (1991)
- [85] S. Dittmaier, Nucl. Phys. B **675** (2003) 447 [arXiv:hep-ph/0308246].
- [86] M. S. Chanowitz, M. Furman and I. Hinchliffe, Nucl. Phys. B **159** (1979) 225.
- [87] G. 't Hooft and M. J. G. Veltman, Nucl. Phys. B **44** (1972) 189.
- [88] P. Breitenlohner and D. Maison, Commun. Math. Phys. **52** (1977) 11.
- [89] E. Byckling and K. Kajantie, “Particle Kinematics”, *John Wiley & Sons, London, 1973*, p. 158ff.
- [90] F. A. Berends, R. Pittau and R. Kleiss, Nucl. Phys. B **424** (1994) 308 [arXiv:hep-ph/9404313].
- [91] F. A. Berends, P. H. Daverveldt and R. Kleiss, Nucl. Phys. B **253** (1985) 441.
- [92] M. Roth, doctoral thesis, DISS-ETH-13363, 1999, arXiv:hep-ph/0008033.
- [93] R. Kleiss and R. Pittau, Comput. Phys. Commun. **83**, 141 (1994) [arXiv:hep-ph/9405257].
- [94] S. Dittmaier and M. Roth, Nucl. Phys. B **642** (2002) 307 [arXiv:hep-ph/0206070].
- [95] S. Eidelman *et al.* [Particle Data Group], Phys. Lett. B **592** (2004) 1.
- [96] S. Dittmaier and M. Krämer, Phys. Rev. D **65** (2002) 073007 [arXiv:hep-ph/0109062].
- [97] C. Amsler *et al.* [Particle Data Group], Phys. Lett. B **667** (2008) 1.
- [98] S. Dittmaier, S. Kallweit and P. Uwer, Phys. Rev. Lett. **100** (2008) 062003 [arXiv:0710.1577 [hep-ph]].
- [99] S. Dittmaier, S. Kallweit and P. Uwer, PoS **RADCOR2007** (2007) 009 [arXiv:0712.3163 [hep-ph]].
- [100] S. Dittmaier, S. Kallweit and P. Uwer, arXiv:0807.0708 [hep-ph].
- [101] J. Pumplin, D. R. Stump, J. Huston, H. L. Lai, P. Nadolsky and W. K. Tung, JHEP **0207** (2002) 012 [arXiv:hep-ph/0201195].
- [102] D. Stump, J. Huston, J. Pumplin, W. K. Tung, H. L. Lai, S. Kuhlmann and J. F. Owens, JHEP **0310** (2003) 046 [arXiv:hep-ph/0303013].

-
- [103] A. D. Martin, W. J. Stirling and R. S. Thorne, Phys. Lett. B **636** (2006) 259 [arXiv:hep-ph/0603143].
- [104] T. Stelzer and W. F. Long, Comput. Phys. Commun. **81** (1994) 357 [arXiv:hep-ph/9401258].
- [105] H. Murayama, I. Watanabe and K. Hagiwara, KEK-91-11 [arXiv:hep-ph/2582015].
- [106] W. Kilian, T. Ohl and J. Reuter, arXiv:0708.4233 [hep-ph].
- [107] T. Gleisberg, S. Höche, F. Krauss, A. Schälicke, S. Schumann and J. C. Winter, JHEP **0402** (2004) 056 [arXiv:hep-ph/0311263].
- [108] W. Beenakker, S. Dittmaier, M. Krämer, B. Plümper, M. Spira and P. M. Zerwas, Nucl. Phys. B **653** (2003) 151 [arXiv:hep-ph/0211352].
- [109] S. Dittmaier, P. Uwer and S. Weinzierl, Phys. Rev. Lett. **98** (2007) 262002 [arXiv:hep-ph/0703120].
- [110] J. M. Campbell, R. K. Ellis and G. Zanderighi, JHEP **0712** (2007) 056 [arXiv:0710.1832 [hep-ph]].
- [111] L. J. Dixon, Z. Kunszt and A. Signer, Phys. Rev. D **60** (1999) 114037 [arXiv:hep-ph/9907305].
- [112] M. Dittmar and H. K. Dreiner, arXiv:hep-ph/9703401.
- [113] W. Beenakker and A. Denner, Nucl. Phys. B **338** (1990) 349.
- [114] Z. Bern, L. J. Dixon and D. A. Kosower, Nucl. Phys. B **412** (1994) 751 [arXiv:hep-ph/9306240].
- [115] R. K. Ellis and G. Zanderighi, JHEP **0802** (2008) 002 [arXiv:0712.1851 [hep-ph]].
- [116] A. Denner and S. Dittmaier, in preparation.

Acknowledgement

The remaining lines are devoted to the people who supported the work on this thesis in various ways.

First of all, I want to thank Stefan Dittmaier, who suggested this investigation. I benefited a lot from his great experience in quantum field theory and collider phenomenology. So I could always rely on getting the decisive advice whenever I got stuck. I'm also grateful to Gerhard Buchalla for his interest in my work.

I would also like to thank Peter Uwer for a very fruitful collaboration and a number of helpful discussions. In particular, he performed a completely independent calculation for the real corrections to the process $WW + \text{jet}$ which have been used as a check.

I'm also grateful to Wolfgang Hollik for giving me the opportunity to work in this great environment at the MPI. Special thanks shall also be addressed here to Thomas Hahn and Peter Breitenlohner for all the support in computer-related emergencies.

I don't want to forget all the members of the institute who created a stimulating and most enjoyable atmosphere both inside and beyond physics. Especially, I want to thank the members of our research group, Marina Billoni, Max Huber, and Tobias Kasprzik, for a lot of useful discussions in particular in our weekly meetings, and my officemates Maike Trenkel and Christoph Reißer for the friendly atmosphere during the last two years. In particular, I'm grateful to Maike and Marina for proof reading parts of the manuscript of this thesis. Besides, I want to thank Maximilian Stahlhofen, the captain of our football team and vice president of our beach-volleyball community for organizing an adequate physical compensation to physics.

Last but not least, I would like to thank my parents for their never-ending support and Zita Neymon de Neyfeldt for all the moral assistance and her patience that was sometimes sorely tried, especially in the last steps of this work.

Lebenslauf

Persönliche Daten

Vorname, Name	<i>Stefan Kallweit</i>
Geburtsdatum	<i>12.04.1981</i>
Geburtsort	<i>München</i>
Familienstand	<i>ledig</i>

Schulische Ausbildung

Grundschule Unterföhring	<i>09/1987 - 07/1991</i>
Maximiliansgymnasium München	<i>09/1991 - 06/2000</i>

Wehrdienst

6./LwAusbRgt 3, Bayreuth	<i>11/2000 - 12/2000</i>
2./FlaRakGrp 33, Bad Aibling	<i>12/2000 - 08/2001</i>

Berufliche Ausbildung

Studium der Physik an der LMU München	<i>10/2001 - 11/2006</i>
Diplomarbeit in Physik am Max-Planck-Institut für Physik, München (Titel: “Vorhersagen für die Prozesse $pp \rightarrow W^+W^- + \text{jet}(\text{jet}) + X$ am LHC”)	<i>11/2005 - 11/2006</i>
Aufnahme in die Studienstiftung des deutschen Volkes	<i>07/2003</i>
Promotionsstudium in Physik an der LMU München	<i>01/2007 - 11/2008</i>

Berufliche Tätigkeit

Lehrer für Mathematik (aushilfsweise) am Maximiliansgymnasium München	<i>01/2005 - 03/2005</i>
Doktorarbeit in Physik am Max-Planck-Institut für Physik, München (Titel: “Precision calculations for gauge-boson pair production with a hadronic jet at hadron colliders”)	<i>01/2007 - 11/2008</i>